USED FUEL DISPOSITION CAMPAIGN

Used Nuclear Fuel Loading and Structural Performance Under Normal Conditions of Transport – Demonstration of Approach and Results on Used Fuel Performance Characterization

Fuel Cycle Research & Development

Prepared for
U.S. Department of Energy
Used Fuel Disposition Campaign
Harold Adkins (PNNL)
Ken Geelhood (PNNL)
Brian Koeppel (PNNL)
Justin Coleman (INL)
John Bignell (SNL)
Gregg Flores (SNL)
Jy-An Wang (ORNL)
Scott Sanborn (PNNL)
Robert Spears (INL)
Nick Klymyshyn (PNNL)
September 30, 2013
FCRD-UFD-2013-000325

USED FUEL DISPOSITION CAMPAIGN
Used Nuclear Fuel Loading and Structural Performance Under Normal Conditions of Transport –
Demonstration of Approach and Results of Used Fuel Performance Characterization
ii   **SEPTEMBER 30, 2013**

USED FUEL DISPOSITION CAMPAIGN
Used Nuclear Fuel Loading and Structural Performance Under Normal Conditions of Transport –
Demonstration of Approach and Results of Used Fuel Performance Characterization
SEPTEMBER 30, 2013   iii

EXECUTIVE SUMMARY

This document addresses Oak Ridge National Laboratory milestone M2FT-13OR0822015 *Demonstration of Approach and Results on Used Nuclear Fuel Performance Characterization.* This report provides results of the initial demonstration of the modeling capability developed to perform preliminary deterministic evaluations of moderate-to-high burnup used nuclear fuel (UNF) mechanical performance under normal conditions of storage (NCS) and normal conditions of transport (NCT) conditions. This report also provides results from the sensitivity studies that have been performed. Finally, discussion on the long-term goals and objectives of this initiative are provided.

Under current U.S. Nuclear Regulatory Commission regulation, it is not sufficient for UNF to simply maintain its integrity during the storage period, it must maintain its integrity in such a way that it can withstand the physical forces of handling and transportation associated with restaging the fuel and moving it to treatment or recycling facilities, or to a geologic repository or other storage facility. Hence it is necessary to understand the performance characteristics of aged UNF cladding and ancillary components under loadings stemming from transport initiatives. Researchers would like to demonstrate that enough information, including experimental support and modeling and simulation capabilities, exists and/or can be generated to establish a preliminary determination of UNF structural performance under normal conditions of transport.

A Research, Development, and Demonstration Plan (Adkins 2013b) was prepared that described a methodology, including development and use of analytical models, to evaluate loading and associated mechanical responses of UNF rods and key structural components during NCT. Since the publication of the Research, Development, and Demonstration Plan, the work described has been completed to implement this plan.

An approach has been developed to obtain transportation loading data that was used by the modeling and simulation team to determine the effect of shock and vibration on the fuel rods and assemblies (Adkins 2013c). The final data describing the shock and vibration has been received and has been used by the modeling and simulation team (Adkins 2013e). Evaluations were performed for representative normal conditions of rail transport involving a rail conveyance capable of meeting the Association of American Railroads Standard S-2043 (AAR 2003). The material properties that feed into the models for the fuel, cladding, and associated transportation hardware have been defined (Geelhood 2013 and Adkins 2013e). Initial conditions of UNF following reactor discharge that feed into various material properties models have been defined (Adkins 2013e). Component temperatures for this demonstration have also been defined (Adkins 2013e).

As mentioned in the Research, Development, and Demonstration Plan, the methodology demonstration is initially focused on structural performance evaluation of Westinghouse Electric 17×17 Optimized Fuel Assembly (conservatively modeled without the intermediated flow mixers) pressurized water reactor fuel assemblies with a discharge burnup range of 30-58 GWd/MTU (assembly average), loaded in a representative high-capacity (≥32 fuel rod

USED FUEL DISPOSITION CAMPAIGN
Used Nuclear Fuel Loading and Structural Performance Under Normal Conditions of Transport -
Demonstration of Approach and Results of Used Fuel Performance Characterization
iv   **SEPTEMBER 30, 2013**

assemblies) transportation package and transported on a 3000 mile rail journey. Geometries for this fuel assembly and the transportation package have been defined (Adkins 2013e).

The modeling and simulation team has been organized into three modeling teams that modeled the UNF at the cask-level, the assembly-level and the fuel rod-level. The methodology for the modeling and simulation work has been fully developed and documented (Adkins 2013f). Failure criteria and a methodology for assessing failure from the calculated fuel rod strain history have been established (Adkins 2013d). Various sensitivity analyses have been identified to evaluate the impact of various material property, initial condition, and modeling uncertainties on the resulting stress and strain predictions and failure prediction (Adkins 2013d). These analyses guided researchers to focus on areas where uncertainties have a significant impact on the failure predictions.

This report documents the final products of this initiative. This report provides results of the initial demonstration of the modeling capability developed to perform preliminary deterministic evaluations of moderate-to-high burnup UNF mechanical performance under NCS and NCT conditions. This report also provides results from the sensitivity studies that have been performed.

Results of a demonstration involving moving high burnup 17×17 OFA fuel in a GBC-32 on a 3000-mile rail journey have been provided. It was determined that peak cladding strains were not large enough to cause structural failure, but cyclic strains roughly projected for the entire route were significant in some cases. The damage ratio for a 3000-mile route was calculated based on a conservative accounting of the vibration and shock loading derived from the representative 10s simulation cases. The total damage for a single rod was then computed by summing the contributions from each of the strain bins. Failure is not expected for damage fractions less than 100%. Cumulative fatigue damage fraction was projected to be 11% of the critical value for the lateral vibration case and 7% for the lateral shock case. Conservatively assuming that the high amplitude shock events occur concurrently with the continuous vibration, the total projected damage is 18% of the critical value. Therefore the fuel rods do not fail during NCT for this demonstration.

Sensitivity studies were performed and the results indicate areas of high, moderate, and low sensitivity. The areas of high sensitivity were found to be;
- Cladding elastic modulus
- Spacer grid stiffness
- Spacer grid location
- Gaps between the assembly and the cask.

The areas of moderate sensitivity are;
- Fuel assembly basket location
- In-reactor fretting wear
- Influence of control components
- Pellet-to-clad bonding.

USED FUEL DISPOSITION CAMPAIGN
Used Nuclear Fuel Loading and Structural Performance Under Normal Conditions of Transport –
Demonstration of Approach and Results of Used Fuel Performance Characterization
SEPTEMBER 30, 2013 v

The areas of low or no sensitivity are;
- Cladding yield stress
- Fuel rod location in assembly
- Temperature distribution
- Fuel rod damping
- Pin pressure influence.

A number of long-term goals and objectives of the Used Fuel Disposition Campaign are discussed in this document as they relate to this initiative and the potential for follow-on work is significant.

USED FUEL DISPOSITION CAMPAIGN
Used Nuclear Fuel Loading and Structural Performance Under Normal Conditions of Transport –
Demonstration of Approach and Results of Used Fuel Performance Characterization
SEPTEMBER 30, 2013   **vii**

ACKNOWLEDGMENTS

USED FUEL DISPOSITION CAMPAIGN
Used Nuclear Fuel Loading and Structural Performance Under Normal Conditions of Transport -
Demonstration of Approach and Results of Used Fuel Performance Characterization
SEPTEMBER 30, 2013 ix

CONTENTS

USED FUEL DISPOSITION CAMPAIGN
Used Nuclear Fuel Loading and Structural Performance Under Normal Conditions of Transport -
Demonstration of Approach and Results of Used Fuel Performance Characterization
x   **SEPTEMBER 30, 2013**

USED FUEL DISPOSITION CAMPAIGN
**Used Nuclear Fuel Loading and Structural Performance Under Normal Conditions of Transport -
Demonstration of Approach and Results of Used Fuel Performance Characterization**
SEPTEMBER 30, 2013 xi

FIGURES

USED FUEL DISPOSITION CAMPAIGN
Used Nuclear Fuel Loading and Structural Performance Under Normal Conditions of Transport -
Demonstration of Approach and Results of Used Fuel Performance Characterization
xii   **SEPTEMBER 30, 2013**

USED FUEL DISPOSITION CAMPAIGN
**Used Nuclear Fuel Loading and Structural Performance Under Normal Conditions of Transport -
Demonstration of Approach and Results of Used Fuel Performance Characterization**
SEPTEMBER 30, 2013 xiii

USED FUEL DISPOSITION CAMPAIGN
Used Nuclear Fuel Loading and Structural Performance Under Normal Conditions of Transport -
Demonstration of Approach and Results of Used Fuel Performance Characterization
xiv   **SEPTEMBER 30, 2013**

USED FUEL DISPOSITION CAMPAIGN
Used Nuclear Fuel Loading and Structural Performance Under Normal Conditions of Transport -
Demonstration of Approach and Results of Used Fuel Performance Characterization
SEPTEMBER 30, 2013 xv

USED FUEL DISPOSITION CAMPAIGN
**Used Nuclear Fuel Loading and Structural Performance Under Normal Conditions of Transport -
Demonstration of Approach and Results of Used Fuel Performance Characterization**
xvi   **SEPTEMBER 30, 2013**

USED FUEL DISPOSITION CAMPAIGN
Used Nuclear Fuel Loading and Structural Performance Under Normal Conditions of Transport -
Demonstration of Approach and Results of Used Fuel Performance Characterization
SEPTEMBER 30, 2013 xvii

USED FUEL DISPOSITION CAMPAIGN
Used Nuclear Fuel Loading and Structural Performance Under Normal Conditions of Transport -
Demonstration of Approach and Results of Used Fuel Performance Characterization
xviii   **SEPTEMBER 30, 2013**

USED FUEL DISPOSITION CAMPAIGN
Used Nuclear Fuel Loading and Structural Performance Under Normal Conditions of Transport -
Demonstration of Approach and Results of Used Fuel Performance Characterization
SEPTEMBER 30, 2013 **xix**

TABLES

USED FUEL DISPOSITION CAMPAIGN
Used Nuclear Fuel Loading and Structural Performance Under Normal Conditions of Transport -
Demonstration of Approach and Results of Used Fuel Performance Characterization
xx **SEPTEMBER 30, 2013**

USED FUEL DISPOSITION CAMPAIGN
**Used Nuclear Fuel Loading and Structural Performance Under Normal Conditions of Transport -
Demonstration of Approach and Results of Used Fuel Performance Characterization**
SEPTEMBER 30, 2013 xxi

USED FUEL DISPOSITION CAMPAIGN
Used Nuclear Fuel Loading and Structural Performance Under Normal Conditions of Transport -
Demonstration of Approach and Results of Used Fuel Performance Characterization
SEPTEMBER 30, 2013 xxiii

ACRONYMS

BE   best estimate
BWR   boiling water reactor

DBTT   ductile-to-brittle-transition temperature
DOE   U.S. Department of Energy

FE   finite element
FEM   finite element model

GBC   generic burnup cask
GWd   gigawatt-days

INL   Idaho National Laboratory

LB   lower bound

MP   material properties
M&S   modeling and simulation
MTU   metric tons (Tonnes) of uranium

NCS   normal conditions of storage
NCT   normal conditions of transport
NRC   U.S. Nuclear Regulatory Commission

OFA   Optimized Fuel Assembly
ORNL   Oak Ridge National Laboratory

PNNL   Pacific Northwest National Laboratory
PSD   power spectral density
PWR   pressurized water reactor

RD&D   research, development, and demonstration

SRS   shock response spectrum

TL   Transportation Loading
TTCI   Transportation Technology Center, Inc.

USED FUEL DISPOSITION CAMPAIGN
Used Nuclear Fuel Loading and Structural Performance Under Normal Conditions of Transport -
Demonstration of Approach and Results of Used Fuel Performance Characterization
xxiv   **SEPTEMBER 30, 2013**

UB   upper bound
UFDC   Used Fuel Disposition Campaign
UNF   used nuclear fuel

USED FUEL DISPOSITION CAMPAIGN
Used Nuclear Fuel Loading and Structural Performance Under Normal Conditions of Transport -
Demonstration of Approach and Results of Used Fuel Performance Characterization
SEPTEMBER 30, 2013   25

USED FUEL DISPOSITION CAMPAIGN
Used Nuclear Fuel Loading and Structural Performance Under Normal Conditions of Transport – Demonstration of Approach of Used Fuel Performance Characterization

1.   INTRODUCTION

The U.S. Department of Energy (DOE) Office of Nuclear Energy, Office of Fuel Cycle Technology has established the Used Fuel Disposition Campaign (UFDC) to conduct the research and development activities related to storage, transportation, and disposal of used nuclear fuel (UNF) and high-level radioactive waste.   Under U.S. Nuclear Regulatory Commission (NRC) regulations, it is not sufficient for UNF to simply maintain its integrity during the storage period. It must maintain its integrity in such a way that it can withstand the physical forces of handling and transportation associated with restaging the fuel and moving it to a different location (such as an interim storage site, a geologic repository, or a treatment/recycling facility).   Hence, understanding mechanical performance under cumulative loading stemming from normal conditions of storage (NCS), transfer (from storage container to transport container if needed), and normal conditions of transport (NCT) is necessary as it establishes part of the safety basis by maintaining the fuel confining boundary (geometry), maintaining criticality safety, and is one of the critical components to the preservation of retrievability. Because of this, an important part of UFDC research and development is related to the mechanical loads on used nuclear fuel, cladding, and key structural components of the fuel assembly during NCT and NCS, and the response of the used fuel and assembly to those loads.

2.   BACKGROUND

In the United States, the UNF inventory continues to increase as nuclear power generation, part of the nation's commercial power generation portfolio, continues to assist in meeting the country's energy demands. At the end of 2012, it was estimated that the commercial nuclear industry had generated approximately 70,000 metric tons (Tonnes) of uranium (MTU) contained in about 245,000 UNF assemblies (140,000 from boiling water reactors [BWRs] and 105,000 from pressurized water reactors [PWRs]). By 2020, the projected total UNF discharges will be approximately 88,000 MTU (Carter et al. 2012). By then, roughly 35,000 MTU is expected to be in dry storage with the remaining 53,000 MTU in the reactor pools. At the time waste acceptance starts, the fuel in dry storage represents a legacy that must be dealt with regardless of what approach is taken to manage newly discharged fuel going forward. By 2060, when all currently licensed reactors will have reached the end of their operational licenses, assuming a 60-year maximum, there will be approximately 140,000 MTU of UNF discharged from the reactor fleet (Carter et al. 2012).

By 1993, 50 percent of all PWR UNF inventory was WE 17×17 type fuel assemblies (Energy Information Administration 1995). Now, almost all PWRs (except combustion engineering plants) use WE 17×17 type fuel assemblies. As such, the WE 17×17 PWR fuel assemblies, or

USED FUEL DISPOSITION CAMPAIGN
Used Nuclear Fuel Loading and Structural Performance Under Normal Conditions of Transport -
Demonstration of Approach and Results of Used Fuel Performance Characterization
26   SEPTEMBER 30, 2013

permutations of this base assembly configuration, will represent the greatest fraction of PWR UNF inventory and is used in this study. The WE 17×17 fuel assembly type should represent the lesser mechanically robust configuration in comparison to other multi-rod PWR configurations because of reduced fuel rod diameter and cladding thickness. As such, the Steering Team, with Implementation Group concurrence, decided that an initial transport packaging candidate must be representative of a high-capacity PWR (≥32 assembly payload) transportation package and would be defined to contain a canisterized payload initially comprising WE 17×17 fuel assemblies. This assembly definition would also leave room to evaluate variants of the WE 17×17 design without making substantial changes to the initial M&S tool definitions.

Given the wide range of dry cask storage systems currently in use and the abundance of WE 17×17 PWR fuel, a generic 32 PWR canister/basket model will be developed and used for the analyses. Finally, generic transportation packaging configurations must be used wherever practical, and yet the packaging configurations must resemble one that could readily be considered for obtaining a Certificate of Compliance for transport purposes. As such, all components that would influence the structural performance need to be captured and accounted for during model generation. An applicable example of this would be the generic cask configuration with a 32-PWR assembly capacity, referred to as the generic burnup cask (GBC)-32 and described in NUREG/CR-6747 (Wagner 2001). It was previously developed to serve as a computational benchmark for criticality burnup credit studies.

Understanding the influence of rail and over-the-road transportation modes is necessary. The most recent national transportation plan (DOE 2009) established that a majority (possibly even greater than 90 percent) of the UNF inventory will be transported by rail. Per this document, DOE selected the mostly rail scenario as the transportation mode to be analyzed in a repository-related environmental impact statement. Additionally, The Office of Civilian Radioactive Waste Management issued a policy stating that dedicated trains will be the usual mode of rail transportation for UNF and high-level radioactive waste. This provides the basis for focusing on the rail transportation mode for this work. A representative rail journey of 3000 miles is selected for this study.

Of particular interest are assemblies that have achieved high burnup, because technical questions have been raised relative to cladding integrity of high burnup fuel, as discussed in NRC Interim Staff Guidance Memorandum 11 (NRC 2003). The current average discharge burnup for PWRs is approximately 48 gigawatt-days GWd/MTU, and for BWRs it is approximately 43 GWd/MTU (EPRI 2010). However, by 2020 it is projected that the average discharge burnups will be 58 GWd/MTU for PWRs and 48 GWd/MTU for BWRs. The peak rod average burnup will be 62 GWd/MTU for both reactor types.

As the burnup increases, a number of changes occur that may affect the performance of the fuel, cladding, and assembly hardware in storage and transportation. These changes include increased thickness of the cladding corrosion layer, increased hydrogen content in the cladding, increased creep strain in the cladding, increased fission gas release, and the formation of the high burnup structure at the surface of the fuel pellets. Because of these changes and the lack of fuel performance data at higher burnups, especially under design basis accident conditions, the

USED FUEL DISPOSITION CAMPAIGN
Used Nuclear Fuel Loading and Structural Performance Under Normal Conditions of Transport -
Demonstration of Approach and Results of Used Fuel Performance Characterization
SEPTEMBER 30, 2013   27

current maximum rod-averaged burnup is limited by the NRC to 62 GWd/MTU (OECD 2012). Newer cladding materials such as ZIRLO™ and M5® were developed to mitigate the effects on cladding associated with these higher burnups, primarily cladding corrosion. However, because these materials are relatively new limited data are available publicly that can be used to determine how these materials may perform under storage and transportation conditions (Hanson et al. 2012).

Depending on the drying process and/or storage conditions, the potential for brittle cladding failure increases substantially because of hydride reorientation. The level of embrittlement that occurs in cladding for a given level and distribution of hydrides is a function of temperature with increasing embrittlement at lower temperatures. Some researchers have characterized this by a ductile-to-brittle-transition temperature (DBTT). As the fuel cools during NCS, it may cool below the DBTT before the fuel is handled and transported at the end of interim storage. If the UNF cladding temperature at the time of transport is below the ductile-to-brittle-transition temperature, the chances for damage to the fuel cladding under NCT will increase.

The implementation of consolidated interim storage of UNF, consistent with one of the Blue Ribbon Commission on America's Nuclear Future recommendations (BRC 2012) and DOE's recently published *Strategy for the Management and Disposal of Used Nuclear Fuel and High-Level Radioactive Waste* (DOE 2013) would necessitate the implementation of a large-scale transportation program. Some of the used fuel in the inventory may be transported at least twice to get it to a repository—once from the reactor spent fuel pool to the consolidated interim storage facility and then to a repository for final disposal—after an unknown storage duration. Given the uncertainty in material properties of high burnup UNF, variability in storage duration, and the potential variability in the magnitude and duration of normal loading during transport, it is appropriate to investigate whether or not single or multiple transports would have a negative impact on fuel integrity and its suitability to meet the regulations regarding retrievability after transport. Hence, understanding performance characteristics of UNF cladding and ancillary components under cumulative loading stemming from NCS, transfer (from storage container to transport container if needed), and NCT is necessary. This understanding establishes the safety basis by maintaining the fuel confining boundary (geometry), maintaining criticality safety, and is one of the critical components to the preservation of retrievability.

Researchers would like to demonstrate that enough information, experimental support, and modeling and simulation capabilities exist to establish a preliminary determination of UNF structural performance under NCT loading. A steering team composed of national laboratories, DOE, and NRC staff met to discuss project feasibility. The group identified the basic information required and established a preliminary path for a successful research, development, and demonstration (RD&D) plan. The Steering Team Meeting took place on December 11-12, 2012. The "Method and Approach" document (Adkins 2013a) was developed to identify the decisions and proceedings of that meeting. An Implementation Group composed of national laboratories, DOE, NRC, and Transportation Technology Center, Inc. (TTCI) staff met February 21-22, 2013 to identify specific inputs needed to develop a focused overall RD&D project implementation plan. Following this meeting a Modeling, Simulation, and Experimental

USED FUEL DISPOSITION CAMPAIGN
Used Nuclear Fuel Loading and Structural Performance Under Normal Conditions of Transport -
Demonstration of Approach and Results of Used Fuel Performance Characterization
28 **SEPTEMBER 30, 2013**

Integration RD&D Plan (Adkins 2013b) was developed. This document describes a methodology, including development and use of analytical models, to evaluate loading and associated mechanical responses of UNF rods and key structural components.

Since the publication of the Research, Development, and Demonstration Plan, the work described has been completed to implement this plan. The input to the modeling and simulation efforts have been defined including rail loading data (Adkins 2013e), material properties (Geelhood 2013 and Adkins 2013e), initial conditions (Adkins 2013e), component temperatures (Adkins 2013e), and assembly and transportation package geometry (Adkins 2013e). The modeling and simulation methodology has been established (Adkins 2013f) and failure criteria and a methodology to assess failure from the modeling and simulation results have been established (Adkins 2013d). Various sensitivity analyses have been identified to evaluate the impact of various material property, initial condition, and modeling uncertainties on the resulting stress and strain predictions and failure prediction (Adkins 2013d).

The work on this initiative was split across 4 national laboratories. Sandia National Laboratory performed modeling on the cask-level and provided some experimental data. Idaho National Laboratory performed modeling on the fuel rod-level. Oak Ridge National Laboratory provided experimental data and confirmatory calculations. Pacific Northwest National Laboratory provided representative material properties, performed modeling on the assembly-level, performed failure assessment, and provided overall project management.

This report documents the final products of this initiative. Results of the initial demonstration of the modeling capability developed to perform preliminary deterministic evaluations of moderate-to-high burnup UNF mechanical performance under NCS and NCT conditions are provided. Results from the sensitivity studies that have been performed are also documented. Finally, discussion on the long-term goals and objectives of this initiative are provided.

3. OBJECTIVES

The objective of the work as described in the RD&D Plan is to determine the mechanical loads on used nuclear fuel, cladding, and key structural components of the fuel assembly during NCT and NCS, and to assess the response of the UNF and assembly hardware to those loads.

Uncertainties in these results will be quantified through sensitivity studies. The work scope will support development and integration of UNF data and analysis capabilities, as well as support the UFDC mission regarding scientific research and technology development to strengthen the technical basis for storage and transportation of UNF. The proposed work scope includes, but is not limited to, collecting information via literature review, soliciting input and contributions from subject matter experts, developing and demonstrating a methodology, performing computational analyses, planning and executing experimental measurements, and preparing a variety of supporting documentation that will feed into and provide the basis for future initiatives. The fundamental near-term objectives of this initiative are stated below and the documentation of the completion of each objective is identified:

USED FUEL DISPOSITION CAMPAIGN
Used Nuclear Fuel Loading and Structural Performance Under Normal Conditions of Transport -
Demonstration of Approach and Results of Used Fuel Performance Characterization
SEPTEMBER 30, 2013   29

- **Perform literature reviews to establish the quantity and type of information available in three specific areas: mechanical loading during storage and transportation; system and UNF material properties; and relevant modeling and simulation techniques.** A detailed literature review was performed to identify, assemble, and document applicable data and information, and identify information gaps. This information has been used to establish databases to support work performed under this initiative, as well as future programs and tasks. A literature review was performed on transportation shock and vibration associated with the normal conditions of transport for rail shipments of used nuclear fuel from commercial light-water reactors. (Maheras et al. 2013). All of this information was used to develop the loading, modeling and simulation, sensitivity, failure, and associated development strategies (Adkins 2013c).

- **Develop a database of information required for modeling via the literature reviews and associated topical influencing factors.** Information related to material properties, specified loading conditions, applicable boundary conditions, etc., have been consolidated into a Material Properties Handbook (Geelhood 2013) and are summarized in Section 5.2, and sensitivity studies have been selected for use in modeling and simulation (M&S) efforts (Adkins 2013d). Uncertainty quantification has been limited to UNF mechanical properties, initial conditions, and various modeling assumptions during this initiative because of the volume of work scheduled to be conducted within the defined performance period and also do to critical information that is not currently available.

- **Apply information from the literature reviews to construct models for performing high-resolution deterministic structural evaluations.** These models (also referred to as M&S tools) have been constructed at three discreet levels; cask-level, assembly-level, and fuel rod-level and are discussed in Section 6. These models have been documented in a fashion that is conducive to future upgrades and modifications/alterations for performing alternate simulations, and are able to accommodate new information as it becomes available. Fundamentally, the models have been constructed so that they may be readily used in future initiatives/assessments to address emergent issues or questions.

- **Select and perform one or more validation cases to establish the credibility of the methodology as well as the models' predictive capability.** The number and type of validation cases have been selected based on availability and pertinence to the deterministic predictions intended to be performed for this initiative. These studies are described in Section 7.

- **Provide an initial demonstration of the developed model's capabilities by performing preliminary deterministic evaluations of moderate-to-high burnup UNF mechanical performance under NCS and NCT conditions.** The current report documents the results of this initial demonstration. Section 8 provides results of the initial demonstration of the modeling capability developed to perform preliminary deterministic evaluations of moderate-to-high burnup UNF mechanical performance under NCS and NCT conditions. Section 8.5 provides results from the sensitivity studies that have been performed. The completion of this demonstration identifies data and information gaps that exist, and the types of testing that might be needed to fill those gaps. It also demonstrates the development and integration of

USED FUEL DISPOSITION CAMPAIGN
**Used Nuclear Fuel Loading and Structural Performance Under Normal Conditions of Transport -
Demonstration of Approach and Results of Used Fuel Performance Characterization**
30   **SEPTEMBER 30, 2013**

UNF data and analysis capabilities, as well as coupling M&S and experimental efforts with focused sensitivity evaluations. Current and future sensitivity evaluations, through simulation, can provide focus for future material testing and examination studies to refine correlations and relationships critical to understanding UNF structural performance and behavior.

The long-term goals and objectives of the initiative are to:

- Provide an analytical assessment of UNF integrity when subjected to NCT.

- Identify the type of ductility demands that would be required to ensure adequate high burnup UNF performance and survivability under a normal transport campaign.

- Answer questions relative to the ability of high burnup UNF to maintain its integrity and retrievability as it moves through each step of the waste management process (storage, transportation, repackaging, and disposal).

- Develop validated models and information to aid in making decisions regarding determination of storage and disposal paths.

- Identify tests that would be sufficient to address technical issues that need to be resolved.

- Contribute to an overarching blueprint for resolving the numerous technical challenges related to extended storage and subsequent transportation of UNF.

These goals and objectives are discussed in detail in Section 9.

4.   OVERVIEW

The remainder of this document will describe in detail the approach for UNF performance characterization that has been developed and give results from the initial demonstration. This initial demonstration will evaluate the structural performance of Westinghouse Electric 17×17 Optimized Fuel Assembly pressurized water reactor fuel assemblies with a discharge burnup range of 30-58 GWd/MTU (assembly average), loaded in a Generic Burnup Cask-32 transportation package and transported on a 3000 mile rail journey. Evaluations have been performed for representative normal conditions of rail transport involving a rail conveyance capable of meeting the Association of American Railroads Standard S-2043 (AAR 2003).

Section 5 describes the modeling inputs that were used for the demonstration. Section 6 describes the modeling approach and basis used for the demonstration. Section 7 describes the validation of models and inputs that was performed. Section 8 provides the model results for this demonstration as well as results from sensitivity studies. Section 9 provides discussion on how these modeling results and sensitivity studies can be used to better inform some of the long term goals of this initiative listed in Section 3.

USED FUEL DISPOSITION CAMPAIGN
Used Nuclear Fuel Loading and Structural Performance Under Normal Conditions of Transport -
Demonstration of Approach and Results of Used Fuel Performance Characterization
SEPTEMBER 30, 2013 31

5. MODELING INPUTS

There are five major modeling inputs to the initial demonstration. These inputs are loading histories of the rail car, component material properties (MP), component temperature, fuel and assembly post-irradiation conditions, and cask, canister, and fuel assembly geometry. This section will provide final documentation of the data and parameters that should be used for each of these items.

5.1 LOADING HISTORIES

In the Loading, M&S Methodology, Sensitivity, and Failure strategy document (Adkins 2013c), an approach for obtaining shock and vibration data was developed. This data was used by the M&S team to determine the effects of the shock and vibration associated with the rail-related NCT on UNF assemblies and rods. The option chosen by the Transportation Loading (TL) team used the extensive data archives and simulation capabilities of TTCI in a three-step process:

1. Obtain existing data for a representative railcar.

2. Use the NUCARS® program (TTCI 2013) to simulate a representative railcar.

3. Use the NUCARS® program to simulate a representative UNF railcar carrying a generic current generation rail transportation cask.

The data provided from task 2 on July 8, 2013 is provided in its processed form below as the Phase I Loads and was used by the M&S team in their initial modeling work. The data from task 3 was provided on August 13, 2013 and is provided in its processed form below as the Phase 3 Loads and was used by the M&S team in their final modeling work.

5.1.1 PHASE I (P1) LOADS

Phase I (P1) loads were extracted from a set of data files received from TTCI on July 8, 2013. Each data file contained an approximately six-minute-duration snapshot of measured acceleration time-history data for two separate rail cars in a single train, taken from a much larger data set of measurements spanning several days and hundreds of miles of track traveled. TTCI performed the initial culling of the larger data set to provide six-minute-duration data snapshots in which large accelerations were observed in the measured accelerations in each of the three directions (axial – along the length of the track, lateral, and vertical). Nineteen unique snapshots were provided for each car, meaning a total of thirty-eight unique snapshots were provided. Data for each car consisted of three-axis acceleration measurements obtained at each end of the rail car. The accelerometers used to obtain the measurements were located along the central axis of the car, spaced approximately 12.42 m apart (Figure 5.1). Measurements were taken at 300 samples per second and post processed with an anti-aliasing algorithm to ensure an accurate reconstruction of the true signal up to 100 Hz from the digitized measured data.

USED FUEL DISPOSITION CAMPAIGN
Used Nuclear Fuel Loading and Structural Performance Under Normal Conditions of Transport -
Demonstration of Approach and Results of Used Fuel Performance Characterization
32   **SEPTEMBER 30, 2013**
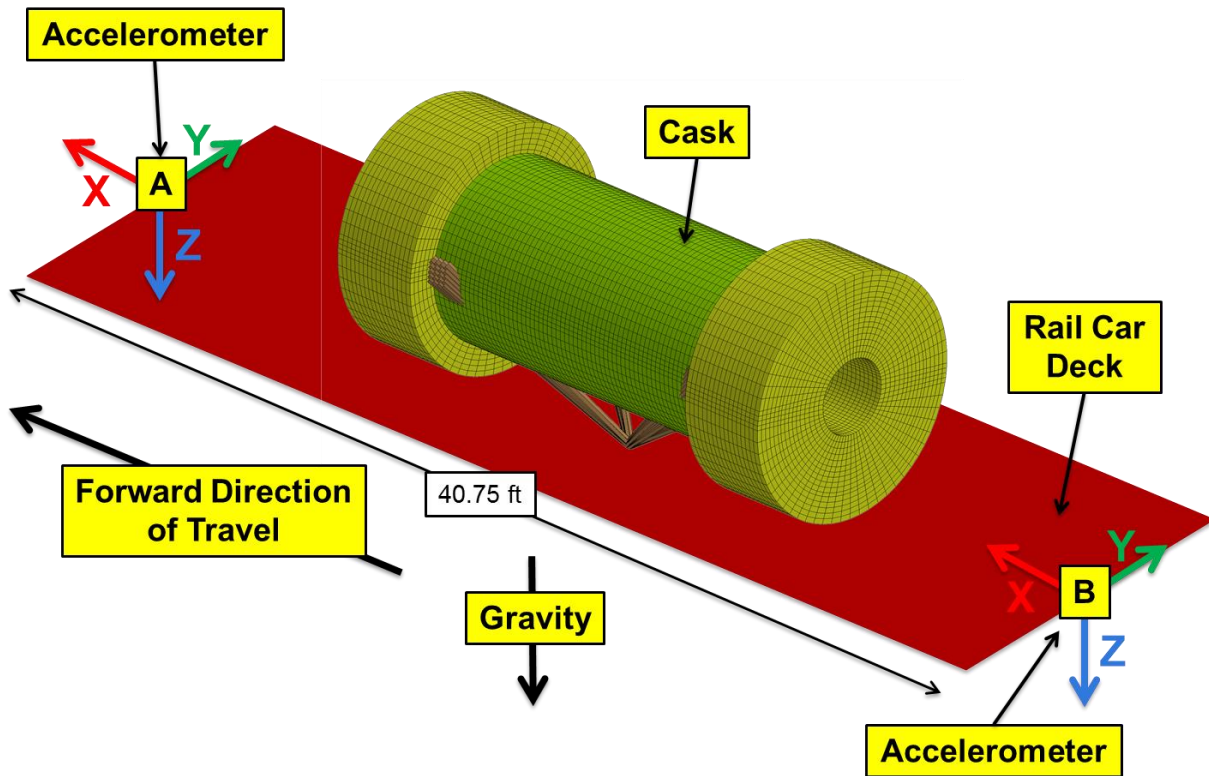
Figure 5.1. Rail Car Acceleration Measurement Locations and Coordinate System

The possibility of nonlinearities (particularly with respect to contact between components) in the response of the cask components to rail car excitations necessitated that explicit nonlinear analyses be performed at the cask model level. While explicit methods for solving transient dynamic problems are very good at handling contact between bodies and severe nonlinearities in response, they require very small time steps to ensure stability in the solution and minimize solution error. These small time steps limit the total length of time that can be effectively and accurately simulated using an explicit method. For the cask assembly model discussed here, the limit on this total length of time is roughly five to ten seconds. For total simulation times much beyond that, the accuracy of the solution becomes suspect, and the computational time required to solve the problem prohibitive. For this reason, ten-second duration load cases were extracted from the six-minute snapshots provided by TTCI. A total of six load cases were produced using a simple selection criterion. Three load cases were designated as shock load cases, and are ten-second duration excerpts from the six-minute snapshots that capture the most severe transient shock event in each of the three directions. The remaining three load cases were designated vibration load cases, and are ten-second duration excerpts from relatively shock free sections of the six-minute snapshots that were selected somewhat at random. While the loads applied in the model consist of either 5 or six degree-of-freedom acceleration time-histories, the selection criteria for both the shock and vibration loads considered only the severity of the accelerations in the direction of interest for that load case. For example, the Shock X (Axial) load case was selected based only on the peak acceleration in the axial direction without consideration of how this acceleration may combine with rail car excitations in the other directions. This is admittedly

USED FUEL DISPOSITION CAMPAIGN
**Used Nuclear Fuel Loading and Structural Performance Under Normal Conditions of Transport -
Demonstration of Approach and Results of Used Fuel Performance Characterization**
SEPTEMBER 30, 2013 33

a simple load case selection methodology that could potentially miss shock or vibration events that are more severe in an off axis direction. However, this seems unlikely considering that a peak load generating event for a rail car will tend to excite the rail car in all directions simultaneously. Therefore, selection of a load case based on peak accelerations in any one direction will tend to capture that one severe load generating event.

The acceleration data provided by TTCI consists of triaxial acceleration data at two points at either end of the rail car. These triaxial acceleration time-histories were converted to six degree-of-freedom acceleration time-histories at the cradle to rail car interface using the equations given below.

$$A_{x_{midpoint}} = \frac{A_{x_{EndA}} + A_{x_{EndB}}}{2}$$

$$A_{y_{midpoint}} = \frac{A_{y_{EndA}} + A_{y_{EndB}}}{2}$$

$$A_{z_{midpoint}} = \frac{A_{z_{EndA}} + A_{z_{EndB}}}{2}$$

$$A_{rx_{midpoint}} = 0$$

$$A_{ry_{midpoint}} = \frac{-\left(A_{z_{EndA}} - A_{z_{EndB}}\right) \times g}{D}$$

$$A_{rz_{midpoint}} = \frac{\left(A_{y_{EndA}} - A_{y_{EndB}}\right) \times g}{D}$$

Note that these equations assume that the rail car is perfectly rigid, which undoubtedly was not the case. Also, note that there was not enough information to determine the rotation of the rail car about the axis connecting the two accelerometers and therefore $A_{rx_{midpoint}}$ was set equal to zero.

After conversion to acceleration time-histories at the rail car mid-point, each six-minute snapshot was processed to remove large rigid body displacements from the accelerations. It is desirable to do this when performing base excitation simulations so as to alleviate post-processing issues and numerical problems that can arise when rigid body displacements are large with respect to much smaller local displacements. To remove the large rigid body displacement, the following steps were undertaken.

1. Each six-minute acceleration time history was converted from the time domain to the frequency domain using a Fast Fourier Transform (FFT) algorithm.
2. The amplitude of the 0.1 Hz and lower frequency components were set identically to zero.

USED FUEL DISPOSITION CAMPAIGN
Used Nuclear Fuel Loading and Structural Performance Under Normal Conditions of Transport -
Demonstration of Approach and Results of Used Fuel Performance Characterization
34   **SEPTEMBER 30, 2013**

3. Each six-minute acceleration time history was then converted back from the frequency domain to the time domain using an inverse Fast Fourier Transform algorithm.
4. Acceleration, velocity, and displacement time-histories, along with Fast Fourier Transform, shock response spectrum (SRS), and power spectral density (PSD) values, were calculated for the before-conversion and after-conversion time-histories and compared to ensure the conversion had been performed correctly and critical characteristics of the original acceleration time-history had not been lost.

Figure 5.2 shows a comparison between an original time-history and a displacement corrected time-history for one component of one six-minute snapshot. Note that in the displacement corrected time history the amplitudes of all of the components of the original acceleration data at and below 0.1 Hz have been set to zero and that the resulting peak displacement has been reduced from over 1000 m to less than 0.1 m (four orders of magnitude). Despite this, the time-domain representation of the acceleration time-history has not been significantly altered and the SRS shows that for all frequencies above 0.1 Hz the signal is unchanged.
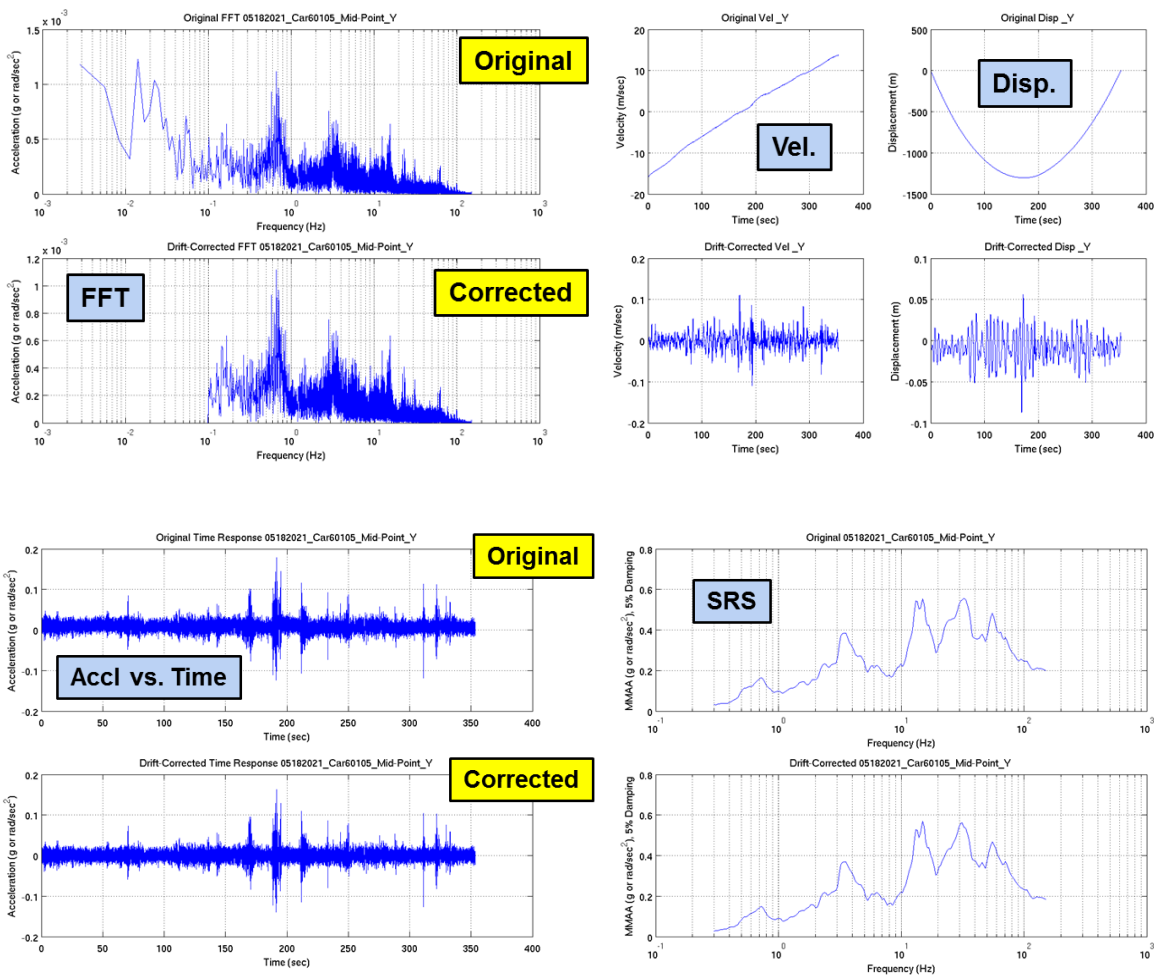
Figure 5.2. Comparison of Original and Displacement Corrected Acceleration Data

USED FUEL DISPOSITION CAMPAIGN
Used Nuclear Fuel Loading and Structural Performance Under Normal Conditions of Transport -
Demonstration of Approach and Results of Used Fuel Performance Characterization
SEPTEMBER 30, 2013 35

Table 5.1 summarizes pertinent details of the six P1 load cases. The data for these cases was made available to the M&S team in electronic form. Note that the X, Y, Z direction designations associated with each load case refer to the TTCI loads coordinate system shown in Figure 5.1. The secondary designator of Axial, Lateral, and Vertical is used to avoid confusion in conversion of loads from the TTCI coordinate system to the coordinate system shown in Figure 6.2 used in the cask FEM described later.

Table 5.1. Cask Assembly Model P1 Load Case Details

Load Case	Source File	Car #	Peak Accel. or g_{rms} (g)	Time (sec)
Shock X (Axial)	05170501	60270	1.269 g	304.1 – 314.1
Shock Y (Lateral)	05200332	60105	0.492 g	35.6 – 45.6
Shock Z (Vertical)	05182021	60105	1.679 g	209.7 – 219.7
Vibration X (Axial)	05170501	60270	0.0079 g_{rms}	125.0 – 135.0
Vibration Y (Lateral)	05211414	60105	0.0105 g_{rms}	70.0 – 80.0
Vibration Z (Vertical)	05211414	60105	0.0241 g_{rms}	225.0 – 235.0

USED FUEL DISPOSITION CAMPAIGN
Used Nuclear Fuel Loading and Structural Performance Under Normal Conditions of Transport -
Demonstration of Approach and Results of Used Fuel Performance Characterization
36 **SEPTEMBER 30, 2013**

The P1 Shock X (Axial) load case was taken from the 05170501 six-minute snapshot for car 60270.
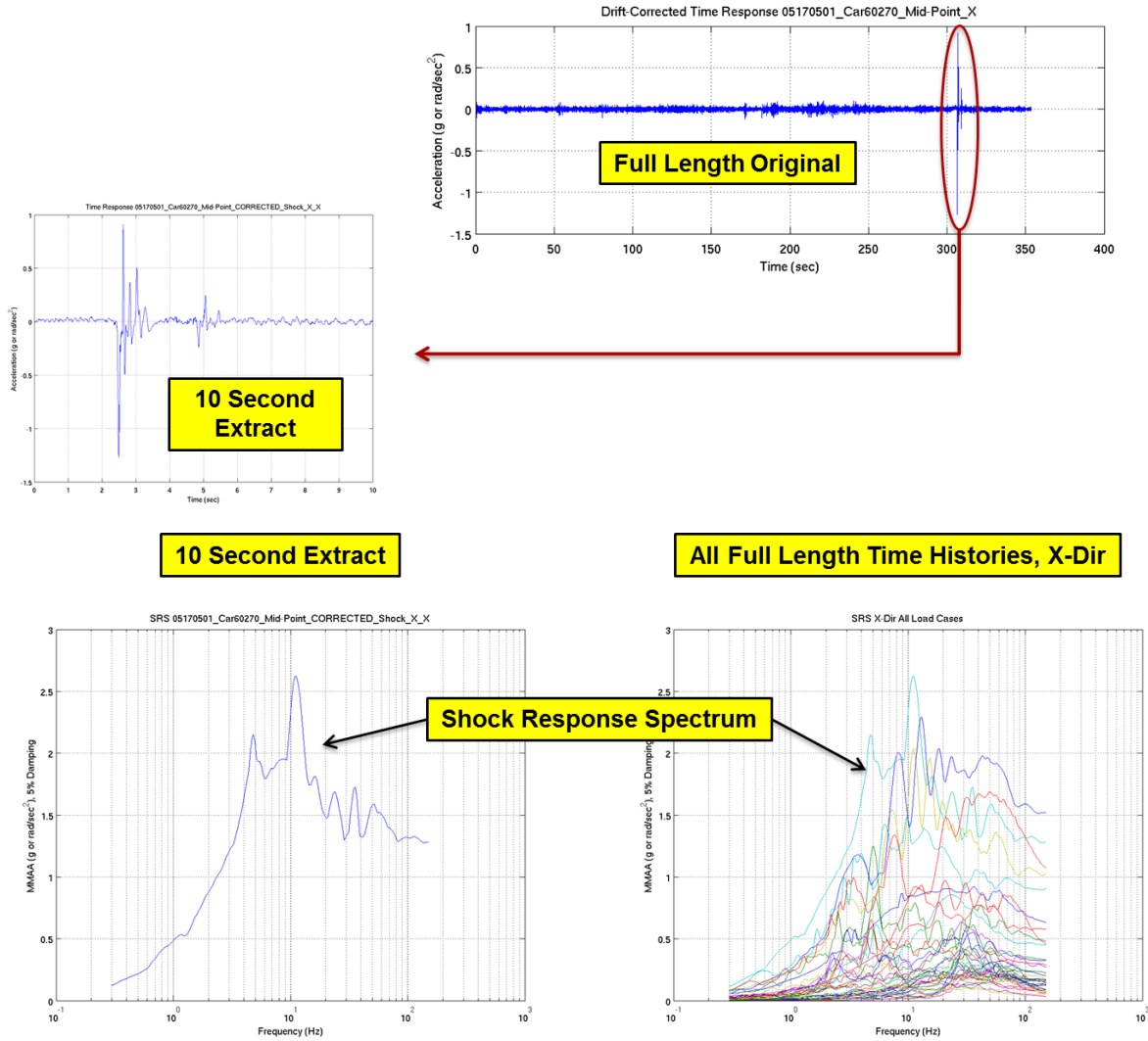
Figure 5.3 illustrates pertinent details of the load case in comparison with all of the six-minute P1 snapshots. The ten-second window extracted from the snapshot was taken from 304.1 seconds to 314.1 seconds. During that time a maximum absolute value acceleration of 1.269 g was measured in the X (Axial) direction. This maximum absolute value acceleration is less than the peak time-domain absolute value acceleration of 1.439 g measured in a different load case, but the SRS for this load case is more broadly and strongly distributed throughout the frequencies of interest (10 to 60 Hz), so it was selected.

USED FUEL DISPOSITION CAMPAIGN
Used Nuclear Fuel Loading and Structural Performance Under Normal Conditions of Transport -
Demonstration of Approach and Results of Used Fuel Performance Characterization
SEPTEMBER 30, 2013 37
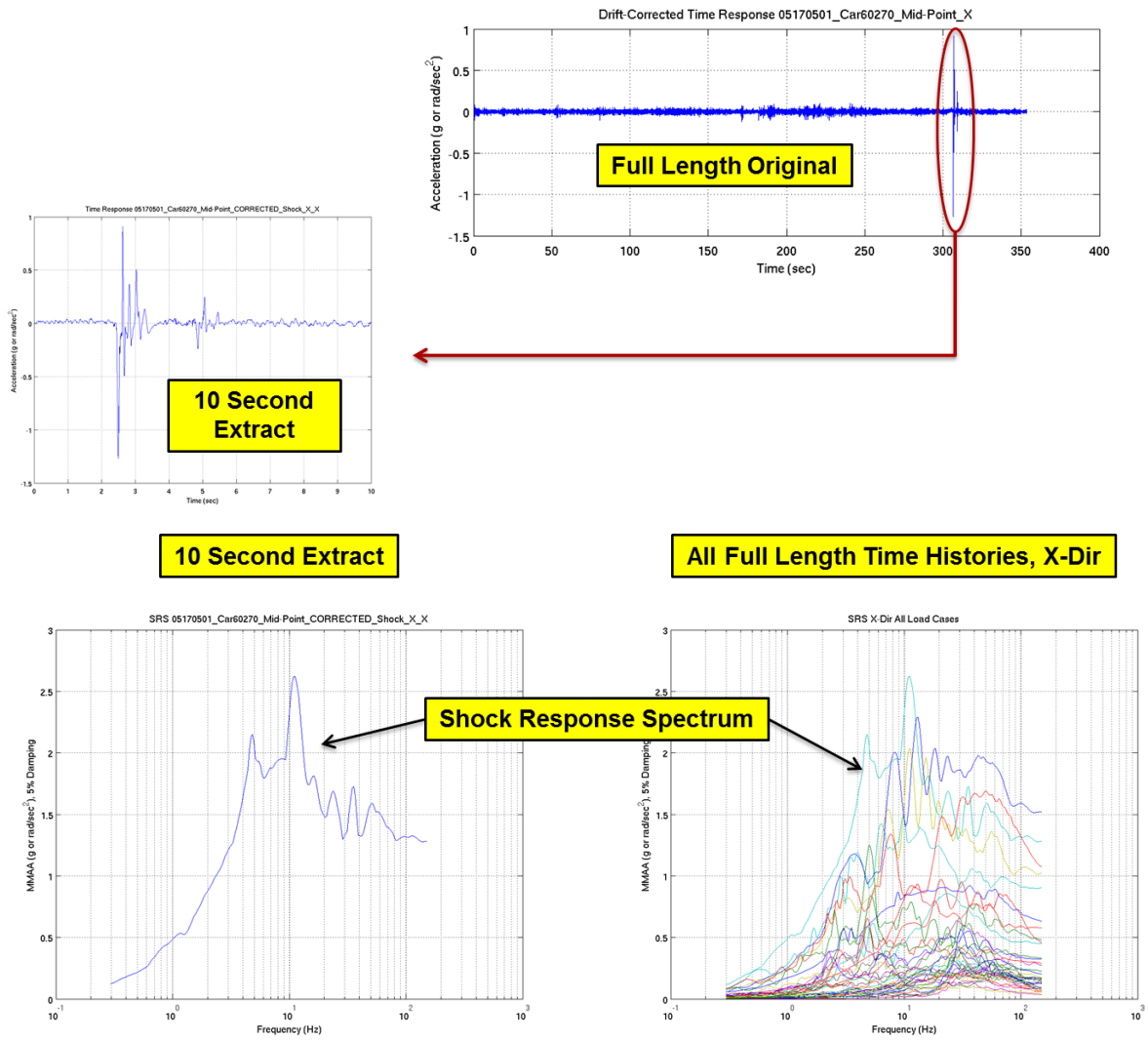
Figure 5.3. P1 Shock X (Axial) Load Case Comparison with Six-Minute Snapshot Loads

USED FUEL DISPOSITION CAMPAIGN
Used Nuclear Fuel Loading and Structural Performance Under Normal Conditions of Transport -
Demonstration of Approach and Results of Used Fuel Performance Characterization
38   **SEPTEMBER 30, 2013**

The P1 Shock Y (Lateral) load case was taken from the 05200332 six-minute snapshot for car 60105. Figure 5.4 illustrates pertinent details of the load case in comparison with all of the six-minute P1 snapshots. The ten-second window extracted from the snapshot was taken from 35.6 seconds to 45.6 seconds. During that time a maximum absolute value acceleration of 0.492g was measured in the Y (Lateral) direction. This maximum absolute value acceleration is less than the peak time-domain absolute value acceleration of 0.718 g measured in a different load case, but the SRS for this load case is more broadly and strongly distributed throughout the frequencies of interest, so it was selected.
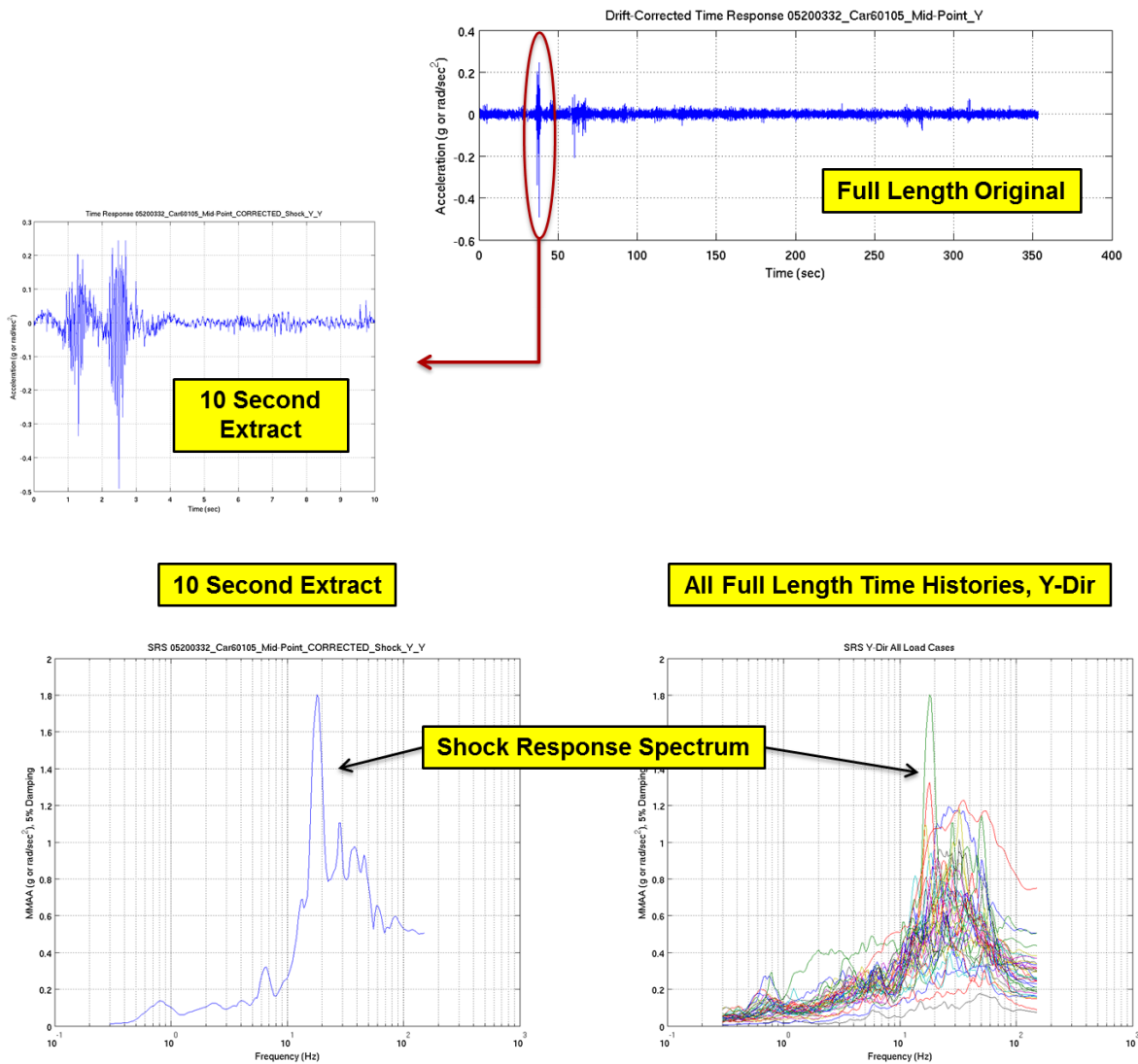
Figure 5.4. P1 Shock Y (Lateral) Load Case Comparison with Six-Minute Snapshot Loads

USED FUEL DISPOSITION CAMPAIGN
Used Nuclear Fuel Loading and Structural Performance Under Normal Conditions of Transport -
Demonstration of Approach and Results of Used Fuel Performance Characterization
SEPTEMBER 30, 2013 39

The P1 Shock Z (Vertical) load case was taken from the 05182021 six-minute snapshot for car 60105. Figure 5.5 illustrates pertinent details of the load case in comparison with all of the six-minute P1 snapshots. The ten-second window extracted from the snapshot was taken from 209.7 seconds to 219.7 seconds. During that time a maximum absolute value acceleration of 1.679 g was measured in the Z (Vertical) direction. This maximum absolute value acceleration is the peak time-domain absolute value acceleration measured in all of the six-minute snapshots.
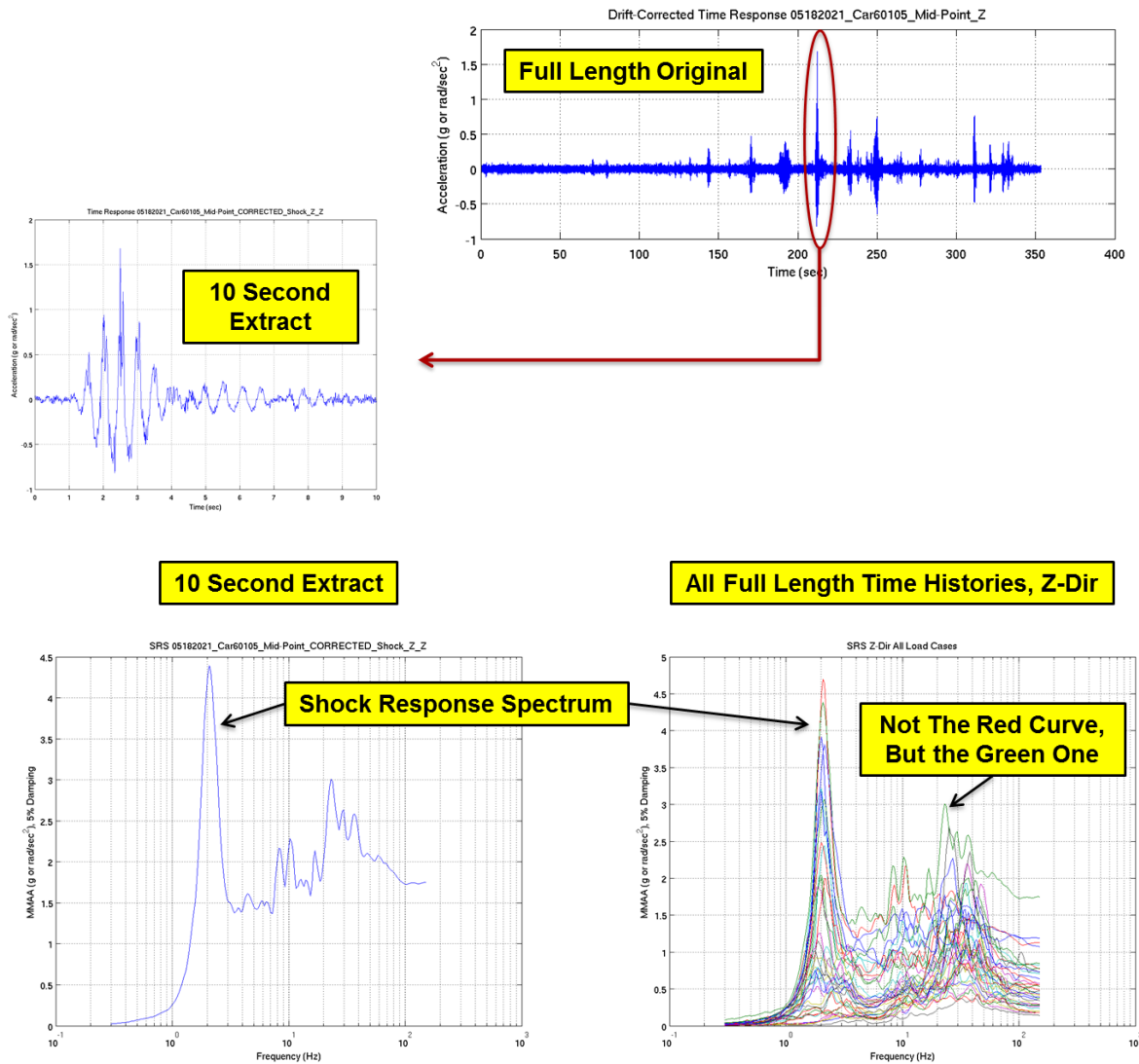
Figure 5.5. P1 Shock Z (Vertical) Load Case Comparison with Six-Minute Snapshot Loads

USED FUEL DISPOSITION CAMPAIGN
Used Nuclear Fuel Loading and Structural Performance Under Normal Conditions of Transport -
Demonstration of Approach and Results of Used Fuel Performance Characterization
40   **SEPTEMBER 30, 2013**

The P1 Vibration X (Axial) load case was taken from the 05170501 six-minute snapshot for car 60270. Figure 5.6 illustrates pertinent details of the load case in comparison with all of the six-minute P1 snapshots. The ten-second window extracted from the snapshot was taken from 125.0 seconds to 135.0 seconds. The PSD root mean square acceleration (g_{rms}) value for the ten-second window is 0.0079 g, whereas the maximum g_{rms} value across all of the six-minute snapshots (which include shock events) is 0.0253 g. While the selected load case does not match the maximum snapshot g_{rms} value, it is a good representation of the vibration environment and is close to the 0.0102 g snapshot case average g_{rms} value.
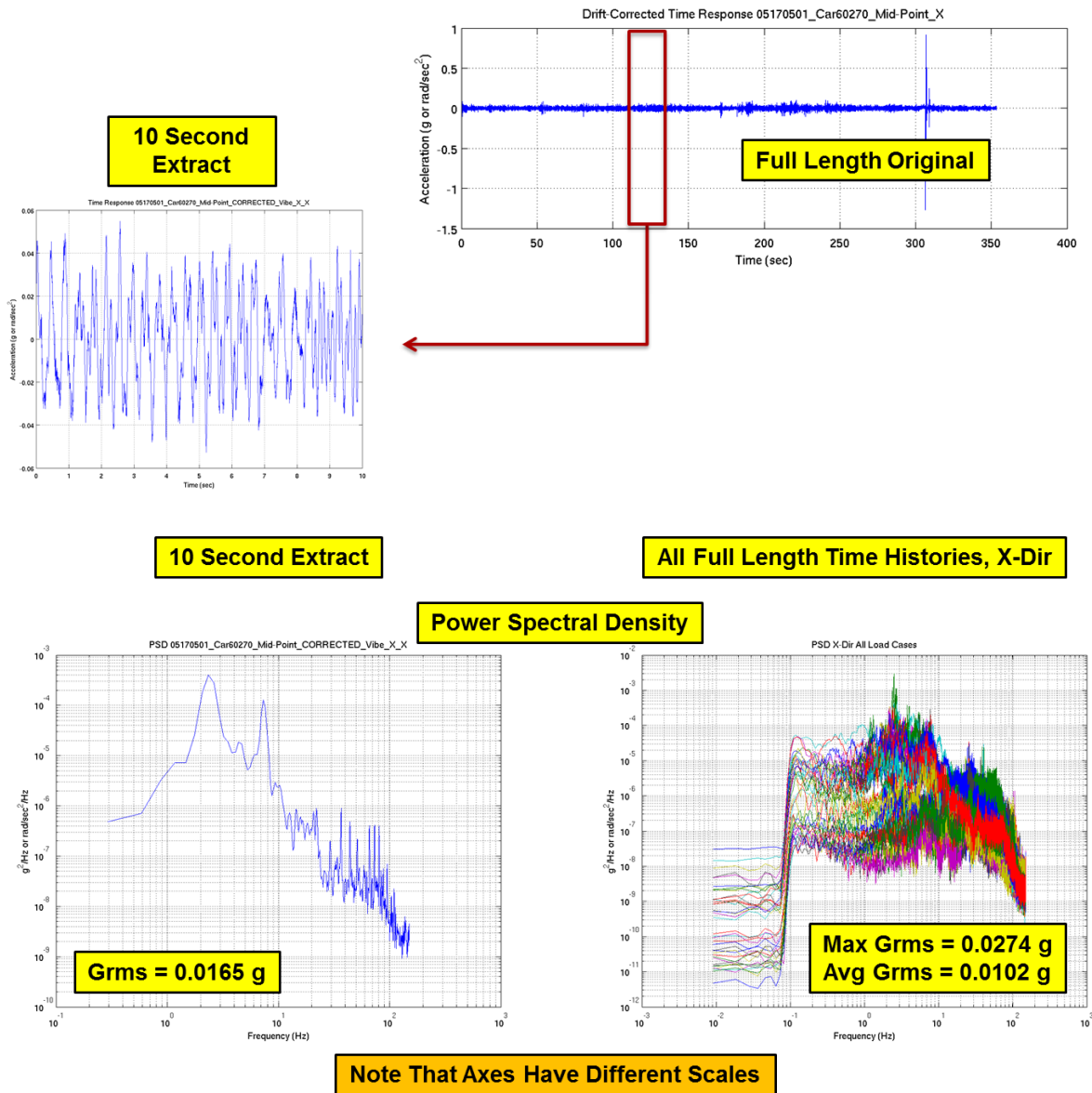
Figure 5.6. P1 Vibration X (Axial) Load Case Comparison with Six-Minute Snapshot Loads

USED FUEL DISPOSITION CAMPAIGN
**Used Nuclear Fuel Loading and Structural Performance Under Normal Conditions of Transport -
Demonstration of Approach and Results of Used Fuel Performance Characterization**
SEPTEMBER 30, 2013 41

The P1 Vibration Y (Lateral) load case was taken from the 05211414 six-minute snapshot for car 60105. Figure 5.7 illustrates pertinent details of the load case in comparison with all of the six-minute P1 snapshots. The ten-second window extracted from the snapshot was taken from 70.0 seconds to 80.0 seconds. The PSD g_{rms} value for the ten-second window is 0.0105 g, whereas the maximum g_{rms} value across all of the six-minute snapshots (which include shock events) is 0.0282 g. While the selected load case does not match the maximum snapshot g_{rms} value, it is a good representation of the vibration environment and is close to the 0.0136 g snapshot average g_{rms} value.
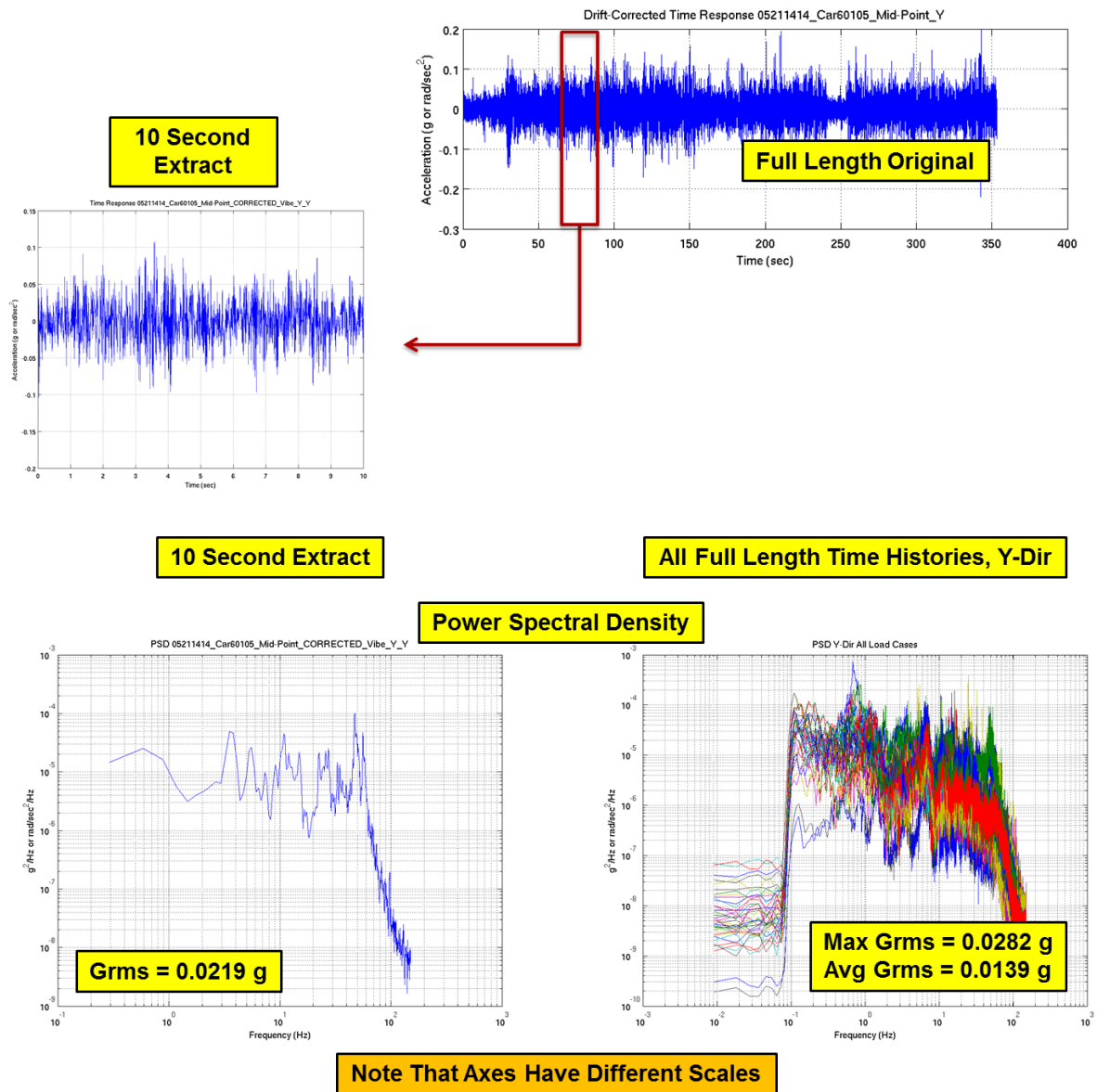
Figure 5.7. P1 Vibration Y (Lateral) Load Case Comparison with Six-Minute Snapshot Loads

USED FUEL DISPOSITION CAMPAIGN
Used Nuclear Fuel Loading and Structural Performance Under Normal Conditions of Transport -
Demonstration of Approach and Results of Used Fuel Performance Characterization
42   SEPTEMBER 30, 2013

The P1 Vibration Z (Vertical) load case was taken from the 05211414 six-minute snapshot for car 60105. Figure 5.8 illustrates pertinent details of the load case in comparison with all of the six-minute P1 snapshots. The ten-second window extracted from the snapshot was taken from 225.0 seconds to 235.0 seconds. The PSD g_{rms} value for the ten-second window is 0.0241 g, whereas the maximum g_{rms} value across all of the six-minute snapshots (which include shock events) is 0.0763 g. While the selected load case does not match the maximum snapshot g_{rms} value, it is a good representation of the vibration environment and is close to the 0.0375 g snapshot average g_{rms} value.
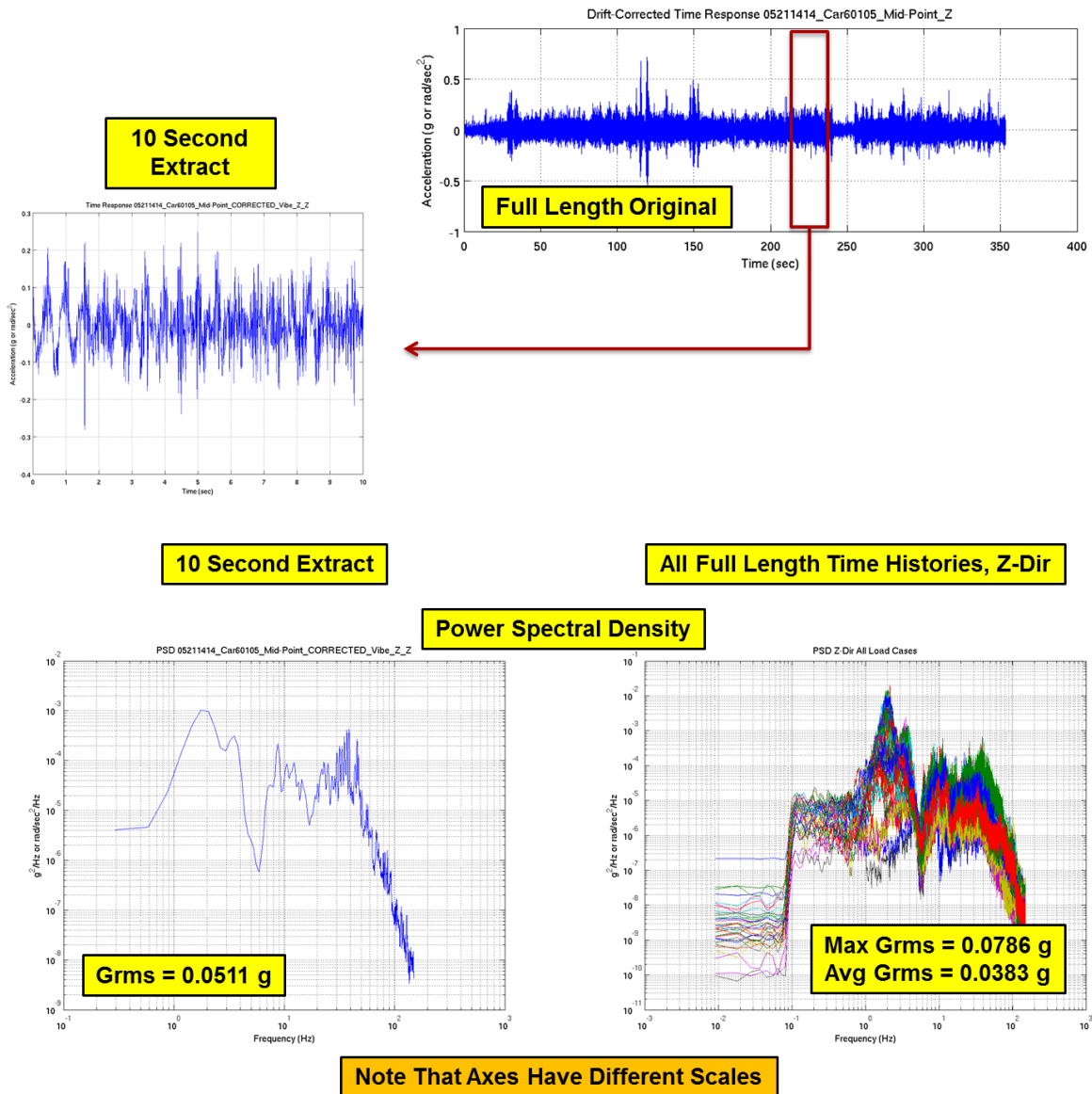
Figure 5.8. P1 Vibration Z (Vertical) Load Case Comparison with Six-Minute Snapshot Loads

USED FUEL DISPOSITION CAMPAIGN
Used Nuclear Fuel Loading and Structural Performance Under Normal Conditions of Transport -
Demonstration of Approach and Results of Used Fuel Performance Characterization
SEPTEMBER 30, 2013 43

5.1.2   PHASE III (P3) LOADS

Phase III (P3) loads were extracted from a set of data files received from TTCI on August 13, 2013. Each data file contained a variable duration (multi-tens-of-minutes) snapshot of rail car acceleration time-history data produced by the NUCARS® (TTCI 2013) software for a single eight-axle, drop-center, rail car (whose design is based on a preliminary rail car design for transport of spent nuclear fuel to Yucca Mountain) as it traversed an approximately 25-mile representative segment of track (referred to as Track 9 by TTCI) at various speeds. The rail car in the NUCARS simulation was loaded with a transportation cask consistent with the cask assembly FEM described later. Acceleration time-histories (consisting of all six degree-of-freedom accelerations at the cradle-to-rail-car interface, sampled at 150 samples per second) were provided for velocities of 10, 20, 24, 30, 40, 50, 53, and 62 mph.

Due to the limitations placed on the length of time that can be effectively simulated using explicit analyses (as described earlier in the discussion of the selection of the P1 load cases), ten-second duration load cases were extracted from the longer NUCARS snapshots provided by TTCI. A total of five load cases were produced. Two load cases were designated as shock load cases, and are ten-second duration excerpts from the longer NUCARS snapshots that capture the most severe transient shock event in each of the three directions. Only two distinct shock load cases were produced. This is because the worst case axial and vertical shocks occur nearly simultaneously and within the same ten second excerpt, thus negating the need for a separate load case for each of these shock events. The remaining three load cases were designated vibration load cases, and are ten second duration excerpts from relatively shock free sections of the longer NUCARS snapshots that contained average power spectral densities for accelerations in each of the three directions.

The data supplied by TTCI for the P3 loads provides six degree-of-freedom accelerations at a single node located at the interface between the cradle and rail car deck. As was done for the P1 load cases, modifications were made to each load case acceleration time-history to remove large rigid body displacements. This modification was performed in a manner analogous to that performed for the P1 load cases.

USED FUEL DISPOSITION CAMPAIGN
**Used Nuclear Fuel Loading and Structural Performance Under Normal Conditions of Transport -
Demonstration of Approach and Results of Used Fuel Performance Characterization**
44   **SEPTEMBER 30, 2013**

Table 5.2 summarizes pertinent details of the five P3 load cases. All of the load cases were taken from the Track 9 snapshot at 62 mph. This snapshot was assumed to represent the most conservative of those provided. Recall from the P1 Load Case discussion that the X, Y, Z direction designations refer to the TTCI loads coordinate system shown in Figure 5.1 and the secondary designator of Axial, Lateral, and Vertical refer to the directions shown in Figure 6.2 used in the cask FEM that is described later.

USED FUEL DISPOSITION CAMPAIGN
Used Nuclear Fuel Loading and Structural Performance Under Normal Conditions of Transport -
Demonstration of Approach and Results of Used Fuel Performance Characterization
SEPTEMBER 30, 2013 **45**

Table 5.2 Cask Assembly Model P3 Load Case Details

Load Case	Source File	Peak Accel. or g_{rms} (g)	Time (sec)
Shock X (Axial)	track9_62mph	0.087 g	815.8 – 825.8
Shock Y (Lateral)	track9_62mph	0.101 g	854.7 – 864.7
Shock Z (Vertical)	track9_62mph	0.335 g	815.8 – 825.8
Vibration X (Axial)	track9_62mph	0.00221 g_{rms}	445.0 – 455.0
Vibration Y (Lateral)	track9_62mph	0.00318 g_{rms}	1185.0 – 1195.0
Vibration Z (Vertical)	track9_62mph	0.00805 g_{rms}	1085.0 – 1095.0

The P3 Shock X (Axial) load case is comprised of the ten-second segment from 815.8 seconds to 825.8 seconds of the 62 mph Track 9 snapshot. Figure 5.9 illustrates pertinent details of the ten-second load case in comparison with the full length snapshot. During the ten-second segment a maximum absolute value acceleration of 0.087 g was imparted to the cask assembly in the X (Axial) direction. This maximum absolute value acceleration is equal to the peak time-domain absolute value acceleration in the full length snapshot.

USED FUEL DISPOSITION CAMPAIGN
Used Nuclear Fuel Loading and Structural Performance Under Normal Conditions of Transport -
Demonstration of Approach and Results of Used Fuel Performance Characterization
46   **SEPTEMBER 30, 2013**
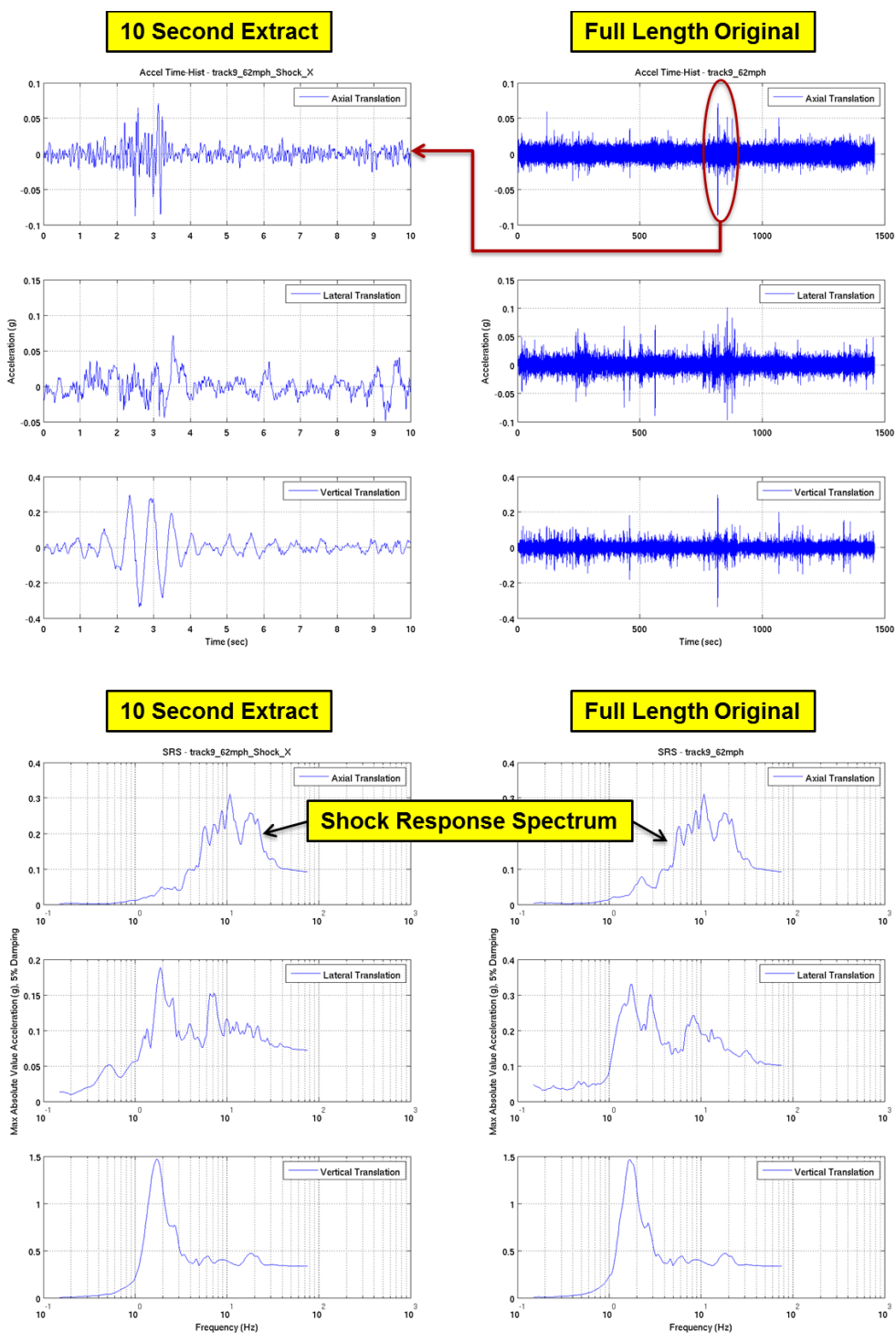
Figure 5.9 P3 Shock X (Axial) Load Case Comparison with Full Length Snapshot

USED FUEL DISPOSITION CAMPAIGN
Used Nuclear Fuel Loading and Structural Performance Under Normal Conditions of Transport -
Demonstration of Approach and Results of Used Fuel Performance Characterization
SEPTEMBER 30, 2013 **47**

The P3 Shock Y (Lateral) load case is comprised of the ten second segment from 854.7 seconds to 864.7 seconds of the 62 mph Track 9 snapshot. Figure 5.10 illustrates pertinent details of the ten-second load case in comparison with the full length snapshot. During the ten-second segment a maximum absolute value acceleration of 0.101 g is imparted to the cask assembly in the Y (Lateral) direction. This maximum absolute value acceleration is equal to the peak time-domain absolute value acceleration in the full length snapshot.

USED FUEL DISPOSITION CAMPAIGN
Used Nuclear Fuel Loading and Structural Performance Under Normal Conditions of Transport -
Demonstration of Approach and Results of Used Fuel Performance Characterization
48   **SEPTEMBER 30, 2013**
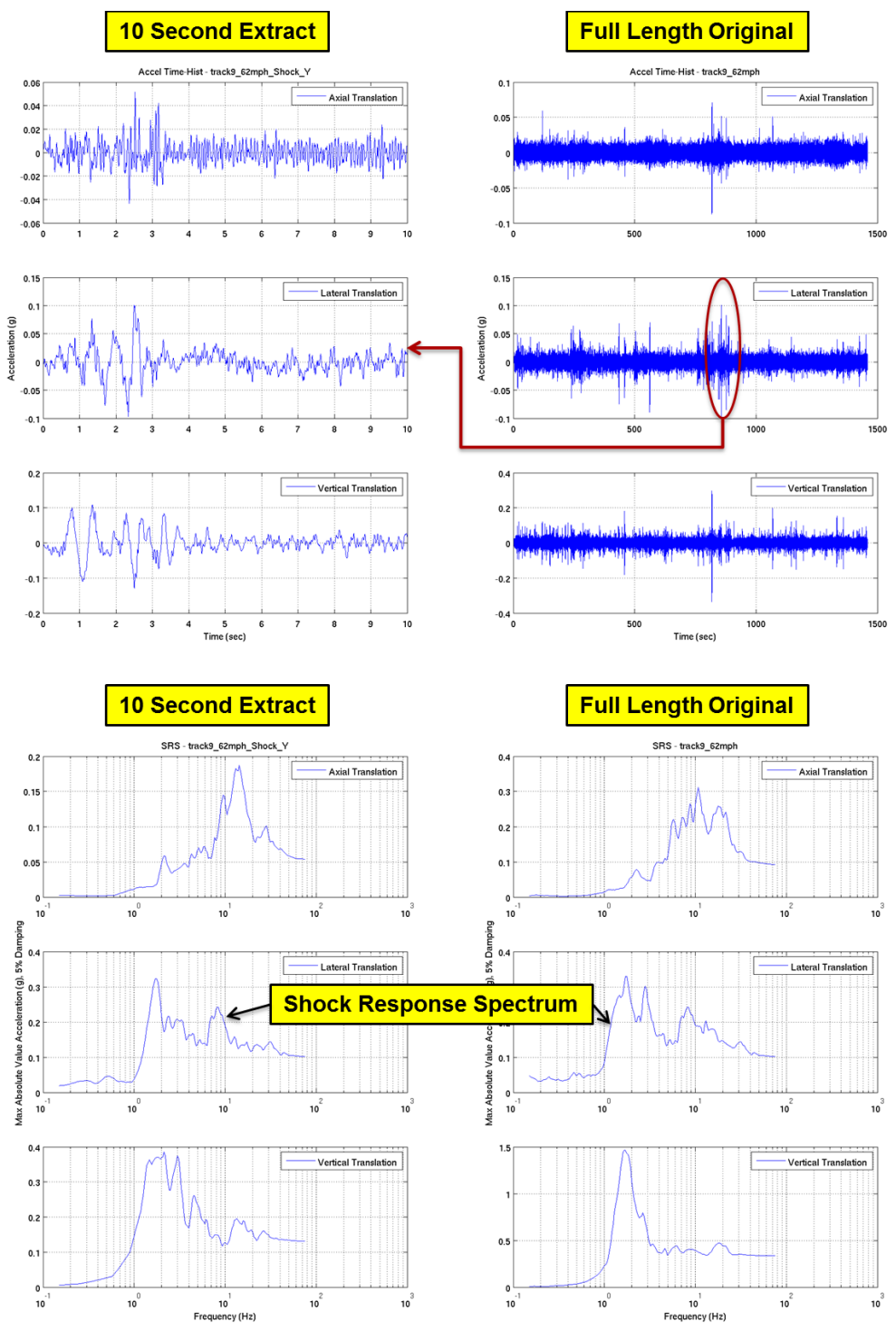
Figure 5.10 P3 Shock Y (Lateral) Load Case Comparison with Full Length Snapshot

USED FUEL DISPOSITION CAMPAIGN
Used Nuclear Fuel Loading and Structural Performance Under Normal Conditions of Transport -
Demonstration of Approach and Results of Used Fuel Performance Characterization
SEPTEMBER 30, 2013 **49**

The P3 Shock Z (Vertical) load case is comprised of the ten second segment from 815.8 seconds to 825.8 seconds of the 62 mph Track 9 snapshot. Figure 5.11 illustrates pertinent details of the ten second load case in comparison with the full length snapshot. During the ten-second segment a maximum absolute value acceleration of 0.335 g is imparted to the cask assembly in the Z (Vertical) direction. This maximum absolute value acceleration is equal to the peak time-domain absolute value acceleration in the full length snapshot.

USED FUEL DISPOSITION CAMPAIGN
Used Nuclear Fuel Loading and Structural Performance Under Normal Conditions of Transport -
Demonstration of Approach and Results of Used Fuel Performance Characterization
50   **SEPTEMBER 30, 2013**
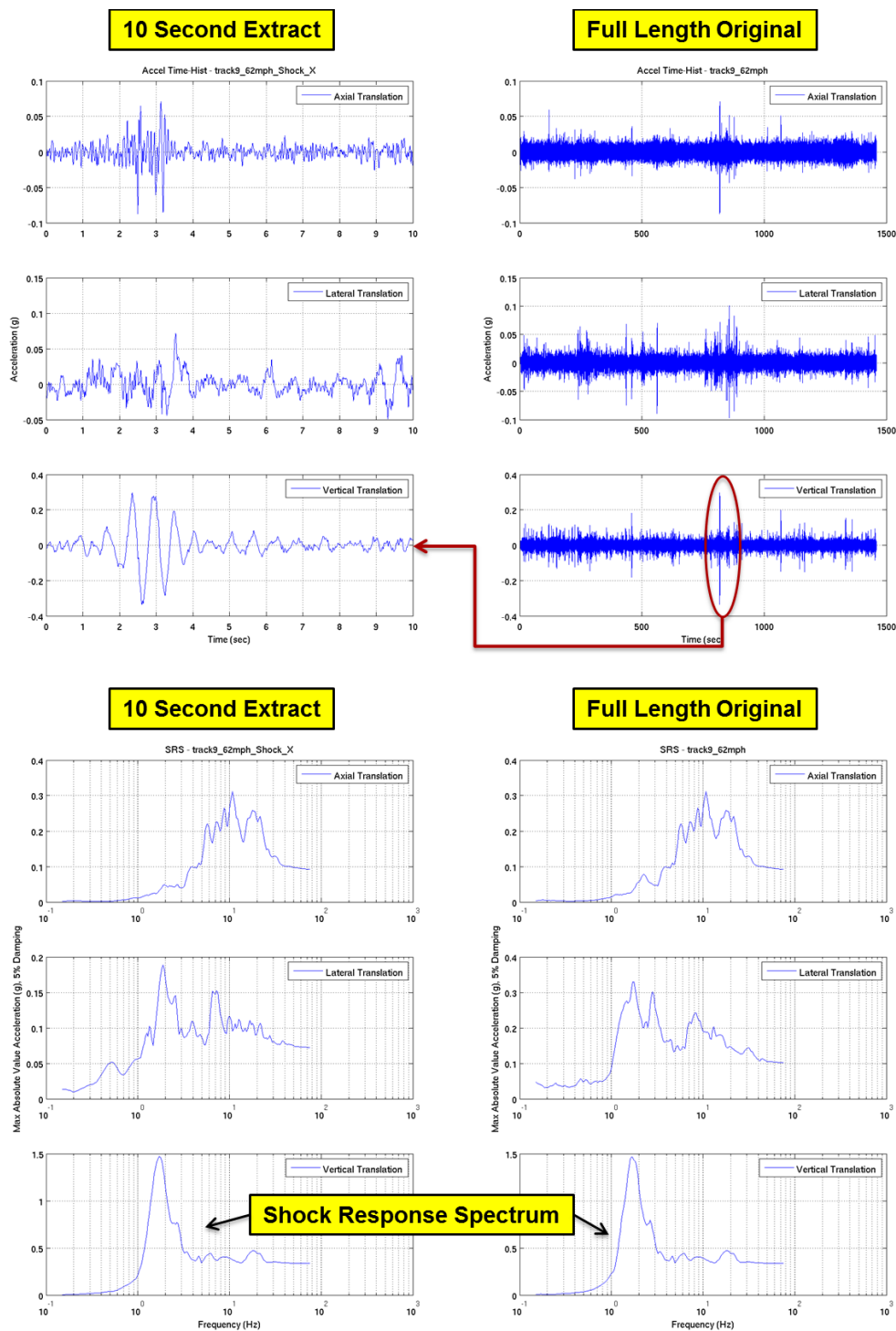
Figure 5.11 P3 Shock Z (Vertical) Load Case Comparison with Full Length Snapshot

USED FUEL DISPOSITION CAMPAIGN
Used Nuclear Fuel Loading and Structural Performance Under Normal Conditions of Transport -
Demonstration of Approach and Results of Used Fuel Performance Characterization
SEPTEMBER 30, 2013 51

The P3 Vibration X (Axial) load case is comprised of the ten second segment from 445.0 seconds to 455.0 seconds of the 62 mph Track 9 snapshot. Figure 5.12 illustrates pertinent details of the ten second load case in comparison with the full length snapshot. The PSD g_{rms} value for the ten second window of 0.00221 g is nearly equal to the g_{rms} value for the full length snapshot (which includes shock events) of 0.00225 g.

USED FUEL DISPOSITION CAMPAIGN
Used Nuclear Fuel Loading and Structural Performance Under Normal Conditions of Transport -
Demonstration of Approach and Results of Used Fuel Performance Characterization
52   **SEPTEMBER 30, 2013**
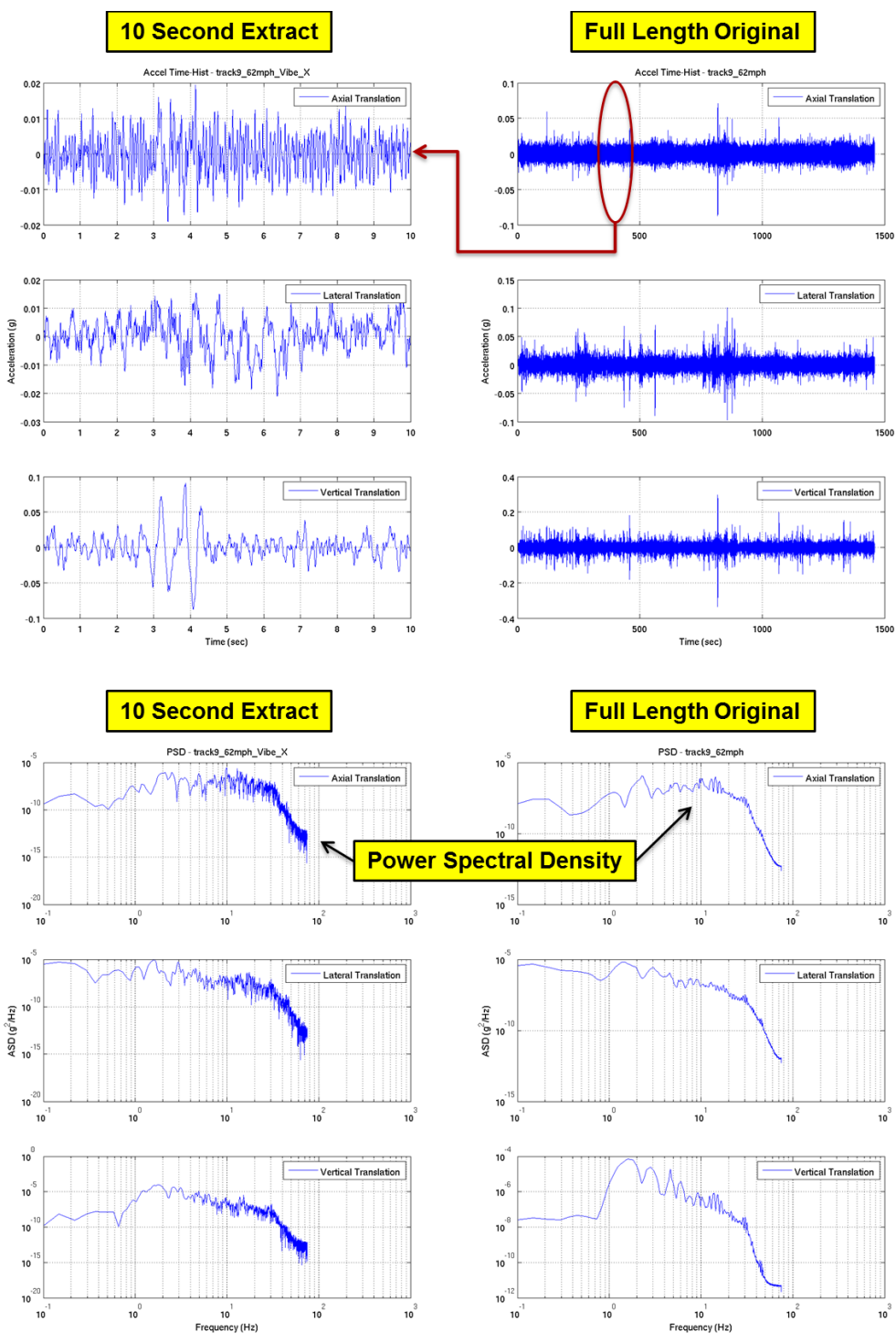
Figure 5.12 P3 Vibration X (Axial) Load Case Comparison with Full Length Snapshot

USED FUEL DISPOSITION CAMPAIGN
Used Nuclear Fuel Loading and Structural Performance Under Normal Conditions of Transport -
Demonstration of Approach and Results of Used Fuel Performance Characterization
SEPTEMBER 30, 2013 53

The P3 Vibration Y (Lateral) load case is comprised of the ten-second segment from 1185.0 seconds to 1195.0 seconds of the 62 mph Track 9 snapshot. Figure 5.13 illustrates pertinent details of the ten-second load case in comparison with the full length snapshot. The PSD g_{rms} value for the ten-second window of 0.00318 g is nearly equal to the g_{rms} value for the full length snapshot (which includes shock events) of 0.00340 g.

USED FUEL DISPOSITION CAMPAIGN
Used Nuclear Fuel Loading and Structural Performance Under Normal Conditions of Transport -
Demonstration of Approach and Results of Used Fuel Performance Characterization
54   **SEPTEMBER 30, 2013**
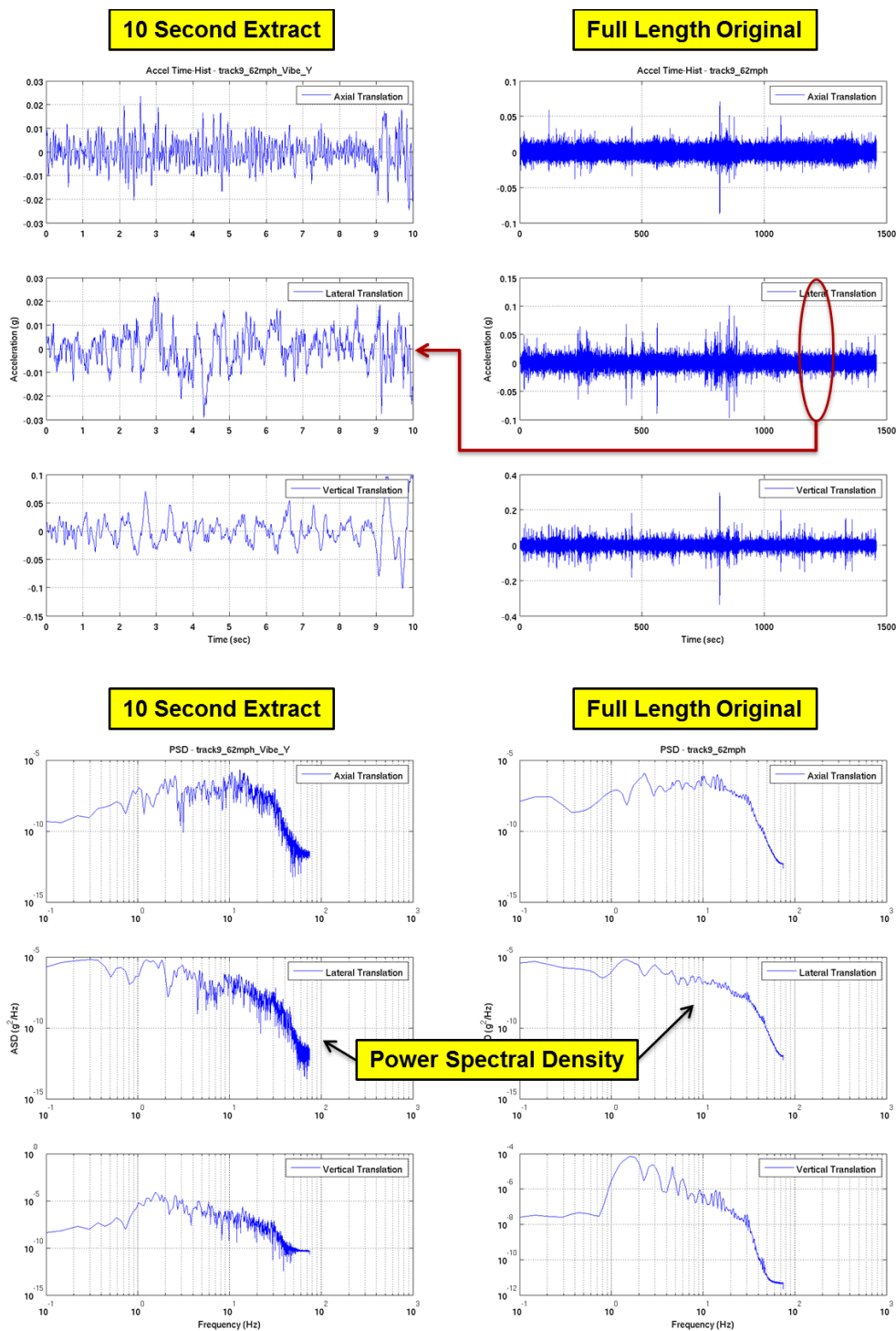
Figure 5.13 P3 Vibration Y (Lateral) Load Case Comparison with Full Length Snapshot

USED FUEL DISPOSITION CAMPAIGN
Used Nuclear Fuel Loading and Structural Performance Under Normal Conditions of Transport -
Demonstration of Approach and Results of Used Fuel Performance Characterization
SEPTEMBER 30, 2013   **55**

The P3 Vibration Z (Vertical) load case is comprised of the ten-second segment from 1085.0 seconds to 1095.0 seconds of the 62 mph Track 9 snapshot. Figure 5.14 illustrates pertinent details of the ten-second load case in comparison with the full length snapshot. The PSD g_{rms} value for the ten-second window of 0.00805 g is nearly equal to the g_{rms} value for the full length snapshot (which includes shock events) of 0.00870 g.

USED FUEL DISPOSITION CAMPAIGN
Used Nuclear Fuel Loading and Structural Performance Under Normal Conditions of Transport -
Demonstration of Approach and Results of Used Fuel Performance Characterization
56   **SEPTEMBER 30, 2013**
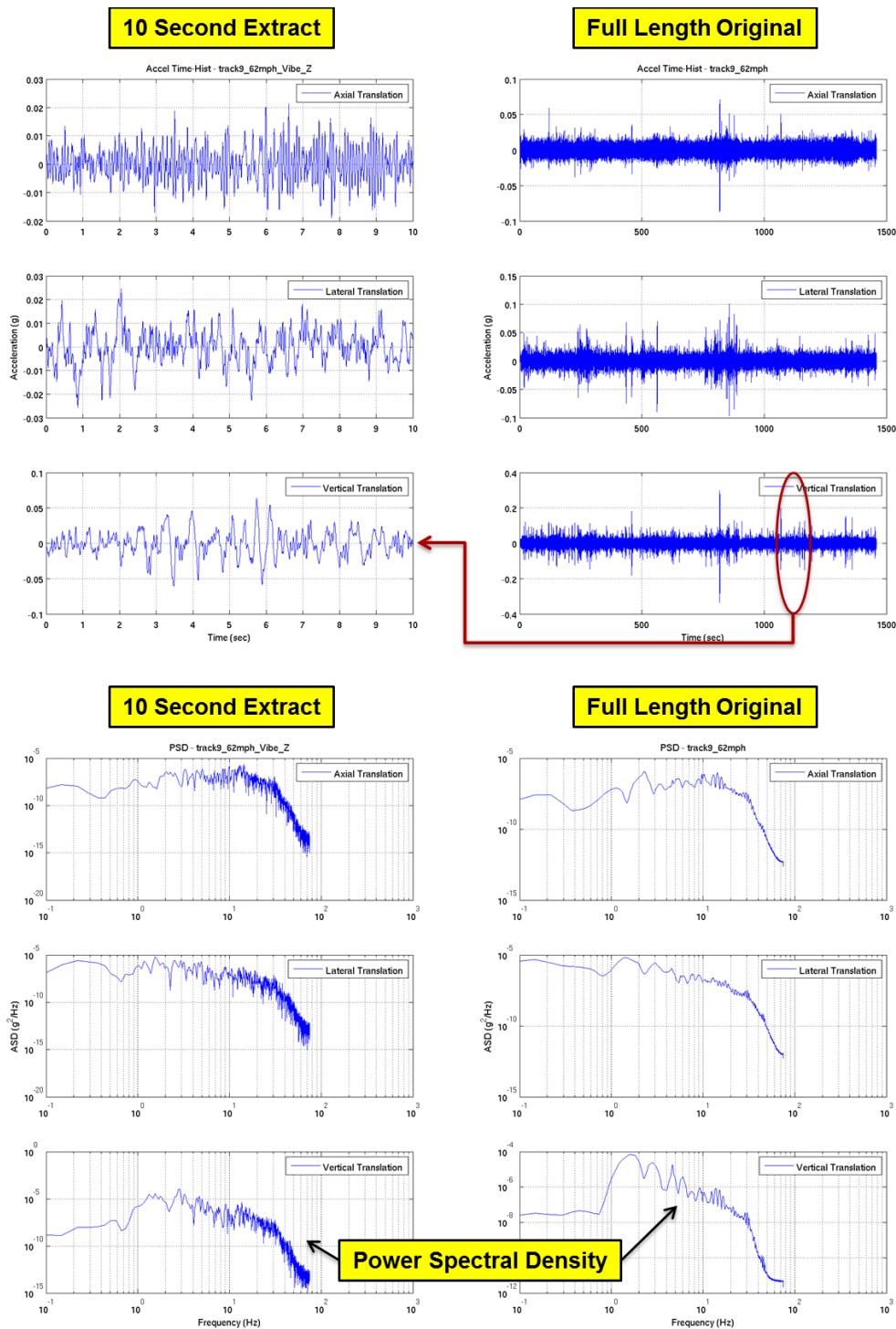
Figure 5.14 P3 Vibration Z (Vertical) Load Case Comparison with Full Length Snapshot

USED FUEL DISPOSITION CAMPAIGN
Used Nuclear Fuel Loading and Structural Performance Under Normal Conditions of Transport -
Demonstration of Approach and Results of Used Fuel Performance Characterization
SEPTEMBER 30, 2013 57

5.1.3   COMPARISON OF P1, P3, AND NUREG CR-0128 LOADS

NUREG/CR-0128 (Magnuson 1980) defines shock and vibration environments for large shipping containers transported by truck. NUREG/CR-0128 is referenced in the vibration environment definition and requirements section (§2.5.6.5) of the U.S. Nuclear Regulatory Commission's "Standard Review Plan for Transportation Packages for Radioactive Materials" (NUREG-1609 1999). For this reason it is appropriate to compare the P1 and P3 load cases discussed above with those described in NUREG/CR-0128 to gain a sense of how similar the rail transportation loads defined here are to those for truck transport (as defined by NUREG/CR-0128).

NUREG/CR-0128 defines shock and vibration environments for two packages, one with a total weight of 44,000 lbs and a second package with a total weight of 56,000 lbs. Figure 5.15a shows a comparison of SRS for the NUREG/CR-0128 shock environment and the P1 and P3 Shock Z (Vertical) load cases. The P1 Shock Z (Vertical) load case is very similar to the NUREG/CR-0128 shock environment, with the most pronounced difference being between 1 and 3 Hz in which the P1 load case shows an increased response magnitude over that of the NUREG/CR-0128 environment. Between 1 and 2 Hz the P3 Shock Z (Vertical) load case is much more in-line with the NUREG/CR-0128 shock environment; however, at frequencies above 2 Hz the P3 load case produces a response well below that of the NUREG/CR-0128 shock environment (approximately 0.4 g versus 1.1 g, respectively). Based on this, the P1 load case can be considered of similar severity to the shock environment defined by NUREG/CR-0128, with the P1 load case potentially producing a response in excess of the NUREG/CR-0128 environment if the cradle/cask/canister/basket/fuel-assembly system responds strongly in the 1 to 3 Hz frequency range. In addition, the P3 load case can be considered more benign than the environment defined by NUREG/CR-0128, unless the cradle/cask/canister/basket/fuel-assembly responds strongly in the 1 to 2 Hz frequency range, in which case the P3 load case and the NUREG/CR-0128 shock environment may produce a response comparable in their severity. For this particular case a rail car was assumed, but when a rail car is designed, the response of the fuel assemblies should be considered.

Figure 5.15b shows a comparison of the envelope of the PSD curves for the NUREG/CR-0128 vibration environments and the PSD curves for the P1 and P3 Vibration Z (Vertical) load cases. Both the P1 and P3 vibration environments contain significantly less power than the NUREG/CR-0128 vibration environment across the frequency range from 1 to 500 Hz. Based on this, the P1 and P3 Vibration Z (Vertical) load cases can be considered more benign than the vibration environments defined by NUREG/CR-0128.

USED FUEL DISPOSITION CAMPAIGN
Used Nuclear Fuel Loading and Structural Performance Under Normal Conditions of Transport -
Demonstration of Approach and Results of Used Fuel Performance Characterization
58 **SEPTEMBER 30, 2013**

Shock Response Spectrum
NUREG CR-0128 vs. P1 and P3 Shock Vertical Load Cases

(a) Shock

Power Spectral Density
NUREG CR-0128 vs. P1 and P3 Vibe Vertical Load Cases

(b) Vibration

Figure 5.15 Comparison of the P1 and P3 Load Cases with the NUREG/CR-0128 Shock and
Vibration Load Environments

USED FUEL DISPOSITION CAMPAIGN
Used Nuclear Fuel Loading and Structural Performance Under Normal Conditions of Transport -
Demonstration of Approach and Results of Used Fuel Performance Characterization
SEPTEMBER 30, 2013   59

5.2   COMPONENT MATERIAL PROPERTIES

Material property correlations for irradiated fuel, cladding, and other assembly components (e.g., grid spacers) have been provided in the Material Properties Handbook (Geelhood 2013). This document also includes material property correlations for the materials in the generic burnup cask (GBC)-32. Since the release of the Material Properties Handbook, the M&S team has requested elastic modulus and density for the neutron shield material used in the GBC-32.

Properties are given below based on values for NS-4-FR given in the NAC International Technical Data Brochure (Danner 1994).

Elastic Modulus: 3.87 GPa
Density: 1.68 g/cm³

The M&S team has exclusively used the material property correlations in the Material Properties Handbook and the properties for the neutron shield material given above.

5.3   COMPONENT TEMPERATURES

A preexisting ANSYS model was utilized to calculate approximate temperatures of various components in a Holtec HI-STAR 100 with an MPC-24 containing Westinghouse WE 17×17 fuel assemblies (Adkins et al. 2006). These temperatures are representative enough of the GBC-32 because of the moderate thermal influence on thermal material properties of the packaging and payload components. These temperature calculations were performed as a function of decay heat within the fuel assembly payload and ambient temperature outside the package. Component temperatures are provided for two limiting cases. The maximum heat load with a high ambient temperature will provide upper bound component temperatures. The minimum heat load with a low ambient temperature will provide lower bound component temperatures.

The maximum decay heat load case used a total distributive heat load of 20 kW and an ambient temperature of 38°C which represents the upper limit that can be transported by the system on an normal hot day per 10 CFR 71.71 (2005). The minimum heat load case used a heat load of 2.7 kW and an ambient temperature of -29°C which represents fuel cooled for 300 years and transported on a normal cold day per 10 CFR 71.71 (2005). Average and maximum component temperatures for each of these cases are shown in Table 5.3. If more detail is desired by the M&S team, the fuel and basket temperatures are shown in Table 5.4 at various axial and radial regions within the GBC-32. Approximate locations of these axial and radial regions are shown in Figure 5.16 and Figure 5.17, respectively.

USED FUEL DISPOSITION CAMPAIGN
**Used Nuclear Fuel Loading and Structural Performance Under Normal Conditions of Transport -
Demonstration of Approach and Results of Used Fuel Performance Characterization**
60 **SEPTEMBER 30, 2013**

Table 5.3. Component Average and Maximum Temperatures for Maximum and Minimum Heat Load Conditions

Component	Maximum Heat Load		Minimum Heat Load	
	Average Temperature	Maximum Temperature	Average Temperature	Maximum Temperature
Fuel	304°C	392°C	56°C	83°C
Basket	293°C	381°C	53°C	79°C
Canister-Right*	141°C	168°C	15°C	19°C
Canister-Side*	149°C	169°C	16°C	21°C
Canister-Left*	227°C	287°C	30°C	41°C
Neutron Shield	103°C	125°C	9°C	14°C
Cask Skin	97°C	123°C	8°C	13°C
Impact Limiters	71°C	109°C	4°C	6°C

*Right and left are the top and bottom of the canister, respectively. The side isaround the diameter of the cask.

Table 5.4. Fuel and Basket Temperatures for Maximum and Minimum Heat Load Conditions in Various Axial and Radial Regions

Location Axial Region: Radial Region*	Maximum Heat Load		Minimum Heat Load	
	Fuel Temperature	Basket Temperature	Fuel Temperature	Basket Temperature
1:1	277°C	281°C	46°C	46°C
1:2	240°C	239°C	38°C	38°C
1:3	199°C	195°C	29°C	29°C
2:1	359°C	355°C	71°C	70°C
2:2	314°C	303°C	60°C	57°C
2:3	261°C	246°C	46°C	43°C
3:1	368°C	363°C	75°C	74°C
3:2	323°C	311°C	63°C	60°C
3:3	270°C	254°C	49°C	46°C
4:1	336°C	330°C	59°C	57°C
4:2	293°C	283°C	50°C	47°C
4:3	246°C	234°C	39°C	37°C

*Axial region midpoints are 471, 358, 246, and 134 cm from bottom of the left end of the cask. Radial region midpoints are 41, 69, and 86 cm from the centerline.

USED FUEL DISPOSITION CAMPAIGN
Used Nuclear Fuel Loading and Structural Performance Under Normal Conditions of Transport -
Demonstration of Approach and Results of Used Fuel Performance Characterization
SEPTEMBER 30, 2013 61
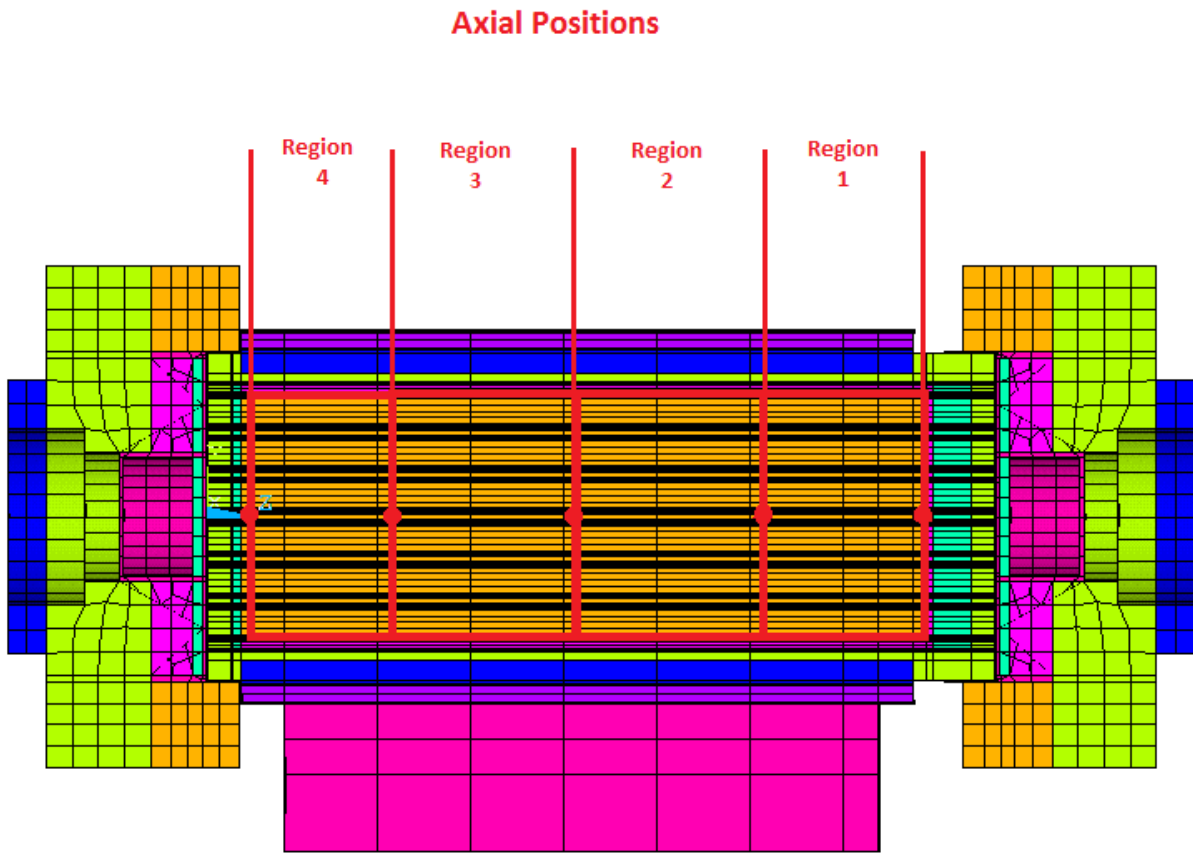
Figure 5.16. Approximate Axial Locations for Fuel and Basket Temperatures

USED FUEL DISPOSITION CAMPAIGN
Used Nuclear Fuel Loading and Structural Performance Under Normal Conditions of Transport -
Demonstration of Approach and Results of Used Fuel Performance Characterization
62 **SEPTEMBER 30, 2013**
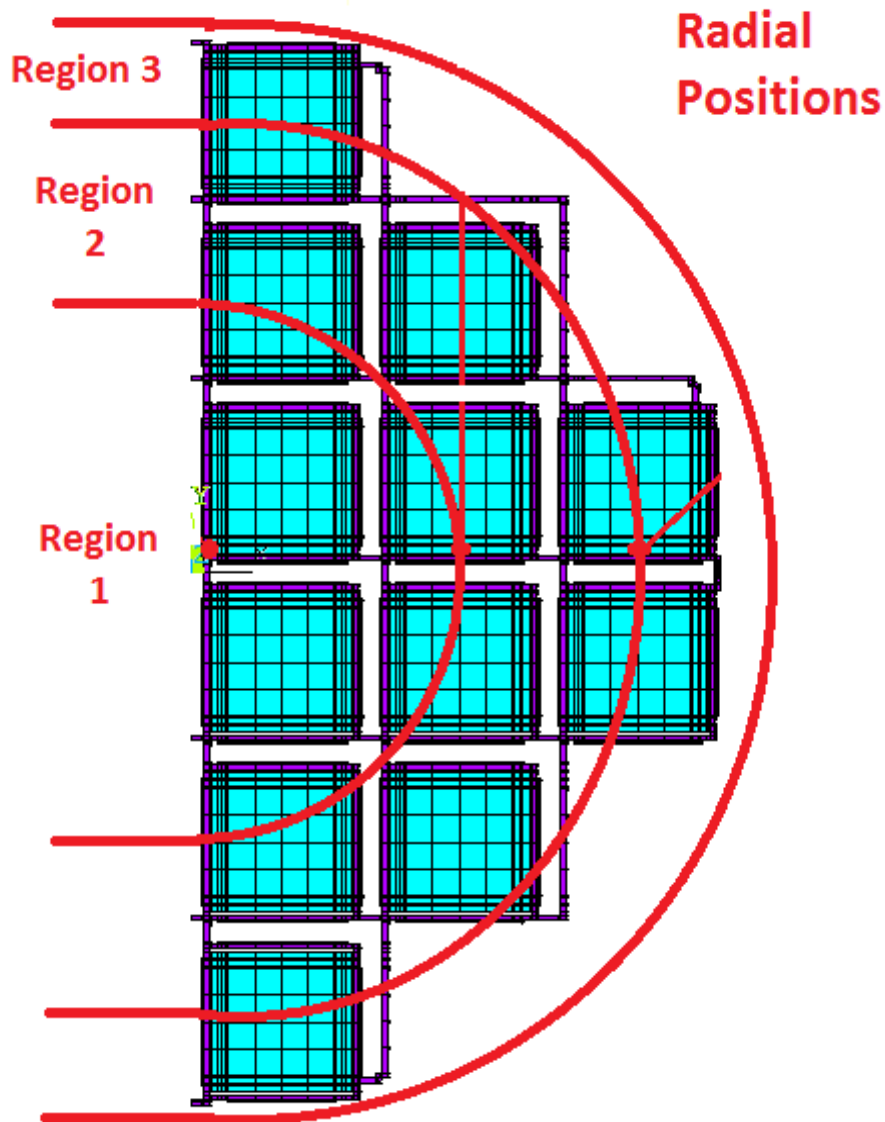
Figure 5.17. Approximate Radial Locations for Fuel and Basket Temperatures

5.4   FUEL AND ASSEMBLY POST-IRRADIATION CONDITIONS

In addition to providing MP correlations for the components in the fuel assemblies and the GBC-32, the Material Properties Handbook (Geelhood 2013) also contains a section that provides representative conditions of fuel rods as a function of burnup and axial location. These conditions include burnup level, fast neutron fluence, corrosion layer thickness and hydrogen content. All of these parameters are input values to various correlations described in the Material Properties Handbook (Geelhood 2013). These tables are reproduced below and were used as necessary to provide initial conditions for the fuel rods being modeled under this initiative.

USED FUEL DISPOSITION CAMPAIGN
**Used Nuclear Fuel Loading and Structural Performance Under Normal Conditions of Transport -
Demonstration of Approach and Results of Used Fuel Performance Characterization
SEPTEMBER 30, 2013** 63

The following tables (Table 5.5 through Table 5.8) show typical conditions at 1-ft intervals for the peak fuel rod from assemblies discharged at 30, 40, 50, and 55 GWd/MTU assembly average burnup. These tables were developed with calculations from FRAPCON-3.4 (Geelhood et al. 2010). No fuel cladding gap is predicted in moderate-to-high burnup fuel when cooled to room temperature. The contact pressure is removed, but there is no effective gap predicted beyond the sum of the fuel and cladding roughness (about 2.5 μm). The conditions shown in these tables are for the peak rod in the assembly. These conditions were conservatively used for all the rods in an assembly. The oxide layer predicted was assumed to be in place on the rod, but offer no load-carrying capability. The cladding should be thinned using the Pillings-Bedworth ratio as discussed in the Material Properties Handbook (Geelhood 2013).

Table 5.5. Typical Conditions for Peak Fuel Rod from PWR Westinghouse 17×17 Fuel Assembly Discharged at Assembly Average Burnup of 30 GWd/MTU

		PWR Westinghouse 17x17 Fuel Assembly								
		Assembly Average Burnup	30 GWd/MTU	Cladding material: Zircaloy-4						
		Peak Rod Average Burnup	32.1 GWd/MTU	Peak Rod Fast Neutron Fluence				5.36E+25 n/m²		
Upper Plenum		Gas Composition 99.0% He, 0.8% Xe, 0.2% Kr			Total void volume = 10.43 cm³			Total Gas = 1.7e-2 Moles		
		Local Burnup	Local Fast Neutron Fluence	Corrosion layer Thickness	Metal Consumed	Hydrogen Concentration	Excess Hydrogen @ 20°C	Excess Hydrogen @ 100°C	Excess Hydrogen @ 200°C	Excess Hydrogen @ 300°C	Excess Hydrogen @ 400°C
		GWd/MTU	n/m²	μm	μm	ppm	ppm	ppm	ppm	ppm	ppm
node 12		24.5	4.11E+25	29.1	18.7	243	243	242	230	178	43
node 11		31.1	5.20E+25	33.8	21.7	281	281	280	268	216	81
node 10		34.1	5.71E+25	33.7	21.6	281	281	280	268	216	81
node 9		34.7	5.81E+25	27.8	17.8	232	232	231	219	167	32
node 8		34.7	5.81E+25	24.3	15.6	204	204	203	191	139	4
node 7		34.7	5.80E+25	19.5	12.5	166	166	165	153	101	0
node 6		34.6	5.79E+25	17.1	11	146	146	145	133	81	0
node 5		34.6	5.78E+25	13.7	8.8	119	119	118	106	54	0
node 4		34.5	5.78E+25	11	7.1	97	97	96	84	32	0
node 3		33.7	5.65E+25	7.8	5	72	72	71	59	7	0
node 2		29.8	4.99E+25	5.1	3.3	50	50	49	37	0	0
node 1		23.4	3.92E+25	2	1.3	26	26	25	13	0	0

USED FUEL DISPOSITION CAMPAIGN
Used Nuclear Fuel Loading and Structural Performance Under Normal Conditions of Transport -
Demonstration of Approach and Results of Used Fuel Performance Characterization
64   **SEPTEMBER 30, 2013**

Table 5.6. Typical Conditions for Peak Fuel Rod from PWR Westinghouse 17×17 Fuel Assembly Discharged at Assembly Average Burnup of 40 GWd/MTU

		PWR Westinghouse 17x17 Fuel Assembly									
		Assembly Average Burnup	40 GWd/MTU	Cladding material: Zircaloy-4							
		Peak Rod Average Burnup	42.6 GWd/MTU	Peak Rod Fast Neutron Fluence			7.13E+25 n/m²				
Upper Plenum		Gas Composition 96.0% He, 3.4% Xe, 0.6% Kr			Total void volume = 10.57 cm³			Total Gas = 1.7e-2 Moles			
		Local Burnup GWd/MTU	Local Fast Neutron Fluence n/m²	Corrosion layer Thickness µm	Metal Consumed µm	Hydrogen Concentration ppm	Excess Hydrogen @ 20°C ppm	Excess Hydrogen @ 100°C ppm	Excess Hydrogen @ 200°C ppm	Excess Hydrogen @ 300°C ppm	Excess Hydrogen @ 400°C ppm
node 12		32.6	5.46E+25	42.5	27.2	353	353	352	340	288	153
node 11		41.3	6.92E+25	51.3	32.9	426	426	425	413	361	226
node 10		45.4	7.60E+25	51.8	33.2	430	430	429	417	365	230
node 9		46.1	7.72E+25	42.7	27.4	355	355	354	342	290	155
node 8		46.2	7.73E+25	36.9	23.7	307	307	306	294	242	107
node 7		46.1	7.71E+25	29.8	19.1	248	248	247	235	183	48
node 6		46	7.70E+25	25.7	16.5	215	215	214	202	150	15
node 5		45.9	7.69E+25	20.9	13.4	176	176	175	163	111	0
node 4		45.9	7.68E+25	17	10.9	145	145	144	132	80	0
node 3		44.8	7.51E+25	12.6	8.1	110	110	109	97	45	0
node 2		39.6	6.63E+25	8.6	5.5	78	78	77	65	13	0
node 1		31.1	5.21E+25	4.4	2.8	45	45	44	32	0	0

USED FUEL DISPOSITION CAMPAIGN
Used Nuclear Fuel Loading and Structural Performance Under Normal Conditions of Transport -
Demonstration of Approach and Results of Used Fuel Performance Characterization
SEPTEMBER 30, 2013   65

Table 5.7. Typical Conditions for Peak Fuel Rod from PWR Westinghouse 17×17 Fuel
Assembly Discharged at Assembly Average Burnup of 50 GWd/MTU

PWR Westinghouse 17x17 Fuel Assembly

Assembly Average Burnup	50 GWd/MTU	Cladding material: Zircaloy-4	
Peak Rod Average Burnup	53.7 GWd/MTU	Peak Rod Fast Neutron Fluence	8.99E+25 n/m²

Upper Plenum — Gas Composition 88.2% He, 10.0% Xe, 1.8% Kr — Total void volume = 10.81 cm³ — Total Gas = 1.9e-2 Moles

	Local Burnup GWd/MTU	Local Fast Neutron Fluence n/m²	Corrosion layer Thickness μm	Metal Consumed μm	Hydrogen Concentration ppm	Excess Hydrogen @ 20°C ppm	Excess Hydrogen @ 100°C ppm	Excess Hydrogen @ 200°C ppm	Excess Hydrogen @ 300°C ppm	Excess Hydrogen @ 400°C ppm
node 12	41.2	6.89E+25	56.8	36.4	472	472	471	459	407	272
node 11	52.1	8.73E+25	71.2	45.6	593	593	592	580	528	393
node 10	57.3	9.58E+25	72.9	46.7	608	608	607	595	543	408
node 9	58.2	9.74E+25	59.8	38.3	497	497	496	484	432	297
node 8	58.2	9.75E+25	50.9	32.6	423	423	422	410	358	223
node 7	58.1	9.73E+25	41	26.3	341	341	340	328	276	141
node 6	58.1	9.72E+25	35.1	22.5	292	292	291	279	227	92
node 5	58	9.70E+25	28.6	18.3	239	239	238	226	174	39
node 4	57.9	9.69E+25	23.5	15.1	197	197	196	184	132	0
node 3	56.6	9.47E+25	17.9	11.5	152	152	151	139	87	0
node 2	49.9	8.36E+25	12.4	7.9	109	109	108	96	44	0
node 1	39.3	6.58E+25	7.1	4.6	66	66	65	53	1	0

Table 5.8. Typical Conditions for Peak Fuel Rod from PWR Westinghouse 17×17 Fuel
Assembly Discharged at Assembly Average Burnup of 55 GWd/MTU

PWR Westinghouse 17x17 Fuel Assembly

Assembly Average Burnup	55 GWd/MTU	Cladding material: Zircaloy-4	
Peak Rod Average Burnup	58.87 GWd/MTU	Peak Rod Fast Neutron Fluence	9.85E+25 n/m²

Upper Plenum — Gas Composition 84.0% He, 13.6% Xe, 2.4% Kr — Total void volume = 10.94 cm³ — Total Gas = 2.0e-2 Moles

	Local Burnup GWd/MTU	Local Fast Neutron Fluence n/m²	Corrosion layer Thickness μm	Metal Consumed μm	Hydrogen Concentration ppm	Excess Hydrogen @ 20°C ppm	Excess Hydrogen @ 100°C ppm	Excess Hydrogen @ 200°C ppm	Excess Hydrogen @ 300°C ppm	Excess Hydrogen @ 400°C ppm
node 12	45.1	7.55E+25	62.8	40.3	522	522	521	509	457	322
node 11	57.1	9.56E+25	79.7	51.1	666	666	665	653	601	466
node 10	62.7	1.05E+26	82.1	52.6	687	687	686	674	622	487
node 9	63.8	1.07E+26	67.2	43.1	560	560	559	547	495	360
node 8	63.8	1.07E+26	57	36.5	474	474	473	461	409	274
node 7	63.7	1.07E+26	45.9	29.4	381	381	380	368	316	181
node 6	63.6	1.07E+26	39.2	25.1	326	326	325	313	261	126
node 5	63.5	1.06E+26	32.1	20.6	267	267	266	254	202	67
node 4	63.4	1.06E+26	26.4	16.9	221	221	220	208	156	21
node 3	62	1.04E+26	20.2	12.9	171	171	170	158	106	0
node 2	54.7	9.16E+25	14.2	9.1	123	123	122	110	58	0
node 1	43.1	7.21E+25	8.4	5.4	77	77	76	64	12	0

USED FUEL DISPOSITION CAMPAIGN
Used Nuclear Fuel Loading and Structural Performance Under Normal Conditions of Transport -
Demonstration of Approach and Results of Used Fuel Performance Characterization
66   **SEPTEMBER 30, 2013**

It is acknowledged that the conditions described here are those of the fuel rod immediately upon discharge from the reactor. It is possible that the conditions of vacuum drying (up to 400°C) and extended dry cask storage (20°C to 400°C for 20 to 60 years) could change the MP and initial conditions provided in the Material Properties Handbook.

One possibility includes hydride reorientation due to the vacuum drying operation. Typically the hydrides in PWR Zircaloy-4 cladding are circumferentially oriented and primarily located in a dense hydride rim along the outer edge of the cladding. If a significant number reorient to the radial direction, it can cause brittle failure to occur in the cladding by providing an easy path for a crack to propagate through the cladding thickness. When hydride reorientation is observed, brittle failure has been observed before yielding of the clad occurs. Work is currently underway on this initiative and other initiatives to evaluate if hydride reorientation has occurred in fuel currently being stored in dry casks, and if so, what the impact on failure or ductility is. The possibility of hydride reorientation will not be examined in the modeling work under the current initiative, although the results of the modeling work for this initiative can be used to assist in assessing the impact of hydride reorientation if it is found to have occurred.

Another possibility includes low temperature/long-term annealing of the irradiation damage in the cladding. Irradiation damage significantly increases the strength of Zircaloy-4 and slightly increases the elastic modulus of Zircaloy-4. If this damage is annealed out, the strength and modulus could be reduced and approach their unirradiated values. Sensitivity studies were performed by the M&S team as described in Adkins (2013d) to address the impact of low temperature/long-term annealing following extended dry cask storage.

One of the sensitivities that was performed is to evaluate the impact of clad thinning due to in-reactor fretting on the potential for failure. In order to perform this sensitivity, it should be assumed that the cladding could be up to 10% thinner in the locations contacted by the springs and dimples on the grid spacers.

One other initial condition is the degree of fuel-clad bonding that has occurred during in-reactor service. It is known that at moderate to high burnup, a fuel-clad bonding layer forms. However, the properties of this layer such as strength or effective friction coefficient are poorly characterized. Therefore, one of the sensitivity studies described in Adkins (2013d) will assess the impact of this uncertainty by evaluating the case with no fuel-clad bonding, and the case with perfect fuel-clad bonding.

5.5 CASK, CANISTER, AND FUEL ASSEMBLY GEOMETRY

The geometry for the rail car conveyance, cask, canister, basket, fuel assemblies, and fuel rods has been defined and a consistent set of values is being used for the modeling at three discreet levels. Figure 5.18 to Figure 5.23 show model overviews of these various components. Table 5.9 lists the dimensions and moments of inertia for the rail car conveyance. Table 5.10 lists the dimensions for the cask assembly. Table 5.11 lists the dimensions for the canister and basket. Table 5.12 lists the dimensions for the fuel assembly spacer blocks. Table 5.13 lists the dimensions for the fuel rods and the fuel assembly.

USED FUEL DISPOSITION CAMPAIGN
Used Nuclear Fuel Loading and Structural Performance Under Normal Conditions of Transport -
Demonstration of Approach and Results of Used Fuel Performance Characterization
SEPTEMBER 30, 2013   **67**
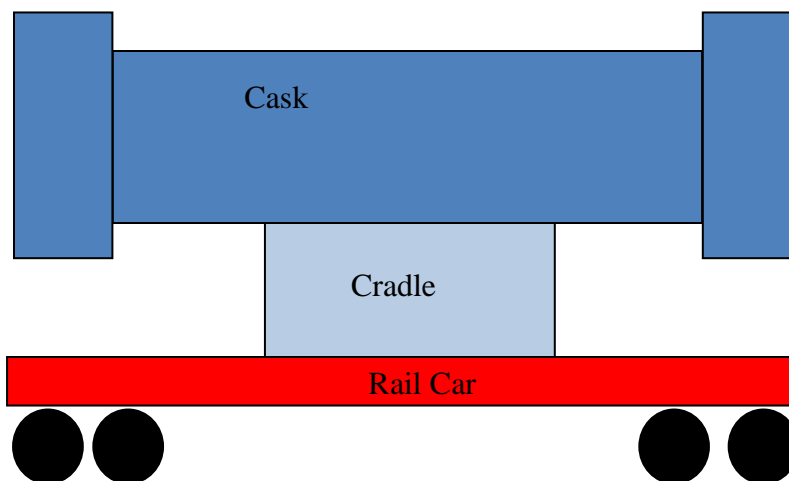
Figure 5.18. Model Overview of Rail Car Conveyance

Table 5.9. Dimensions and Moments of Inertia for the Rail Car Conveyance

Dimension	Value
Total Cask Length with Impact Limiters	7.26 m
Height of Cask above Rail Car Deck	3.40 m
Height of Cask Center of Gravity above Rail Car Deck	1.775 m
Gap between Rail Car Deck and Impact Limiter	0.15 m
Cradle height	1.775 m
Cradle width	2.550 m
Cradle length	4.510 m
Height of Cradle Center of Gravity above Rail Car Deck	0.8875 m
Moment of inertia of cask with impact limiters about center of gravity	
IXX	490300 kg-m²
IYY	490800 kg-m²
IZZ	104100 kg-m²
Moment of inertia of cradle about center of gravity	
IXX	26638 kg-m²
IYY	30439 kg-m²
IZZ	10946 kg-m²
Moment of inertia of cradle about top of rail car deck	
IXX	37356 kg-m²
IYY	30439 kg-m²
IZZ	21665 kg-m²
Mass of cradle	13600 kg

USED FUEL DISPOSITION CAMPAIGN
Used Nuclear Fuel Loading and Structural Performance Under Normal Conditions of Transport -
Demonstration of Approach and Results of Used Fuel Performance Characterization
68   **SEPTEMBER 30, 2013**
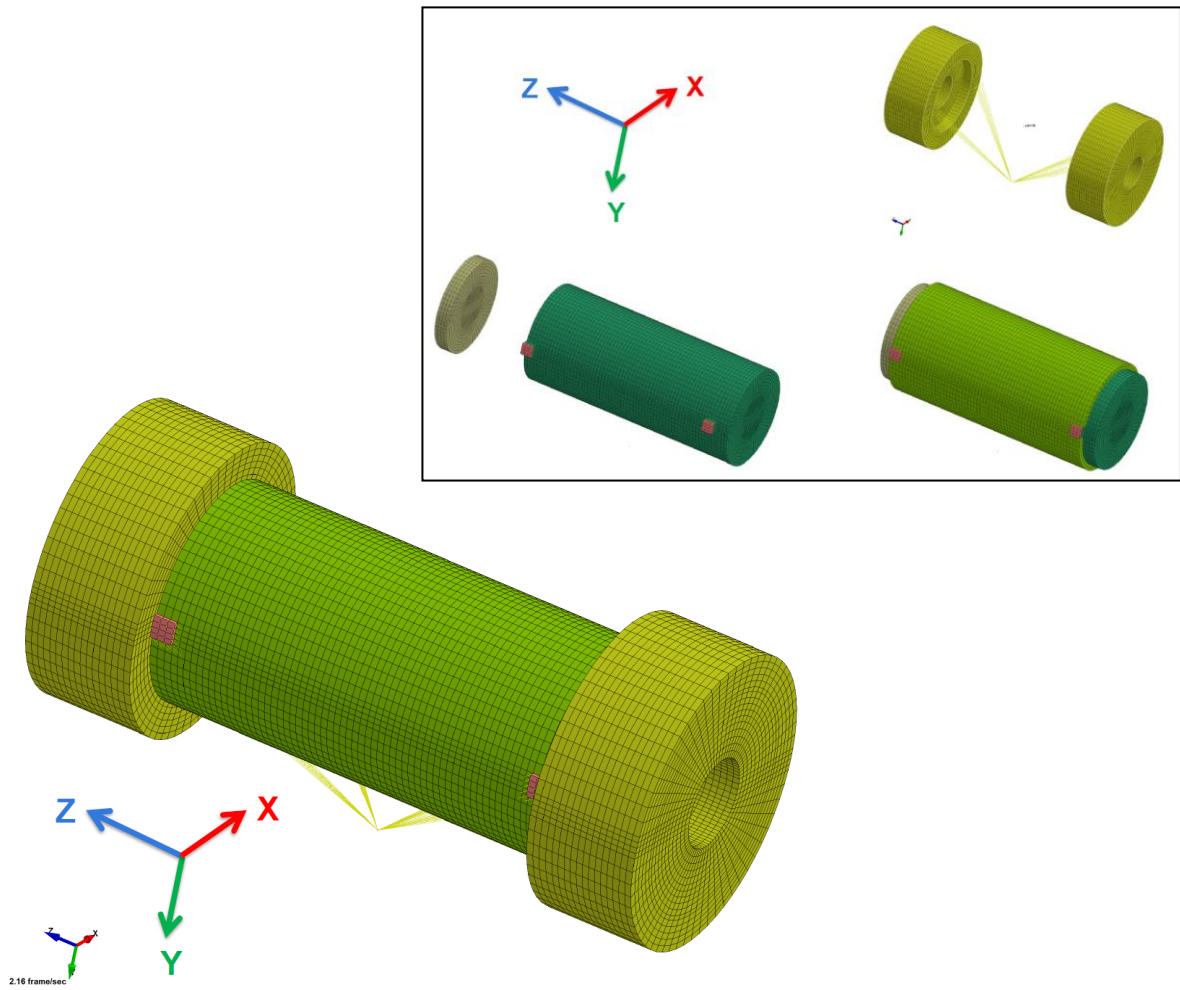
Figure 5.19. Model Overview of Cask and Cask Components

USED FUEL DISPOSITION CAMPAIGN
Used Nuclear Fuel Loading and Structural Performance Under Normal Conditions of Transport -
Demonstration of Approach and Results of Used Fuel Performance Characterization
SEPTEMBER 30, 2013 69

Table 5.10. Dimensions for Cask Assembly

Dimension	Value
Cask Body Outer Length	5.360 m
Cask Body Outer Diameter	5.360 m
Cask Body Radial Wall Thickness	200 mm
Cask Body Top Thickness	300 mm
Cask Body Bottom Thickness	300 mm
Trunnion Size (Length and Width)	250 mm
Trunnion Radial Distance from Cask Centerline	1.275 m
Trunnion Axial Distance From Cask Mid-Point	2.255 m
Neutron Shield Length	4.760 m
Neutron Shield Outer Diameter	2.450 m
Neutron Shield Radial Thickness	132.5 mm
Impact Limiter Length	1.250 m
Impact Limiter Cask Overlap Length	300 mm
Impact Limiter Outer Diameter	3.250 m
Impact Limiter Inner Diameter	2.185 m
Impact Limiter Cutout Hole Diameter	1.000 m
Cask Center to Rail Car Deck Distance	1.775 m
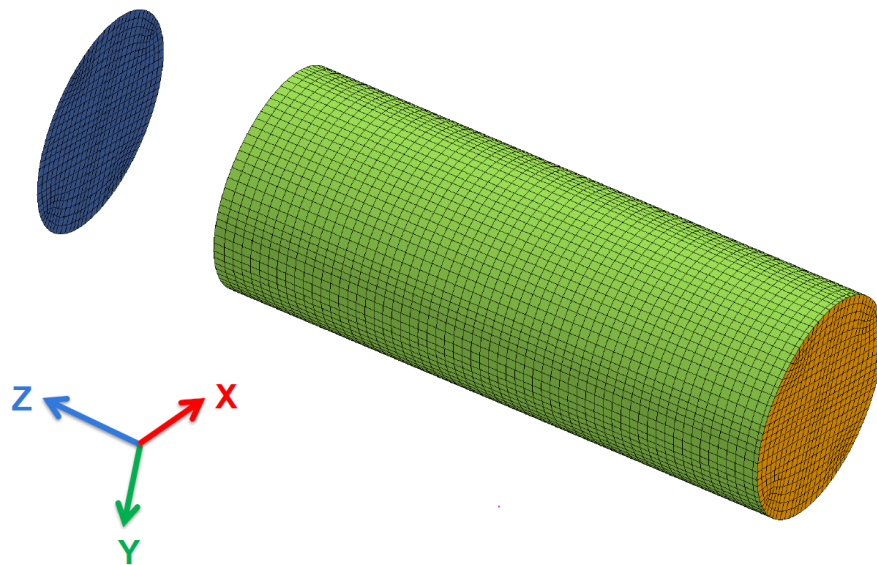
Figure 5.20. Model Overview of Canister

USED FUEL DISPOSITION CAMPAIGN
Used Nuclear Fuel Loading and Structural Performance Under Normal Conditions of Transport -
Demonstration of Approach and Results of Used Fuel Performance Characterization
70   **SEPTEMBER 30, 2013**
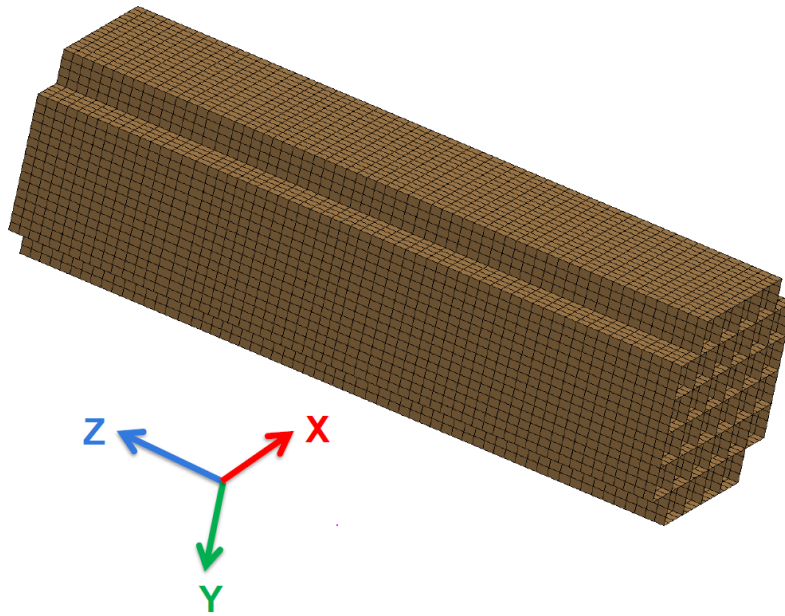
Figure 5.21. Model Overview of Basket

Table 5.11. Dimensions for Canister and Basket

Dimension	Value
Canister Outer Length	4.750 m
Canister Radial Wall Thickness	12.5 mm
Canister Top Thickness	150 mm
Canister Bottom Thickness	50 mm
Basket Lateral Support Structure Wall Thickness	7.5 mm
Canister to Cask Clearance	5.0 mm
Basket Cell Length	4.525 m
Basket Cell Configuration	4-6-6-6-6-4
Basket Cell Inside Dimension (Including Boral Panel)	220 mm
Basket Cell Wall Thickness Without Boral Panel	7.5 mm
Basket Boral Panel Thickness	2.5 mm
Basket Cell Wall Thickness Including Boral Panel	10 mm
Basket Cell Centerline to Cell Centerline Spacing (Pitch)	230 mm
Basket Boral Panel Width	190.5 mm
Basket Boral Panel Length	4.525 m
Basket Boral Panel Boron Carbide Thickness	2.0 mm
Basket Boral Panel Aluminum Face Sheet Thickness (x2)	0.25 mm
Basket Outer Dimensions	1.3875 m
Basket to Canister Lateral Clearance	5.0 mm
Basket to Canister Axial Clearance	12.5 mm

USED FUEL DISPOSITION CAMPAIGN
Used Nuclear Fuel Loading and Structural Performance Under Normal Conditions of Transport -
Demonstration of Approach and Results of Used Fuel Performance Characterization
SEPTEMBER 30, 2013 **71**
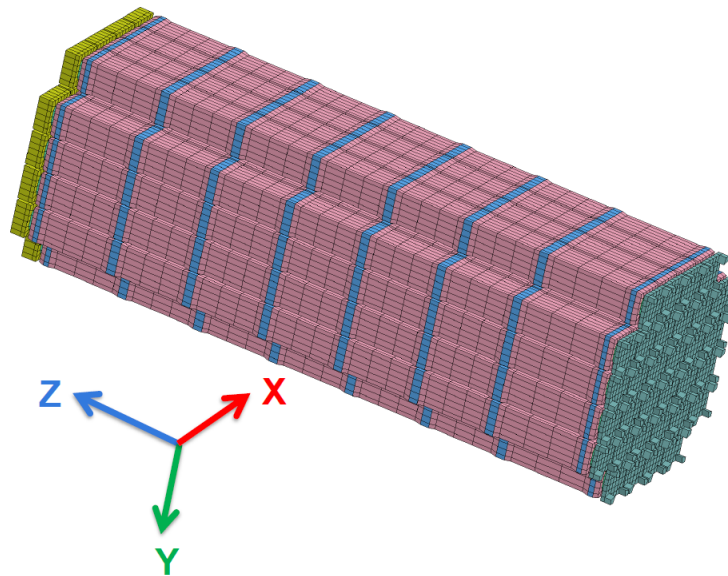
Figure 5.22. Model Overview of Fuel Assemblies

Table 5.12. Dimensions for Fuel Assembly Spacer Blocks

Dimension	Value
Fuel Assembly to Spacer Block Axial Clearance	10 mm
Bottom Spacer Block Wall Thickness	10 mm
Bottom Spacer Block Lateral Clearance to Basket	5 mm
Bottom Spacer Block Length	140 mm
Bottom Spacer Block Size	210 mm
Bottom Spacer Block Stepped Down Tube Size	160 mm
Top Spacer Block Wall Thickness	10 mm
Top Spacer Block Lateral Clearance to Basket	50 mm
Top Spacer Block Length	140 mm
Top Spacer Block Size	120 mm
Top Spacer Block Stepped Down Tube Size	70 mm

USED FUEL DISPOSITION CAMPAIGN
Used Nuclear Fuel Loading and Structural Performance Under Normal Conditions of Transport -
Demonstration of Approach and Results of Used Fuel Performance Characterization
72   **SEPTEMBER 30, 2013**
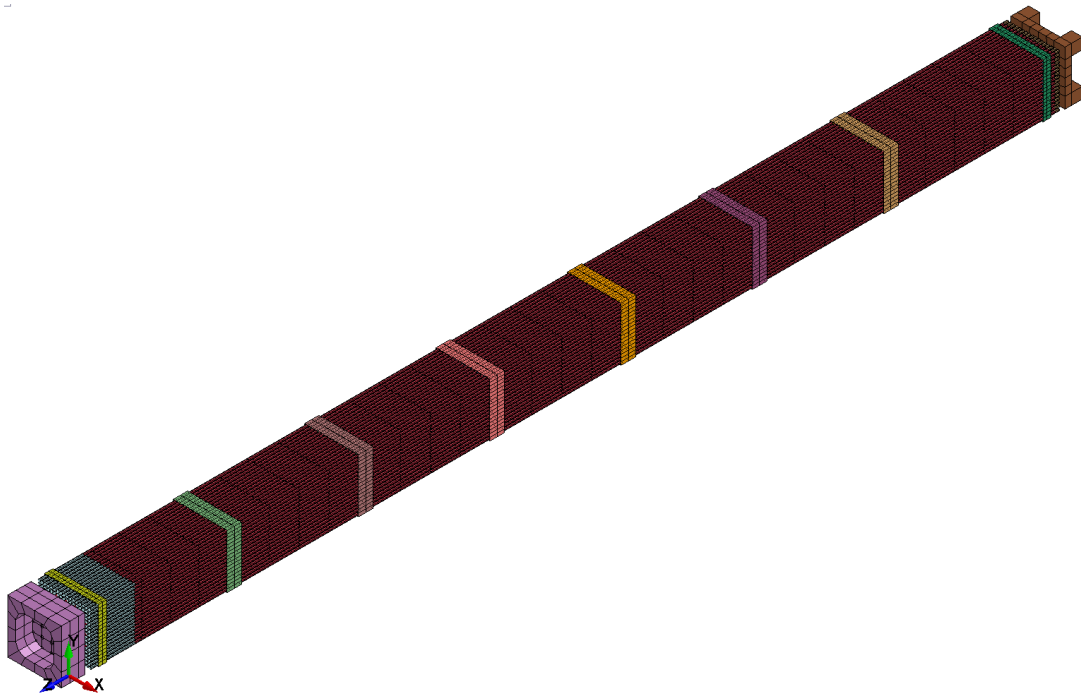
Figure 5.23. Model Overview of Single Fuel Assembly

Table 5.13. Dimensions for Fuel Rods and Fuel Assembly

Dimension	Value
Fuel rod cladding outer diameter	9.144 mm
Rod pitch	12.598 mm
Lower plenum/end plug outer diameter	9.144 mm
Lower plenum/end plug inner diameter	6.175 mm
Bottom plenum/end plug length	17.475 mm
Upper plenum/end plug outer diameter	9.144 mm
Upper plenum/end plug inner diameter	6.175 mm
Upper plenum/end plug length	176.454 mm
Guide tube outer diameter	12.04 mm
Guide tube inner diameter	11.43 mm
Intermediate (Zircaloy) spacer inner shell thickness	0.457 mm
Intermediate (Zircaloy) spacer outer shell thickness	0.66 mm
Intermediate (Zircaloy) spacer axial length	57.15 mm
Intermediate (Zircaloy) spacer horizontal width	214.2 mm
Top and bottom end (Inconel) spacer inner shell thickness	0.267 mm
Top and bottom end (Inconel) spacer outer shell thickness	0.432 mm
Top and bottom end (Inconel) spacer axial length	33.579 mm

USED FUEL DISPOSITION CAMPAIGN
Used Nuclear Fuel Loading and Structural Performance Under Normal Conditions of Transport -
Demonstration of Approach and Results of Used Fuel Performance Characterization
SEPTEMBER 30, 2013 73

Table 5.13 (continued)

Dimension	Value
Top and bottom end (Inconel) spacer horizontal width	214.2 mm
Fraction of total spacer grid length to the length from spacer grid edge to dimple	0.1
Bottom nozzle overall height	69.545 mm
Bottom nozzle width and depth	213.97 mm
Bottom nozzle plate thickness	25.4 mm
Bottom nozzle leg thickness	43.993 mm
Top nozzle overall height	93.218 mm
Top nozzle overall height with control rod assembly	285.2 mm
Top nozzle width and depth	213.462 mm
Top nozzle plate thickness	12.7 mm
Top nozzle side wall thickness	12.7 mm
Distance from base of bottom nozzle to:	
top of 1st spacer grid	157.226 mm
top of 2nd spacer grid	789.432 mm
top of 3rd spacer grid	1311.402 mm
top of 4th spacer grid	1833.372 mm
top of 5th spacer grid	2355.342 mm
top of 6th spacer grid	2877.312 mm
top of 7th spacer grid	3399.282 mm
top of 8th spacer grid	3910.584 mm
Distance from bottom of bottom nozzle to bottom of top nozzle	3.964813 m
Distance from top of bottom nozzle to bottom of fuel rods	19.901 mm
Distance from top of fuel rods to bottom of top nozzle	25.743 mm
Overall length of assembly (without hold down assembly)	4.058031 m
Overall length of assembly (with control rod assembly)	4.250 m

6. MODELING APPROACH AND BASIS

The general modeling approach is shown schematically in Figure 6.1 along with the identified inputs and outputs. The modeling and simulation methodology has been described in detail previously (Adkins 2013f). In general, the modeling and simulation approach consists of three levels of sub-models. As described in the Modeling, Simulation, and Experimental Integration

USED FUEL DISPOSITION CAMPAIGN
**Used Nuclear Fuel Loading and Structural Performance Under Normal Conditions of Transport -
Demonstration of Approach and Results of Used Fuel Performance Characterization**
74 **SEPTEMBER 30, 2013**

RD&D Plan (Adkins 2013b), this methodology will utilize finite element analysis sub-modeling techniques to accurately model the complete spent nuclear fuel transport system on the railcar (rail car, cask restraint structure, cask, basket, and fuel). This sub-modeling approach will allow for more detailed finite element models of individual system components, faster analysis run times for the individual sub-models, and flexibility when updating or modifying the sub-models to incorporate better excitation data, initial material properties, or other pertinent information. The cask modeling effort interfaces with the transportation loading (TL) Team by using excitations from the railcar bed. These excitation loads are used to define the boundary conditions for the fully loaded cask model. The system dynamics are then sequentially evaluated at the cask-level, fuel assembly-level, and fuel rod-level. The predicted loads and deformations on the fuel rods were finally output to the MP team for failure evaluation. All levels of sub-modeling used input component temperatures, fuel post-irradiation conditions and material properties from a common source as appropriate.
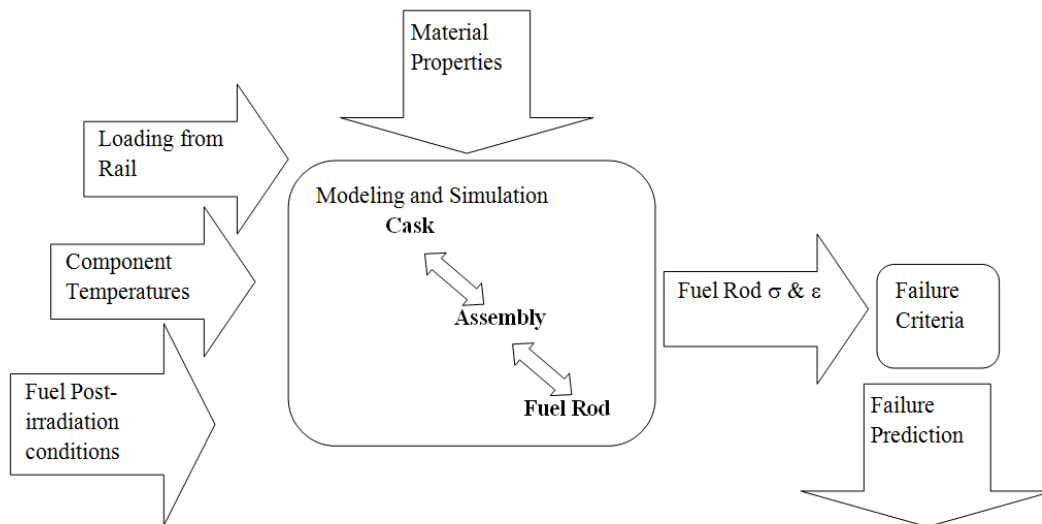
Figure 6.1. Overview of Modeling Approach with Inputs and Outputs

Final modeling inputs that will be used for each area identified in Figure 6.1 as well as the final geometry for the cask and the fuel assembly have been identified. Construction of model geometry, meshing, and implementation of material properties has been completed at each of the different levels of the modeling effort, and numerical results have been generated.

Section 8 will describe the results of the initial demonstration including the assessment of failure or no failure and the results from the sensitivity analyses.

USED FUEL DISPOSITION CAMPAIGN
Used Nuclear Fuel Loading and Structural Performance Under Normal Conditions of Transport -
Demonstration of Approach and Results of Used Fuel Performance Characterization
SEPTEMBER 30, 2013   75

6.1   MODELING APPROACH AT THE CASK-LEVEL

The cask FEM is the highest assembly-level FEM and the means by which loads at the fuel assembly, resulting from transportation environments defined at the rail car, were determined. Inputs to the model included material property and temperature distribution data provided in Geelhood (2013) and Adkins (2013e), rail car excitation data from TTCI (Adkins 2013e and Urban et al. 2013), and data defining the simplified sub-models used to represent the fuel assemblies from the Pacific Northwest National Laboratory (PNNL) detailed-fuel-assembly modeling team. Outputs from the model included shock and vibration environments defined as acceleration time-histories at each basket cell location. (More detail on the outputs is provided in Section 6.1.3) These were provided to the detailed-fuel-assembly modeling team to enable their simulations of the response of individual rods within a fuel assembly for each load case.

6.1.1   MODELING APPROACH AND BASIS

The cask model consists of several major components, namely the cask, canister, fuel basket, and fuel assemblies. It was intended to be generic in design, with the basic dimensions loosely based on the GBC-32 definition provided by Wagner (2001). The total mass of the cask in the cask assembly FEM was approximately 123,000 kg (270,000 lbm) exclusive of the approximately 13,600 kg (30,000 lbm) cradle. The specific component mass breakdown for the cask FEM is given in Table 6.1 and Table 6.2. Due to the nature of how actual fuel transportation casks are configured, namely with gaps between the cask and canister, the canister and basket, and the basket and fuel assemblies, there is potential for nonlinearity in the response of the system to transportation loads (largely dependent on the amplitude of any excitations it may be subject to). For this reason, interface gaps between the cask and canister, the canister and basket, and the basket and surrogate fuel assemblies were each explicitly included in the model, and the response of the cask assembly determined through explicit transient dynamic analyses using the general purpose finite element program LS-DYNA (2013).

USED FUEL DISPOSITION CAMPAIGN
Used Nuclear Fuel Loading and Structural Performance Under Normal Conditions of Transport -
Demonstration of Approach and Results of Used Fuel Performance Characterization
76   **SEPTEMBER 30, 2013**

Table 6.1. Cask Assembly Model FEM Component Mass Breakdown (Fuel Assemblies with Control Components)

Inertia Tensor (kg - m^2)						
Ixx	Ixy	Ixz		501,300	0	0
Iyx	Iyy	Iyz	=	0	501,800	-25
Izx	Izy	Izz		0	-25	104,900

Total Mass of Body (kg)	123,144

Center of Mass (m)	
X	0.0
Y	0.0
Z	0.0

Component	Sub-Component	Block Number	Mass (kg)			Weight (lbm)		
			Sub-Component	Component(s)	Single Fuel Assem.	Sub-Component	Component(s)	Single Fuel Assem.
Cask	Body	100	49,860	89,109	N/A	109,922	196,452	N/A
	Trunions	105	98			217		
	Top	110	8,828			19,464		
	Bottom	115	5,892			12,990		
	Nuetron Shield	120	7,658			16,884		
	Impact Limiters	130	16,772			36,977		
Canister	Body	200	2,533	7,600	N/A	5,584	16,755	N/A
	Top	210	2,873			6,335		
	Bottom	220	958			2,112		
	Basket Supports	230	1,235			2,724		
Basket	Basket	300	4,643	5,206	N/A	10,235	11,477	N/A
	Bottom Spacer Blocks	510	440			970		
	Top Spacer Blocks	520	123			271		
Fuel Assembly	Lower Tie Plates	401	189	21,229	663	416	46,802	1,463
	Rods - Exterior	402	8,174			18,021		
	Rods - Interior	403	9,055			19,962		
	Spacer Grids - Exterior	404	709			1,564		
	Spacer Grids - Interior	405	33			74		
	Tie Plate Transitions	406	116			256		
	Upper Tie Plate	407	342			754		
	Control Rod Assembly	408	2,611			5,756		
	Total		123,144		N/A	271,486		N/A

USED FUEL DISPOSITION CAMPAIGN
Used Nuclear Fuel Loading and Structural Performance Under Normal Conditions of Transport -
Demonstration of Approach and Results of Used Fuel Performance Characterization
SEPTEMBER 30, 2013 77

Table 6.2. Cask Assembly Model FEM Component Mass Breakdown (Fuel Assemblies without Control Components)

Inertia Tensor (kg - m^2)						
Ixx	Ixy	Ixz		492,500	0	0
Iyx	Iyy	Iyz	=	0	492,900	9
Izx	Izy	Izz		0	9	104,300

Total Mass of Body (kg)	120,739

Center of Mass (m)	
X	0.0
Y	0.0
Z	0.0

Component	Sub-Component	Block Number	Mass (kg)			Weight (lbm)		
			Sub-Component	Component(s)	Single Fuel Assem.	Sub-Component	Component(s)	Single Fuel Assem.
Cask	Body	100	49,860	89,109	N/A	109,922	196,452	N/A
	Trunions	105	98			217		
	Top	110	8,828			19,464		
	Bottom	115	5,892			12,990		
	Nuetron Shield	120	7,658			16,884		
	Impact Limiters	130	16,772			36,977		
Canister	Body	200	2,533	7,600	N/A	5,584	16,755	N/A
	Top	210	2,873			6,335		
	Bottom	220	958			2,112		
	Basket Supports	230	1,235			2,724		
Basket	Basket	300	4,643	5,411	N/A	10,235	11,930	N/A
	Bottom Spacer Blocks	510	569			1,253		
	Top Spacer Blocks	520	200			441		
Fuel Assembly	Lower Tie Plates	401	189	18,618	582	416	41,046	1,283
	Rods - Exterior	402	8,174			18,021		
	Rods - Interior	403	9,055			19,962		
	Spacer Grids - Exterior	404	709			1,564		
	Spacer Grids - Interior	405	33			74		
	Tie Plate Transitions	406	116			256		
	Upper Tie Plate	407	342			754		
	Control Rod Assembly	408	0			0		
	Total		120,739		N/A	266,183		N/A

USED FUEL DISPOSITION CAMPAIGN
Used Nuclear Fuel Loading and Structural Performance Under Normal Conditions of Transport -
Demonstration of Approach and Results of Used Fuel Performance Characterization
78   SEPTEMBER 30, 2013

As part of the sensitivity studies that have been undertaken, several model temperature distribution and gap model configurations were created. Two temperature configurations were created based on the information in Adkins (2013e) designated "hot" and "cold" that are intended to be bounding and represent the likely hot and cold cask-canister-basket-fuel temperature distributions during transport. The specific component temperatures used for each case are listed in Table 6.3. Note that the listed temperatures were evenly applied across whole components (e.g., the basket had a single temperature applied to it due to weak influence.). In addition, two gap configurations were created in which cask-to-canister, canister-to-basket, and basket-to-fuel assembly clearances were varied. These two configurations were designated as "nominal" and "large clearance" and the specific component-to-component gaps utilized are listed in Table 6.4.

Table 6.3. Cask Assembly Model Component Temperatures

| Case | Component Temp | | | | | |
| | Basket | | Canister | | Cask | |
	(°F)	(°C)	(°F)	(°C)	(°F)	(°C)
Hot	560.0	293.3	342.0	172.2	194.6	90.3
Cold	127.7	53.2	68.9	20.5	44.0	6.7

Table 6.4. Cask Assembly Model Component-to-Component Gaps

Dimension	GBC-32	Cask FEM Large Clearance	Cask FEM Nominal
Canister-to-Cask Clearance (Radial and Each End)	---	10 mm	5.0 mm
Basket-to-Canister Lateral Clearance (Radial)	---	10 mm	5.0 mm
Basket-to-Canister Axial Clearance (Each End)	---	25 mm	12.5 mm
Fuel-Assembly-to-Basket Lateral Clearance (All Sides)	---	6.0 mm	2.9 mm
Fuel-Assembly-to-Spacer-Block Axial Clearance (Each End)	---	20 mm	10 mm
Top Spacer Block Lateral Clearance to Basket (All Sides)	---	53.1 mm	50 mm
Bottom Spacer Block Lateral Clearance to Basket (All Sides)	---	8.1 mm	5 mm

Each model was subject to several load cases. Each load case consisted of an excerpt from rail car acceleration time-history data measured over a longer time period provided by TTCI (Adkins 2013e) (referred to as Phase I or P1 loads) or from longer rail car acceleration time-history data based on NUCARS simulations (Urban et al. 2013) (referred to as Phase III or P3 loads) also provided by TTCI. Each load case was ten seconds in duration, and consisted of five degree-of-freedom (P1 load cases) or six degree-of-freedom (P3 load cases) acceleration time-histories defined at the rail car to cask cradle interface. For the P1 load cases, the sixth degree-of-freedom, roll about the longitudinal axis of the rail car, could not be determined from the data provided by TTCI, and therefore excitation in that degree-of-freedom was zero for all load cases. To generate each load case six separate ten-second long excerpts were extracted from each of the longer duration P1 and P3 TTCI provided time-histories. From each data set (P1 and P3) three excerpts were selected to capture a peak shock event, one for each coordinate direction of "axial"

USED FUEL DISPOSITION CAMPAIGN
Used Nuclear Fuel Loading and Structural Performance Under Normal Conditions of Transport -
Demonstration of Approach and Results of Used Fuel Performance Characterization
SEPTEMBER 30, 2013   79

along the track, "lateral", and "vertical". The remaining three excerpts were selected to capture a representative continuous vibration (excluding any major shock loads), again with one excerpt for each of the three ("axial", "lateral", and "vertical") directions. For the P3 load cases, two of the shock load cases were identical (P3 Shock X (Axial) and P3 Shock Z (Vertical)), and therefore the P3 load case set consisted of only five distinct load cases. The selection of these load cases, and the specific characteristics of each load case, has been discussed earlier. Each load case was introduced to the cask assembly FEM by specifying all six degree-of-freedom accelerations at the cradle base node (referred to as the "rail car node" or node 100 in the FEM) located at the interface between the rail car deck and cradle.

6.1.2   MODEL DESCRIPTION

The cask and cradle portion of the cask assembly model was comprised of the cask body, neutron shield, impact limiters, and cask cradle (Figure 6.2). The cask body consists of a 200 mm thick open hollow cylinder 5.3675 m long and 2.185 m in outer diameter. Four securement and handling trunnions were located mid-height on each side of the cask body 4.510 m apart (center-to-center) with the outer interface surface located 1.275 m radially out from the cask body central axis. The cask lid and cask body bottom plate were both 300 mm thick. The cask body and lid material were type 304 stainless steel. Surrounding the cask body along 4.760 m of its length was a 132.5 mm thick neutron shield. The neutron shield was made from an NS-4-FR-like material. The impact limiters attached to each end of the cask body were 1.250 m long and 3.250 m in outer diameter. Each impact limiter overlaps the cask body by 300 mm. The impact limiters were made from a crushable aluminum honeycomb material. The total assembled length of the cask was 7.2675 m, width was 3.250 m, and height including cradle was 3.400 m. Additional cask dimensions are listed in Table 6.5. A total of 61,852 reduced integration 8-node hexahedral elements were used to represent the cask components in the FEM, and 80 Hughes-Liu linear beam elements with cross section integration were used to represent the cradle. Contact between the cradle elements and the cask body was not included because the cradle elements do not represent a true geometric recreation of a cradle structure and are simply intended to transfer the rail car excitations to the four trunnions on the cask body. (This is why the cradle elements appear to pass through the body of the cask in Figure 6.2 and Figure 5.1) Because the cask and cradle materials were expected to remain well within their elastic range during normal transport conditions, linear elastic material models were used to represent the materials for each of these components. This is true also for the neutron shielding material which may be a viscoelastic material in an actual cask that would provide some amount of vibration damping. Elastic material model parameters, adjusted to account for the temperatures listed in Table 6.3, were taken from Geelhood (2013). The specific elastic material model parameters used in the model are list in Table 6.6.

USED FUEL DISPOSITION CAMPAIGN
Used Nuclear Fuel Loading and Structural Performance Under Normal Conditions of Transport -
Demonstration of Approach and Results of Used Fuel Performance Characterization
80   **SEPTEMBER 30, 2013**
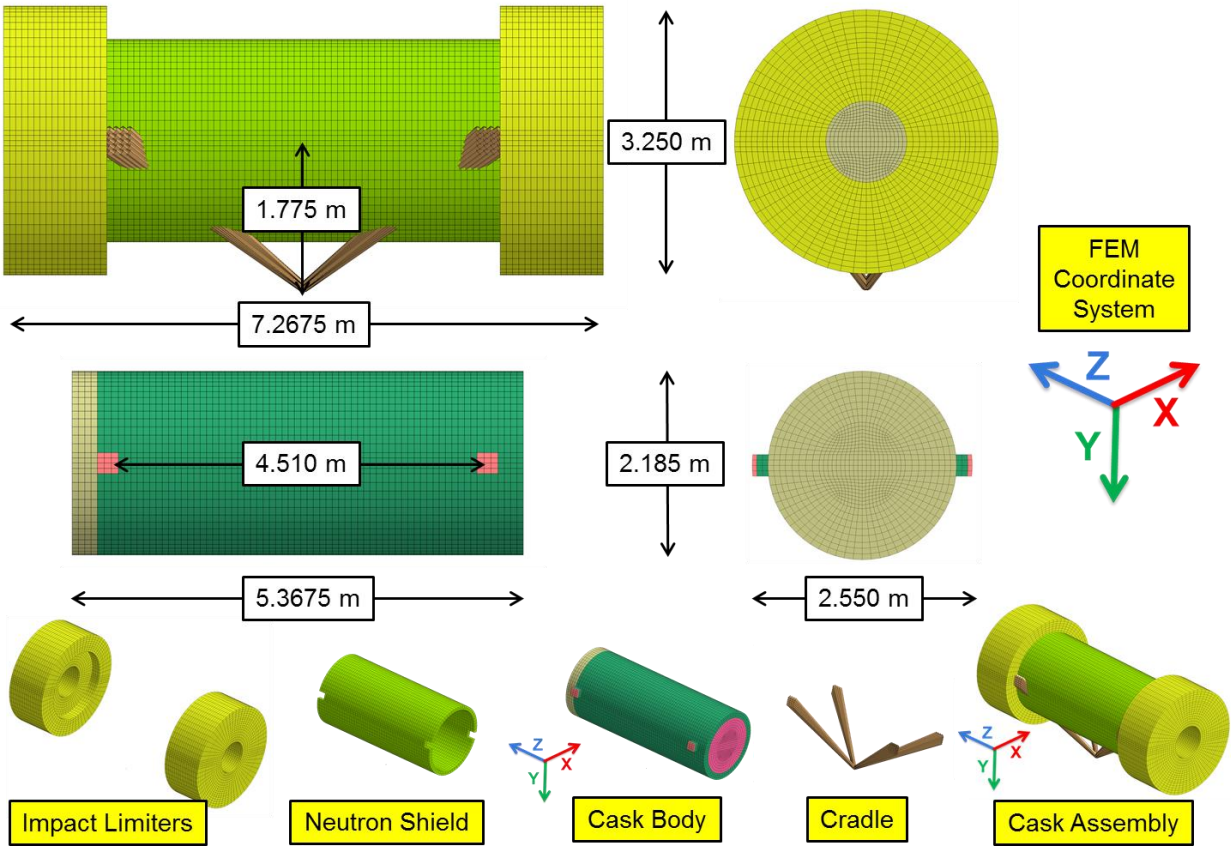
Figure 6.2. Cask Components of Cask Assembly Model

USED FUEL DISPOSITION CAMPAIGN
Used Nuclear Fuel Loading and Structural Performance Under Normal Conditions of Transport -
Demonstration of Approach and Results of Used Fuel Performance Characterization
SEPTEMBER 30, 2013 **81**

Table 6.5. Cask Assembly, Cask Component, and Cradle Dimensions

Dimension	GBC-32	Cask FEM
Cask Assembly Length	---	7.2675 m
Cask Assembly Width	---	3.250 m
Cask Assembly Height	---	3.400 m

Dimension	GBC-32	Cask FEM
Cradle Length (Cask Trunnion Longitudinal Center-to-Center Spacing)	---	4.510 m
Cradle Width (Cask Width at Trunnions)	---	2.550 m
Cradle Height (Cask Center to Cradle/Rail-Car-Deck Interface)	---	1.775 m

Dimension	GBC-32	Cask FEM
Cask Body Outer Length	4.708 m	5.3675 m
Cask Body Outer Diameter	2.150 m	2.185 m
Cask Body Radial Wall Thickness	200 mm	200 mm
Cask Body Top Thickness	300 mm	300 mm
Cask Body Bottom Thickness	300 mm	300 mm
Trunnion Size (Length and Width)	---	250 mm
Trunnion Radial Distance from Cask Centerline	---	1.275 m
Trunnion Longitudinal Center-to-Center Distance	---	4.510 m
Neutron Shield Length	---	4.760 m
Neutron Shield Outer Diameter	---	2.450 m
Neutron Shield Radial Thickness	---	132.5 mm
Impact Limiter Length	---	1.250 m
Impact Limiter Cask Overlap Length	---	300 mm
Impact Limiter Outer Diameter	---	3.250 m
Impact Limiter Inner Diameter	---	2.185 m
Impact Limiter Cutout Hole Diameter	---	1.000 m

USED FUEL DISPOSITION CAMPAIGN
Used Nuclear Fuel Loading and Structural Performance Under Normal Conditions of Transport -
Demonstration of Approach and Results of Used Fuel Performance Characterization
82   **SEPTEMBER 30, 2013**

Table 6.6. Material Model Parameters Used in the Cask Assembly FEM.

Material	Component	Temperature Case	Temperature (K)	(C)	Density (kg/m³)	E (GPa)	ν
304SS	Cask	Hot	364	90	7860	192	0.295
		Cold	280	7	7860	199	0.289
	Canister	Hot	445	172	7860	185	0.302
		Cold	294	21	7860	198	0.290
	Basket and Spacer Blocks	Hot	567	293	7860	174	0.450
		Cold	326	53	7860	195	0.292
Nuetron Shield	Neutron Shield	Hot & Cold	293	20	1680	4	0.300
Aluminum Honeycomb	Impact Limiter	Hot & Cold	293	20	988	4	0.100
High Stiffness Material	Cradle	Hot & Cold	293	20	785	2000	0.260

USED FUEL DISPOSITION CAMPAIGN
Used Nuclear Fuel Loading and Structural Performance Under Normal Conditions of Transport -
Demonstration of Approach and Results of Used Fuel Performance Characterization
SEPTEMBER 30, 2013 83

The canister and basket portion of the cask assembly model were comprised of the canister body, canister lid, and basket (Figure 6.3). The canister body consisted of a 12.5 mm thick open hollow cylinder 4.750 m long and 1.775 m in outer diameter. The canister lid and canister bottom plate were 150 mm and 50 mm thick, respectively. Running longitudinally along the inner wall of the canister were four separate structures that provide lateral and vertical support to the basket during cask transport. These support structures consisted of 7.5 mm thick plate elements that run the full length of the basket. The canister component materials were all type 304 stainless steel. The basket consisted of 32 open-ended square cells constructed from 7.5 mm thick plate material. These basket plates were also of type 304 stainless steel. Attached to each cell wall, with the exception of the cell walls on the exterior surface of the basket, were Boral (boron carbide and aluminum) neutron poison plates that run the full length of the basket. The mass and geometric dimensions (for contact) of the Boral plates were included in the model, but they were assumed to contribute no structural stiffness to the basket cell walls. Additional canister and basket dimensions are listed in Table 6.7. A total of 9,920 reduced integration 4-node shell elements were used to represent the canister components in the FEM, and 18,240 reduced integration 4-node shell elements for the basket components. Because the canister and basket materials were expected to remain well within their elastic range during normal transport conditions, linear elastic material models were used to represent the materials for each of these components. Elastic material model parameters, adjusted to account for the temperatures listed in Table 6.3, were taken from Geelhood (2013). The specific elastic material model parameters used in the model are list in Table 6.6.

USED FUEL DISPOSITION CAMPAIGN
Used Nuclear Fuel Loading and Structural Performance Under Normal Conditions of Transport -
Demonstration of Approach and Results of Used Fuel Performance Characterization
84   **SEPTEMBER 30, 2013**
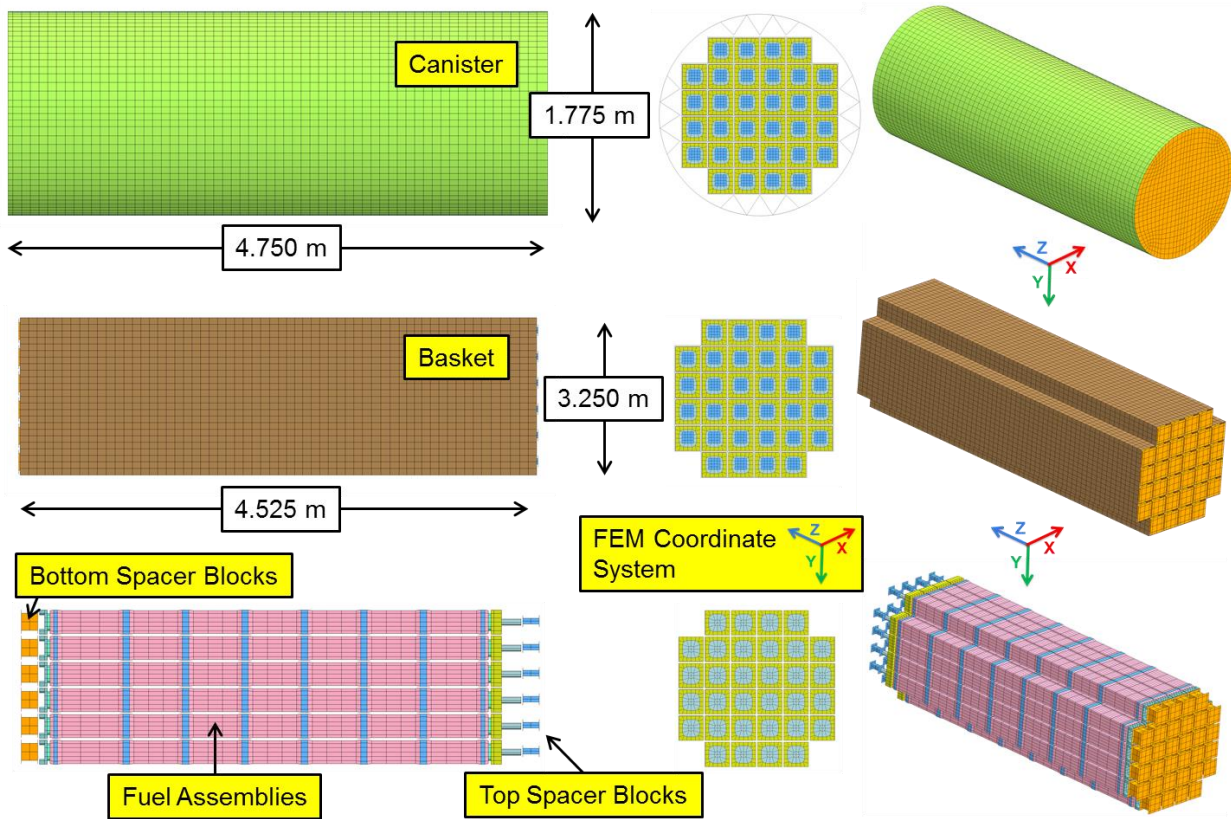
Figure 6.3. Canister, Basket, and Fuel Assembly Components of Cask Assembly Model

USED FUEL DISPOSITION CAMPAIGN
Used Nuclear Fuel Loading and Structural Performance Under Normal Conditions of Transport -
Demonstration of Approach and Results of Used Fuel Performance Characterization
SEPTEMBER 30, 2013   85

Table 6.7. Canister and Basket Dimensions

Dimension	GBC-32	Cask FEM
Canister Outer Length	---	4.750 m
Canister Outer Diameter	---	1.775 m
Canister Radial Wall Thickness	---	12.5 mm
Canister Top Thickness	---	150 mm
Canister Bottom Thickness	---	50 mm
Basket Lateral Support Structure Wall Thickness	---	7.5 mm

Dimension	GBC-32	Cask FEM
Basket Cell Length	3.658 m	4.525 m
Basket Cell Configuration	4-6-6-6-6-4	4-6-6-6-6-4
Basket Cell Inside Dimension (Including Boral Panel)	220 mm	220 mm
Basket Cell Wall Thickness Without Boral Panel	7.5 mm	7.5 mm
Basket Boral Panel Thickness	2.54 mm	2.5 mm
Basket Cell Wall Thickness Including Boral Panel	10.04 mm	10 mm
Basket Cell Centerline to Cell Centerline Spacing (Pitch)	237.6 mm	230 mm
Basket Boral Panel Width	190.5 mm	190.5 mm
Basket Boral Panel Length	3.658 m	4.525 m
Basket Boral Panel Boron Carbide Thickness	2.06 mm	2.0 mm
Basket Boral Panel Aluminum Face Sheet Thickness (x2)	0.254 mm	0.25 mm
Basket Outer Dimensions	---	1.3875 m

The fuel assembly and spacer block portion of the cask assembly model was comprised of 32 individual fuel assemblies and 64 top and bottom spacer blocks (Figure 6.3 and Figure 6.4). Two fuel assembly configurations were used. The first configuration includes a representation of the control rod assembly components. This fuel assembly was 4.228 m in length and had a maximum width and height of 214.2 mm set by the spacer grid dimensions. The second configuration did not include the control rod assembly components. It had a total length of 4.058 m and identical width and height dimensions as the fuel assembly with control components. Additional fuel assembly dimensions are listed in Table 6.8. The simplified fuel assembly model was provided by the detailed-fuel-assembly modeling team, with material property and mesh characteristics determined largely by them. A short overview of the models is provided here. The various portions of the fuel assembly model (e.g., tie plates, spacer grids, fuel rods, etc.) were represented with either an isotropic or orthotropic elastic material model with parameters selected for those models so as to match the dynamic response characteristics of the simplified model to that of the detailed-fuel-assembly model. A total of 54,656 reduced integration and 1280 full integration 8-node hexahedral elements were used to represent the 32 fuel assemblies without control components in the FEM, whereas a total of 55,296 reduced integration and 1280 full integration 8-node hexahedral elements were used to represent the 32 fuel assemblies with control components.

USED FUEL DISPOSITION CAMPAIGN
Used Nuclear Fuel Loading and Structural Performance Under Normal Conditions of Transport -
Demonstration of Approach and Results of Used Fuel Performance Characterization
86   SEPTEMBER 30, 2013

Both types of fuel assembly were significantly shorter than the interior length of the canister which necessitated that spacer blocks be used to limit the amount of axial movement of the fuel assemblies in the basket during transport. Two types of spacer blocks were employed. The first type, the bottom spacer block, was composed of a 160 mm x 160 mm square type 304 stainless steel tube with a wall thickness of 10 mm, capped on each end with 10 mm thick square plates with dimensions of 210 mm by 210 mm. The bottom spacer block had a total length of 154.58 mm in the case of the fuel assembly with control components, and 239.74 mm for the fuel assembly without control components. Each bottom spacer block was free floating within the fuel basket, but because of the relatively small clearances between each spacer block and its surrounding cell walls its overall movement was limited (see Table 6.4). The second type of spacer block was the top spacer block which was composed of a 70 mm by 70 mm square type 304 stainless steel tube with a wall thickness of 10 mm, capped on each end with 10 mm thick square plates with dimensions of 120 mm by 120 mm. The top spacer block has a total length of 154.58 mm in the case of the fuel assembly with control components, and 307.55 mm for the fuel assembly without control components. In the case of the fuel assembly without control components, the top spacer block extended into a cavity that existed on the upper tie plate so as to maintain a gap between the spacer block and fuel assembly that was consistent with the fuel assembly with control components case. Unlike the bottom spacer block, the top spacer block was not free floating, but rather was attached to the lid of the canister. Additional spacer block dimensions are listed in Table 6.8. The bottom and top spacer block material was type 304 stainless steel. Because the spacer block materials were expected to remain well within their elastic range during normal transport conditions, linear elastic material models were used. Elastic material model parameters, adjusted to account for the temperatures listed in Table 6.3, were taken from Geelhood (2013). The specific elastic material model parameters used in the model are list in Table 6.6. A total of 3,072 reduced integration 4-node shell elements were used to represent the 64 spacer blocks in the FEM with fuel assemblies that did include control components, whereas a total of 3,840 reduced integration 4-node shell elements were used to represent the 64 spacer blocks in the FEM with fuel assemblies that did not include control components.

USED FUEL DISPOSITION CAMPAIGN
Used Nuclear Fuel Loading and Structural Performance Under Normal Conditions of Transport -
Demonstration of Approach and Results of Used Fuel Performance Characterization
SEPTEMBER 30, 2013 87

Fuel Assembly With Control Components

4.228 m

Fuel Assembly Without Control Components

4.058 m

Top Spacer Block Without Control Components

Bottom Spacer Block

Top Spacer Block With Control Components

Figure 6.4. Fuel Assembly and Spacer Block Components of Cask Assembly Model

USED FUEL DISPOSITION CAMPAIGN
**Used Nuclear Fuel Loading and Structural Performance Under Normal Conditions of Transport -
Demonstration of Approach and Results of Used Fuel Performance Characterization**
88   **SEPTEMBER 30, 2013**

Table 6.8. Fuel Assembly and Spacer Block Dimensions

Dimension	GBC-32	Cask FEM
Top Spacer Block Wall Thickness	---	10 mm
Bottom Spacer Block Wall Thickness	---	10 mm
Top Spacer Block Lateral Clearance to Basket (All Sides)	---	50 mm
Bottom Spacer Block Lateral Clearance to Basket (All Sides)	---	5 mm
Top Spacer Block Length (Fuel Assembly With Control Components)	---	154.58 mm
Top Spacer Block Length (Fuel Assembly Without Control Components)	---	307.55 mm
Bottom Spacer Block Length (Fuel Assembly With Control Components)	---	154.58 mm
Bottom Spacer Block Length (Fuel Assembly Without Control Components)	---	239.74 mm
Top Spacer Block Plate Height and Width	---	120 mm
Bottom Spacer Block Plate Height and Width	---	210 mm
Top Spacer Block Tube Height and Width	---	70 mm
Bottom Spacer Block Tube Height and Width	---	160 mm

Dimension	GBC-32	Cask FEM
Fuel Assembly Total Length (Without Control Rod Assembly)	---	4.05803 m
Fuel Assembly Total Length (With Control Rod Assembly)	---	4.228338 m
Fuel Assembly Upper Tie Plate Thickness	---	93.2 mm
Fuel Assembly Upper Tie Plate Thickness with Control Rod Assembly	---	263.508 mm
Fuel Assembly Upper Tie Plate Size	---	213.5 mm
Fuel Assembly Lower Tie Plate Thickness	---	69.5 mm
Fuel Assembly Lower Tie Plate Size	---	214.0 mm
Fuel Assembly End Spacer Grid Thickness	---	33.0 mm
Fuel Assembly End Spacer Grid Size	---	214.2 mm
Fuel Assembly Interior Spacer Grid Thickness	---	57.1 mm
Fuel Assembly Interior Spacer Grid Size	---	214.2 mm
Fuel Assembly Total Number of Spacer Grids	---	8
Fuel Assembly Bottom of Lower Tie Plate to Top of 1st Spacer Grid	---	157.2 mm
Fuel Assembly Bottom of Lower Tie Plate to Top of 2nd Spacer Grid	---	789.4 mm
Fuel Assembly Bottom of Lower Tie Plate to Top of 3rd Spacer Grid	---	1311.4 mm
Fuel Assembly Bottom of Lower Tie Plate to Top of 4th Spacer Grid	---	1833.4 mm
Fuel Assembly Bottom of Lower Tie Plate to Top of 5th Spacer Grid	---	2355.3 mm
Fuel Assembly Bottom of Lower Tie Plate to Top of 6th Spacer Grid	---	2877.3 mm
Fuel Assembly Bottom of Lower Tie Plate to Top of 7th Spacer Grid	---	3399.3 mm
Fuel Assembly Bottom of Lower Tie Plate to Top of 8th Spacer Grid	---	3910.6 mm

Contact between bodies in the cask assembly FEM was handled in LS-DYNA using a penalty based surface-to-surface algorithm that includes a friction model with the ability to specify differing static and dynamic coefficients of friction. For all analyses performed, these values were conservatively assumed equal to 0.2 and 0.1, respectively. A small amount of structural

damping was also included in the cask assembly FEM using a mass and stiffness proportional Rayleigh damping algorithm. For all analyses performed, Rayleigh damping parameters were selected such that all components in the cask assembly FEM had a structural damping of approximately 2% of critical throughout the frequency range of 1.0 Hz to 500 Hz.

6.1.3   CASK MODEL OUTPUT

For each simulation performed, acceleration-velocity-displacement data in all six degrees-of-freedom were extracted at a series of locations on the rail car (rail car node), basket, and fuel assemblies. This data was produced at a rate of 1000 samples per second to provide ample fidelity in the measured response quantities for follow on modeling. Table 6.9 describes the specific output locations in more detail. Acceleration-velocity-displacement time-history data from each cask assembly model simulation for all points on the basket and spacer blocks were provided to the detailed-fuel-assembly modeling team for use in their modeling.

Table 6.9. Cask Assembly Model Data Output Locations

Component and Location	Node ID Range
Rail Car – Node at Interface Between Cradle and Rail Car Deck	100
Basket Cell – Center	🔵 1XX's, Where XX = 01 to 31
Basket Cell – Corners at Fuel Assembly Ends, Mid-Point, and Quarter Points	🔴 10,0XX's, Where XX = 01 to 05
Basket Cell – Corners at Fuel Assembly Spacer Grid Mid-Points	🔴 10,0XX's, Where XX = 11 to 18
Basket Cell – Horiz. Walls at Fuel Assembly Ends, Mid-Point, and Quarter Points	🟠 20,0XX's, Where XX = 01 to 05
Basket Cell – Horiz. Walls at Fuel Assembly Spacer Grid Mid-Points	🟠 20,0XX's, Where XX = 11 to 18
Basket Cell – Vert. Walls at Fuel Assembly Ends, Mid-Point, and Quarter Points	🟢 30,0XX's, Where XX = 01 to 05
Basket Cell – Vert. Walls at Fuel Assembly Spacer Grid Mid-Points	🟢 30,0XX's, Where XX = 11 to 18
Top Spacer Block – Mid-point of Face On Fuel Assembly Side	40,0XX's, Where XX = 01 to 32
Bottom Spacer Block – Mid-point of Face On Fuel Assembly Side	50,0XX's, Where XX = 01 to 32
Fuel Assembly – Bottom Spacer Grid Mid-Points	1,000,000's

USED FUEL DISPOSITION CAMPAIGN
Used Nuclear Fuel Loading and Structural Performance Under Normal Conditions of Transport -
Demonstration of Approach and Results of Used Fuel Performance Characterization
90 **SEPTEMBER 30, 2013**
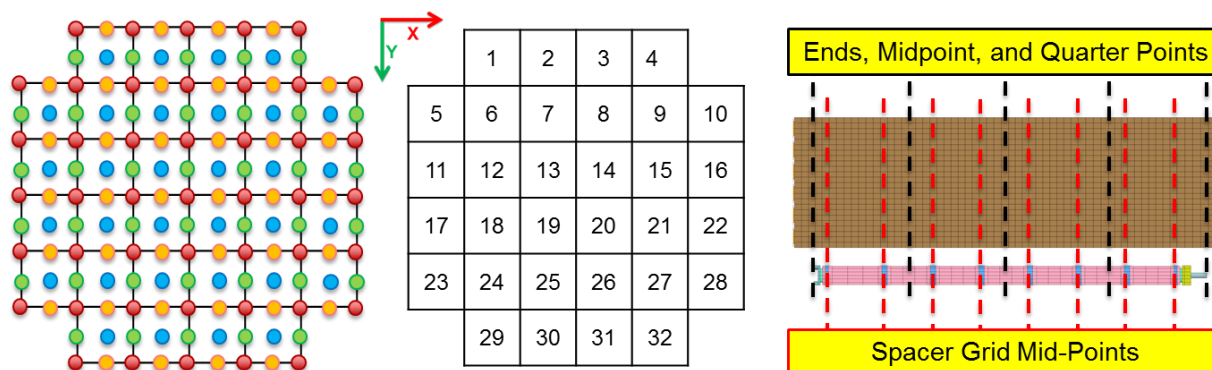
6.2   MODELING APPROACH AT THE ASSEMBLY-LEVEL

The PWR assembly model is a three-dimensional LS-DYNA explicit transient FEM of a single full Westinghouse 17×17 Optimized Fuel Assembly (OFA). The model includes geometric representations of the major structural components in a full single assembly including the upper nozzle/tie plate, lower nozzle/tie plate, guide/measurement tubes, spacer grids, and fuel rods (Figure 6.5). Additionally, the inclusion of a control head assembly was also considered since such activated hardware may be transported simultaneously with the assembly and adds additional mass that may influence the dynamic response. This assembly submodel is used to estimate the stresses and strains on the fuel rod cladding during transient dynamic shock and vibration events that occur under NCT.

Figure 6.5. WE 17×17 OFA PWR Fuel Assembly Submodel (w/o Control Components)

6.2.1   MODELING APPROACH AND BASIS

The objective of the assembly-level submodel is to determine the stress and strain states in all of the fuel rods in a single assembly during TL. A detailed three-dimensional model using the explicit finite element analysis code LS-DYNA (LSTC 2013) was created to evaluate the transient dynamic loading during shock and vibration events.

6.2.1.1   ASSUMPTIONS

The following are the major assumptions and simplifications made in the assembly submodel:

- The fuel rod (fuel pellets, cladding, plenum spring, thimbles, etc.) was modeled as a solid beam with effective bending stiffness, mass and damping properties.

USED FUEL DISPOSITION CAMPAIGN
**Used Nuclear Fuel Loading and Structural Performance Under Normal Conditions of Transport -
Demonstration of Approach and Results of Used Fuel Performance Characterization
SEPTEMBER 30, 2013** 91

- The spacer grid slots were modeled as a simplified box structure, and spacer grid leaf springs/dimples were modeled as translational springs.

- Leaf springs and dimples were assumed to be fully relaxed due to in-core creep; i.e. there was no preload in the springs or dimples.

- The basket was modeled as a rectangular enclosure and assumed rigid during transient dynamic events.

- Only the end plates of the spacer blocks were modeled as part of the basket enclosure.

- Temperature fields for mechanical property assignment were assumed constant with four axial zones along the assembly.

- Friction coefficients of 0.2 static and 0.1 dynamic were conservatively assumed.

- Cladding strains at the outer diameter of the fuel rods were the primary result of interest.

- Thermal strains were not considered.

- Intermediate flow mixers were neglected because they were assumed to be completely deteriorated and not present.

6.2.1.2   GEOMETRY

The geometry of the WE 17×17 OFA assembly was taken primarily from the physical descriptions and dimensions provided in the available public documents (e.g., DOE-RW-0184 1987, Mays et al. 1998) to provide the key dimensions as summarized in (Adkins 2013e). Simplified geometries were used for the upper nozzle/tie plate, bottom nozzle/tie plate, and control head assembly to eliminate unnecessary geometric details. These simplified structures retained the proper mass and acceptable inertial properties and there are not expected to be significantly different interactions with the other components. The assembly was then supported within a box structure representative of a single basket compartment. This structure consisted of a rectangular box with open ends to represent the basket side walls, and the same initial gap sizes used in the cask model between the assembly and basket were maintained. Only the end plate surfaces of each spacer block that face each assembly were modeled.

6.2.1.3   MESHING

The model mesh of the assembly submodel is shown in Figure 6.6. The fuel rods and guide tubes were meshed with 2-node Hughes-Liu beam elements with a solid circular cross section for the fuel rods and a thin wall tube for the guide tubes. The spacer grids were meshed with 4-node reduced integration Belytschko-Tsay shell elements. The complex geometric details of the numerous possible spacer grid, leaf spring, dimples, and flow diverter configurations were not modeled. Rather the rods were laterally supported by two orthogonal sets of translational springs in every slot (each vertical and horizontal set consisted of one leaf spring at the geometric center

USED FUEL DISPOSITION CAMPAIGN
Used Nuclear Fuel Loading and Structural Performance Under Normal Conditions of Transport -
Demonstration of Approach and Results of Used Fuel Performance Characterization
92   **SEPTEMBER 30, 2013**

of the slot and two dimples separated by a distance of 46 mm). Guide tubes were rigidly connected to the corresponding slots in the spacer grids via the LS-DYNA "spotweld" connection such that bending moments were properly transferred. The top and bottom tie plates were modeled with 8-node constant stress brick elements. The tie plates were similarly connected with the guide tubes to transfer bending moments. For models with the control head assembly, a single large diameter beam was connected via smaller diameter beams to the 24 guide/measurement tube locations of the top nozzle. This transferred the moment of the cantilevered head assembly mass to the guide tubes and upper tie plate, but any consideration of control head axial sliding within the guide tubes was neglected. The basket and spacer block plates surrounding the assembly were meshed with shells.

Explicit finite element (FE) calculations require that the model integration time step be smaller than the shortest duration for stress wave propagation through an element (Courant-Friedrichs-Levy stability criterion). To maximize the permissible time step and reduce the total solution time, elements with small dimensions were eliminated from the model as much as possible. Alternatively, mass can also be judiciously added to small elements to increase the density and reduce the local wave propagation speed, but the added mass must be small relative to the actual mass of the structure so as to not significantly affect the overall problem response. In anticipation of long solution times for the vibration cases, special care was taken in model meshing to maximize the time step which was initially of the order of 1e-7 s. The mesh was coarsened to produce reasonable solution times. In particular, the biggest problem region was with the spacer grids. The spacer grids were significantly coarsened to only two elements per side of each slot. The spacer grids springs also had a small time step, but a small added mass (<1% of the entire assembly) was added automatically during solution to boost the time step. The geometry of the tie plates/nozzles was also modified to eliminate small elements. These modifications increased the permissible time step of the overall model to 2.1e-6 s. The resulting mesh after modifications is shown in Figure 6.6 through Figure 6.12. The model consisted of approximately 140k nodes and 60k elements. The simplified control head assembly was also added to the model for some of the sensitivity analyses (Figure 6.13). The model mass summary is shown in Table 6.10. The mass of the control rods was estimated from data provided in Mays et al., 1998 for the silver-indium-cadmium control rod material with stainless steel clad.

Contact between interacting components was implemented in several locations. General surface-to-surface contact with friction was defined between the grids and tie plates of the assembly and the basket walls. A beam-to-surface contact definition included the fuel rods to capture potential contact between the rods and basket during lateral vibration. Node-to-surface contact with friction was defined between the spacer block end plates and the tie plates/nozzles and/or control head assembly. Tied node-to-surface contact was assigned between the spacer grid and the springs representing the leaf springs and dimples. This method was chosen over using common nodes to permit spring placement at their actual locations on the spacer grid independent of the local grid mesh density (which was necessarily coarsened to increase the time step). Finally, the control rods were attached to the spacer grids using rigid constraints via the generalized spot weld option.

USED FUEL DISPOSITION CAMPAIGN
**Used Nuclear Fuel Loading and Structural Performance Under Normal Conditions of Transport -
Demonstration of Approach and Results of Used Fuel Performance Characterization
SEPTEMBER 30, 2013** 93
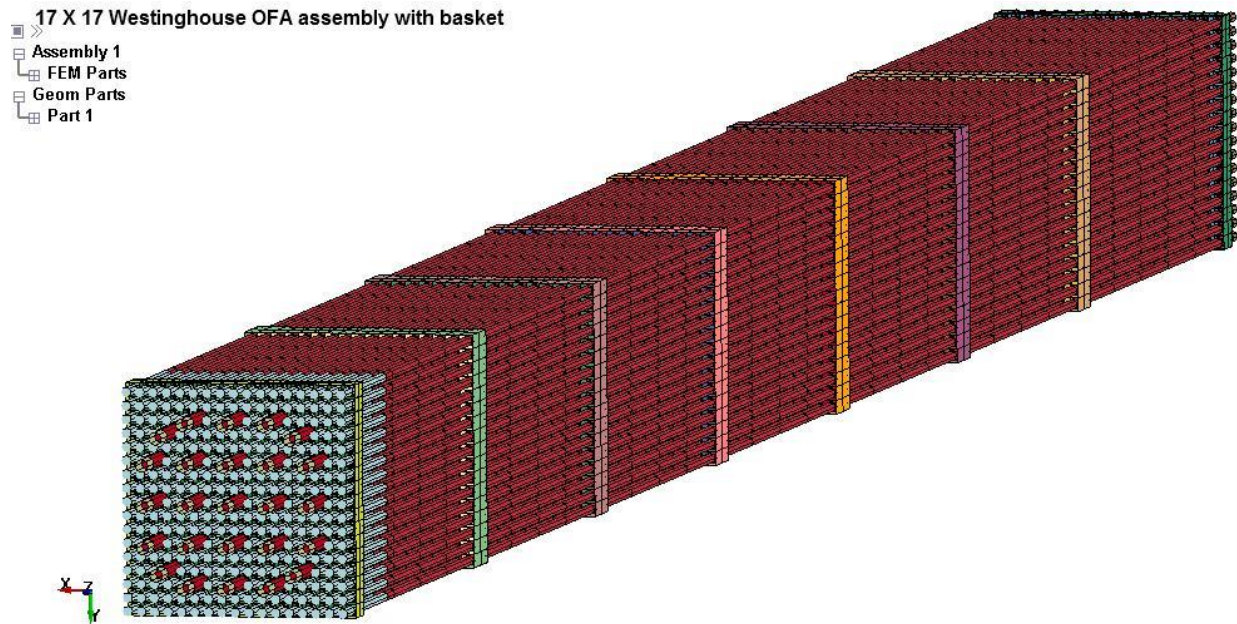
Figure 6.6. WE 17×17 OFA PWR Fuel Assembly Submodel (End Tie Plates/Nozzles Removed)
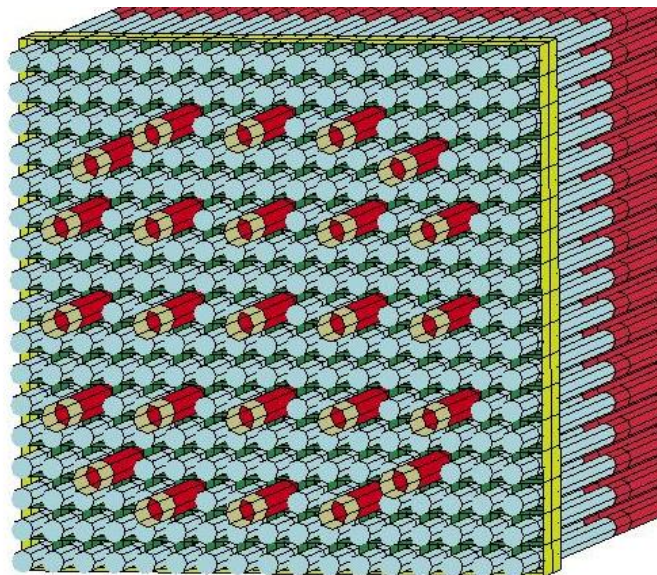
Figure 6.7. Fuel Rods and Guide Tubes at Upper End Spacer Grid

USED FUEL DISPOSITION CAMPAIGN
Used Nuclear Fuel Loading and Structural Performance Under Normal Conditions of Transport -
Demonstration of Approach and Results of Used Fuel Performance Characterization
94   **SEPTEMBER 30, 2013**
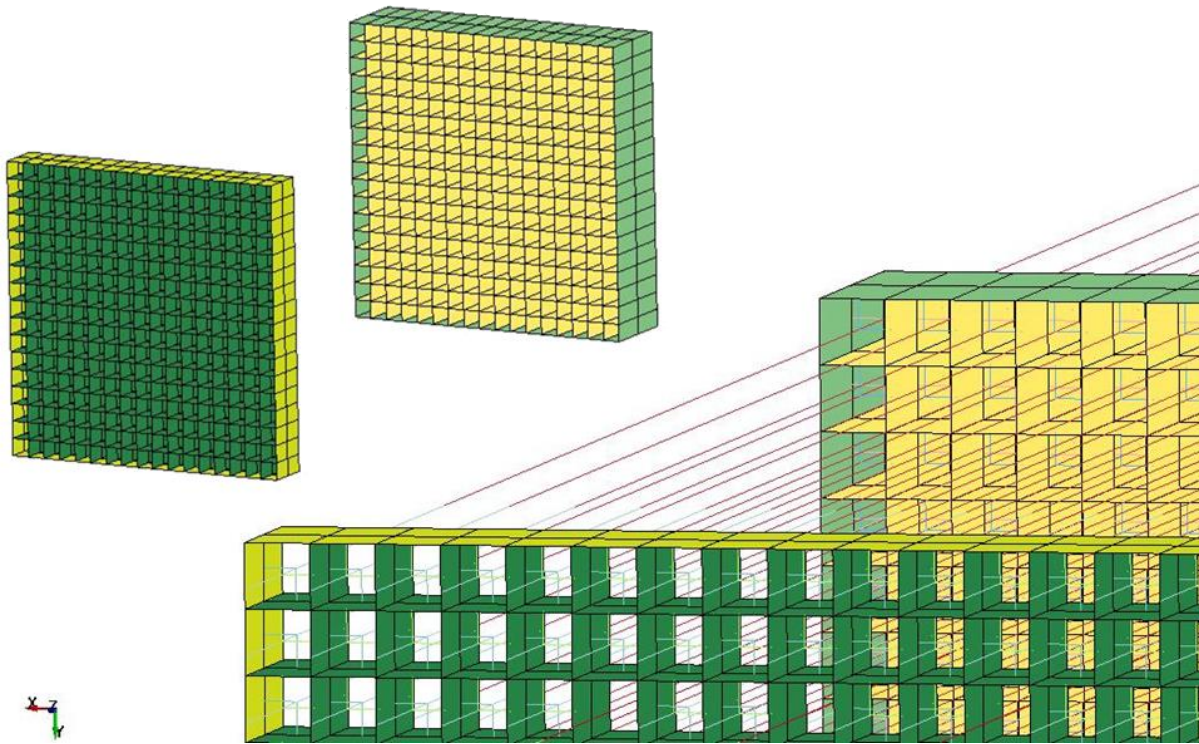
Figure 6.8. End Inconel and Middle Zircaloy Spacer Grids with Fuel Rods (Beam Elements Are Represented As Lines) Supported by Spring Elements Representing the Two Leaf Springs and Four Dimples within Each Slot
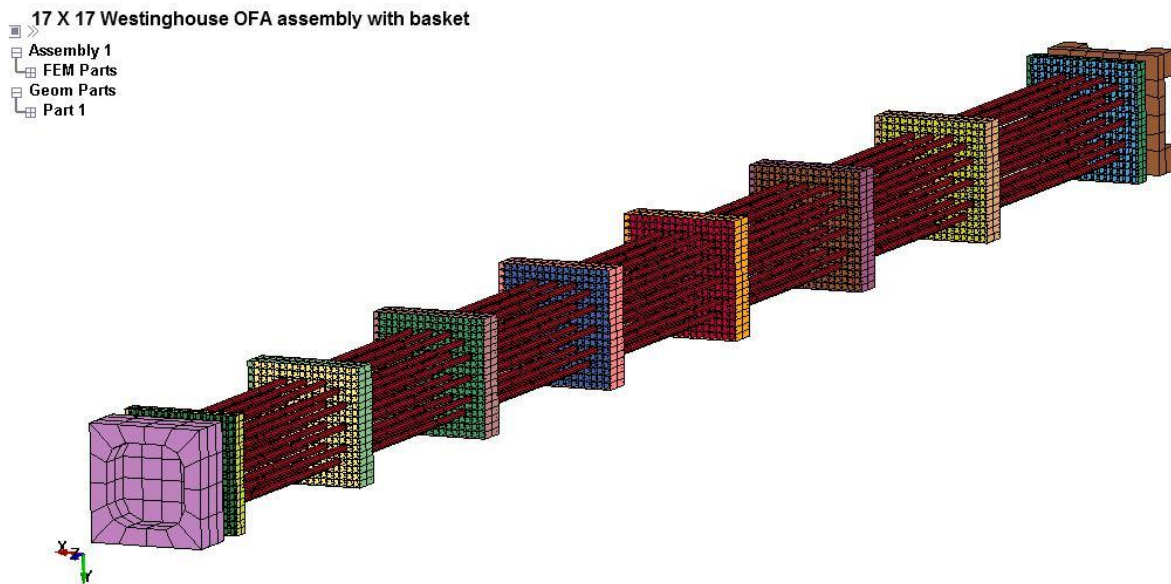
Figure 6.9. Assembly Support Skeleton Consisting of the Guide Tubes, Spacer Grids, Lower Tie Plate/Nozzle, and Upper Tie Plate/Nozzle

USED FUEL DISPOSITION CAMPAIGN
Used Nuclear Fuel Loading and Structural Performance Under Normal Conditions of Transport -
Demonstration of Approach and Results of Used Fuel Performance Characterization
SEPTEMBER 30, 2013 **95**
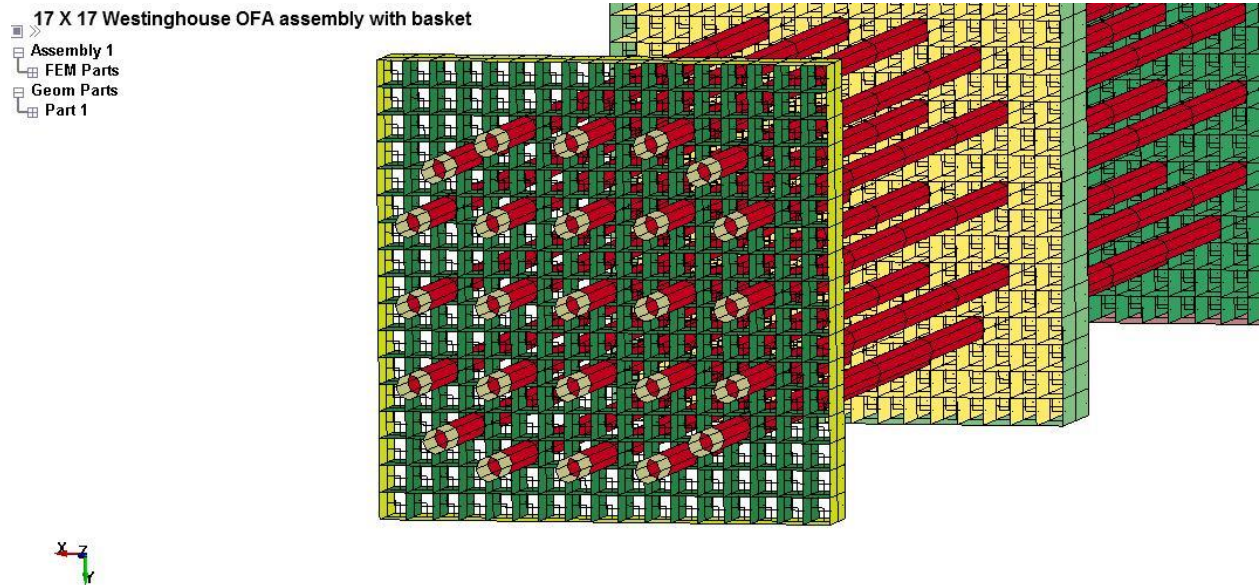
Figure 6.10. Guide Tubes Rigidly Attached to the Spacer Grids
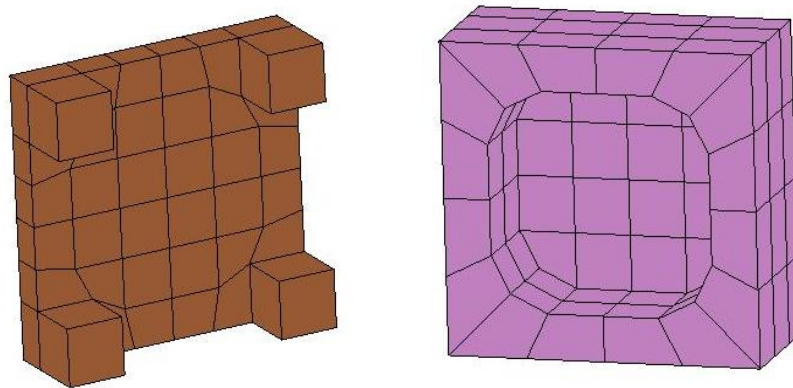
Figure 6.11. Simplified Representation of the Lower and Upper Tie Grids/Nozzles

USED FUEL DISPOSITION CAMPAIGN
Used Nuclear Fuel Loading and Structural Performance Under Normal Conditions of Transport -
Demonstration of Approach and Results of Used Fuel Performance Characterization
96 **SEPTEMBER 30, 2013**
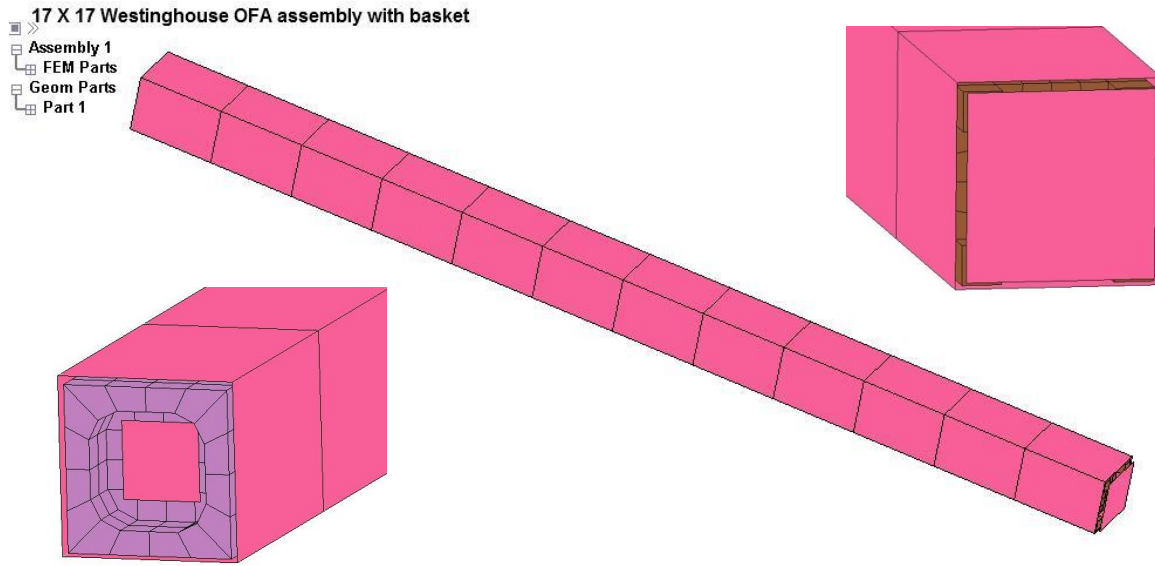
Figure 6.12. Compartment Walls and Spacer Block End Plates Forming the Basket Enclosure for the Assembly Submodel
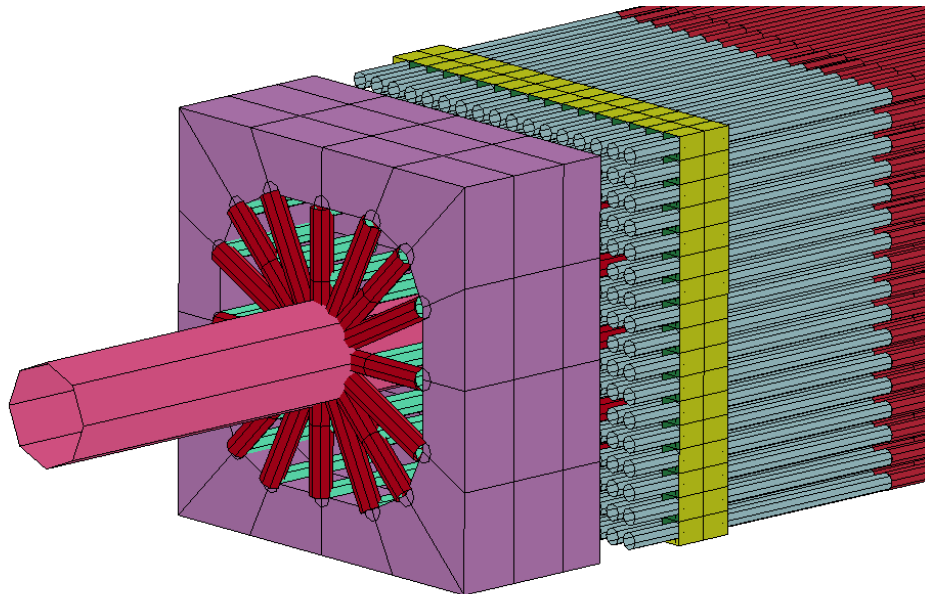
Figure 6.13. Simplified Beam Element Control Head Assembly Added to the Top Tie Plate/Nozzle and Connected to the Control Rods

USED FUEL DISPOSITION CAMPAIGN
Used Nuclear Fuel Loading and Structural Performance Under Normal Conditions of Transport -
Demonstration of Approach and Results of Used Fuel Performance Characterization
SEPTEMBER 30, 2013 **97**

Table 6.10. Mass Properties of the WE 17×17 OFA PWR Model

Component	Reference Mass (kg)	Model Mass (kg)
Fuel Rods (264×)	591.6	591.1
Guide Tubes (25×)	9.5	9.5
Bottom Spacer Grid	0.9	0.9
Top Spacer Grid	0.9	0.9
Middle Spacer Grids (6×)	7.0	7.0
Bottom Tie Plate/Nozzle	5.9	5.9
Top Tie Plate/Nozzle	6.9	6.9
Total	622.7	622.2
Control Rods (24×)		66.0
Control Head Assembly		15.7
Total		81.7

6.2.1.4 MATERIAL PROPERTIES

Material properties for most of the assembly components were taken from the previous summary report on typical component materials (Geelhood, 2013). These properties are dependent on temperature and level of irradiation and plots are shown in the supporting document. Density and temperature-dependent stress-strain properties were implemented as available into the bilinear elastic-plastic model MAT_004. Thermal expansion effects were ignored. The top and bottom spacer grids were Inconel-718, the middle spacer grids were Zircaloy-4, the guide tubes were Zircaloy-4, and the tie plates/nozzles were stainless steel grade 304. For the fuel rods, effective beam properties were used based on the single rod-level analyses. An effective rod bending stiffness (elastic modulus multiplied by area moment of inertia) of 8.3 Pa-m^4 was assumed for the lower bound (LB), 49.3 Pa-m^4 for the upper bound (UB), and 45.1 Pa-m^4 for the best estimate (BE) value. The effective modulus was then calculated from the selected bending stiffness and the area moment of inertia based on a solid circular cross section with clad outer diameter of 0.360". With this approach, the bending strains at the outer diameter of the fuel rod are the same as the outer bending strains of the actual cladding and suitable for use in subsequent failure and fatigue analyses.

For the leaf spring and dimple properties of the spacer grids, spring stiffness values were used based on initial single rod-level analyses of the spacer grid slot. For the modal and initial sensitivity analyses using P1 loading, spring stiffness values of 121 N/mm and 311 N/mm were used for the Inconel leaf spring and dimple, respectively, based on the initial slope of the predicted response from the spring deformation analyses conducted as part of this study. Spring stiffness values of 49 N/mm and 126 N/mm were used for the Zircaloy leaf spring and dimple, respectively. For the cases with the final data from the NUCARS simulations (P3 loading), a more complete nonlinear elastic spring response based on the single spacer grid slot analysis was

USED FUEL DISPOSITION CAMPAIGN
**Used Nuclear Fuel Loading and Structural Performance Under Normal Conditions of Transport -
Demonstration of Approach and Results of Used Fuel Performance Characterization**
98   **SEPTEMBER 30, 2013**

implemented. These springs were defined to act primarily in compression with only a relatively low stiffness in tension to approximate possible gap opening between the spring/dimple and the rod during loading (Figure 6.14). The initial slopes of these nonlinear curves are 121 N/mm and 1019 N/mm for the Inconel leaf spring and dimple, respectively, and 49 N/mm and 413 N/mm for the Zircaloy leaf spring and dimple, respectively. Under compression, the single spacer grid slot and spring stiffness analyses predicted the load to reach a peak and then reduce with further deformation. For this model, the compressive load was not allowed to drop after the peak load was reached and a flat response was assumed for further deformation. It is noted that the rod will contact the spacer grid slot wall (when the spring bottoms out) after traveling about 1.7 mm. The initial compressive slopes of these more complete nonlinear elastic responses match the spring stiffness values used in the modal and initial sensitivity analyses.
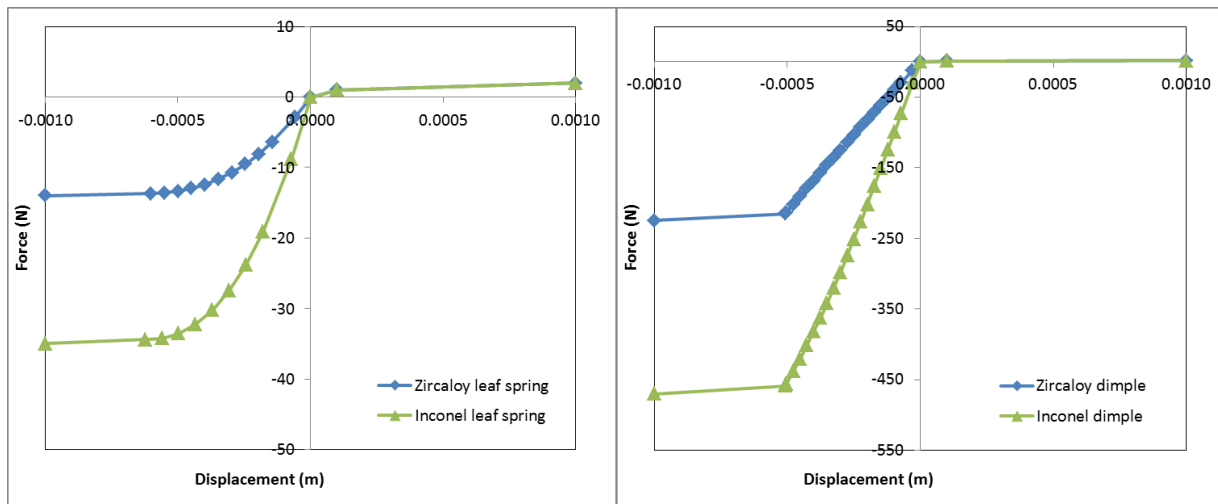
Figure 6.14. Force deflection curves for spacer grid leaf springs and dimples.

Damping in the fuel rods used Raleigh damping parameters estimated from the single fuel rod analyses conducted as part of this study. For the contact elements, a static friction coefficient of 0.2 and a dynamic coefficient of 0.1 were used.

6.2.1.5   LOADS

A gravitational body load of 9.807 m/s^2 was applied to all components during both the initialization and the transient dynamic phases of the model solution. A uniform temperature load was applied to four regions along the assembly length for assignment of temperature-dependent MP. The hot case consisted of an assembly at the center of the cask with temperatures of 550.07, 632.64, 641.4, and 641.40 K defined across 4 axial regions. The cold cases consist of an assembly at the periphery of the cask with temperatures of 302.26, 319.13, 322.17, and 312.36 K defined across 4 axial regions.

USED FUEL DISPOSITION CAMPAIGN
Used Nuclear Fuel Loading and Structural Performance Under Normal Conditions of Transport -
Demonstration of Approach and Results of Used Fuel Performance Characterization
SEPTEMBER 30, 2013 99

6.2.1.6   BOUNDARY CONDITIONS

During the initialization stage, the basket walls were constrained while the assembly was allowed to establish contact with the basket floor due to gravitational loading. During the transient excitation, acceleration time-histories from the cask-level analysis were applied to the basket and spacer block plates. For the basket compartment side walls and spacer block plates, a rigid body was generated between all basket nodes and a node at the basket centroid. Rotational and translational accelerations from the cask-level model for the centroid of a specific basket compartment were applied to the center rigid body node which then appropriately transfers the rigid body translations and rotations to all of the nodes on the basket and spacer block plate boundaries. Further details on the model input history data is provided in Section 6.2.2.1.

6.2.1.7   SOLUTION PROCEDURE

The solution procedure for the assembly model included an initialization step to establish contact due to gravity followed by a transient dynamic calculation. During the initialization step, the gravitational body load was imposed on the model and the assembly came to rest on the floor of the basket. This step induced the initial strain in the fuel rod cladding due to sagging of the rods between the grid supports. The transient dynamic calculation was then initiated with application of the loading time-histories. Cladding strains in all of the rods were output for post-processing and subsequent use in the failure analysis effort.

USED FUEL DISPOSITION CAMPAIGN
Used Nuclear Fuel Loading and Structural Performance Under Normal Conditions of Transport -
Demonstration of Approach and Results of Used Fuel Performance Characterization
100 **SEPTEMBER 30, 2013**

6.2.2 UPSTREAM AND DOWNSTREAM COMMUNICATIONS

6.2.2.1 MODEL INPUTS

The assembly-level submodel received inputs from both the rod-level and cask-level models. Based on the rod-level analyses, data regarding the fuel rod bending stiffness (LB, UB, and BE), fuel rod Raleigh damping parameters due to possible pellet-clad interactions, spacer grid leaf spring stiffness, spacer grid dimple stiffness, and cladding tensile bending stress concentration due to pellet-pellet gaps were utilized. Based on the cask-level analyses, the six degree-of-freedom motion (X, Y, and Z translational and rotational accelerations) was obtained for the entire basket. Based on the basket compartment of interest, the appropriate acceleration histories provide the time-dependent accelerations representing the selected shock or vibration excitation. Acceleration time-histories were additionally processed via filtering to eliminate high frequency numerical noise generated in the cask-level model output accelerations, but no further drift correction was performed. Bounding cases with broadened response curves that encompass the responses of all 32 individual basket compartments were also evaluated to ensure maximum rod excitation for a final conservative evaluation of each loading condition.

6.2.2.2 MODEL OUTPUTS

The assembly submodel predicted the stresses and strains of the fuel rod cladding for the simulated loading duration. From this data history, the peak cladding strain or stress was identified for failure analysis of an overloading condition. This data history was also used to determine the cyclic strain history for the loading duration using rainflow counting procedures (ASTM E1049-85 2011). Therefore, the model results were analyzed to determine the cladding peak strain and cyclic strain history for use by the failure analysis team.

The assembly model data history was also used to determine the cyclic strain history of the fuel cladding for fatigue failure calculations. For each fuel rod beam element in the model, the resultant axial force and the two resultant bending moments about the local element axes were tabulated for each loading history. Using this unfiltered data, the elastic axial strain and bending strains were computed at four locations on the outer surface of the cladding (Figure 6.15) according to the equations below where E is the elastic modulus, F_{axial} is the resultant axial force, r is the clad outer radius, $K_{tension}$ is the tensile stress concentration factor, and M_{bend1} and M_{bend2} are the resultant local beam bending moments. Tensile bending strains were multiplied by the stress concentration factor of 1.38 based on analysis of the single rod with fuel pellets. This analysis showed that the local tensile bending stress in the cladding was higher than the compressive bending stress because the individual fuel pellets can support a compressive load but likely do not carry tension at the pellet-pellet interface. Therefore cladding on the tensile side during fuel rod bending must carry more of the load, and this effect was included in the strain history calculations. At each of these locations on the rods, rainflow counting procedures (ASTM E1049-85, 2011) were used to compute the amplitudes and total number of strain cycles experienced by the cladding. The rainflow algorithm is a useful method to obtain a set of strain reversal cycles of various amplitudes from a complex time history. The fatigue limit curves

USED FUEL DISPOSITION CAMPAIGN
Used Nuclear Fuel Loading and Structural Performance Under Normal Conditions of Transport -
Demonstration of Approach and Results of Used Fuel Performance Characterization
SEPTEMBER 30, 2013 101

presented in Section 6.4 are used to determine the fatigue damage at each location, and the location with the highest damage was selected for further post-processing. Finally, the histogram of strain cycle amplitudes at the worst rod location for the 10s simulation window was output for a prediction of total damage under the entire transport route.

$$\varepsilon_1 = \frac{1}{E}\left(\frac{F_{axial}}{\pi r^2} + K_{tension}\left(\frac{M_{bend1}r}{\frac{\pi}{4}r^4}\right)\right)$$

$$\varepsilon_3 = \frac{1}{E}\left(\frac{F_{axial}}{\pi r^2} - \left(\frac{M_{bend1}r}{\frac{\pi}{4}r^4}\right)\right)$$

$$\varepsilon_2 = \frac{1}{E}\left(\frac{F_{axial}}{\pi r^2} + K_{tension}\left(\frac{M_{bend2}r}{\frac{\pi}{4}r^4}\right)\right)$$

$$\varepsilon_4 = \frac{1}{E}\left(\frac{F_{axial}}{\pi r^2} - \left(\frac{M_{bend2}r}{\frac{\pi}{4}r^4}\right)\right)$$
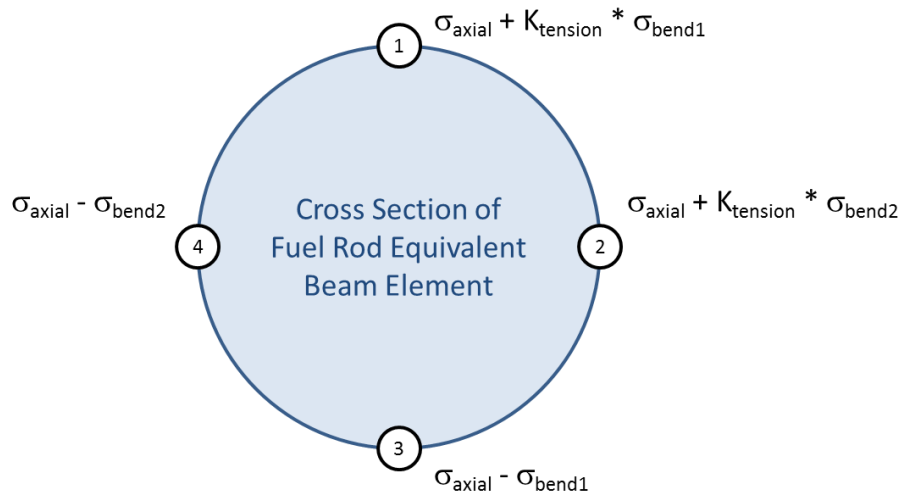
Figure 6.15. Calculation locations of beam cladding strains.

USED FUEL DISPOSITION CAMPAIGN
Used Nuclear Fuel Loading and Structural Performance Under Normal Conditions of Transport -
Demonstration of Approach and Results of Used Fuel Performance Characterization
102   **SEPTEMBER 30, 2013**

6.2.2.3   SURROGATE DEFINTION

The surrogate fuel assembly model was used to represent an individual assembly in the cask-level model. The surrogate model was defined to sufficiently represent the mass, stiffness, and inertial properties of the individual fuel assembly to capture the fundamental modes of its dynamic response. It was previously planned to use the detailed assembly submodel to create a superelement for the surrogate; however, the authors discovered software bugs in the LS-DYNA program which could not be resolved by the developers in sufficient time for testing and use in this task. Instead, an approach of using a coarsely-meshed continuum representation of the assembly with effective properties was utilized. The model used solid mechanics calculations for beam and plate bending to compute effective orthotropic normal and shear moduli for the simplified assembly shown in Figure 6.16. Effective densities were calculated based on the surrogate volume. Modal analysis of the surrogate assembly was then performed and the results were compared to modal results of the full detailed assembly. The computed orthotropic normal and shear moduli ratios were then further scaled by a constant value to better match the first few bending and torsion modes of the assembly. The comparison of the mass, inertia, and modal properties between the two models are shown in Table 6.11 and Table 6.12. The surrogate model was deemed sufficiently similar to the detailed model based on the reasonable matching of these properties. Next, the required time step of the surrogate assembly model was improved. Element sizing was adjusted and geometry of the upper and lower plates was modified to improve the time step to 2.5e-6 s for use in the cask-level analyses (Figure 6.17).

USED FUEL DISPOSITION CAMPAIGN
**Used Nuclear Fuel Loading and Structural Performance Under Normal Conditions of Transport -
Demonstration of Approach and Results of Used Fuel Performance Characterization**
SEPTEMBER 30, 2013 **103**
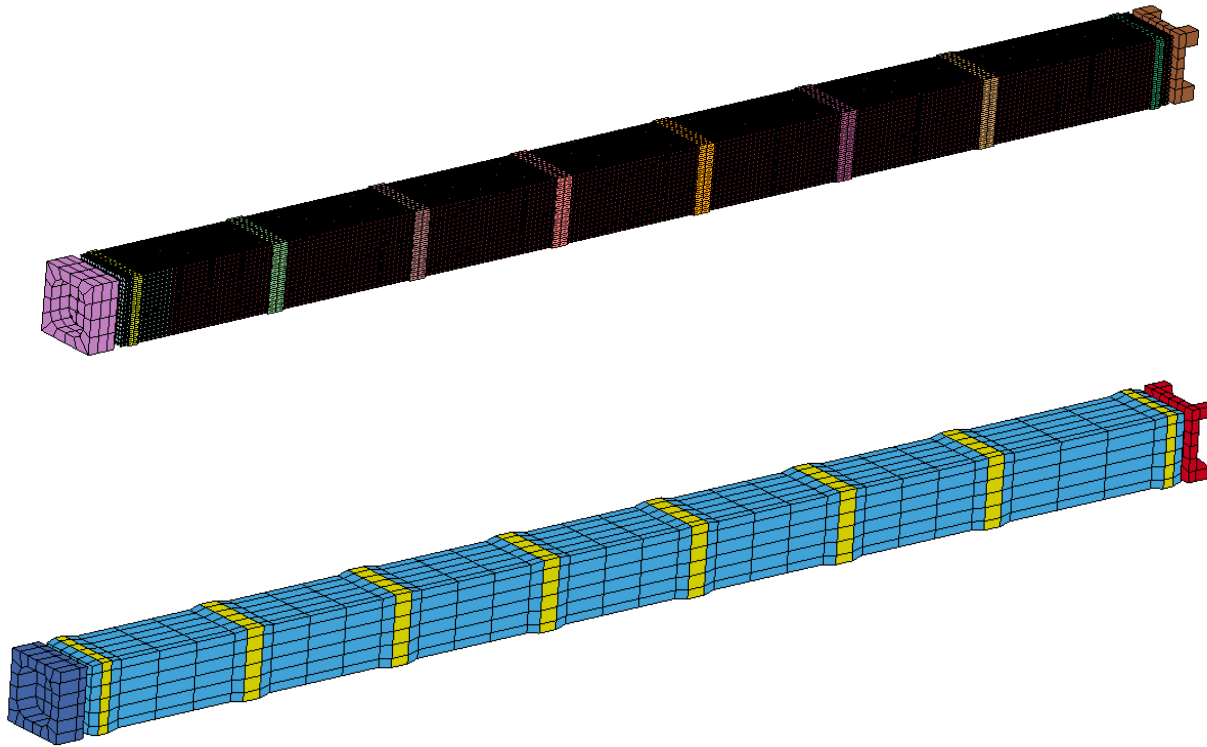
Figure 6.16. Detailed and Simplified Assembly Surrogate Model for Use in Cask-level Analyses
(w/o control components)

Table 6.11. Mass and Inertia of Surrogate and Detailed Assemblies

	Detailed	Surrogate
Total Mass (kg)	623.3	622.4
Ixx (kg-m^2)	809	808
Iyy (kg-m^2)	809	808
Izz (kg-m^2)	4.91	4.58

Table 6.12. Modal Frequencies of Surrogate and Detailed Assemblies

Mode #	Mode	Frequency (Hz)	
		Detailed	Surrogate
1	Z Torsion	4.48	4.46
2,3	XY Flexure	5.33	6.06
4	Z Torsion	9.07	8.89
5,6	XY Flexure	10.25	9.98
7	Z Torsion	14.07	13.27

USED FUEL DISPOSITION CAMPAIGN
Used Nuclear Fuel Loading and Structural Performance Under Normal Conditions of Transport -
Demonstration of Approach and Results of Used Fuel Performance Characterization
104 **SEPTEMBER 30, 2013**
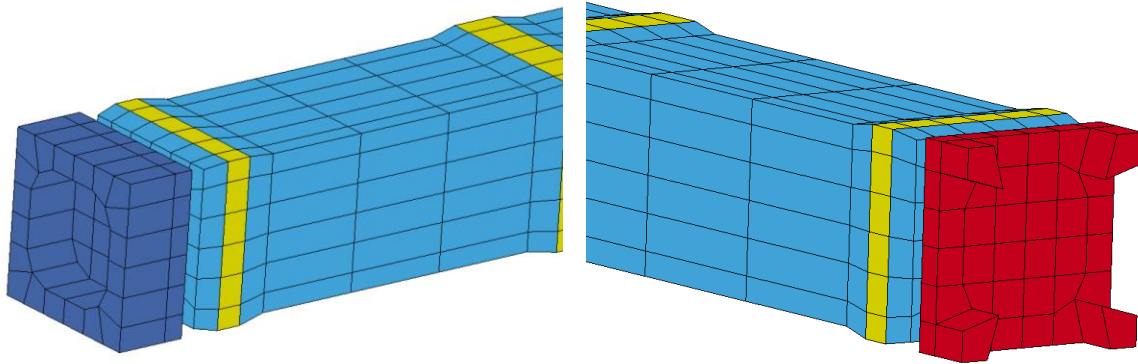
Figure 6.17. Modified Tie Plate and Spacer Grid Geometry to Increase the Time Step of the
Surrogate Assembly

6.3   MODELING APPROACH AT THE FUEL ROD-LEVEL AND BASIS

The knowledge and characterization of material states for high burnup fuel, cladding, and the pellet-clad interface is based on limited experimental data and subject to additional complex behaviors such as chips, voids, primary ridging (from thermal expansion and clad creep-down and often termed "bambooing" from the cladding's similar appearance to a bamboo stalk), secondary ridging (from fuel fracturing/swelling and differential thermal expansion), and local stresses due to pellet edge-clad interactions. For the effort to provide effective mechanical properties of a fuel rod, model evaluations will only consider the effect of complete bonding versus frictional sliding. The single rod sub-modeling effort included a detailed three-dimensional representation of the fuel pin and cladding to investigate the influence of possible gaps between the pellet and cladding on structural dynamic performance. The effort also included a detailed submodel of one individual fuel rod slot in a grid spacer (Figure 6.18). This sub-modeling effort provided equivalent beam properties (i.e., stiffness and damping) and spring and shell properties for the grid spacers, springs, and dimples to the assembly model discussed in Section 6.2 Modeling Approach at the Assembly-Level.

USED FUEL DISPOSITION CAMPAIGN
Used Nuclear Fuel Loading and Structural Performance Under Normal Conditions of Transport -
Demonstration of Approach and Results of Used Fuel Performance Characterization
SEPTEMBER 30, 2013 **105**
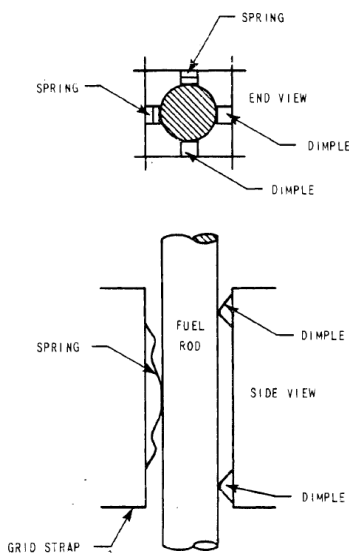
Figure 6.18. Typical Spring and Dimple Support of Fuel Rod in Fuel Assembly Grid

Given the significant variation in the fuel rod geometry and MP (and a lack of substantial data on MP and material state), two approaches were available for obtaining representative fuel rod response: probabilistic or deterministic. Since a probabilistic analysis would require hundreds of model runs to establish reasonable confidence in the rod response (e.g., seismic codes use 80th percentile non-exceedance probability), a deterministic approach was chosen to provide a representative response.

The deterministic approach employed was taken from the seismic community (based on ASCE 4, "Seismic Analysis of Safety-Related Nuclear Structures and Commentary") and uses three estimates on MP: LB, BE, and UB. A flat and broadened response spectrum was also used to account for uncertainty in the model. Since there is a wide range of uncertainty for the structural MP for irradiated fuel (currently there is a lack of high burnup fuel performance data) and also a wide range of uncertainty on material state (i.e., cracked pellets, bambooing of rods, and the pellet-cladding interface) the proposed approach will "tune" the BE response of the PWR assembly. This was accomplished by providing equivalent beam LB and UB (a window), stiffness, and damping parameters from the model developed in this section to the assembly-level model. Then the PWR response can be tuned to a broadened response spectrum at the assembly-level.

6.3.1   MODELING APPROACH AND BASIS

This section describes in detail the modeling approach and basis used at the fuel rod-level. Included in this section are descriptions of the fuel rod stiffness and damping model, the fuel rod FE mesh, MP, and geometry, the fuel rod loading and response, the optimization relating the displacement equation to the FEM data, and the fuel rod viscous damping.

USED FUEL DISPOSITION CAMPAIGN
Used Nuclear Fuel Loading and Structural Performance Under Normal Conditions of Transport -
Demonstration of Approach and Results of Used Fuel Performance Characterization
106   SEPTEMBER 30, 2013

6.3.1.1   DETAILED FUEL ROD STIFFNESS AND DAMPING MODEL

The WE 17×17 type PWR OFA assembly is modeled using a preexisting PNNL model with the fuel rods being represented by beam elements. The important parameters to define the dynamic behavior of the PWR assembly are stiffness (linear elastic MP) and damping (Rayleigh damping). Given the potential for geometric nonlinear behavior (i.e., contact between the pellets and cladding) and potential variation in MP in the actual fuel rods, a detailed rod evaluation was necessary to develop the equivalent beam properties. As discussed above the intent of the detailed fuel rod evaluation was to establish reasonable LB, BE, and UB properties that could be used to define the fuel rod equivalent beam properties in the PWR assembly model. The properties of interest were flexural rigidity, Poisson's ratio, density, cross sectional geometry, and Rayleigh damping. Material nonlinearity (elastic/plastic response) was not evaluated in this detailed model because significant material nonlinearity was not expected during NCT. However if the PWR assembly model shows the potential for significant material nonlinearity then additional evaluation would be necessary.

The basic approach to the fuel rod evaluation can be summarized in the five steps below:

- Generate a simply supported FEM for a portion of a fuel rod that accurately considers geometric nonlinearity

- Apply a distributed load to excite a first mode response

- Establish optimization that best relates the displacement equation to the FEM data using nonlinear regression

- Modify the modeled length, the modeled interaction (tied or in contact), and friction coefficient (where contact is defined) and repeat the above steps to establish viscous damping versus natural frequency, flexural rigidity, and friction

- Define linear beam mass, flexural rigidity and Rayleigh damping parameters equivalent to the nonlinear fuel rod model. This data was provided to the PWR assembly model.

The conclusions of the detailed fuel rod modeling effort documented below are that damping in the fuel rod due to pellet-clad interaction is low. Also the large change in beam flexural rigidity occurs when going from the non-tied beam case (i.e., the pellets and clad are all modeled in contact with various values of friction used) to the tied beam case. The values of friction used herein have little effect on the flexural rigidity.

6.3.1.2   FUEL ROD FINITE ELEMENT MESH, MATERIAL PROPERTIES, AND GEOMETRY

The fuel rod FE meshes were each a simply supported portion of the fuel rod as shown in Figure 6.19 This model included fuel pellets (shown with the red and orange elements) and cladding (shown with the light blue elements). The model used nominal dimensions for the fuel pellet and cladding from DOE (1987), pages 2A-349 to 2A-354. The cladding length was modeled to match the length of the enclosed fuel pellets.

USED FUEL DISPOSITION CAMPAIGN
Used Nuclear Fuel Loading and Structural Performance Under Normal Conditions of Transport -
Demonstration of Approach and Results of Used Fuel Performance Characterization
SEPTEMBER 30, 2013 107
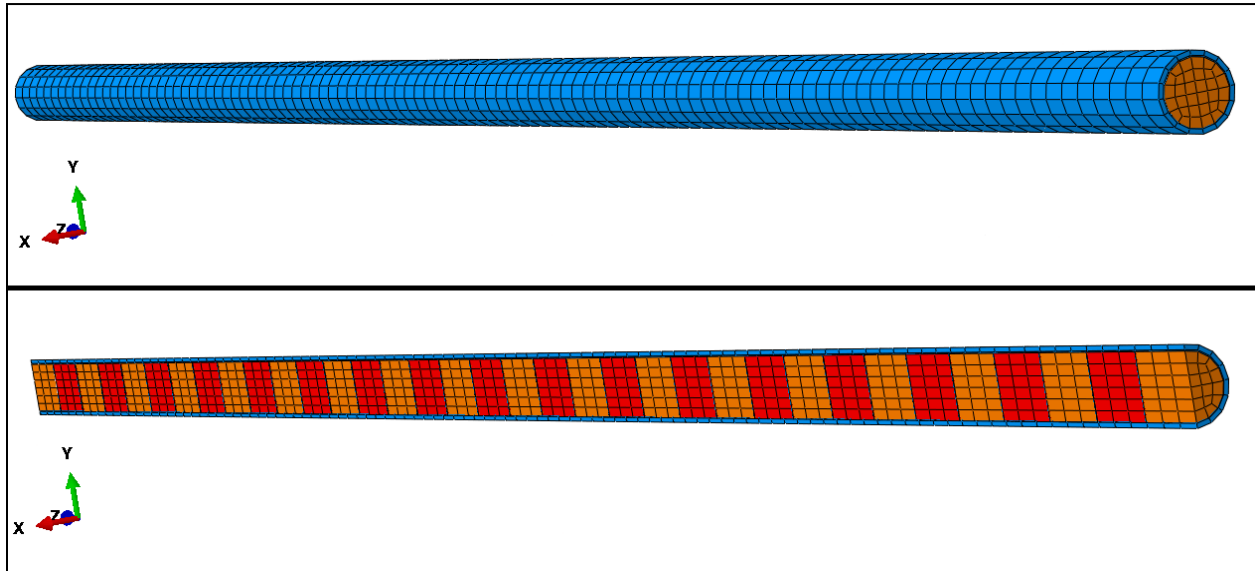
Figure 6.19. Full 35 Fuel Pellet Mesh for the Fuel Rod (Top) and Cut-Away of the Mesh to
Show the Internal Structure (Bottom)

The mesh shown in Figure 6.19 was generated with solid linear continuum shell elements for the cladding and solid reduced integration linear brick elements for the fuel pellet elements. These element types are selected because they produce reasonable results for the mesh density shown and they work well in implicit or explicit solvers. Surfaces were defined on the fuel pellets and cladding such that pellet-to-pellet and pellet-to-clad interactions could be in contact or tied. When pellet-to-clad surfaces were tied, the outer nodes of the fuel pellets move with a strain free displacement to the inner surface of the cladding. Otherwise, the contact definition does not affect the geometry. The boundary conditions necessary for the simply supported beam behavior are enforced with coupling constraints attached to the ends of the clad. Each coupling constraint uses a reference node that has the boundary conditions applied to it. The reference node is placed in the center of the cladding cross section and couples the response of the reference node with the cross section of the cladding (as shown in Figure 6.20.). A coupling definition is more desirable than a rigid connection because a coupling does not artificially stiffen the cross section by forcing it to stay round. The boundary condition on one coupling node is fixed translation in all directions and fixed rotation along the axis of the fuel rod. The boundary condition on the other coupling node is fixed translation in the two directions perpendicular to the axis of the fuel rod. Allowing one end of the fuel rod to displace along the axis of the fuel rod prevents the fuel rod from being artificially stiffened by having to elongate the fuel rod to allow a simply supported displacement. For models where the pellets are not tied, they are not restrained from leaving the cladding. They are held in place by friction and gravity.

USED FUEL DISPOSITION CAMPAIGN
Used Nuclear Fuel Loading and Structural Performance Under Normal Conditions of Transport -
Demonstration of Approach and Results of Used Fuel Performance Characterization
108   **SEPTEMBER 30, 2013**
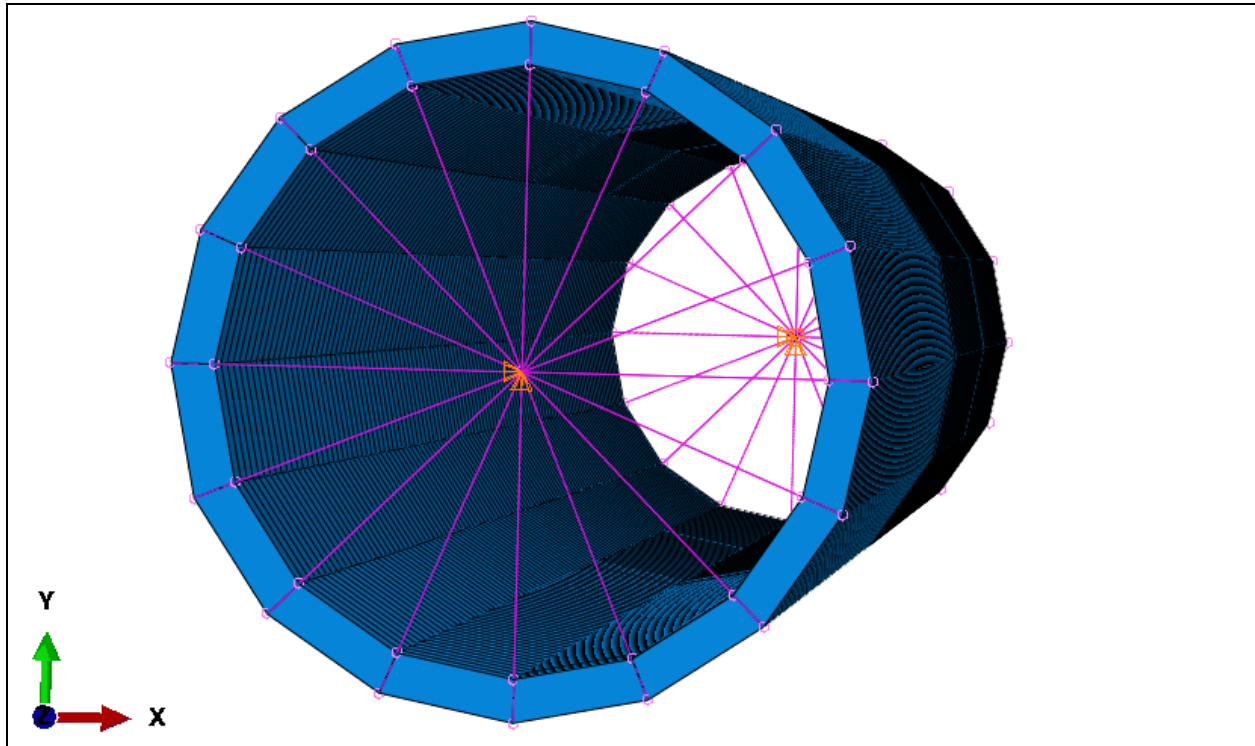
Figure 6.20. Couplings, Cladding, and Cladding Restraints

The UB response occurred when all of the fuel pellets along with the cladding were tied together thus acting as a continuous beam. The LB response occurred when all of the fuel pellets along with the cladding were in contact (i.e., nodes not tied) thus the cladding is primarily responsible for the stiffness of the fuel rod. The BE response occurred when the fuel pellets were tied to the cladding but in contact with each other. An expected actual fuel rod may have pellets that are cracked and in contact with each other, the cladding may exhibit "bambooing," and the overall stiffness may change during transport due to crack growth. These conditions could be imposed on this mesh if the deformation and cracking were known. Given the significant variability associated with possible deformation and cracking, the UB and LB are intended to reasonably envelope possible fuel rod response. The BE gives an initial guess as to actual fuel rod response. However, the final PWR assembly model runs were based on selecting a fuel rod stiffness, between UB and LB, that ensure that the peak response occurs.

The following are the fuel rod and fuel pellet geometry used in the fuel rod model.

Fuel Rod and Fuel Pellet Geometry

$d_{co} := 0.360 \cdot in = 9.144 \cdot mm$ — Outside diameter of the cladding.

$t_c := 0.0225 \cdot in = 0.5715 \cdot mm$ — Thickness of the cladding.

$d_{ci} := d_{co} - 2 \cdot t_c = 8.001 \cdot mm$ — Inside diameter of the cladding.

$A_c := \frac{\pi}{4} \cdot \left(d_{co}^2 - d_{ci}^2\right) = 15.39 \cdot mm^2$ — Cross sectional area of the cladding.

$I_c := \frac{\pi}{64} \cdot \left(d_{co}^4 - d_{ci}^4\right) = 142.0 \cdot mm^4$ — Area moment of inertia for the cladding.

$d_p := 0.3088 \cdot in = 7.844 \cdot mm$ — Outside diameter of the fuel pellet.

$A_p := \frac{\pi}{4} \cdot d_p^2 = 48.318 \cdot mm^2$ — Cross sectional area of the fuel pellet.

$I_p := \frac{\pi}{64} \cdot d_p^4 = 185.786 \cdot mm^4$ — Area moment of inertia for the fuel pellet.

$L_p := \frac{144.00 \cdot in}{284} = 12.879 \cdot mm$ — Length of the fuel pellet.

$m_{cp} := \rho_{z4} \cdot A_c + \rho_{uo} \cdot A_p = 0.599 \cdot \frac{kg}{m}$ — Modeled mass of the cladding and fuel pellet.

$L_c := \begin{pmatrix} L_p \cdot 35 \\ L_p \cdot 50 \\ L_p \cdot 70 \\ L_p \cdot 100 \end{pmatrix} \qquad L_c = \begin{pmatrix} 450.8 \\ 644.0 \\ 901.5 \\ 1287.9 \end{pmatrix} \cdot mm$ — Length of the modeled cladding. These lengths are established by matching clad lengths with 35, 50, 70, and 100 stacked fuel pellets respectively.

$EI_{LB\_t} := E_{z4}(T_{400}, \Delta_o, C_o, \Phi_{lo}) \cdot I_c = 8.6 \cdot Pa \cdot m^4$ — Theoretical lower bound flexural rigidity.

$EI_{UB\_t} := E_{z4}(T_o, \Delta_o, C_o, \Phi_{hi}) \cdot I_c \ldots = 49.2 \cdot Pa \cdot m^4$
$\qquad + E_{uo}(T_o, D_o, Bu_{lo}) \cdot I_p$ — Theoretical upper bound flexural rigidity.

USED FUEL DISPOSITION CAMPAIGN
Used Nuclear Fuel Loading and Structural Performance Under Normal Conditions of Transport -
Demonstration of Approach and Results of Used Fuel Performance Characterization
110 **SEPTEMBER 30, 2013**

6.3.1.3 FUEL ROD LOADING AND RESPONSE

In the FEM the first mode fuel rod response was excited by applying loading over two steps. In the first step, the loading was applied statically as a constant 1g load and a superimposed 0.4 g sine wave load as shown in Figure 6.21. The sine wave load is zero at the fuel rod model ends and 0.4 g in the center. This magnitude of loading was considered reasonable and relatively conservative because higher loading can be expected in actual motions and the damping tends to increase with increased motion. In the second step, the sine wave portion of the load was removed to produce a first mode, free vibration response that was evaluated dynamically. The response was tracked using the vertical motion of a node midway along the cladding length.
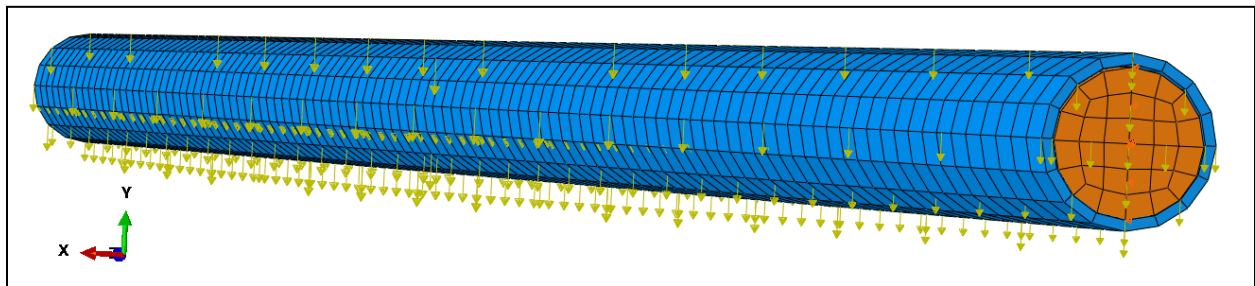
Figure 6.21 Distributed Load on the Fuel Rod

Figure 6.22 shows example vertical motions for the center of a fuel rod. These motions are from a single fuel rod mesh that has fuel pellets that are free to move. The difference in the curves is the friction coefficient that is used. The red curve is for a friction coefficient of 0.1, the blue curve is for a friction coefficient of 0.75, and the brown curve is for a friction coefficient of 1.5.
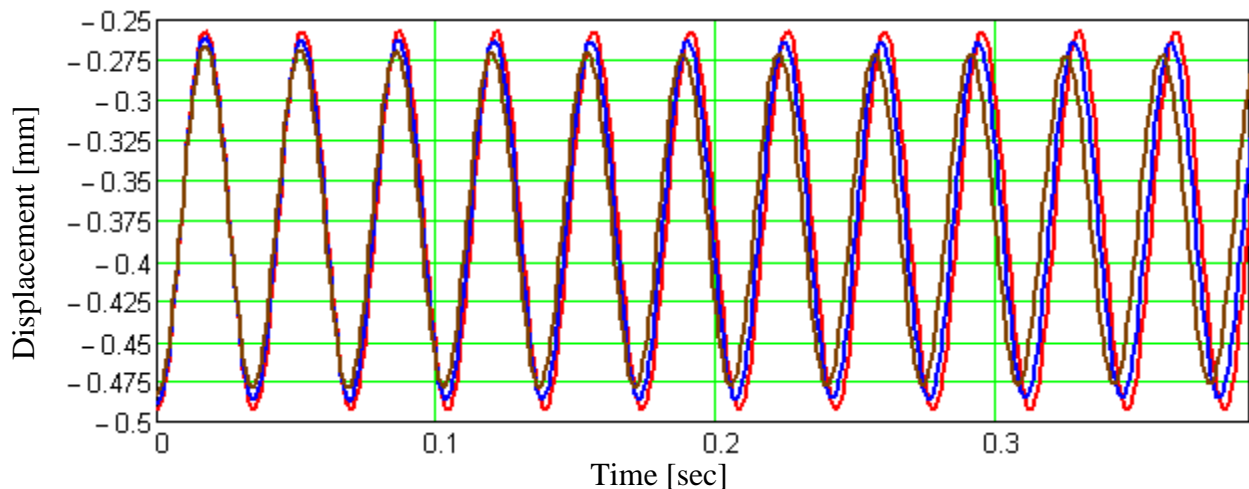
Figure 6.22 Three Example Vertical Motions for a Single Fuel Rod Mesh Defined with Different Friction Coefficients

USED FUEL DISPOSITION CAMPAIGN
Used Nuclear Fuel Loading and Structural Performance Under Normal Conditions of Transport -
Demonstration of Approach and Results of Used Fuel Performance Characterization
SEPTEMBER 30, 2013 **111**

6.3.1.4   OPTIMIZATION RELATING THE DISPLACEMENT EQUATION TO THE FINITE ELEMENT MODEL DATA

The beam elements representing the fuel rods in the PWR assembly are linear in their response. Consequently, their center motion (for similar boundary conditions and loading) follows the equation for free response of an underdamped simple oscillator. The displacement equation for this motion is given below. (It should be noted that the equation below finds damping under the assumption that the model is a simple spring-mass-damper. Because the damping needs to accommodate a simply supported beam, the damping found here needs to be scaled before including it in the PWR assembly model. This is discussed further in Section 6.3.1.5.) Below is the displacement equation of a single degree-of-freedom system.

$$y(t, \zeta, \omega, Y_a, \phi, y_g) := Y_a \cdot e^{-\zeta \cdot \omega \cdot t} \cdot \sin\left(\sqrt{1 - \zeta^2} \cdot \omega \cdot t + \phi\right) + y_g$$

Displacement equation of a single degree-of-freedom system.

where:

ζ - Viscous damping ω - Angular natural frequency y - Vertical position t - Time

ϕ - Phase angle Y_a - Wave amplitude y_g - Wave offset

Given the displacement equation and the FEM data, optimization relating the two can be performed. This is done using nonlinear regression. To perform the nonlinear regression, the following functions are defined:

$$\frac{dy}{d\zeta} = y_\zeta(t, \zeta, \omega, Y_a, \phi, y_g) := -Y_a \cdot \omega \cdot t \cdot e^{-\zeta \cdot \omega \cdot t} \cdot \left(\sin\left(\sqrt{1 - \zeta^2} \cdot \omega \cdot t + \phi\right) + \frac{\zeta}{\sqrt{1 - \zeta^2}} \cdot \cos\left(\sqrt{1 - \zeta^2} \cdot \omega \cdot t + \phi\right) \right)$$

$$\frac{dy}{d\omega} = y_\omega(t, \zeta, \omega, Y_a, \phi, y_g) := Y_a \cdot t \cdot e^{-\zeta \cdot \omega \cdot t} \cdot \left(\cos\left(\sqrt{1 - \zeta^2} \cdot \omega \cdot t + \phi\right) \cdot \sqrt{1 - \zeta^2} - \zeta \cdot \sin\left(\sqrt{1 - \zeta^2} \cdot \omega \cdot t + \phi\right) \right)$$

$$\frac{dy}{dY_a} = y_{Ya}(t, \zeta, \omega, Y_a, \phi, y_g) := e^{-\zeta \cdot \omega \cdot t} \cdot \sin\left(\sqrt{1 - \zeta^2} \cdot \omega \cdot t + \phi\right)$$

$$\frac{dy}{d\phi} = y_\phi(t, \zeta, \omega, Y_a, \phi, y_g) := Y_a \cdot e^{-\zeta \cdot \omega \cdot t} \cdot \cos\left(\sqrt{1 - \zeta^2} \cdot \omega \cdot t + \phi\right)$$

$$\frac{dy}{dy_g} = y_{yg}(t, \zeta, \omega, Y_a, \phi, y_g) := 1$$

Using the defined functions, the optimized values for viscous damping, angular natural frequency, wave amplitude, phase angle, and wave offset can be found iteratively. Initially, a reasonable guess for these values is made. This is shown below along with definitions for the vectors containing the FEM data to be fit.

USED FUEL DISPOSITION CAMPAIGN
Used Nuclear Fuel Loading and Structural Performance Under Normal Conditions of Transport -
Demonstration of Approach and Results of Used Fuel Performance Characterization
112   **SEPTEMBER 30, 2013**

$A = \begin{pmatrix} \zeta & \omega & Y_a & \phi & y_g \end{pmatrix}^T$ \qquad Initial guess values.

$i = 0 .. last(t)$ \qquad Counting variable.

y_{dat} - Vertical position data from the finite element model.

t_{dat} - Time associated with the vertical position data.

Note: y_{dat} and t_{dat} are vectors and y_{dat_i} and t_{dat_i} are scalar values at the ith position in the given vector. Likewise, $A_0 = \zeta$, $A_1 = \omega$, ...

The iterations that follow are performed as shown below:

Iteration loop

$y_{\zeta\_v_i} = y_\zeta\left(t_{dat_i}, A_0, A_1, A_2, A_3, A_4\right)$ \qquad $y_{\phi\_v_i} = y_\phi\left(t_{dat_i}, A_0, A_1, A_2, A_3, A_4\right)$

$y_{\omega\_v_i} = y_\omega\left(t_{dat_i}, A_0, A_1, A_2, A_3, A_4\right)$ \qquad $y_{yg\_v_i} = y_{yg}\left(t_{dat_i}, A_0, A_1, A_2, A_3, A_4\right)$

$y_{Ya\_v_i} = y_{Ya}\left(t_{dat_i}, A_0, A_1, A_2, A_3, A_4\right)$ \qquad $D_i = y_{dat_i} - y\left(t_{dat_i}, A_0, A_1, A_2, A_3, A_4\right)$

$Z = augment\left(y_{\zeta\_v}, y_{\omega\_v}, y_{Ya\_v}, y_{\phi\_v}, y_{yg\_v}\right)$

$\Delta A = \left(Z^T \cdot Z\right)^{-1} \cdot \left(Z^T \cdot D\right)$ \qquad Change in the optimize values.

$A = A + \Delta A$ \qquad New optimize values.

In the iteration loop, vectors are defined for each function defined previously. These vectors are augmented into an array "Z" and an additional vector "D" is defined as the difference between the data and displacement equation values. The change in optimized values and new optimized values can then be found with this array and vector. The iteration loop is repeated until the following is true.

$$\varepsilon = \sum_{j=0}^{last(A)} \left| \frac{\Delta A_j}{A_j} \right| < 10^{-6}$$

USED FUEL DISPOSITION CAMPAIGN
Used Nuclear Fuel Loading and Structural Performance Under Normal Conditions of Transport -
Demonstration of Approach and Results of Used Fuel Performance Characterization
SEPTEMBER 30, 2013 113

Upon completion of the nonlinear regression, the optimized values for viscous damping, angular natural frequency, wave amplitude, phase angle, and wave offset are defined. Using these values optimized natural frequency and flexural rigidity can also be defined as follows:

$$\begin{pmatrix} \zeta & \omega & Y_a & \phi & y_g \end{pmatrix}^T = A \qquad$$ Optimized values output from the nonlinear regression.

$$f = \frac{\omega}{2 \cdot \pi} \qquad$$ Optimized value for natural frequency.

$$f = \frac{\pi^2}{2 \cdot \pi \cdot L_c^2} \cdot \sqrt{\frac{E \cdot I}{m_{cp}}} \qquad$$ Natural frequency of the first mode of a simply supported beam.

Solving for flexural rigidity:

$$E \cdot I = \frac{4 \cdot f^2 \cdot L_c^4 \cdot m_{cp}}{\pi^2} \qquad$$ Optimized value for flexural rigidity.

Example results from the nonlinear regression are shown in Figure 6.23. Figure 6.23 shows the FE data (red curve) and displacement equation results using the optimized values for viscous damping, angular natural frequency, wave amplitude, phase angle, and wave offset (blue dots).
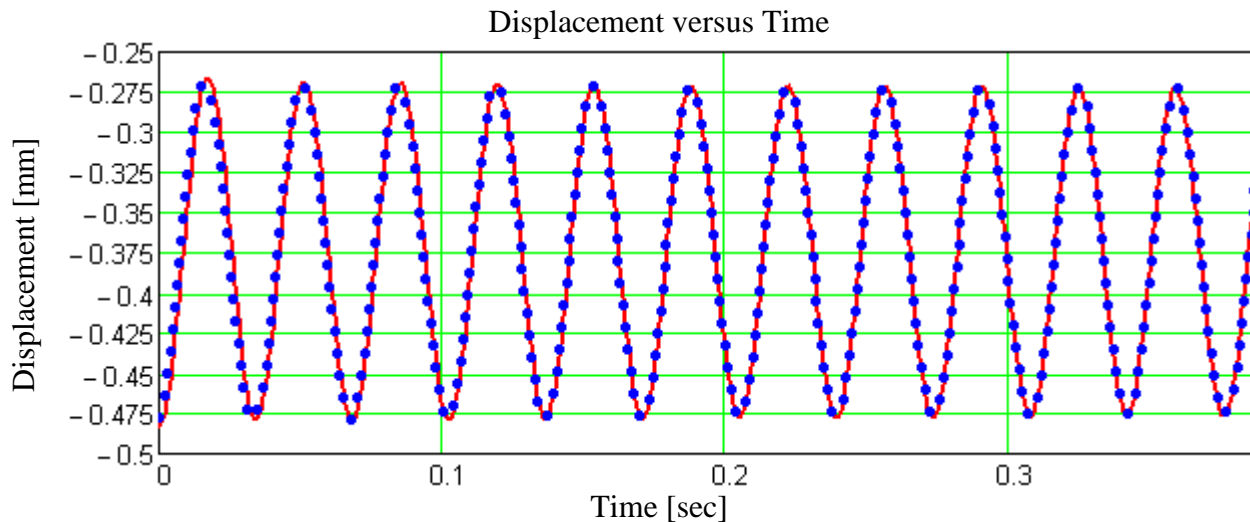
Figure 6.23. Example Finite Element Data (Red Curve) and Displacement Equation Results (Blue Dots)

USED FUEL DISPOSITION CAMPAIGN
Used Nuclear Fuel Loading and Structural Performance Under Normal Conditions of Transport -
Demonstration of Approach and Results of Used Fuel Performance Characterization
114 **SEPTEMBER 30, 2013**

6.3.1.5 *FUEL ROD VISCOUS DAMPING VERSUS NATURAL FREQUENCY, FLEXURAL RIGIDITY, AND FRICTION*

Given the flexibility and potential gapping of the grid straps, the grid straps will most likely not act as rigid supports during the vibrational response of the fuel rods. Most likely, the first mode of the fuel rods will occur with a shape that has nodes at a greater spacing than the grid straps. To accommodate this uncertainty, simply supported beam models are run in this evaluation to accommodate fuel rod open span lengths of a little less than one OFA grid strap which is 520.7 mm (20.5 in) spacing to more than two times the OFA grid strap spacing.

Varying the open span length of the fuel rod models makes it possible to establish the appropriate viscous damping versus natural frequency. Varying the friction coefficient (where pellet-to-pellet and/or pellet-to-cladding contact is defined and not tied) makes it possible to establish the appropriate viscous damping versus natural frequency. The range of friction coefficients is from 0.1 to 1.5. Varying the fuel pellet and cladding interaction (as in tied or in contact) makes it possible to establish the appropriate viscous damping versus flexural rigidity.

The approach described in Section 6.3.1.4 is calculated as though the model is a simple spring-mass-damper. Because the damping needs to accommodate a simply supported beam, the calculated viscous damping values need to be scaled before including them in the PWR assembly model. To find how the viscous damping needs to be scaled, a virtual work derivation is performed. In the derivation, the virtual work for viscous damping in a simply supported beam is equated to the virtual work for viscous damping in a simple spring-mass-damper (where the entire beam has a rigid body deflection). The derivation is solved to find the relationship between the simply supported beam viscous damping and simple spring-mass-damper viscous damping. As such,

$$\delta W = \int_0^L c(z) \cdot v_t(z,t) \cdot \delta v(z,t)\, dz \qquad \text{Virtual work related to viscous damping.}$$

where:

W - Work L - Beam length c - Viscous damping coefficient v - Beam displacement

z - Position along the beam t - Time

Note: δ - Implies virtual t as a subscript - Implies a time derivative.

Since the beam acts in a first mode motion, the beam displacement can be broken into a shape function which varies only in position and a motion function which varies only in time.

USED FUEL DISPOSITION CAMPAIGN
Used Nuclear Fuel Loading and Structural Performance Under Normal Conditions of Transport -
Demonstration of Approach and Results of Used Fuel Performance Characterization
SEPTEMBER 30, 2013   **115**

$$v_t(z,t) = \psi(z) \cdot y_t(t) \qquad \text{Velocity of the beam.}$$

$$\delta v(z,t) = \psi(z) \cdot \delta y(t) \qquad \text{Virtual displacement of the beam.}$$

where:

ψ - Shape function y - Motion function

Substituting:

$$\delta W = \int_0^L c(z) \cdot \left(\psi(z) \cdot y_t(t)\right) \cdot \left(\psi(z) \cdot \delta y(t)\right) dz \quad = \quad y_t(t) \cdot \delta y(t) \cdot \int_0^L c(z) \cdot \psi(z)^2 dz$$

For the viscous damping coefficient being a constant as in this problem:

$$\delta W = c \cdot y_t(t) \cdot \delta y(t) \cdot \int_0^L \psi(z)^2 dz \qquad \text{Virtual work related to viscous damping.}$$

Having the function for virtual work, it can be defined unique to the simply supported beam and simple mass-spring-damper and equated.

$$\psi\_b(z) = \sin\left(\frac{\pi}{L} \cdot z\right) \qquad \text{Shape function for the simply supported beam.}$$

$$\psi\_s(z) = 1 \qquad \text{Shape function for the simple spring-mass-damper.}$$

Note: _b in the subscript - Implies simply supported beam.

      _s in the subscript - Implies simple spring-mass-damper.

$$\delta W\_b = c\_b \cdot y_t(t) \cdot \delta y(t) \cdot \int_0^L \psi\_b(z)^2 dz \qquad \text{Virtual work related to viscous damping for the simply supported beam.}$$

$$\delta W\_b = c\_s \cdot y_t(t) \cdot \delta y(t) \cdot \int_0^L \psi\_s(z)^2 dz \qquad \text{Virtual work related to viscous damping for the simple spring-mass-damper.}$$

USED FUEL DISPOSITION CAMPAIGN
Used Nuclear Fuel Loading and Structural Performance Under Normal Conditions of Transport -
Demonstration of Approach and Results of Used Fuel Performance Characterization
116   **SEPTEMBER 30, 2013**

Equating, substituting, and solving for the viscous damping coefficient relationship:

$$\delta W_{\_b} = \delta W_{\_s} \implies c_{\_b} \cdot y_t(t) \cdot \delta y(t) \cdot \int_0^L \psi_{\_b}(z)^2 \, dz = c_{\_s} \cdot y_t(t) \cdot \delta y(t) \cdot \int_0^L \psi_{\_s}(z)^2 \, dz$$

$$\implies c_{\_b} \cdot \int_0^L \psi_{\_b}(z)^2 \, dz = c_{\_s} \cdot \int_0^L \psi_{\_s}(z)^2 \, dz \implies c_{\_b} \cdot \int_0^L \sin\left(\frac{\pi}{L} \cdot z\right)^2 \, dz = c_{\_s} \cdot \int_0^L 1^2 \, dz$$

$$\implies c_b \cdot \frac{L}{2} = c_s \cdot L \implies c_b = 2 \cdot c_s$$

C_{cr} - Critical damping for the actual model.

$$\frac{c_b}{C_{cr}} = 2 \cdot \frac{c_s}{C_{cr}} \implies \zeta_b = 2 \cdot \zeta_s \qquad$$ Viscous damping for the simply supported beam as a function of the center point data viscous damping.

The above derivation shows that the viscous damping, derived as described in Section 6.3.1.4 has to be doubled to be correctly input as viscous damping for a linear beam.

To provide data for an appropriate range of open span length, friction coefficient, and contact definition, ten model runs were performed. Table 6.13 lists general modeling information for the model runs and Table 6.14 provides a summary of important input and optimized results. The models are primarily focused on varying friction and length with no ties in the model. The expectation is that the viscous damping can be best characterized by studying it where it is a maximum. The viscous damping should go to zero as the model becomes completely tied because the friction and contact that represent the primary energy losses are no longer present. The viscous damping, natural frequency, and flexural rigidity (E·I) values in Table 6.13 were derived as described in Section 6.3.1.4. The viscous damping is then doubled to make it appropriate for input to a linear beam with Rayleigh damping.

To ensure a good curve fit, each model was run for not less than 11 cycles. The curve fit was then performed on the entire model run and cycles 3-8 to ensure that the natural frequency and damping did not change (within four significant digits). This provided confidence that enough data was provided to get a good curve fit and no significant anomaly occurred near the start of the model run which would skew the data.

USED FUEL DISPOSITION CAMPAIGN
Used Nuclear Fuel Loading and Structural Performance Under Normal Conditions of Transport -
Demonstration of Approach and Results of Used Fuel Performance Characterization
SEPTEMBER 30, 2013   117

Table 6.13. Fuel Rod Finite Element Model General Information

Model number	Number of Fuel Pellets in the Model	ABAQUS/Standard Input File for Static Loading*	ABAQUS/Explicit Input File for Dynamic Response*
1	100	notie_100_SI_static.inp	notie_100_SI_exp.inp
2	70	notie_70_SI_static.inp	notie_70_SI_exp.inp
3	70	notie_70_SI_static_0_75.inp	notie_70_SI_exp_0_75.inp
4	50	notie_50_SI_static.inp	notie_50_SI_exp.inp
5	50	notie_50_SI_static_0_75.inp	notie_50_SI_exp_0_75.inp
6	35	notie_35_SI_static.inp	notie_35_SI_exp.inp
7	35	notie_35_SI_static_0_75.inp	notie_35_SI_exp_0_75.inp
8	35	notie_35_SI_static_1_5.inp	notie_35_SI_exp_1_5.inp
9	35	cirtie_35_SI_static.inp	cirtie_35_SI_exp.inp
10	35	fulltie_35_SI_static.inp	fulltie_35_SI_exp.inp

* All of the input files were generated in ABAQUS/CAE (fuel_rod_exp_OFA_SI_mm.cae).

Table 6.14. Fuel Rod Finite Element Model Input and Results

Model number	Contact Definition	Length [mm]	Friction Coefficient	Viscous Damping	Frequency [Hz]	$E \cdot I$ [Pa·m^4]
1	No Ties	1287.9	0.1	0.0000821	3.5	8.29
2	No Ties	901.53	0.1	0.0000936	7.2	8.33
3	No Ties	901.53	0.75	0.000522	7.2	8.36
4	No Ties	643.95	0.1	0.000164	14.1	8.34
5	No Ties	643.95	0.75	0.000877	14.2	8.39
6	No Ties	450.76	0.1	0.0000844	28.8	8.32
7	No Ties	450.76	0.75	0.000548	28.9	8.36
8	No Ties	450.76	1.5	0.00105	29.1	8.5
9	Clad-Pellet Tie	450.76	0.1	0.0000136	67.1	45.06
10	All Tied	450.76	0.1	0.00000181	70.1	49.29

Given the results in Table 6.14, the following definitions can be made:

$EI_{LB} = 8.3 \cdot Pa \cdot m^4$ Evaluated lower bound flexural rigidity.

$EI_{BE} = 45.1 \cdot Pa \cdot m^4$ Evaluated best estimate flexural rigidity.

$EI_{UB} = 49.3 \cdot Pa \cdot m^4$ Evaluated upper bound flexural rigidity.

USED FUEL DISPOSITION CAMPAIGN
Used Nuclear Fuel Loading and Structural Performance Under Normal Conditions of Transport -
Demonstration of Approach and Results of Used Fuel Performance Characterization
118   **SEPTEMBER 30, 2013**

When comparing the evaluated flexural rigidity to the theoretical flexural rigidity (calculated earlier), the evaluated LB is lower than theoretical and the evaluated UB is higher than theoretical. These differences are small and their existence can be expected. The primary reason for the evaluated LB being lower than theoretical is that the evaluated model allows the section to soften by ovalization where this was not considered for the theoretical value. The primary reason for the evaluated UB being higher than theoretical is that the evaluated model swells the fuel pellet to tie it to the clad where this was not considered for the theoretical value.

The results in Table 6.14 can be used to establish viscous damping versus natural frequency, friction, and flexural rigidity. In the PWR assembly model, Rayleigh damping will be used. The equation for Rayleigh damping is given below:

$$\zeta = \frac{\alpha}{\omega} + \beta \cdot \omega \qquad \text{Rayleigh damping equation.}$$

where:

ω - Angular natural frequency α - Mass damping factor β - Stiffness damping factor

Considering the data in Table 6.14, it appears that a reasonable Rayleigh damping function could simply have a linear variation with respect to friction and flexural rigidity. Since there is a less than 3% change in the flexural rigidity for the first eight models, it will be assumed constant for these model runs. This makes it possible to perform a linear regression of the data to optimize the mass damping factor and stiffness damping factor as a function of friction coefficient. Following this optimization, the Rayleigh damping function will be defined to linearly go to zero as flexural rigidity goes to that of the "all tied" model. If the data reasonably/conservatively agrees with this assumption, no further optimization is needed.

Below is the definition for the mass damping factor and the stiffness damping factor to be optimized by linear regression:

$$\alpha = C_0 \cdot fn \qquad \text{Mass damping factor.}$$

$$\beta = C_1 \cdot fn \qquad \text{Stiffness damping factor.}$$

where:

fn - Friction coefficient C_0 - Mass damping constant C_1 - Stiffness damping constant

Considering the inclusion of the friction coefficient above, the linear regression can be performed as shown below:

$$\zeta_i \approx \frac{C_0 \cdot fn_i}{\omega_i} + C_1 \cdot fn_i \cdot \omega_i \qquad \begin{array}{l}\text{Rayleigh damping equation for optimization (where the}\\ \text{subscript "i" indicates a single set of data).}\end{array}$$

Minimize: $F(\omega) =$

USED FUEL DISPOSITION CAMPAIGN
Used Nuclear Fuel Loading and Structural Performance Under Normal Conditions of Transport -
Demonstration of Approach and Results of Used Fuel Performance Characterization
SEPTEMBER 30, 2013 **119**

$$\sum_{i=0}^{last(\omega)} \left(\frac{C_0 \cdot fn_i}{\omega_i} + C_1 \cdot fn_i \cdot \omega_i - \zeta_i \right)^2$$

$$\frac{\partial}{\partial \alpha} \left[\sum_{i=0}^{last(\omega)} \left(\frac{C_0 \cdot fn_i}{\omega_i} + C_1 \cdot fn_i \cdot \omega_i - \zeta_i \right)^2 \right] = 0 \implies \sum_{i=0}^{last(\omega)} \left[\frac{2 \cdot fn_i}{\omega_i} \cdot \left(\frac{C_0 \cdot fn_i}{\omega_i} + C_1 \cdot fn_i \cdot \omega_i - \zeta_i \right) \right] = 0$$

$$\frac{\partial}{\partial \beta} \left[\sum_{i=0}^{last(\omega)} \left(\frac{C_0 \cdot fn_i}{\omega_i} + C_1 \cdot fn_i \cdot \omega_i - \zeta_i \right)^2 \right] = 0 \implies \sum_{i=0}^{last(\omega)} \left[2 \cdot fn_i \cdot \omega_i \cdot \left(\frac{C_0 \cdot fn_i}{\omega_i} + C_1 \cdot fn_i \cdot \omega_i - \zeta_i \right) \right] = 0$$

$$\begin{bmatrix} \sum_{i=0}^{last(\omega)} \left(fn_i^2 \cdot \omega_i^{-2} \right) & \sum_{i=0}^{last(\omega)} fn_i^2 \\ \sum_{i=0}^{last(\omega)} fn_i^2 & \sum_{i=0}^{last(\omega)} \left(fn_i^2 \cdot \omega_i^2 \right) \end{bmatrix} \cdot \begin{pmatrix} C_0 \\ C_1 \end{pmatrix} = \begin{bmatrix} \sum_{i=0}^{last(\omega)} \left(\zeta_i \cdot fn_i \cdot \omega_i^{-1} \right) \\ \sum_{i=0}^{last(\omega)} \left(\zeta_i \cdot fn_i \cdot \omega_i \right) \end{bmatrix}$$

$$\begin{pmatrix} C_0 \\ C_1 \end{pmatrix} = \begin{bmatrix} \sum_{i=0}^{last(\omega)} \left(fn_i^2 \cdot \omega_i^{-2} \right) & \sum_{i=0}^{last(\omega)} fn_i^2 \\ \sum_{i=0}^{last(\omega)} fn_i^2 & \sum_{i=0}^{last(\omega)} \left(fn_i^2 \cdot \omega_i^2 \right) \end{bmatrix}^{-1} \cdot \begin{bmatrix} \sum_{i=0}^{last(\omega)} \left(\zeta_i \cdot fn_i \cdot \omega_i^{-1} \right) \\ \sum_{i=0}^{last(\omega)} \left(\zeta_i \cdot fn_i \cdot \omega_i \right) \end{bmatrix}$$

Using the results from the first eight model runs (and converting natural frequency to angular natural frequency as needed in the equation above), the constants can be found.

$C_0 = 3.39 \times 10^{-2}$ Mass damping constant

$C_1 = 3.07 \times 10^{-6}$ Stiffness damping constant

Figure 6.24 shows a plot of the optimized Rayleigh damping curves (using the constants above) and FEM data (from the first eight model runs shown in Table 6.13). Considering the results in Figure 6.24, the assumption of the viscous damping linearly changing with friction appears reasonably accurate. The main discrepancy between the curves and data points results from the

USED FUEL DISPOSITION CAMPAIGN
Used Nuclear Fuel Loading and Structural Performance Under Normal Conditions of Transport -
Demonstration of Approach and Results of Used Fuel Performance Characterization
120   SEPTEMBER 30, 2013

Rayleigh damping curve shape. As can be seen in Figure 6.24, the five data points below 20 Hz show an upward trend that fits well to a Rayleigh damping curve shape. The three points above 20 Hz take a downward trend which makes fitting a Rayleigh damping curve more difficult. In general, the viscous damping considered here is very minimal and the optimization is considered reasonable.
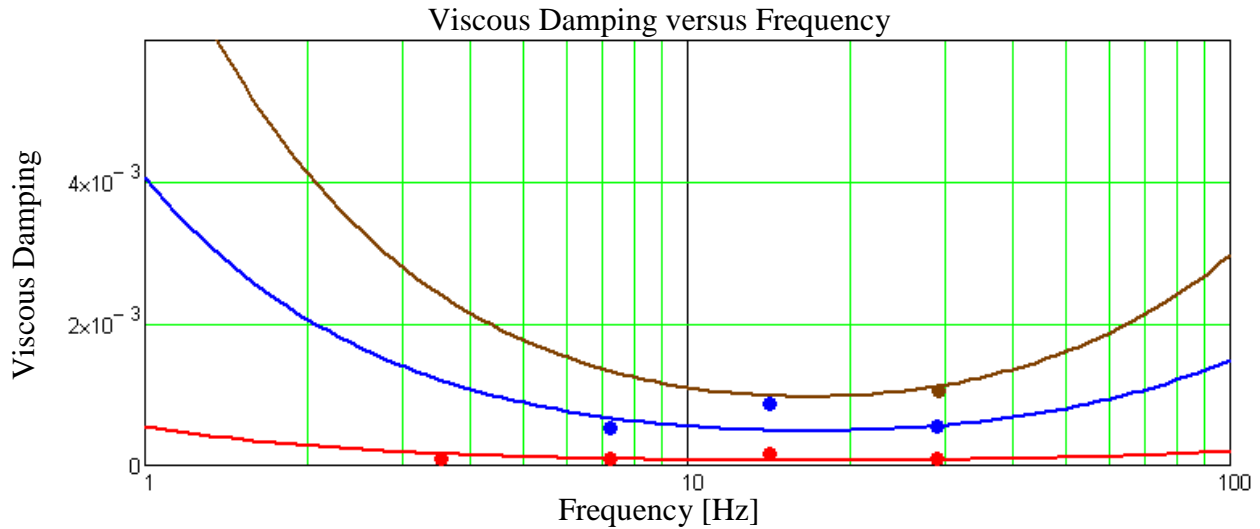
Figure 6.24. Optimized Rayleigh Damping Curves and Finite Element Model Data Points for Friction Coefficients of 0.1 (Red), 0.75 (Blue), and 1.5 (Brown)

As discussed above, the next step is to define a Rayleigh damping function that linearly goes to zero as flexural rigidity goes to that of the "all tied" model. The results of this are checked against the three FE models run with a length of 450.76 mm, a friction coefficient of 1.0, and different contact definitions. Below are the definitions for the mass damping factor and stiffness damping factor with the flexural rigidity included. Figure 6.25 shows the comparison of the Rayleigh damping (with the defined damping factors) versus flexural rigidity curve and the FEM data points.

$$\alpha = \frac{\left(EI_{UB} - EI\right) \cdot \left(C_0 \cdot fn\right)}{EI_{UB} - EI_{LB}} \qquad \text{Mass damping factor.}$$

$$\beta = \frac{\left(EI_{UB} - EI\right) \cdot \left(C_1 \cdot fn\right)}{EI_{UB} - EI_{LB}} \qquad \text{Stiffness damping factor.}$$

where:

fn - Friction coefficient C_0 - Mass damping constant C_1 - Stiffness damping constant

EI - Flexural rigidity EI_{UB} - Maximum flexural rigidity EI_{LB} - Minimum flexural rigidity

Viscous Damping versus Flexural Rigidity (E·I)
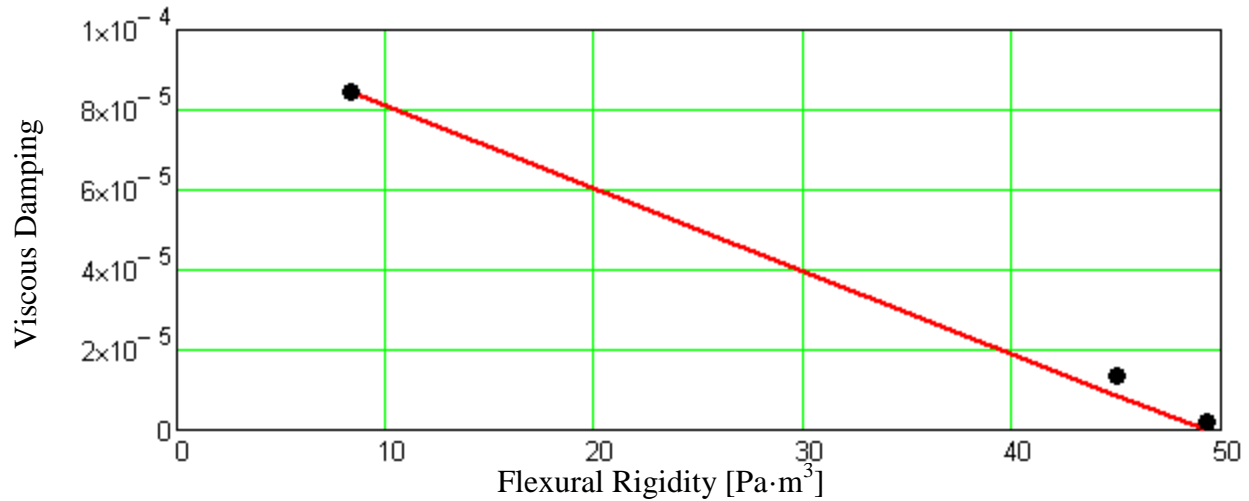
Figure 6.25. Rayleigh Damping versus Flexural Rigidity Curve and Finite Element Model Data Points

Figure 6.25 shows a plot considering that Rayleigh damping linearly goes to zero as flexural rigidity goes to that of the "all tied" model. The data reasonably/conservatively agrees with the FEM data point. Consequently, no further optimization is necessary.

6.3.2 MATERIAL PROPERTIES

The material property data used in the FE models are mostly defined using equations from Geelhood (2013). However selected cladding and density and fuel pellet Poisson's ratio are consistent with Avallone et al. (1996) and the fuel density is calculated with data from the description for the WE 17×17 type PWR OFA from DOE (1987), pages 2A-349 to 2A-354.

The fuel rod cladding is fabricated using Zircaloy-4 and the pellets are UO_2. The OFA assembly has grids that are fabricated of either Zircaloy-4 or Inconel 718. Therefore the MP used in determining the equivalent grid shell thickness and equivalent nonlinear spring and dimple behavior are Zircaloy-4 and Inconel 718. The details on the MP used in the models are provided in Table 6.15.

USED FUEL DISPOSITION CAMPAIGN
Used Nuclear Fuel Loading and Structural Performance Under Normal Conditions of Transport -
Demonstration of Approach and Results of Used Fuel Performance Characterization
122   SEPTEMBER 30, 2013

Table 6.15. Material Properties Used in the Fuel Rod Models

Material	Bound	Temperature (Kelvin)	Modulus of Elasticity (Pa)	Poisson's Ratio	Density (kg/m^3)	Fast Neutron Fluence (n/m^2)
Zircaloy-4	Upper Bound	295	9.165×10^{10}	0.318	6.59×10^3	12.5×10^{25}
	Lower Bound	673	6.022×10^{10}	0.338	6.59×10^3	0
Inconel 718	Upper Bound	295	1.982×10^{11}	0.29	8.193×10^3	
	Lower Bound	673	1.795×10^{11}	0.29	8.193×10^3	
UO$_2$	Upper Bound	295	9.165×10^{10}	0.21	1.029×10^4	1.25×10^{26}
	Lower Bound	673	1.66×10^{11}	0.21	1.029×10^4	0

The calculations for the material property definitions provided in Table 6.15 are given below:

Zircaloy-4 Tubing (Fuel Cladding) Material Property equations

T - Temperature in Kelvin. (A reasonable range of temperatures for this evaluation is considered to occur between room temperature and 400°C.)

$\Delta_o := 0.0012$ - Average oxygen concentration minus oxygen concentration of as-received cladding. Always use 0.0012 kg oxygen/kg Zircaloy.

$C_o := 0.5$ - Cold work (unit-less ratio of areas). Use 0.5 for Zircaloy-4 and ZIRLO™. Use 0.0 for M5™.

Φ - Fast neutron fluence (n/m^2). (A reasonable range of fast neutron fluences for this evaluation is considered to occur between 0 and 12.5×10^{25} n/m^2 given that this is representative of the range of values given in Geelhood et al. (2013).)

$$K_{E1}(T_o, \Delta_o) := \left(6.61 \cdot 10^{11} + 5.912 \cdot 10^8 \cdot T_o\right) \cdot \Delta_o$$ First modulus of elasticity equation constant.

$$K_{E2}(C_o) := -2.6 \cdot 10^{10} \cdot C_o$$ Second modulus of elasticity equation constant.

$$K_{E3}(\Phi_o) := 0.88 + 0.12 \cdot e^{\dfrac{-\Phi_o}{10^{25}}}$$ Third modulus of elasticity equation constant.

USED FUEL DISPOSITION CAMPAIGN
Used Nuclear Fuel Loading and Structural Performance Under Normal Conditions of Transport -
Demonstration of Approach and Results of Used Fuel Performance Characterization
SEPTEMBER 30, 2013   123

Given the previous definitions, the modulus of elasticity is
defined by:

$$K_{G2}(C_o) := -0.867 \cdot 10^{10} \cdot C_o \qquad \text{First shear modulus equation constant.}$$

$$E_{z4}(T_o, \Delta_o, C_o, \Phi_o) := \frac{1.088 \cdot 10^{11} - 5.475 \cdot 10^7 \cdot T_o + K_{E1}(T_o, \Delta_o) + K_{E2}(C_o)}{K_{E3}(\Phi_o)} \cdot Pa$$

$$K_{G1}(T_o, \Delta_o) := \left(7.07 \cdot 10^{11} + 2.315 \cdot 10^8 \cdot T_o\right) \cdot \Delta_o \qquad \text{Second shear modulus equation constant.}$$

$$K_{G3}(\Phi_o) := 0.88 + 0.12 \cdot e^{\frac{-\Phi_o}{10^{25}}} \qquad \text{Third shear modulus equation constant.}$$

And is defined as:

$$G_{z4}(T_o, \Delta_o, C_o, \Phi_o) := \frac{4.04 \cdot 10^{10} - 2.168 \cdot 10^7 \cdot T_o + K_{G1}(T_o, \Delta_o) + K_{G2}(C_o)}{K_{G3}(\Phi_o)} \cdot Pa$$

$$v_{z4}(T_o, \Delta_o, C_o, \Phi_o) := \frac{E_{z4}(T_o, \Delta_o, C_o, \Phi_o)}{2 \cdot G_{z4}(T_o, \Delta_o, C_o, \Phi_o)} - 1 \qquad \text{Poisson's ratio.}$$

$$\rho_{z4} = 6.587 \times 10^3 \frac{kg}{m^3} \qquad \text{Mass density.}$$

To generate plots of modulus of elasticity versus temperature and fast neutron fluence to
establish upper and lower bound:

$T_o := 295 \quad K \qquad$ Room temperature.

$T_{400} := 673.15 \quad K \quad$ Temperature at 400°C.

$\Phi_{lo} := 0 \qquad$ Lowest considered fast neutron fluence (n/m2).

$\Phi_{hi} := 12.5 \cdot 10^{25} \quad$ Highest considered fast neutron fluence (n/m2).

$$T_{gr} := T_o, T_o + \frac{T_{400} - T_o}{100} \; .. \; T_{400} \qquad \text{Temperature plotting values.}$$

$$\Phi_{gr} := \Phi_{lo}, \Phi_{lo} + \frac{\Phi_{hi} - \Phi_{lo}}{100} \; .. \; \Phi_{hi} \qquad \text{Fast neutron fluence plotting values.}$$
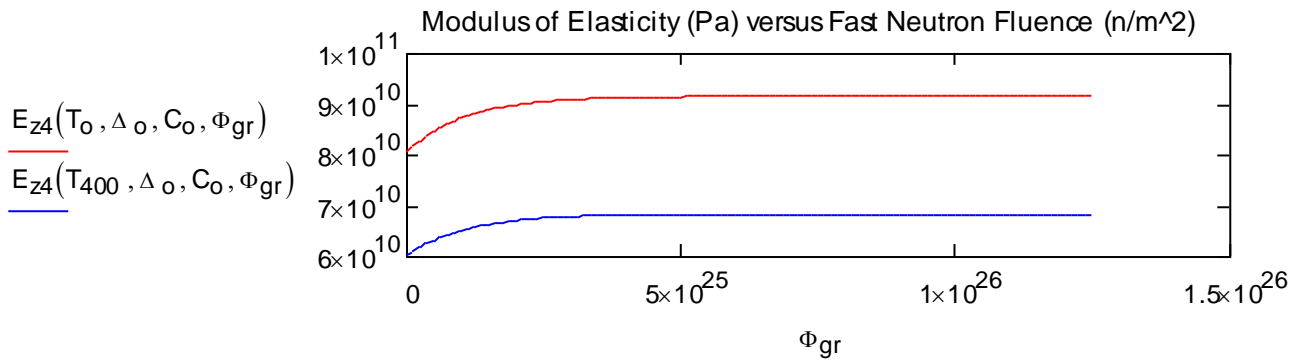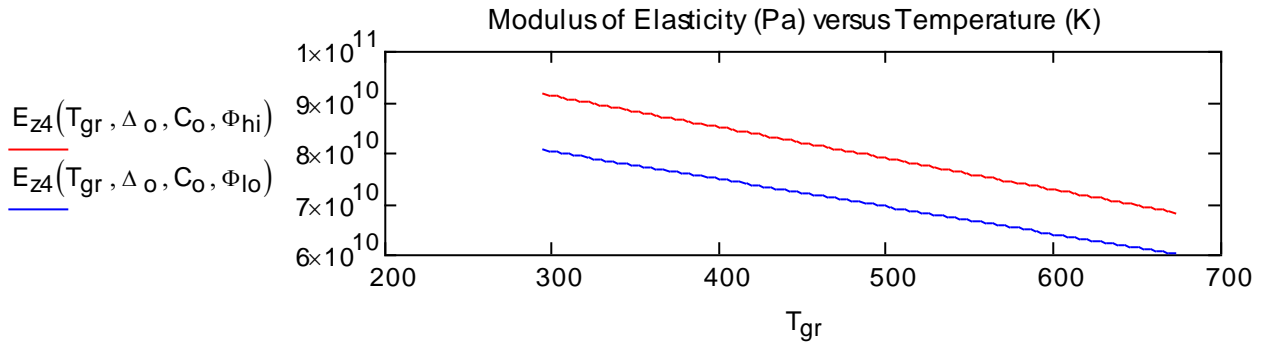
USED FUEL DISPOSITION CAMPAIGN
Used Nuclear Fuel Loading and Structural Performance Under Normal Conditions of Transport -
Demonstration of Approach and Results of Used Fuel Performance Characterization
124   **SEPTEMBER 30, 2013**

Which yields:

Considering the plots above, the UB modulus of elasticity occurs at the lowest temperature and highest fast neutron fluence and the LB modulus of elasticity occurs at the highest temperature and lowest fast neutron fluence.

USED FUEL DISPOSITION CAMPAIGN
Used Nuclear Fuel Loading and Structural Performance Under Normal Conditions of Transport -
Demonstration of Approach and Results of Used Fuel Performance Characterization
SEPTEMBER 30, 2013 125

Fuel Material Property Equations

T — Temperature in Kelvin. (A reasonable range of temperatures for this evaluation is considered to occur between room temperature and 400°C.)

$D_o := 0.95$ — Fuel density (fraction of theoretical density). (The defined value is from DOE (1987), page 2A-352.)

Bu — Burnup (GWd/MTU). (A reasonable range of fast neutron fluences for this evaluation is considered to occur between 0 and 55 GWd/MTU. The upper limit is selected because bonding is present around the circumference above this value per Geelhood et al. (2013), page 51.)

The modulus of elasticity is defined as:

$$E_{uo}(T_o, D_o, Bu_o) := \left[2.334 \cdot 10^{11} \cdot \left[1 - 2.752 \cdot (1 - D_o) \right] \cdot \left(1 - 1.0915 \cdot 10^{-4} \cdot T_o \right) \cdot \left(1 - 2.0 \cdot 10^{-3} \cdot Bu_o \right) \right] \cdot Pa$$

$\nu_{uo} := 0.21$ \hspace{3cm} Poisson's ratio.

$$\rho_{uo} := \frac{4.01 \cdot lbm}{\frac{\pi}{4} \cdot (0.3088 \cdot in)^2 \cdot 144.00 \cdot in}$$ \hspace{2cm} Mass density.

$$\rho_{uo} = 1.029 \times 10^4 \frac{kg}{m^3}$$

To generate plots of modulus of elasticity versus temperature and burnup to establish upper and lower bound the following conditions are defined:

$T_o = 295$ \quad K \hspace{2cm} Room temperature.

$T_{400} = 673.15$ \quad K \quad Temperature at 400°C.

$Bu_{lo} := 0$ \hspace{2.5cm} Lowest burnup (GWd/MTU).

$Bu_{hi} := 55$ \hspace{2.5cm} Highest burnup (GWd/MTU).

$$T_{gr} := T_o, T_o + \frac{T_{400} - T_o}{100} \ .. \ T_{400}$$ \hspace{2cm} Temperature plotting values.

$$Bu_{gr} := Bu_{lo}, Bu_{lo} + \frac{Bu_{hi} - Bu_{lo}}{100} \ .. \ Bu_{hi}$$ \hspace{2cm} Burnup plotting values.
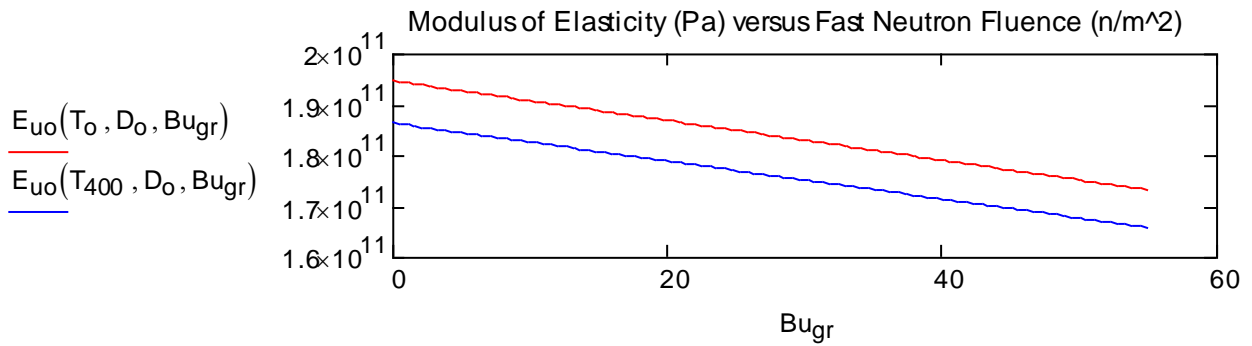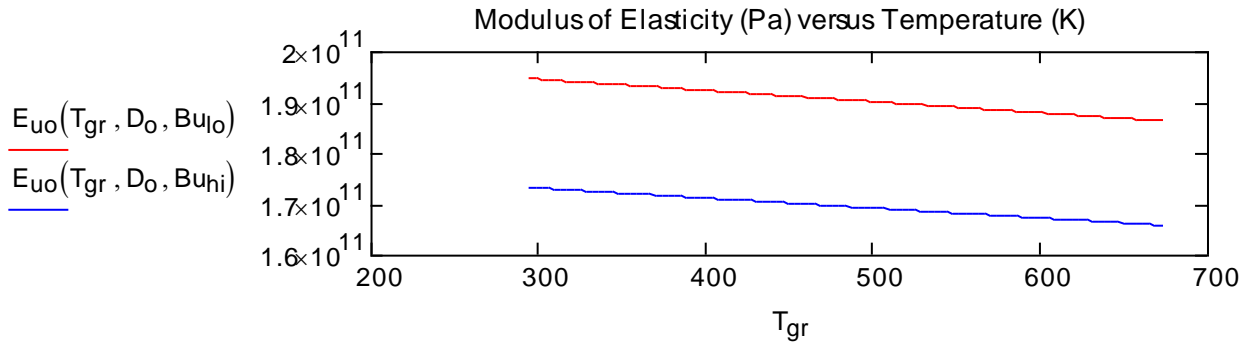
USED FUEL DISPOSITION CAMPAIGN
Used Nuclear Fuel Loading and Structural Performance Under Normal Conditions of Transport -
Demonstration of Approach and Results of Used Fuel Performance Characterization
126   **SEPTEMBER 30, 2013**

Modulus of Elasticity (Pa) versus Temperature (K)

$E_{uo}(T_{gr}, D_o, Bu_{lo})$

$E_{uo}(T_{gr}, D_o, Bu_{hi})$

Modulus of Elasticity (Pa) versus Fast Neutron Fluence (n/m^2)

$E_{uo}(T_o, D_o, Bu_{gr})$

$E_{uo}(T_{400}, D_o, Bu_{gr})$

Considering the plots above, the UB modulus of elasticity occurs at the lowest temperature and lowest burnup and the LB modulus of elasticity occurs at the highest temperature and highest burnup.

Using the equations above, the following UB and LB MP can be found.

USED FUEL DISPOSITION CAMPAIGN
Used Nuclear Fuel Loading and Structural Performance Under Normal Conditions of Transport -
Demonstration of Approach and Results of Used Fuel Performance Characterization
SEPTEMBER 30, 2013 **127**

Upper Bound Model Material Properties

$T_o = 295$ K   Room temperature.

Clad Material Properties

$\Delta_o = 0.0012$ Average oxygen concentration minus oxygen concentration of as-received cladding. Always use 0.0012 kg oxygen/kg Zircaloy.

$C_o = 0.5$ Cold work (unit-less ratio of areas). Use 0.5 for Zircaloy-4 and ZIRLO™. Use 0.0 for M5™.

$\Phi_{hi} = 1.25 \times 10^{26}$ Fast neutron fluence (n/m2).

$E_{z4}(T_o, \Delta_o, C_o, \Phi_{hi}) = 9.165 \times 10^7 \cdot \dfrac{kg \cdot mm}{s^2 \cdot mm^2}$ Modulus of elasticity.

$\nu_{z4}(T_o, \Delta_o, C_o, \Phi_{hi}) = 0.318$ Poisson's ratio.

$\rho_{z4} = 6.587 \times 10^{-6} \cdot \dfrac{kg}{mm^3}$ Mass density.

Fuel Material Properties

$D_o = 0.95$ Fuel density (fraction of theoretical density).

$Bu_{Io} = 0$ Burnup (GWd/MTU). This value is selected as conservatively stiff.

$E_{uo}(T_o, D_o, Bu_{Io}) = 1.948 \times 10^8 \cdot \dfrac{kg \cdot mm}{s^2 \cdot mm^2}$ Modulus of elasticity.

$\nu_{uo} = 0.21$ Poisson's ratio.

$\rho_{uo} = 1.029 \times 10^{-5} \cdot \dfrac{kg}{mm^3}$ Mass density.

USED FUEL DISPOSITION CAMPAIGN
Used Nuclear Fuel Loading and Structural Performance Under Normal Conditions of Transport -
Demonstration of Approach and Results of Used Fuel Performance Characterization
128 **SEPTEMBER 30, 2013**

Lower Bound Model Material Properties

$T_{400} = 673.15$ K Temperature at 400°C.

Clad Material Properties

$\Delta_o = 0.0012$ Average oxygen concentration minus oxygen concentration of as-received cladding. Always use 0.0012 kg oxygen/kg Zircaloy.

$C_o = 0.5$ Cold work (unit-less ratio of areas). Use 0.5 for Zircaloy-4 and ZIRLO™. Use 0.0 for M5™.

$\Phi_{lo} = 0$ Fast neutron fluence (n/m2). This is set to zero to make it conservatively soft.

$E_{z4}(T_{400}, \Delta_o, C_o, \Phi_{lo}) = 6.022 \times 10^7 \cdot \dfrac{kg \cdot mm}{s^2 \cdot mm^2}$ Modulus of elasticity.

$\nu_{z4}(T_{400}, \Delta_o, C_o, \Phi_{lo}) = 0.338$ Poisson's ratio.

$\rho_{z4} = 6.587 \times 10^{-6} \cdot \dfrac{kg}{mm^3}$ Mass density.

Fuel Material Properties

$D_{400} := 0.95$ Fuel density (fraction of theoretical density).

$Bu_{hi} = 55$ Burnup (GWd/MTU). This value is selected because bonding is present around the circumference above this value.

$E_{uo}(T_{400}, D_{400}, Bu_{hi}) = 1.66 \times 10^8 \cdot \dfrac{kg \cdot mm}{s^2 \cdot mm^2}$ Modulus of elasticity.

$\nu_{uo} = 0.21$ Poisson's ratio.

$\rho_{uo} = 1.029 \times 10^{-5} \cdot \dfrac{kg}{mm^3}$ Mass density.

6.3.3 UPSTREAM AND DOWNSTREAM COMMUNICATIONS

The information generated in this detailed fuel rod, grid spacer, and spring analysis is provided to the PWR assembly model. At the PWR assembly-level model this information will be used to "tune" the assembly to the input response spectra at the basket location. The tuning is performed within the LB, UB material property window.

USED FUEL DISPOSITION CAMPAIGN
**Used Nuclear Fuel Loading and Structural Performance Under Normal Conditions of Transport -
Demonstration of Approach and Results of Used Fuel Performance Characterization
SEPTEMBER 30, 2013** 129

Additionally the stress increase due to fuel rod bending is calculated and provided to the PWR assembly-level model. This multiplier is used at the PWR assembly-level on the bending stress output.

6.4   FAILURE DETERMINATION

The primary purpose of this initiative is to determine if the loads that UNF is subjected to under rail-related NCT are sufficient to cause failure in the cladding and/or assembly structure. The modeling activities described in the previous Section 4 and in the Loading, M&S Methodology, Sensitivity, and Failure strategy document (Adkins 2013c) can provide computed stress and strain histories for the fuel rods based on input loading from the rail car, material properties given in Geelhood (2013), temperature distribution, and the initial conditions. Additionally, an interim failure criteria and a methodology to assess failure against these criteria has been established in order to determine if these stress and strain histories are sufficient to cause cladding failure.

Various material properties that can be used as failure criteria (e.g. yield strength, uniform elongation, fracture toughness, fatigue strength) have been identified in the Material Properties Handbook (Geelhood 2013). The loading experienced by UNF under rail-related NCT will consist of shock and vibrational loads. A methodology has been developed to analyze the potential for failure for the shock loads separately from the vibrational loads. Also, with the vibrational loads it is anticipated that the loading will not consist of a constant amplitude loading over the entire transportation time. Rather, it will likely consist of several different amplitude loadings occurring with different frequencies. In order to accommodate this, a methodology to calculate a cumulative fatigue damage fraction based on a number of difference cycles at a number of different stress or strain amplitudes must be developed. This cumulative damage fraction will be combined with the damage fraction from the shock loading and then be used to assess the potential for failure for a given stress and strain history.

6.4.1   INTERIM FAILURE CRITERIA

Various material properties that can be used as failure criteria have been proposed in the Material Properties Handbook (Geelhood 2013). These criteria provide a first-order estimate of failure of UNF under NCT. The potential failure modes where criteria could be established are:

- **Fatigue failure**: Failure of the rods due to excessive strain cycling at low amplitude. The mechanism causing this strain cycling would be vibration normal to the axial direction of the fuel rods as they are transported by rail or road. This is the most likely failure mechanism for UNF under NCT. For this activity, the O'Donnell fatigue-design curve for irradiated Zircaloy was used to assess failure under vibrational loading.

USED FUEL DISPOSITION CAMPAIGN
Used Nuclear Fuel Loading and Structural Performance Under Normal Conditions of Transport -
Demonstration of Approach and Results of Used Fuel Performance Characterization
130   SEPTEMBER 30, 2013

- **Classic failure due to excessive stress or strain**: This type of failure could be caused by a large shock load that does not cause impact on the fuel rods due to a normal event such as rail car coupling. Because these events are assumed to occur under NCT, this type of failure was examined. For this activity, the uniform elongation (plastic strain at maximum load) was used to assess failure under excessive stress or strain.

- **Failure due to impact loading on the rods**: There is no anticipated impact loading for UNF under NCT. This type of loading is typically characterized by the fracture toughness of a material and is more applicable for accident and drop scenarios that are not considered in this work. The Material Properties Handbook (Geelhood 2013) provides a fracture toughness model that could be used if such a failure mechanism were considered. For this activity, failure due to impact loading will not be considered.

6.4.2   FAILURE APPLICATION METHODOLOGY

The cladding stress and strain history predicted by the detailed UNF assembly model informed by the assembly and cask models under rail-related NCT conditions was used to determine cladding integrity. The cladding stress and strain history was broken down into shock events and vibrational loading.

For shock events, the maximum predicted cladding strain was compared to predicted uniform elongation at the appropriate conditions. For vibrational loading, the strain history was broken up into various cyclic strain magnitudes and the calculated number of occurrences. Because it is anticipated that there will be a different number of cyclic strains at different magnitudes, a damage fraction was calculated that includes the cyclic loadings at various amplitudes. This approach known as the Rainflow-counting algorithm (Matsuishi and Endo 1968) is often used to calculate failure due to fatigue and is included in ASTM E 1049-85 (ASTM 2005).

To calculate the fatigue damage fraction, the vibrational loading history was broken up into a number of strain amplitudes and the number of cycles at each of these amplitudes. For each strain amplitude, fatigue strength, S, was calculated according to:

$$S = \tfrac{1}{2} E \varepsilon_T$$

Where:

  S = fatigue strength
  E = elastic modulus
  ε_T = total strain change over cycle

For each fatigue strength calculated, the fatigue-design curve was used to determine the allowable number of cycles at that strain amplitude and a damage fraction was calculated by dividing the anticipated number of cycles at that strain amplitude by the number allowed at that amplitude. The cumulative damage fraction was calculated by adding the individual damage

USED FUEL DISPOSITION CAMPAIGN
Used Nuclear Fuel Loading and Structural Performance Under Normal Conditions of Transport -
Demonstration of Approach and Results of Used Fuel Performance Characterization
SEPTEMBER 30, 2013 131

fractions for each strain amplitude to the damage fraction from each shock loading event according to:

$$Damage\ Fraction = \sum_{i=1}^{n} \frac{N_i}{(N_{allow})_i} + \sum_{j=1}^{m} \frac{(\varepsilon_{plastic})_j}{UE_j}$$

Where:

N_i = number of anticipated cycles at a given strain amplitude
N_{allow} = number of allowable cycles at a given strain amplitude
$\varepsilon_{plastic}$ = plastic strain from a given shock loading event
UE = uniform elongation for given shock loading event

The methodology described above to analyze the potential for failure from shock and vibration is shown graphically in Figure 6.26.

If the comparisons of the cladding stress and strain history to these failure criteria show that the fuel assembly performance during NCT is significantly below the established failure criteria, then this may provide adequate demonstration that the cladding will not experience gross failure. If the resulting FEM stress/strain history indicates conditions that are close (e.g., within 80%) to the established failure criteria, then further experimental work may be required to refine the current failure curves.

USED FUEL DISPOSITION CAMPAIGN
Used Nuclear Fuel Loading and Structural Performance Under Normal Conditions of Transport -
Demonstration of Approach and Results of Used Fuel Performance Characterization
132
SEPTEMBER 30, 2013

Strain vs. time history from FEA

Vibrational loads
(small or no plastic strain & >20 cycles)
Compare number of cycles and stress amplitude to fatigue-design curve.
ε_1 with N_1 cycles
ε_2 with N_2 cycles
…
ε_n with N_n cycles

Shock loads
(significant plastic strain & <20 cycles)
Compare maximum plastic strain to uniform elongation

$$Damage\ Fraction = \sum_{i=1}^{n} \frac{N_i}{(N_{allow})_i} + \sum_{j=1}^{m} \frac{(\varepsilon_{plastic})_j}{UE_j}$$

Is damage fraction < 1?

Figure 6.26. Methodology to Analyze the Potential for Failure for the Shock Loads and Vibrational Loads

USED FUEL DISPOSITION CAMPAIGN
Used Nuclear Fuel Loading and Structural Performance Under Normal Conditions of Transport -
Demonstration of Approach and Results of Used Fuel Performance Characterization
SEPTEMBER 30, 2013   133

7.   MODELING VALIDATION

Extensive validation has been performed to ensure that that the results for the initial demonstration are the current best estimate. Modeling inputs including the loading histories and the material properties have been validated. The assembly-level FEA models have been validated against the results of the surrogate fuel assembly tested on the shaker table at SNL (McConnell et al. 2013). The fatigue failure limit has been compared to a large body of literature data as well as recent fatigue data from ORNL. This section describes the validation that has been performed in each of these areas.

7.1   NUCARS

The NUCARS® program (TTCI 2013) has been used to provide the acceleration data used by the modeling team as described in Section 5.1. TTCI had previously provided the M&S team with load and vibration data archived at the Transportation Technology Center for a representative railcar. TTCI worked with the M&S team to select the dataset to be as representative as possible of the likely loading, and shock and vibration environment of the railcars that would be used to carry used nuclear fuel transportation casks.

In order to validate the predictions that would later be provided by NUCARS® shown in Section 5.1, TTCI conducted NUCARS® simulations of a railcar with similar characteristics to the representative railcar for which archived data was available. The objective of these simulations was to demonstrate that NUCARS® can be used to reasonably simulate the shock and vibration environment of actual railcars. Simulations were performed over tracks and routes with characteristics as close as possible to the track and route conditions for which the archived data was collected.

The result of these simulations was that there is a good comparison between modeling and test results for lateral and vertical accelerations (Urban et al 2013). Based on these comparisons it is reasonable to assume the loading histories given in Section 5.1 are representative of what will be expected for UNF under NCT from the DOE defined transport that meeting AAR Sepcification 2043 (2003).

7.2   SHAKER TABLE

The SNL fuel assembly shaker table test campaign offered a source of validation data for the PWR fuel assembly model. The test campaign subjected a surrogate fuel assembly to shock acceleration loads while the surrogate fuel assembly was instrumented with a number of accelerometers and strain gauges. Comparison of the body of recorded test data to the calculated model results offered quantifiable evidence of the model's ability to predict realistic response in two key areas:

   1.) <u>Dynamic Response of the Fuel Assembly</u>: Fuel assemblies are not expected to behave like rigid bodies. They are complex structures comprised of long bundles of tubes that

USED FUEL DISPOSITION CAMPAIGN
Used Nuclear Fuel Loading and Structural Performance Under Normal Conditions of Transport -
Demonstration of Approach and Results of Used Fuel Performance Characterization
134   **SEPTEMBER 30, 2013**

are simply supported at the spacer grid locations, but otherwise have freedom to move within the gap space between its neighbors. Under sufficiently large loads, the fuel cladding can make contact with its neighbors, making the dynamic response of the fuel assembly nonlinear and difficult to predict without this type of detailed finite element model. It is also to be expected that the general dynamic response of the fuel assembly structure will change in relation to the magnitude of the loads it is subjected to. Accelerometers were placed at various locations around the fuel assembly surrogate. This technique allows a direct comparison to the model's predicted acceleration, velocity, and displacement history. There are some difficulties in determining the correct velocity and displacement from the available accelerometer data (the raw data requires filtering and drift correction) but the finite element model calculates all three as part of its solution.

2.) <u>Local Strains</u>: One of the major interests of the test campaign was to determine the amount of strain that can be expected in cladding. Strain gauges were placed at a number of locations on the three Zircaloy-4 cladding tubes. The strain gauge data offered direct comparison of model-predicted strains to recorded strains at specific locations on the surrogate fuel cladding. This data offered a direct validation of the model's ability to predict cladding strains under the type of loading scenario investigated.

The model validation effort is not complete, but enough comparisons between test and model results have been completed to assert that the model reasonably approximates the observed fuel assembly behavior in the two categories described above. One caveat to this validation is that the SNL test series covers only a certain range of the potential fuel assembly response. A comparison between the shaker test loads and the NCT loads is needed to determine if the NCT response is within or outside the bounds tested by the shaker.

A detailed report of the shaker table modeling is provided by Klymyshyn et al. (2013). The shaker test report is provided by McConnell et al. (2013). The two types of validation are discussed in the following two subsections, and a summary and conclusions is presented in 7.2.3.

7.2.1   DYNAMIC RESPONSE OF THE FUEL ASSEMBLY

The fuel assembly shaker test was performed using a thick-walled aluminum box structure to represent the fuel compartment and a fuel assembly test surrogate that used the skeleton of a real unirradiated fuel assembly with fuel cladding and fuel replaced by copper tubes with lead wire inside to represent the mass of the fuel. Three of the cladding tubes were the typical Zircaloy-4 material instead of copper, and the strain on these tubes was recorded with strain gauges. The finite element model closely represented the features of the surrogate fuel assembly, the basket structure, and the plates that attached it to the vertical shaker table. The basket and fuel assembly were oriented in the horizontal direction, as expected for transport conditions, and the shaker drove the middle of the basket.

Pre-test predictions (1) anticipated a very mild response from the fuel assembly under the test loads. The maximum liftoff from the basket floor was predicted to be less than one millimeter for the fuel assembly center of mass, with potentially higher liftoff at the ends (still on the order

USED FUEL DISPOSITION CAMPAIGN
Used Nuclear Fuel Loading and Structural Performance Under Normal Conditions of Transport -
Demonstration of Approach and Results of Used Fuel Performance Characterization
SEPTEMBER 30, 2013   135

of millimeters) due to the fuel assembly's ability to flex along its length. This prediction was generally confirmed by the test observers, who noted no significant liftoff of the assembly. This is consistent with the basket and fuel assembly accelerometer data, which did not record any major impacts of the fuel assembly against the floor or ceiling of the basket.

The pre-test predictions also showed some potential "chattering", where the fuel assembly briefly lifted off the basket floor and returned. This was observed in all three of the calculated relative motion histories (acceleration, velocity, and displacement) of the fuel assembly and shaker. The test observers reported the sound of chattering, the sound of the fuel assembly surrogate tapping against the basket.

The pre-test predictions also showed an apparent frequency-dependent amplification of the fuel assembly acceleration response to the excitation loads. In the frequency domain, the composition of the artificial shock load is clearly apparent − SNL used a number of decaying sinusoids with discrete frequencies to define their shock load. These showed up as peaks in the frequency domain decomposition of the shaker acceleration history using FFT (the Fast Fourier Transform operation). Comparing the FFT of the shaker acceleration to the fuel assembly CG acceleration, there was a clear amplification of the excitation in the fuel assembly response in some frequency bands (up to about 150 Hz) and a clear attenuation or non-responsiveness of the fuel assembly (roughly, above 150 Hz). Accelerometer test data located at the middle grid spacer is the best available approximation of the fuel assembly surrogate CG, and this data generally agrees with the frequencies of the frequency response of the model. The work of comparing the shaker test results to the model results is still ongoing, but the middle spacer grid acceleration data confirms that the dominant response range is roughly up to 150 Hz.

The post-test models used the precise acceleration history recorded by an accelerometer placed at the middle of the basket base plate as the base excitation load, and the model was loaded with the best approximation of the actual test. These models confirmed the same general dynamic behavior predicted by the pre-test predictions and the test observations. Specific comparisons of the final post-test model results and the recorded transducer data to determine the accuracy of the model have not been completed, but the general dynamic behavior of the fuel assembly model matches the behavior of the test surrogate to the extent that it has been studied to date.

7.2.2   LOCAL STRAINS

Strain gauges were applied to the shaker table test campaign fuel assembly surrogate at a number of locations. Results from three specific strain gauges were the main focus of comparison in Section 7.2.1. These gages were located on the fuel rod with the longest span (between grid spacers) on the top middle Zircaloy-4 cladding. One strain gauge was located on the cladding in the center of the span, and the two others were located at the ends of the span, as close to either spacer grid as possible. In the model, peak element integration point values were extracted from the elements corresponding to the strain gauge locations. This offered the best direct comparison available.

USED FUEL DISPOSITION CAMPAIGN
Used Nuclear Fuel Loading and Structural Performance Under Normal Conditions of Transport -
Demonstration of Approach and Results of Used Fuel Performance Characterization
136   **SEPTEMBER 30, 2013**

In the test results, the peak recorded strain was on the order of 200 µε (micro strains, equal to 1E-6 mm/mm), which is well within the material's elastic region. This is an indication that very little structural deformation occurred in the surrogate fuel assembly during the test. The peak strains calculated by the post-test version of the model are on the order of 700 µε. While this could be interpreted as an error of 350%, the strains involved are so small that this is more favorably considered to be an error of 500 µε (possibly due to the fact that the strain gages were only excited to 2-3% of their designed strain range), which is an order of magnitude smaller than the 0.2% offset definition for material yield (0.002 mm/mm for yield, 0.0005 mm/mm error). The significance of the calculated difference in strains is still being considered, but from a validation standpoint it can be concluded that when the test produces very small strains in the test surrogate, the model also calculates very small strains.

One consideration that can potentially bring the model strains closer to the actual test strains is that the model was solved with single precision solver (due to time constraints). An assessment of the effect of using single precision versus double precision at specific strain gauge locations through time suggests the average strain error is ±10 µε, with a maximum instantaneous error of ±480 µε. The average error confirms single precision offers a reasonable estimate of the double precision results, but the instantaneous peak error suggests the confidence in calculating the peak strain from a single precision model is relatively low, compared to the magnitude of strains that developed in the shaker table test campaign.

7.2.3   SUMMARY AND CONCLUSIONS

The shaker table test campaign performed by SNL offers an opportunity to validate the PWR fuel assembly model. One important observation that can be made about the test campaign is that it caused very mild dynamic excitation of the fuel assembly and caused very low strains in the cladding. The validation the test data offers is in the same mild response range. Initial model results for the current railcar NCT evaluation suggest the response range may be similar to the SNL shaker test range, or it may be somewhat above it.

The fuel assembly model dynamic response compares well with the observations made by witnesses to the shaker testing, in terms of the fuel assembly chattering within the fuel compartment and the fact that the excitation was not strong enough to cause the fuel assembly to rise off the basket floor to strike the basket ceiling. Accelerometer data does not show any major impacts, and it confirms that the dynamic response is strongest in the 0-150 Hz range, as predicted by the model.

The peak strains recorded in testing are miniscule, on the order of 200 µε, which would need to increase by a factor of more than 30 to reach the Zircaloy-4 yield limit. The model similarly predicts tiny strains, with a slightly higher magnitude (only a 10x margin on the yield limit). The mismatch between the recorded strains and the calculated strains is considered to be a numerical issue related to the calculation of very small numbers. A comparison between single precision and double precision solvers is recommended for the rail NCT evaluation, to determine if this particular case is sensitive to the precision.

USED FUEL DISPOSITION CAMPAIGN
Used Nuclear Fuel Loading and Structural Performance Under Normal Conditions of Transport -
Demonstration of Approach and Results of Used Fuel Performance Characterization
SEPTEMBER 30, 2013   137

7.3   MATERIAL PROPERTIES

The material properties that have a significant impact on the structural performance of UNF are the cladding elastic modulus and cladding yield stress. For both of these properties, best-estimate models taken from vetted NRC fuel performance codes are provided as a function of temperature and irradiation level in the Material Properties Handbook (Geelhood 2013). Additionally, uncertainty bands are established for these models and distributions of the predicted minus measured values are provided.

However, it has been noted that the data used to develop and validate these models are from cladding that was recently (approximately 6 months) removed from the reactor. The short term vacuum drying operation at temperatures up to 400°C is not expected to cause any changes, but the 20 or more years spent in dry cask storage at 100°C-400°C may result in annealing of irradiation damage or in grain growth. In order to assess the potential for annealing to occur, sensitivity studies have been performed using the prediction for the irradiated values as well as for the unirradiated values. The cladding elastic modulus is not a strong function of fluence (12% increase from the unirradiated condition to the highly irradiated condition) such that the maximum difference from annealing will be 12%.The cladding yield stress is a strong function of fluence and the unirradiated strength could be half of the irradiated strength. The results of the sensitivity studies related to these material properties are discussed in Section 8.5.

The elastic properties of the fuel will also impact the overall rigidity of the fuel rod. For this property, best-estimate models are provided as a function of temperature and irradiation level in the Material Properties Handbook (Geelhood 2013). Additionally, uncertainty bands are established for these models and distributions of the predicted minus measured values are provided. Bounding values for the fuel elastic modulus are selected in the calculation of overall rigidity of the fuel rod.

The other material properties such as the cask materials have low uncertainty and have been used successfully for many other applications.

7.4   FUEL ROD-LEVEL MODELING

A validation problem was performed and is described in Section 8.5.8.13 to help demonstrate that the fuel rod-level models provide an accurate stress concentration to be passed on to the assembly-level. This validation problem demonstrates that the model is providing good results.

Another level of validation performed was the verification and validation on the FEA software, ABAQUS, used for the fuel rod modeling work. In addition to the extensive verification and validation (V&V) performed by the software vendor ABAQUS, Idaho National Laboratory (INL) has an internal software quality assurance (SQA) program. This SQA program requires the internal V&V of analysis software, in this case ABAQUS. ECAR-1698 (Idaho National Laboratory 2011) documents INL's internal V&V of ABAQUS using a number of test problems. The most recent V&V was performed in early November 2012, using the operating system on

USED FUEL DISPOSITION CAMPAIGN
**Used Nuclear Fuel Loading and Structural Performance Under Normal Conditions of Transport -
Demonstration of Approach and Results of Used Fuel Performance Characterization**
138   **SEPTEMBER 30, 2013**

the INL compute server Quark. On November 21, 2012 the validation script approved in ECAR-1698 Rev. 0 was rerun on compute server Quark and the results were in agreement with the results discussed in ECAR-1698 Rev. 0. Therefore, ABAQUS/Explicit and /Standard Version 6.11-1 are considered verified and validated for Quark.

INL's calculations for this document were performed with ABAQUS 6.12-2 on the computer server Quark at INL. Because a formal V&V has not been performed on ABAQUS 6.12-2 at INL, a verification of the calculation capability in ABAQUS 6.12-2 is provided below. The most complex model run performed, shown in Figure 8.83, was rerun using INL's validated version of ABAQUS, 6.11-1. Figure 7.1 shows the results of the model run performed with the validated version of ABAQUS 6.11-1. Since the stress states in Figure 8.83 (ABAQUS 6.12-2) and Figure 7.1 (ABAQUS 6.11-1) are identical, ABAQUS 6.12-2 is deemed to provide accurate results for the structural dynamics calculations presented in this report.
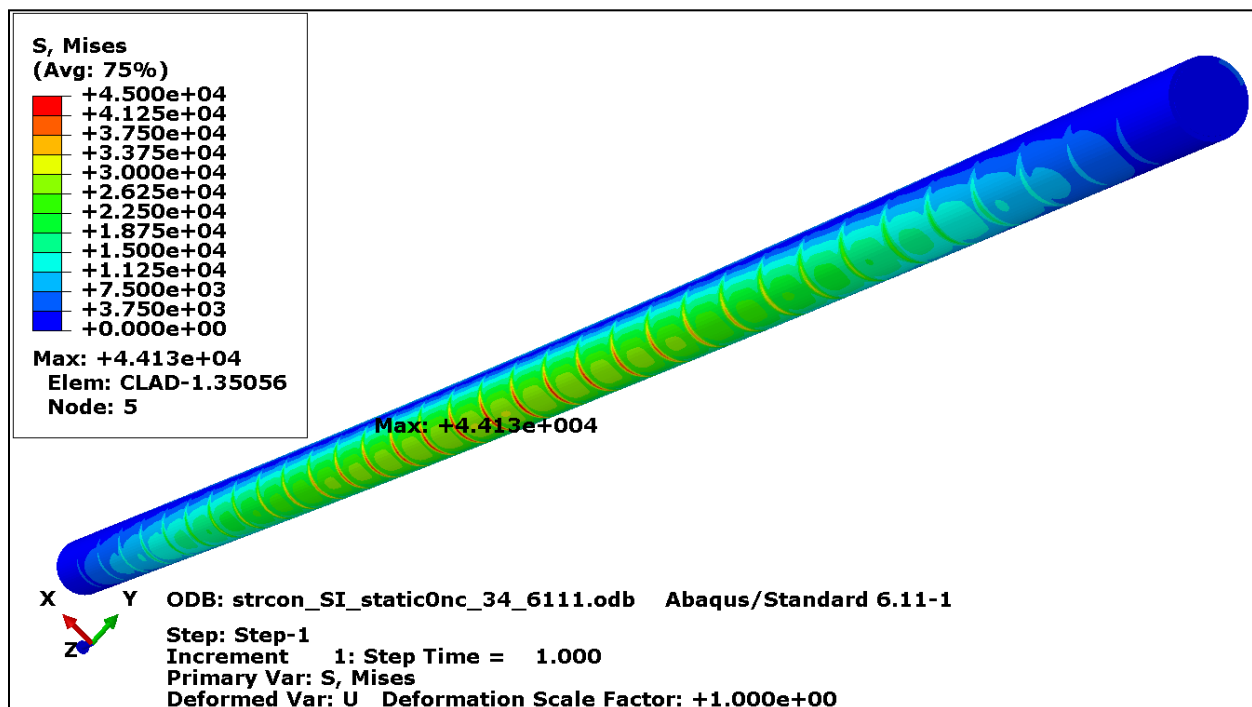
Figure 7.1. Full Model Stress Results for the Simply Supported Beam for validation.

7.5   FAILURE LIMITS

Various material properties that can be used as failure criteria (e.g., yield strength, uniform elongation, fracture toughness, and fatigue strength) have been proposed in the Material

USED FUEL DISPOSITION CAMPAIGN
**Used Nuclear Fuel Loading and Structural Performance Under Normal Conditions of Transport -
Demonstration of Approach and Results of Used Fuel Performance Characterization**
SEPTEMBER 30, 2013 139

Properties Handbook (Geelhood 2013). Several concerns have recently been raised over the applicability of these properties as failure criteria for UNF under NCT. These concerns primarily relate to the fact that much of the data used to develop these models was not completely prototypic to the expected conditions and loading of UNF under NCT.

One particular concern was raised as to the applicability of the proposed fatigue failure criterion (O'Donnell and Langer 1964) to UNF under NCT. In particular the concern was related to the fact that none of the data used by O'Donnell and Langer was completely prototypic of the expected loading of UNF under NCT. Additionally, none of the irradiated data were irradiated under the same PWR environmental conditions and likely did not contain the same level of corrosion or distribution of hydrides as UNF. Finally, the data did not include the impact of pellets bonded to the cladding as expected for UNF.

In order to address these concerns, a thorough literature review was performed to identify other fatigue data tested under different conditions that could potentially address the applicability of the current fatigue failure criterion to UNF under NCT. The literature review was able to provide some additional insight into the influence of the following parameters on fatigue failure in Zircaloy (Wisner et al 1994, Soniak et al 1994, Mehan and Wiesinger 1961, Lin 1998, Pandarinathan and Vasudevan 1980):

- Temperature dependence

- Irradiation dependence

- Hydrogen dependence (for some orientations and distributions of hydrides)

- Geometry, stress state, and sample orientation.

Additionally, recent data from ORNL (Wang and Wang, 2013) taken on unirradiated Zircaloy filled with epoxy, loaded with alumina pellets and bonded with epoxy, and loaded with alumina pellets with no bonding, was able to provide additional insight into:

- Influence of the presence of a bonded pellet and an unbonded pellet on unirradiated tubes (note: these tests did not have the prototypical high burnup distribution of hydrides).

This section discusses the data used to develop the O'Donnell and Langer fatigue failure criteria and the data from the literature review ORNL used to further validate its use for UNF under NCT.

7.5.1   O'DONNELL AND LANGER FATIGUE FAILURE CRITERIA

The Material properties document (Geelhood, 2013) identifies the O'Donnell and Langer (1964) failure curves as the initial fatigue failure criteria that should be used to assess failure of used nuclear fuel under normal conditions of transport.

USED FUEL DISPOSITION CAMPAIGN
**Used Nuclear Fuel Loading and Structural Performance Under Normal Conditions of Transport -
Demonstration of Approach and Results of Used Fuel Performance Characterization**
140   **SEPTEMBER 30, 2013**

O'Donnell and Langer collected a large quantity of data from unirradiated and irradiated Zircaloy samples tested under various orientations between 21°C and 315°C. Based on these data two different fatigue-design curves were constructed which represents a lower bound of the available data. This curve was constructed by applying a factor of safety of either 2 on the stress amplitude or a factor of 20 on the number of cycles to failure, whichever is more conservative. This method of constructing fatigue-design curves is the recommended method stated by the U.S. Nuclear Regulatory Commission in the standard review plan (NRC 2007). In fact, the O'Donnell and Langer fatigue-design curves are often used by fuel vendors in their in-reactor fatigue safety analyses.

The Zircaloy samples used by O'Donnell and Langer consisted of Zircaloy sheet samples tested transverse to the direction of rolling and parallel to the direction of rolling. Additionally, welded material was tested both transverse and parallel to the direction of welding. The data does not identify which measurements come from which samples, and these differences could account for the scatter observed in these data. However, it is noted that the final fatigue-design curves bound all the data from the different sample types.

The Zircaloy samples were tested at 21°C and 315°C. It is noted that the samples tested at 21°C exhibited slightly higher fatigue strength than those tested at elevated temperature. The irradiated Zircaloy samples were irradiated to a fast neutron fluence of 1.5×10^{21} n/cm² to 5.5×10^{21} n/cm² which corresponds to burnup levels of 9 to 33 GWd/MTU under PWR conditions. It is also noted that these samples were irradiated in a more inert environment than that of fuel rods under PWR conditions. As such, these samples did not have a thick (20-80μm) oxide layer or significant hydrogen (200-600ppm) concentration such as is usually observed in moderate to high burnup PWR fuel cladding.

Two types of fatigue tests were performed on these samples. Axial tension and compression tests were performed on samples and bending tests were performed on samples. For the bending tests, different tests were performed with the mean stress either being zero, or some larger value. It was determined that the bending tests with some positive mean stress were more limiting than those with zero mean stress.

The data is shown as stress vs. cycles to failure. For all tests, this stress is calculated according to the formula:

$$S = \tfrac{1}{2} E \varepsilon_T$$

Where:
S = Fatigue failure stress
E = elastic modulus evaluated at test temperature
ε_T = total change in strain

For the tests where the yield stress is exceeded, this formula gives a stress value which, although fictitious, is proportional to strain and is a good measure of the damage being done. Figure 7.2

USED FUEL DISPOSITION CAMPAIGN
Used Nuclear Fuel Loading and Structural Performance Under Normal Conditions of Transport -
Demonstration of Approach and Results of Used Fuel Performance Characterization
SEPTEMBER 30, 2013 141

and Figure 7.3 show the O'Donnell and Langer fatigue-design curves for unirradiated and irradiated Zircaloy and the supporting data.
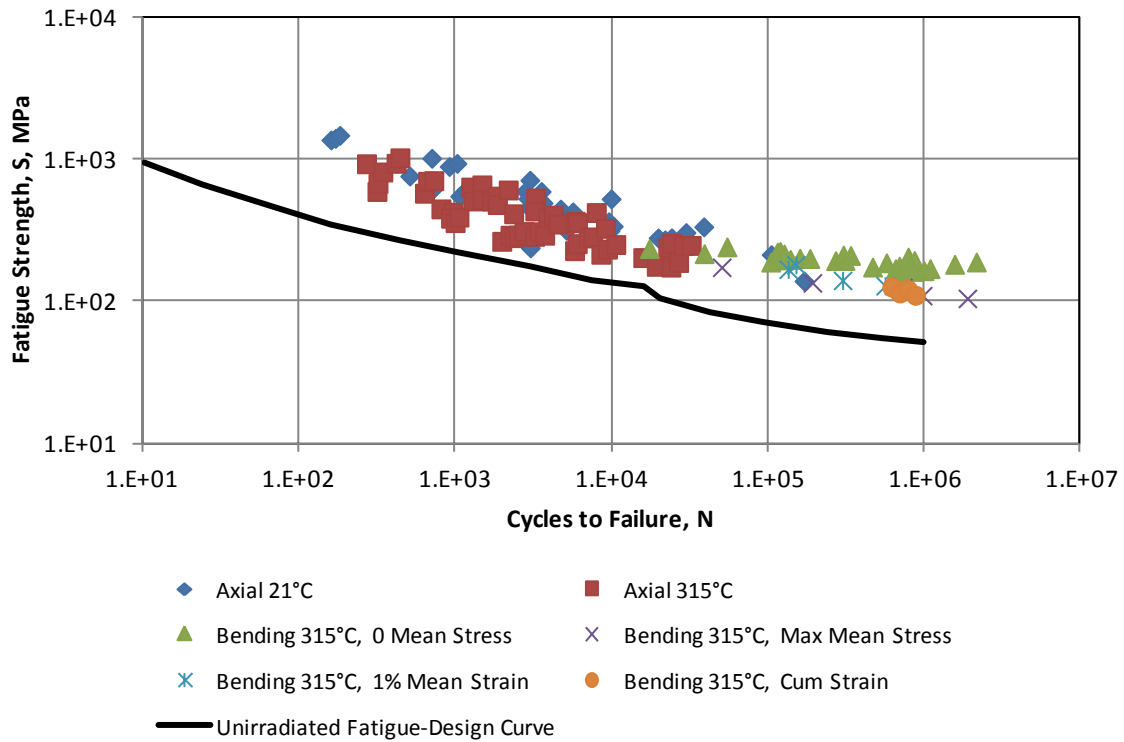
Figure 7.2. Fatigue-design Curve and Supporting Data for Unirradiated Zircaloy Proposed by O'Donnell and Langer

USED FUEL DISPOSITION CAMPAIGN
Used Nuclear Fuel Loading and Structural Performance Under Normal Conditions of Transport -
Demonstration of Approach and Results of Used Fuel Performance Characterization
142   **SEPTEMBER 30, 2013**
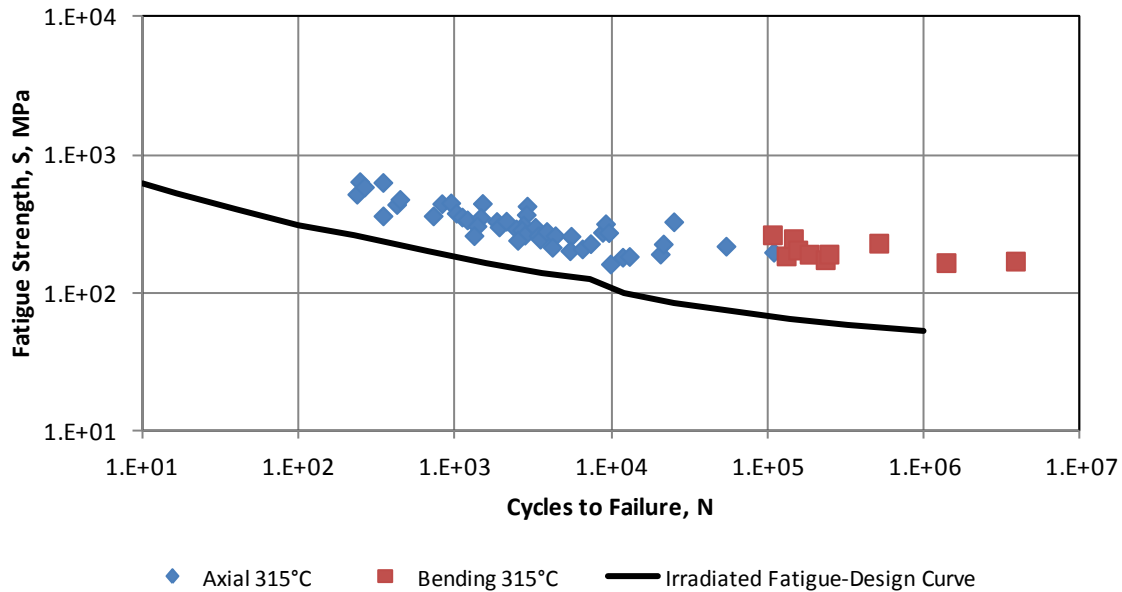
Figure 7.3. Fatigue-design Curve and Supporting Data for Irradiated Zircaloy Proposed by
             O'Donnell and Langer

7.5.2   OTHER FATIGUE DATA

It is acknowledged that the O'Donnell and Langer fatigue data is not completely representative of the starting state and loading conditions that will be experienced by used nuclear fuel under normal conditions of transport. In order to address concerns over these differences, other fatigue data was collected and is described in this section.

7.5.2.1   WISNER DATA

Wisner et al. (1994) collected fatigue data from axial tension and compression tests performed on irradiated and unirradiated Zircaloy sheet material tested transverse to the rolling direction. All tests were performed at 343°C. The irradiated samples were irradiated under BWR spectrum in an inert capsule to fluence levels between 1×10^{21} n/cm² to 1.5×10^{22} n/cm² which corresponds to burnup levels of 6 to 90 GWd/MTU under PWR conditions. Due to the fact that these samples were irradiated in an inert capsule, these samples did not have a thick (20-80µm) oxide layer or significant hydrogen (200-600ppm) concentration such as is usually observed in moderate to high burnup PWR fuel cladding.

These data are shown in Figure 7.4. It can be seen from this figure that there is little difference between the irradiated and unirradiated data.

USED FUEL DISPOSITION CAMPAIGN
Used Nuclear Fuel Loading and Structural Performance Under Normal Conditions of Transport -
Demonstration of Approach and Results of Used Fuel Performance Characterization
SEPTEMBER 30, 2013 143
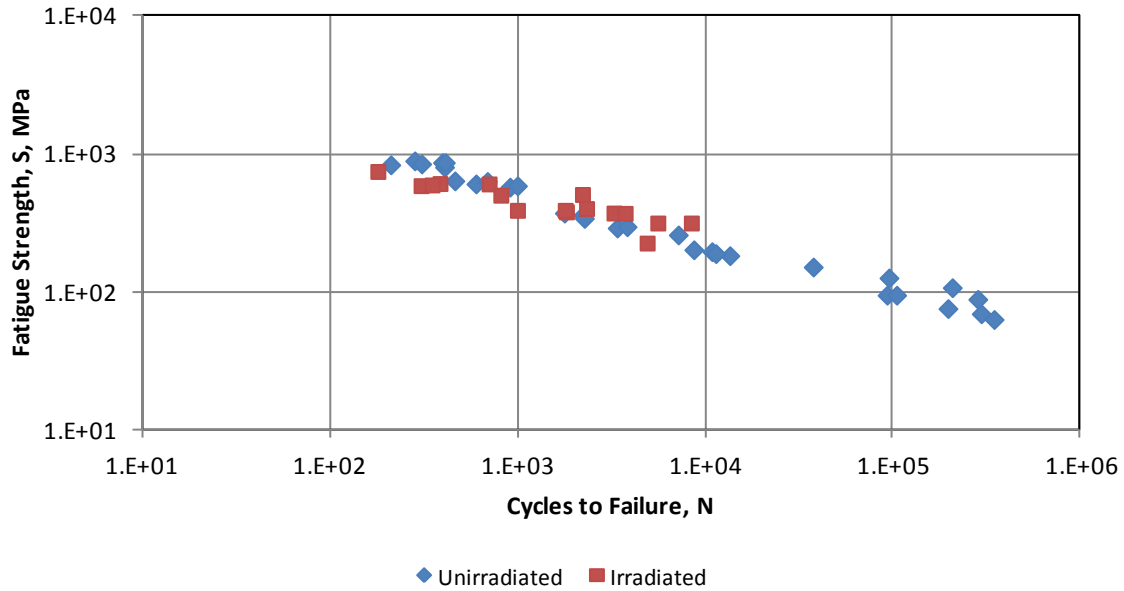
Figure 7.4. Wisner et al. (1994) Fatigue Data

Figure 7.5 and Figure 7.6 show the Wisner data along with the O'Donnell data and fatigue-design curve for irradiated and unirradiated material, respectively. The Wisner and O'Donnell data are mostly in agreement, except for the high cycle unirradiated data, which is somewhat lower than the O'Donnell data, but still bounded by the fatigue-design curve. This may be due to the fact that the Wisner data was all tested in the transverse direction, which will be shown later to have lower fatigue strength than in the rolling direction. However, the O'Donnell data consists of samples tested in both directions, but it is unknown if any of these high cycle data are taken on transverse samples.

USED FUEL DISPOSITION CAMPAIGN
Used Nuclear Fuel Loading and Structural Performance Under Normal Conditions of Transport -
Demonstration of Approach and Results of Used Fuel Performance Characterization
144   **SEPTEMBER 30, 2013**
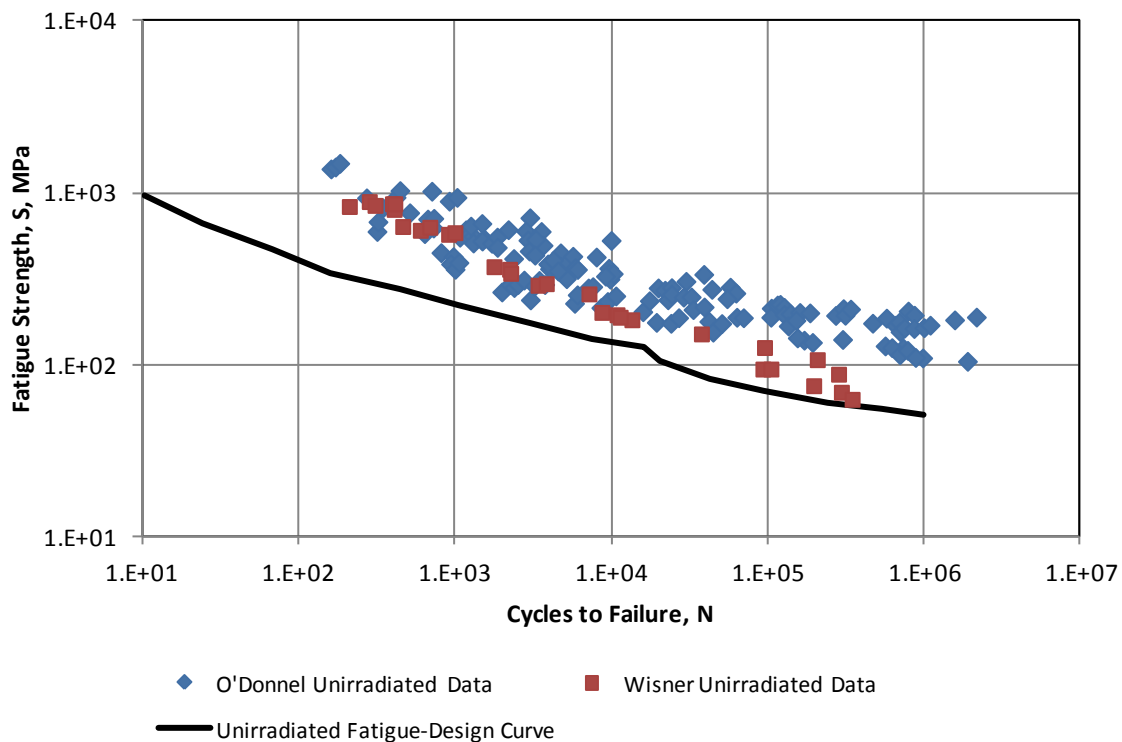
Figure 7.5. Wisner et al. (1994) Unirradiated Fatigue Data with O'Donnell Data and Fatigue-
design Curve

USED FUEL DISPOSITION CAMPAIGN
Used Nuclear Fuel Loading and Structural Performance Under Normal Conditions of Transport -
Demonstration of Approach and Results of Used Fuel Performance Characterization
SEPTEMBER 30, 2013 145

Figure 7.6. Wisner et al. (1994) Irradiated Fatigue Data with O'Donnell Data and Fatigue-design Curve

7.5.2.2   SONIAK DATA

Soniak et al. (1994) collected fatigue data from pressure tests performed on irradiated and unirradiated Zircaloy cladding tubes. All tests were performed at 350°C. The irradiated samples were taken from fuel rods irradiated in a French PWR and from fuel rods irradiated in a French experimental reactor (CAP). The cladding irradiated in the French PWR was irradiated to fluence levels between 3.8×10^{21} n/cm² to 1.1×10^{22} n/cm² which corresponds to burnup levels of 26 to 63 GWd/MTU under PWR conditions. Due to the fact that these samples were irradiated fuel rods from a PWR, these samples did have a thick oxide layer (between 29-65µm) and significant hydrogen concentration (between 280-600ppm) such as is usually observed in moderate to high burnup PWR fuel cladding.

The cladding irradiated in the French experimental reactor was irradiated under lower water temperature than the PWR fuel and only had oxide thickness of 12µm and hydrogen concentration of 60 ppm.

These data are shown in Figure 7.7. It can be seen from this figure that there is no difference between the irradiated and unirradiated data at 10^4 cycles, but with increasing cycles, the irradiate fatigue strength decreases relative to the unirradiated fatigue strength. It is interesting to note that the CAP fatigue strength does not decrease as much as the PWR fatigue strength. Since there was little hydrogen in the CAP samples, this comparison may show the impact of irradiation alone (CAP data) and the impact of irradiation and hydrogen (PWR data)

USED FUEL DISPOSITION CAMPAIGN
Used Nuclear Fuel Loading and Structural Performance Under Normal Conditions of Transport -
Demonstration of Approach and Results of Used Fuel Performance Characterization
146   **SEPTEMBER 30, 2013**
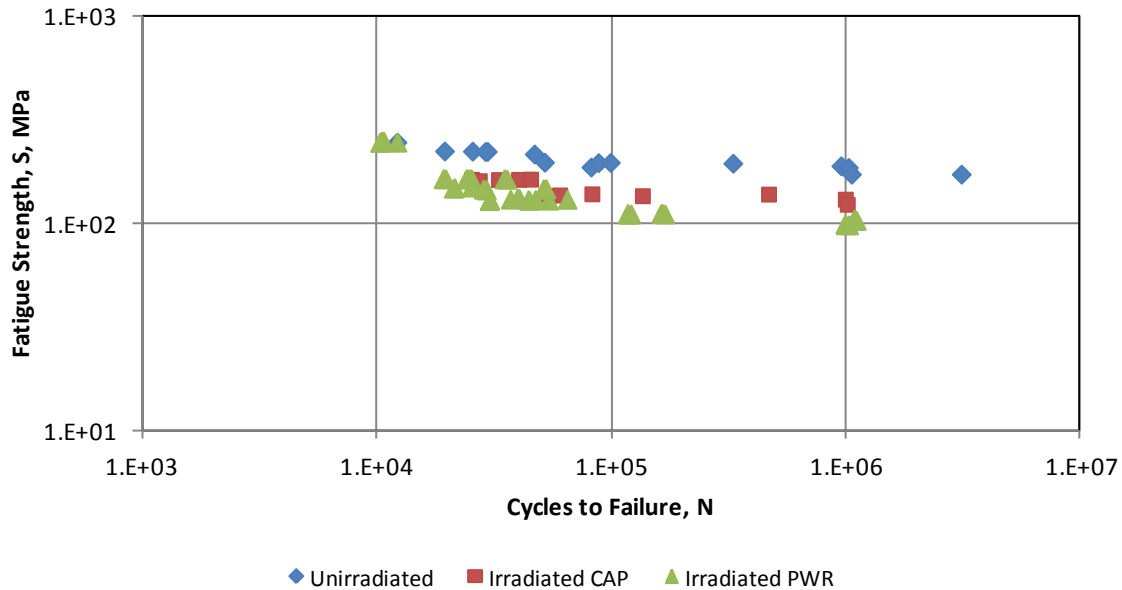
Figure 7.7. Soniak et al. (1994) Fatigue Data

Soniak et al (1994) performed various tests to determine the effect of hydrogen concentration on irradiated cladding fatigue strength. Figure 7.8 shows a plot of all the 4 cycle (52 GWd/MTU) data taken from different axial elevation such that different hydrogen levels could be examined. It can be seen from this figure that the impact of increasing hydrogen level between 280 ppm and 600 ppm appears to be negligible. Clearly as seen previously there is an impact of increasing the hydrogen from 60 ppm (CAP data) to 280-600 ppm (PWR data), but that effect seems to quickly saturate.

USED FUEL DISPOSITION CAMPAIGN
Used Nuclear Fuel Loading and Structural Performance Under Normal Conditions of Transport -
Demonstration of Approach and Results of Used Fuel Performance Characterization
SEPTEMBER 30, 2013   **147**
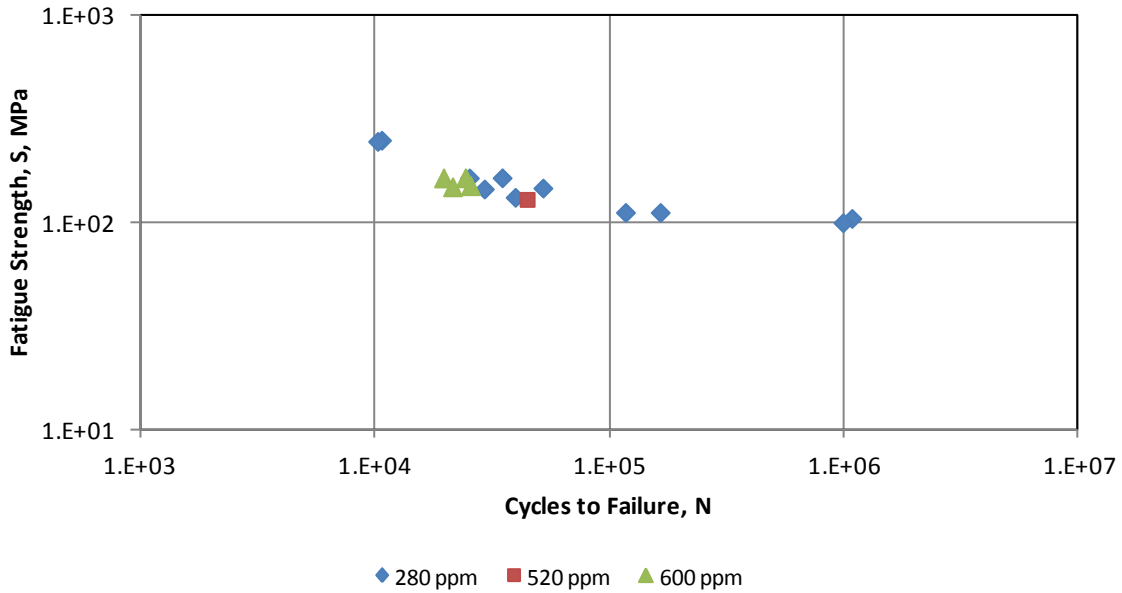
Figure 7.8. Soniak et al. (1994) 4-cycle PWR Irradiated Fatigue Data at Different Hydrogen
        Concentrations

Figure 7.9 and Figure 7.10 show the Soniak data along with the O'Donnell data and fatigue-design curve for irradiated and unirradiated material, respectively. The Soniak and O'Donnell unirradiated data are in excellent agreement. For the irradiated data, the CAP data with low hydrogen concentrations are in good agreement with the O'Donnell data. The PWR data exhibits lower fatigue strength than the O'Donnell data, possibly due to the presence of hydrogen in these samples. However, the Soniak data are all bounded by the fatigue-design curve. If more conservatism was desired in the fatigue-design curve, the curve could be lowered in the higher cycle range ($>10^4$ cycles) by the difference between the Soniak PWR data and the O'Donnell data.

USED FUEL DISPOSITION CAMPAIGN
Used Nuclear Fuel Loading and Structural Performance Under Normal Conditions of Transport -
Demonstration of Approach and Results of Used Fuel Performance Characterization
148   **SEPTEMBER 30, 2013**
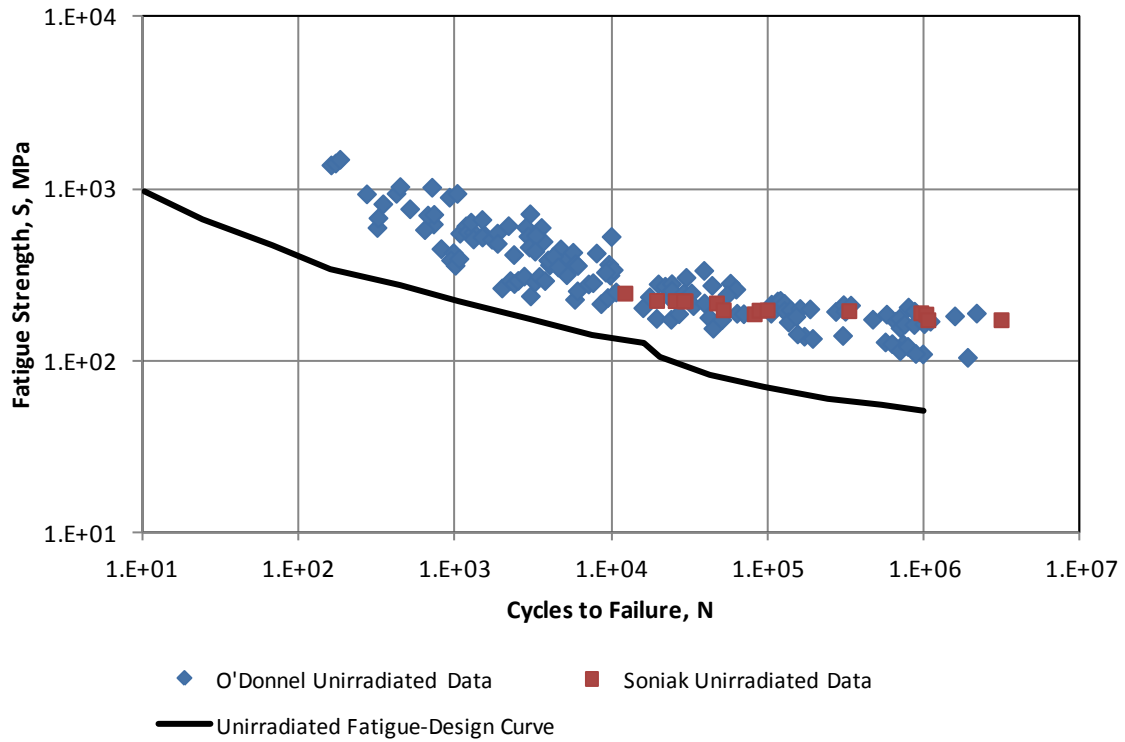
Figure 7.9. Soniak et al. (1994) Unirradiated Fatigue Data with O'Donnell Data and Fatigue-
Design Curve

USED FUEL DISPOSITION CAMPAIGN
Used Nuclear Fuel Loading and Structural Performance Under Normal Conditions of Transport -
Demonstration of Approach and Results of Used Fuel Performance Characterization
SEPTEMBER 30, 2013   **149**
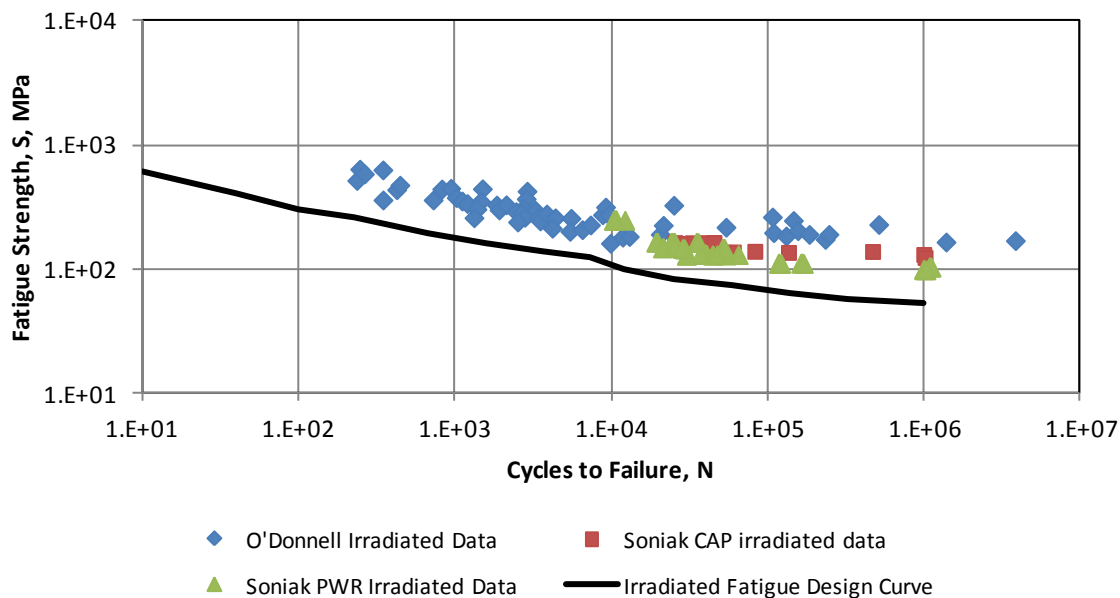
Figure 7.10. Soniak et al. (1994) Irradiated Fatigue Data with O'Donnell Data and Fatigue-
              Design Curve

7.5.2.3   MEHAN DATA

Mehan and Wiesinger (1961) collected fatigue data from axial tension and compression tests
performed on unirradiated Zircaloy sheet material tested transverse and longitudinal to the
rolling direction. Tests were performed at 25°C, 315°C, and 482°C. Most samples were as-
received with 12 ppm hydrogen, although some were hydrided to 500 ppm. In this way, the
effect of orientation (transverse vs. longitudinal), temperature (25°C – 482°C) and hydrogen (12-
500 ppm) could be examined.

These data are shown in Figure 7.11 and Figure 7.12 for the longitudinal and transverse
orientations respectively. These figures show a clear trend of reduced fatigue strength with
increased temperature. Additionally, Figure 7.11 shows that there is a small reduction in fatigue
strength between 12ppm and 500 ppm hydrogen. Figure 7.13 shows the data at two different
temperatures for the transverse and longitudinal orientations. This comparison shows that the
fracture strength is lower in the transverse orientation than in the longitudinal orientation.

USED FUEL DISPOSITION CAMPAIGN
Used Nuclear Fuel Loading and Structural Performance Under Normal Conditions of Transport -
Demonstration of Approach and Results of Used Fuel Performance Characterization
150 **SEPTEMBER 30, 2013**
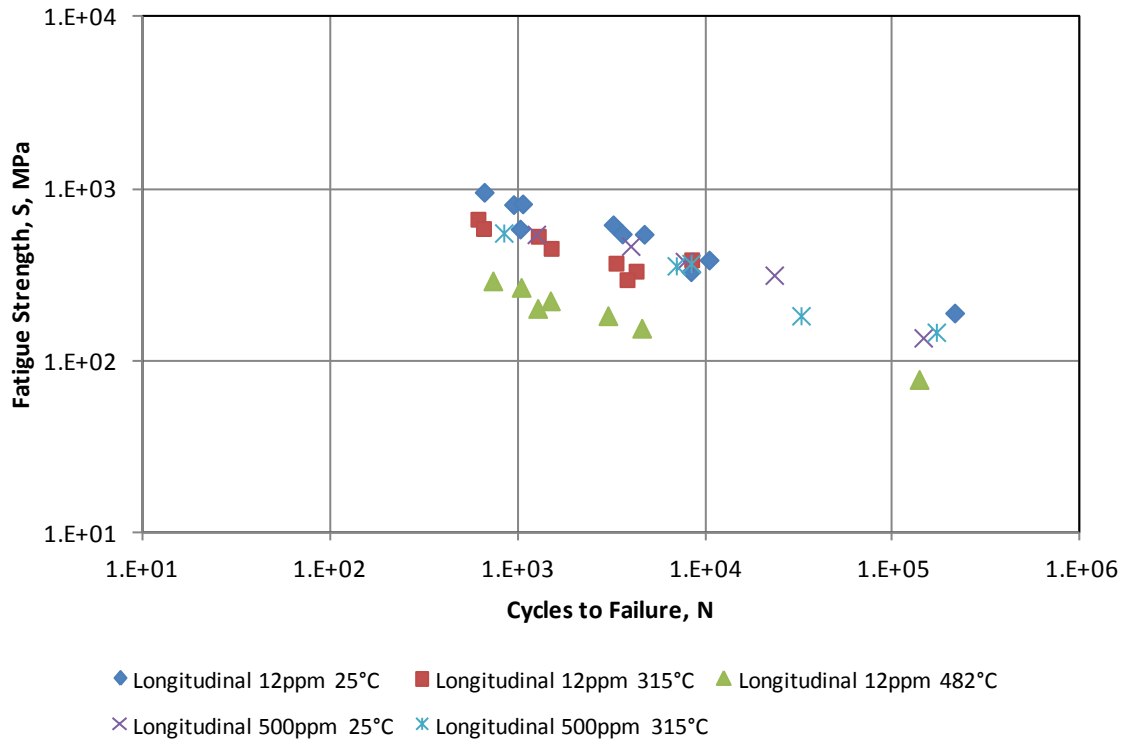
Figure 7.11. Mehan and Wiesinger (1961) Fatigue Data for Samples Tested In Longitudinal
Orientation

USED FUEL DISPOSITION CAMPAIGN
Used Nuclear Fuel Loading and Structural Performance Under Normal Conditions of Transport -
Demonstration of Approach and Results of Used Fuel Performance Characterization
SEPTEMBER 30, 2013   **151**
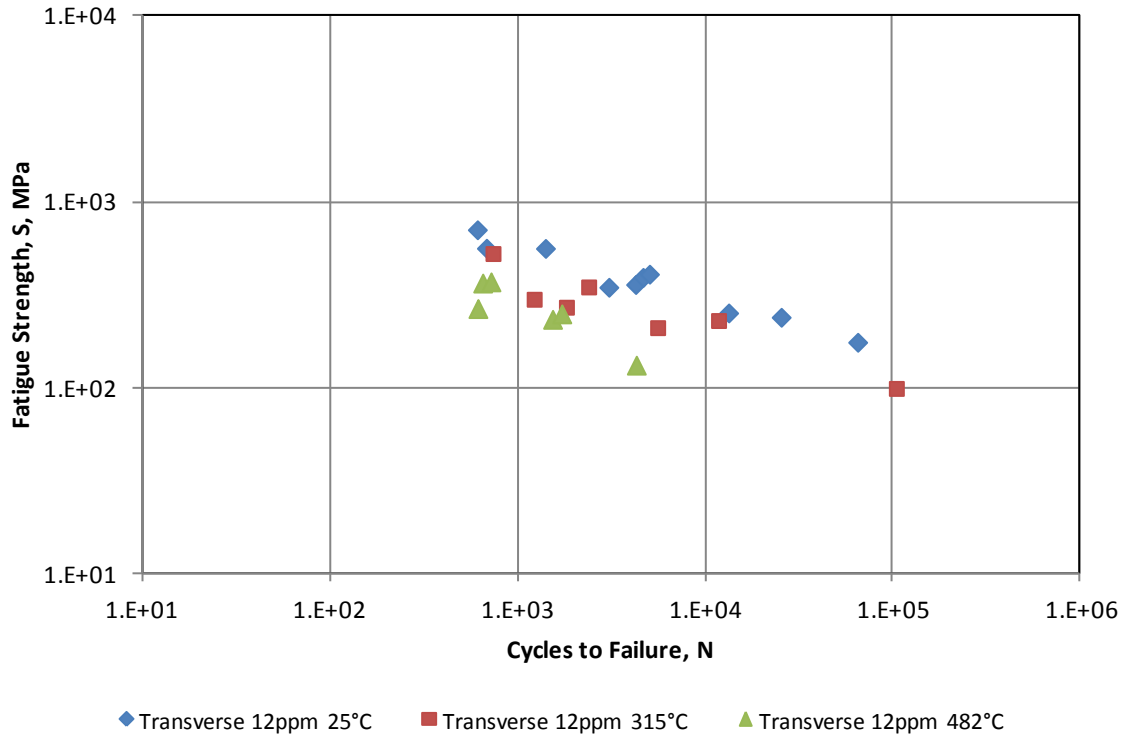
Figure 7.12. Mehan and Wiesinger (1961) Fatigue Data for Samples Tested in Transverse Orientation

USED FUEL DISPOSITION CAMPAIGN
Used Nuclear Fuel Loading and Structural Performance Under Normal Conditions of Transport -
Demonstration of Approach and Results of Used Fuel Performance Characterization
152   **SEPTEMBER 30, 2013**
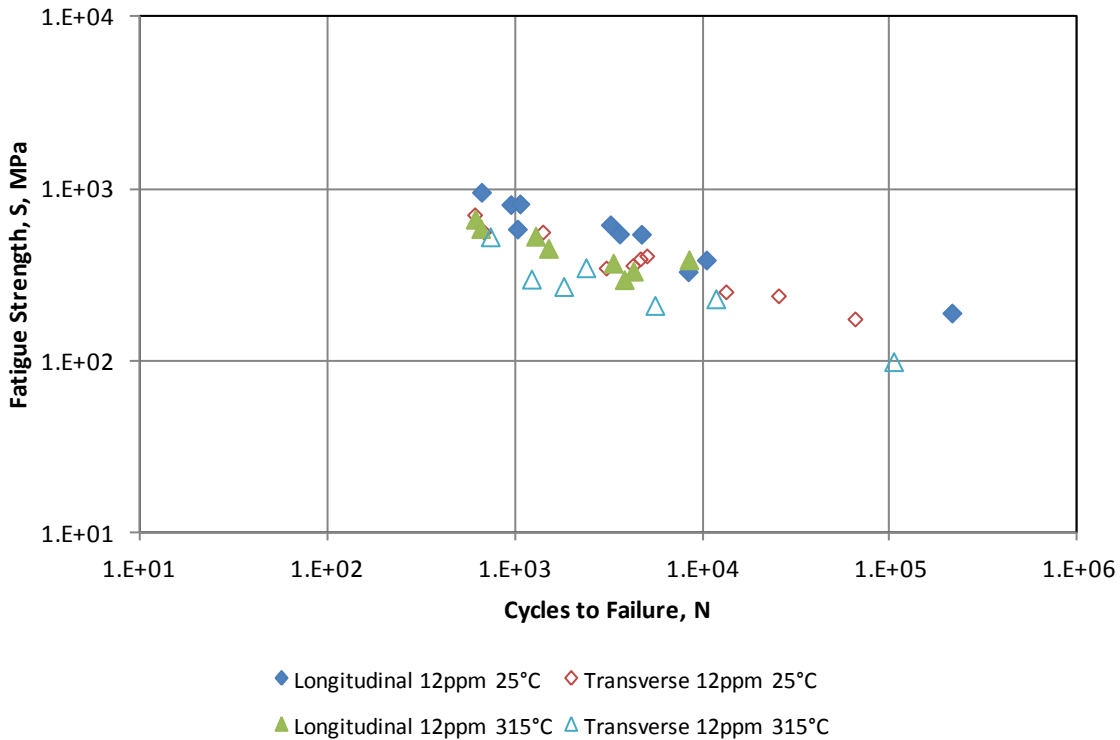
Figure 7.13. Mehan and Wiesinger (1961) Fatigue Data for Samples Tested In Longitudinal and
Transverse Orientation

Figure 7.14shows the Mehan and Wiesinger data along with the O'Donnell data and fatigue-design curve for unirradiated material. The Mehan and Wiesinger and O'Donnell unirradiated data are in excellent agreement for those samples taken at 25°C and 315°C. All these data are bounded by the fatigue-design curve. Those data taken at 482°C are below the other data and some are not bounded by the fatigue design curve. It is noted that 482°C is greater than the temperature limit for storage of used nuclear fuel which is 400°C.

USED FUEL DISPOSITION CAMPAIGN
Used Nuclear Fuel Loading and Structural Performance Under Normal Conditions of Transport -
Demonstration of Approach and Results of Used Fuel Performance Characterization
SEPTEMBER 30, 2013 153
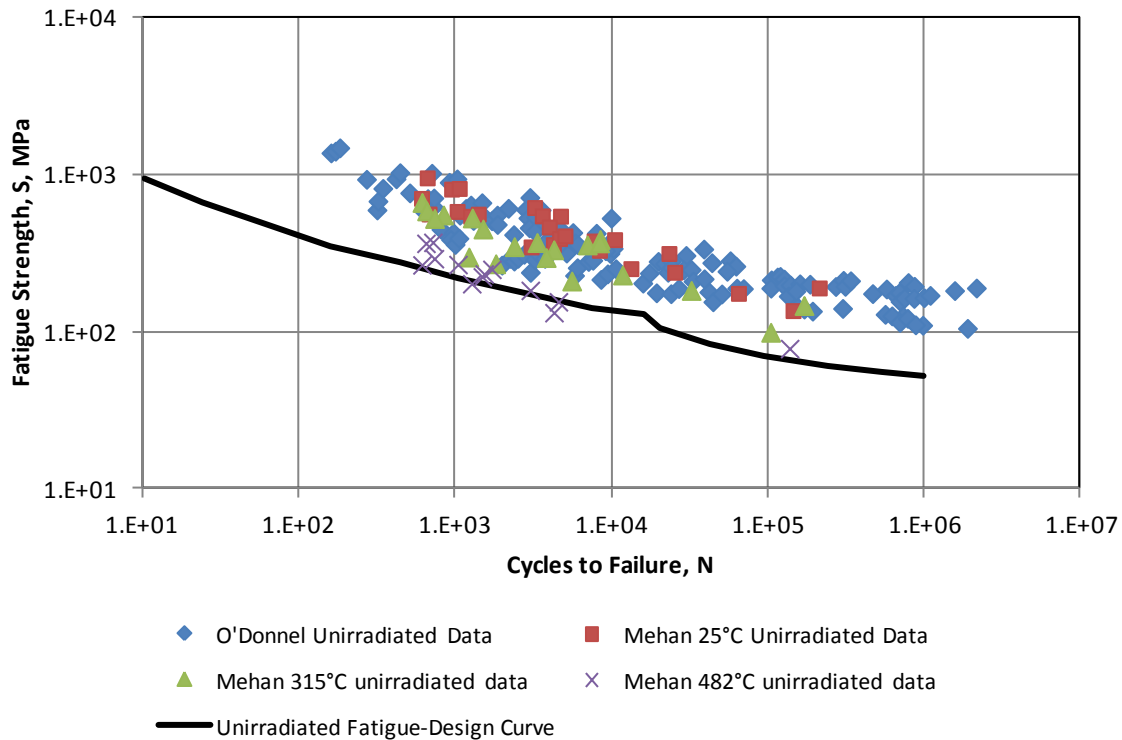
Figure 7.14. Mehan and Wiesinger (1961) Unirradiated Fatigue Data with O'Donnell Data and Fatigue-Design Curve

7.5.2.4 LIN DATA

Lin (1998) collected fatigue data from reverse bending tests unirradiated Zircaloy and zirconium sheet material. Tests were performed at 25°C. This study focused on the fatigue behavior at high cycles (10^5 to 10^7 cycles).

These data are shown in Figure 7.15. These data show that there is no difference in the fatigue strength of Zircaloy-4 and zirconium at high cycles.

USED FUEL DISPOSITION CAMPAIGN
Used Nuclear Fuel Loading and Structural Performance Under Normal Conditions of Transport -
Demonstration of Approach and Results of Used Fuel Performance Characterization
154   **SEPTEMBER 30, 2013**
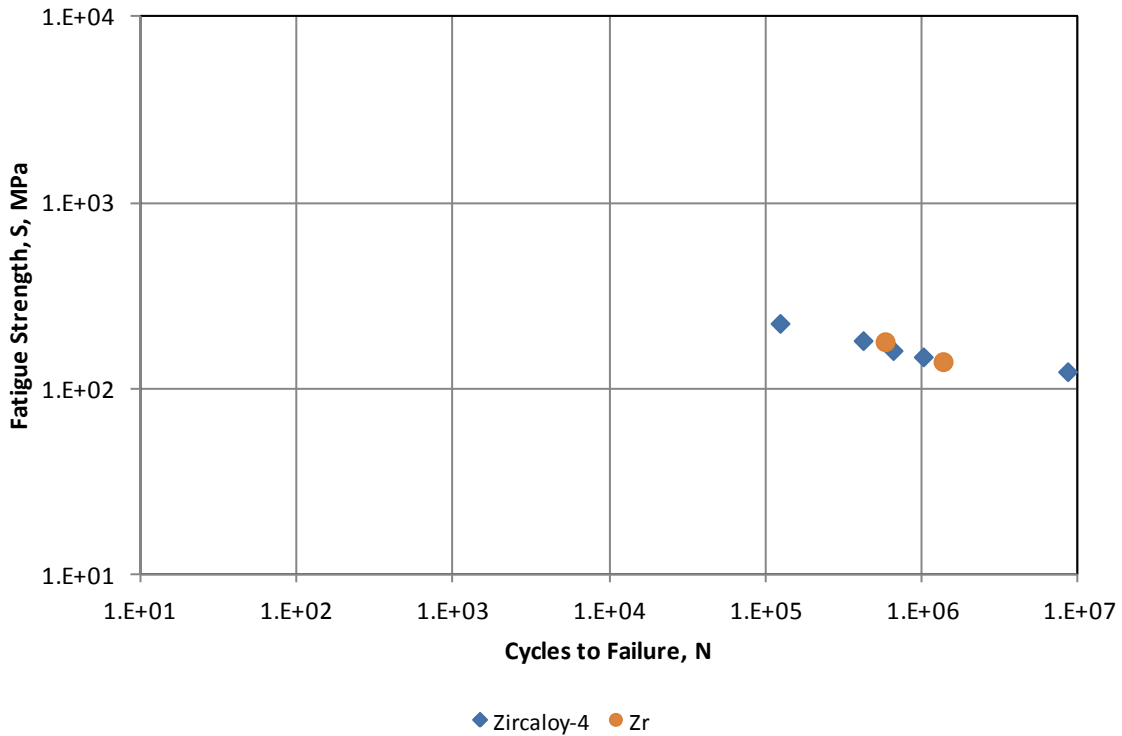
Figure 7.15. Lin (1998) Fatigue Data for Zircaloy-4 and Zirconium Samples

Figure 7.16 shows the Lin data along with the O'Donnell data and fatigue-design curve for unirradiated material. The Lin and O'Donnell unirradiated data are in excellent agreement. All these data are bounded by the fatigue-design curve. Although the fatigue-design curve only extends to 10^6 cycles, these data indicate that the curve could be extended to use a constant value between 10^6 cycles and 10^7 cycles.

USED FUEL DISPOSITION CAMPAIGN
Used Nuclear Fuel Loading and Structural Performance Under Normal Conditions of Transport -
Demonstration of Approach and Results of Used Fuel Performance Characterization
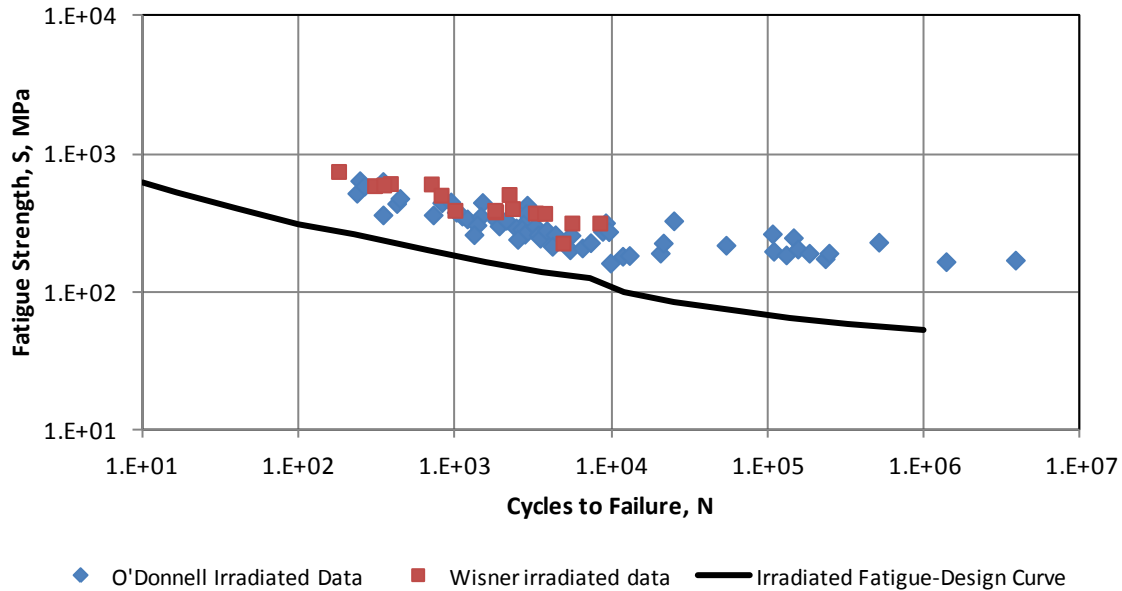**SEPTEMBER 30, 2013**   155
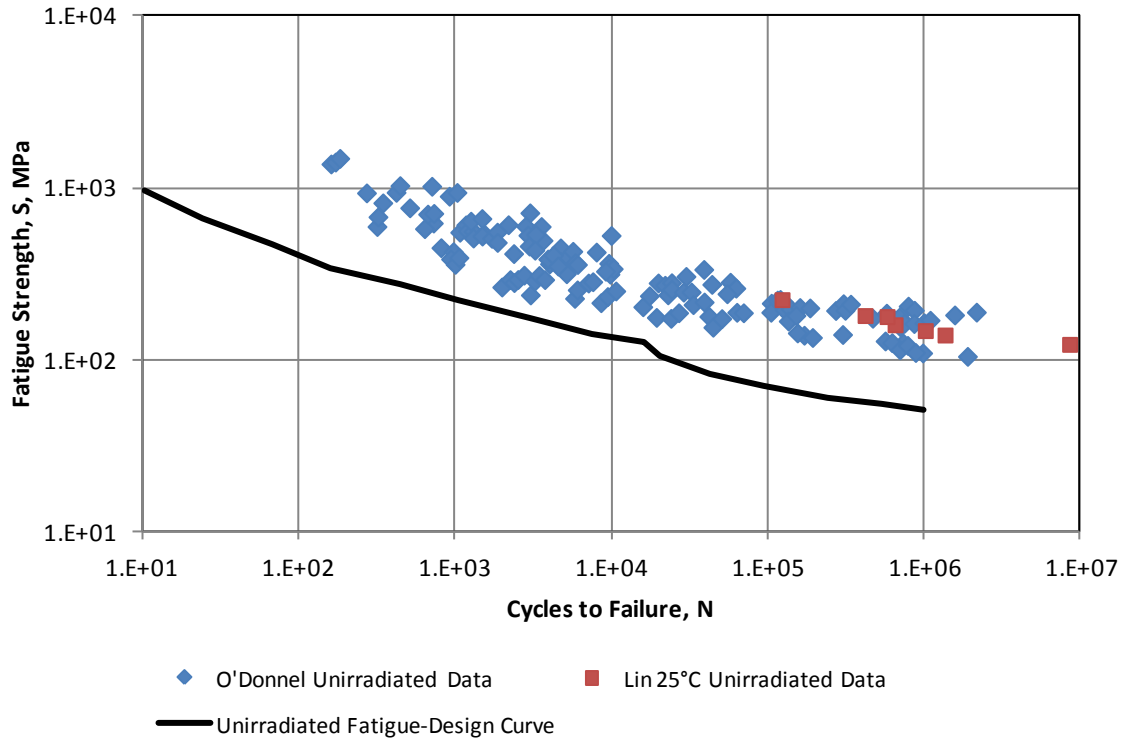
Figure 7.16. Lin (1998) Unirradiated Fatigue Data with O'Donnell Data and Fatigue-Design
Curve

7.5.2.5 *PANDARINATHAN DATA*

Pandarinathan and Vasudevan (1980) collected fatigue data from bending tests on unirradiated
Zircaloy cladding tubes. Tests were performed at 25°C, 300°C, and 350°C. These data are
interesting because the geometry of the test (bending cladding tubes) is most similar to the
loading that is expected during normal transportation conditions for used nuclear fuel.

These data are shown in Figure 7.17. These data show a small reduction in fatigue strength with
increasing temperature.

USED FUEL DISPOSITION CAMPAIGN
Used Nuclear Fuel Loading and Structural Performance Under Normal Conditions of Transport -
Demonstration of Approach and Results of Used Fuel Performance Characterization
156   **SEPTEMBER 30, 2013**
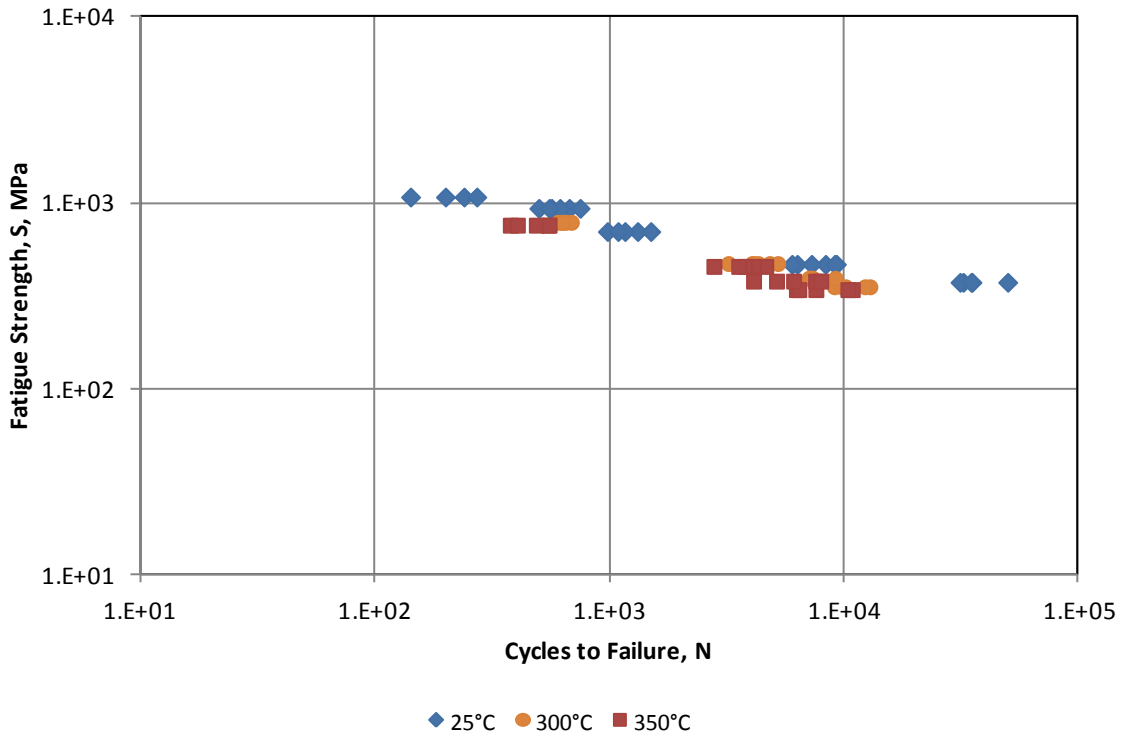
Figure 7.17. Pandarinathan and Vasudevan (1980) Fatigue Data for Zircaloy Samples

Figure 7.18 shows the Pandarinathan data along with the O'Donnell data and fatigue-design curve for unirradiated material. The Pandarinathan and O'Donnell unirradiated data are in excellent agreement. All these data are bounded by the fatigue-design curve. These data demonstrate that tube bending fatigue data provide similar fatigue strengths as axial tension and compression tests and bend tests on sheet.

USED FUEL DISPOSITION CAMPAIGN
Used Nuclear Fuel Loading and Structural Performance Under Normal Conditions of Transport -
Demonstration of Approach and Results of Used Fuel Performance Characterization
SEPTEMBER 30, 2013 157
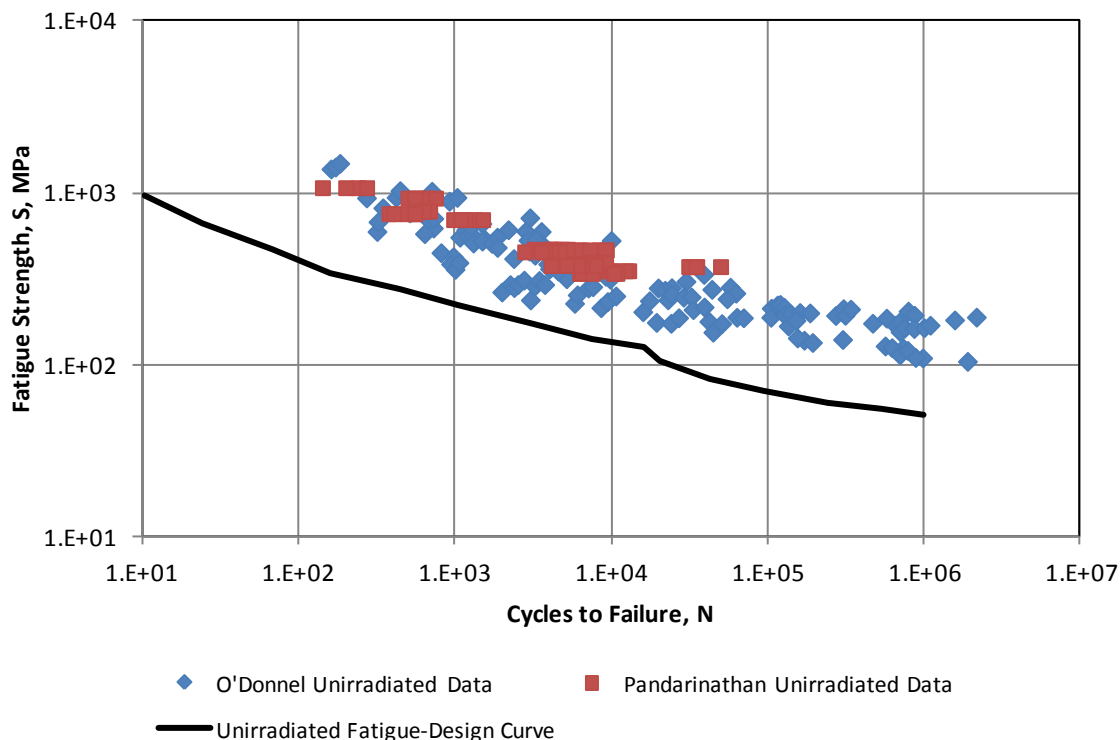
Figure 7.18. Pandarinathan and Vasudevan (1980) Unirradiated Fatigue Data with O'Donnell
Data and Fatigue-Design Curve

7.5.2.6 ORNL DATA

Oak Ridge National Laboratory (ORNL) has collected fatigue data from bending tests on unirradiated Zircaloy tubes with various ways of simulating the presence of bonded and un-bonded pellets (Wang and Wang 2013). Tests were performed at 25°C. Some of the tubes were completely filled with epoxy, some were loaded with alumina pellets bonded with epoxy, and some were simply loaded with alumina pellets. These data are interesting because the geometry of the test (bending cladding tubes) is most similar to the loading that is expected during normal transportation conditions for used nuclear fuel and while unirradiated, attempt to identify the impact of the presence of bonded UO_2 pellets.

These data are shown in Figure 7.19. These data generally show similar results for the different internal configurations. It is noted that the one low data point with alumina pellets only was identified to have a structural flaw which resulted in decreased fatigue lifetime.

USED FUEL DISPOSITION CAMPAIGN
Used Nuclear Fuel Loading and Structural Performance Under Normal Conditions of Transport -
Demonstration of Approach and Results of Used Fuel Performance Characterization
158   **SEPTEMBER 30, 2013**
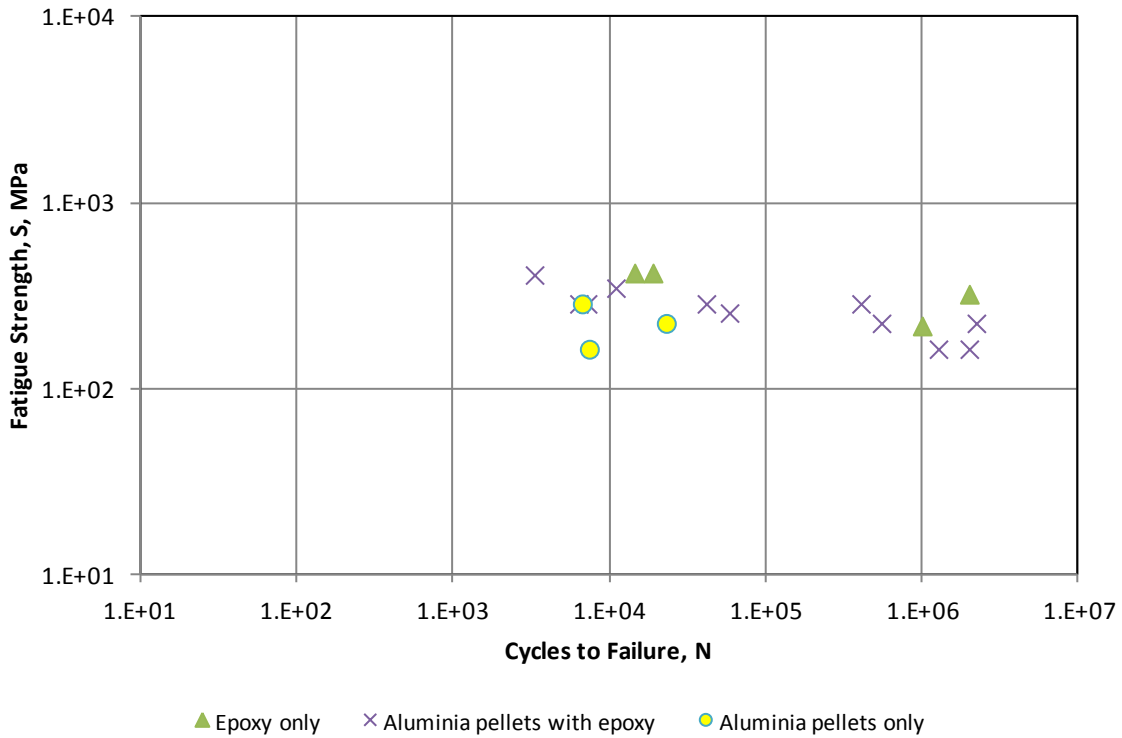
Figure 7.19. ORNL Fatigue Data for Zircaloy Samples

Figure 7.20 shows the ORNL data along with the O'Donnell data and fatigue-design curve for unirradiated material. The ORNL and O'Donnell unirradiated data are in excellent agreement. All these data are bounded by the fatigue-design curve. These data demonstrate that unirradiated tubes loaded with bonded and unbounded pellets tested under bending fatigue provide similar fatigue strengths as axial tension and compression tests and bend tests on sheet.

USED FUEL DISPOSITION CAMPAIGN
Used Nuclear Fuel Loading and Structural Performance Under Normal Conditions of Transport -
Demonstration of Approach and Results of Used Fuel Performance Characterization
SEPTEMBER 30, 2013 159
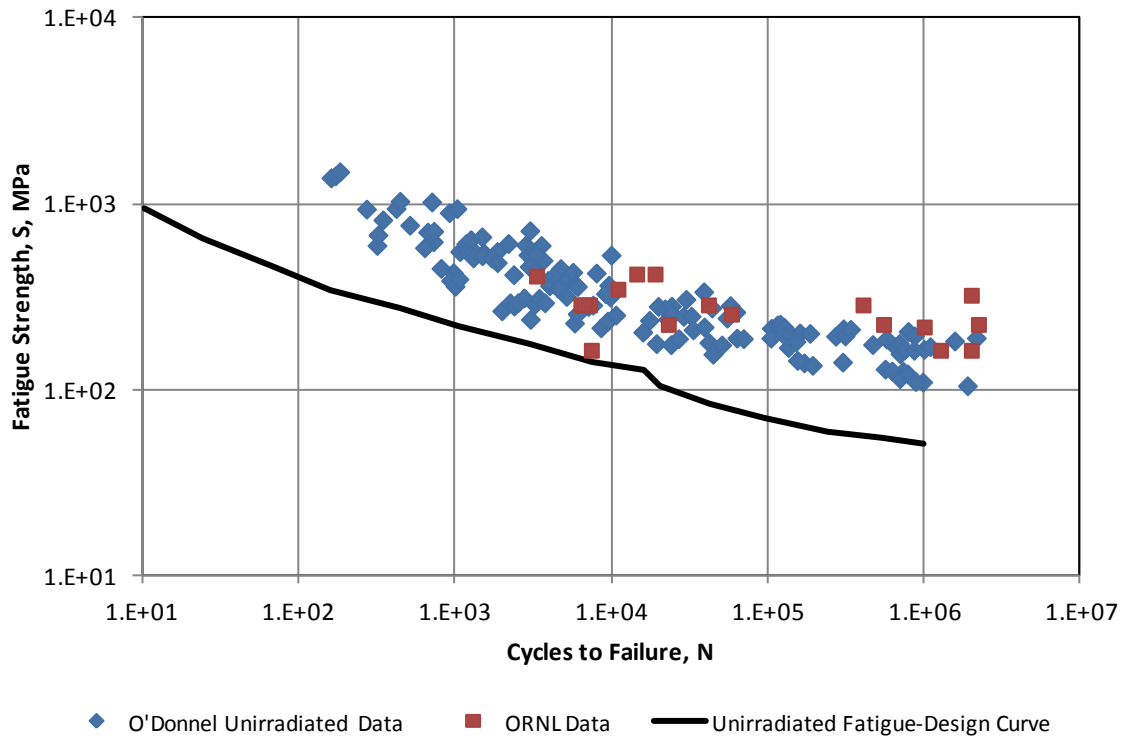
Figure 7.20. ORNL Unirradiated Fatigue Data with O'Donnell Data and Fatigue-Design Curve

USED FUEL DISPOSITION CAMPAIGN
Used Nuclear Fuel Loading and Structural Performance Under Normal Conditions of Transport -
Demonstration of Approach and Results of Used Fuel Performance Characterization
160 **SEPTEMBER 30, 2013**

7.5.3   APPLICABILITY OF O'DONNELL FATIGUE FAILURE CRITERIA TO TRANSPORTATION OF USED NUCLEAR FUEL

This section will describe the applicability of the selected fatigue failure criteria to UNF under NCT.

7.5.3.1   CONDITION OF USED NUCLEAR FUEL

The condition of used nuclear fuel is outlined in Table 7.1.

Table 7.1. Condition of Used Nuclear Fuel under Normal Conditions of Transportation

Parameter	Value
Temperature	20°C to 400°C
Burnup/Fluence	35 to 62 GWd/MTU 5.8×10^{21} to 1.0×10^{22} n/cm²
Hydrogen content	200 to 600 ppm (up to 800 ppm at local places)
Geometry	Rods with UO_2 pellets bonded inside Subjected to cyclic bending loads

7.5.3.2   IMPACT OF TEMPERATURE ON FATIGUE

Although there is some amount of scatter in fatigue strength data, all the data sets that performed measurements on Zircaloy samples at various temperatures demonstrated some reduction in fatigue strength with increasing temperature. O'Donnell and Langer (1964) showed a small reduction in fatigue strength from 21°C to 315°C for unirradiated samples. Mehan and Wiesinger (1961) showed reduction in fatigue strength from 25°C to 315°C to 482°C for unirradiated samples. Pandarinathan and Vasudevan (1980) showed reduction in fatigue strength from 25°C to 315°C to 482°C.

All the irradiated samples (O'Donnell and Langer 1964, Wisner et al 1994, Soniak et al 1994) were tested at elevated temperature (315°C to 351°C) which should provide a lower bound fatigue strength for used nuclear fuel under conditions of normal transportation.

The only data that were not bounded by the fatigue-design curve were those tested by Mehan and Wiesinger (1961) at 482°C. It is noted that this temperature is considerably above the upper limit of temperature for conditions of normal storage and transportation of UNF. Additionally, it can be seen in Figure 7.21that 482°C (755K) is close to the temperature where irradiated Zircaloy exhibits a rapid decrease in yield strength. This decrease in yield strength will cause a greater fraction of any cyclic strain to be plastic strain which will most likely lead to lower fatigue strength. For reference, the temperature limit for NCS and NCT is 400°C (673K) which is still in the area of higher yield strength.

USED FUEL DISPOSITION CAMPAIGN
**Used Nuclear Fuel Loading and Structural Performance Under Normal Conditions of Transport -
Demonstration of Approach and Results of Used Fuel Performance Characterization
SEPTEMBER 30, 2013** 161

The Mehan and Wiesinger (1961) data at 482°C should not be used in the development of a fatigue-design curve. It is concluded that the current design curves for irradiated and unirradiated Zircaloy are adequate for the temperature range of used nuclear fuel under NCT.
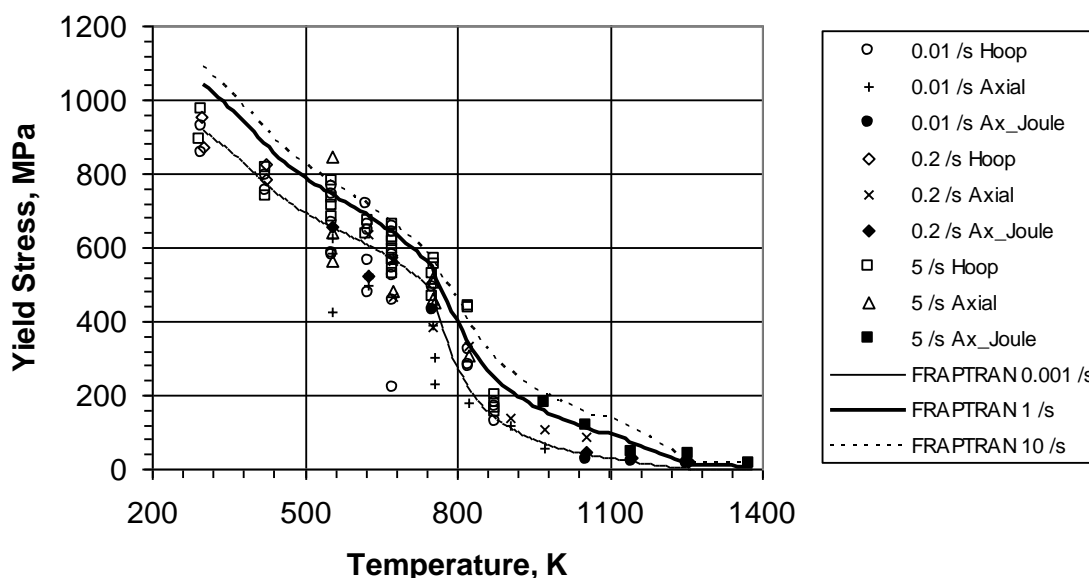
Figure 7.21. Yield Stress of Irradiated SRA Zircaloy-4 from the PROMETRA Database as a Function of Temperature. Also Shown for Comparison are FRAPTRAN Model Predictions

7.5.3.3 IMPACT OF IRRADIATION ON FATIGUE

O'Donnell and Langer (1964) noted somewhat lower fatigue strength in irradiated Zircaloy relative to unirradiated Zircaloy between 10^1 and 10^5 cycles and little to no difference between irradiated and unirradiated Zircaloy from 10^5 and 10^7 cycles. Because of these observations, the fatigue-design curve for irradiated Zircaloy is lower than that for the unirradiated Zircaloy between 10 and 10^5 cycles and the same as that for unirradiated Zircaloy above 10^5 cycles.

Wisner et al. (1994) noted no difference between irradiated and unirradiated Zircaloy for less than 10^4 cycles. Soniak et al. (1994) also noted no difference between irradiated and unirradiated Zircaloy at 10^4 cycles, but decreased fatigue strength of irradiated Zircaloy for cycles greater than 10^4 up to 10^6 cycles.

The fatigue-design curve for irradiated Zircaloy provided considerably more margin for the high cycle data than the low cycle data from O'Donnell and Langer (1964). The inclusion of the Soniak data which noted some decrease in fatigue strength for the high cycle irradiated data

USED FUEL DISPOSITION CAMPAIGN
Used Nuclear Fuel Loading and Structural Performance Under Normal Conditions of Transport -
Demonstration of Approach and Results of Used Fuel Performance Characterization
162   **SEPTEMBER 30, 2013**

makes the margin to the fatigue design curve consistent at all cycles as can be seen in Figure 7.10. As discussed in Section 7.5.2.2, the Soniak data demonstrated that the effect of fluence quickly saturates and is constant up to high fluence levels.

It is concluded that the current irradiated fatigue-design curve is adequate for the expected fluence levels found in nuclear fuel under NCT.

7.5.3.4   IMPACT OF HYDROGEN ON FATIGUE

Mehan and Wiesinger (1961) observed a slight decrease in the fatigue strength of unirradiated Zircaloy between 12 ppm and 500 ppm. This decrease was noted at both 25°C and 315°C. However, the impact of the hydrogen was less than the impact of testing sheet in the transverse and longitudinal directions. The samples used in this test were recrystallized annealed and as such would have had a significant fraction of radial hydrides in the hydrogen charged samples. The presence of radial hydrides does not appear to have a large impact on the fatigue strength of unirradiated Zircaloy. All the variations with respect to hydrogen content are well bounded by the unirradiated fatigue-design curve.

Soniak et al (1994) observed a small decrease in fatigue strength of irradiated Zircaloy between 60 ppm and 280-600ppm. However, no difference was observed in the fatigue strength between 280ppm and 600 ppm. The Soniak data is interesting for spent fuel under NCT because the samples were taken directly from irradiated PWR cladding and have the hydride morphology typical of spent fuel under NCT. All the Soniak data are well bounded by the irradiated fatigue-design curve despite the presence of hydrides. Because of the insensitivity of the fatigue strength to hydrogen between 280 ppm and 600ppm, it is not likely that local variations in hydrogen content sometimes observed in cladding will cause a change in the local fatigue strength.

It is concluded that the current irradiated fatigue-design curve is adequate for the hydrogen concentrations, orientations, and distributions found in nuclear fuel under NCT.

7.5.3.5   IMPACT OF GEOMETRY, STRESS STATE, AND SAMPLE ORIENTATION ON FATIGUE

As noted in Table 7.1, used nuclear fuel rods under NCT will be subjected to cyclic bending loads which could cause fatigue failure if the load and/or the cycles are great enough. The texture and grain structure of a drawn Zircaloy fuel tube is similar to the texture and grain structure of a rolled Zircaloy plate. The axial direction of a fuel tube is similar to that of the direction parallel to the rolling direction (longitudinal direction). The hoop direction of a fuel tube is similar to that of the direction transverse to the rolling direction. These directions are shown in Figure 7.22

USED FUEL DISPOSITION CAMPAIGN
Used Nuclear Fuel Loading and Structural Performance Under Normal Conditions of Transport -
Demonstration of Approach and Results of Used Fuel Performance Characterization
SEPTEMBER 30, 2013 163
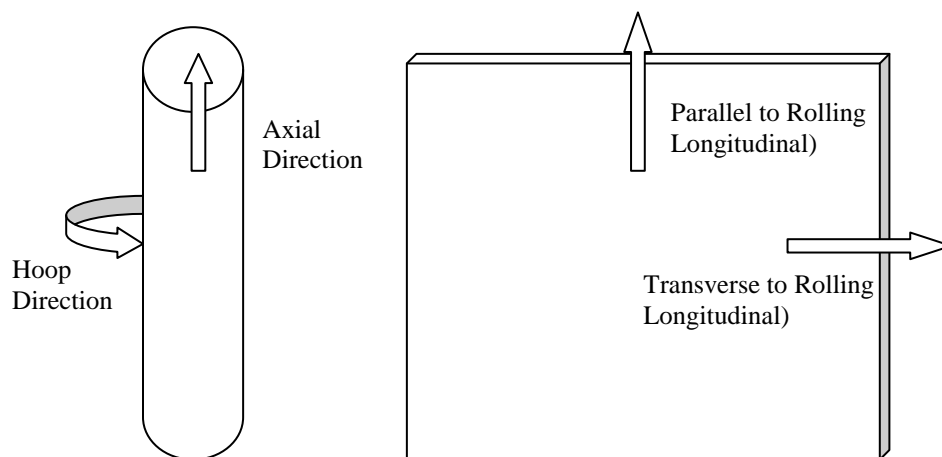
Figure 7.22. Directions in Drawn Tubes and Rolled Sheet

Because of these similarities, bending of a fuel rod will be similar to bending of a rolled sheet oriented in the longitudinal direction (tension and compression parallel to the rolling direction) and axial tension and compression tests on a rolled sheet oriented in the longitudinal direction. Tests that are less applicable to bending of a fuel rod would include cyclic pressure tests (tension and no stress in the hoop direction), bending of a rolled sheet oriented in the transverse direction (tension and compression transverse to the rolling direction) and axial tension and compression tests on a rolled sheet oriented in the transverse direction. Although these tests are not as applicable, it has already been demonstrated that Zircaloy exhibits lower fatigue strength in the transverse direction than in the longitudinal direction.   Therefore these tests will provide fatigue strengths that will be lower than that seen under NCT for used nuclear fuel.

In addition to geometry and sample orientation, stress state could have an impact on fatigue strength for used nuclear fuel under NCT. Fortunately, the data described in this report come from a number of different stress states including uniaxial stress, bending stress, biaxial stress, as well as bending of actual fuel rods. Therefore any impact of stress state may be deduced from these data.

Pandarinathan and Vasudevan (1980) performed bending tests on unirradiated cladding tubes. The data from these tests are in excellent agreement with the O'Donnell unirradiated data and are in fact on the high side of the scatter in the O'Donnell data (see Figure 7.18). This would indicate that bending of tubes results in similar or greater fatigue strength than other test geometries. ORNL data (Wang and Wang 2013) demonstrated that bending tests on tubes loaded with pellets either in the bonded or unbounded conditions are also in excellent agreement with the O'Donnell unirradiated data. This provides further indication that bending of tubes results in similar or greater fatigue strength than other test geometries regardless of their contents and that the presence of pellets (bonded or unbounded) does not have a significant impact on the fatigue strength of unirradiated tubes.

USED FUEL DISPOSITION CAMPAIGN
Used Nuclear Fuel Loading and Structural Performance Under Normal Conditions of Transport -
Demonstration of Approach and Results of Used Fuel Performance Characterization
164   **SEPTEMBER 30, 2013**

Mehan and Wiesinger (1961) observed lower fatigue strength for samples tested in the transverse direction than in the longitudinal direction. Based on this one might expect that the Soniak pressure loading tests which place the largest stress in the hoop direction (similar to the transverse direction) may also exhibit lower fatigue strengths than bending tests. However, this was not the case. As seen for the unirradiated samples in Figure 7.9, the pressure loading tests give similar fatigue strengths to other test geometries. Based on this, it is likely that the irradiated samples tested by Soniak under pressure loading will provide relevant data to used nuclear fuel under NCT.

Other irradiated data is available, such as O'Donnell (axial and bending) and Wisner (axial), but neither have the typical hydrogen levels that the Soniak PWR irradiated data do. However, the fact that the O'Donnell, Wisner, and Soniak CAP data which all have low hydrogen data are in good agreement indicates that these test geometries give similar fatigue strength and the small difference seen Soniak PWR data relative to the other irradiated data is a result of differences in hydrogen rather than difference in sample geometries or stress states.

It is concluded that the current irradiated fatigue-design curve is adequate for the loading conditions typical of nuclear fuel under NCT.

USED FUEL DISPOSITION CAMPAIGN
Used Nuclear Fuel Loading and Structural Performance Under Normal Conditions of Transport -
Demonstration of Approach and Results of Used Fuel Performance Characterization
SEPTEMBER 30, 2013 **165**

7.5.4 FATIGUE FAILURE CRITERIA FOR TRANSPORTATION OF USED NUCLEAR FUEL

Figure 7.23 shows all the irradiated Zircaloy fatigue data and the fatigue-design curve proposed by O'Donnell for irradiated Zircaloy. It has been shown that the Soniak PWR irradiated data is highly applicable to used nuclear fuel under NCT. This figure demonstrates that the proposed fatigue-design curve bounds these and all irradiated data with an adequate margin of safety.
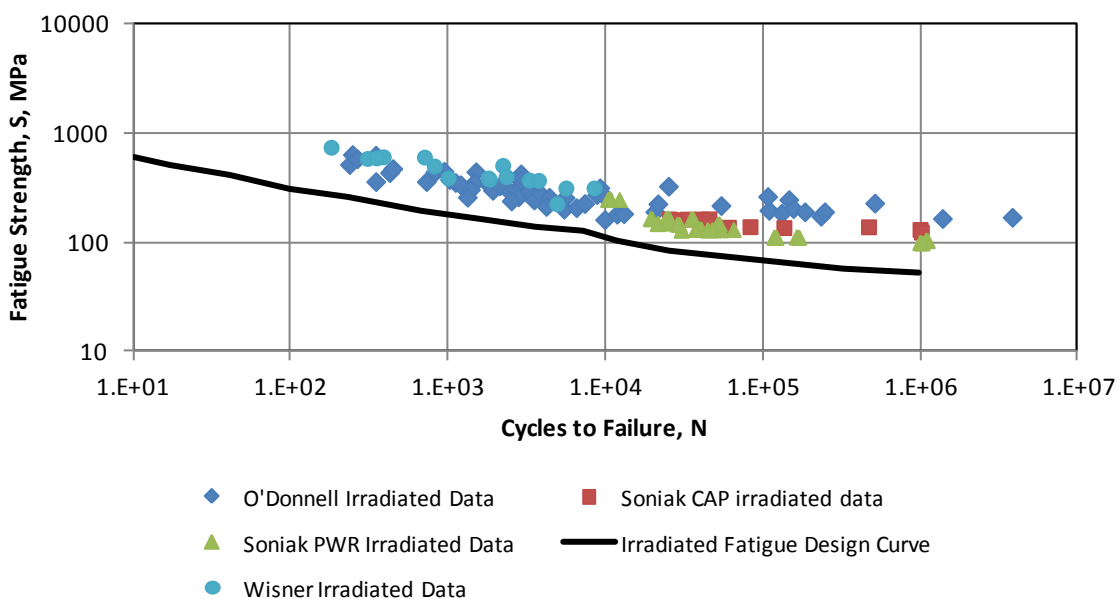
Figure 7.23. All Irradiated Fatigue Data and Irradiated Fatigue-Design Curve Applicable To Used Nuclear Fuel under NCT

One question related to fatigue lifetime is what the impact of in-reactor stress cycling is on the fatigue lifetime of used nuclear fuel. For example, will a fuel rod that has been subjected to stress cycling in-reactor exhibit a lower fatigue strength than one that was subjected to in-reactor stress cycling? Soniak et al. (1994) examined cladding tubes from PWRs following 2 and 4 cycles of irradiation without power cycling, and compared them to cladding tubes from PWRs following 2, 3, and 5 cycles of irradiation. The fatigue life of those that had power cycling were identical or even slightly higher than those that did not have power cycling, indicating that in-reactor stress cycling does not impact the out-of reactor fatigue strength.

One thing that has not been demonstrated experimentally, is the impact of the fuel pellet and the fuel/clad bonding layer and the impact of typical hydrides on tube bending on the fatigue strength of spent nuclear fuel under NCT through tests on irradiated cladding with actual high burnup UO_2 pellets. The U.S. Nuclear Regulatory Commission (NRC) Office of Research (RES) is conducting a test program at the Oak Ridge National Laboratory (ORNL) to measure the fatigue strength of sections of irradiated fuel rods containing fuel under cyclic bending

USED FUEL DISPOSITION CAMPAIGN
Used Nuclear Fuel Loading and Structural Performance Under Normal Conditions of Transport -
Demonstration of Approach and Results of Used Fuel Performance Characterization
166 **SEPTEMBER 30, 2013**

conditions. These data are expected to be available in the fall/winter 2013 timeframe. The results from these tests should be compared to the irradiated data that has been collected here, and in particular, the Soniak PWR irradiated data to determine the impact, if any, of the pellets, the pellet/clad bonding layer, or the hydrides on fatigue strength of used nuclear fuel under NCT. If a significant impact is discovered, the current fatigue-design curve can be adjusted to provide a conservative bound to these new data.

Another potential issue that should be determined, but currently no testing is planned to address, are the influence of hydride reorientation to radial hydrides. This is because hydrided cladding may fracture in the elastic region if stresses are perpendicular to the hydride and the influence of radial stress that may be imparted on the cladding from the spacer grid springs during bending in NCT.

Based on the data available, the O'Donnell and Langer irradiated fatigue failure criteria represents the current best fatigue failure limit for UNF under NCT.

8.   RESULTS OF THE INITIAL DEMONSTRATION

The results of the initial demonstration are provided in this section. Cask-level results and fuel rod-level results that feed into the assembly-level model will be provided in Sections 8.1 and 8.2, respectively. The assembly-level results provided in Section 8.3 include the calculated strain histories that are predicted for the selected loading times. These results are extrapolated over the entire 3000 mile journey and a damage fraction and assessment of failure is made in Section 8.4. Although this initial demonstration is provided for a nominal case with best-estimate modeling assumptions and inputs, sensitivity analyses have been performed to determine the relative impact of various input and modeling uncertainties on the final model predictions. The results of these sensitivity analyses are provided in Section 8.5. Finally, a summary of the results of the initial demonstration is given in Section 8.6.

8.1   CASK-LEVEL RESULTS

Table 8.1 lists the cask-level simulations that were performed. The intent of these analyses was two-fold. First, to determine the general characteristics of the shock and vibration environments generated at the fuel assemblies due to the rail car excitations provided (P1 and P3 Load Cases); and second to assess the sensitivities of those response characteristics to a limited set of previously identified parameters such as basket cell location, cask assembly component temperature, component-to-component gap size, and the inclusion or exclusion of fuel assembly control components. A detailed discussion of the results from each of the cases described in Table 8.1 is provided in Appendix A. A brief overview of the main findings from the analyses is provided next.

Table 8.1 Cask Assembly Model Simulation Matrix

Load Case	Control Components	Temperature	Gap Size
P1 Shock X (Axial)	With	Hot	Nominal
P1 Shock Y (Lateral)	With	Hot	Nominal
P1 Shock Z (Vertical	With	Hot	Nominal
P1 Vibe X (Axial)	With	Hot	Nominal
P1 Vibe Y (Lateral)	With	Hot	Nominal
P1 Vibe Z (Vertical)	With	Hot	Nominal
P3 Shock Y (Lateral)	With	Hot	Nominal
P3 Shock Z (Vertical	With	Hot	Nominal
P3 Vibe X (Axial)	With	Hot	Nominal
P3 Vibe Y (Lateral)	With	Hot	Nominal
P3 Vibe Z (Vertical)	With	Hot	Nominal
P3 Shock Y (Lateral)	Without	Hot	Nominal
P3 Shock Z (Vertical)	Without	Hot	Nominal
P3 Shock Y (Lateral)	With	Cold	Nominal
P3 Shock Z (Vertical)	With	Cold	Nominal
P3 Shock Y (Lateral)	With	Hot	Large Clearance
P3 Shock Z (Vertical)	With	Hot	Large Clearance

For the cask assembly as realized in the cask assembly FEM, the shock and vibration loads derived from the P1 data provided by TTCI produced significant excitations at the fuel assembly-level. In the axial and vertical shock cases, the rail car loads were sufficient enough to result in slip and/or vertical separation of the fuel assemblies in the basket and impact of the fuel assemblies against either the basket cell walls or the top or bottom spacer blocks. It is worth noting that the P1 shock load in the vertical direction is consistent with the shock environment defined for truck transport as described in NUREG/CR-0128 and therefore may provide some indication of the severity of the truck transport shock loading environment as well. P1 vibration loads were more benign than the P1 shock loads with respect to their ability to produce fuel assembly slip and vertical separation, but they still tended to produce excitations at the fuel assemblies of significant magnitude in the frequency range of concern, namely between 10 and 40 Hz (rigid body translation is observed between 0 and 10 Hz).

The P3 shock and vibration loads derived from the NUCARS® simulations performed by TTCI produced basket cell excitations significantly reduced from those of the P1 shock load cases. However, the P3 shock loads were still sufficient enough to induce sliding of the fuel assemblies in the basket and impact of the fuel assemblies against either the basket cell walls or the top or bottom spacer blocks. Vertical separation between the fuel assembly and basket cell wall was significantly reduced or entirely eliminated in the P3 simulations. The P3 vibration loads were generally more benign than even the P1 vibration loads, but still produced excitations at the fuel assemblies of significant magnitude in the frequency range between 10 and 40 Hz.

USED FUEL DISPOSITION CAMPAIGN
Used Nuclear Fuel Loading and Structural Performance Under Normal Conditions of Transport -
Demonstration of Approach and Results of Used Fuel Performance Characterization
168   **SEPTEMBER 30, 2013**

8.2   FUEL ROD-LEVEL RESULTS

The information generated in this detailed fuel rod, grid spacer, and spring analysis was provided to the PWR assembly-level model. At the PWR assembly-level model this information was used to "tune" the assembly to the input response spectra at the basket location. The tuning was performed within the LB, UB material property window.

Additionally the stress increase due to fuel rod bending is calculated and provided to the PWR assembly-level. This multiplier was used at the PWR assembly-level on the bending stress output. The bending stress in the cladding without stress concentration is $3.219 \cdot 10^4$ kPa (as calculated in Section 8.5.8.2) Consequently, the stress concentration column of Table 8.12 is the percent stress increase (or decrease if it is negative) above this bending stress value for the stress concentration region on top of the cladding.

8.2.1.1   LINEAR BEAM ELEMENTS PROPERTIES FOR THE PWR ASSEMBLY MODEL

Given the evaluation for the geometrically nonlinear, simply supported fuel rod model in Section 6.3.1, the following properties can be used to define linear beam element properties that generate similar results.

$m_{cp} = 0.599 \dfrac{kg}{m}$ Modeled mass of the cladding and fuel pellet.

$EI_{LB} = 8.3 \cdot Pa \cdot m^4$ Evaluated lower bound flexural rigidity.

$EI_{BE} = 45.1 \cdot Pa \cdot m^4$ Evaluated best estimate flexural rigidity.

$EI_{UB} = 49.3 \cdot Pa \cdot m^4$ Evaluated upper bound flexural rigidity.

$$\alpha\,(EI, fn) := \frac{\left(49.3 \ Pa \cdot m^4 - EI\right) \cdot \left(3.39 \times 10^{-2} \cdot fn\right)}{41.0 \ Pa \cdot m^4}$$ Mass damping factor for Rayleigh damping.

$$\beta\,(EI, fn) := \frac{\left(49.3 \ Pa \cdot m^4 - EI\right) \cdot \left(3.07 \times 10^{-6} \cdot fn\right)}{41.0 \ Pa \cdot m^4}$$ Stiffness damping factor for Rayleigh damping.

where

EI - Flexural rigidity.

fn - Friction coefficient (the damping factors were evaluated for a range of $0.1 < fn < 1.5$).

USED FUEL DISPOSITION CAMPAIGN
Used Nuclear Fuel Loading and Structural Performance Under Normal Conditions of Transport -
Demonstration of Approach and Results of Used Fuel Performance Characterization
SEPTEMBER 30, 2013 169

As an example to demonstrate the use of these properties, a linear beam model is run that is similar to the nonlinear model run (using a model similar to Figure 6.21) of the 450.8 mm long rod with a 0.75 friction coefficient. The linear beam model has a mesh density similar to that of the nonlinear beam with 250 elements along its length. The example uses the properties above along with a LB cladding modulus, Poisson's ratio, and the outside diameter of the cladding. The other needed properties are calculated.

The following show the effective properties to be used in the PWR assembly-level model.

USED FUEL DISPOSITION CAMPAIGN
Used Nuclear Fuel Loading and Structural Performance Under Normal Conditions of Transport -
Demonstration of Approach and Results of Used Fuel Performance Characterization
170   SEPTEMBER 30, 2013

(The material properties below are based on those derived in Section 6.3.2)

$$E_{z4}\left(T_{400}, \Delta_o, C_o, \Phi_{lo}\right) = 6.022 \times 10^7 \cdot \frac{kg \cdot mm}{s^2 \cdot mm^2}$$

Lower bound cladding modulus of elasticity.

$$\nu_{z4}\left(T_{400}, \Delta_o, C_o, \Phi_{lo}\right) = 0.338$$

Poisson's ratio.

$$d_{co} = 9.144 \cdot mm$$

Outside diameter of the cladding.

Find Rayleigh damping factors, section thickness, and density:

$$EI_{ex} := 8.36 \cdot Pa \cdot m^4$$

Flexural rigidity (from the nonlinear model for comparison).

$$fn_{ex} := 0.75$$

Friction coefficient (from the nonlinear model for comparison).

$$\alpha_{ex} := \alpha\left(EI_{ex}, fn_{ex}\right) = 2.539 \times 10^{-2}$$

Mass damping factor for Rayleigh damping.

$$\beta_{ex} := \beta\left(EI_{ex}, fn_{ex}\right) = 2.299 \times 10^{-6}$$

Stiffness damping factor for Rayleigh damping.

$$I_{ex} := \frac{EI_{ex}}{E_{z4}\left(T_{400}, \Delta_o, C_o, \Phi_{lo}\right)} = 138.834 \cdot mm^4$$

Area moment of inertia for the cladding.

$$d_{ci\_ex} := \sqrt[4]{d_{co}^4 - \frac{64 \cdot I_{ex}}{\pi}} = 8.032 \cdot mm$$

Inside diameter of the cladding.

$$t_{ex} := \frac{1}{2} \cdot \left(d_{co} - d_{ci\_ex}\right) = 0.5558 \cdot mm$$

Thickness of the cladding.

$$A_{c\_ex} := \frac{\pi}{4} \cdot \left(d_{co}^2 - d_{ci\_ex}^2\right) = 15.00 \cdot mm^2$$

Cross sectional area of the cladding.

$$\rho_{ex} := \frac{m_{cp}}{A_{c\_ex}} = 3.992 \times 10^{-5} \cdot \frac{kg}{mm^3}$$

Density of the cladding.

Running the linear beam model and deriving natural frequency as described in Section 6.3.1.4 (and then doubling the viscous damping) produces the following data for comparison:

$$\omega_{ex} = 180.9$$

Natural frequency of the linear beam.

$$\zeta_{ex} = 5.712 \times 10^{-4}$$

Viscous damping of the linear beam.

$$\omega_{nl} = 181.6$$

Natural frequency of the nonlinear beam.

$$\zeta_{nl} = 5.475 \times 10^{-4}$$

Viscous damping of the nonlinear beam.

USED FUEL DISPOSITION CAMPAIGN
Used Nuclear Fuel Loading and Structural Performance Under Normal Conditions of Transport -
Demonstration of Approach and Results of Used Fuel Performance Characterization
SEPTEMBER 30, 2013   171

Based on comparing the linear beam results to the nonlinear model run (using a model similar to Figure 6.21), the error in the natural frequency for the linear beam results is less than 1% and could be explained with round off error. The error in the viscous damping is about 4%. About 2% of this is related to the damping factor functions not producing a Rayleigh damping value that exactly matches that resulting from the nonlinear analysis. Default bulk viscosity in the solver could contribute along with round off error to explain the other 2%. Given that the viscous damping is very small, the observed difference may be considered to be reasonable. (It should be noted that, for scoping analyses, the above comparison was rerun with a much more coarse mesh. The results showed that the natural frequency error was still not significantly different but the viscous damping error went up significantly. The coarser mesh was then rerun again with a target damping of 5% and the error was not significant in either natural frequency or damping. These scoping runs indicate that the method produces accurate results but the damping is small enough that it is sensitive to small inaccuracies in calculation. Given how small the damping is, this sensitivity is not expected to significantly affect the results of the PWR assembly-level model.)

8.3   ASSEMBLY-LEVEL RESULTS

The assembly submodel analyses were performed for the Phase 3 (P3) loading conditions based on the hypothetical S-2406 compliant rail car and NUCARS simulations. The results of these preliminary analyses are shown in Section 8.3.1. The final evaluations with the PWR assembly-level model are to use bounding data for the shock and vibration events for a conservative estimate of maximum fuel rod deformation. These results are shown in Section 8.3.2.

8.3.1   PRELIMINARY ANALYSES AND RESULTS USING NUCARS TRANSPORTATION DATA

The assembly submodel analyses were repeated for the new loading conditions based on the hypothetical S-2406 compliant rail car and NUCARS simulations. Acceleration time histories for the lateral shock, vertical/longitudinal shock, lateral vibration, vertical vibration, and longitudinal vibration cases were obtained from the cask-level analyses and applied to the assembly-level submodel. The maximum accelerations for this rail car are expected to be less severe than those of the coal car used in the initial sensitivity analyses. Preliminary results using these input loads are reported here to demonstrate the procedure for evaluation of cyclic fatigue loading. Due to project time constraints, the acceleration input histories used here were simply filtered to eliminate high frequency noise and were not drift corrected. The basket accelerations output from the cask-level analyses based on the NUCARS dataset will next be made bounding for all basket cells, broadened, and drift corrected for the final demonstration case.

The maximum cladding strains and distributions of the peak-to-peak strain cycles for the simulated 10s window are shown in Figure 8.1. The highest cladding strain of 3.87e-4 was observed in the vertical shock case, while the lateral shock case showed strains of only 2.34e-4. Maximum strains of 1.54e-4 to 2.02e-4 were observed in the vibration cases with the vertical excitation again being worse. The distributions of cyclic cladding strains are similar for all of

USED FUEL DISPOSITION CAMPAIGN
Used Nuclear Fuel Loading and Structural Performance Under Normal Conditions of Transport -
Demonstration of Approach and Results of Used Fuel Performance Characterization
172   **SEPTEMBER 30, 2013**

the cases in that a greater number of low amplitude cycles occur and the frequency of occurrence then tends to decrease in number for higher amplitude cycles. The shock loads do show a higher amplitude peak in the histogram due to the particular event itself as expected by definition. The contribution of each of these cycle bins to the total fatigue damage is shown in Figure 8.2. It is observed that the high amplitude cycles contribute the most to fatigue damage even though the occurrence counts are much lower. The low amplitude high frequency vibrations do not contribute much damage, which is beneficial from a modeling standpoint that any high frequency numerical noise in the solution does not affect the damage assessment. The occurrence frequency and cyclic amplitude for the shock events is assumed to be the same for all rail speeds, but the cyclic strains are scaled by the different amplitudes of the 10 shock events in the 350-second window evaluated. For the vibration cases, the damage distribution is broader due to the influence of the rail car speed. The strain amplitude is assumed to vary with the speed of the car and the total damage accounts for the duration at each speed range during the 3000 mile route with a total duration of 94 hours. For the speed distribution shown in Figure 8.3, the damage contribution in the vibration cases is shown to be greatest for the 45-50 mph range (Figure 8.4). Therefore, the highest strain was observed in the analyzed 10-second window corresponding to 62.5 mph operation, but the train spends much more time at lower speeds which ultimately contribute more to the overall fatigue damage and broaden the histogram of damage versus cyclic strain amplitude (Figure 8.2). This analysis emphasizes the importance of the rail car route characteristics on the cumulative fatigue damage of the cladding.

The total fatigue damage levels for the cases are summarized in Table 8.2 and Figure 8.5. The highest damage was observed in the vertical vibration case followed by the lateral shock case. The total predicted damage is less than 1% of the allowable fatigue. This suggests that the nominal cladding layer would not exhibit a fatigue-type failure based on the assumed state and fatigue properties of the cladding, but the gross assumptions about extrapolation of response from a small 10-second time window to a 3000 mile trip still warrants careful future consideration.

USED FUEL DISPOSITION CAMPAIGN
Used Nuclear Fuel Loading and Structural Performance Under Normal Conditions of Transport -
Demonstration of Approach and Results of Used Fuel Performance Characterization
SEPTEMBER 30, 2013 173
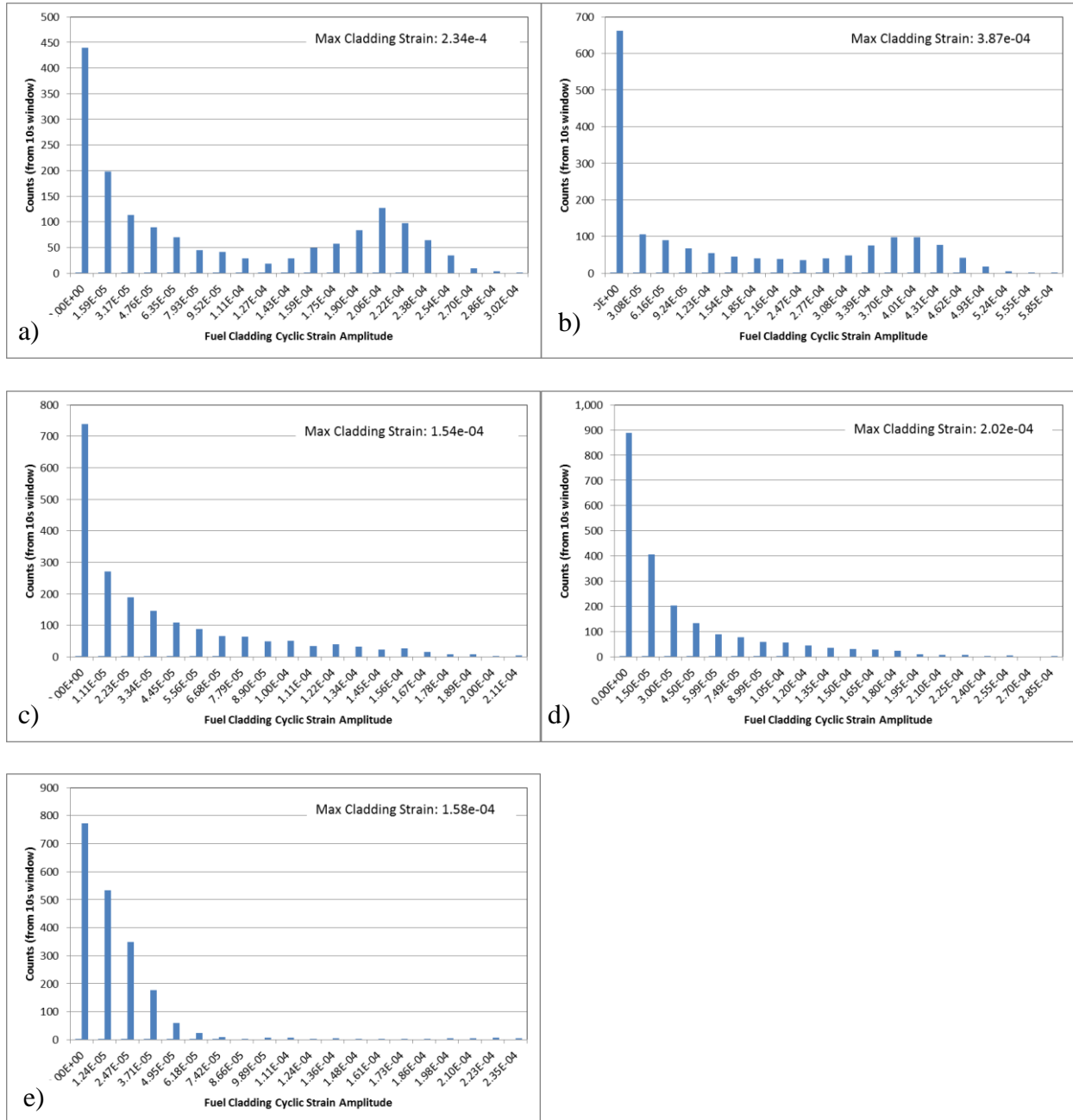
Figure 8.1. Distribution of Cladding Strain Cycles for the 10-second Window of the a) Lateral Shock, b) Vertical/Longitudinal Shock, c) Lateral Vibration, d) Vertical Vibration, and e) Axial Vibration Cases

USED FUEL DISPOSITION CAMPAIGN
Used Nuclear Fuel Loading and Structural Performance Under Normal Conditions of Transport -
Demonstration of Approach and Results of Used Fuel Performance Characterization
174   **SEPTEMBER 30, 2013**
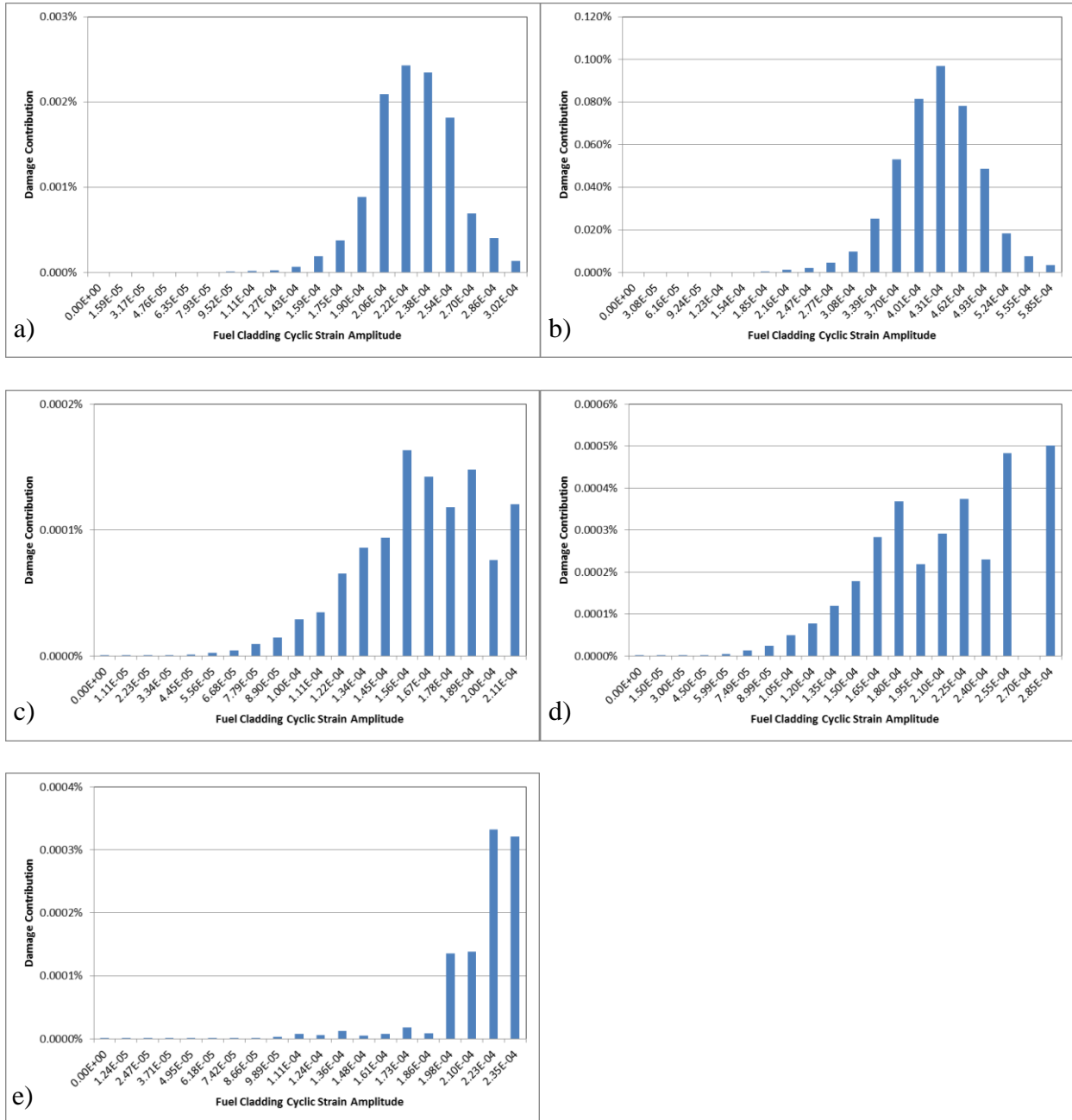
Figure 8.2. Distribution of Fatigue Damage Contribution as a Function of Cyclic Strain Amplitude for the 10-second Window of the a) Lateral Shock, b) Vertical/Longitudinal Shock, c) Lateral Vibration, d) Vertical Vibration, and e) Axial Vibration Cases

USED FUEL DISPOSITION CAMPAIGN
Used Nuclear Fuel Loading and Structural Performance Under Normal Conditions of Transport -
Demonstration of Approach and Results of Used Fuel Performance Characterization
SEPTEMBER 30, 2013 **175**
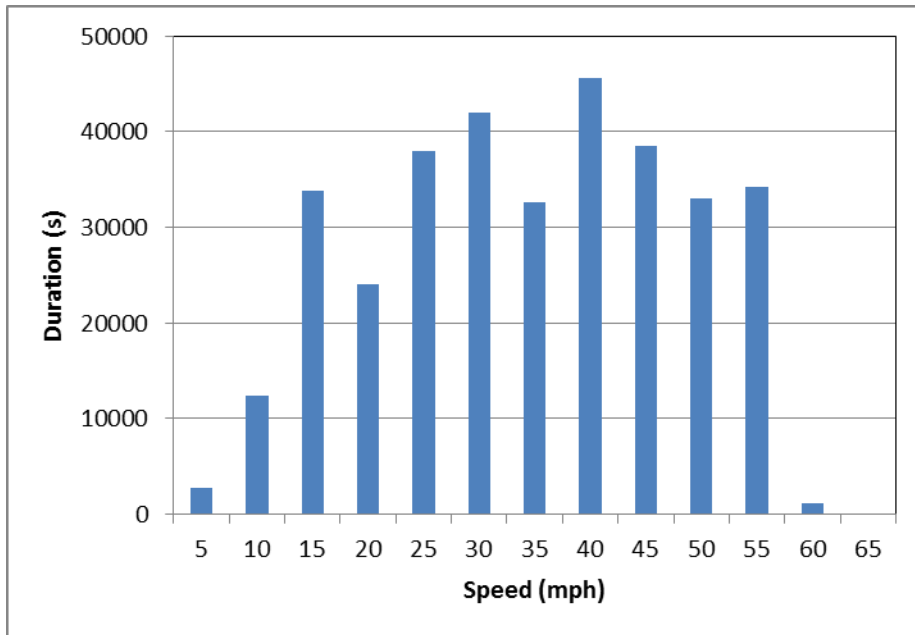
Figure 8.3. Duration of the Rail Car Operation at Different Speeds for a 3000 Mile Route

USED FUEL DISPOSITION CAMPAIGN
Used Nuclear Fuel Loading and Structural Performance Under Normal Conditions of Transport -
Demonstration of Approach and Results of Used Fuel Performance Characterization
176 **SEPTEMBER 30, 2013**
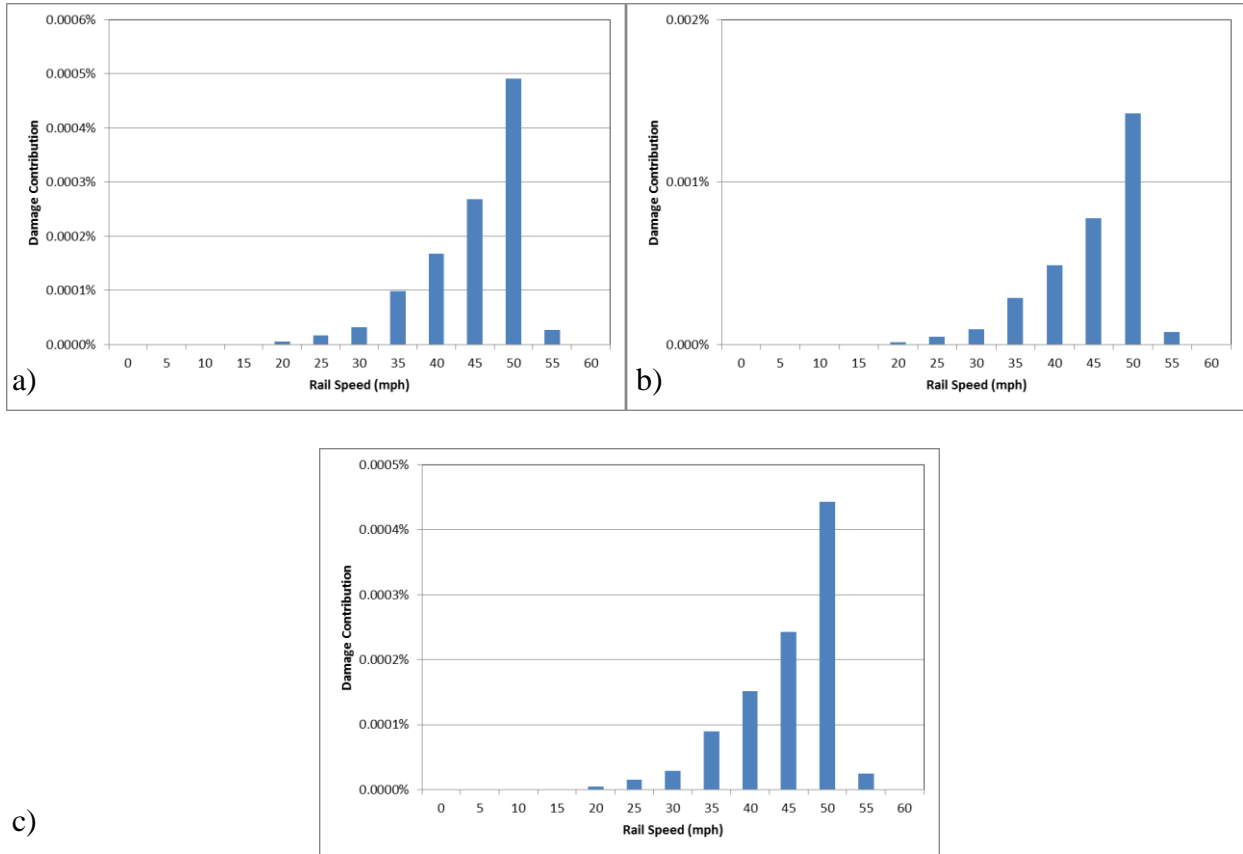
Figure 8.4. Distribution of Fatigue Damage Contribution as a Function of Rail Speed for the a) Lateral Vibration, b) Vertical Vibration, and c) Axial Vibration Cases

Table 8.2. Total Cladding Fatigue Damage Due to Shock and Vibration Loading

Case	Description	Maximum Cladding Strain	Maximum Cyclic Strain Amplitude	Total Fatigue Damage
P3-1	Lateral Shock	2.34E-04	3.17E-04	0.011%
P3-2	Vertical/Longitudinal Shock	3.87E-04	6.16E-04	0.432%
P3-3	Lateral Vibration	1.54E-04	2.23E-04	0.001%
P3-4	Vertical Vibration	2.02E-04	3.00E-04	0.003%
P3-5	Longitudinal Vibration	1.58E-04	2.47E-04	0.001%
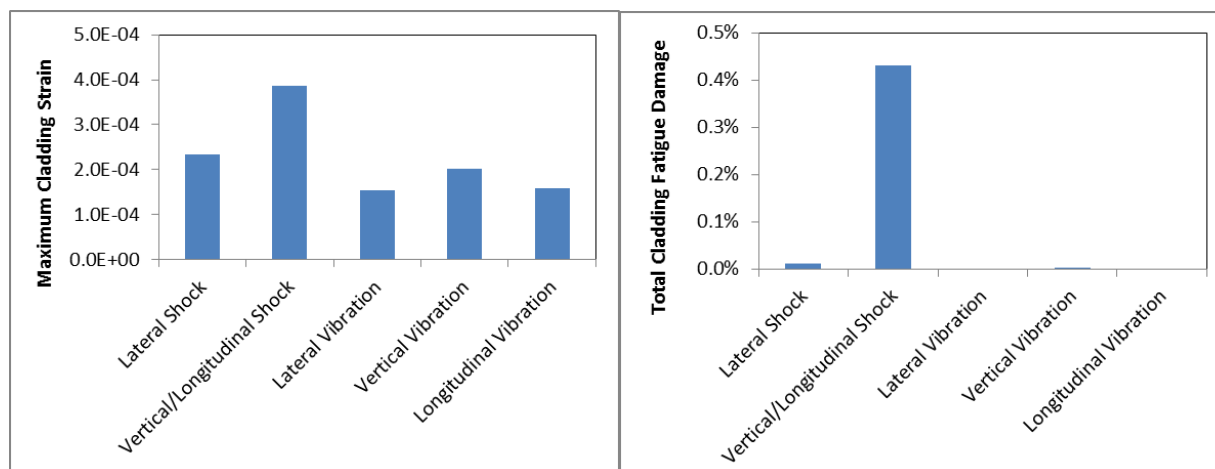
Figure 8.5. Comparison of Maximum Cladding Strain and Total Fatigue Damage for P3 Shock and Vibration Cases

8.3.2 FINAL ANALYSES USING BROADENED LOAD SPECTRA DERIVED FROM P3 NUCARS TRANSPORTATION DATA

The final evaluations with the assembly-level submodel are to use bounding and broadened data for the shock and vibration events for a conservative estimate of maximum fuel rod deformation. This analysis is necessary primarily because of the large uncertainty with the final material state of the fuel rod during transport. The effective rod stiffness and corresponding natural frequency of vibration depends on many factors (e.g., the irradiated material properties, temperature, pellet-clad bonding) which may exhibit considerable variation but are difficult to experimentally characterize. Particular fuel rods may or may not have strong amplification of the input loading depending on how well the frequency content of the excitation load matches the rod response with its particular mechanical properties. If the particular rod definition used in the simulation does not have a natural frequency at the frequency where a strong input loading peak exists (which is likely), then the predicted cladding strain may be greatly underestimated. To ensure that the rod responds in the dynamic loading events simulated here, peaks in the input loading spectrum are broadened to ensure that the modeled rod will be appropriately excited.

8.3.2.1 BROADENED P3 INPUT LOAD SPECTRA

The loading spectra for all 32 basket assemblies obtained from the cask-level model using the P3 NUCARS input were evaluated for the five final data sets. The rigid body translational and rotational accelerations of the basket compartments were obtained from the cask-level results. The bounding spectrum was determined for the three translational and three rotational basket accelerations and then broadened based on the potential variation in fuel rod stiffness due to temperature, material properties, and pellet-clad bonding. The broadened curves will ensure that

USED FUEL DISPOSITION CAMPAIGN
Used Nuclear Fuel Loading and Structural Performance Under Normal Conditions of Transport -
Demonstration of Approach and Results of Used Fuel Performance Characterization
178   **SEPTEMBER 30, 2013**

the maximum response of the rods will be excited. 10-second time histories were then generated based on the broadened spectra and used as loading for the PWR assembly model. The corresponding spectra are shown in Figure 8.6-Figure 8.15. The corresponding acceleration and displacement time histories are shown in Figure 8.16-Figure 8.20. The broadening has particularly enhanced the lateral vibration amplitude with peaks of ~6 m/s^2 for the lateral shock case and ~4 m/s^2 for the vertical shock case. The peak lateral acceleration was also 1.5 m/s^2 for the lateral and vertical vibration cases. Therefore, higher loading and cladding strains are expected for the broadened lateral shock and vibration cases.

USED FUEL DISPOSITION CAMPAIGN
Used Nuclear Fuel Loading and Structural Performance Under Normal Conditions of Transport -
Demonstration of Approach and Results of Used Fuel Performance Characterization
SEPTEMBER 30, 2013 179
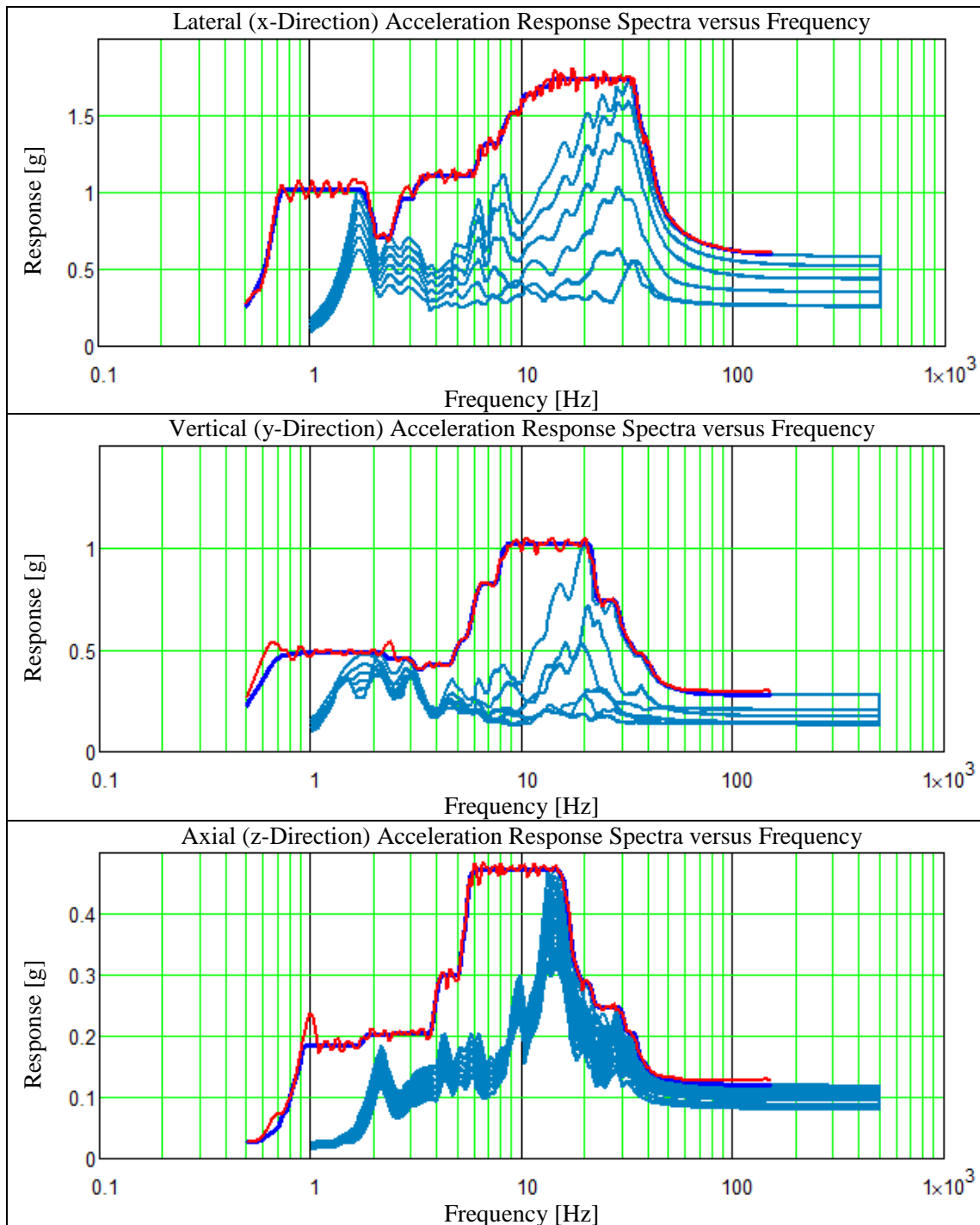
Figure 8.6. Translational Response Spectra for "Shock_Lateral_Cell_Response_Data" with Cell Data (Blue-Gray Curves), Broadened Target (Blue Curve) and Modified Time History Response (Red Curve)

USED FUEL DISPOSITION CAMPAIGN
Used Nuclear Fuel Loading and Structural Performance Under Normal Conditions of Transport -
Demonstration of Approach and Results of Used Fuel Performance Characterization
180   **SEPTEMBER 30, 2013**
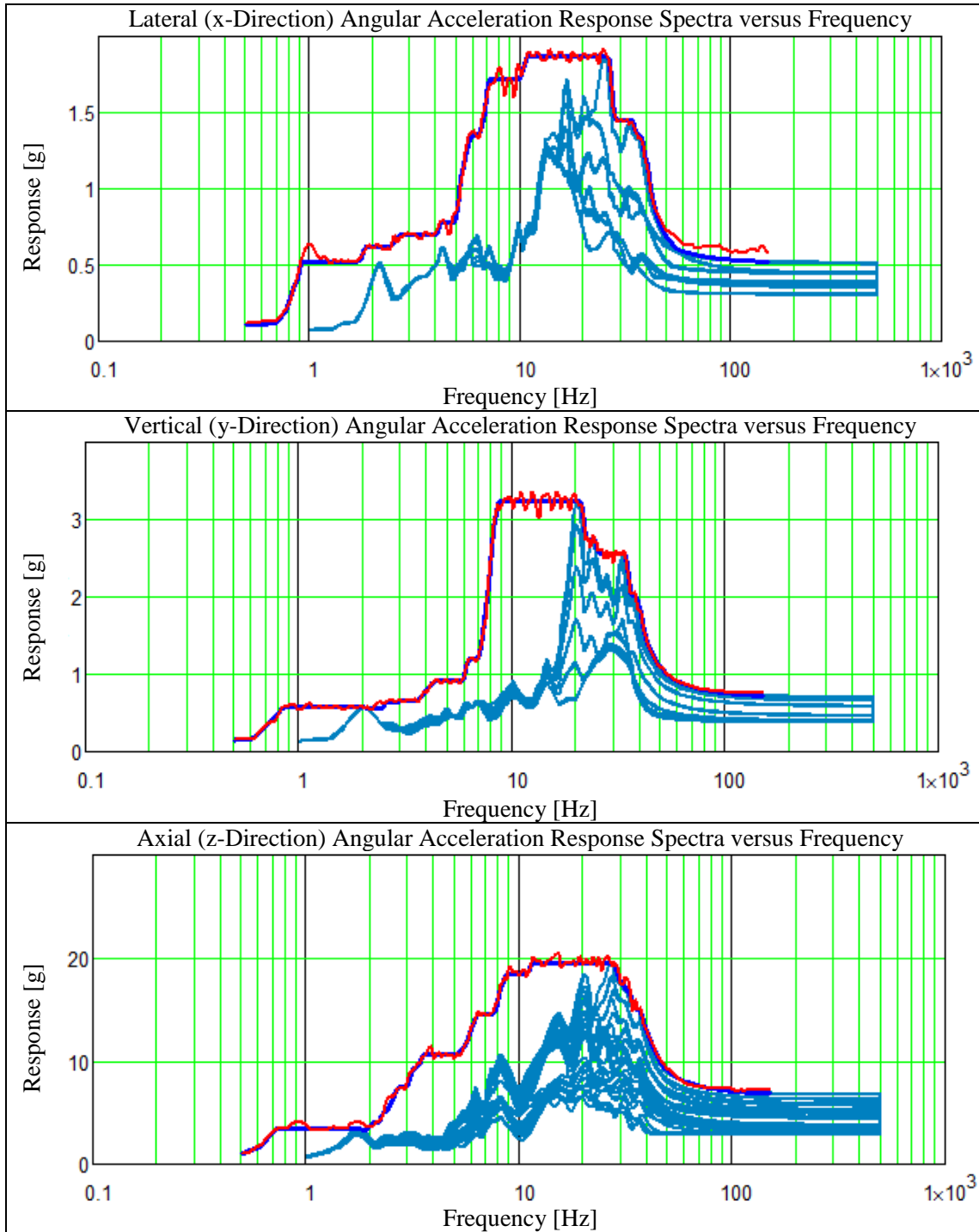
Figure 8.7. Rotational Response Spectra for "Shock_Lateral_Cell_Response_Data" with Cell
Data (Blue-Gray Curves), Broadened Target (Blue Curve) and Modified Time
History Response (Red Curve)

USED FUEL DISPOSITION CAMPAIGN
**Used Nuclear Fuel Loading and Structural Performance Under Normal Conditions of Transport -
Demonstration of Approach and Results of Used Fuel Performance Characterization
SEPTEMBER 30, 2013** **181**
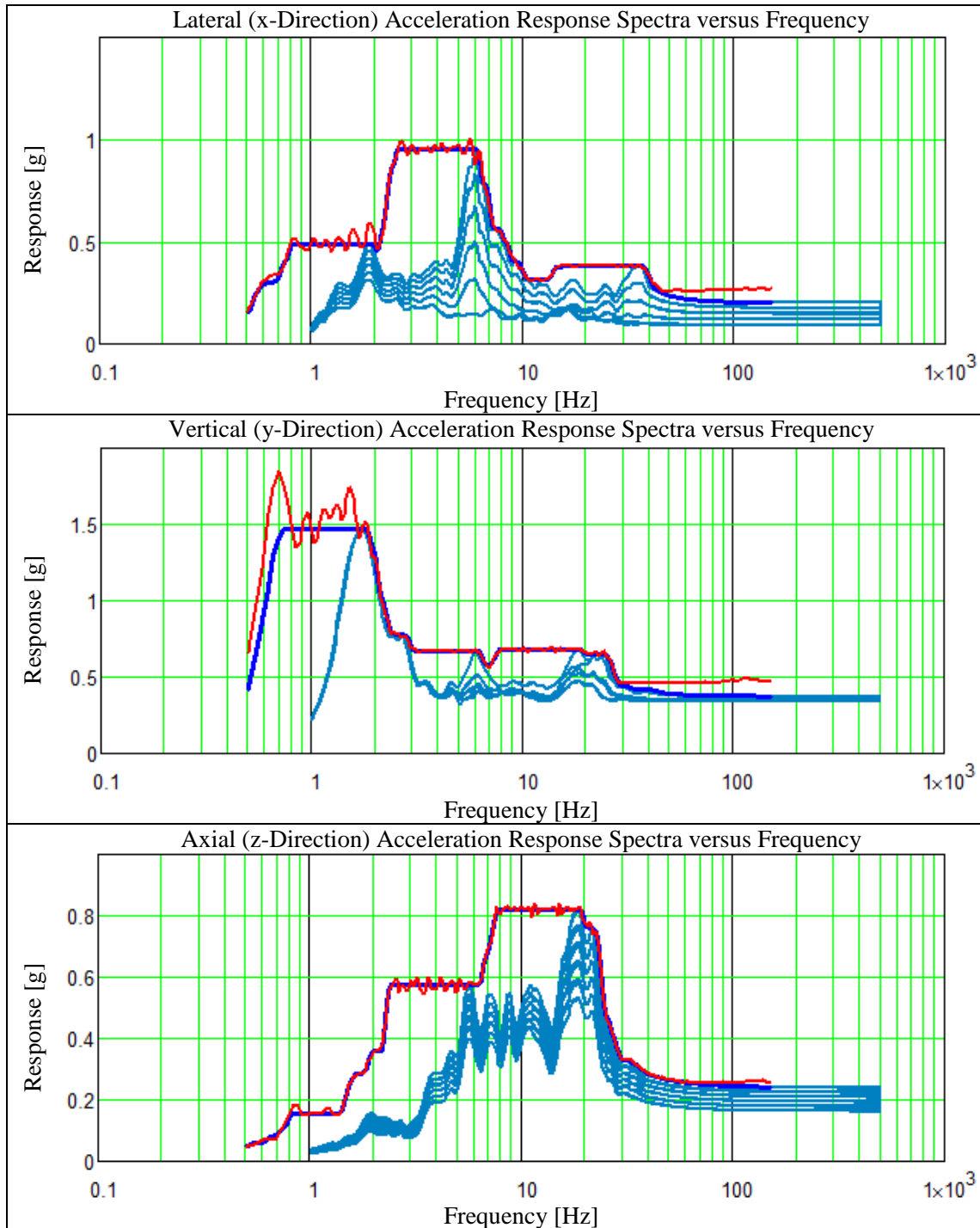
Figure 8.8. Translational Response Spectra for "Shock_Vertical_Cell_Response_Data" with
Cell Data (Blue-Gray Curves), Broadened Target (Blue Curve) and Modified Time
History Response (Red Curve)

USED FUEL DISPOSITION CAMPAIGN
**Used Nuclear Fuel Loading and Structural Performance Under Normal Conditions of Transport -
Demonstration of Approach and Results of Used Fuel Performance Characterization**
182   **SEPTEMBER 30, 2013**
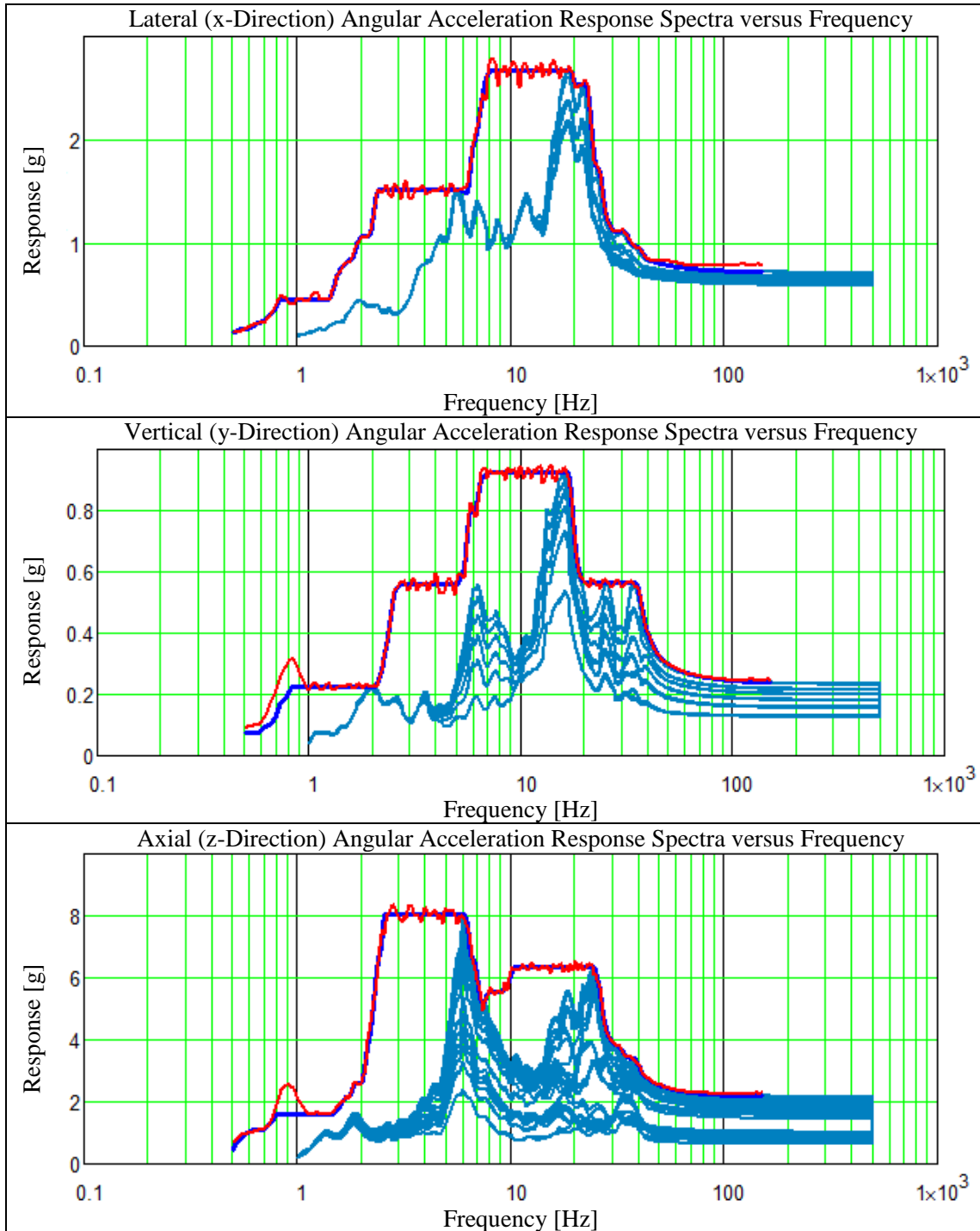
Figure 8.9. Rotational Response Spectra for "Shock_Vertical_Cell_Response_Data" With Cell
Data (Blue-Gray Curves), Broadened Target (Blue Curve) and Modified Time
History Response (Red Curve)

USED FUEL DISPOSITION CAMPAIGN
Used Nuclear Fuel Loading and Structural Performance Under Normal Conditions of Transport -
Demonstration of Approach and Results of Used Fuel Performance Characterization
SEPTEMBER 30, 2013   183
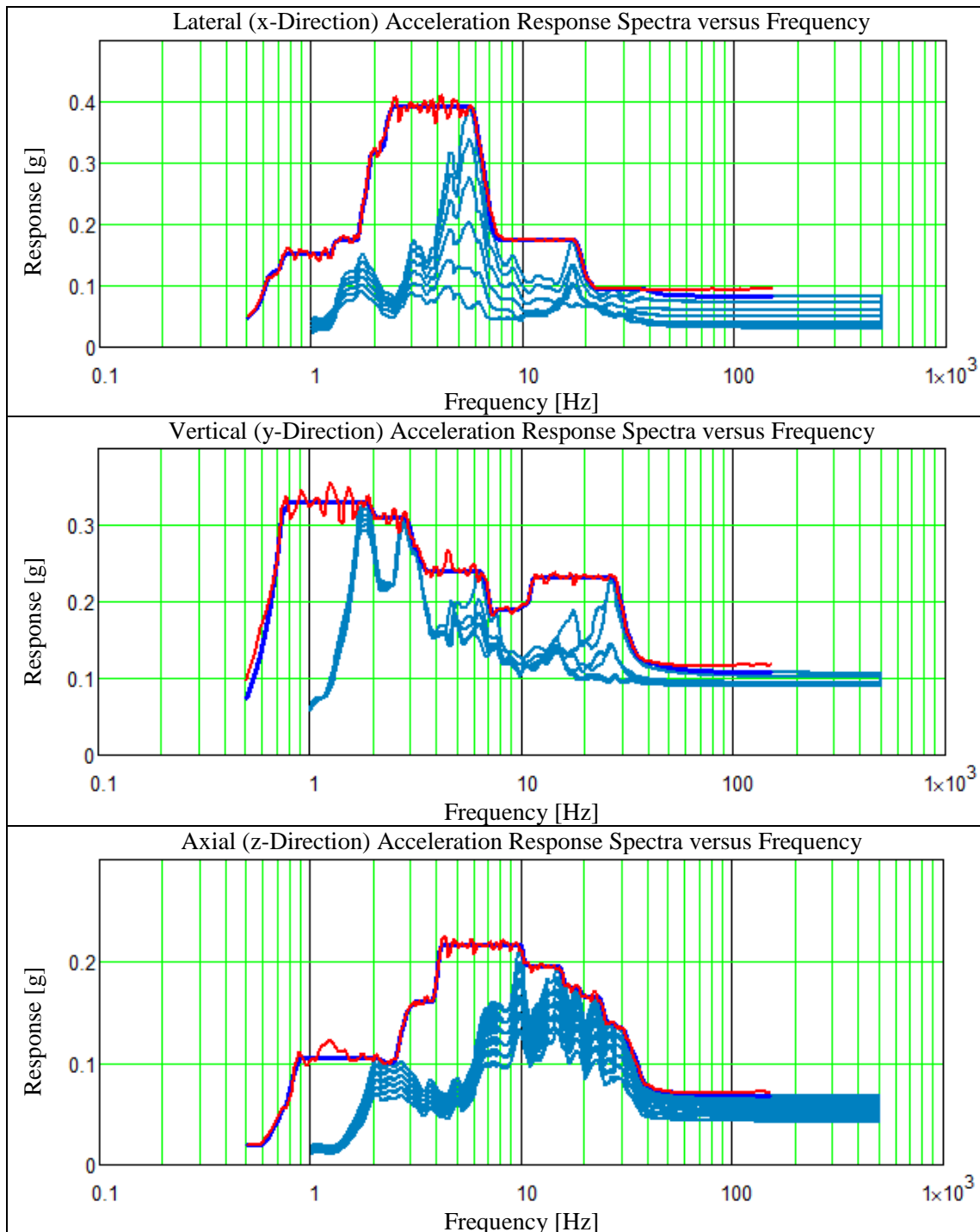
Figure 8.10. Translational Response Spectra for "Vibe_Axial_Cell_Response_Data" with Cell
Data (Blue-Gray Curves), Broadened Target (Blue Curve) and Modified Time
History Response (Red Curve)

USED FUEL DISPOSITION CAMPAIGN
Used Nuclear Fuel Loading and Structural Performance Under Normal Conditions of Transport -
Demonstration of Approach and Results of Used Fuel Performance Characterization
184 **SEPTEMBER 30, 2013**
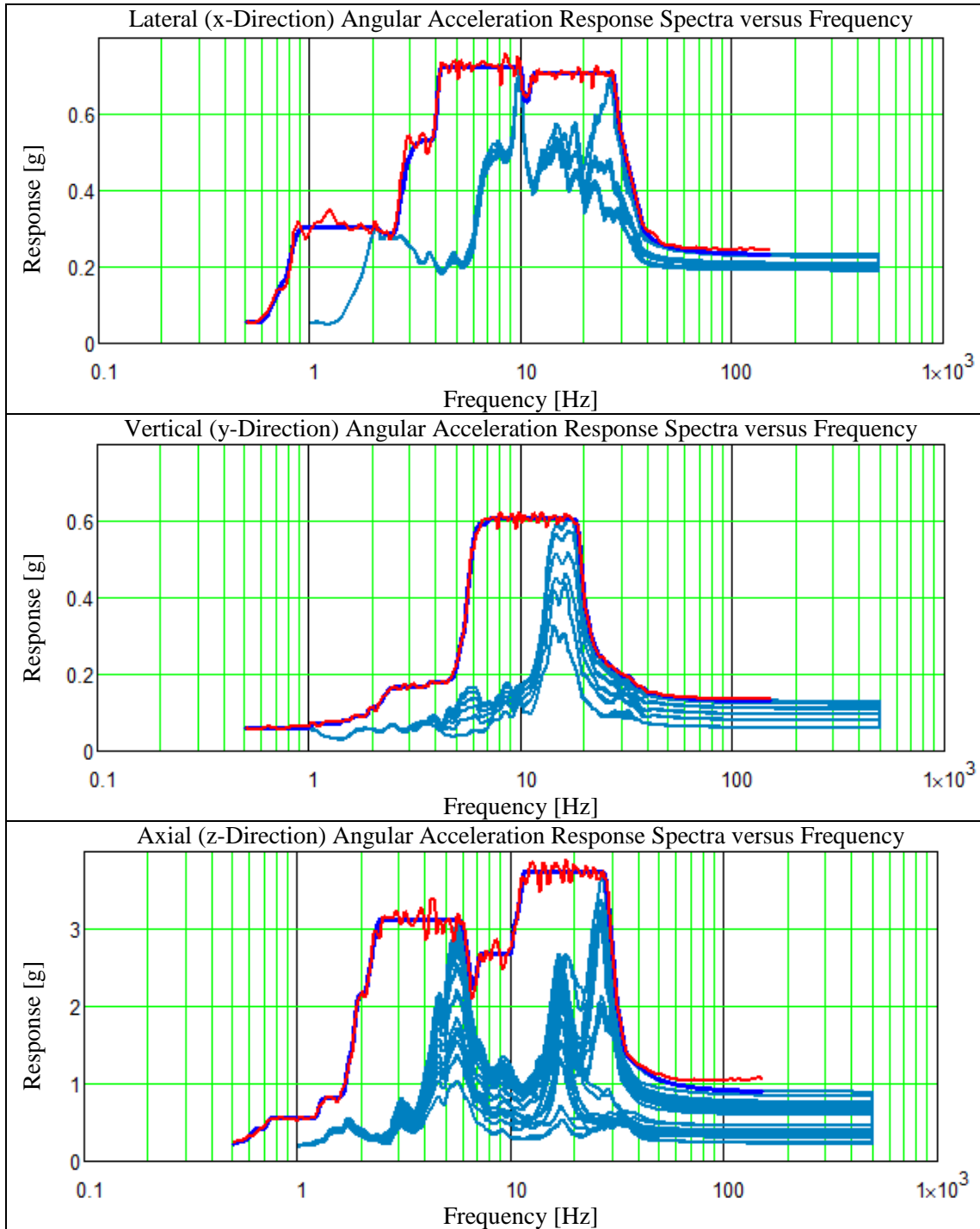
Figure 8.11. Rotational Response Spectra for "Vibe_Axial_Cell_Response_Data" with cell Data (Blue-Gray Curves), Broadened Target (Blue Curve) and Modified Time History Response (Red Curve)

USED FUEL DISPOSITION CAMPAIGN
Used Nuclear Fuel Loading and Structural Performance Under Normal Conditions of Transport -
Demonstration of Approach and Results of Used Fuel Performance Characterization
SEPTEMBER 30, 2013 185
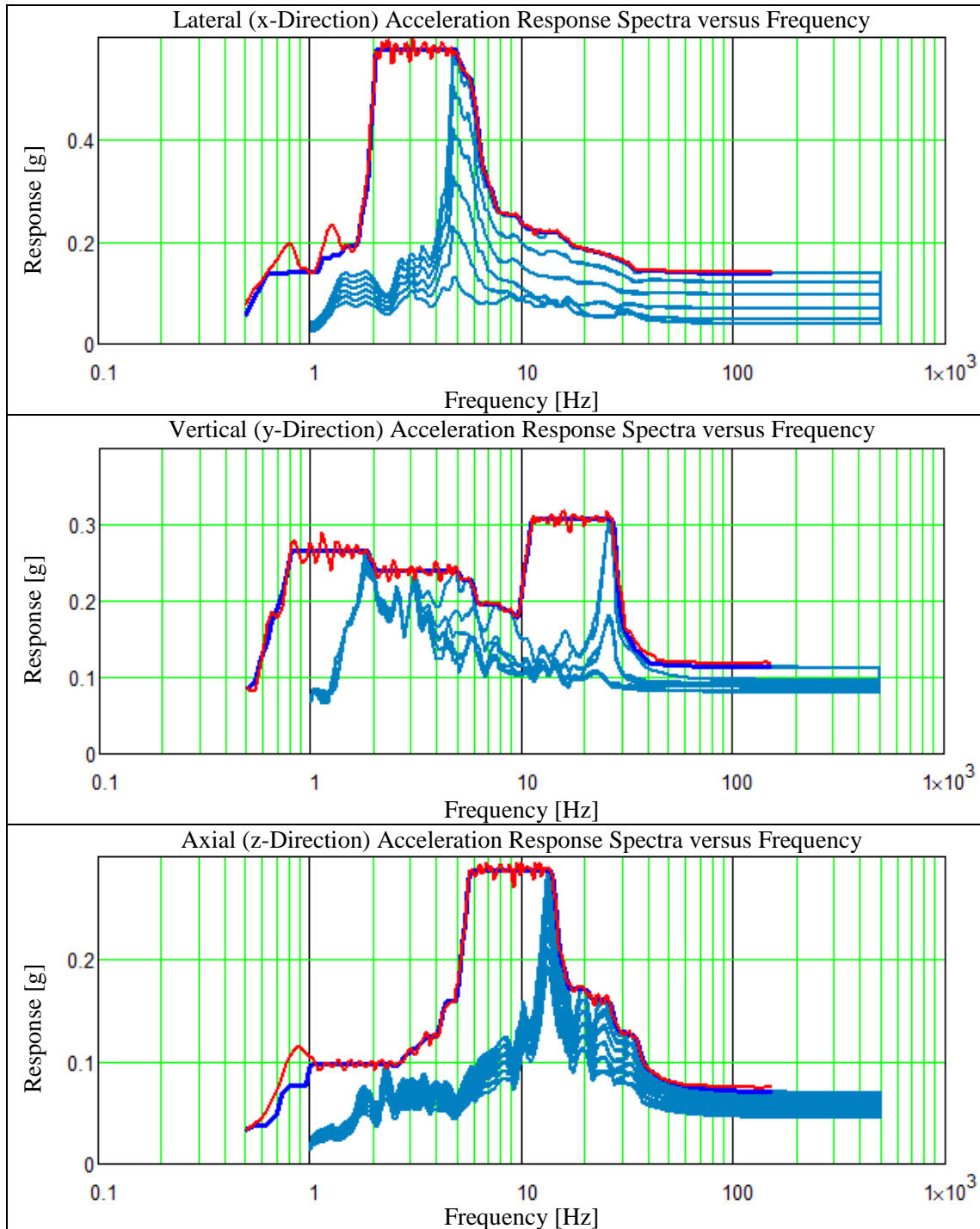
Figure 8.12. Translational Response Spectra for "Vibe_Lateral_Cell_Response_Data" with Cell Data (Blue-Gray Curves), Broadened Target (Blue Curve) and Modified Time History Response (Red Curve)

USED FUEL DISPOSITION CAMPAIGN
Used Nuclear Fuel Loading and Structural Performance Under Normal Conditions of Transport -
Demonstration of Approach and Results of Used Fuel Performance Characterization
186   **SEPTEMBER 30, 2013**
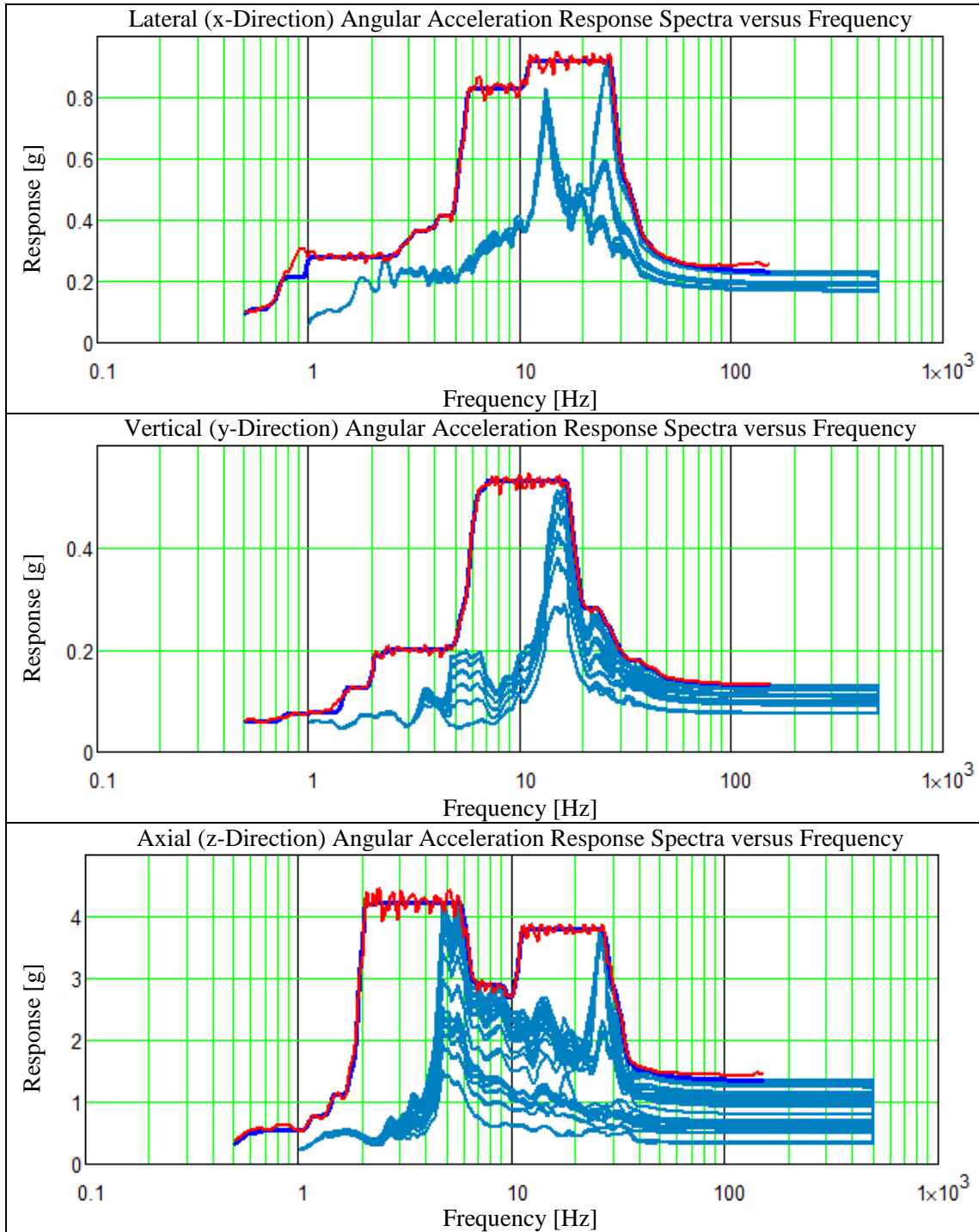
Figure 8.13. Rotational Response Spectra for "Vibe_Lateral_Cell_Response_Data" with Cell Data (Blue-Gray Curves), Broadened Target (Blue Curve) and Modified Time History Response (Red Curve)

USED FUEL DISPOSITION CAMPAIGN
Used Nuclear Fuel Loading and Structural Performance Under Normal Conditions of Transport -
Demonstration of Approach and Results of Used Fuel Performance Characterization
SEPTEMBER 30, 2013 187
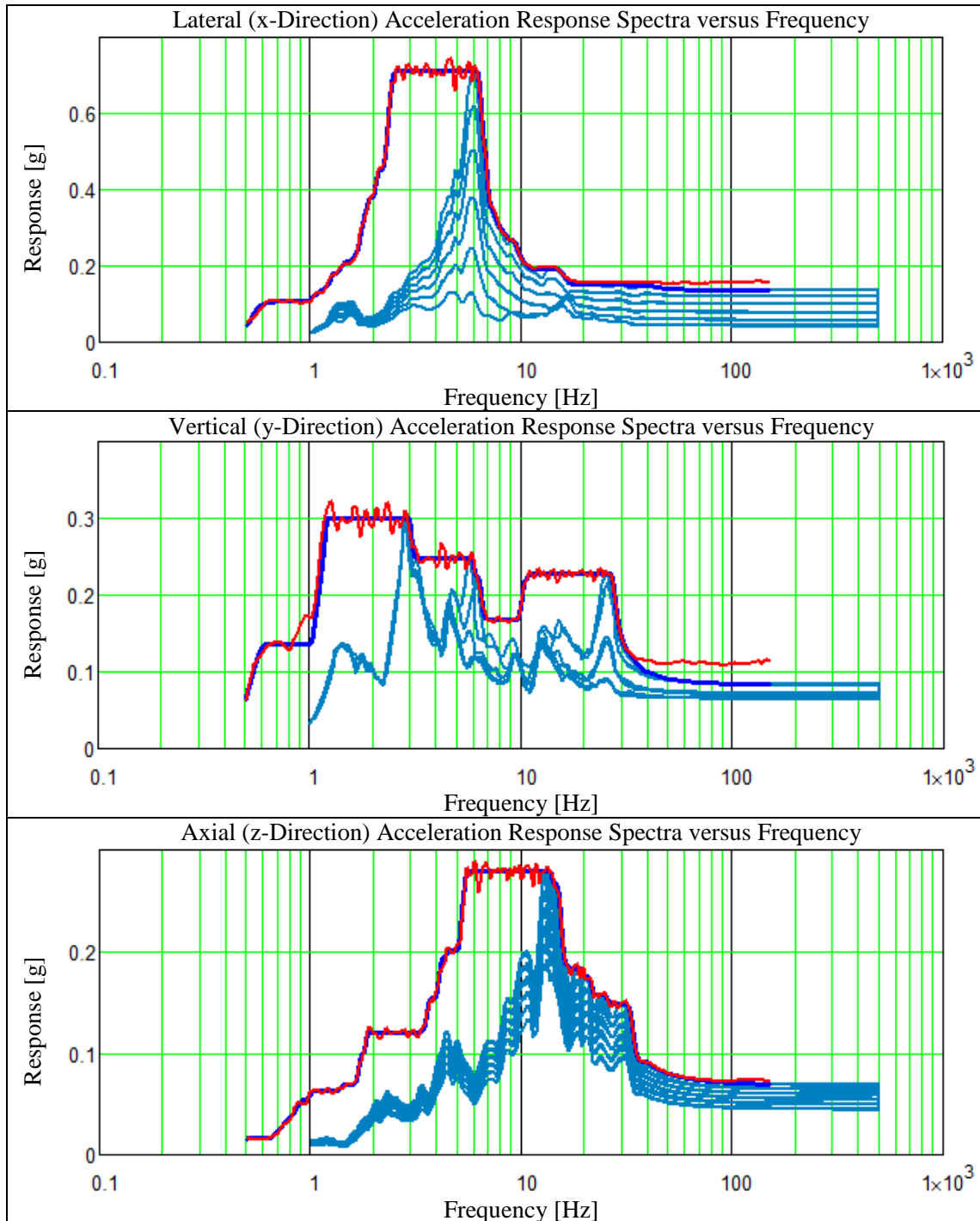
Figure 8.14. Translational Response Spectra for "Vibe_Vertical_Cell_Response_Data" with Cell
Data (Blue-Gray Curves), Broadened Target (Blue Curve) and Modified Time
History Response (Red Curve)

USED FUEL DISPOSITION CAMPAIGN
Used Nuclear Fuel Loading and Structural Performance Under Normal Conditions of Transport -
Demonstration of Approach and Results of Used Fuel Performance Characterization
188   **SEPTEMBER 30, 2013**
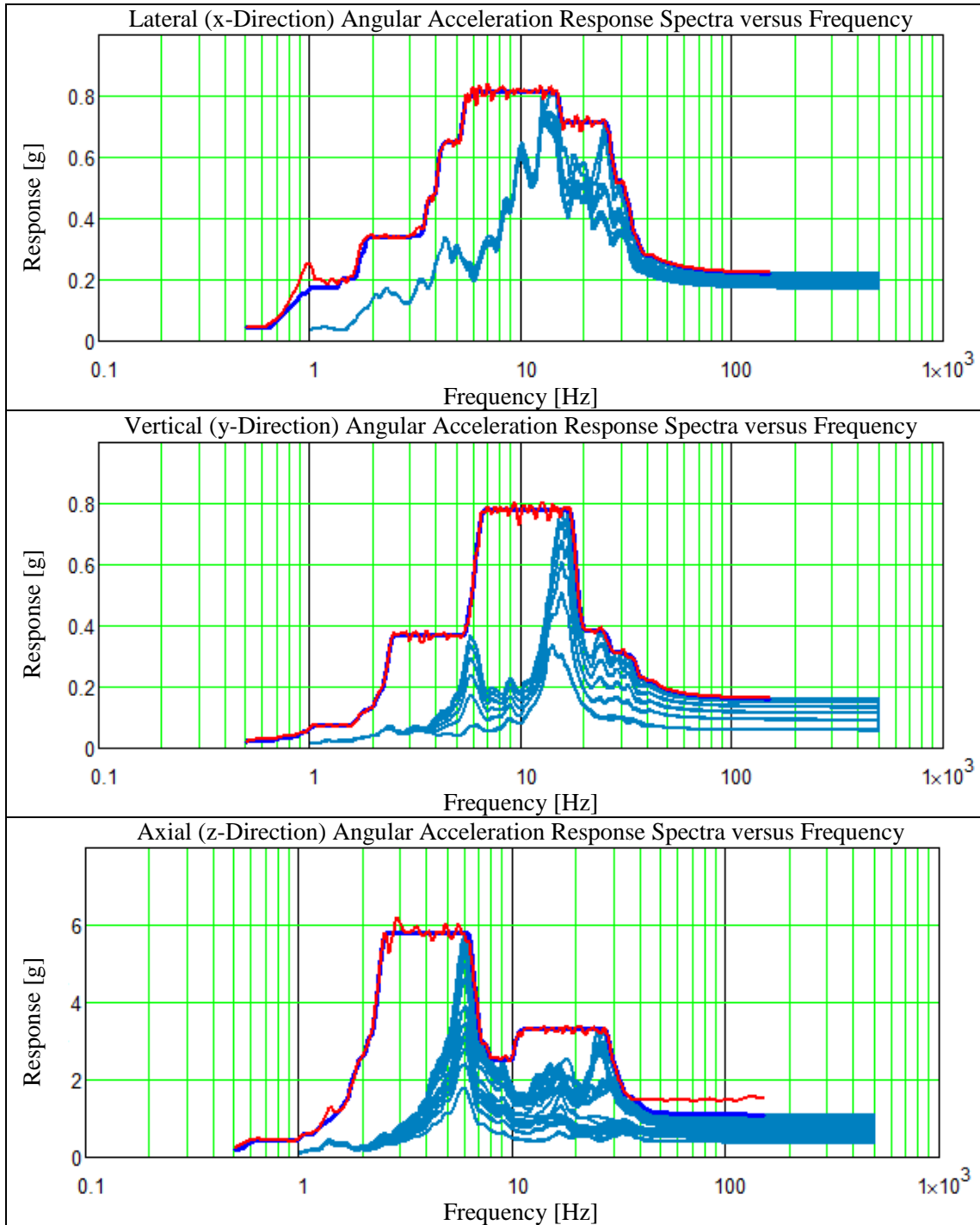
Figure 8.15. Rotational Response Spectra for "Vibe_Vertical_Cell_Response_Data" with Cell Data (Blue-Gray Curves), Broadened Target (Blue Curve) and Modified Time History Response (Red Curve)

USED FUEL DISPOSITION CAMPAIGN
Used Nuclear Fuel Loading and Structural Performance Under Normal Conditions of Transport -
Demonstration of Approach and Results of Used Fuel Performance Characterization
SEPTEMBER 30, 2013 189
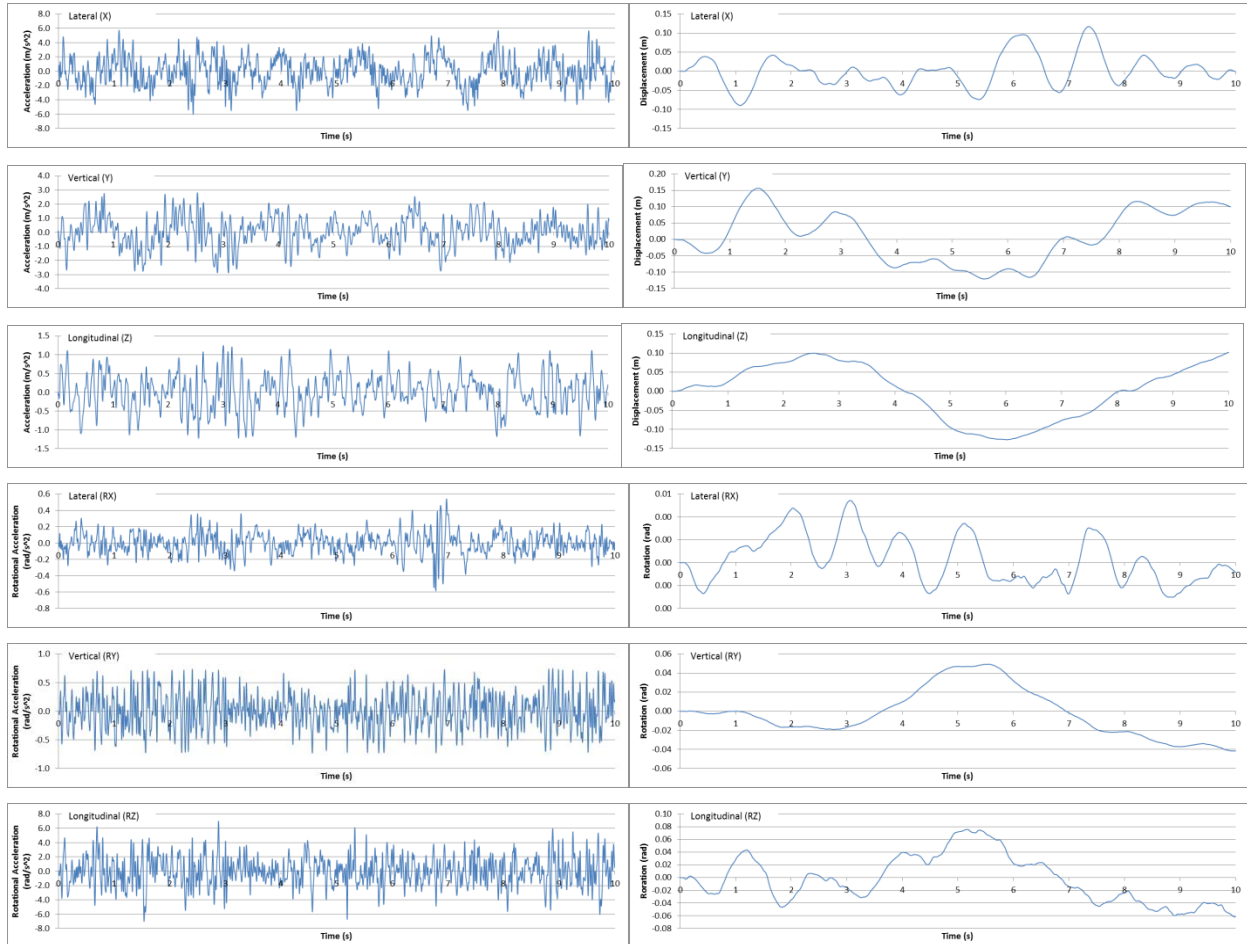
Figure 8.16. Acceleration and Displacement/Rotation Input Time Histories for Broadened P3 Lateral Shock Case

USED FUEL DISPOSITION CAMPAIGN
Used Nuclear Fuel Loading and Structural Performance Under Normal Conditions of Transport -
Demonstration of Approach and Results of Used Fuel Performance Characterization
190   **SEPTEMBER 30, 2013**
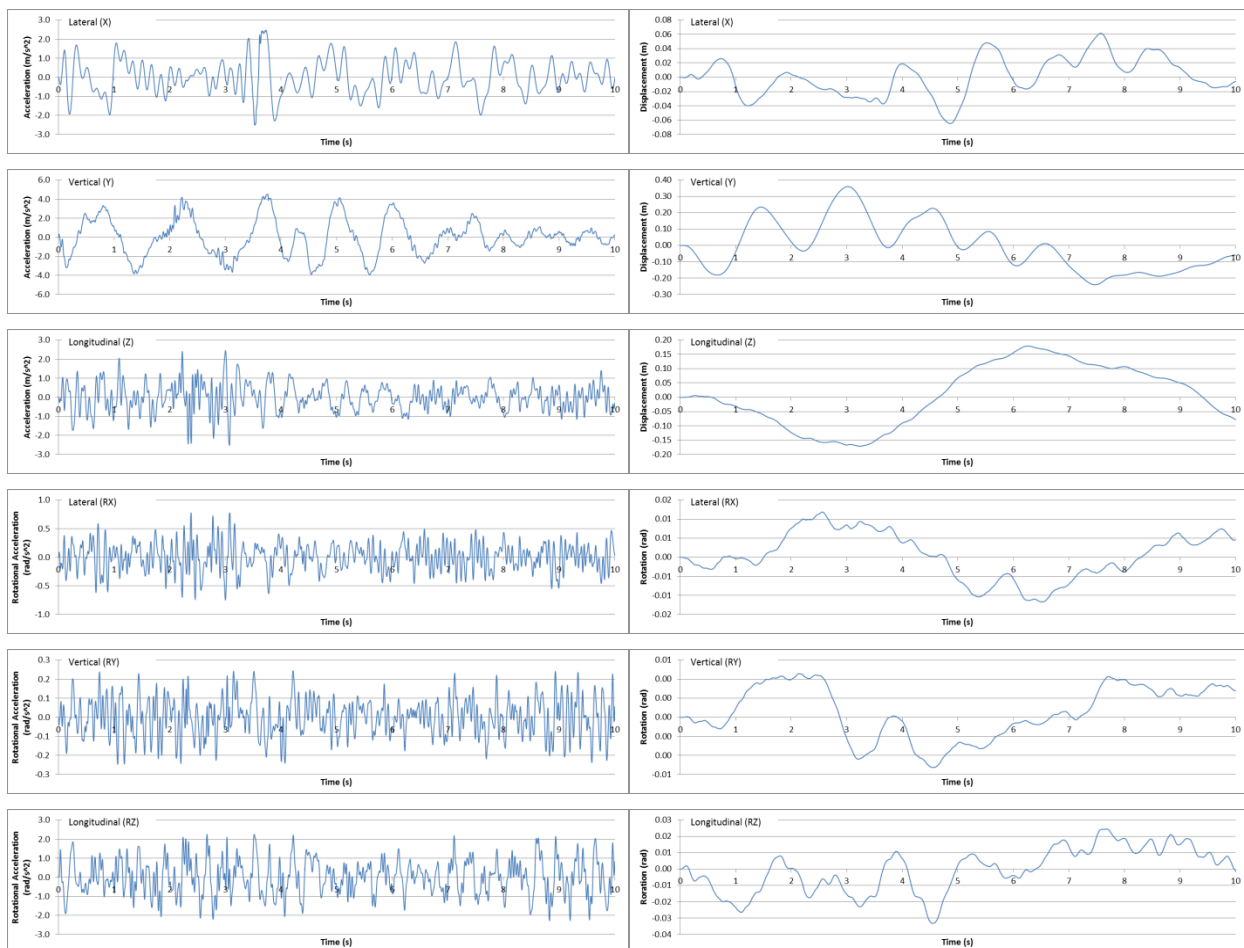
Figure 8.17. Acceleration and Displacement/Rotation Input Time Histories for Broadened P3 Vertical/Longitudinal Shock Case

USED FUEL DISPOSITION CAMPAIGN
Used Nuclear Fuel Loading and Structural Performance Under Normal Conditions of Transport -
Demonstration of Approach and Results of Used Fuel Performance Characterization
SEPTEMBER 30, 2013 191
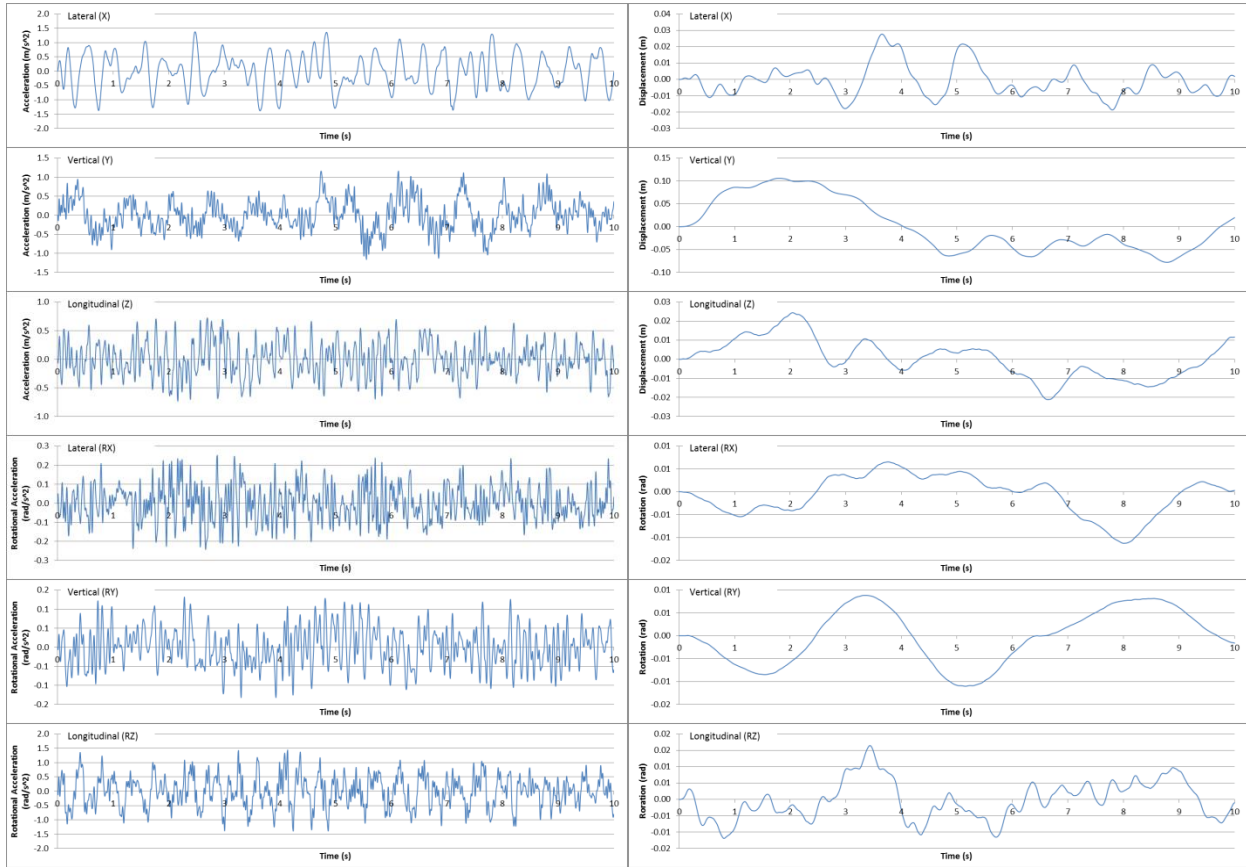
Figure 8.18. Acceleration and Displacement/Rotation Input Time Histories for Broadened P3 Lateral Vibration Case

USED FUEL DISPOSITION CAMPAIGN
Used Nuclear Fuel Loading and Structural Performance Under Normal Conditions of Transport -
Demonstration of Approach and Results of Used Fuel Performance Characterization
192   **SEPTEMBER 30, 2013**
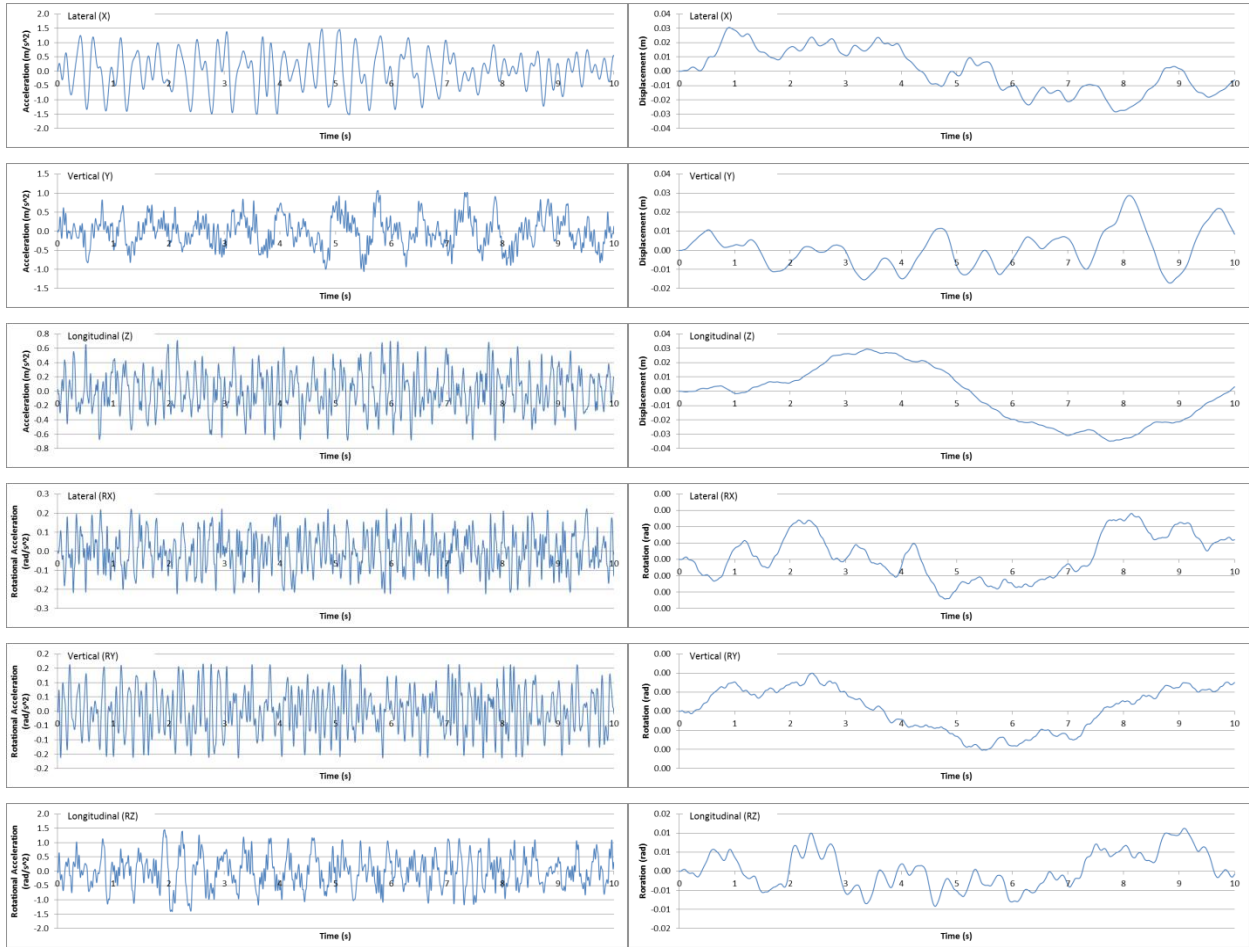
Figure 8.19. Acceleration and Displacement/Rotation Input Time Histories for Broadened P3 Vertical Vibration Case

USED FUEL DISPOSITION CAMPAIGN
Used Nuclear Fuel Loading and Structural Performance Under Normal Conditions of Transport -
Demonstration of Approach and Results of Used Fuel Performance Characterization
SEPTEMBER 30, 2013 **193**
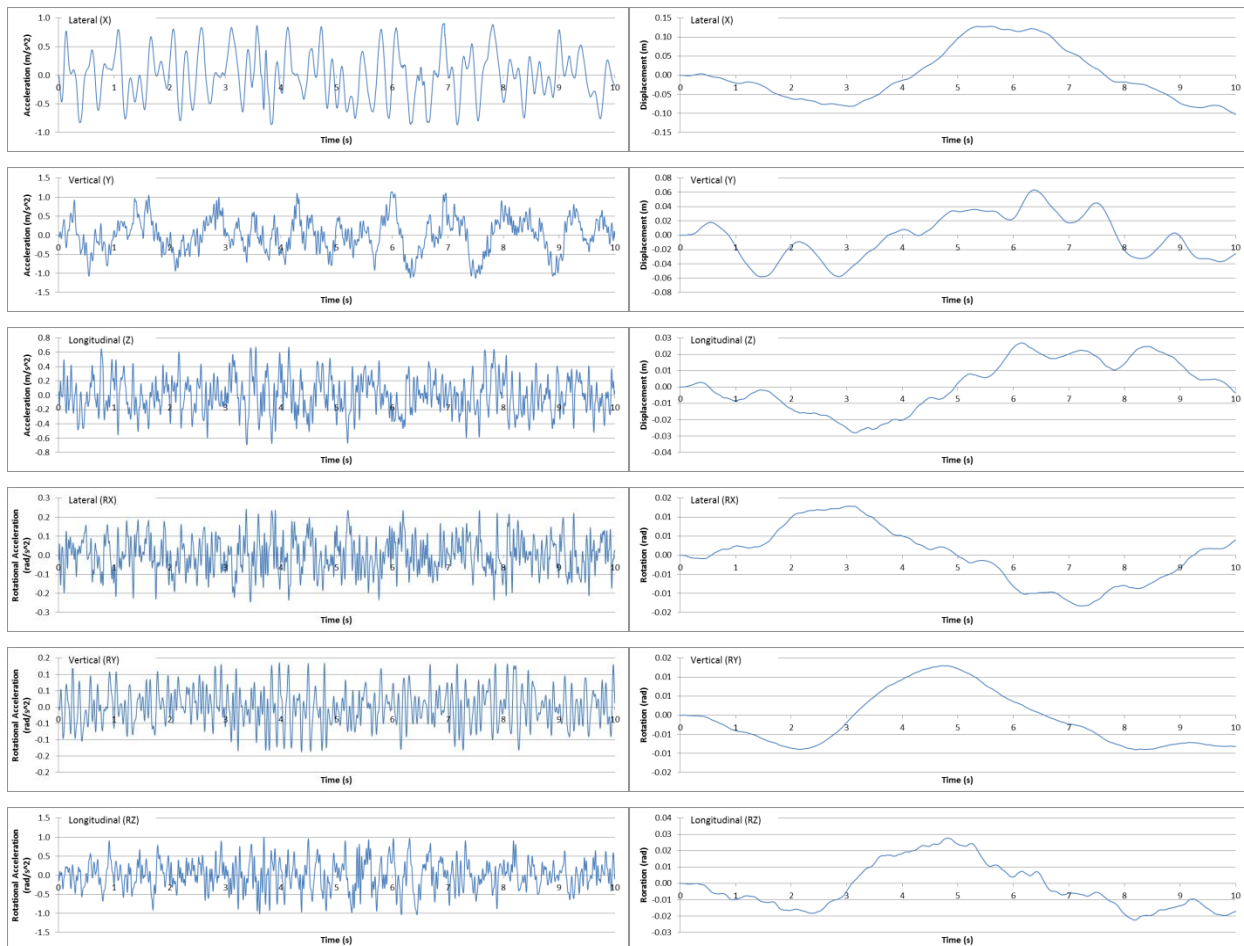
Figure 8.20. Acceleration and Displacement/Rotation Input Time Histories for Broadened P3 Longitudinal Vibration Case

8.3.2.2   *RESULTS FOR BROADENED P3 LOADING*

The assembly analyses were repeated for the two shock cases and three vibration cases of the broadened P3 loading set. The enhanced loading resulted in rigid body motion of the assembly within the basket. Plots of the difference between the displacements of the assembly CG and the basket CG are shown in Figure 8.21-Figure 8.23. The relative motion of the CG's is an indicator of the assembly's relative displacements for sliding in the lateral direction, sliding in the axial direction, or vertical separation of the assembly from the basket floor. The increased lateral loading resulted in significant lateral sliding for the two shock cases (Figure 8.21) leading to successive impacts with the basket side walls as well as longitudinal sliding (Figure 8.22). The large axial sliding for the lateral shock case results from the combination of basket rotation and axial acceleration such that the assembly continues to slip downhill towards the bottom of the basket. No vertical separation was observed for any of the cases as vertical loading did not exceed 1 g and only a small compressive displacement of the assembly CG towards the basket floor was observed (Figure 8.23).

USED FUEL DISPOSITION CAMPAIGN
Used Nuclear Fuel Loading and Structural Performance Under Normal Conditions of Transport -
Demonstration of Approach and Results of Used Fuel Performance Characterization
194   SEPTEMBER 30, 2013

The frequency response of the assembly is shown by Fast Fourier Transforms of the rigid body translational accelerations of the assembly and the basket (i.e. the input excitation) in Figure 8.24-Figure 8.26. It is observed that there is generally no assembly response for frequencies less than ~8 Hz. Amplification of the accelerations begins above ~10 Hz with large amplification of the vertical accelerations around 25 Hz. All of the accelerations above ~30 Hz are amplified consistent with the expected natural frequency of the fuel rods at 50-60 Hz based on the varying span between spacer grid supports.
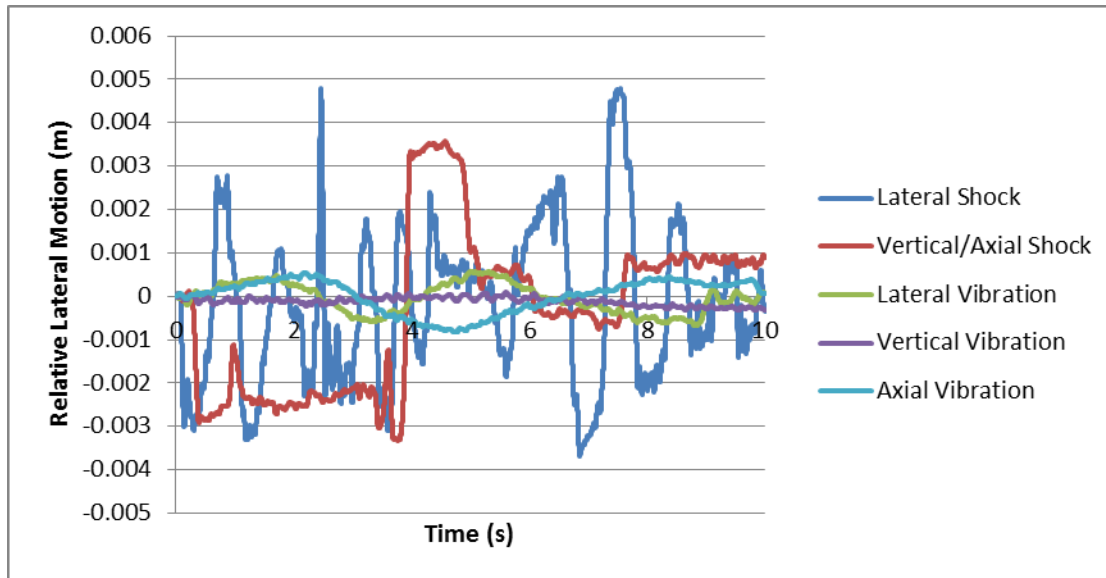
Figure 8.21. Lateral Motion of the Assembly CG Relative to the Basket CG for the Broadened P3 Shock Cases

USED FUEL DISPOSITION CAMPAIGN
Used Nuclear Fuel Loading and Structural Performance Under Normal Conditions of Transport -
Demonstration of Approach and Results of Used Fuel Performance Characterization
SEPTEMBER 30, 2013 195
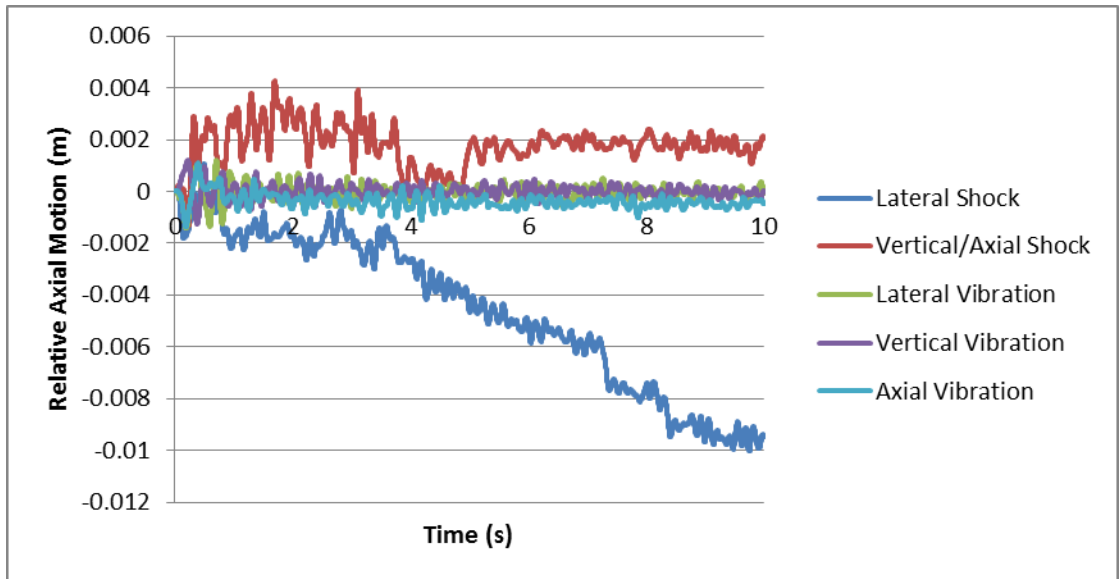
Figure 8.22. Axial Motion of the Assembly CG Relative to the Basket CG for the Broadened P3 Vertical/Axial Shock Case
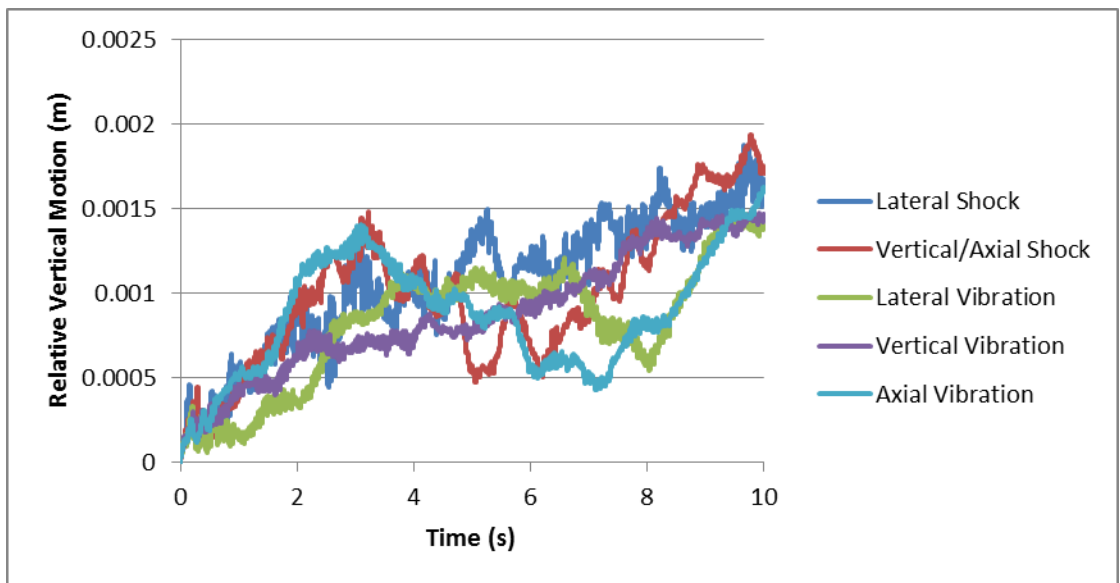
Figure 8.23. Vertical Motion of the Assembly CG Relative to the Basket CG for the Broadened P3 Shock Cases

USED FUEL DISPOSITION CAMPAIGN
Used Nuclear Fuel Loading and Structural Performance Under Normal Conditions of Transport -
Demonstration of Approach and Results of Used Fuel Performance Characterization
196 **SEPTEMBER 30, 2013**
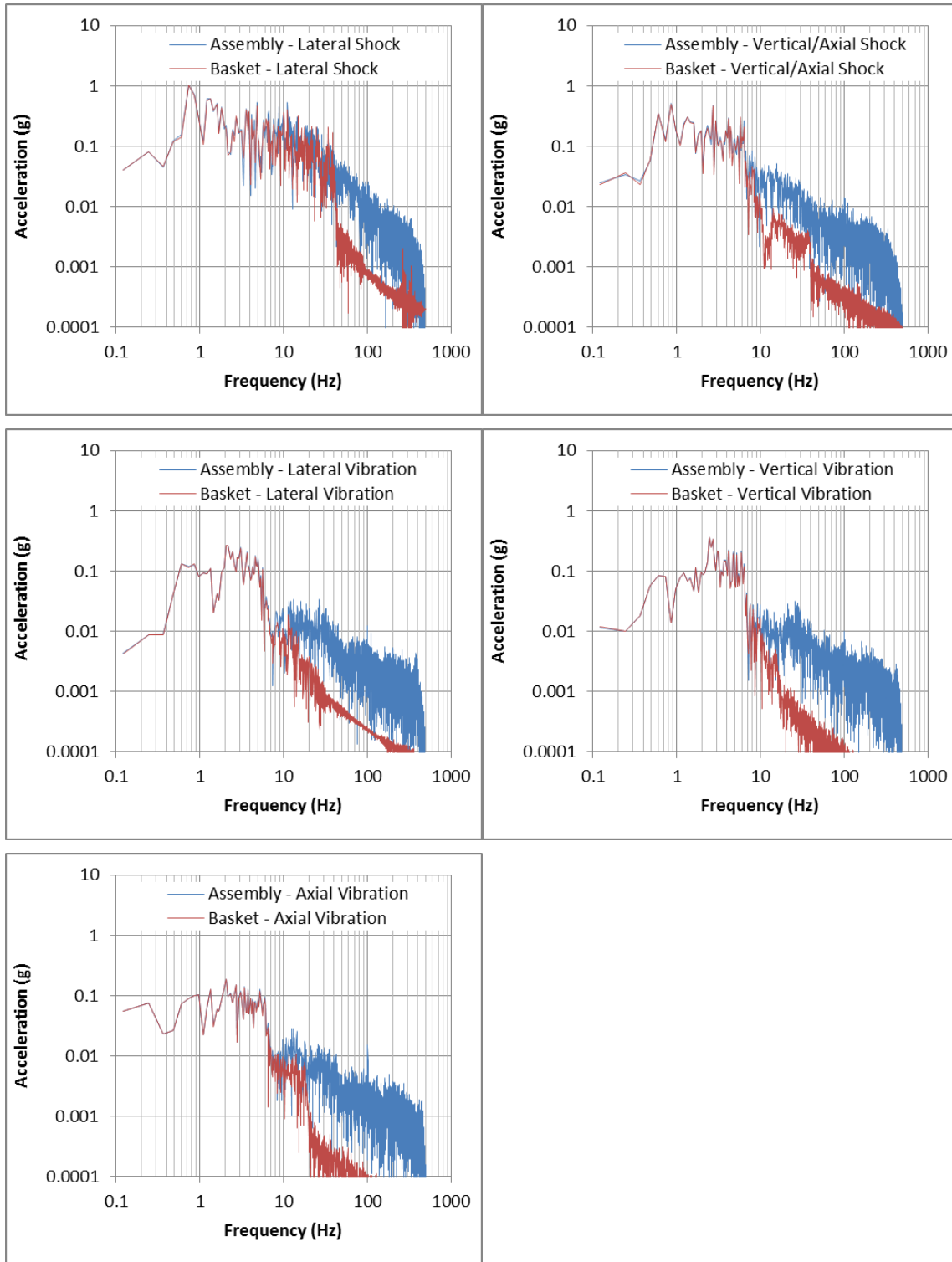
Figure 8.24. FFT of the Assembly and Basket Lateral Accelerations for the Broadened P3 Cases

USED FUEL DISPOSITION CAMPAIGN
**Used Nuclear Fuel Loading and Structural Performance Under Normal Conditions of Transport -
Demonstration of Approach and Results of Used Fuel Performance Characterization
SEPTEMBER 30, 2013** 197
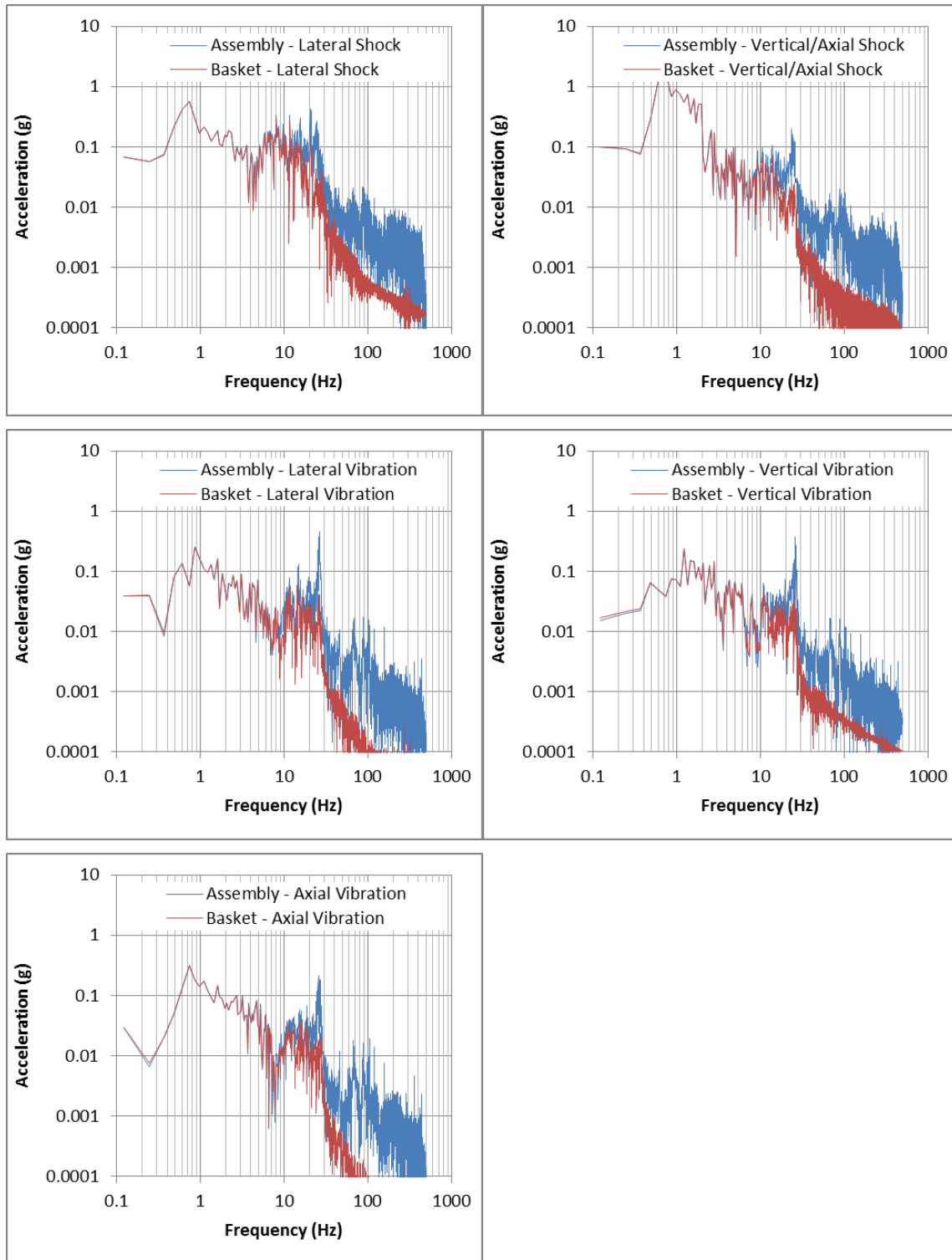
Figure 8.25. FFT of the Assembly and Basket Vertical Accelerations for the Broadened P3 Cases

USED FUEL DISPOSITION CAMPAIGN
Used Nuclear Fuel Loading and Structural Performance Under Normal Conditions of Transport -
Demonstration of Approach and Results of Used Fuel Performance Characterization
198   **SEPTEMBER 30, 2013**
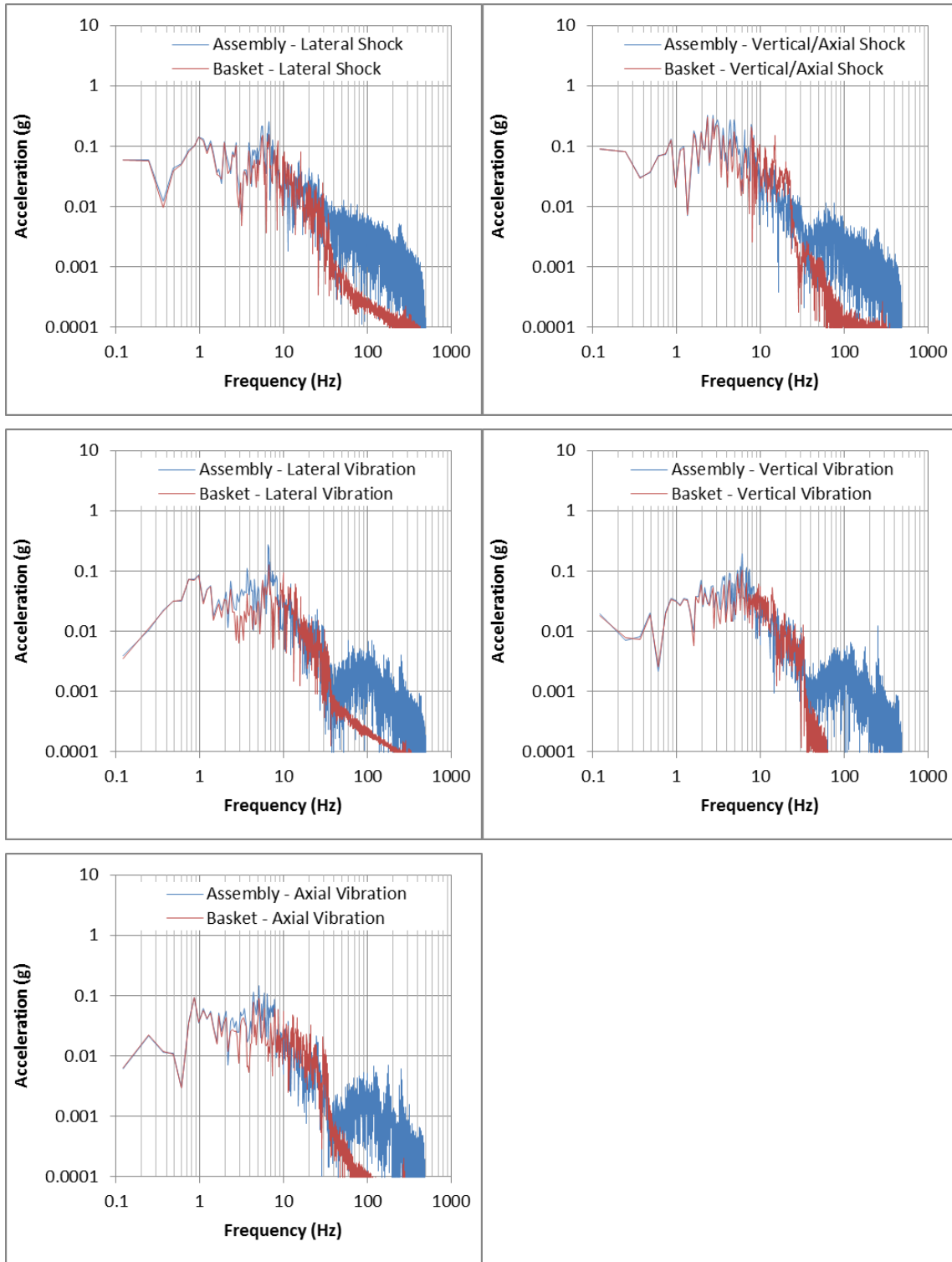
Figure 8.26. FFT of the Assembly and Basket Axial Accelerations for the Broadened P3 Cases

USED FUEL DISPOSITION CAMPAIGN
Used Nuclear Fuel Loading and Structural Performance Under Normal Conditions of Transport -
Demonstration of Approach and Results of Used Fuel Performance Characterization
SEPTEMBER 30, 2013 **199**

The maximum cladding strains and the distribution of the cyclic strain amplitudes is shown in Figure 8.27. The highest cladding strain of 7.52e-4 was observed in the lateral shock cases. The vertical/axial shock case had a peak cladding strain of 6.41e-4 while the strains ranged from 3.82e-4 to 5.55e-4 in the vibration cases. These strain levels from the broadened P3 loading are 2-3 times greater than those observed with the P3 loading and indicates the effect of the peak broadening. The results for both the cyclic strain amplitude and distribution the two shock cases are very similar. For the vibration cases, the axial and vertical cases had lower peak amplitudes compared to the shock cases, but the lateral vibration case had a similarly large magnitude. The resulting fatigue damage levels at each strain amplitude are shown for these cases in Figure 8.28 and summarized in Table 8.3. Due to the higher strain magnitudes induced by the broadened input excitations, the predicted fatigue damage level is now more than 10 times greater than the P3 loading. The maximum clad fatigue damage fraction is 11% and occurs for the lateral vibration case. This is considerably higher, but still remains below the lower fatigue threshold value for all of the shock and vibration cases.

USED FUEL DISPOSITION CAMPAIGN
Used Nuclear Fuel Loading and Structural Performance Under Normal Conditions of Transport -
Demonstration of Approach and Results of Used Fuel Performance Characterization
200 **SEPTEMBER 30, 2013**
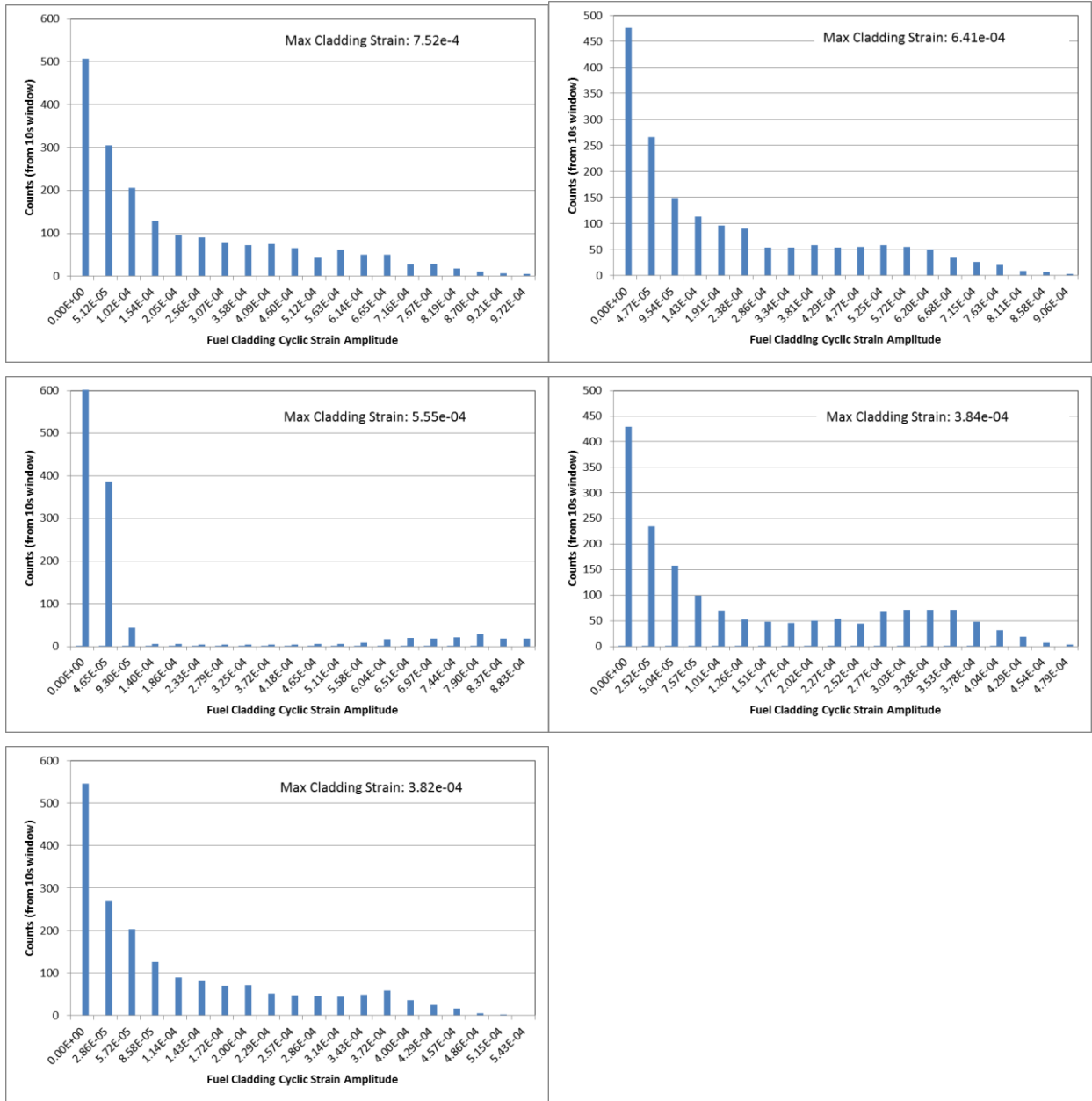
Figure 8.27. Distribution of Cladding Strain Cycles for the 10-second Window of the a) Lateral Shock, B) Vertical/Longitudinal Shock, C) Lateral Vibration, D) Vertical Vibration, and e) Axial Vibration Cases for Broadened P3 Loading

USED FUEL DISPOSITION CAMPAIGN
Used Nuclear Fuel Loading and Structural Performance Under Normal Conditions of Transport -
Demonstration of Approach and Results of Used Fuel Performance Characterization
SEPTEMBER 30, 2013   201
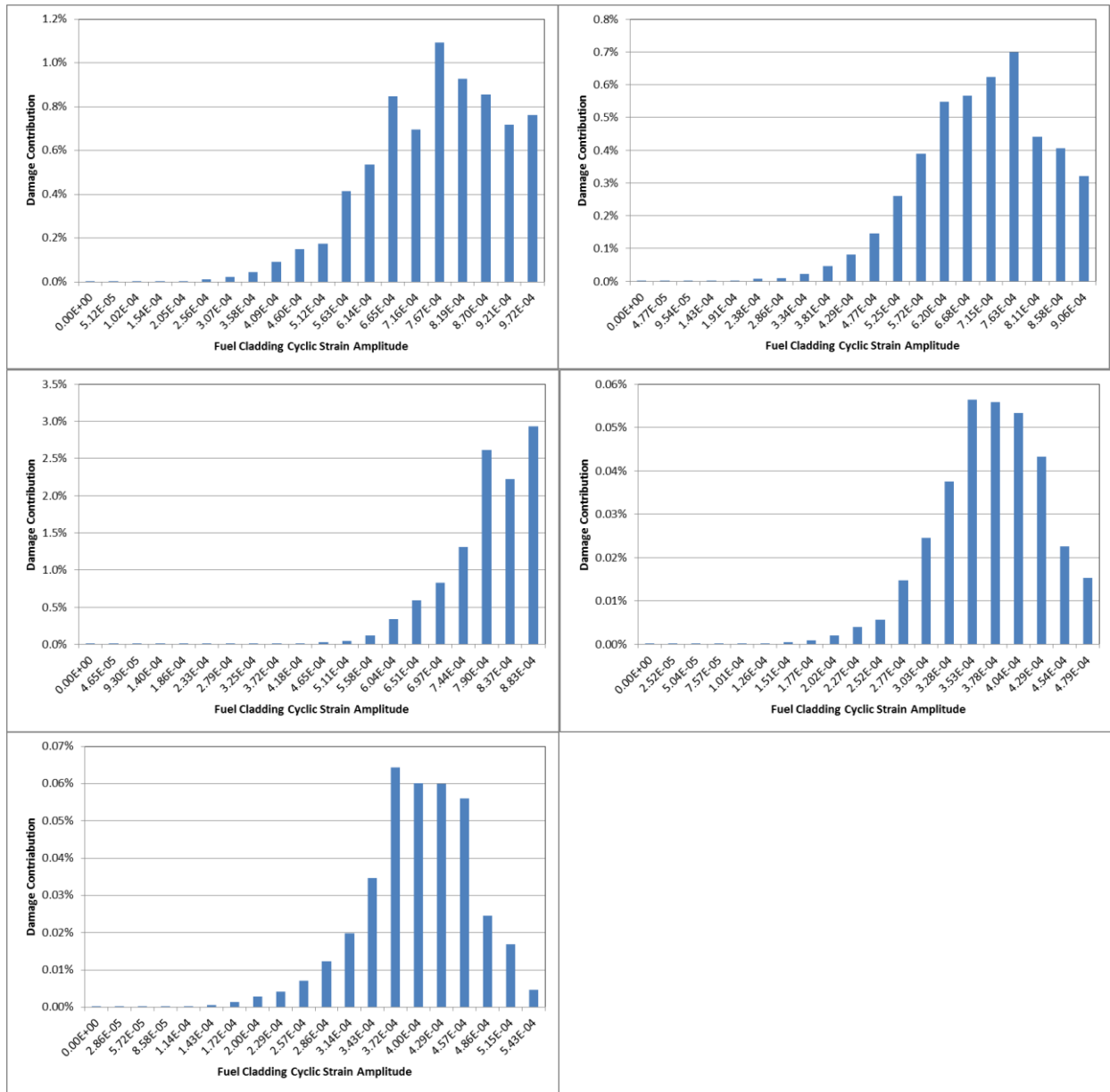
Figure 8.28. Distribution of Fatigue Damage Contribution as a Function of Cyclic Strain
Amplitude for the 10-second Window of the a) Lateral Shock, b)
Vertical/Longitudinal Shock, c) Lateral Vibration, d) Vertical Vibration, and e)
Axial Vibration Cases Using Broadened P3 Loading

USED FUEL DISPOSITION CAMPAIGN
Used Nuclear Fuel Loading and Structural Performance Under Normal Conditions of Transport -
Demonstration of Approach and Results of Used Fuel Performance Characterization
202   **SEPTEMBER 30, 2013**
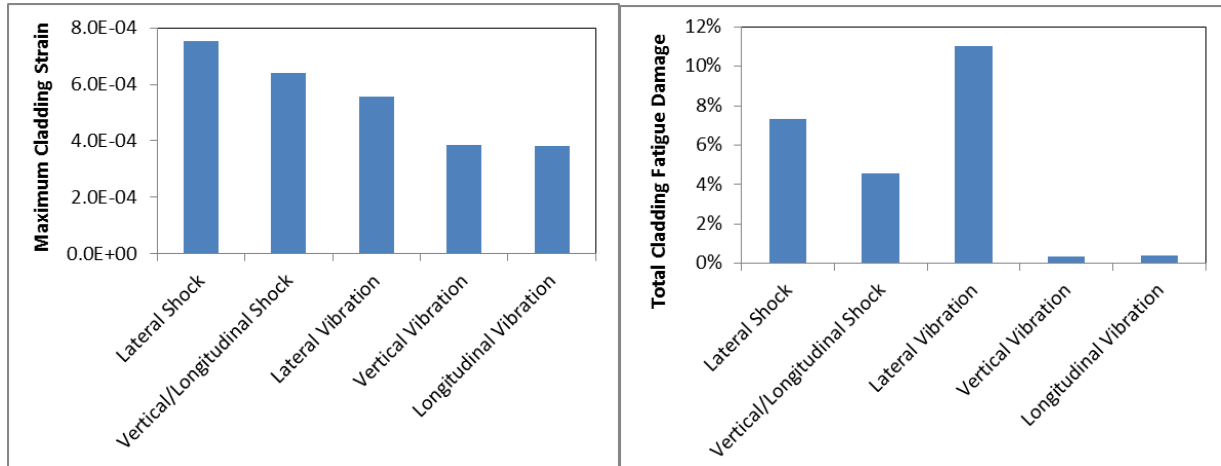
Figure 8.29. Cladding Maximum Cyclic Strain Amplitude and Total Fatigue Damage for Broadened P3 Loading

Table 8.3. Total Cladding Fatigue Damage Due to Broadened P3 Loading

Case	Description	Maximum Cladding Strain	Maximum Cyclic Strain Amplitude	Total Fatigue Damage
P3-1b	Lateral Shock	7.52E-04	1.02E-03	7.34%
P3-2b	Vertical/Longitudinal Shock	6.41E-04	9.54E-04	4.57%
P3-3b	Lateral Vibration	5.55E-04	9.30E-04	11.04%
P3-4b	Vertical Vibration	3.84E-04	5.04E-04	0.34%
P3-5b	Longitudinal Vibration	3.82E-04	5.72E-04	0.37%

8.3.2.3   DISCUSSION OF CLADDING FATIGUE RESULTS

The cladding fatigue results based on the best estimate fuel rod and the final P3 load set indicated that the total fatigue damage fraction in the cladding was less than 1% of the lower threshold value, and all of the rods in all of the cases are predicted to maintain containment. The cladding fatigue results based on the broadened P3 loading indicate similar results though they were closer to the failure limit as expected. The results showed that the highest stressed point (including a tensile stress concentration factor for possible occurrence at a pellet-pellet interface) on a particular fuel rod at the worst location in the basket exhibited a damage level of 11% of the bounding threshold for the known fatigue strength of unirradiated or irradiated Zircaloy-4 (Figure 7.23). It is common that fatigue damage limits of materials almost always have an inherently wide variability though, as evidenced by the wide scatter of this experimental data which is plotted on log-log axes. To more easily visualize a comparison of the fatigue results to the fatigue experimental data, the total damage computed from the spectrum of peaks was converted to an effective number of cycles at the stress level corresponding to the maximum binned cyclic strain. The results for the P3 and broadened P3 load cases are shown with the

USED FUEL DISPOSITION CAMPAIGN
Used Nuclear Fuel Loading and Structural Performance Under Normal Conditions of Transport -
Demonstration of Approach and Results of Used Fuel Performance Characterization
SEPTEMBER 30, 2013 203

experimental data in Figure 8.30. This shows that the results obtained in this effort (which account for the unknown material property variability and location in the basket through the broadened and bounded input definitions) put the cladding much closer to the region where fatigue damage is possible. The argument could also be made that the 11% damage from the lateral vibration case would actually be higher since additional damage will occur from high magnitude shock events. Even if the total damage from the lateral shock and vibration cases are summed, the 18% damage level is still less than the fatigue threshold. It is also noted that these points are at lower stress/strain levels than that used for the majority of the experimental fatigue tests. Additional data on irradiated specimens for this stress/strain level may be useful to ensure the lower threshold for fatigue strength in this range is adequately captured. Therefore, these analyses show that cladding fatigue damage is predicted to be below the threshold, but additional effort to reducing the assumptions in the failure analysis procedure would be valuable to make a better evaluation of cumulative fatigue damage effects.

This modeling approach can be further refined by focusing future research efforts on two key areas that would greatly reduce the greatest unknowns in the developed approach. The first effort would be to fully characterize the entire loading history of the rail route. While the loading inputs selected for the simulated shock and vibration events were highly representative of a hypothetical S-2403 compliant car on an actual physical route, extensive characterization and analysis of the entire loading history was not able to be completed for the fatigue damage analysis. It was assumed that the 5 minute window (from which the 10s loading history was derived) was representative of the entire 94 hour trip. This likely overestimated the number and magnitude of shock events that occurred in the trip, thereby making the aggressive fatigue damage estimate conservative. For vibration, only the representative amplitude from the 10s window was evaluated though. A more thorough approach similar to that used in the standards for design of rail components should be pursued. This approach completely characterizes the full spectrum of the expected loads in a Road Environment Percent Occurrence Spectra (REPOS) by giving the cyclic load minimum/maximum magnitudes and percent occurrence for all occurring load combinations (AAR 2011). This type of data is available in the standard for other selected rail car types, but they are not representative of the car design, truck design, and payload expected for shipping of a spent fuel cask. Therefore, the REPOS should be developed for this particular car design (or any future car designed specifically for UNF transport), and such detailed loading information with the number of occurrences for each event would provide a much better assessment and combination of the total trip shock and vibration events under NCT for use in the failure analyses.

The second key effort would be to improve characterization of the fuel rod stiffness and fatigue limits under cycling conditions. The bonding and amount of load transfer at the pellet-clad interface has a tremendous influence on the bending stiffness of the rod. The broadened input loading was required to address this uncertainty and puts more energy into the dynamic event. By better characterizing the flexural properties of the actual irradiated rod, any deviations from perfect bonding would lead to lower flexural stiffness. This ultimately could be beneficial or

USED FUEL DISPOSITION CAMPAIGN
Used Nuclear Fuel Loading and Structural Performance Under Normal Conditions of Transport -
Demonstration of Approach and Results of Used Fuel Performance Characterization
204 **SEPTEMBER 30, 2013**

detrimental on the final fatigue results, but the added information would reduce the amount of peak broadening necessary in the input load profile to account for uncertain properties. The pellet-clad bonding and stiffness may also change with time and cycling, so testing such as that proposed by ORNL for fuel rod cyclic bending would provide additional insight to mechanical properties changes with cumulative loading. Such testing results of irradiated clad could also provide more experimental fatigue failure data at the lower stress levels predicted by the models. Much of the data in Figure 8.30 is obtained for higher stress levels, uses specimen geometries other than tubes, and is primarily for unirradiated Zircaloy. Additional fatigue data on representative bending geometries of irradiated materials would be extremely valuable in ensuring the true fatigue limit of the high burn-up cladding material state has been adequately quantified.
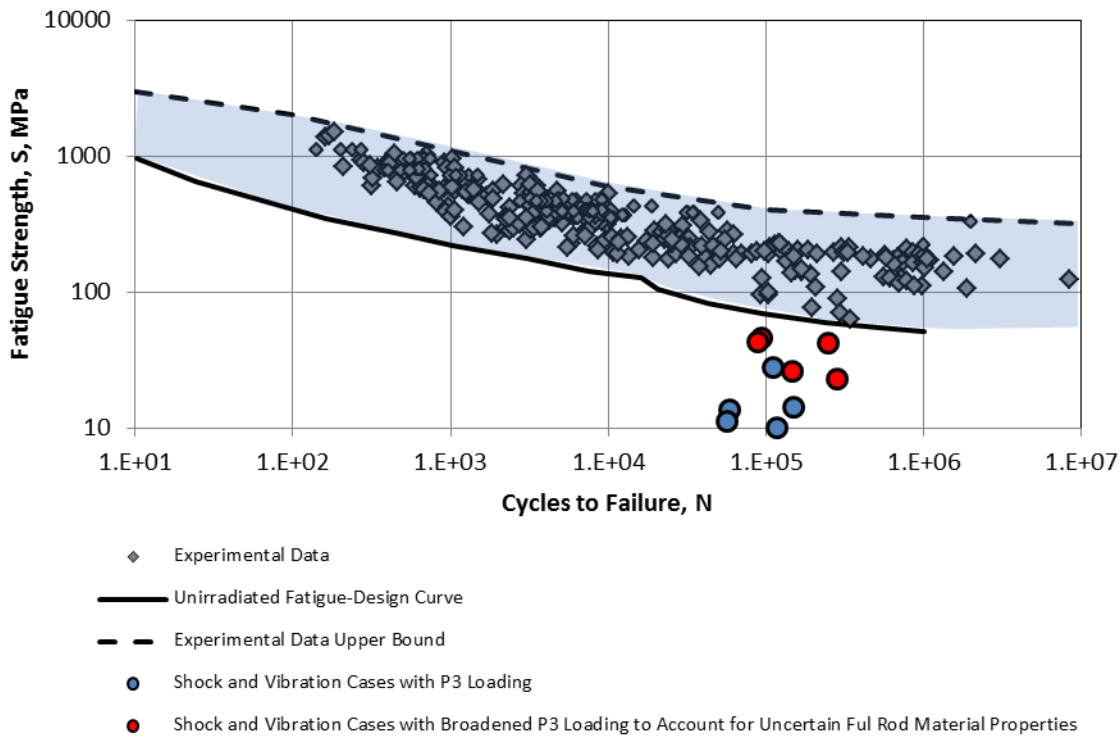
Figure 8.30. Clad Fatigue Damage Summary for Shock and Vibration Cases with P3 and Broadened P3 Loading

8.4   FAILURE ASSESSMENT

Materials such as the Zircaloy cladding may be susceptible to cumulative damage and fatigue failure under cyclic loading conditions as documented by Geelhood (2013). This type of material failure depends strongly on the initial material state, nature of the loading cycles, and participating damage mechanisms (which depends on the temperature state), so predictions for

USED FUEL DISPOSITION CAMPAIGN
Used Nuclear Fuel Loading and Structural Performance Under Normal Conditions of Transport -
Demonstration of Approach and Results of Used Fuel Performance Characterization
SEPTEMBER 30, 2013   205

lifetime under high cycle fatigue loading generally have large scatter in the lifetime predictions even for more common engineering materials. Therefore, an approach utilizing the available fatigue material data and the predicted dynamic loading from the numerical models are used to make an estimate of fuel cladding survival, but ultimately more testing of actual irradiated fuel properties/mechanisms and further characterization of the transportation loading history will be needed to better characterize fatigue response under all possible transport conditions. The approach presented compares the number of cycles a fuel rod undergoes at certain strains during a representative 3000 mile rail transport and compares these cycles to Figure 8.31 (Geelhood 2013).
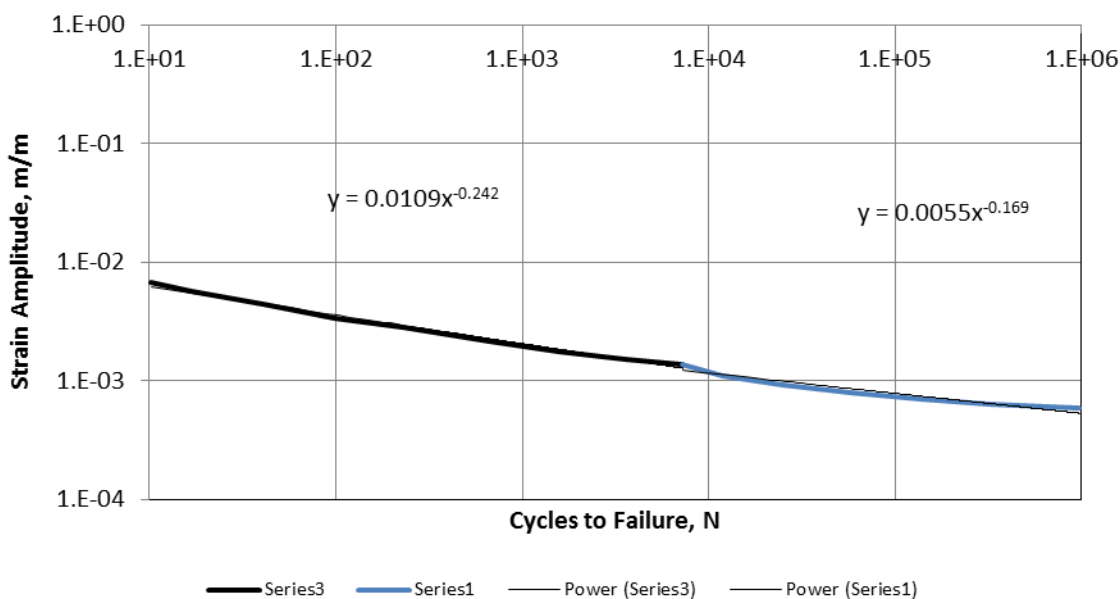
Figure 8.31. O'Donnell Fatigue-Design Curve for Irradiated Zircaloy

The approach to evaluation of failure under cyclic loading is as follows: The assembly-level submodel predicts the strain history for a 10-second window under vibration and shock loading conditions. This assembly-level model provides a conservative measure of maximum strain in the fuel cladding using the following approach. Ten-second time history analysis, for five unique time history sets, is performed at the cask-level to provide six degree-of-freedom time histories at each of the 32 basket locations (shown as grey-blue curves in Figure 8.32). The response spectrum for each time history is plotted and these plots are reviewed to determine which cell location produces the maximum response. Next, these response spectra are broadened to account for material property uncertainty (see the blue curve in Figure 8.32). This approach is described in more detail in a separate section in this document. Modified time histories are generated to provide the appropriate magnitude and frequency content so that their response spectrum fits the broadened response spectrum shown as the red curve in Figure 8.32. These time histories are used as inputs to the assembly-level analysis. This should cause maximum fuel

USED FUEL DISPOSITION CAMPAIGN
Used Nuclear Fuel Loading and Structural Performance Under Normal Conditions of Transport -
Demonstration of Approach and Results of Used Fuel Performance Characterization
206   SEPTEMBER 30, 2013

rod response, within the range of material property uncertainty, in the assembly-level analysis, thus producing the maximum cladding strains.
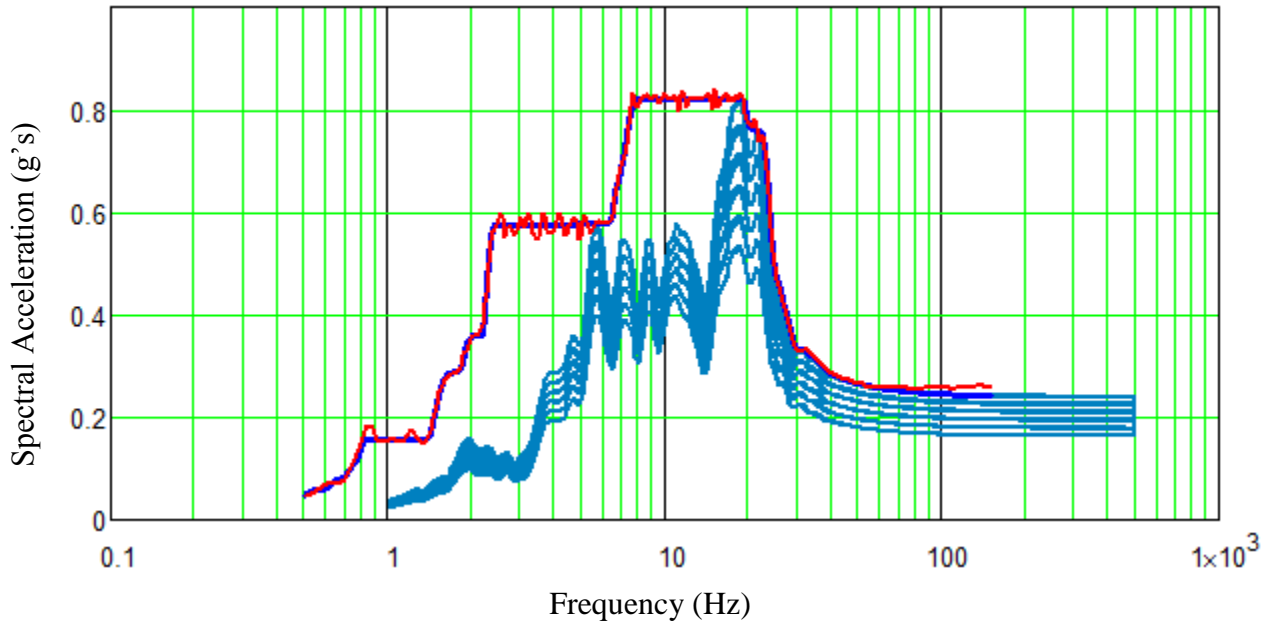
Figure 8.32. Vertical Shock Spectra Due to Longitudinal Input with Broadened Response

It is presently assumed that the response within this 10-second window is representative of the entire trip. The ten-second shock and vibration time histories were selected from 350 second time histories provided by TTCI. Figure 8.33 shows a 350 second vertical "shock" (the project chose each shock time history to represent that which produced the maximum acceleration value in a given direction) time history from TTCI with a 10-second window around the maximum acceleration. Figure 8.34 shows a 350-second vertical "vibration" (the project chose each vibration time history to represent that which produces a representative vibration due to normal transport away from a shock event) time history from TTCI with a 10-second window around normal vibration. Therefore results from the 10-second shock assembly-level runs should produce maximum representative shock strains for a 350-second TTCI time history data set. Results from the 10-second vibration assembly-level runs should produce maximum representative vibration strains for the 350-second TTCI time history data set.

USED FUEL DISPOSITION CAMPAIGN
Used Nuclear Fuel Loading and Structural Performance Under Normal Conditions of Transport -
Demonstration of Approach and Results of Used Fuel Performance Characterization
SEPTEMBER 30, 2013   207
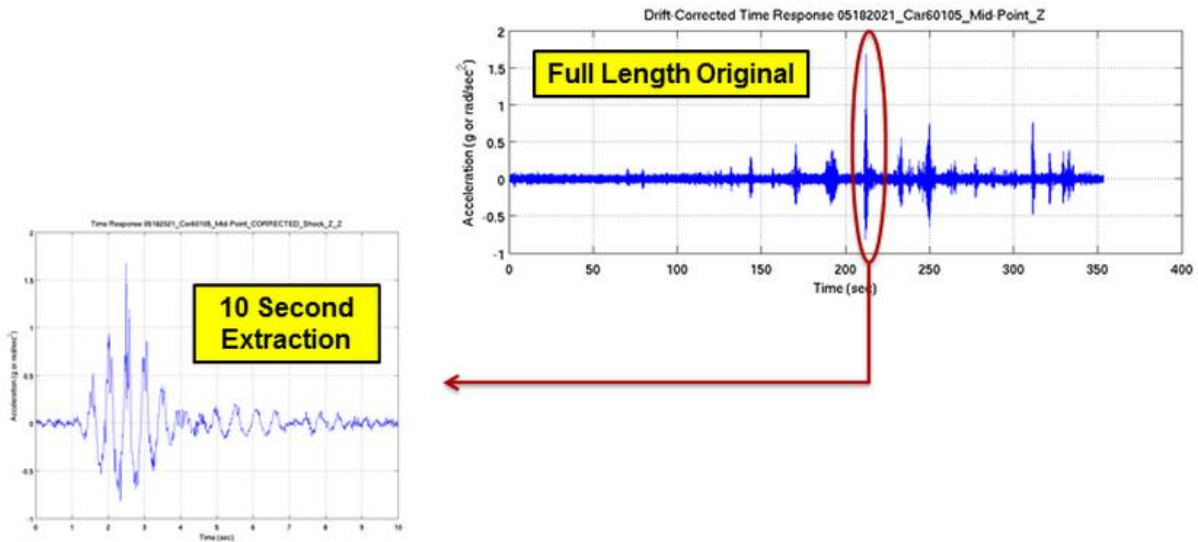
Figure 8.33. 350-second Vertical Shock Time History from TTCI Showing Extracted 10-second
Window
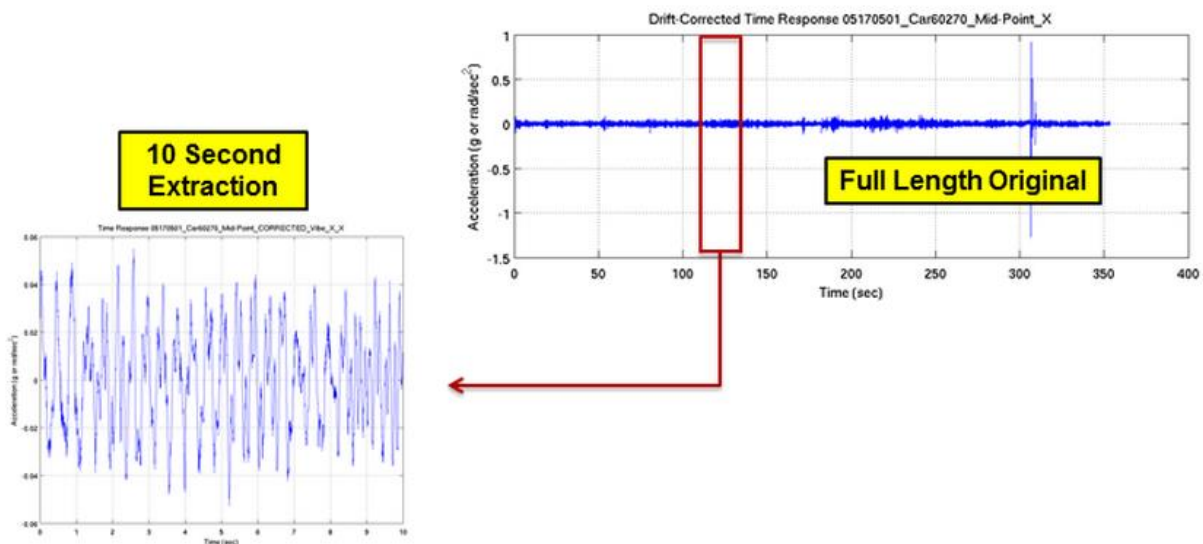
Figure 8.34. 350-second Vertical Vibration Time History from TTCI Showing Extracted 10-
second Window

The assumption is that these strain cycles can be extrapolated to the 3000-mile trip and generation of a first estimate for fatigue damage. The strain cycles from the bounding shock assembly-level analysis and the bounding vibration assembly-level analysis are used to calculate the damage ratio (which is the total number of cycles divided by the critical number of cycles, or the number of cycles for fuel rod cladding failure). For the bounding vibration run the cyclic

USED FUEL DISPOSITION CAMPAIGN
Used Nuclear Fuel Loading and Structural Performance Under Normal Conditions of Transport -
Demonstration of Approach and Results of Used Fuel Performance Characterization
208   **SEPTEMBER 30, 2013**

strain magnitudes for cladding of all of the fuel rods in the assembly are tabulated from the assembly-level submodel, and data from the location with the highest predicted damage is placed in a histogram with 20 bins. Based on each cyclic strain magnitude, a critical number of cycles to failure can be estimated based on the identified Zircaloy-4 fatigue limits (Figure 8.31). However, before these 10-second results can be extrapolated to the full trip duration, a simplified accounting for rail speed variation during the trip is included. Evaluation of the vertical and lateral peak accelerations of the proposed AAR 2406-compliant rail car on the selected track indicated that the peak minimum/maximum acceleration values are approximately linear with rail speed (Figure 8.35 and Figure 8.36).
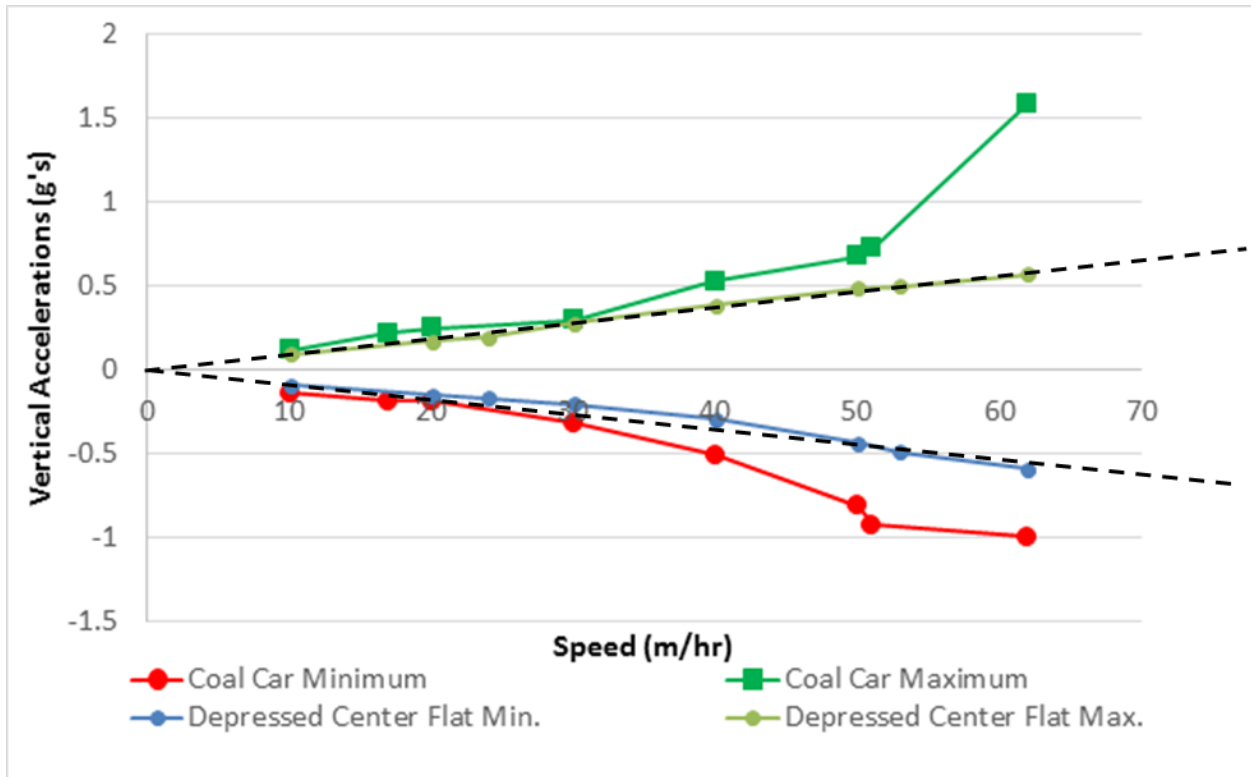
Figure 8.35. Vertical Acceleration Versus Train Speed. Depressed Center Car is Assumed to be
Representative of AAR 2406 Compliant Rail Car

USED FUEL DISPOSITION CAMPAIGN
Used Nuclear Fuel Loading and Structural Performance Under Normal Conditions of Transport -
Demonstration of Approach and Results of Used Fuel Performance Characterization
SEPTEMBER 30, 2013 209
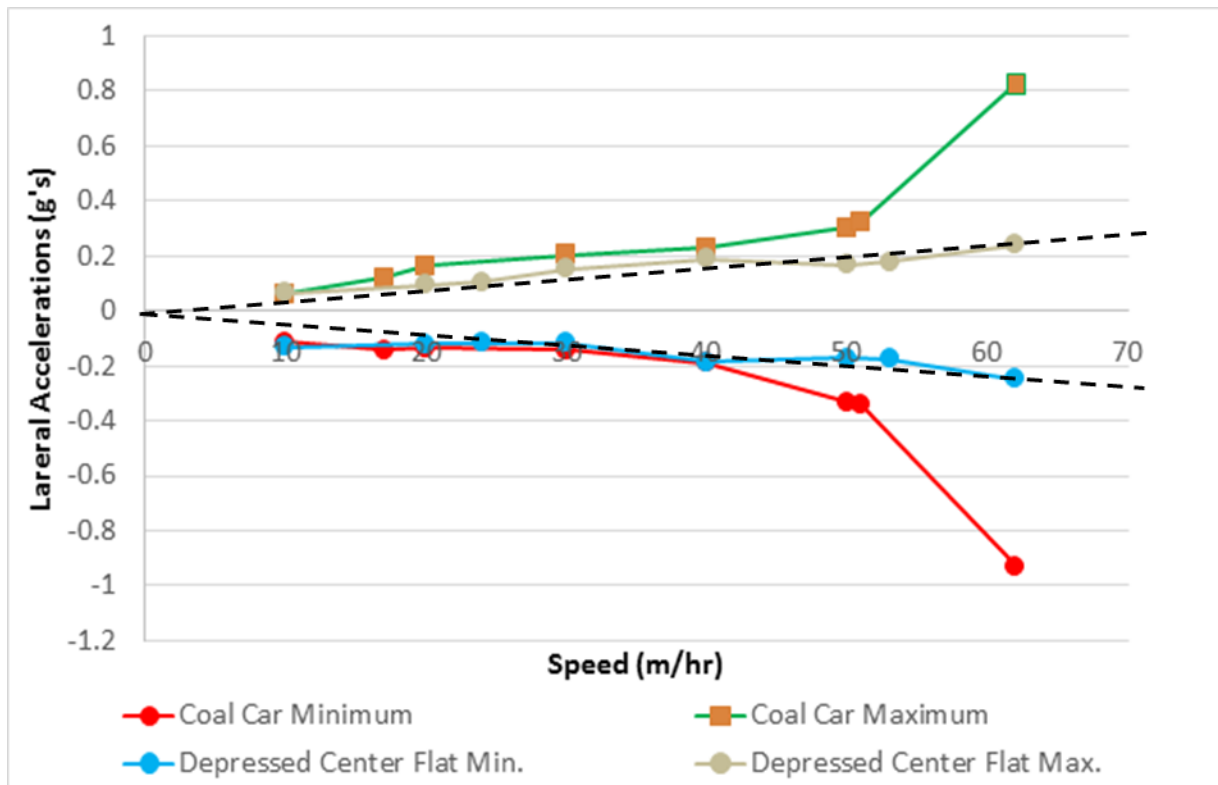
Figure 8.36. Lateral Acceleration Versus Train Speed. Depressed Center Car is Assumed to be
Representative of 2406 Compliant Rail Car

It is therefore assumed that the amplitude of vibration is linear with rail speed and the measured strain in the rods is proportional to the amplitude. This assumption should be validated since it is possible the strain is dependent on amplitude and frequency. Certain train speeds likely produce different frequency content motion which may excite fuel rod response at lower speeds. An example of this is when watching trains travel down a track at lower speeds, the displacement of the train cars side to side appears to be greater than when the train is traveling at high speed.

The characteristic speed profile of the simulated rail route is shown by the histogram in Figure 8.37, from which the duration of loading at each speed can be calculated.

USED FUEL DISPOSITION CAMPAIGN
Used Nuclear Fuel Loading and Structural Performance Under Normal Conditions of Transport -
Demonstration of Approach and Results of Used Fuel Performance Characterization
210   **SEPTEMBER 30, 2013**

	0	5	10	15	20	25	30	35	40	45	50	55	60	65	70
Speed (mph)	5.0	9.7	13.	13.	13.	9.8	10.	7.9	6.9	6.3	1.7	0.1	0.0	0.0	
Distance (miles)	0.0	0.8	3.9	3.9	7.9	10.	9.8	15.	15.	14.	16.	0.6	0.0	0.0	0.0
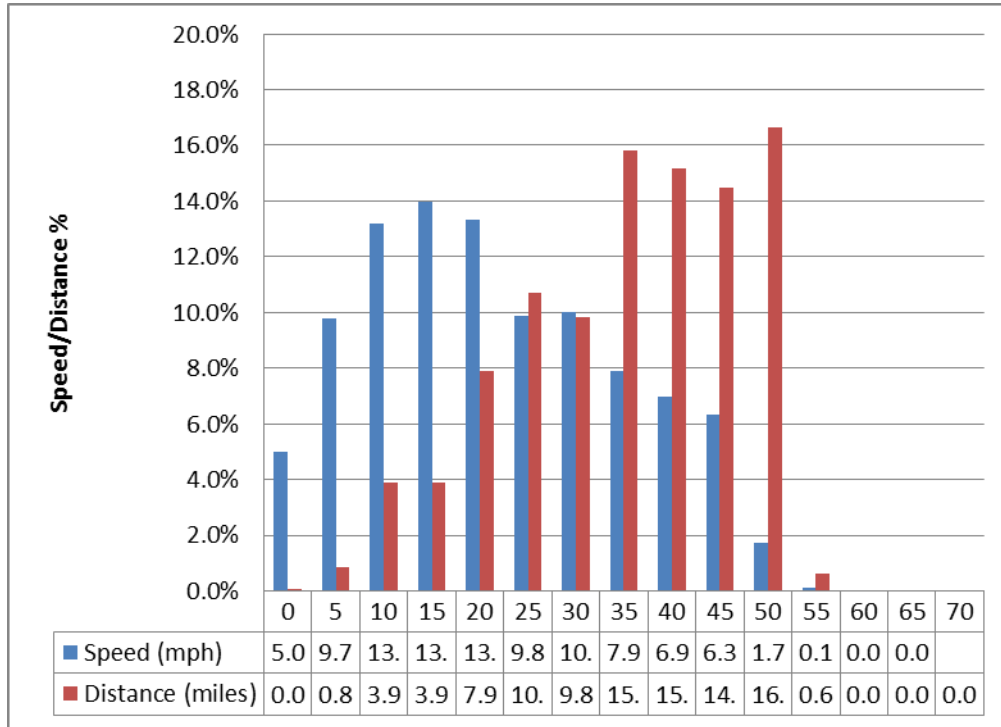
Figure 8.37. Histogram Showing Speed and Distance of a Representative Rail Car Run

For the vibration run the damage ratio for a 3000-mile trip is assumed to have the speed distribution given in Figure 8.37 to provide the duration at each speed. The number of strain cycles at each speed is then computed by multiplying the cycles in the 10-second simulated window by (time in seconds/10). The strain cycle magnitudes are then scaled linearly by the speed ratio (speed bin/speed simulated) where the simulated speed in the 10-second window was 62.5 mph. Once the strain magnitudes and cycle counts are known for each speed bin, the partial damage contribution is calculated as $N_{cycle}/N_{critical}$ where the critical value is computed from the fatigue limit curve fits in Figure 8.31. For strains less than 1.13e-3, the relationship strain=$0.0055*N_{crit}^{-0.169}$ is used, while for larger strains the relationship strain=$0.0109*N_{crit}^{-0.242}$ is used. It is assumed that the damage is linear such that individual damage contributions from different strain amplitudes can be added together. The partial damage contributions are then summed to determine the total damage to the fuel cladding over the 3000-mile route. A value greater than 1.0 indicates that the cladding has reached its fatigue limit.

The shock run damage ratio is calculated by reviewing Figure 8.38 (which is the vertical cask-level input shock time history) and determining that approximately 10 unique shock events (event defined as approximately 10 seconds) occur in a 350-second time history. A finite element analysis is performed for the maximum 10 second shock event (1.65 g, Figure 8.38) which produces a number of cycles for each strain bin. The other nine shock events shown in Figure 8.38 have amplitudes that are less than the peak. Therefore, based on the previous assumption that strain is proportional to amplitude, these other shock events are calculated by

USED FUEL DISPOSITION CAMPAIGN
Used Nuclear Fuel Loading and Structural Performance Under Normal Conditions of Transport -
Demonstration of Approach and Results of Used Fuel Performance Characterization
SEPTEMBER 30, 2013 211

defining a linear relationship between the maximum vibration strain and maximum shock strain versus amplitude shown in Figure 8.39. Using the equation of the line defined in Figure 8.39, a multiplier is calculated for adjusting the maximum shock strains (Table 8.4) based on the amplitude of the peaks. The corresponding number of cycles for each strain bin is defined by the maximum shock finite element analysis. The number of total shock cycles for the 3000 mile trip is calculated by using the time of rail transport for the trip, which is calculated to be 338,013 seconds. Dividing this number by 350 seconds yields 966 individual 350-second windows. Therefore to estimate the damage ratio for shock events, for a 3000-mile trip, the adjusted maximum strains for each unique shock event (10 events, Figure 8.38) are used with the corresponding cycles, and multiplied by 10 and then by 966. The damage ratio from the bounding shock event should then be added to the bounding damage ratio for the vibration event to produce the total damage ratio.
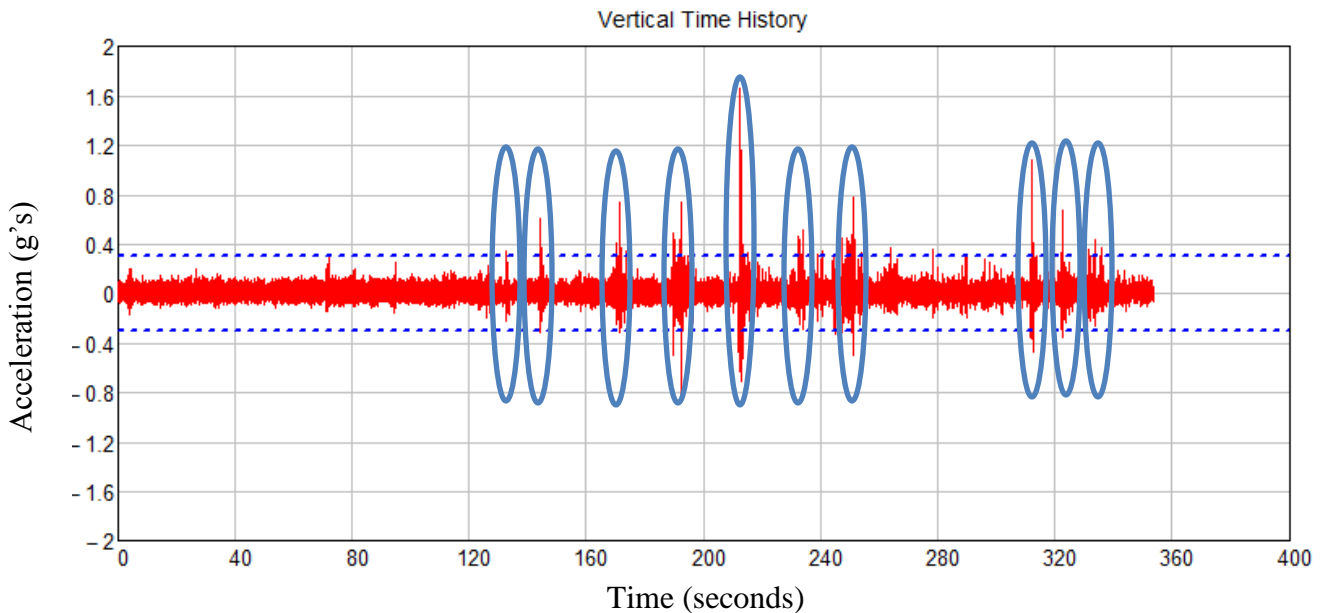
Figure 8.38. Vertical TTCI Input to Cask-level Analysis Showing the Shock Events

USED FUEL DISPOSITION CAMPAIGN
Used Nuclear Fuel Loading and Structural Performance Under Normal Conditions of Transport -
Demonstration of Approach and Results of Used Fuel Performance Characterization
212 **SEPTEMBER 30, 2013**
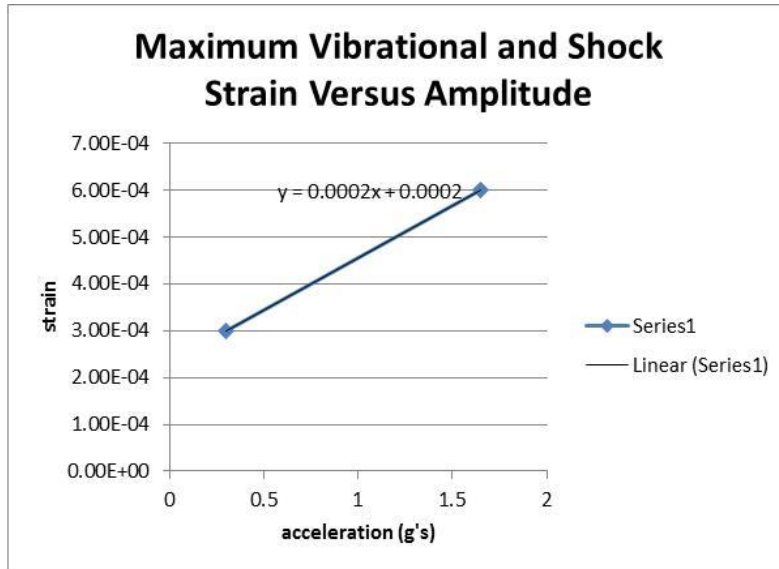
Figure 8.39. Maximum Vibration and Shock Strain versus Acceleration

Table 8.4. Multiplier to Use On Maximum Shock Strains to Estimate Cycles

Acceleration values of peak shock for each 10 second shock event (From Figure)	Estimated maximum strain at "g" value	Multiplier to use on maximum shock strains
0.38	0.0003	0.53
0.6	0.0004	0.61
0.78	0.0004	0.68
0.78	0.0004	0.68
1.65	0.0006	1.00
0.5	0.0003	0.57
0.8	0.0004	0.69
1.1	0.0005	0.80
0.75	0.0004	0.67
0.45	0.0003	0.56

Example results are shown in Section 8.3.1. The results show that for the vibration case, there are a larger number of low amplitude cycles and a progressively smaller number of high amplitude cycles. The high amplitude events have a greater overall damage contribution though. Even though the duration at different speeds is broad with most time spent at 35-40 mph, the maximum damage contribution happens from the travel 45-50 mph. Overall though, the summed damage for the initial cases to date have been less than 26% of the critical value considering the strain cycling due to both vibration and shock.

USED FUEL DISPOSITION CAMPAIGN
Used Nuclear Fuel Loading and Structural Performance Under Normal Conditions of Transport -
Demonstration of Approach and Results of Used Fuel Performance Characterization
SEPTEMBER 30, 2013   213

8.5   SENSITIVITY ANALYSES

The sensitivity analyses that were performed are shown below in Table 8.5. This table includes brief summaries of the result of each study. The full results of these studies are shown in the following sections.

Table 8.5. Results of Sensitivity Analyses to be Performed for this Initiative

Analysis	Section	Result
Cladding elastic modulus	8.5.1	**High Sensitivity:** Best estimate fuel rod stiffness and damping parameters developed at the rod-level analysis and provided to assembly-level analysis. Rod-level analysis also developed a range of fuel rod flexural rigidity (range of material uncertainty). The basket response spectra (generated by the cask-level analysis) are broadened by the range in flexural rigidity uncertainty. Time histories are fit to these broadened response spectra and are used in the best estimate assembly-level analysis. At the assembly-level, modal analysis indicates a wide range of natural frequencies between the upper and lower bound rod stiffness values indicating the importance of the integrity and load carrying capability of the pellet-clad interface.
Cladding yield stress	8.5.2	**No Sensitivity:** Full range of yield stress from irradiated to unirradiated are well above expected cladding bending stress.
Spacer grid stiffness	8.5.3	**High Sensitivity:** Analysis at the rod-level performed to produce equivalent shell thickness that provides similar lateral displacements to one with springs and dimples. At the assembly-level, modal analysis indicated that the spring stiffness values have a strong influence on the natural frequencies of the fuel rods, so different designs and the possibility of spring relaxation or gap formation could significantly influence the rod response.
Spacer grid location	8.5.4	**High Sensitivity:** Larger grid-to-grid distance gives a longer unsupported fuel rod span with a lower natural frequency that leads to higher bending strains in the vicinity of the spacer grid.
Fuel assembly basket location	8.5.5	**Moderate Sensitivity:** Basket location does matter for the assembly loading, so methods to provide a bounding case for all of the basket compartments would be advantageous to ensure the worst basket location has been evaluated.
Fuel rod location in assembly	8.5.6	**Low Sensitivity:** Little evidence has been observed in the various cases so far to suggest that different fuel rods locations in the spacer grids behave significantly differently from each other.

USED FUEL DISPOSITION CAMPAIGN
Used Nuclear Fuel Loading and Structural Performance Under Normal Conditions of Transport -
Demonstration of Approach and Results of Used Fuel Performance Characterization
214   **SEPTEMBER 30, 2013**

Analysis	Section	Result
Temperature distribution	8.5.7	**Low Sensitivity:** The effects of temperature on the materials' elastic moduli (not including the fuel rod itself) had a small effect on the response and cladding strains.
In-reactor fretting wear	8.5.8	**Moderate Sensitivity:** Increase or decrease in nominal bending stress calculated and a multiplier is provided to the assembly-level model to account for this. The multiplier is approximately 1.41 times the bending stress.
Gaps between assembly and cask support structure	8.5.9	**High Sensitivity:** For loads consistent with the P3 shock loads and for the range of clearances investigated, the gaps are of significant importance in determining the severity of the excitations at each fuel assembly, particularly for excitations in the lateral and axial rotation directions.
Influence of control components	8.5.10	**Moderate Sensitivity:** The added mass and stiffness at the top of the assembly from inclusion of the control assembly resulted in lower strains for the cladding.
Fuel rod damping	8.5.1	**Low Sensitivity:** Damping was determined to be minimal in the fuel rods. However, the damping Rayleigh damping parameters provided to the assembly-level analysis was determined by varying the coefficient of friction and bonding at the pellet-pellet and pellet-clad interfaces.
Pellet-to-clad bonding	8.5.8	**Moderate Sensitivity:** Increase or decrease in nominal bending stress calculated and a multiplier is provided to the assembly-level model to account for this. The multiplier is approximately 1.38 times the bending stress.
Pin pressure influence	8.5.8	**Low Sensitivity:** Internal pin pressure influence reduces the stress concentration caused by pellet-to-clad bonding and in-reactor fretting wear. Therefore this effect was not considered in the final analysis

8.5.1   CLADDING ELASTIC MODULUS AND FUEL ROD DAMPING

As discussed in Section 6.3.2, the potential in variation of the elastic modulus is captured by using LB and UB elastic modulus. These values are used to generate LB and UB stiffness. This provides a material property window for the PWR assembly-level which allows them to tune to the response of the input.

The greatest source of variability or uncertainty in this modeling effort is the state of the fuel rod cladding and its associated physical/mechanical properties. The variability of mechanical properties due to irradiation and damage as well as physical factors such as the state and load carrying capacity of the pellet-clad interface greatly influence the dynamic characteristics of the fuel rod. Therefore, the UB, LB, and BEs rod stiffness values generated by the rod-level analyses were evaluated in modal analyses. Based on analysis of free vibration with no constraints on the

USED FUEL DISPOSITION CAMPAIGN
Used Nuclear Fuel Loading and Structural Performance Under Normal Conditions of Transport -
Demonstration of Approach and Results of Used Fuel Performance Characterization
SEPTEMBER 30, 2013 215

assembly, the first modes involve the entire assembly with torsion and flexure modes of vibration. The first torsion and flexure modes are ~4-5 Hz and followed subsequently by their higher order harmonics. These types of modes may be active if the basket has significant flexure, the spacer grid springs develop gaps, or the assembly lifts off the basket floor. At higher frequencies, the fuel rods begin to vibrate on the leaf spring and dimples within the spacer grids. These modes can be active at all times including while the assembly remains in contact with the basket wall.

As expected, there is considerable variation in the modal response from the bounding fuel rod stiffness values because the flexure natural frequency of a simply supported beam varies with the square root of the elastic modulus (Table 8.6). The fuel rod stiffness had the largest influence on the fuel rod flexure modes. The first fuel rod flexure mode was ~28 Hz for the LB rod stiffness, ~49 Hz for the BE stiffness, and ~51 Hz for the UB stiffness. The ratio of the UB/LB flexural mode frequencies was ~1.8 compared to the root modulus ratio of ~2.4, where the difference is attributed to the influence of the elastic supports (i.e., spacer grid springs) on the fuel rods. Due to the large number of fuel rods, the fuel rod flexure then exhibits numerous similar modes over a ~0.5 Hz frequency range. This primarily involves the rods in the lower half of the assembly since this span between spacer grids here is larger than the rest of the assembly (0.63 m versus 0.52 m). Flexural modes for the fuel rods with the smaller span at the top of the assembly begin around 59 Hz for the BE stiffness. So the default assembly geometry of the WE 17×17 OFA contains two distinct rod flexure natural frequency bands and regions that may be activated during transient loading (Figure 8.41). The lower frequency assembly flexure and torsion modes also changed as expected with rod stiffness, but the magnitude of the difference was smaller since these modes depend more on the combined stiffness properties of the guide tube and spacer grid support skeleton. Therefore, the rod state and its associated flexure properties will be a critical parameter to determine if the assembly has potential natural frequencies close to the frequency content of the TL environment. To account for the uncertainty in the rod stiffness properties, cases using broadened bounding load spectra will be evaluated to ensure that maximum rod response is achieved.
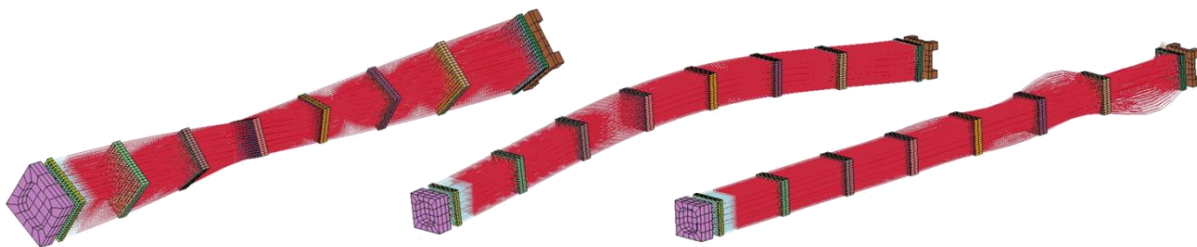
Figure 8.40. Typical Mode Shapes of the Assembly Submodel Including Assembly Torsion, Assembly Flexure, and Fuel Rod Flexure

USED FUEL DISPOSITION CAMPAIGN
Used Nuclear Fuel Loading and Structural Performance Under Normal Conditions of Transport -
Demonstration of Approach and Results of Used Fuel Performance Characterization
216 **SEPTEMBER 30, 2013**
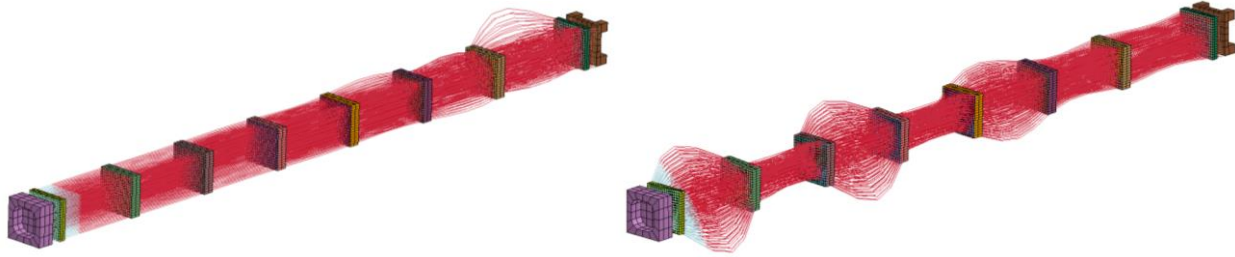
Figure 8.41. Lower Frequency (49 Hz) Mode Shapes Involving Fuel Rods at the Bottom of the Assembly and Higher Frequency (59 Hz) Fuel Rod Flexural Modes Involving Fuel Rods at the Top of the Assembly Due to Different Spacer Grid Spans

Table 8.6. Assembly Modal Results for Different Fuel Rod Stiffness Values

Mode #	Participating Component	Shape	Frequency (Hz)		
			BE cold	LB cold	UB cold
1	assembly	torsion	4.5	4.2	4.5
2/3	assembly	flexure	5.3	4.7	5.3
4	assembly	torsion	9.2	8.3	9.2
5/6	assembly	flexure	10.2	8.3	10.4
7	assembly	torsion	14.3	12.1	14.5
8/9	assembly	flexure	16.4	12.1	16.7
10	assembly	torsion	20.4	16.0	20.7
11/12	assembly	flexure	23.7	16.0	24.4
13	assembly	torsion	27.6	20.3	28.2
14/15	assembly	flexure	32.7	20.3	33.9
16	assembly	torsion	36.2	24.4	37.2
17/18	assembly	flexure	43.2	24.5	44.9
19	assembly	torsion	46.4	27.8	47.9
20+	fuel rod	flexure	48.8	27.9	50.5

8.5.2   CLADDING YIELD STRESS

As discussed in the material properties handbook (Geelhood 2013), there may be a significant level of uncertainty associated with the cladding yield stress. In addition to a calculated standard error of 65 MPa for the yield stress correlation relative to the data, it is also acknowledged that some annealing of irradiation damage following reactor discharge could lower the yield stress of the cladding prior to transportation . An example of the change in yield stress with fast fluence

USED FUEL DISPOSITION CAMPAIGN
Used Nuclear Fuel Loading and Structural Performance Under Normal Conditions of Transport -
Demonstration of Approach and Results of Used Fuel Performance Characterization
SEPTEMBER 30, 2013 217

in Zircaloy-4 at 315°C is shown in Figure 8.42. Annealing has the potential to change the yield stress from about 600 MPa at the time of discharge to 360 MPa if all the irradiation defects were annealed out.
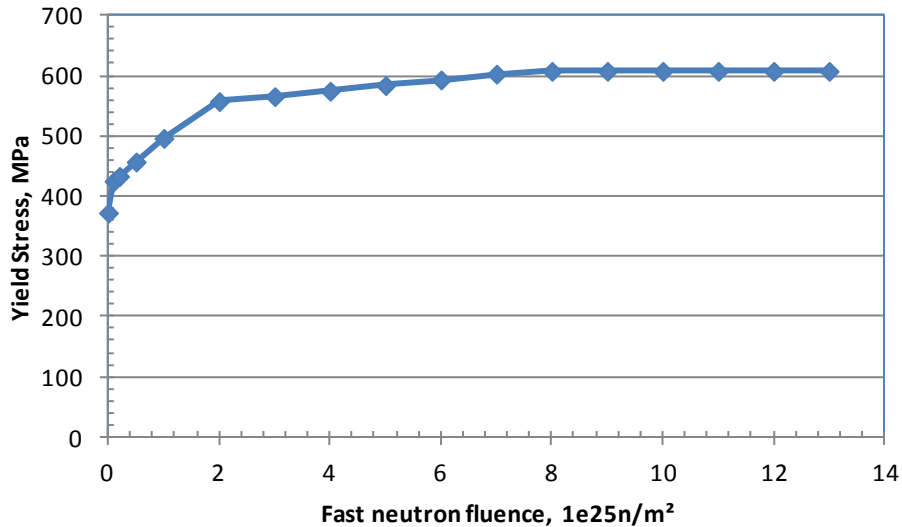
Figure 8.42. Change in Yield Stress with Increasing Fast Neutron Fluence at 315°C

As noted in Section 0, the nominal cladding bending stress for NCT is expected to be 32 MPa. Various uncertainties are only expected to increase this value by 40% to about 45 MPa. Since this is well below the yield stress of either irradiated or unirradiated Zircaloy, the impact of potential ex-reactor annealing will not affect the results of this demonstration. Regardless, the cladding will remain in the elastic region.

8.5.3   SPACER GRID AND SPRING AND SIMPLE STIFFNESS

Sensitivities of the spacer grid stiffness and the spring and dimple stiffness were assessed at both the fuel rod-level and the assembly-level. The following sections give the results of these sensitivity assessments at each level.

8.5.3.1   *SENSITIVITY AT THE FUEL ROD-LEVEL*

Detailed grid spacer slots include springs and dimples that restrain movement of fuel rods through contact interaction. Due to time constraints it is not reasonable to provide this level of detail in the PWR assembly model performed at the assembly-level. Therefore the effort documented in this section focuses on providing equivalent grid slot shell properties and equivalent spring properties to represent the actual springs and dimples. These values are provided to the assembly-level to use in their PWR assembly model. It is necessary to have detailed drawings or measurements of a grid spacer slot to numerically model the performance.

USED FUEL DISPOSITION CAMPAIGN
**Used Nuclear Fuel Loading and Structural Performance Under Normal Conditions of Transport -
Demonstration of Approach and Results of Used Fuel Performance Characterization**
218 **SEPTEMBER 30, 2013**

Since vendor drawings were not available, measurements were taken on an AREVA Advanced Mark-BW 17×17 which is on display at the Idaho National Laboratory (INL) (Figure 8.43).

Figure 8.43. AREVA Advanced Mark-BW 17×17 Fuel Assembly

Using these measurements, a detailed grid spacer analysis was performed using ABAQUS. Details on the MP are provided in Table 6.15. Details on FE properties, and applied loads are provided below.

The FE code ABAQUS was used to develop the equivalent shell thickness and spring and dimple behavior. The objective of these models is to determine the equivalent stiffness values for the springs and dimples and determine the equivalent shell response of the fuel rod slot that does not include the geometrical details of the spring and dimples (this is the geometric configuration that will be used by the PWR assembly-level analysis, see Figure 8.44).

8.5.3.1.1   *EQUIVALENT GRID SLOT SENSITIVITY*

The equivalent grid slot study investigates what shell thickness is required for a coarsely-meshed (3 mesh elements across slot width and 2 mesh elements across slot width) slot to produce similar lateral response to a finely-meshed grid slot that includes the springs and dimples (see Figure 8.44). To accomplish this, a load is applied to the individual slots (Figure 8.45) and the horizontal displacement measured at a node measured at either end and in the middle of the edge highlighted in Figure 8.45. The required equivalent shell thicknesses for both the Inconel and Zircaloy coarsely-meshed models are provided in Table 8.7. Note that the change in the modulus of elasticity value has no effect on the relative percent difference between the fine- and coarse-meshed models.

USED FUEL DISPOSITION CAMPAIGN
Used Nuclear Fuel Loading and Structural Performance Under Normal Conditions of Transport -
Demonstration of Approach and Results of Used Fuel Performance Characterization
SEPTEMBER 30, 2013   219

Table 8.7. Required Equivalent Shell Thicknesses for the Inconel and Zircaloy Coarsely-Meshed
Models

	Actual Shell Thickness (mm)	Equivalent Shell Thickness for 2 Shell Elements Across (mm)	Equivalent Shell Thickness for 2 Shell Elements Across (mm)
Inconel Shell	0.381	0.330	0.343
Zircaloy-4 Shell	0.381	0.330	0.343
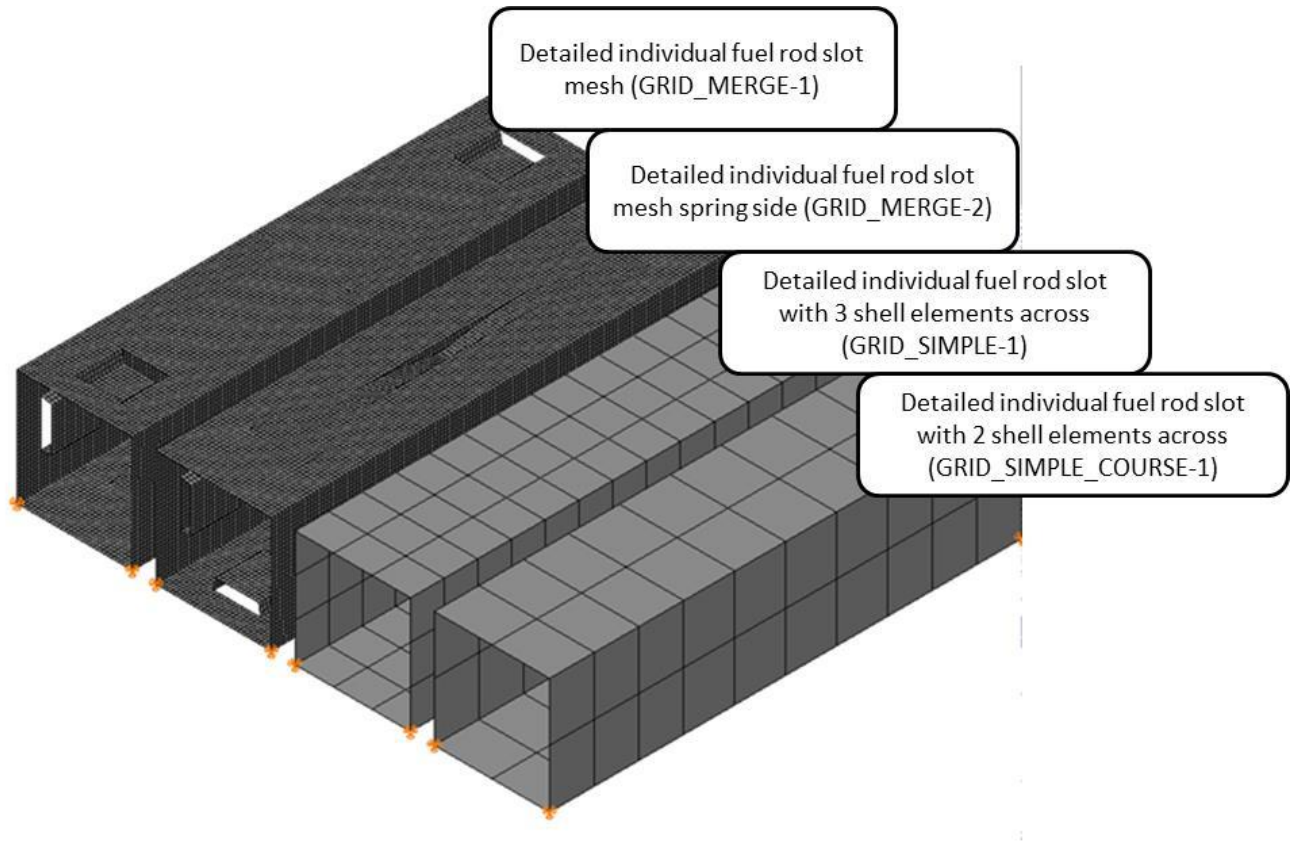
Figure 8.44. Detailed and Simplified Finite Element Model of Individual Fuel Rod Slot

USED FUEL DISPOSITION CAMPAIGN
Used Nuclear Fuel Loading and Structural Performance Under Normal Conditions of Transport -
Demonstration of Approach and Results of Used Fuel Performance Characterization
220 **SEPTEMBER 30, 2013**
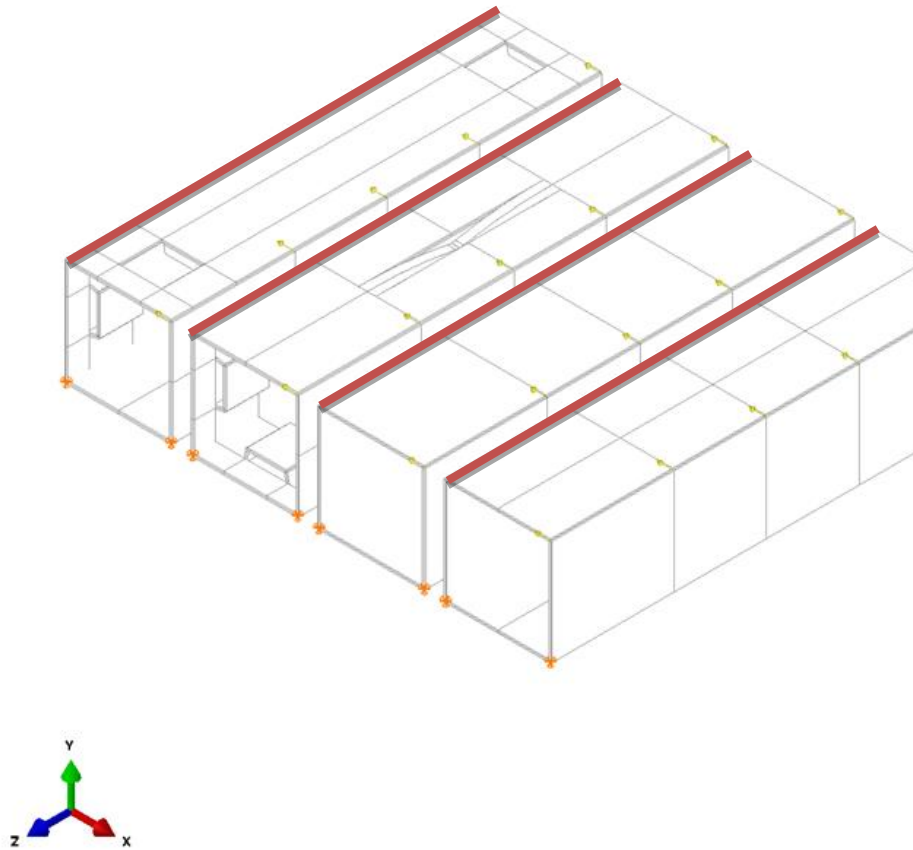
Figure 8.45. Detailed and Simplified Finite Element Model of Individual Fuel Rod Slot Showing Load Application Locations

The model runs and results for the Inconel runs are presented in Figure 8.46-Figure 8.48. These model runs show that if the shell thickness values presented in Table 8.7 are used the percent difference between the detailed finely-meshed slots and the coarsely-meshed slots are less than 5 percent.

USED FUEL DISPOSITION CAMPAIGN
Used Nuclear Fuel Loading and Structural Performance Under Normal Conditions of Transport -
Demonstration of Approach and Results of Used Fuel Performance Characterization
SEPTEMBER 30, 2013 221
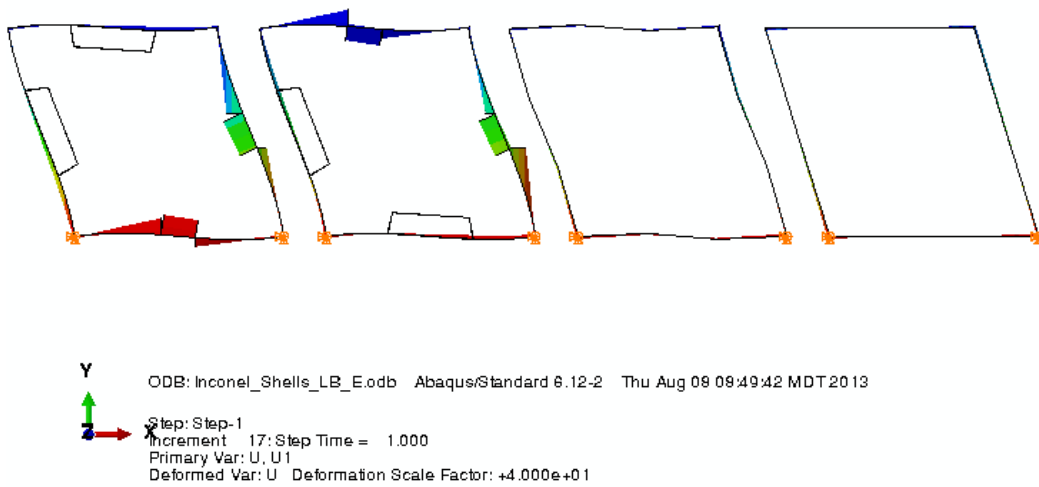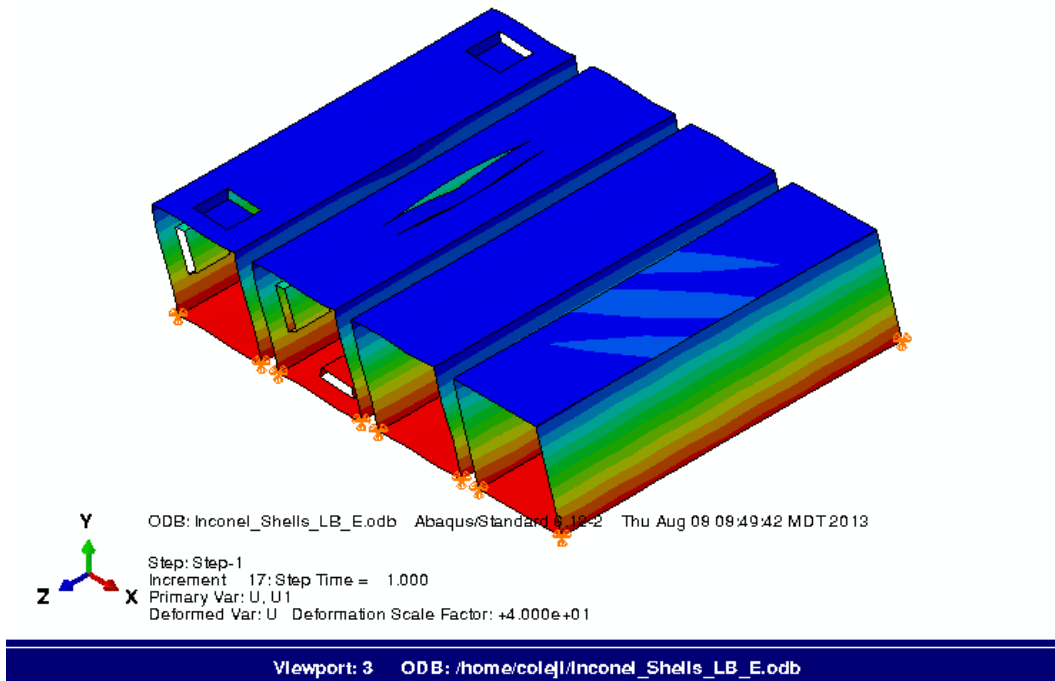
Figure 8.46. Deflection of Inconel Model

USED FUEL DISPOSITION CAMPAIGN
**Used Nuclear Fuel Loading and Structural Performance Under Normal Conditions of Transport -
Demonstration of Approach and Results of Used Fuel Performance Characterization**
222   **SEPTEMBER 30, 2013**

Model Name: Inconel_shells_UB UNITS: SI				
Node Identifier	Fine Mesh Dimple (Shell Thickness = 0.381 mm)	Fine Mesh Spring(Shell Thickness = 0.381 mm)	Mesh 3 Elements (Shell Thickness = 0.343 mm)	Mesh 2 Elements (Shell Thickness = 0.330 mm)
GRID_MERGE-1 N:59	-0.0900			
GRID_MERGE-1 N:63	-0.0900			
GRID_MERGE-1 N:66	-0.0884			
GRID_MERGE-2 N:73		-0.0897		
GRID_MERGE-2 N:79		-0.0882		
GRID_MERGE-2 N:93		-0.0897		
GRID_SIMPLE-1 N: 6			-0.0915	
GRID_SIMPLE-1 N: 11			-0.0933	
GRID_SIMPLE-1 N: 17			-0.0933	
GRID_SIMPLE_COURSE-1 N:23				-0.0863
GRID_SIMPLE_COURSE-1 N:27				-0.0871
GRID_SIMPLE_COURSE-1 N:29				-0.0871

Equivalent Spring Percent Diff for UB_Inconel				
Percent Difference in Lateral Deflection	Average of Fine Mesh Dimple and Fine Mesh Spring	Percent Difference Between Average deflection and Mesh 3	Percent Difference Between Average deflection and Mesh 2	
	-0.0899	1.75	4.21	
	-0.0891	4.47	2.35	
	-0.0891	4.51	2.31	

Figure 8.47. Results of the Detailed and Simplified Finite Element Model of Individual Fuel Rod Slot Showing Deflection Values in (mm) for the Upper Bound Inconel Percent Difference. Notice that the percent difference for the 2 mesh and 3 mesh cases are all less than 5 percent.

Model Name: Inconel_shells_LB_E.odb UNITS: SI				
Node Identifier	Fine Mesh Dimple (Shell Thickness = 0.381 mm)	Fine Mesh Spring(Shell Thickness = 0.381 mm)	Mesh 3 Elements (Shell Thickness = 0.343 mm)	Mesh 2 Elements (Shell Thickness = 0.330 mm)
GRID_MERGE-1 N:59	-0.0994			
GRID_MERGE-1 N:63	-0.0994			
GRID_MERGE-1 N:66	-0.0977			
GRID_MERGE-2 N:73		-0.0991		
GRID_MERGE-2 N:79		-0.0974		
GRID_MERGE-2 N:93		-0.0991		
GRID_SIMPLE-1 N: 6			-0.1010	
GRID_SIMPLE-1 N: 11			-0.1031	
GRID_SIMPLE-1 N: 17			-0.1031	
GRID_SIMPLE_COURSE-1 N:23				-0.0953
GRID_SIMPLE_COURSE-1 N:27				-0.0962
GRID_SIMPLE_COURSE-1 N:29				-0.0962

Equivalent Spring Percent Diff for LB_Inconel				
Percent Difference in Lateral Deflection	Average of Fine Mesh Dimple and Fine Mesh Spring	Percent Difference Between Average deflection and Mesh 3	Percent Difference Between Average deflection and Mesh 2	
	-0.0993	1.75	4.21	
	-0.0984	4.47	2.35	
	-0.0984	4.51	2.31	

Figure 8.48. Results of the Detailed and Simplified Finite Element Model of Individual Fuel Rod Slot Showing Deflection Values in (mm) for the Upper Bound Inconel Percent

USED FUEL DISPOSITION CAMPAIGN
Used Nuclear Fuel Loading and Structural Performance Under Normal Conditions of Transport -
Demonstration of Approach and Results of Used Fuel Performance Characterization
SEPTEMBER 30, 2013 223

Difference. Notice that the percent difference for the 2 mesh and 3 mesh cases are all less than 5 percent.

The model runs and results for the Zircaloy-4 runs are presented in Figure 8.49 and Figure 8.50. These model runs show that if the shell thickness values presented in Table 8.7 are used the percent difference between the detailed finely-meshed slots and the coarsely-meshed slots are less than 5 percent.

USED FUEL DISPOSITION CAMPAIGN
Used Nuclear Fuel Loading and Structural Performance Under Normal Conditions of Transport -
Demonstration of Approach and Results of Used Fuel Performance Characterization
224 **SEPTEMBER 30, 2013**
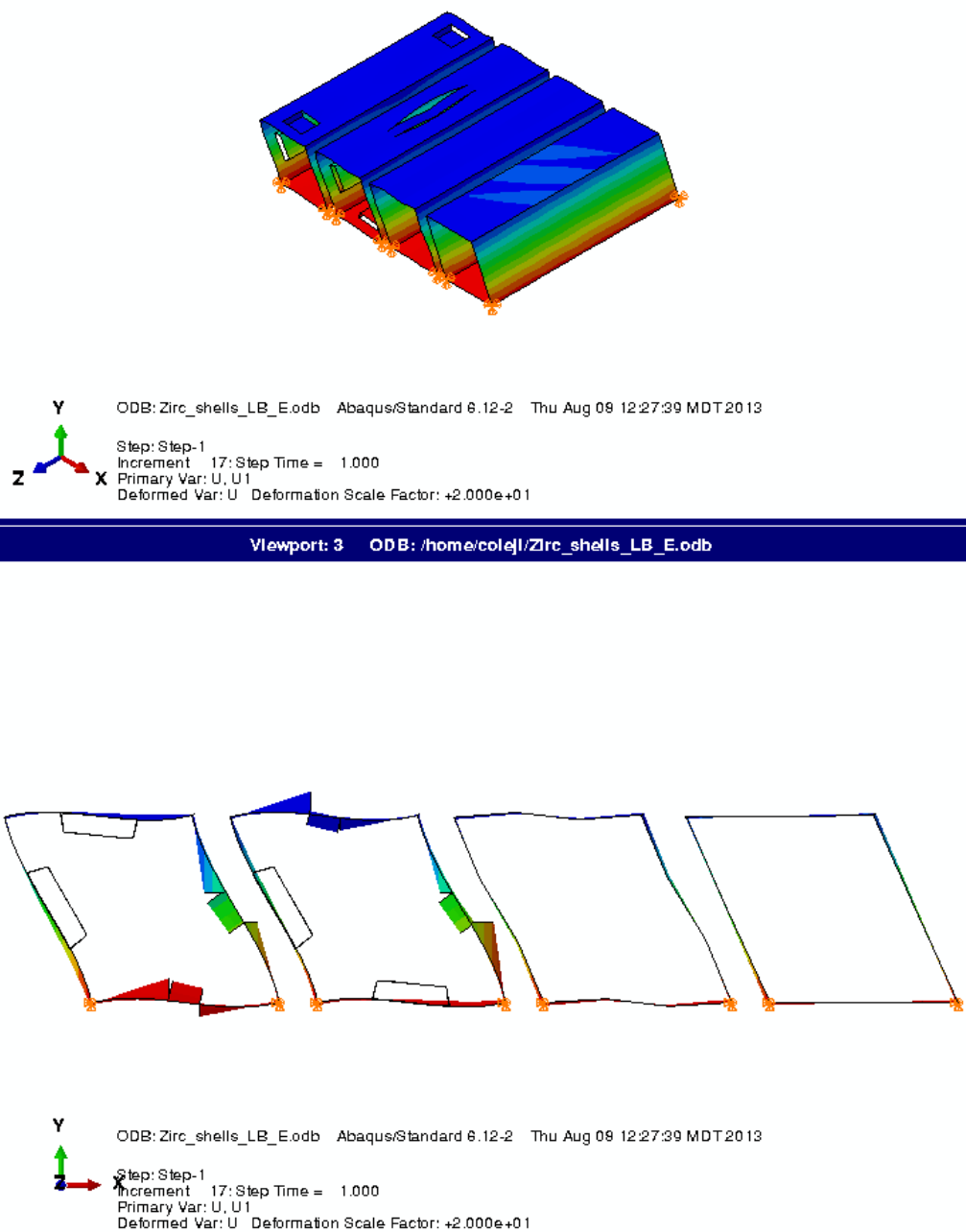
Figure 8.49. Deflection of Zircaloy-4 Model

USED FUEL DISPOSITION CAMPAIGN
Used Nuclear Fuel Loading and Structural Performance Under Normal Conditions of Transport -
Demonstration of Approach and Results of Used Fuel Performance Characterization
SEPTEMBER 30, 2013   225

Model Name: Zirc_shells_LB_E.od UNITS: SI				
Node Identifier	Fine Mesh Dimple (Shell Thickness = 0.381 mm)	Fine Mesh Spring(Shell Thickness = 0.381 mm)	Mesh 3 Elements (Shell Thickness = 0.343 mm)	Mesh 2 Elements (Shell Thickness = 0.330 mm)
GRID_MERGE-1 N:59	-0.2897			
GRID_MERGE-1 N:63	-0.2897			
GRID_MERGE-1 N:66	-0.2844			
GRID_MERGE-2 N:73		-0.2885		
GRID_MERGE-2 N:79		-0.2835		
GRID_MERGE-2 N:93		-0.2885		
GRID_SIMPLE-1 N: 6			-0.2925	
GRID_SIMPLE-1 N: 11			-0.2984	
GRID_SIMPLE-1 N: 17			-0.2984	
GRID_SIMPLE_COURSE-1 N:23				-0.2756
GRID_SIMPLE_COURSE-1 N:27				-0.2783
GRID_SIMPLE_COURSE-1 N:29				-0.2783

Equivalent Spring Percent Diff

Percent Difference in Lateral Deflection	Average of Fine Mesh Dimple and Fine Mesh Spring	Percent Difference Between Average deflection and Mesh 3	Percent Difference Between Average deflection and Mesh 2
	-0.2891	1.16	4.89
	-0.2866	3.96	3.00
	-0.2864	4.02	2.93

Figure 8.50. Results of the Detailed and Simplified Finite Element Model of Individual Fuel Rod Slot Showing Deflection Values in (mm) for the Lower Bound Zircaloy-4 Percent Difference. Notice that the percent difference for the 2 mesh and 3 mesh cases are all less than 5 percent.

8.5.3.1.2   SPRING STIFFNESS SENSITIVITY

The prototypic spacer grid spring assembly assumed in this task consists of a central leaf spring between two support dimples. One grid spacer spring and one dimple are also modeled and loads are applied at the locations where the fuel rod contact is expected. From this model a nonlinear load displacement curve is calculated to determine the spring and dimple stiffness. Figure 8.51 shows the locations of load application and the boundary conditions. The pinned boundary conditions are applied along the edges so that the model is only calculating the response of the spring and dimple.

USED FUEL DISPOSITION CAMPAIGN
Used Nuclear Fuel Loading and Structural Performance Under Normal Conditions of Transport -
Demonstration of Approach and Results of Used Fuel Performance Characterization
226   SEPTEMBER 30, 2013
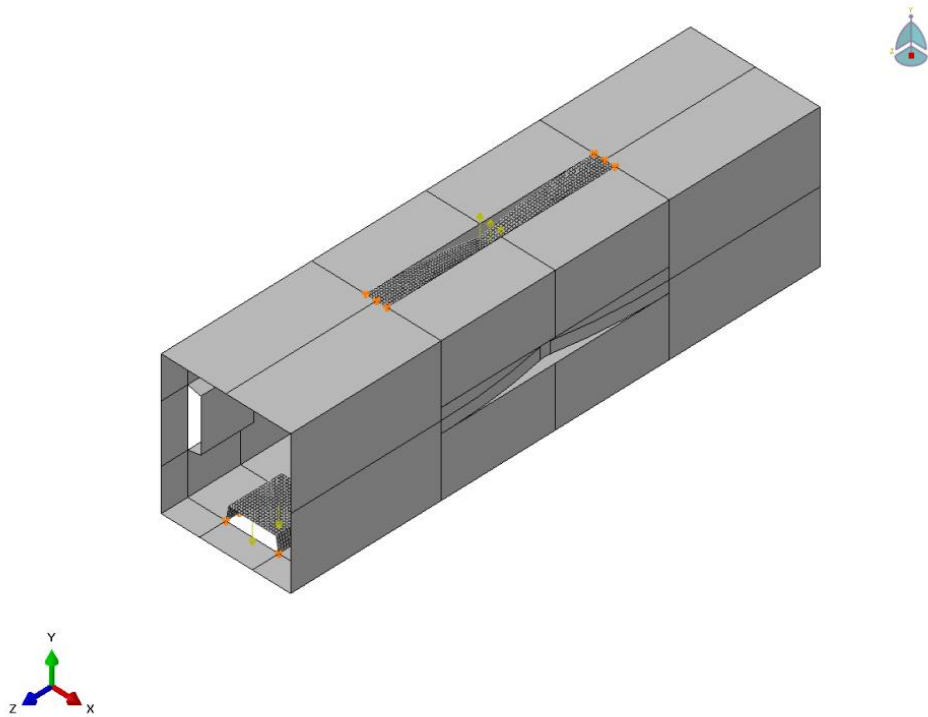
Figure 8.51. Detailed and Simplified Finite Element Model of an Individual Spring and Dimple
Showing the Applied Load and Boundary Conditions

The applied loading produces the spring and dimple load deflection curves shown in Figure 8.52
- Figure 8.55.

USED FUEL DISPOSITION CAMPAIGN
**Used Nuclear Fuel Loading and Structural Performance Under Normal Conditions of Transport -
Demonstration of Approach and Results of Used Fuel Performance Characterization**
SEPTEMBER 30, 2013 **227**
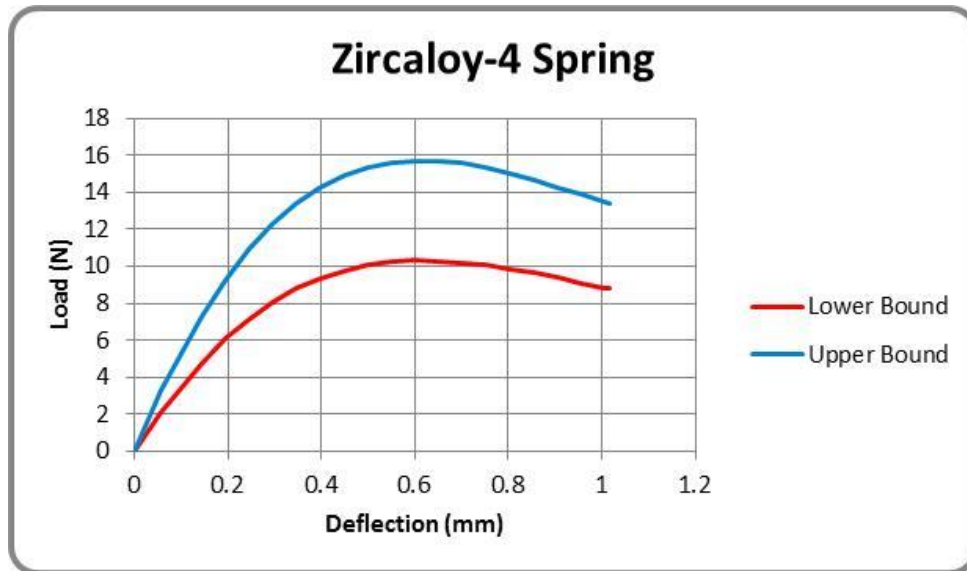
Figure 8.52. Load versus Deflection curve of Zircaloy-4 Spring Showing the Lower and Upper
Bound Modulus of Elasticity Response
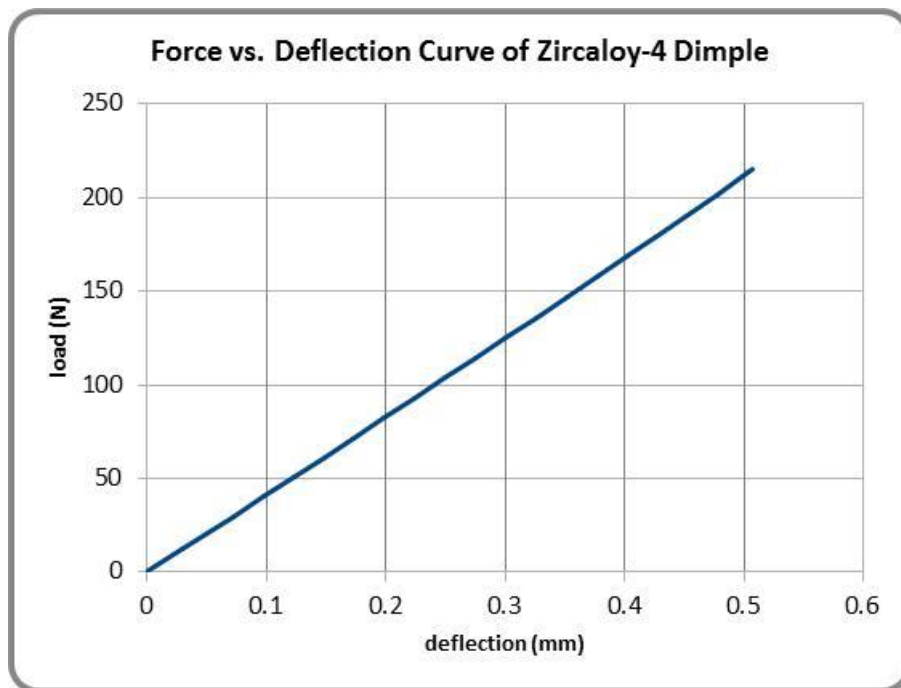
Figure 8.53. Load versus Deflection Curve of Zircaloy-4 Dimple

USED FUEL DISPOSITION CAMPAIGN
Used Nuclear Fuel Loading and Structural Performance Under Normal Conditions of Transport -
Demonstration of Approach and Results of Used Fuel Performance Characterization
228   **SEPTEMBER 30, 2013**
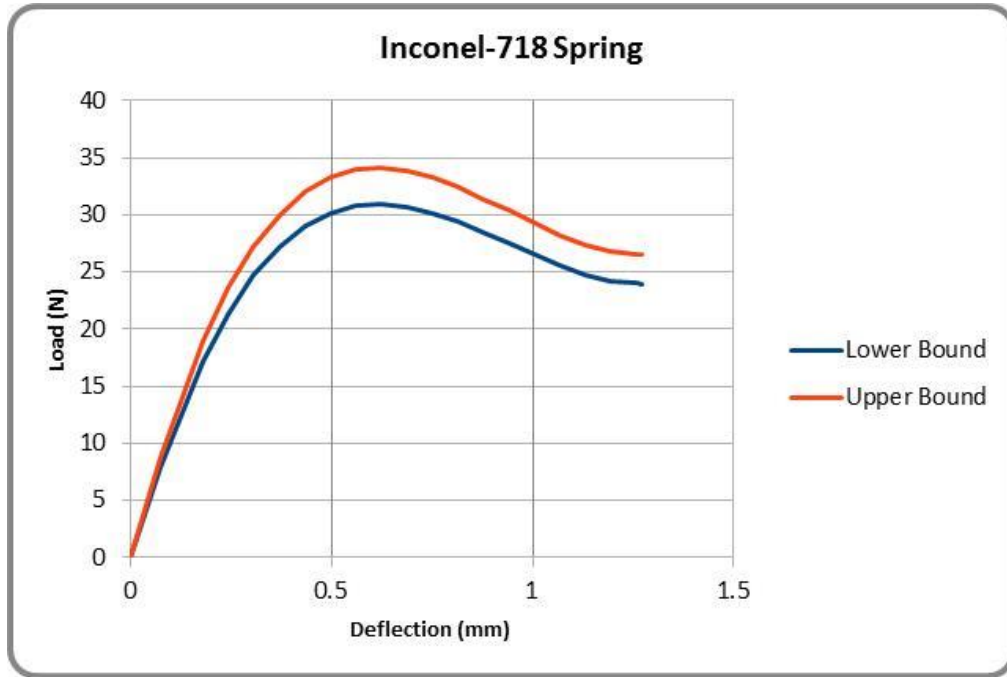
Figure 8.54. Load versus Deflection Curve of Inconel Spring Showing the Lower and Upper Bound Modulus of Elasticity Response
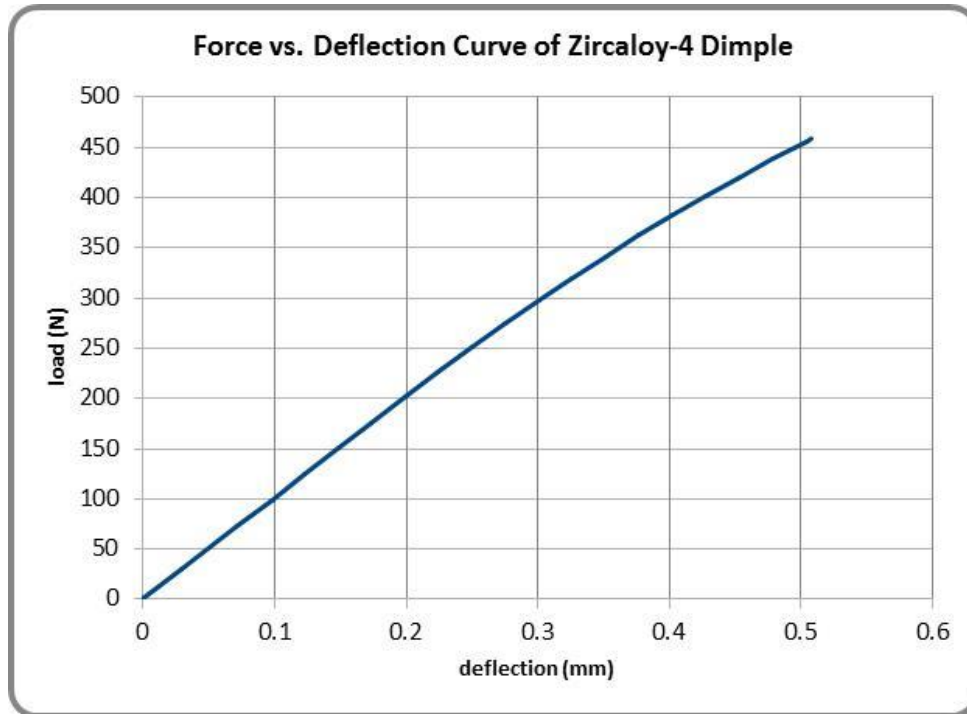
Figure 8.55. Load versus Deflection Curve of Inconel Dimple

USED FUEL DISPOSITION CAMPAIGN
Used Nuclear Fuel Loading and Structural Performance Under Normal Conditions of Transport -
Demonstration of Approach and Results of Used Fuel Performance Characterization
SEPTEMBER 30, 2013 **229**

8.5.3.2 *SENSITIVITY AT THE ASSEMBLY-LEVEL*

The stiffness of spacer grid leaf springs is difficult to identify from the literature due to proprietary grid designs, but limited available data presented in an earlier report (Adkins 2013c) indicates that the stiffness varies considerably between different manufacturers, designs, and grid material. The preload on the spacer grid springs also tends to reduce during reactor operations due to creep and stress relaxation. Therefore, the support of the rod by the spacer grid may be considerably different for different grid designs and burnup levels which would ultimately affect the rod natural frequencies.

8.5.3.2.1 *MODAL ANALYSES*

Modal analyses were performed to compare the results with the nominal spring stiffness to those with 10✕ and 1/10✕ the nominal spring stiffness. Both the leaf spring and dimple stiffness values were scaled by the same factor. The results are shown in Table 8.8. It was observed that the 1/10✕ reduced spacer grid stiffness reduced the assembly vibration frequencies by 5-14% and the fuel rod flexure frequency by 15%. Increasing the spacer grid stiffness by 10✕ was observed to eliminate some of the lower frequency assembly modes and increase the first fuel rod flexure frequency by 38%. Based on expected loading, the rail transport is expected to have low frequency content in the 2-50 Hz range (Figure 8.56). Relaxation of the springs and formation of possible gaps would then reduce the natural frequency of the rod span below the 48.8 Hz nominal value and possibly excite a greater response to such loading.

USED FUEL DISPOSITION CAMPAIGN
Used Nuclear Fuel Loading and Structural Performance Under Normal Conditions of Transport -
Demonstration of Approach and Results of Used Fuel Performance Characterization
230   **SEPTEMBER 30, 2013**

Table 8.8. Assembly Modal Results for Different Spacer Grid Spring Stiffness Values

Mode #	Participating Component	Shape	Frequency (Hz)		
			BE cold (1✕)	BE cold (1/10 ✕)	BE cold (10 ✕)
1	assembly	torsion	4.5	3.9	
2/3	assembly	flexure	5.3	4.7	6.4
4	assembly	torsion	9.2	8.0	6.8
5/6	assembly	flexure	10.2	8.9	
7	assembly	torsion	14.3	12.8	13.6
8/9	assembly	flexure	16.4	14.8	13.7
10	assembly	torsion	20.4	18.5	20.5
11/12	assembly	flexure	23.7	21.8	21.7
13	assembly	torsion	27.6	25.6	27.9
14/15	assembly	flexure	32.7	30.9	30.3
16	assembly	torsion	36.2	34.2	36.1
17/18	assembly	flexure	43.2		39.5
19	assembly	torsion	46.4		44.7
20+	fuel rod	flexure	48.8	41.4	67.1

USED FUEL DISPOSITION CAMPAIGN
Used Nuclear Fuel Loading and Structural Performance Under Normal Conditions of Transport -
Demonstration of Approach and Results of Used Fuel Performance Characterization
SEPTEMBER 30, 2013 231
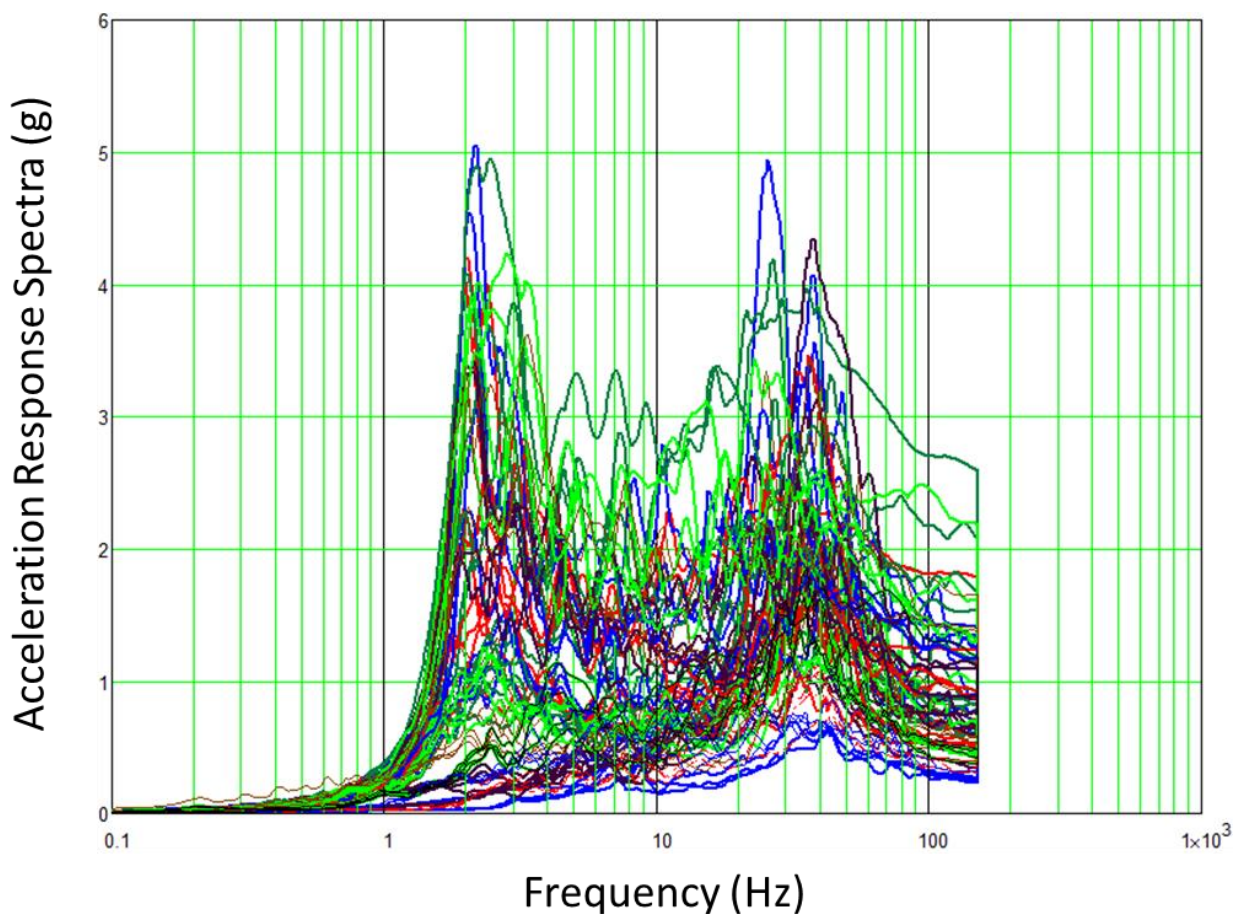
Figure 8.56. Vertical Cask Loading Response Spectra from the Initial TTCI Rail Car Data

8.5.3.2.2   *TRANSIENT DYNAMIC ANALYSES*

The assembly model was run for a lateral vibration case to identify sensitivity of the cladding strain when using modified spring stiffness values. Models were run with linear stiffness values in compression decreased by a factor of 10 from the initial slopes of the nominal nonlinear spring curves (discussed in subsection 6.2.1.4) and shown in Figure 8.57. Stiffness values were modified by the same scale factor for all of the leaf springs and dimples in every spacer grid. The softer springs were slightly more beneficial to the cladding strains. The maximum cladding strain with the softer springs reduced 16% from 0.622e-3 to 0.521e-3, and there was a similar small benefit in the number of cyclic events as shown in Figure 8.58 (note that in this Figure the presented counts are the sum of all locations on all beam elements in the model, which gives a measure of the total cyclic response but does not indicate the cycle count for any individual location). The additional compliance reduces the high local bending strains in the vicinity of the three-point support of the spacer grid when the unsupported rod span is laterally deflected.

USED FUEL DISPOSITION CAMPAIGN
Used Nuclear Fuel Loading and Structural Performance Under Normal Conditions of Transport -
Demonstration of Approach and Results of Used Fuel Performance Characterization
232   **SEPTEMBER 30, 2013**
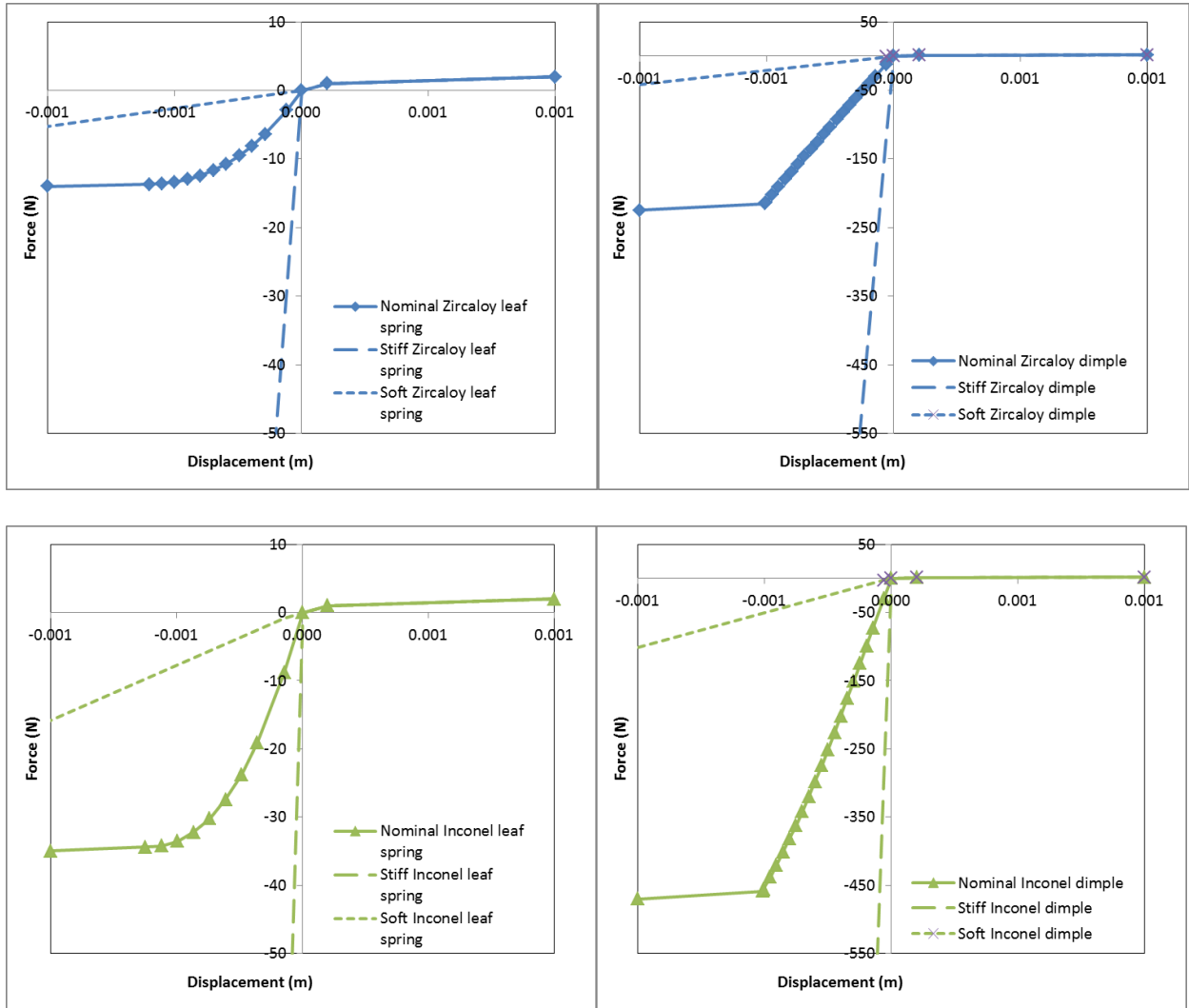
Figure 8.57. Modified Stiffness Values for Inconel and Zircaloy Spacer Grid Leaf Springs and Dimples

USED FUEL DISPOSITION CAMPAIGN
Used Nuclear Fuel Loading and Structural Performance Under Normal Conditions of Transport -
Demonstration of Approach and Results of Used Fuel Performance Characterization
SEPTEMBER 30, 2013 233
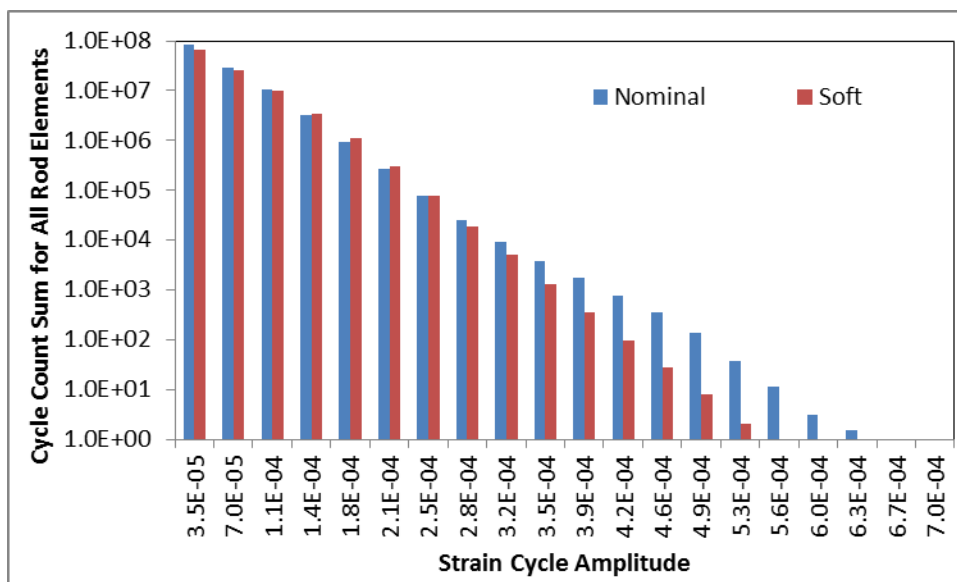
Figure 8.58. Cyclic Strain History for the Assembly with Modified Spacer Grid Spring Stiffness

8.5.4   SPACER GRID LOCATION

The number and location of the spacer grids may vary for different assemblies and manufacturers. No documented alternate spacer grid layouts were able to be identified for the WE 17×17 OFA assembly. To consider a case where greater unsupported rods spans could be possibly used in a design, a case was run by moving the spacer grid location to provide a larger unsupported rod span (Figure 8.59). The bottom spacer grid of the default model was moved further up the assembly by 15.2 cm (6 in) to increase the bottom span from 0.632 m to 0.785 m. This will tend to decrease the rod flexural natural frequency which again moves it closer to the frequencies of the rail car loading.

Figure 8.59. Fuel Rod Modal Deformation Shown on the Alternate Spacer Grid Design Case for the Sensitivity Analysis

8.5.4.1   MODAL ANALYSES

Modal analyses were performed to compare the results with the larger rod span to the nominal case (Table 6.10). There was only 1-2% difference for the low frequency assembly modes. As expected for the fuel rod flexure though, frequency decreased about 29% from 49 Hz to 35 Hz.

USED FUEL DISPOSITION CAMPAIGN
Used Nuclear Fuel Loading and Structural Performance Under Normal Conditions of Transport -
Demonstration of Approach and Results of Used Fuel Performance Characterization
234   **SEPTEMBER 30, 2013**

Again, this moves the rod flexure natural frequency closer to some of the high amplitude content in the preliminary vertical load spectrum (Figure 8.56) where more response would be expected. These results are shown in Table 8.9.

Table 8.9. Assembly Modal Results for Larger Grid Span

Mode #	Participating Component	Shape	Frequency (Hz)	
			Normal Grid Span	Larger Grid Span
1	assembly	torsion	4.5	4.5
2/3	assembly	flexure	5.3	5.3
4	assembly	torsion	9.2	9.2
5/6	assembly	flexure	10.2	10.0
7	assembly	torsion	14.3	14.1
8/9	assembly	flexure	16.4	16.2
10	assembly	torsion	20.4	20.2
11/12	assembly	flexure	23.7	24.3
13	assembly	torsion	27.6	27.8
14/15	assembly	flexure	32.7	33.4
16	assembly	torsion	36.2	
17/18	assembly	flexure	43.2	
19	assembly	torsion	46.4	
20+	fuel rod	flexure	48.8	34.6

8.5.4.2   *TRANSIENT DYNAMIC ANALYSES*

The assembly model was run for the P1 vertical shock case with the nominal spacer grid locations and an alternate grid location where the bottom span was further increased by 6 in. This had a significant effect on the response. The rod exhibited much higher bending stresses at the spacer grid locations near the longer span, resulting in higher cladding strains. The highest strains tended to be concentrated in the first Zircaloy grid from the bottom of the assembly and located generally on the top side of the assembly (Figure 8.60). The maximum cladding strain increased 120% from 5.77e-4 to 1.27e-3 and the cyclic strain distribution showed a large number of high magnitude cycles (Figure 8.61). Note that in this figure the presented counts are the sum of all locations on all beam elements in the model, which gives a measure of the total cyclic response but does not indicate the cycle count for any individual location. Future modeling activities should include a literature review of the spacer grid spans in different assembly designs to quantify the possible unsupported rod lengths that exist in the used fuel inventory.

USED FUEL DISPOSITION CAMPAIGN
Used Nuclear Fuel Loading and Structural Performance Under Normal Conditions of Transport -
Demonstration of Approach and Results of Used Fuel Performance Characterization
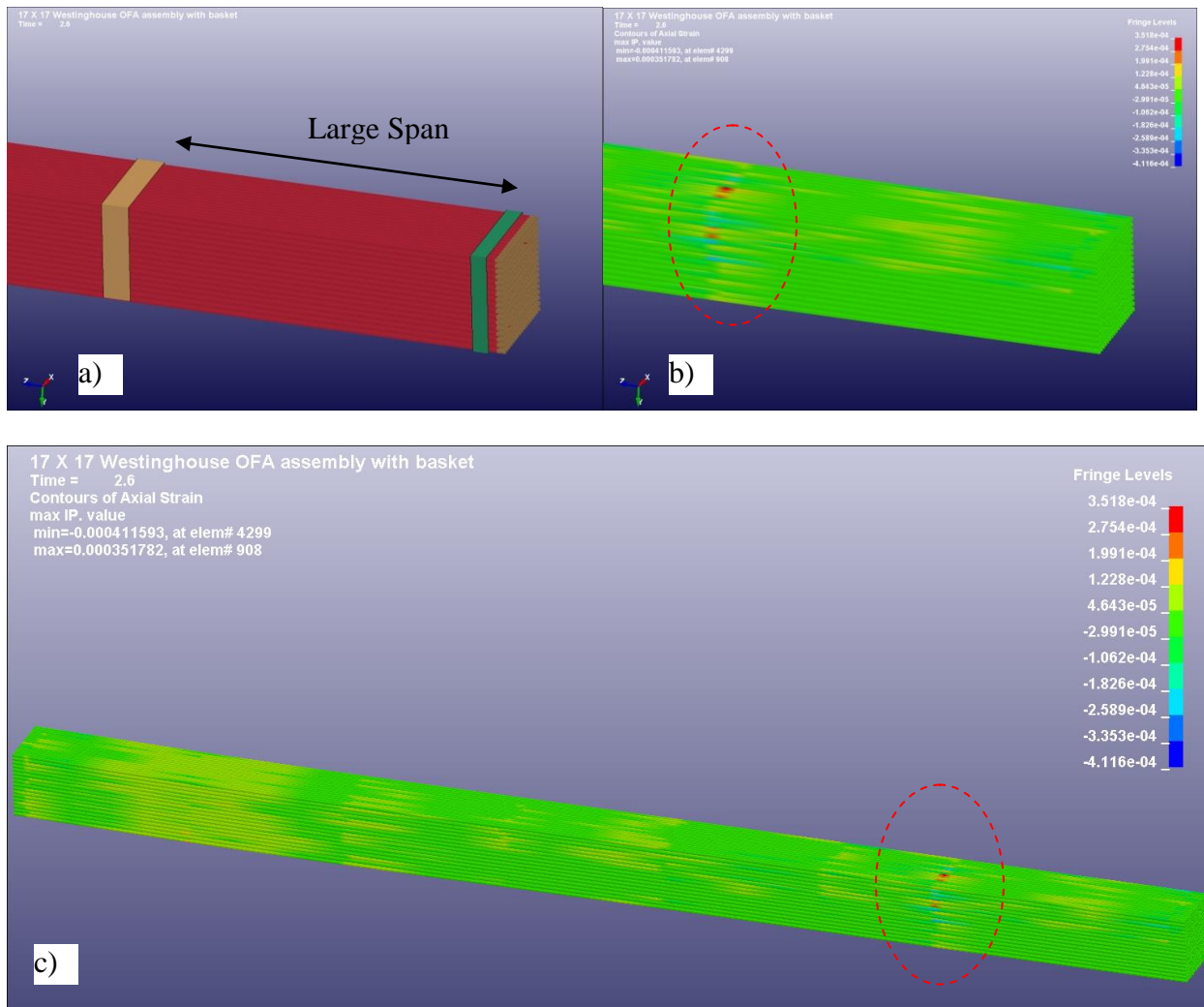SEPTEMBER 30, 2013   235

Figure 8.60. Location and Fuel Rod Axial Strains Concentrated under the Spacer Grid When the
        Span between Grids is Increased

USED FUEL DISPOSITION CAMPAIGN
Used Nuclear Fuel Loading and Structural Performance Under Normal Conditions of Transport -
Demonstration of Approach and Results of Used Fuel Performance Characterization
236 **SEPTEMBER 30, 2013**
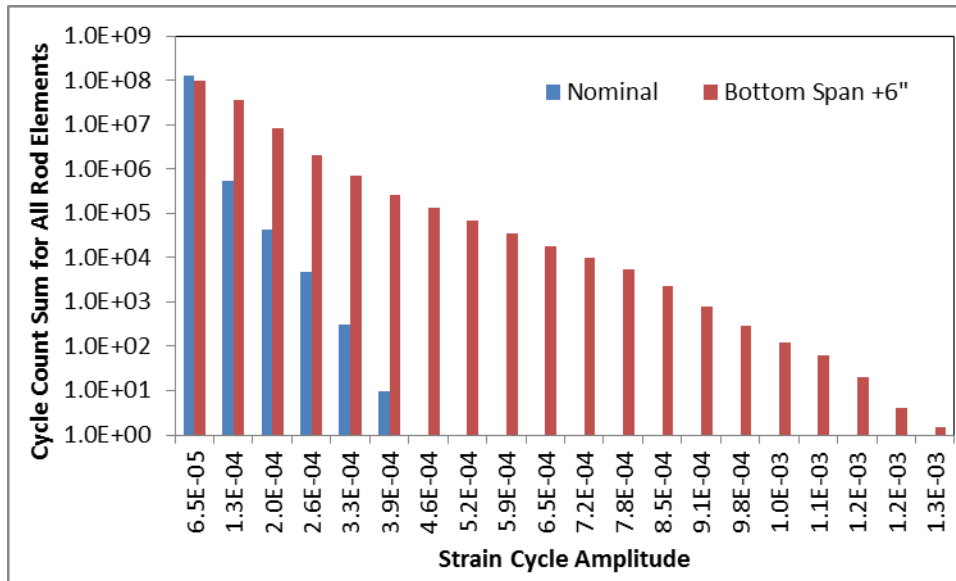
Figure 8.61. Cyclic Strain History for the Assembly with Nominal and Modified Grid Spacer Locations

8.5.5 FUEL ASSEMBLY BASKET LOCATION

The assemblies in different compartments of the basket may experience different excitations that will affect the predicted loads on the rods. These differences are due to several reasons. First, the local compliance of the basket itself may change due to its construction and support (e.g., the middle compartment versus the outside compartment). Second, the compartment accelerations will be different due to rotation of the cask/cradle about the rail car deck (e.g., the compartment at the top of the basket may have more lateral acceleration due to low speed roll of the rail car). Third, there is an inherent temperature distribution on the cask such that the central compartment is hotter than outside compartments which have a small effect on MP. Therefore, this sensitivity analysis helps to identify the region within the basket that may present the worst conditions for the assembly.

The assembly model was run with the vertical shock loading case inputs for basket cells #1 and #20 (see Table 6.9 for basket cell numbering). Cell #20 is near the center of the basket while cell #1 is on the outer corner. For cell #1, the maximum strain increased 40% from 5.77e-4 to 8.05e-4 and the number of cycles (summed for all beam elements in the model) increased at the higher strain levels (Figure 8.62). Since the response is different and strains are moderately higher, evaluation of different basket compartments is important but not computationally feasible for this task. For this reason, the use of bounding spectra to capture the response of all the basket locations will be beneficial to ensure that the worst-case basket loading has been accounted for.

USED FUEL DISPOSITION CAMPAIGN
Used Nuclear Fuel Loading and Structural Performance Under Normal Conditions of Transport -
Demonstration of Approach and Results of Used Fuel Performance Characterization
SEPTEMBER 30, 2013 237
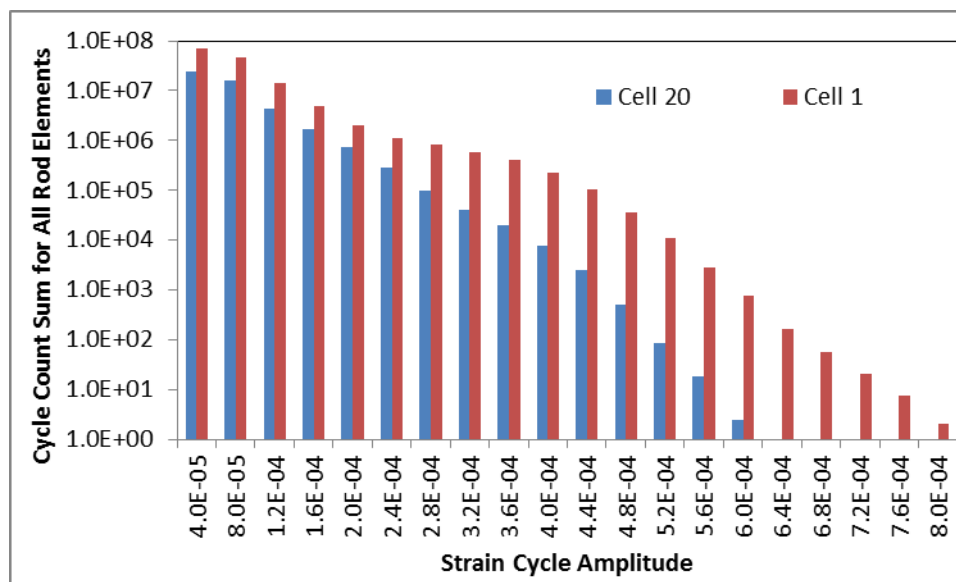
Figure 8.62. Cyclic Strain History for Basket Cells #1 and #20.

8.5.6 FUEL ROD LOCATION IN ASSEMBLY

For a given assembly, different rods within the assembly may inherently receive more loading due to interactions with the basket. Since the assembly submodel includes all of the fuel rods, every case can be evaluated to identify the fuel rod with the highest strains. The fuel rod with the highest cladding strain during the event as well as the fuel rod with the most severe fatigue cycling can be identified. It was expected and observed that the highest fuel rod bending loads occur in the spacer grids support locations. Regarding individual fuel rods that may be more susceptible to damage, analyses of the cases have not indicated any rods to clearly have higher damage. Based on the analysis of the lateral shock case, the maximum element strain was tabulated for each of the 264 fuel rods and plotted in a contour plot shown in Figure 8.63. There is not a clear distribution of the strains, but generally the rods with the lowest strains are within the center of the assembly. For this figure, the top of the plot corresponds to the bottom of the assembly resting on the basket floor, so the rods here may also tend to have lower strains since they can contact the basket for support to limit deflections. Certain rods may have more particular sensitivity to other load orientations though, so a more automated way to establish the rod strain/damage mapping will be pursued for evaluation of the different load cases.

USED FUEL DISPOSITION CAMPAIGN
Used Nuclear Fuel Loading and Structural Performance Under Normal Conditions of Transport -
Demonstration of Approach and Results of Used Fuel Performance Characterization
238   **SEPTEMBER 30, 2013**
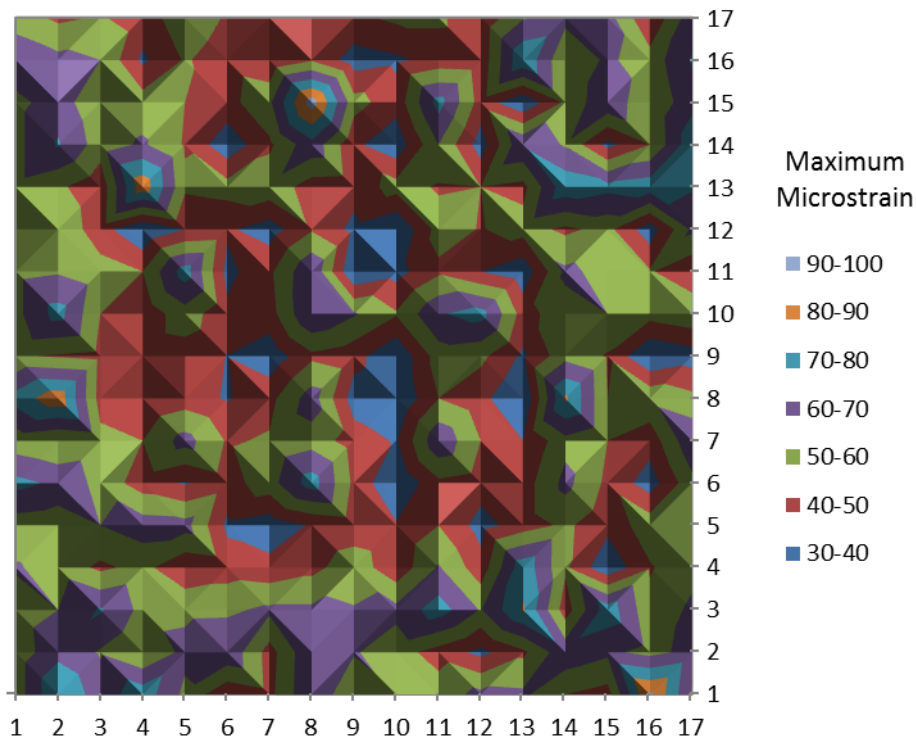
Figure 8.63. Maximum Cladding Strain Mapping for Each Fuel Rod in the 17×17 Assembly

8.5.7   TEMPERATURE DISTRIBUTION

The elastic modulus of the fuel assembly materials is temperature-dependent and generally decreases with temperature. Changes to the elastic moduli affect the local stiffness and vibration characteristics. The distribution of temperature throughout the cask also means that elastic properties will vary spatially. The effect of the temperature distribution and associated elastic material property changes was evaluated by considering the potential extreme hot and cold distributions. The hot case consists of an assembly at the center of the cask with temperatures of 550.07-641.4 K defined across 4 axial regions. The cold cases consist of an assembly at the periphery of the cask with temperatures of 302.26-322.17 K defined across 4 axial regions.

8.5.7.1   MODAL ANALYSES

Modal analyses were performed with the assembly submodel at each of the temperature cases, and the results are shown in Table 8.10. It should be noted that the effective beam stiffness for the fuel rod and the spacer grid springs do not include temperature effects, so this analysis is primarily testing the influence of temperature on the elastic MP of the grids and guide tubes. The effect of the temperature on the elastic moduli is small for the temperature range used here, so changes to the modal frequencies were correspondingly small with a difference of no more than 3%. Therefore, it expected that the dynamic mechanical response of the assembly is essentially

USED FUEL DISPOSITION CAMPAIGN
Used Nuclear Fuel Loading and Structural Performance Under Normal Conditions of Transport -
Demonstration of Approach and Results of Used Fuel Performance Characterization
SEPTEMBER 30, 2013   239

the same for this expected temperature range within the transport cask. This also suggests that a single surrogate assembly definition can be reasonably used for any location in the basket.

Table 8.10. Assembly Modal Results for Different Temperatures

Mode #	Participating Component	Shape	Frequency (Hz)					
			BE cold	BE hot	LB cold	LB hot	UB cold	UB hot
1	assembly	torsion	4.5	4.4	4.2	4.1	4.5	4.4
2/3	assembly	flexure	5.3	5.2	4.7	4.6	5.3	5.2
4	assembly	torsion	9.2	9.0	8.3	8.1	9.2	9.0
5/6	assembly	flexure	10.2	10.0	8.3	8.1	10.4	10.2
7	assembly	torsion	14.3	14.1	12.1	11.8	14.5	14.2
8/9	assembly	flexure	16.4	16.2	12.1	11.9	16.7	16.5
10	assembly	torsion	20.4	20.1	16.0	15.7	20.7	20.4
11/12	assembly	flexure	23.7	23.5	16.0	15.8	24.4	24.2
13	assembly	torsion	27.6	27.3	20.3	20.0	28.2	27.9
14/15	assembly	flexure	32.7	32.6	20.3	20.0	33.9	33.7
16	assembly	torsion	36.2	35.9	24.4	24.1	37.2	36.9
17/18	assembly	flexure	43.2	43.0	24.5	24.1	44.9	44.7
19	assembly	torsion	46.4	46.1	27.8	27.8	47.9	47.6
20+	fuel rod	flexure	48.8	48.7	27.9	27.9	50.5	50.5

8.5.7.2   TRANSIENT DYNAMIC ANALYSES

The assembly model with material properties for the hot and cold conditions was run with the P1 vertical shock loading case. The different temperature affects the elastic properties of the spacer grids, guide tubes, and upper/lower nozzles, but the properties of the fuel rods themselves remained the same with best estimate equivalent stiffness. Therefore, the surrounding support structure of the fuel rods is expected to become slightly stiffer (i.e., higher modulus) for the cold case. For the cold condition, the maximum strain increased only 21% from 5.77e-4 to 7.00e-4 and the total number of cycles (summed for all beam elements in the model) increased at the higher strain levels (Figure 8.64), but overall the effect on the response was small.
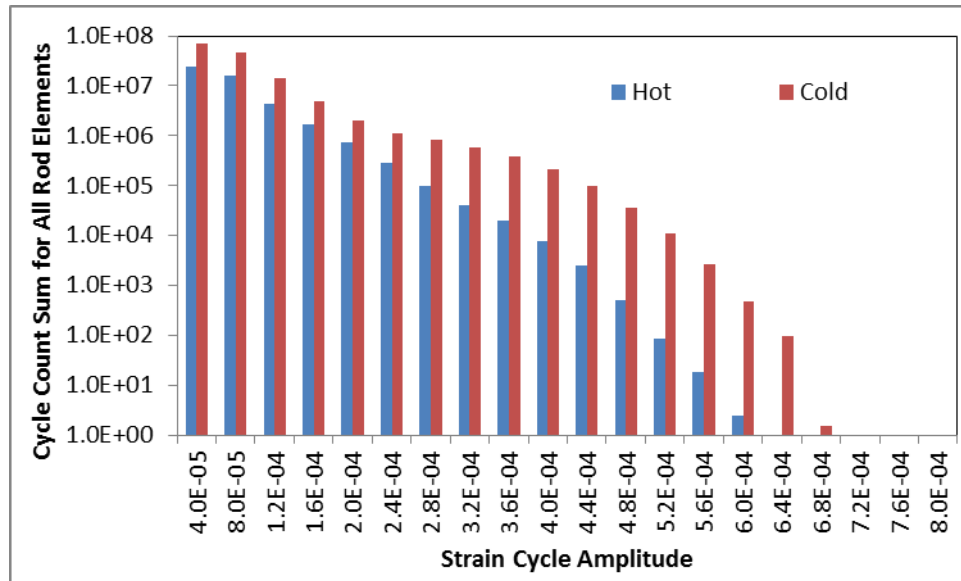
USED FUEL DISPOSITION CAMPAIGN
Used Nuclear Fuel Loading and Structural Performance Under Normal Conditions of Transport -
Demonstration of Approach and Results of Used Fuel Performance Characterization
240 **SEPTEMBER 30, 2013**

Figure 8.64. Cyclic Strain History at Hot and Cold Cask Conditions

8.5.8   IN-REACTOR FRETTING WEAR, PIN PRESSURE INFLUENCE, AND PELLET-TO-CLAD BONDING

The following sections discuss the detailed fuel rod stress concentration, MP, and FEMs and results.

8.5.8.1   DETAILED FUEL ROD STRESS CONCENTRATION MODEL

A FE sensitivity study is performed to understand the possible stress concentration in the cladding due to having a moment applied to a fuel rod containing fuel pellets that are not bonded to each other. The study is performed with nominal cladding and fuel pellet dimensions except the fuel pellet diameter which is expanded to make contact with the inside diameter of the cladding. The model includes two fuel pellets and cladding that is sufficiently long to contain them. The loading on the model is pure bending. Given that neighboring fuel pellets are not bonded, this loading causes the fuel pellets to spread slightly on the tensile side of the section. Along the length of the fuel pellets, the fuel pellets offer support to the clad. Where the gap occurs, a stress concentration occurs in the cladding.

Additionally, a sensitivity study is performed to address wear that can occur from in-reactor rubbing of a grid spacer dimple against the fuel rod. This sensitivity study uses the same model as described above except two wear marks are included in the model at 90 degrees from each other around the axis of the fuel rod. The wear marks are centered on the plane where the fuel pellets meet. They are 5.08 mm (0.2 in.) long with a maximum depth of 10% of the cladding thickness.   The shape of the wear marks is modeled using a cylindrically shaped cut

USED FUEL DISPOSITION CAMPAIGN
Used Nuclear Fuel Loading and Structural Performance Under Normal Conditions of Transport -
Demonstration of Approach and Results of Used Fuel Performance Characterization
SEPTEMBER 30, 2013   241

perpendicular to the axis of the fuel rod and producing the defined dimensions. The results of this study show how much the stress concentration is increased if a wear mark occurs where two disconnected fuel pellets meet.

The scope of the study includes two parts. The first part is the sensitivity study for the cladding stress concentration resulting from adjacent, unbounded fuel pellets with no cladding wear. The scope for this part includes evaluating two different coefficients of friction and two different axial support scenarios for the fuel pellets. The two coefficients of friction are 0 and 1.5. These two values are sufficient to establish a trend relative to what causes conservative results and further models could be run if necessary. The two axial support scenarios include not allowing and allowing the fuel pellets to move axially inside the cladding. When the bending load is applied, the fuel pellets only carry a compressive load where fuel pellets meet. This creates a load that tends to displace the pellets axially. Not allowing axial movement implies that neighboring fuel pellets are bonded to the cladding well enough to resist the axial loads. Allowing axial movement implies that axial movement is only suppressed by friction or cladding deformation. (It should be noted that model restraints are included to ensure that if the fuel pellets slide apart to where there is no compressive load between them, they will still remain touching at one point.) Inclusion of internal pressure in this sensitivity study is not expected to increase the stress concentration. However, the model described above with the highest stress concentration will be rerun with the inclusion of an expected internal pressure to ensure that the stress concentration is not increased. Additionally, considering that the stress concentrations produce highly localized stresses, a final run for the highest stress concentration model will be performed with a much finer mesh to ensure convergence.

The scope for the second part is the sensitivity study for the cladding stress concentration resulting from adjacent, unbounded fuel pellets with cladding wear. This sensitivity study is performed only on the scenario from the first part that produces the largest stress concentration. Two scenarios are run for this part which include without and with internal pressure.

In general, the study is intended to produce reasonable stress concentration results that error to the conservative side. Table 8.11 below lists all of the model runs used in the sensitivity study. Additional model runs were performed for validation and they are described in the body of the evaluation. All of the models were run as geometric nonlinear with no material plasticity.

USED FUEL DISPOSITION CAMPAIGN
Used Nuclear Fuel Loading and Structural Performance Under Normal Conditions of Transport -
Demonstration of Approach and Results of Used Fuel Performance Characterization
242   **SEPTEMBER 30, 2013**

Table 8.11. Sensitivity Study Models

Model Number	Coefficient of Friction	Fuel Pellets Axially Contained	Internal Pressure Included	Wear Included	Finer Meshed
1	0	yes	no	no	no
2	1.5	yes	no	no	no
3	0	no	no	no	no
4	1.5	no	no	no	no
5*	0	no	yes	no	no
6*	0	no	no	no	yes
7*	0	no	no	yes	no
8*	0	no	yes	yes	no
9*	0	no	no	yes	yes

* Model parameters selected based on the results of earlier models.

8.5.8.2 *FUEL ROD MATERIAL PROPERTIES, GEOMETRY, STRESS CONSIDERING NO STRESS CONCENTRATION, AND INTERNAL PRESSURE*

The fuel rod and fuel pellet MP used in this evaluation are the LB MP defined for the detailed fuel rod stiffness and damping model. The fuel rod and fuel pellet geometry used in this evaluation are same as defined for the detailed fuel rod stiffness and damping model except the pellet outer diameter is adjusted to fit the inner diameter of the fuel rod in this evaluation. These MP and relevant geometer are repeated below for information.

Additionally, the bending stress considering no stress concentration must be established as a reference for stress concentration. Given that the models are run with geometric nonlinearity, the selection of the applied moment can have some influence on the resulting stress concentration. In these models where the pellets resist ovalization of the cladding, these effects should be minimal. The selected moment (of 10^7 kg·mm^2/s^2) is relatively high but not high enough to induce material yielding. (The units were selected to produce scalar numbers that best produced contact convergence in the FE solver.)

Finally, there exists a potential for an internal pressure. The representative internal pressure is calculated below with the ideal gas law using data from Geelhood et al. (2013), page 18 and a temperature of 400°C. The material properties and geometry below are from values defined in Sections 6.3.1 and 6.3.2.

<u>Lower Bound Model Material Properties</u>

$T_{400} = 673.15$ K   Temperature at 400°C.

Clad Material Properties

$E_{z4sc} = 6.022 \times 10^7 \cdot \dfrac{kg \cdot mm}{s^2 \cdot mm^2}$ Modulus of elasticity.

$\nu_{z4sc} = 0.338$ Poisson's ratio.

$\rho_{z4} = 6.587 \times 10^{-6} \cdot \dfrac{kg}{mm^3}$ Mass density.

Fuel Material Properties

$E_{uosc} = 1.66 \times 10^8 \cdot \dfrac{kg \cdot mm}{s^2 \cdot mm^2}$ Modulus of elasticity.

$\nu_{uo} = 0.21$ Poisson's ratio.

$\rho_{uo} = 1.029 \times 10^{-5} \cdot \dfrac{kg}{mm^3}$ Mass density.

<u>Fuel Rod and Fuel Pellet Geometry</u>

$d_{co} = 9.144$ mm   Outside diameter of the cladding.

$t_c = 0.5715$ mm   Thickness of the cladding.

$d_{ci} = 8.001$ mm   Inside diameter of the cladding.

$A_c = 15.39$ mm^2 Cross sectional area of the cladding.

$I_c = 142.0$ mm^4 Area moment of inertia for the cladding.

$L_p = 12.879$ mm   Length of the fuel pellet.

$2 \cdot L_p = 25.758$ mm   Length of the cladding for this evaluation.

USED FUEL DISPOSITION CAMPAIGN
Used Nuclear Fuel Loading and Structural Performance Under Normal Conditions of Transport -
Demonstration of Approach and Results of Used Fuel Performance Characterization
244   **SEPTEMBER 30, 2013**

Fuel Rod Stress Considering No Stress Concentration

$$M_{sc} := 10^7 \cdot kg \cdot \frac{mm^2}{s^2}$$

Moment applied to the cladding.

$$\sigma_{sc} := \frac{M_{sc} \cdot \frac{d_{co}}{2}}{I_c}$$

Cladding bending stress.

$$\sigma_{sc} = 3.219 \times 10^5 \cdot \frac{kg \cdot mm}{s^2 \cdot mm^2} \qquad \sigma_{sc} = 3.219 \times 10^5 \cdot kPa \qquad (\sigma_{sc} = 4.669 \times 10^4 \cdot psi)$$

Fuel Rod Internal Pressure

Ideal gas law: $p \cdot V = n \cdot R \cdot T$

$$T_{c400} := 673.15 \cdot K$$

Temperature at 400°C.

$$R_c := 8.314 \cdot \frac{J}{K \cdot mol}$$

Universal gas constant.

$$n_c := 0.02 \cdot mol$$

Number of moles (from Geelhood et al. (2013), p. 18).

$$V_c := 10.94 \cdot cm^3$$

Total void volume (from Geelhood et al. (2013), p. 18).

$$p_c := \frac{n_c \cdot R_c \cdot T_{c400}}{V_c}$$

Cladding internal pressure.

$$p_c = 1.023 \times 10^4 \cdot \frac{kg \cdot mm}{s^2 \cdot mm^2} \qquad p_c = 1.023 \times 10^4 \cdot kPa \qquad (p_c = 1.484 \times 10^3 \cdot psi)$$

USED FUEL DISPOSITION CAMPAIGN
Used Nuclear Fuel Loading and Structural Performance Under Normal Conditions of Transport -
Demonstration of Approach and Results of Used Fuel Performance Characterization
SEPTEMBER 30, 2013   **245**

8.5.8.3 *FUEL ROD FINITE ELEMENT MODELING AND RESULTS FOR MODEL 1*

Model 1 for the fuel rod consists of cladding, two fuel pellets, and two rigid surfaces (see Figure 8.65 and Figure 8.66). It is run with a coefficient of friction of 0 and the fuel pellets are axially constrained with the rigid surfaces.

Figure 8.65 shows the full mesh and a cut-away of the mesh for model 1. Figure 8.66 shows the cladding elements, the elements for a single fuel pellet, and the elements for the rigid surfaces. The cladding elements are solid linear brick elements that are enhanced by incompatible modes (C3D8I Abaqus). The fuel elements are fully integrated solid linear brick elements (C3D8 Abaqus). The rigid surfaces are three-dimensional rigid elements (R3D4 Abaqus) with reference points at their centers.

USED FUEL DISPOSITION CAMPAIGN
Used Nuclear Fuel Loading and Structural Performance Under Normal Conditions of Transport -
Demonstration of Approach and Results of Used Fuel Performance Characterization
246 **SEPTEMBER 30, 2013**
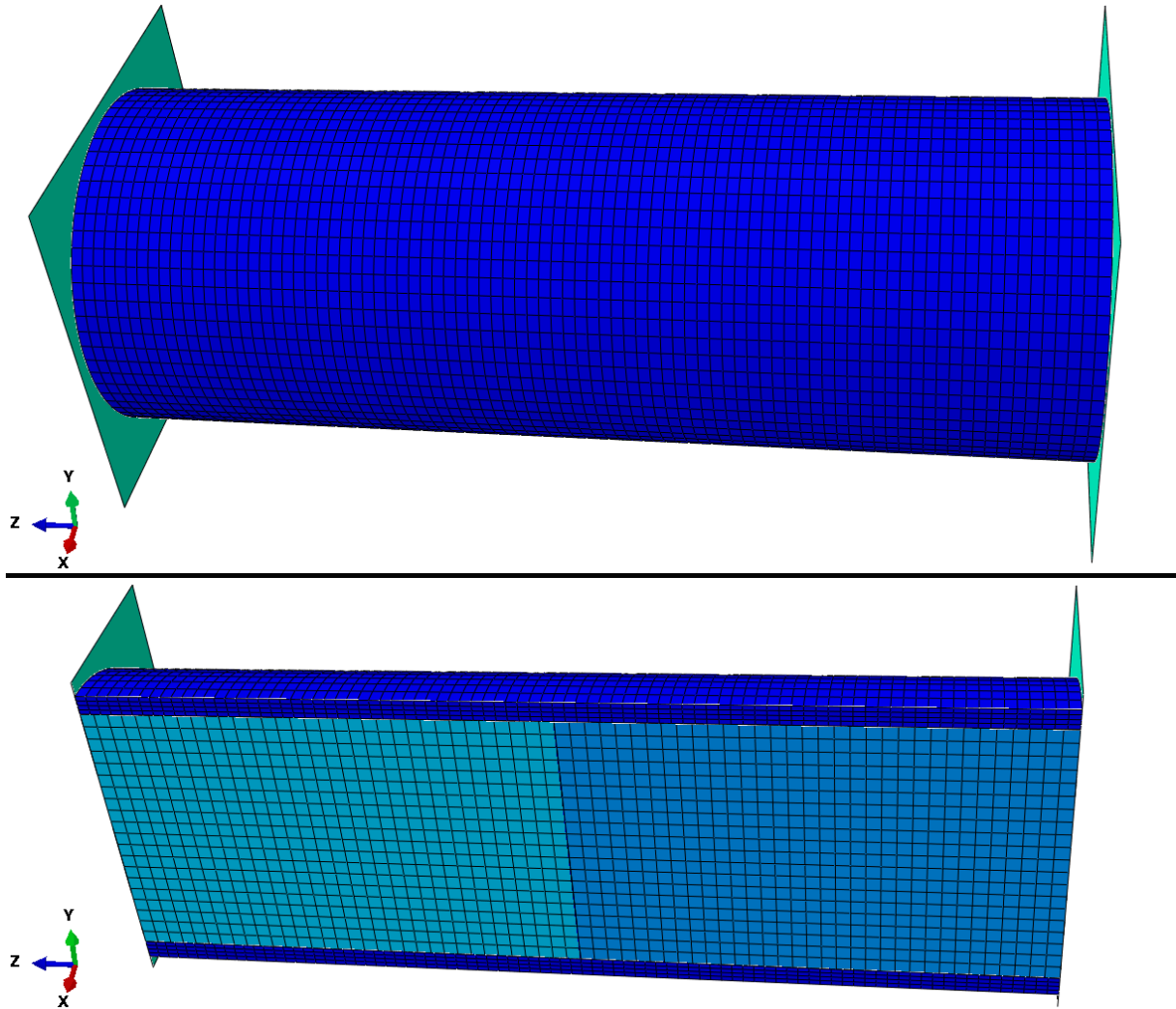
Figure 8.65. Model 1 Full Mesh and Cut-Away Mesh

USED FUEL DISPOSITION CAMPAIGN
**Used Nuclear Fuel Loading and Structural Performance Under Normal Conditions of Transport -
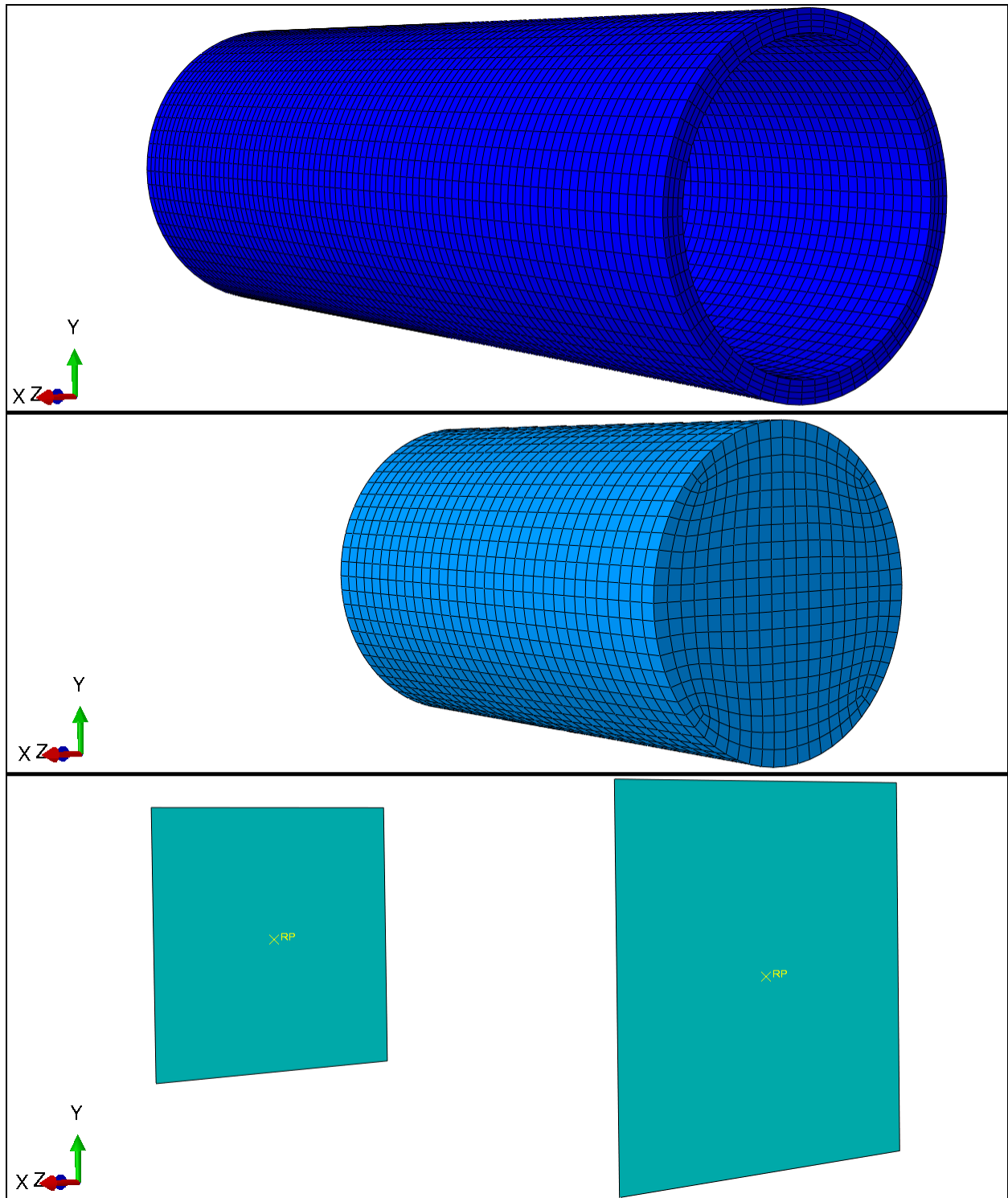Demonstration of Approach and Results of Used Fuel Performance Characterization
SEPTEMBER 30, 2013** 247

Figure 8.66. Model 1 Cladding Elements (Top), Fuel Pellet Elements (Middle), and Rigid
Surface Elements (Bottom)

USED FUEL DISPOSITION CAMPAIGN
Used Nuclear Fuel Loading and Structural Performance Under Normal Conditions of Transport -
Demonstration of Approach and Results of Used Fuel Performance Characterization
248 **SEPTEMBER 30, 2013**

To load and/or restrain the ends of the cladding, couplings are added to the ends of the cladding (see Figure 8.67). Each coupling has a reference point at the center of the cladding cross section. This reference point is where the given load and/or restraint is applied. The loads are transferred to the cross section with a continuum distributing coupling. To ensure that the fuel pellets do not move axially, rigid surfaces are added. The rigid surfaces also have reference nodes that share the locations of the coupling reference nodes. The reference node of each surface is tied to the reference node of the respective coupling. The rigid surfaces then move with the cladding cross section and only contact the fuel pellets.

The coupling in the most negative z-direction has a fixed restraint applied to it. The coupling in the most positive z-direction has a 10^7 kg·mm^2/s^2 moment applied to it in the positive x-direction.
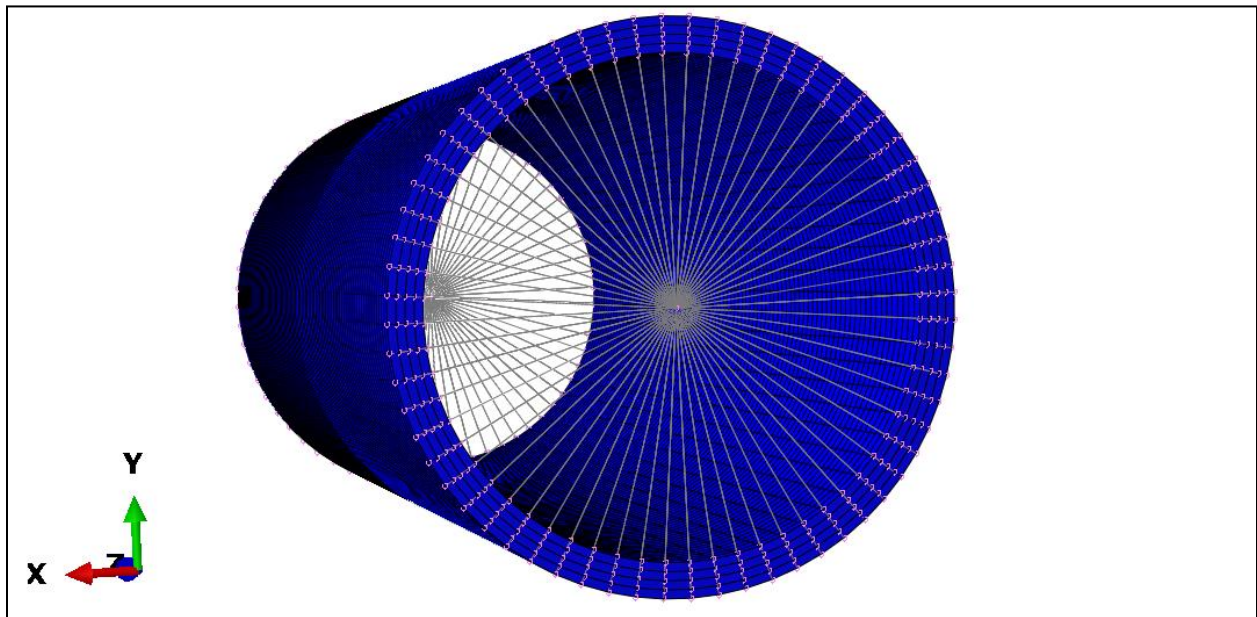
Figure 8.67. Model 1 Cladding Elements with Couplings Shown at the Ends

The stress results for model 1 are shown in Figure 8.68. The three plots include a cut-away of the full model with the overall maximum stress identified, a top view of the cladding only with the cladding high stress identified, and a bottom view of the cladding only.

USED FUEL DISPOSITION CAMPAIGN
Used Nuclear Fuel Loading and Structural Performance Under Normal Conditions of Transport -
Demonstration of Approach and Results of Used Fuel Performance Characterization
SEPTEMBER 30, 2013   249

Figure 8.68. Full Model Cut-Away, Cladding Top, and Cladding Bottom Model 1 Stress Results

USED FUEL DISPOSITION CAMPAIGN
Used Nuclear Fuel Loading and Structural Performance Under Normal Conditions of Transport -
Demonstration of Approach and Results of Used Fuel Performance Characterization
250   **SEPTEMBER 30, 2013**

8.5.8.4   FUEL ROD FINITE ELEMENT MODELING AND RESULTS FOR MODEL 2

Model 2 for the fuel rod consists of cladding, two fuel pellets, and two rigid surfaces. It differs from model 1 only in coefficient of friction. The model 2 coefficient is friction 1.5.

The stress results for model 2 are shown in Figure 8.69. The three plots include a cut-away of the full model with the overall maximum stress identified, a top view of the cladding only with the cladding high stress identified, and a bottom view of the cladding only.
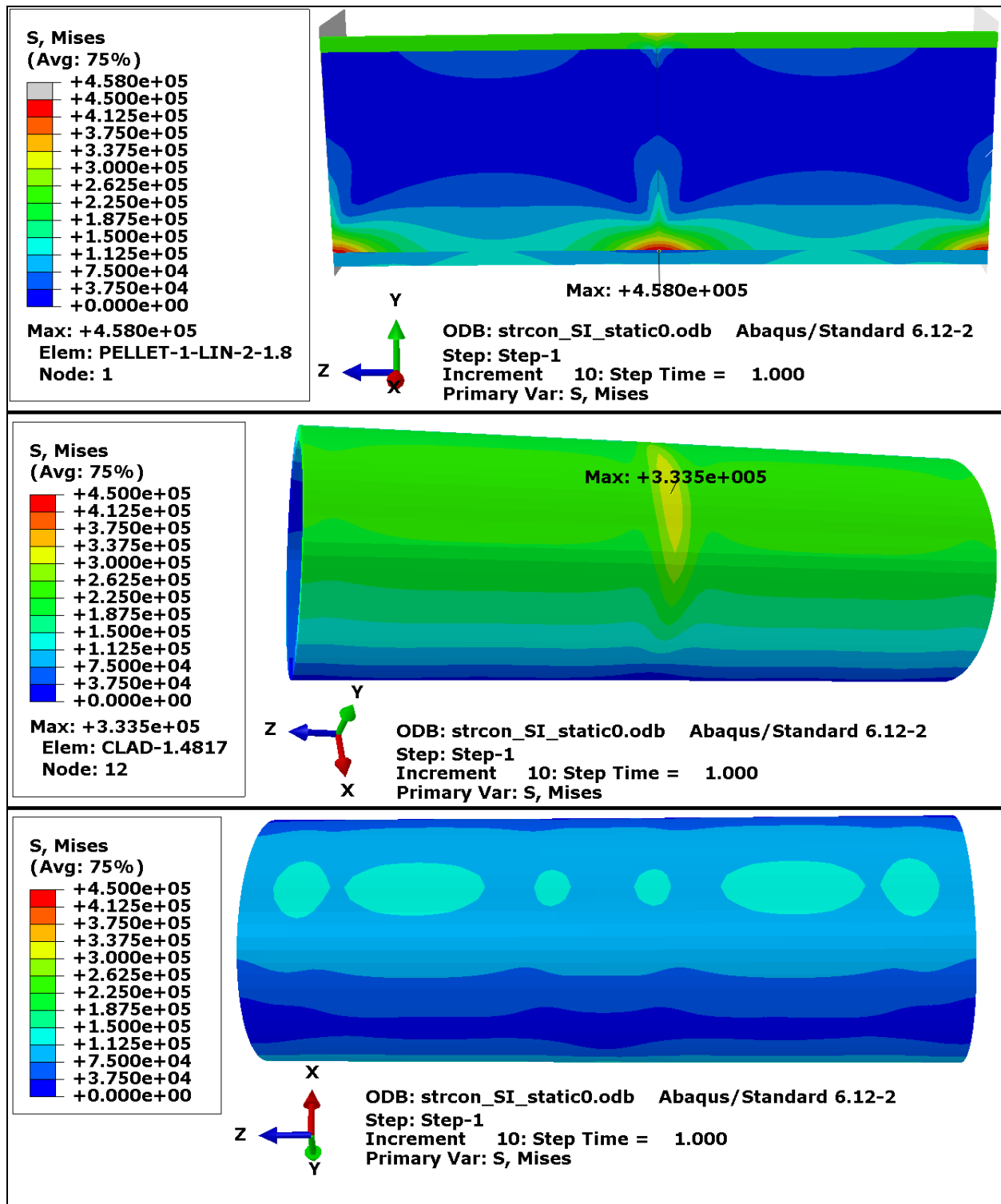
USED FUEL DISPOSITION CAMPAIGN
Used Nuclear Fuel Loading and Structural Performance Under Normal Conditions of Transport -
Demonstration of Approach and Results of Used Fuel Performance Characterization
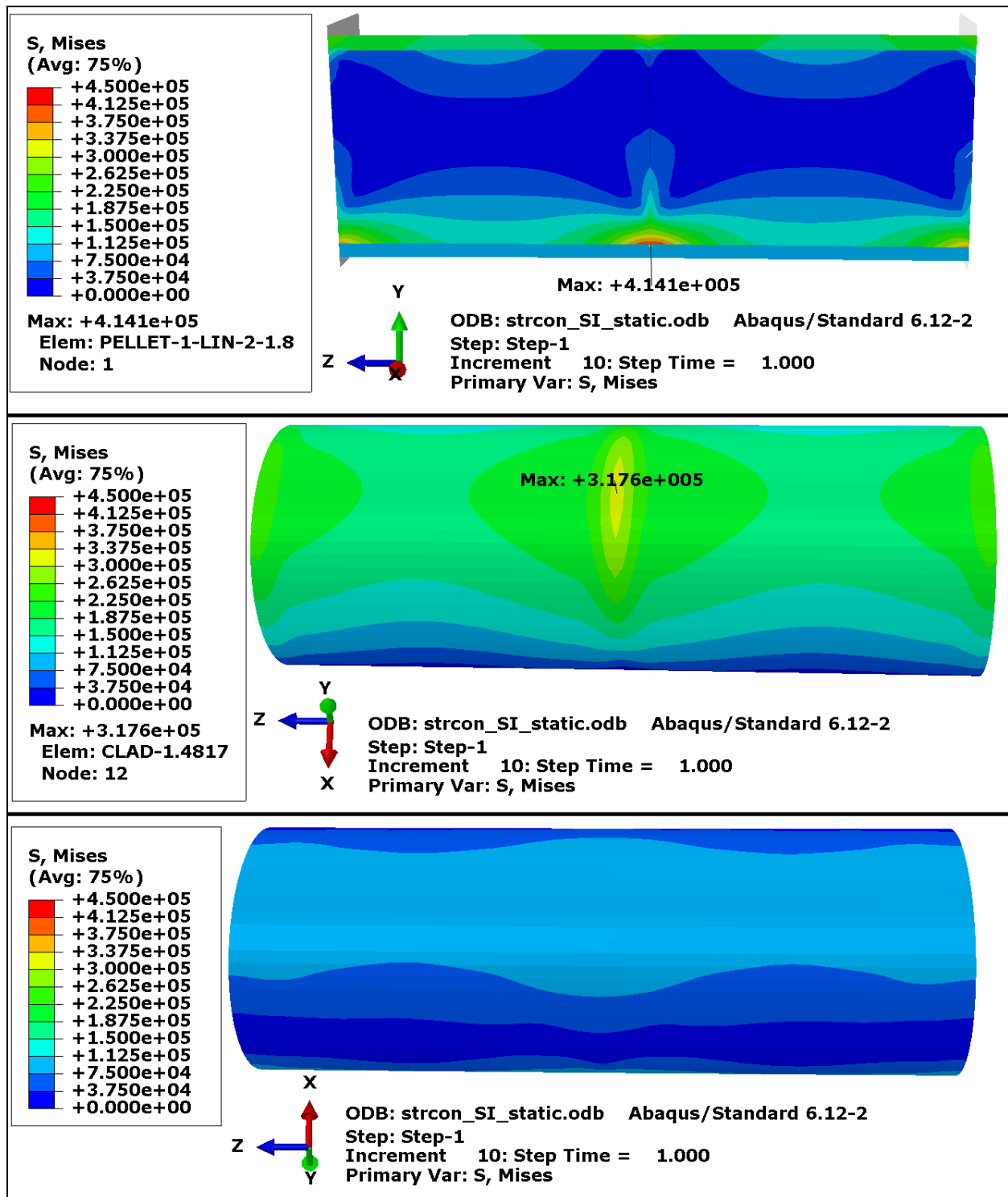SEPTEMBER 30, 2013   251

Figure 8.69. Full Model Cut-Away, Cladding Top, and Cladding Bottom Model 2 Stress Results

USED FUEL DISPOSITION CAMPAIGN
Used Nuclear Fuel Loading and Structural Performance Under Normal Conditions of Transport -
Demonstration of Approach and Results of Used Fuel Performance Characterization
252   **SEPTEMBER 30, 2013**

8.5.8.5   *FUEL ROD FINITE ELEMENT MODELING AND RESULTS FOR MODEL 3*

Model 3 for the fuel rod consists of cladding and two fuel pellets (see Figure 8.70). It is run with a coefficient of friction of 0 and the fuel pellets are not axially constrained.

Figure 8.70 shows the full mesh and a cut-away of the mesh for model 3. The cladding and fuel pellet meshes are the same as those for model 1 (shown in Figure 8.66). However, there are no rigid surfaces in model 3.
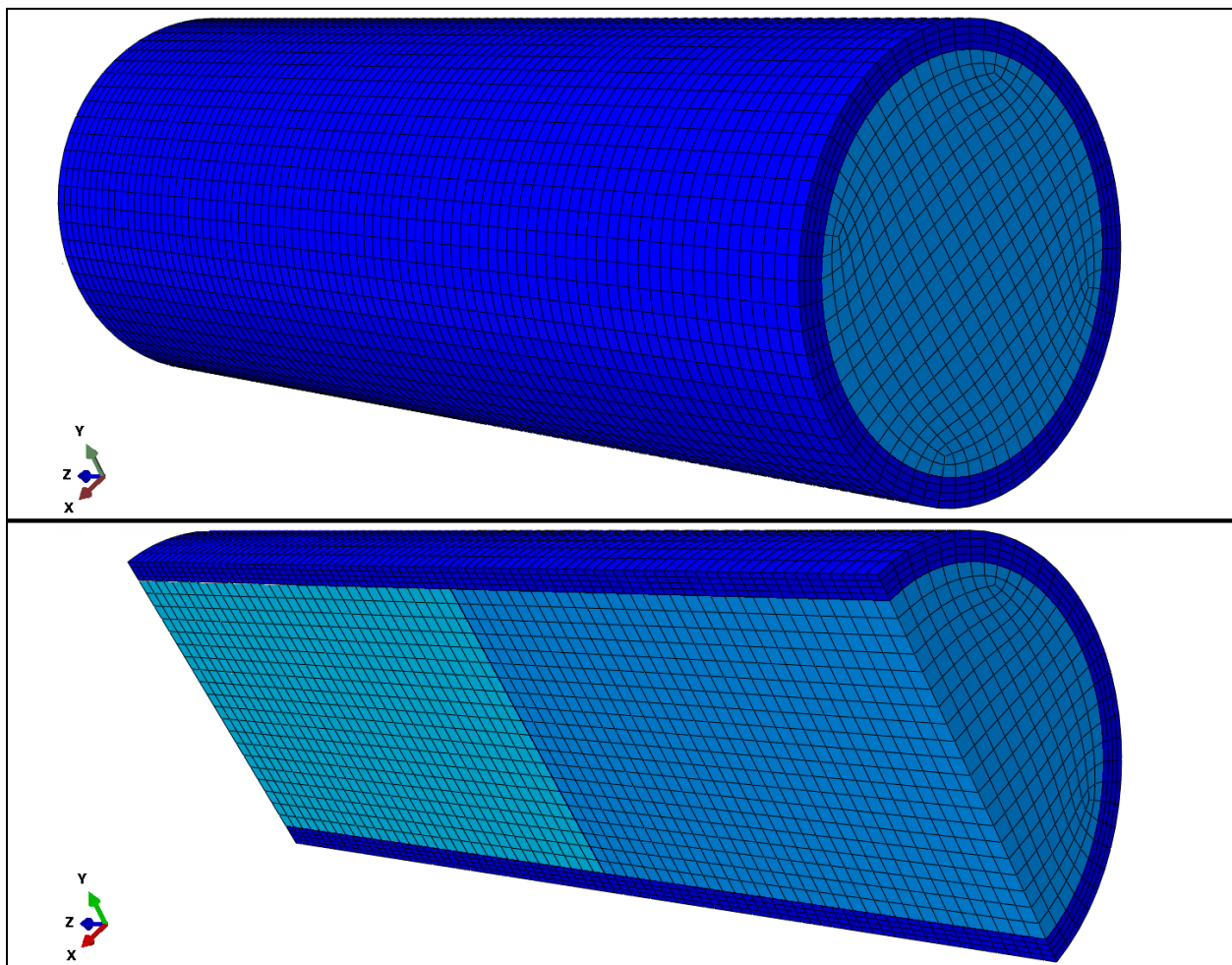

Figure 8.70. Full Mesh and Cut-Away Mesh for Model 3

To load and/or restrain the ends of the cladding, couplings are added to the ends of the cladding similar to those in model 1 (see Figure 8.71). Each coupling has a reference point at the center of the cladding cross section. For the fuel rod loading in this model, the coupling in the most

USED FUEL DISPOSITION CAMPAIGN
Used Nuclear Fuel Loading and Structural Performance Under Normal Conditions of Transport -
Demonstration of Approach and Results of Used Fuel Performance Characterization
SEPTEMBER 30, 2013 **253**

negative z-direction has a 10^7 kg·mm^2/s^2 moment applied to it in the negative x-direction. The coupling in the most positive z-direction has a 10^7 kg·mm^2/s^2 moment applied to it in the positive x-direction. For the fuel rod restraints, the coupling in the most negative z-direction is fixed in x- and y-translation and y- and z-rotation. The plane running through the center of the cladding has translation fixed in the z-direction. These cladding restraints are not intended to carry any load. Instead, they are used to make a stable model run. For the fuel pellet restraints, a z-translational restraint is applied to the two pellet nodes where contact can always exist without adversely affecting the model results. These fuel pellet restraints are not intended to carry a significant load and are needed to create a stable model.
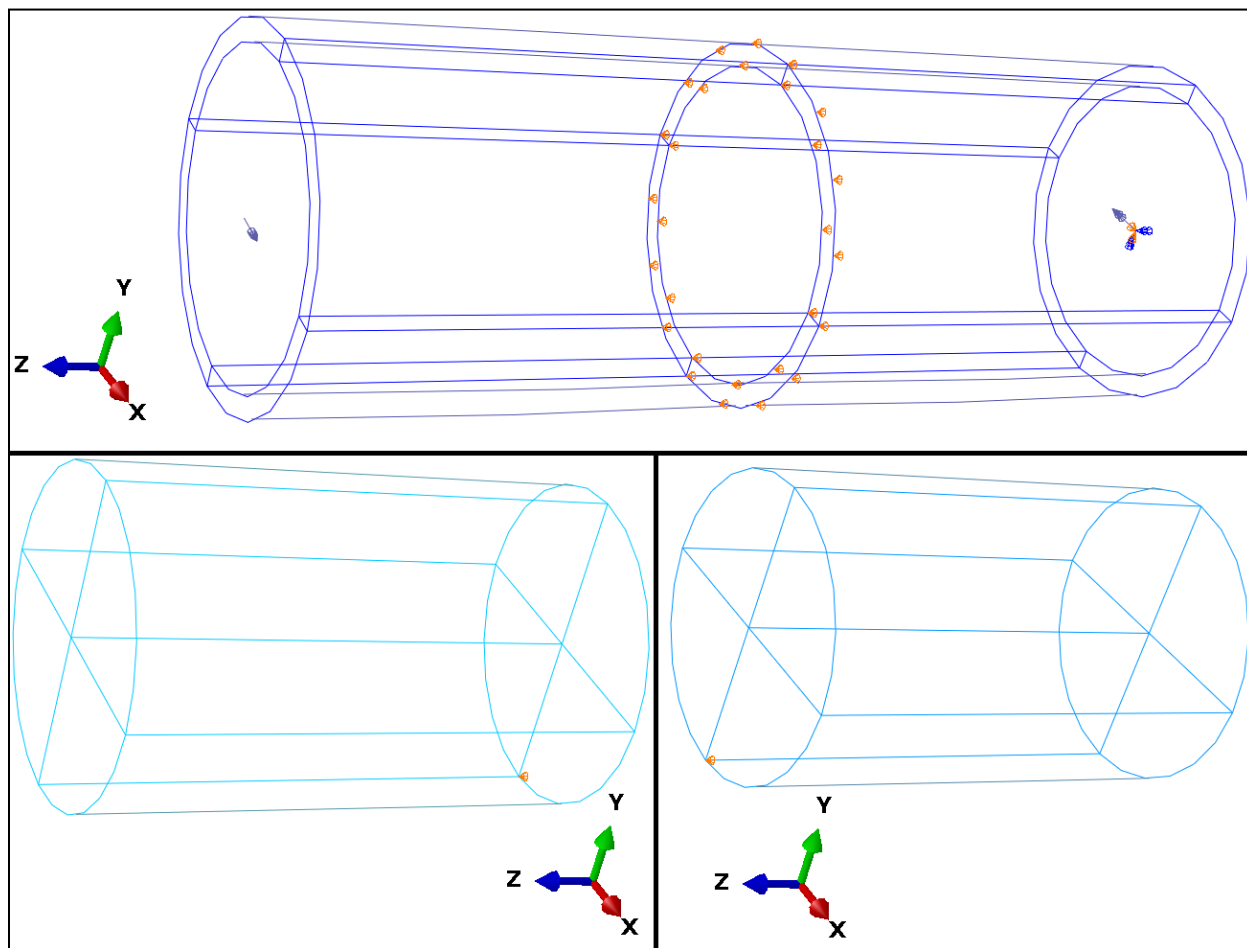

Figure 8.71. Model 3 Restraints and Loads

The stress results for model 3 are shown in Figure 8.72. The three plots include a cut-away of the full model with the overall maximum stress identified, a top view of the cladding only with the cladding high stress identified, and a bottom view of the cladding only.

USED FUEL DISPOSITION CAMPAIGN
Used Nuclear Fuel Loading and Structural Performance Under Normal Conditions of Transport -
Demonstration of Approach and Results of Used Fuel Performance Characterization
254   SEPTEMBER 30, 2013

Figure 8.72. Full Model Cut-Away, Cladding Top, and Cladding Bottom Model 3 Stress Results

USED FUEL DISPOSITION CAMPAIGN
Used Nuclear Fuel Loading and Structural Performance Under Normal Conditions of Transport -
Demonstration of Approach and Results of Used Fuel Performance Characterization
SEPTEMBER 30, 2013 **255**

8.5.8.6   *FUEL ROD FINITE ELEMENT MODELING AND RESULTS FOR MODEL 4*

Model 4 for the fuel rod consists of cladding and two fuel pellets. It differs from model 3 only in coefficient of friction. The model 4 coefficient is friction 1.5.

The stress results for model 4 are shown in Figure 8.73. The three plots include a cut-away of the full model with the overall maximum stress identified, a top view of the cladding only with the cladding high stress identified, and a bottom view of the cladding only.
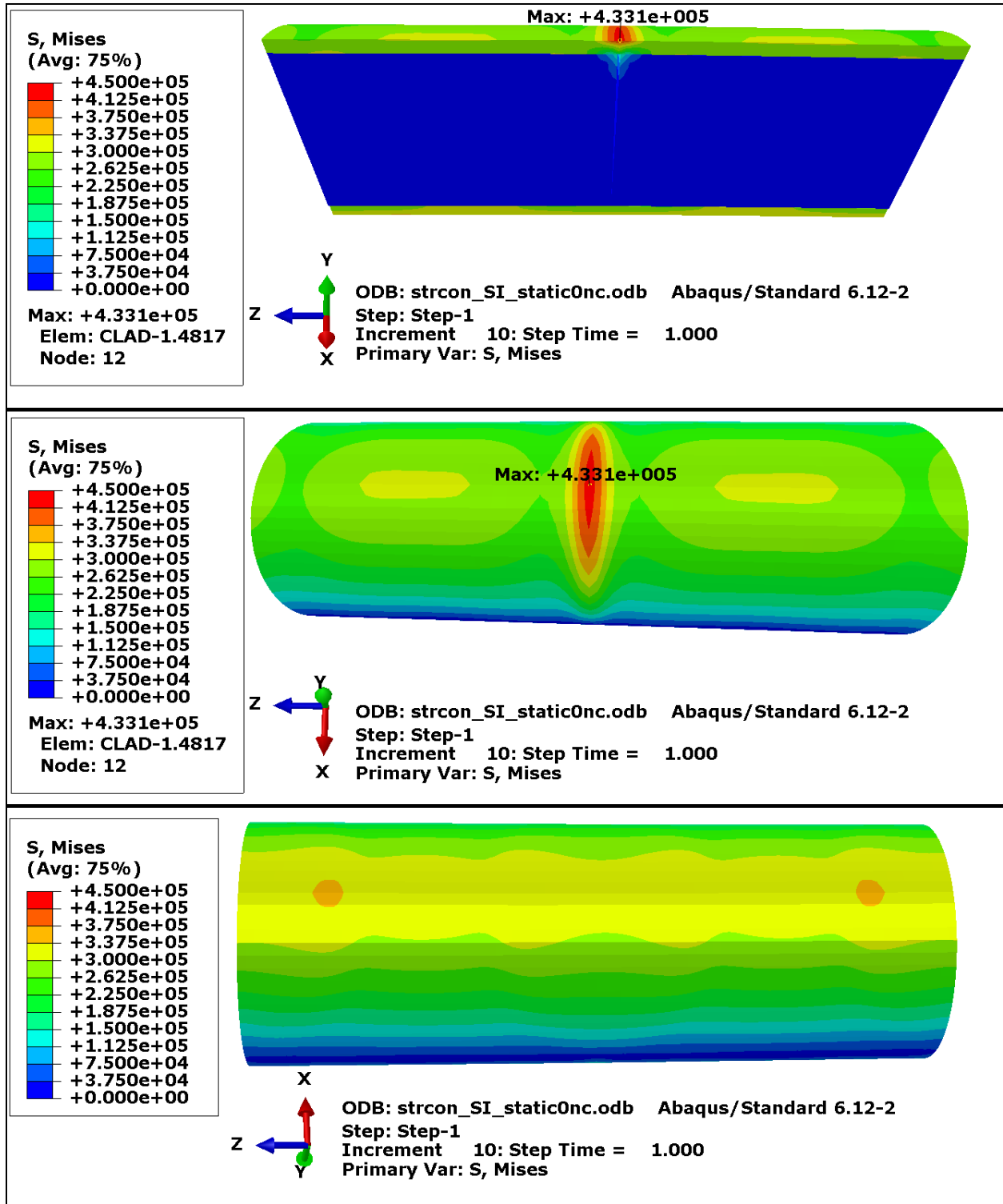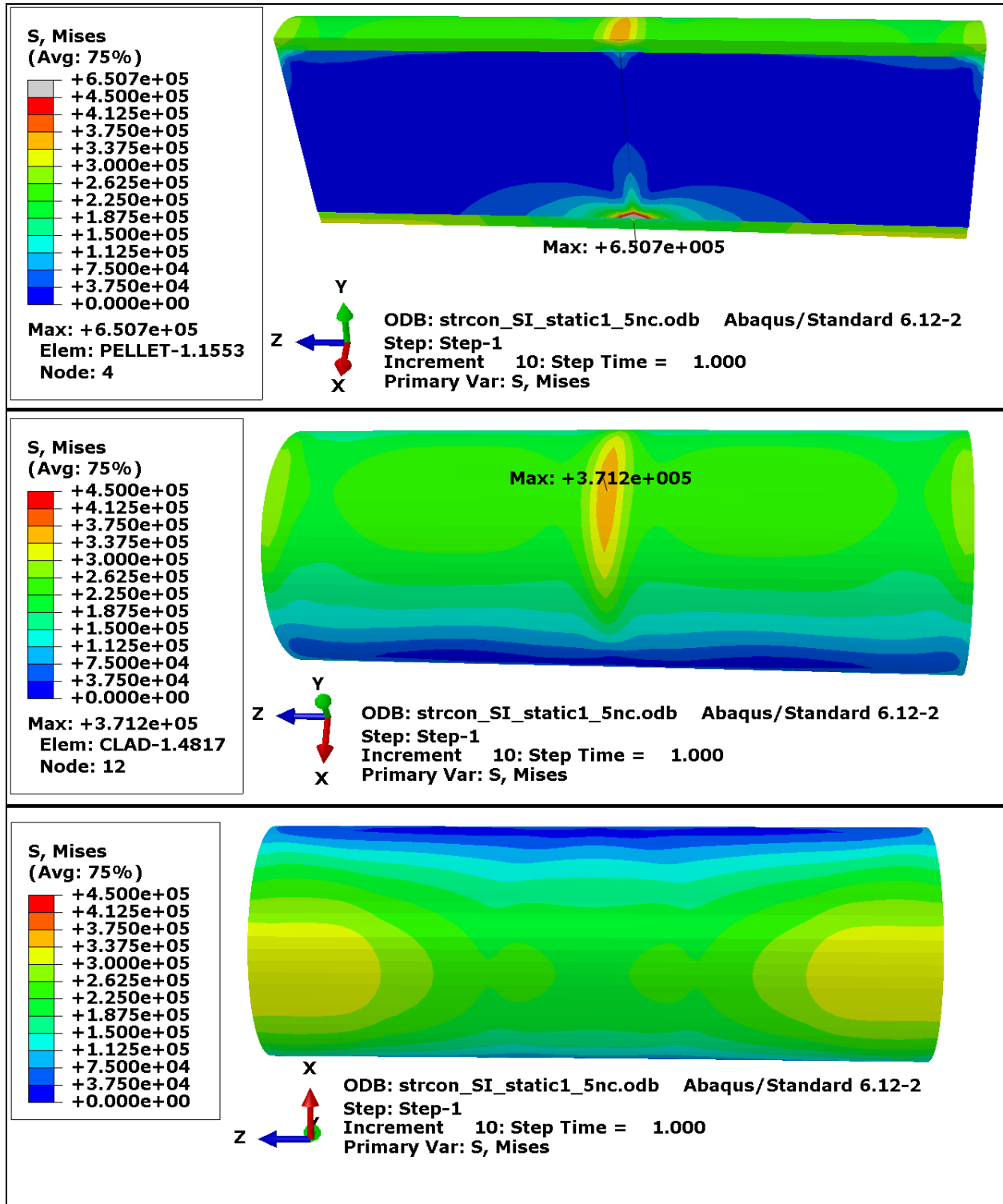
USED FUEL DISPOSITION CAMPAIGN
Used Nuclear Fuel Loading and Structural Performance Under Normal Conditions of Transport -
Demonstration of Approach and Results of Used Fuel Performance Characterization
256   SEPTEMBER 30, 2013

Figure 8.73. Full Model Cut-Away, Cladding Top, and Cladding Bottom Model 4 Stress Results

USED FUEL DISPOSITION CAMPAIGN
Used Nuclear Fuel Loading and Structural Performance Under Normal Conditions of Transport -
Demonstration of Approach and Results of Used Fuel Performance Characterization
SEPTEMBER 30, 2013 257

8.5.8.7   FUEL ROD FINITE ELEMENT MODELING AND RESULTS FOR MODEL 5

Considering models 1 – 4, the highest stress concentration occurred in model 3. Consequently, model 5 is the same as model 3 except model 5 has an internal pressure (of $1.023 \cdot 10^4$ kPa) on the cladding. (This pressure is calculated in Section 8.5.8.2.)

The stress results for model 5 are shown in Figure 8.74. The three plots include a cut-away of the full model with the overall maximum stress identified, a top view of the cladding only with the cladding high stress in the stress concentration region identified, and a bottom view of the cladding only with the cladding high stress identified.
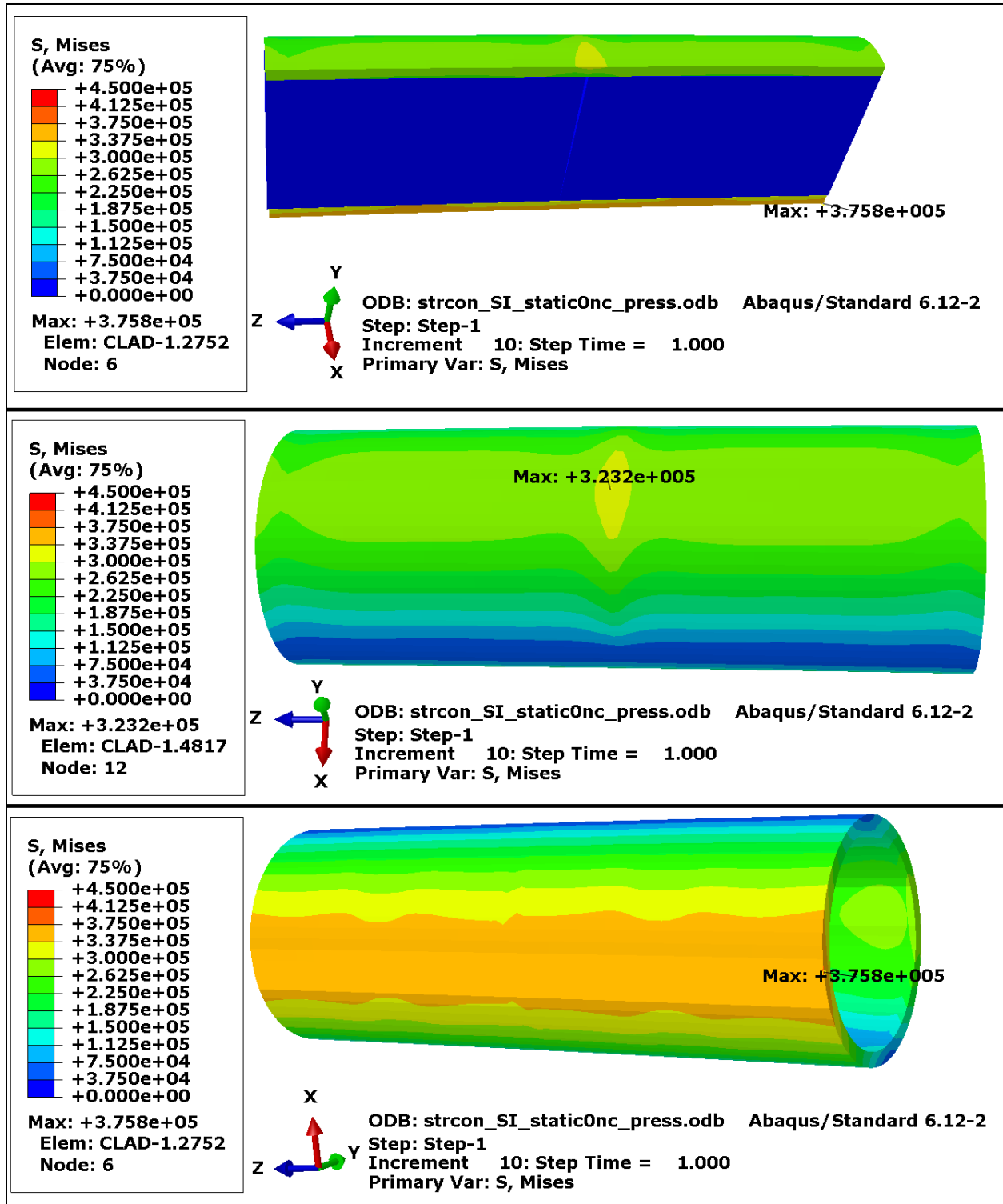
USED FUEL DISPOSITION CAMPAIGN
**Used Nuclear Fuel Loading and Structural Performance Under Normal Conditions of Transport -
Demonstration of Approach and Results of Used Fuel Performance Characterization**
258   **SEPTEMBER 30, 2013**

Figure 8.74. Full Model Cut-Away, Cladding Top, and Cladding Bottom Model 5 Stress Results

USED FUEL DISPOSITION CAMPAIGN
Used Nuclear Fuel Loading and Structural Performance Under Normal Conditions of Transport -
Demonstration of Approach and Results of Used Fuel Performance Characterization
SEPTEMBER 30, 2013 **259**

8.5.8.8   *FUEL ROD FINITE ELEMENT MODELING AND RESULTS FOR MODEL 6*

Considering models 1 – 5, the highest stress concentration occurred in model 3. Given that the stress concentration causes a large stress gradient in a small area, model 6 is run with a finer mesh to check convergence. Consequently, model 6 is the same as model 3 except the mesh density has been doubled in every direction. Figure 8.75 shows how the cladding and fuel pellets have been meshed for model 6.
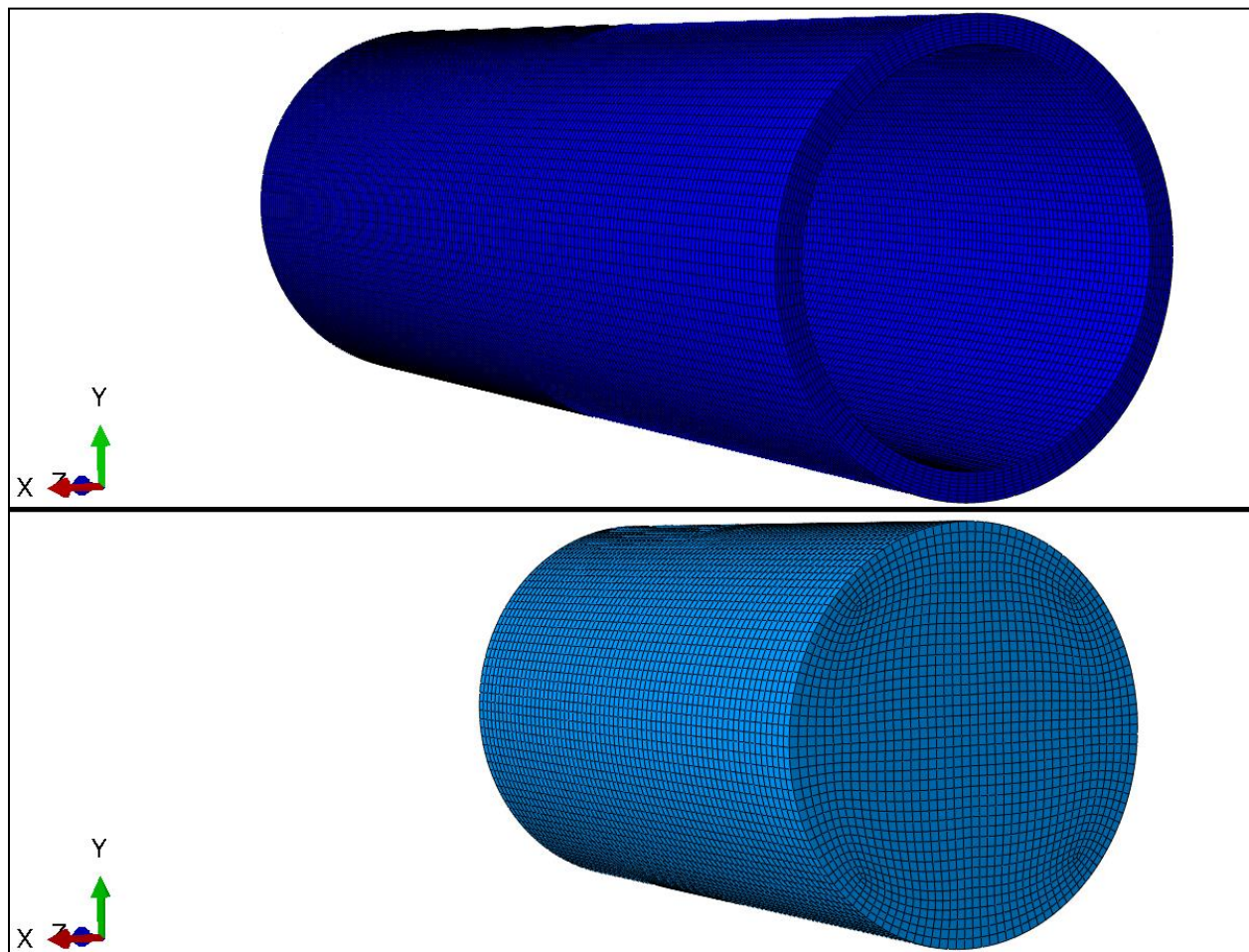

Figure 8.75. Model 6 Cladding Elements (Top) and Fuel Pellet Elements (Bottom)

The stress results for model 6 are shown in Figure 8.76. The three plots include a cut-away of the full model with the overall maximum stress identified, a top view of the cladding only with the cladding high stress identified, and a bottom view of the cladding only. As can be seen in the comparison of the results, the stress only increased by about 2 %, consequently further refinement is not necessary.
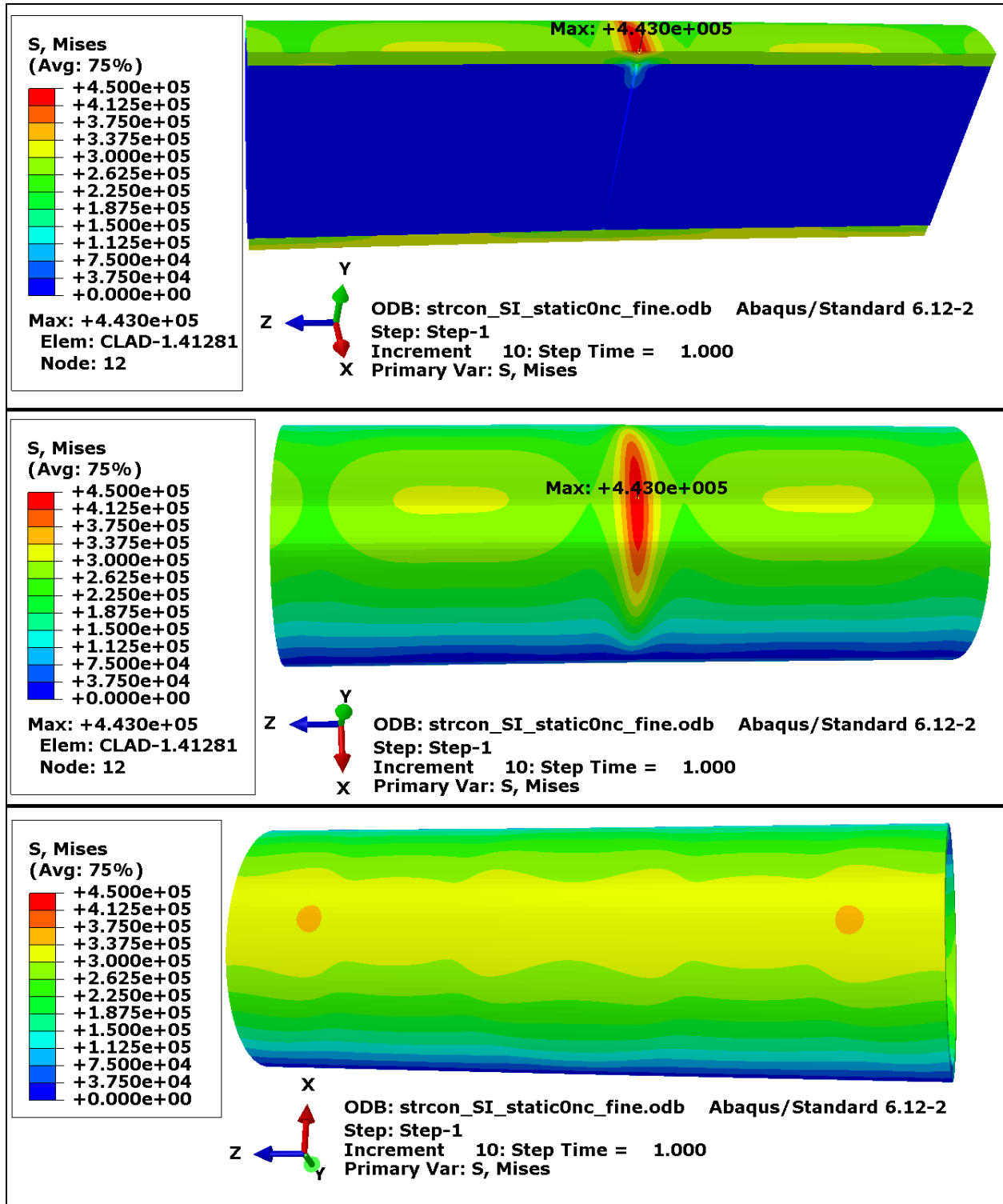
USED FUEL DISPOSITION CAMPAIGN
Used Nuclear Fuel Loading and Structural Performance Under Normal Conditions of Transport -
Demonstration of Approach and Results of Used Fuel Performance Characterization
260   SEPTEMBER 30, 2013

Figure 8.76. Full Model Cut-Away, Cladding Top, and Cladding Bottom Model 6 Stress Results

USED FUEL DISPOSITION CAMPAIGN
Used Nuclear Fuel Loading and Structural Performance Under Normal Conditions of Transport -
Demonstration of Approach and Results of Used Fuel Performance Characterization
SEPTEMBER 30, 2013 **261**

8.5.8.9   *FUEL ROD FINITE ELEMENT MODELING AND RESULTS FOR MODEL 7*

Considering models 1 – 4, the highest stress concentration occurred in model 3. Consequently, model 7 will be the same as model 3 except two wear marks are included on the cladding mesh at 90 degrees from each other around the axis of the fuel rod. As shown in Figure 8.77, the wear marks are centered on the plane where the fuel pellets meet. They are 5.08 mm (0.2 in.) long with a maximum depth of 10% of the cladding thickness. The shape of the wear marks is modeled using a cylindrically shaped cut perpendicular to the axis of the fuel rod and producing the defined dimensions.
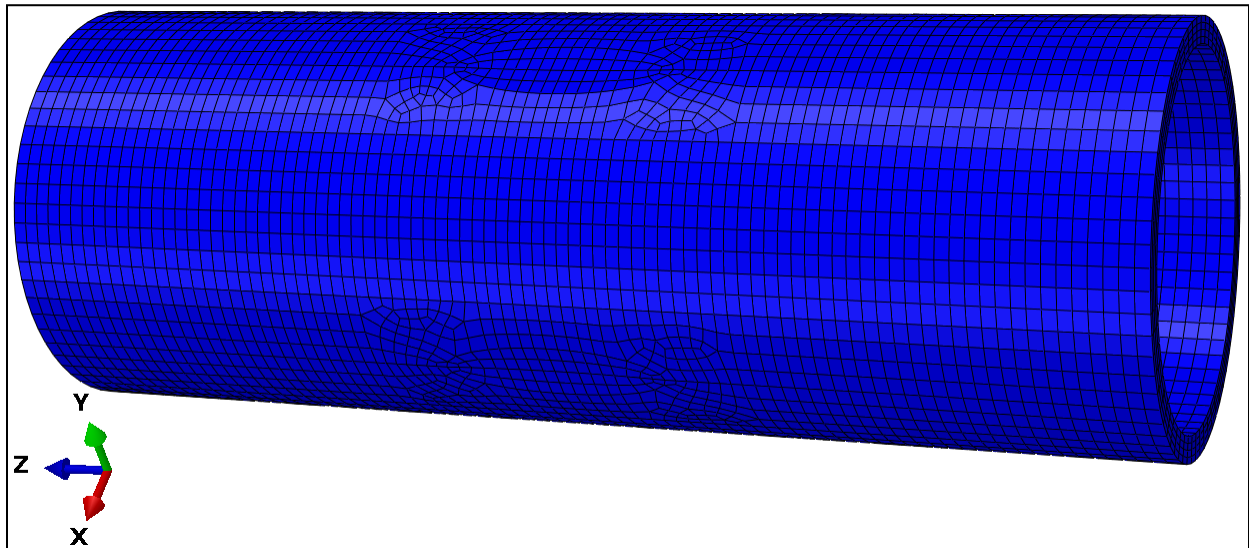

Figure 8.77. Model 7 Cladding Elements

The stress results for model 7 are shown in Figure 8.78. The three plots include a cut-away of the full model with the overall maximum stress identified, a top view of the cladding only with the cladding high stress identified, and a bottom view of the cladding only.
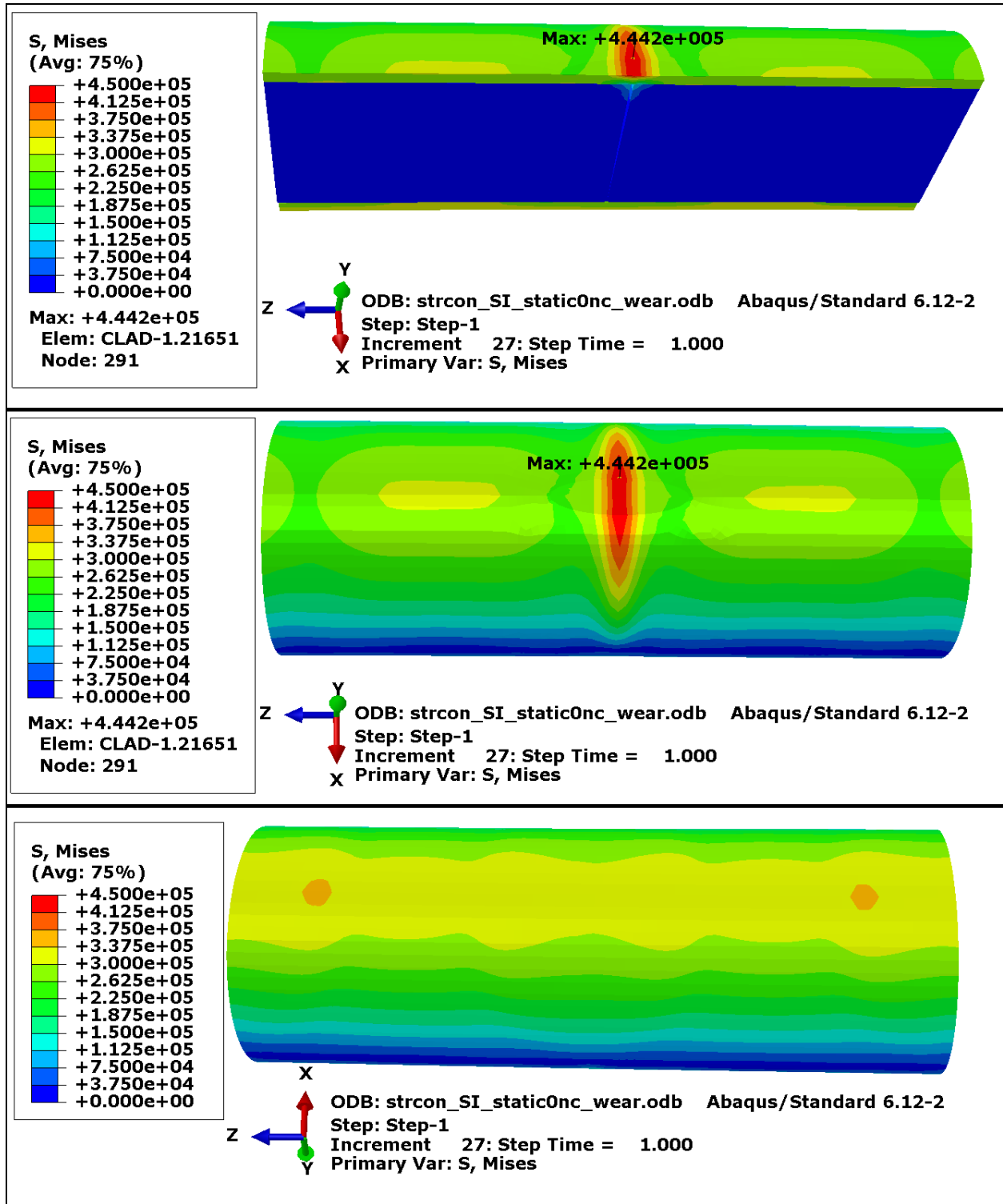
USED FUEL DISPOSITION CAMPAIGN
Used Nuclear Fuel Loading and Structural Performance Under Normal Conditions of Transport -
Demonstration of Approach and Results of Used Fuel Performance Characterization
262   SEPTEMBER 30, 2013

Figure 8.78. Full Model Cut-Away, Cladding Top, and Cladding Bottom Model 7 Stress Results

USED FUEL DISPOSITION CAMPAIGN
Used Nuclear Fuel Loading and Structural Performance Under Normal Conditions of Transport -
Demonstration of Approach and Results of Used Fuel Performance Characterization
SEPTEMBER 30, 2013 **263**

8.5.8.10 FUEL ROD FINITE ELEMENT MODELING AND RESULTS FOR MODEL 8

Model 8 is the same as model 7 except model 8 has an internal pressure (of $1.023 \cdot 10^4$ kPa) on the cladding. (This pressure is calculated in Section 8.5.8.2.)

The stress results for model 8 are shown in Figure 8.79. The three plots include a cut-away of the full model with the overall maximum stress identified, a top view of the cladding only with the cladding high stress in the stress concentration region identified, and a bottom view of the cladding only with the cladding high stress identified.
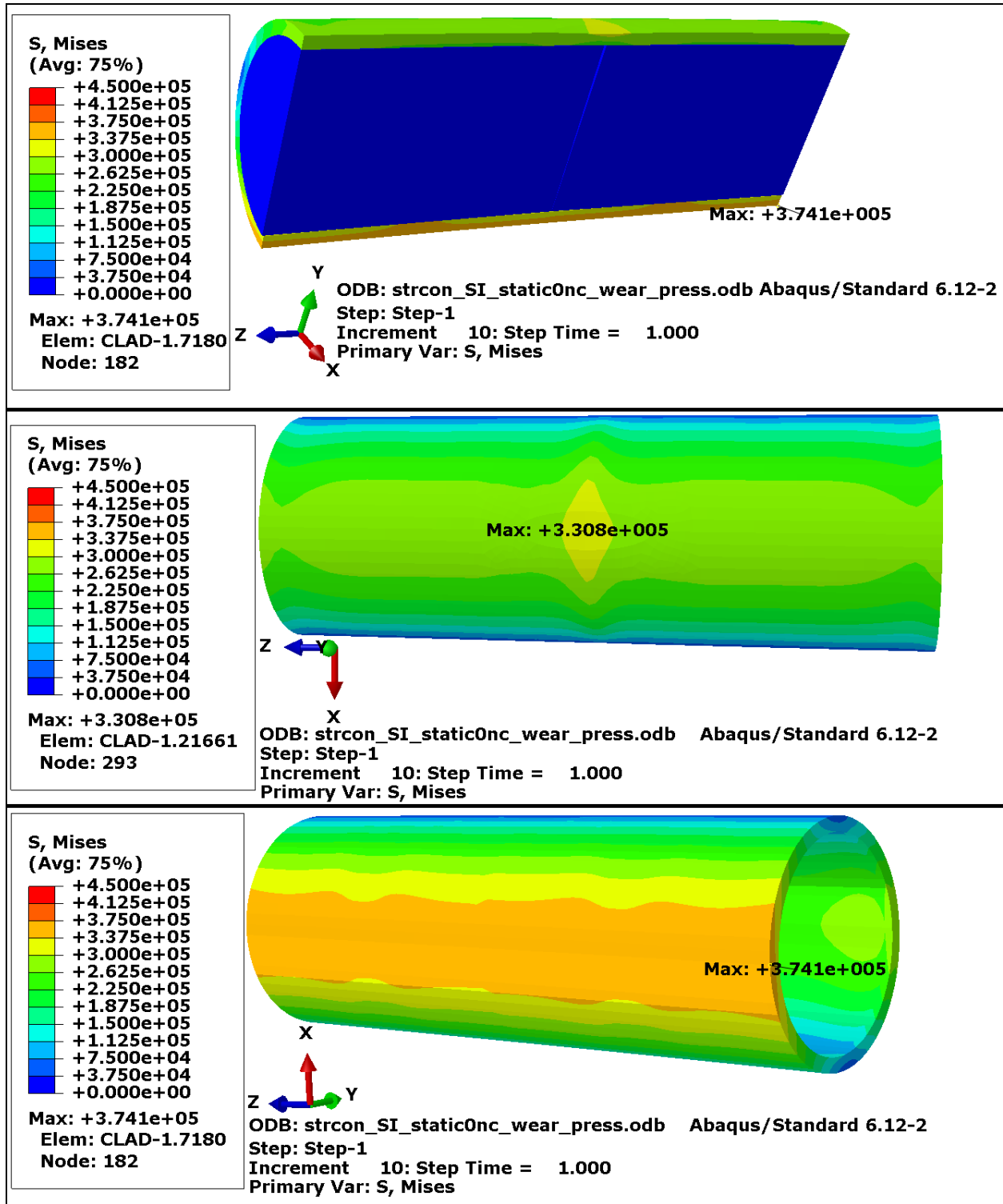
USED FUEL DISPOSITION CAMPAIGN
Used Nuclear Fuel Loading and Structural Performance Under Normal Conditions of Transport -
Demonstration of Approach and Results of Used Fuel Performance Characterization
264   SEPTEMBER 30, 2013

Figure 8.79. Full Model Cut-Away, Cladding Top, and Cladding Bottom Model 8 Stress Results

USED FUEL DISPOSITION CAMPAIGN
Used Nuclear Fuel Loading and Structural Performance Under Normal Conditions of Transport -
Demonstration of Approach and Results of Used Fuel Performance Characterization
SEPTEMBER 30, 2013 265

8.5.8.11   *FUEL ROD FINITE ELEMENT MODELING AND RESULTS FOR MODEL 9*

Similar to model 6 being a fine meshed version of model 3, model 9 is a fine meshed version of model 7. Model 7 is meshed finer because model 7 has higher stresses than model 8 and model 7 has more stress concentration than model 3.

The fuel pellets in model 9 are meshed that same as in model 6. The cladding mesh is shown in Figure 8.80. Otherwise, the model run is just like model 7.
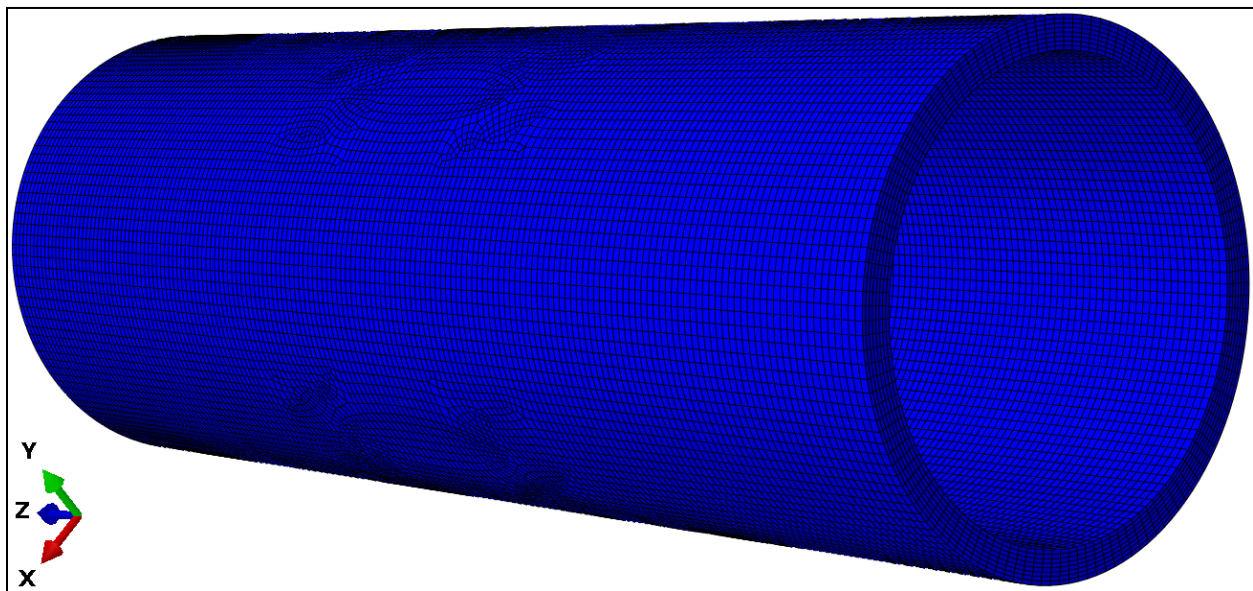
Figure 8.80. Model 9 Cladding Elements

The stress results for model 9 are shown in Figure 8.81. The three plots include a cut-away of the full model with the overall maximum stress identified, a top view of the cladding only with the cladding high stress identified, and a bottom view of the cladding only. As can be seen in the comparison of the results, the stress only increased by about 2 %, consequently further refinement is not necessary.
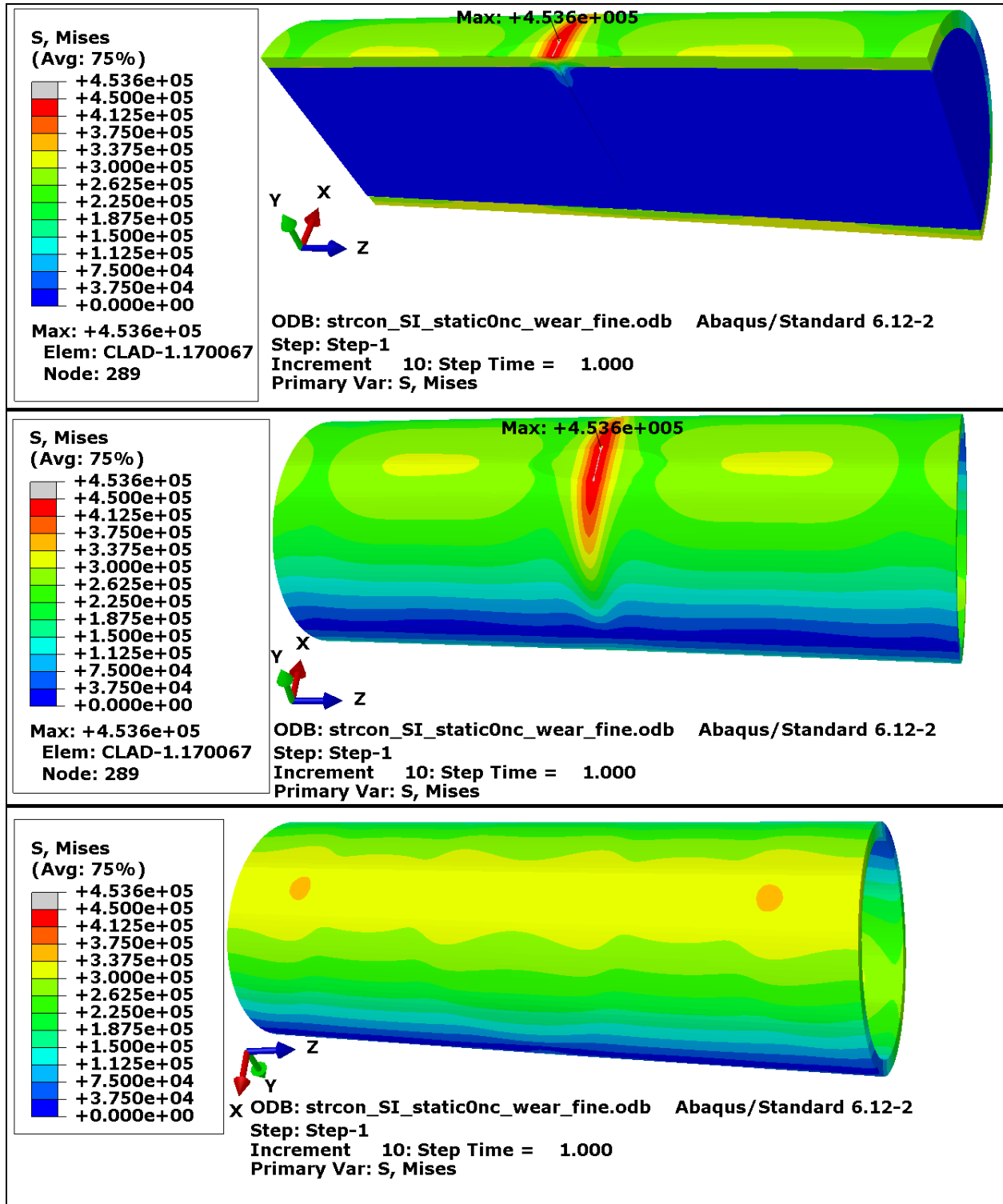
USED FUEL DISPOSITION CAMPAIGN
Used Nuclear Fuel Loading and Structural Performance Under Normal Conditions of Transport -
Demonstration of Approach and Results of Used Fuel Performance Characterization
266   SEPTEMBER 30, 2013

Figure 8.81. Full Model Cut-Away, Cladding Top, and Cladding Bottom Model 9 Stress Results

USED FUEL DISPOSITION CAMPAIGN
**Used Nuclear Fuel Loading and Structural Performance Under Normal Conditions of Transport -
Demonstration of Approach and Results of Used Fuel Performance Characterization
SEPTEMBER 30, 2013** 267

8.5.8.12   SUMMARY OF RESULTS

Table 8.12 below shows a summary of results for the sensitivity study. The bending stress in the cladding without stress concentration is $3.219 \cdot 10^4$ kPa (as calculated in Section 8.5.8.2.) Consequently, the stress concentration column of Table 8.12 is the percent stress increase (or decrease if it is negative) above this bending stress value for the stress concentration region on top of the cladding. (It is possible for the stress concentration values to be lower than the bending stress in the cladding without stress concentration. This is because the bending stress in the cladding without stress concentration only considers the cladding, whereas in the models it is possible for the fuel pellets to carry a significant portion of the load.)

Table 8.12. Sensitivity Study Model Stress Concentration Results

Model Number	Coefficient of Friction	Fuel Pellets Axially Contained	Internal Pressure Included	Wear Included	Finer Meshed	Stress Difference
1	0	yes	no	no	no	3.6 %
2	1.5	yes	no	no	no	-1.3 %
3	0	no	no	no	no	34.5 %
4	1.5	no	no	no	no	15.3 %
5*	0	no	yes	no	no	0.4 %
6*	0	no	no	no	yes	37.6 %
7*	0	no	no	yes	no	38.0 %
8*	0	no	yes	yes	no	2.8 %
9*	0	no	no	yes	yes	40.9 %

* Model parameters selected based on the results of earlier models.

Based on Table 8.12, the highest nominal dimensions stress concentration is 38.0 % and the highest stress concentration including wear is 40.9 %. These should be conservative values as they are based on a frictionless assumption along with no axial fuel pellet restraint.

The bottom (compressive side) of the fuel rod models shows minimal stress concentration in general.

8.5.8.13   VALIDATION PROBLEM

To help demonstrate that the models provide as accurate stress concentration a validation problem was developed. The validation problem is a uniformly loaded simply supported beam where 34 pellets are modeled inside cladding. There is no friction and essentially no axial

USED FUEL DISPOSITION CAMPAIGN
Used Nuclear Fuel Loading and Structural Performance Under Normal Conditions of Transport -
Demonstration of Approach and Results of Used Fuel Performance Characterization
268   **SEPTEMBER 30, 2013**

restraint. (Given that complete lack of axial restraint makes an unstable model, some minimal guidance was provided.)

Figure 8.82 shows the full mesh and a cut-away of the mesh for the simply supported beam. The mesh density and pellet and clad interaction are similar to that in model 3. The basic loading for this model is a uniform gravitational load of $67420 \cdot mm/s^2$. For the basic restraints, there are couplings at either end of the cladding (similar to those shown in Figure 8.67). The basic restraints include x- and y-translation on both couplings and z-rotation in addition on the coupling in the most negative z location. The x- and z-restraints are added for model stability and not intended to carry load. Additional cladding restraints for model stability are (similar to model 3 shown in Figure 8.71) z-translational restraints on the cross section in the center of the cladding. Additional pellet restraints added for stability include an x-translational restraint on the vertical cross section through the axis of the pellets. This prevents unnecessary rotation of the pellets. Also, the 17th pellet in the positive z-direction from the end of the cladding has a single z-translational restraint on its uppermost point which is the compressive side of the bending moment (similar to that for one fuel pellet in model 3 as shown in Figure 8.71). This ensures that the pellets remain in place. Finally for stability, there is a positive z-direction $1 \cdot mm/s^2$ acceleration load applied to pellets 1-17 (moving in the positive z-direction) and a negative z-direction $1 \cdot mm/s^2$ acceleration load applied to pellets 18-34 (moving in the positive z-direction).

USED FUEL DISPOSITION CAMPAIGN
Used Nuclear Fuel Loading and Structural Performance Under Normal Conditions of Transport -
Demonstration of Approach and Results of Used Fuel Performance Characterization
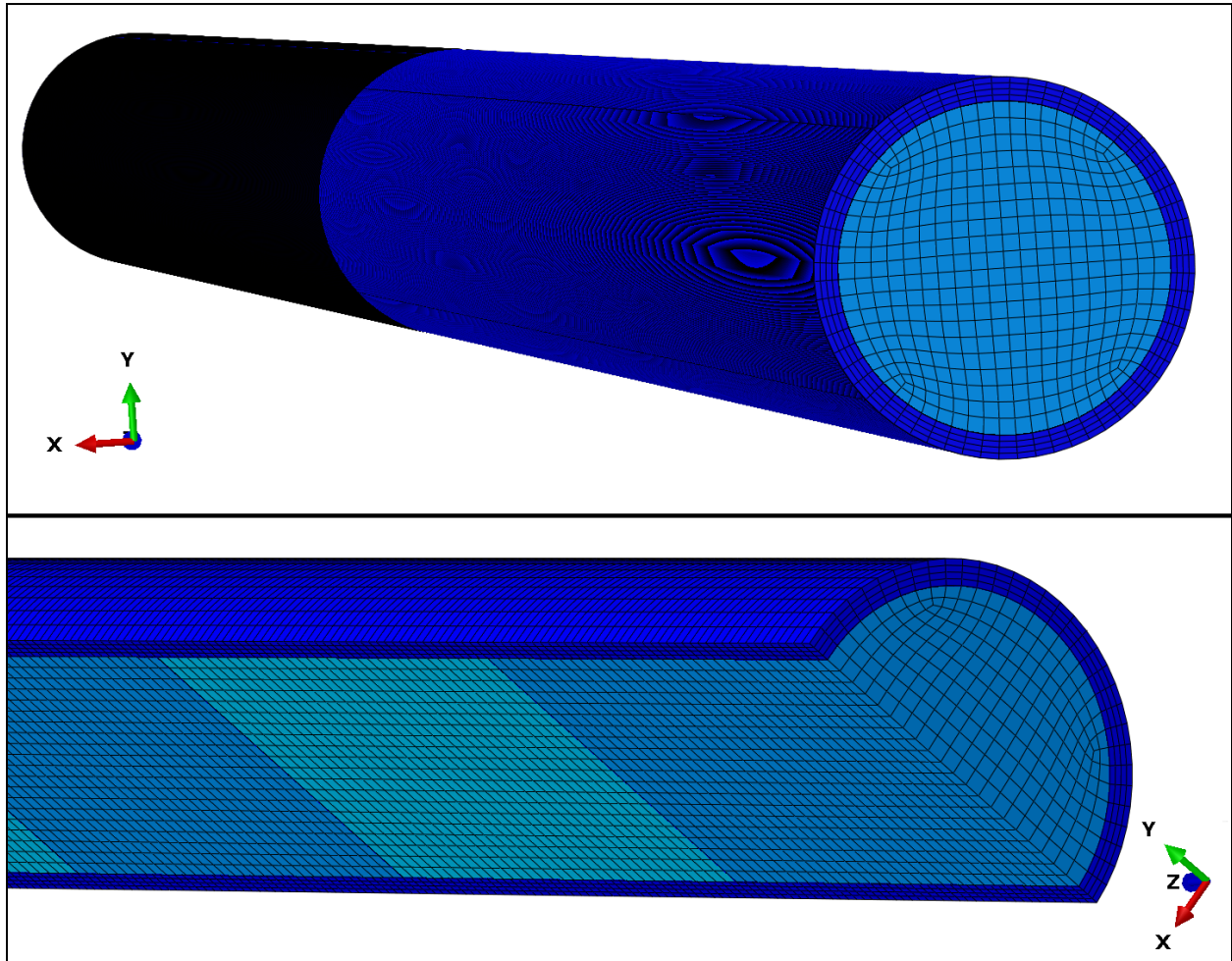**SEPTEMBER 30, 2013** 269

Figure 8.82. Full Mesh and Cut-Away Mesh for the Simply Supported Beam

The stress results for the simply supported beam are shown in Figure 8.83. The three plots include a cut-away of the full model with the overall maximum stress identified, a top view of the cladding only with the cladding high stress identified, and a bottom view of the cladding only.

USED FUEL DISPOSITION CAMPAIGN
Used Nuclear Fuel Loading and Structural Performance Under Normal Conditions of Transport -
Demonstration of Approach and Results of Used Fuel Performance Characterization
270   **SEPTEMBER 30, 2013**
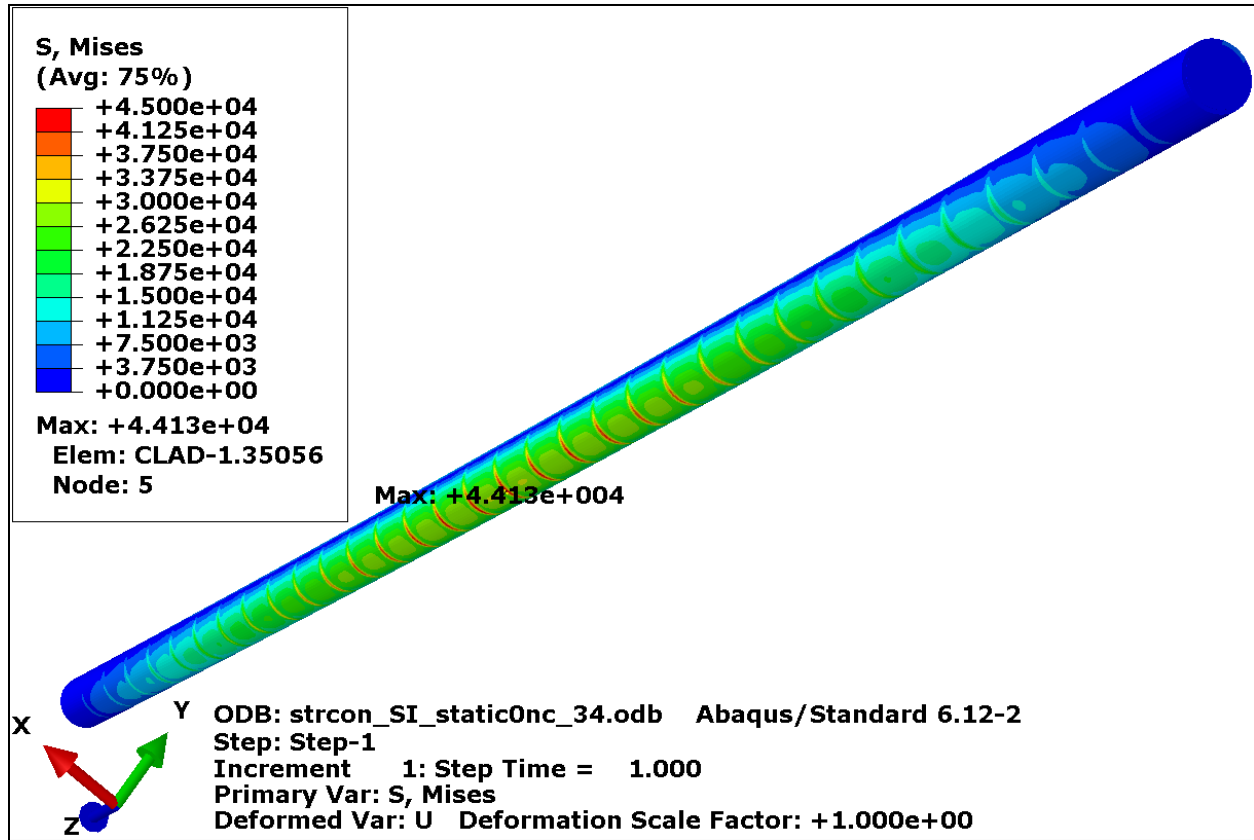
Figure 8.83. Full Model Stress Results for the Simply Supported Beam

The high stress in the simply supported beam model (shown in Figure 8.83) occurs at the center of the cladding. The moment in the cladding at this location is $9.949 \cdot 10^5$ kg·mm^2/s^2. Below is a calculation of the beam stresses that would be expected with no stress concentration:

$$M_v := 9.949 \cdot 10^5 \cdot kg \cdot \frac{mm^2}{s^2}$$

Moment at the center of the cladding.

$$\sigma_v := \frac{M_v \cdot \frac{d_{co}}{2}}{I_c}$$

Cladding bending stress.

$$\sigma_v = 3.203 \times 10^4 \cdot \frac{kg \cdot mm}{s^2 \cdot mm^2} \qquad \sigma_v = 3.203 \times 10^4 \cdot kPa$$

If this moment at the center of the simply supported beam is applied to model 3, the stress pattern appears as shown in Figure 8.72 and the maximum stress is $4.342 \cdot 10^4$ kPa. This is about a 1.6 % difference in stress as compared to the simply supported beam model. If the stress

USED FUEL DISPOSITION CAMPAIGN
Used Nuclear Fuel Loading and Structural Performance Under Normal Conditions of Transport -
Demonstration of Approach and Results of Used Fuel Performance Characterization
SEPTEMBER 30, 2013   271

concentration for model 3 (shown as 34.5 % in Table 8.12) is applied to the cladding bending stress calculated above, the stress is $4.308 \cdot 10^4$ kPa. This is about a 2.4 % difference in stress as compared to the simply supported beam model. The difference in both comparisons is minimal. The minimal difference in the first comparison is an indication that the constant moment application in the two pellet models is reasonable. The minimal difference in the second comparison is an indication that, in addition to the moment application, the nonlinear model produces near linear results for a change in load that is approximately one order of magnitude.

8.5.8.14   *FUEL ROD STIFFNESS SENSITIVITY TO PELLET-PELLET AND PELLET-CLAD INTERFACES*

ORNL used finite element analysis to investigate the impacts of interfacial bonding efficiency at pellet-pellet and pellet-clad interfaces. The simulation studies were validated and benchmarked with ORNL reversal bending fatigue test results on surrogate stainless steel rods with alumina-pellets. The results of this sensitivity study are provided by Wang et al. (2013). A summary of the results and the potential impact on NCT are provided below.

Based on FEA simulation results ORNL determined that with good interface bonding and without fuel pellet and clad fracture, the pellets in the surrogate rod will carry more bending moment resistance than the clad under normal transportation vibration. Upon fuel pellet failure including de-bonding at the pellet-pellet interfaces, the load carrying capacity shifts from fuel pellets to the clad, and the clad starts to carry nearly all of the bending moment at the pellet-pellet interface region. With good cohesion bonding at the pellet-clad interfaces, the pellets can still provide support to the clad and carry a sufficient portion of the bending moment resistance.

Upon further de-bonding at the pellet-clad interfaces, the embedded pellets can no longer provide effective structural support to the clad as well as assist the load transfer within the surrogate rod system. Thus, the majority of the load carrying capacity shifts to the clad throughout the entire gauge section.

The immediate consequence of interface de-bonding is the load carrying capacity shift from fuel to clad, as well as the reduction of flexural rigidity. This shift in flexural rigidity will shift the natural frequency of the PWR assembly down, which may tune to the response of the input motion from rail car transport.

The NCT modeling effort documented herein accounts for this uncertainty in material property and material state by using "best estimate" fuel rod properties and broadening the input PWR response spectra and modifying the assembly time histories to fit this broadened response (Figure 8.84 visually provides the raw and broadened response spectra). These response spectra are broadened based on the percentage of uncertainty in the material properties. This provides more input energy to the PWR assembly and gives a wider frequency range of peak acceleration response for the assembly to respond to. For example Figure 8.84 provides a hypothetical PWR assembly first mode of response around 15 Hz (black line). If the raw time histories that produce the response spectra shown as the blue curves are used, the PWR assembly response will be

USED FUEL DISPOSITION CAMPAIGN
**Used Nuclear Fuel Loading and Structural Performance Under Normal Conditions of Transport -
Demonstration of Approach and Results of Used Fuel Performance Characterization**
272   **SEPTEMBER 30, 2013**

relatively low, however if time histories are used that fit the broadened response spectrum, the PWR assembly response will be much greater.
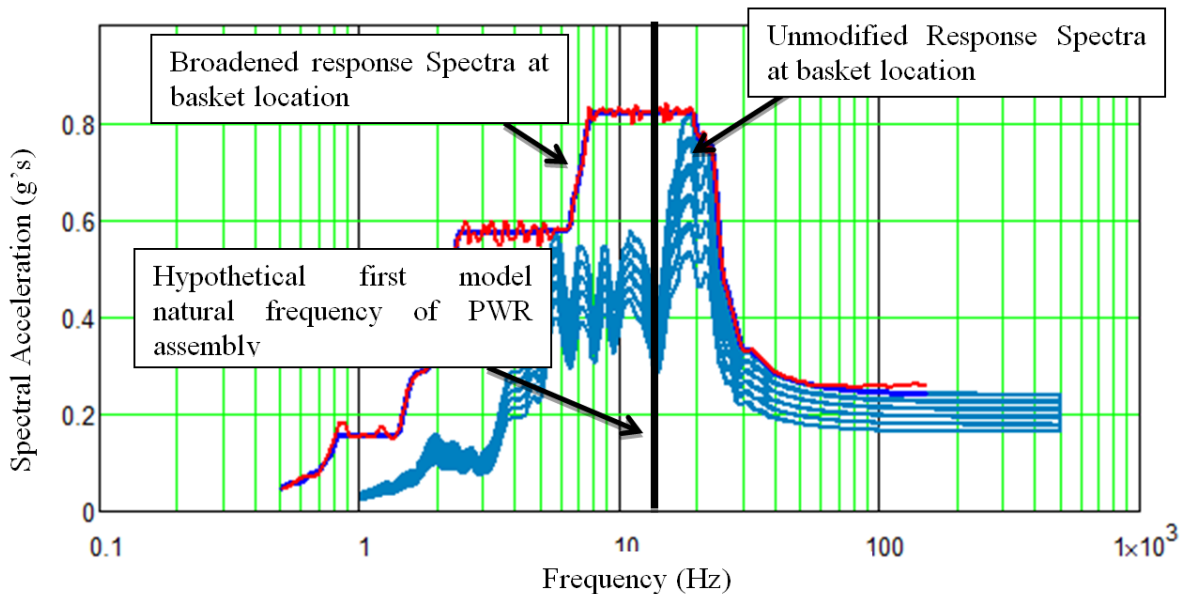

Figure 8.84. Raw and Broadened Response Spectra at Basket Location

This approach should produce conservative results. Additional sensitivity studies could be performed on the pellet-pellet-clad interface to reduce this conservatism and provide a better estimate on high burn-up fuel rod flexural rigidity and fuel rod natural frequency.

8.5.9   GAPS BETWEEN ASSEMBLY AND CASK AND OTHER CASK-LEVEL INPUT PARAMETERS

Analyses to investigate the sensitivity of the basket cell response to the input parameters of cask component temperature, component-to-component gap size, and inclusion or exclusion of control components with the fuel assembly have been completed for the P3 shock load cases. Results from these analyses (that are discussed in detail in Appendix A) indicate that cask component temperature, for loads consistent with the P3 shock loads and for the range of temperatures expected, are relatively unimportant in determining the severity of the excitations at each fuel assembly. Loads generated at each cell location are essentially identical for the hot and cold temperature configurations. The inclusion or exclusion of the control assembly components with each fuel assembly, again for loads consistent with the P3 shock loads and for the fuel assembly investigated, is only of moderate importance in determining the severity of the excitations at each fuel assembly. Significant differences exist between the excitation produced at each cell location when control components are included or excluded from the model. Which configuration represents the more severe configuration must be assessed at the detailed fuel assembly-level.   The component-to-component gap size, again for loads consistent with the P3

USED FUEL DISPOSITION CAMPAIGN
Used Nuclear Fuel Loading and Structural Performance Under Normal Conditions of Transport -
Demonstration of Approach and Results of Used Fuel Performance Characterization
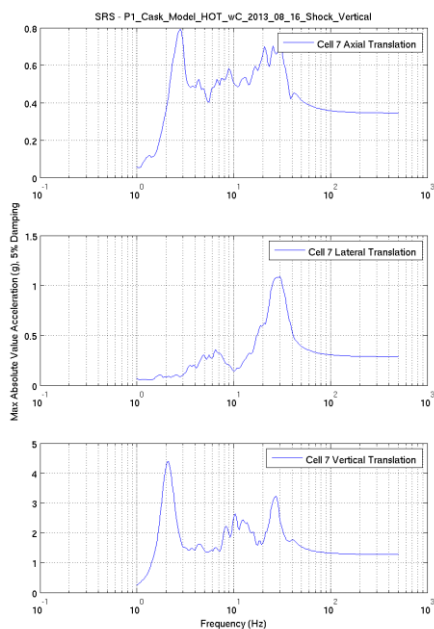**SEPTEMBER 30, 2013** 273

shock loads and for the range of clearances investigated, is of significant importance in determining the severity of the excitations at each fuel assembly, particularly for excitations in the lateral and axial rotation directions. In general larger clearances between components result in increased excitation levels at each fuel assembly and therefore larger clearance configurations can generally be considered more severe.

Results from all of the analyses performed indicate that cell location within the basket is also of critical importance, with the characteristics of the response at each cell location significantly affected by the cell location. For example, cells located on the exterior edges of the basket display different response characteristics when excited in the vertical direction. Consider the response of exterior cell 5 and interior cell 7 (locations shown in Table 6.9) given in Figure 8.85 to the loading of the P1 Shock Z (Vertical) load case. The magnitude of the response in the vertical direction at 30 Hz is significantly different between the exterior cell (cell 5) which has a greater magnitude of response at 30 Hz, and the interior cell (cell 7) at the same frequency. This difference results in differing amplitudes of vertical separation between the fuel assembly and basket at the two locations. Or, alternatively consider the response of cell 2 located on the upper side of the basket and cell 30 located on the lower side of the basket given in Figure 8.86 to the loading of the P1 Vibration Y (Lateral) load case. The magnitude of the responses in the lateral direction at 6 and 30 Hz are significantly different between these two cells, with greater SRS acceleration magnitudes experienced at cell 2 on the upper side of the basket than at cell 30 located on the lower side of the basket. This is likely the result of rocking of the canister in the cask and racking of the basket. Which cell represents the worst case cell configuration must be assessed at the detailed fuel assembly-level. The response of the fuel assembly will depend not only on the magnitude of any input excitation, but also upon the specific frequencies at which that excitation occurs.
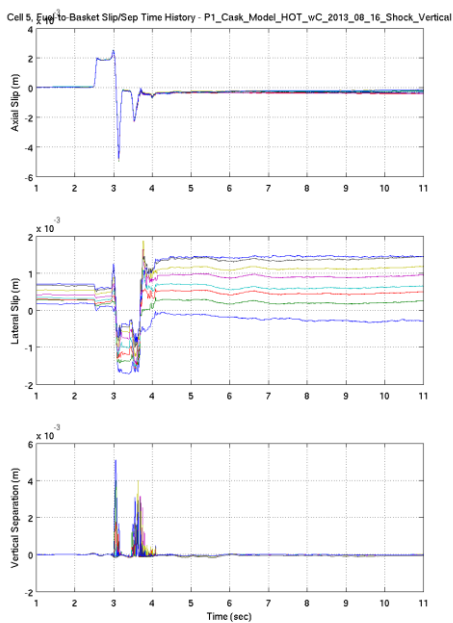
Finally, the severity of the response at any given basket cell will also be heavily influenced by whether the input excitations produce vertical separation and/or sliding of the fuel assembly in the basket and ultimately impact of the assembly against the basket wall, or top or bottom spacer blocks. If sliding and/or separation occurs that results in impact, the severity of the impact may be the single most important factor in determining the severity of the transportation loads.
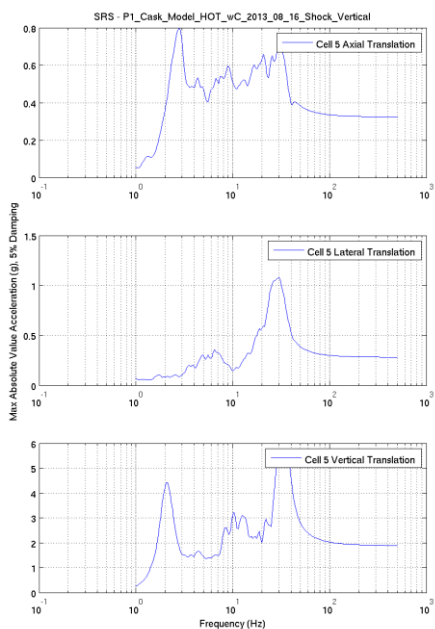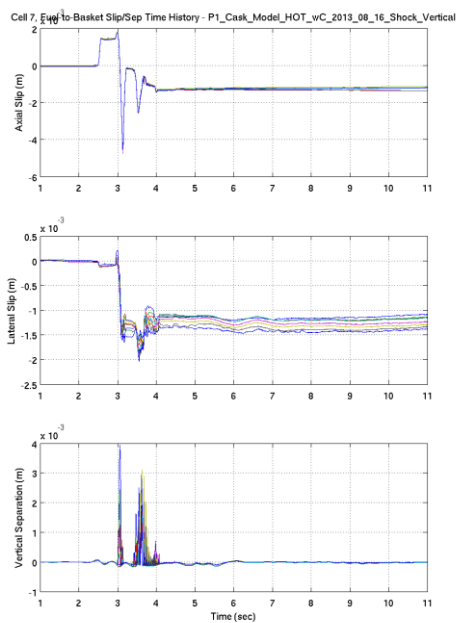
USED FUEL DISPOSITION CAMPAIGN
Used Nuclear Fuel Loading and Structural Performance Under Normal Conditions of Transport -
Demonstration of Approach and Results of Used Fuel Performance Characterization
274   **SEPTEMBER 30, 2013**

(c) Exterior Cell 5 – SRS   (d) Interior Cell 7 – SRS
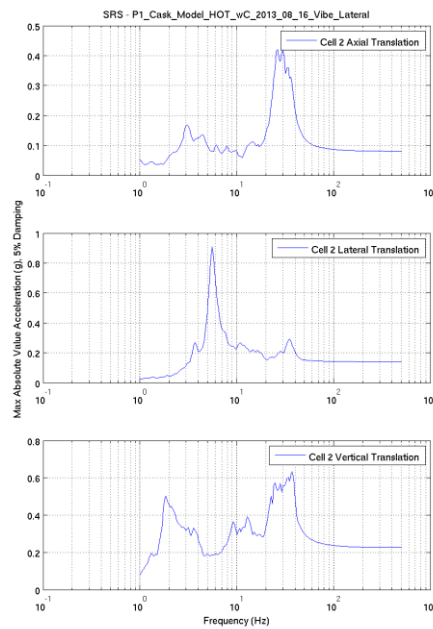

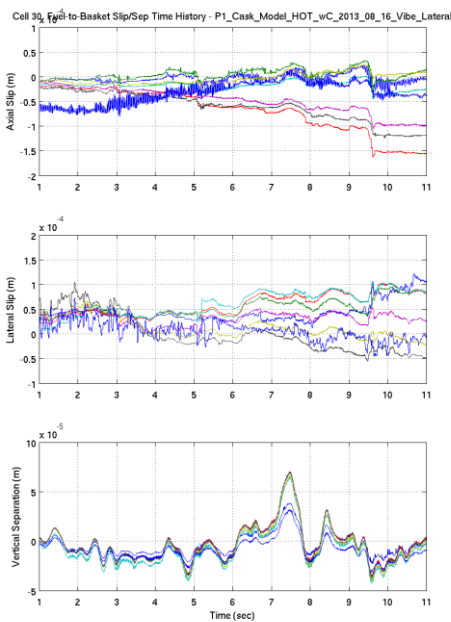(c) Exterior Cell 5 – Slip/Sep   (d) Interior Cell 7 – Slip/Sep

Figure 8.85. Comparison of Response in the Vertical Direction between an Interior and Exterior Cell.

USED FUEL DISPOSITION CAMPAIGN
Used Nuclear Fuel Loading and Structural Performance Under Normal Conditions of Transport -
Demonstration of Approach and Results of Used Fuel Performance Characterization
SEPTEMBER 30, 2013 **275**
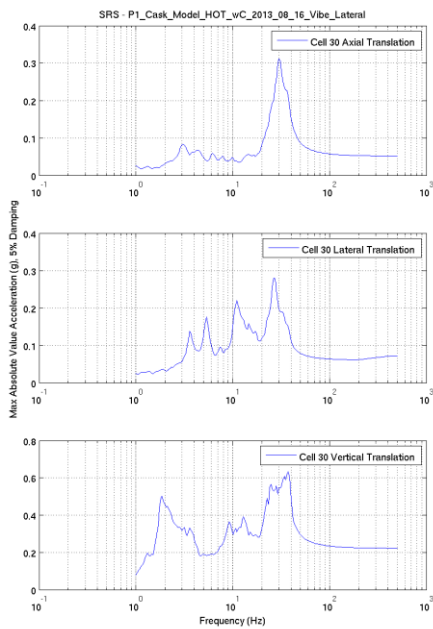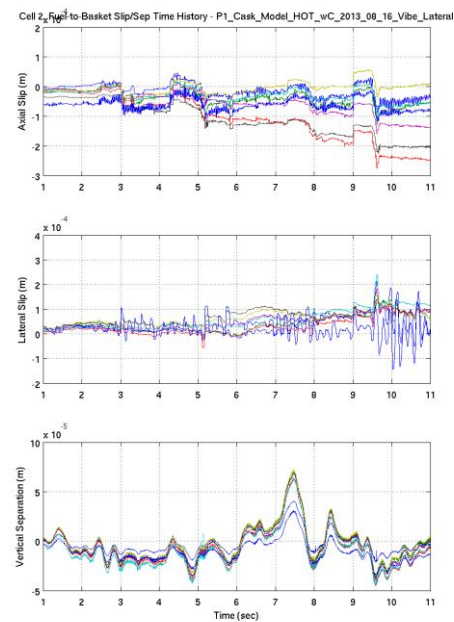
(c) Upper Cell 30 – SRS   (d) Lower Cell 2 – SRS

(c) Upper Cell 30 – Slip/Sep   (d) Lower Cell 2 – Slip/Sep

Figure 8.86. Comparison of Response in the Lateral Direction between an Upper and Lower Cell.

Other potentially important parameters that should be considered in future sensitivity analyses, that have not been investigated here, are the static and dynamics coefficients of friction between

USED FUEL DISPOSITION CAMPAIGN
Used Nuclear Fuel Loading and Structural Performance Under Normal Conditions of Transport -
Demonstration of Approach and Results of Used Fuel Performance Characterization
276   **SEPTEMBER 30, 2013**

interacting bodies (most notably between the cell and basket – which in the cask assembly FEM were equal to 0.2 and 0.1, respectively), structural damping (which in the cask assembly FEM was equal to approximately 2% of critical damping throughout the frequency range of 1.0 Hz to 500 Hz), specifics related to how contact is analytically modeled within the code, sensitivities to input load characteristics, and design details of the cradle-cask-canister-basket assembly. Each of these parameters are likely important and could potentially affect important characteristics of the response (including response magnitude, frequency content, the occurrence of slip and impact, etc.).

8.5.10   INFLUENCE OF CONTROL COMPONENTS

Addition of activated hardware such as control components to the fuel assembly during transport adds additional mass and stiffness to the assembly. Additional mass is added to the guide tubes from the inserted control rods and to the upper nozzle with the overhanging control head assembly. The insertion of the control rods will also affect the total bending stiffness of the guide tubes, but this effect is neglected in the model since the stiffness increase is difficult to quantify for the sliding components and uncertain material composition. Therefore, the effect of the added mass to the assembly is primarily evaluated with this analysis.

8.5.10.1   MODAL ANALYSES

Modal analyses were performed with and without the control head assembly. The results are summarized in Table 8.13. It was observed that the lower frequencies of the assembly modes were reduced approximately 3-7% due to the added mass, while the first fuel rod flexure frequency was unaffected since it vibrates independent of the support skeleton on the leaf springs and dimples. The effect of the control head mass may be more apparent for the dynamic transient analyses where the cantilevered mass may induce additional bending stresses in the upper portion of the assembly.

USED FUEL DISPOSITION CAMPAIGN
Used Nuclear Fuel Loading and Structural Performance Under Normal Conditions of Transport -
Demonstration of Approach and Results of Used Fuel Performance Characterization
SEPTEMBER 30, 2013 277

Table 8.13. Assembly Modal Results for Inclusion of Control Components

Mode #	Participating Component	Shape	Frequency (Hz) w/o control head	Frequency (Hz) w/ control head
1	assembly	torsion	4.5	4.3
2/3	assembly	flexure	5.3	4.9
4	assembly	torsion	9.2	8.9
5/6	assembly	flexure	10.2	9.5
7	assembly	torsion	14.3	13.9
8/9	assembly	flexure	16.4	15.2
10	assembly	torsion	20.4	19.8
11/12	assembly	flexure	23.7	22.2
13	assembly	torsion	27.6	26.8
14/15	assembly	flexure	32.7	30.7
16	assembly	torsion	36.2	35.2
17/18	assembly	flexure	43.2	40.7
19	assembly	torsion	46.4	45.1
20+	fuel rod	flexure	48.8	48.8

8.5.10.2 TRANSIENT DYNAMIC ANALYSES

The assembly model with and without the control head assembly was run for the vertical shock case. The same identical loading input from the cask-level model with control rod assembly was used for each model. The fuel rod cladding experienced strains of higher magnitude without the control head assembly. The peak cladding strain value for the case without the control head remained small but increased 40% from 5.77e-4 to 8.05e-4 with the distribution of strain cycles (summed for all beam elements in the model) as shown in Figure 8.87.

USED FUEL DISPOSITION CAMPAIGN
Used Nuclear Fuel Loading and Structural Performance Under Normal Conditions of Transport -
Demonstration of Approach and Results of Used Fuel Performance Characterization
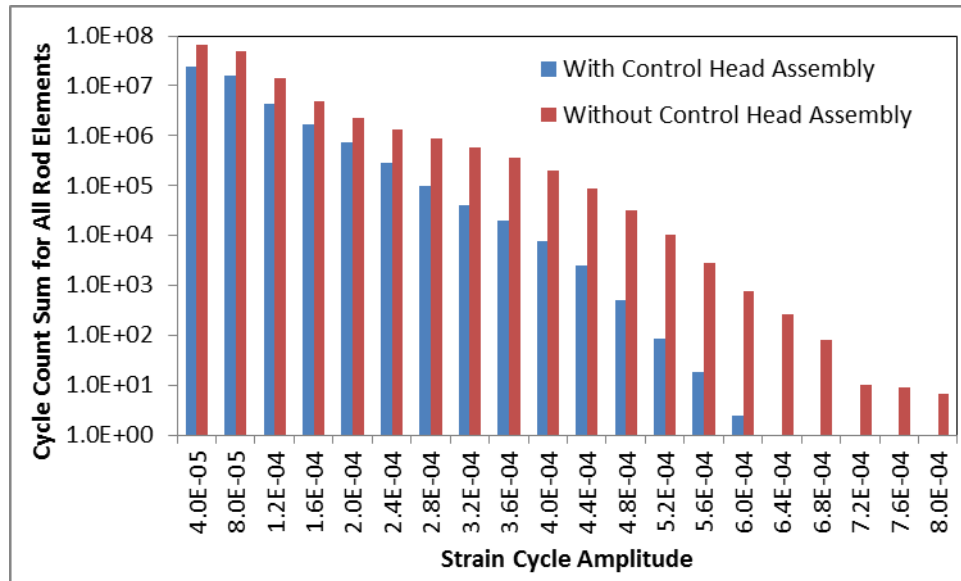**278** **SEPTEMBER 30, 2013**

Figure 8.87. Cyclic Strain History with and without Control Rods and Control Head Assembly

8.6 SUMMARY

Results of the initial demonstration are provided in this section, including results from the cask-level modeling, the fuel rod-level modeling, and the assembly-level modeling. Based on the results of these models, the fuel rods were assessed against the selected failure criteria.

For the cask assembly as currently realized in the cask assembly FEM, the shock and vibration loads derived from the P1 data provided by TTCI produce significant excitations at the fuel assembly-level. In the axial and vertical shock cases, the rail car loads are sufficient enough to result in slip and/or vertical separation of the fuel assemblies in the basket and impact of the fuel assemblies against either the basket cell walls or the top or bottom spacer blocks. Based on this observation alone, the P1 transportation loads as realized in the selected load cases appear to be severe enough to be of concern. However, detailed modeling at the fuel assembly-level is required to definitively assess this. It is worth noting that the P1 shock load in the vertical direction is consistent with the shock environment defined for truck transport as described in NUREG/CR-0128 and therefore may be some indication of the severity of the truck transport shock loading environment. P1 vibration loads, while somewhat more benign with respect to their ability to produce fuel assembly slip and vertical separation than the P1 shock loads, still tend to produce excitations at the fuel assemblies of significant magnitude in the frequency range of concern, namely between 10 and 40, that further modeling at the detailed fuel assembly-level is required to assess these loads for their severity.

For the cask assembly as currently realized in the cask assembly FEM, the shock and vibration loads derived from the P3 data provided by TTCI produce excitations at the fuel assembly-level significantly reduced from those of the P1 shock load cases. However, the P3 shock loads are still sufficient enough to induce sliding of the fuel assemblies in the basket and impact of the fuel assemblies against either the basket cell walls or the top or bottom spacer blocks. Based on this observation, and the sensitivity of the response severity to component-to-component gap size, the P3 transportation loads as realized in the selected load cases appear to have the potential to be severe enough in some instances to be of concern. Detailed modeling at the fuel assembly-level is required to definitively assess this. Also, additional sensitivity studies are required to more fully quantify the importance of uninvestigated parameters such as coefficients of friction between interacting bodies, structural damping, and analytical handling of contact within the FE code, input load characteristics, and design details of the cradle-cask-canister-basket assembly on the severity of the load environments generated at each fuel assembly. Finally, while the P3 vibration loads are generally more benign than even the P1 vibration loads, they still produce excitations at the fuel assemblies of significant magnitude in the frequency range of concern for the fuel assemblies that detailed fuel assembly-level modeling to assess their import is warranted.

The rod-level analysis provides best estimate stiffness and damping properties of a high burn-up fuel rod based on nominal dimensions. It also quantifies the range of flexural rigidity of high burn-up fuel based on various bounding conditions between the pellet-pellet and pellet-clad interface. This range of fuel rod flexural rigidity defines the material property uncertainty range which is used to broaden assembly-level response spectra. Time histories are generated to fit these broadened response spectra and used as input to the assembly-level PWR analysis.

At the assembly-level, a detailed model of the WE 17×17 OFA PWR assembly was constructed in LS-DYNA. Preliminary sensitivity analyses of the various model options were tested by modal analysis to evaluate the effects on natural frequencies of the entire fuel assembly and the individual fuel rods. Preliminary transient dynamic analysis with P1 loading was used to evaluate the fuel rod strain history. The fuel rod stiffness, spacer grid spring stiffness, and spacer grid locations had a strong influence on the assembly and fuel rod natural frequencies and resulting fuel cladding strains. Location of the assembly in the basket and the addition of control components had a smaller but moderate influence on the maximum cladding strains observed in the transient response. Temperature and fuel rod location in the assembly had only a small influence on the natural frequencies and resulting transient response. Transient dynamic cases using P3 loading based on NUCARS simulation were then performed and indicated that the vertical shock had the most potential for high cladding deformation and strain. Additional transient dynamic cases were also ran with inputs derived from the P3 loading to identify a bounding envelope encompassing the response of all 32 basket compartments and peak broadened to account for uncertainty in the fuel rod stiffness. This loading was significant enough to still cause lateral and axial sliding of the assembly within the basket and impact with the side walls, but the assembly did not separate from the basket floor due to vertical loading. Significant amplification of the assembly response was observed for all cases at frequencies above 40 Hz consistent with the estimated rod natural frequencies of 50-60 Hz. The lateral shock

USED FUEL DISPOSITION CAMPAIGN
**Used Nuclear Fuel Loading and Structural Performance Under Normal Conditions of Transport -
Demonstration of Approach and Results of Used Fuel Performance Characterization**
280 **SEPTEMBER 30, 2013**

case exhibited the highest cladding strain in the transient dynamic model, but the lateral vibration case had the highest potential fatigue damage.

The predicted cladding strains were not large enough to cause structural failure, but cyclic strains roughly projected for the entire route were significant in some cases. A rain-flow counting procedure was used to compute the magnitude and number of cladding strain cycles for each fuel rod element in the assembly. These strain cycles are binned and counted for the 10s simulation time. These are extrapolated for a 3000 mile trip and the damage contribution for each strain bin is calculated as the number of cycles the fuel rods hit over the projected 3000 mile journey divided by the critical number of cycles to failure. The total damage for a single rod was then computed by summing the contributions from each of the strain bins. Failure is not expected for damage fractions less than 100%. For the P3 loading without peak broadening, loading was fairly benign and cumulative fatigue damage fraction was less than 1% for all of the cases considered. With the broadened P3 loading, lateral excitations were larger and cumulative fatigue damage for the lateral vibration case was projected to be 11% of the critical value based on the representative 10s window response. The cumulative fatigue damage fraction for the lateral shock case was 7% for a conservative accounting of frequent high amplitude shock events over the entire route. Fatigue damage projections for the vertical shock were 5% while the vertical and longitudinal vibration cases were less than 1%.

Therefore, considering that the total damage from summation of the worst shock and vibration cases is ~18% of the expected fatigue limit, the fuel rods do not fail during NCT given the assumptions listed.

9. LONG TERM GOALS AND OBJECTIVES

As mentioned in Section 3, there are a number of long term goals and objectives associated with the initiative. Based on the results of the successful demonstration reported herein, recommendations are made on how to best address the long term goals and objectives.

9.1 ANALYTICAL ASSESSMENT OF UNF INTEGRITY UNDER NCT

One of the long term goals of this initiative is to provide an analytical assessment of UNF integrity when subjected to NCT. An initial demonstration of these analytical capabilities has been provided. Future work would include implementing refined material properties models and failure criteria informed from targeted testing activities as well as more complete model integration to provide modeling of various scenarios without the current modular modeling approach.

The current modeling tools that have been developed under this initiative could be used to investigate a number of different scenarios and mechanisms. A list of possible future modeling activities is shown below.

USED FUEL DISPOSITION CAMPAIGN
**Used Nuclear Fuel Loading and Structural Performance Under Normal Conditions of Transport -
Demonstration of Approach and Results of Used Fuel Performance Characterization
SEPTEMBER 30, 2013** 281

- Hypothetical cumulative influences (storage, transfer, transport…)
- Consideration of other fuel configuration candidates (e.g., GE 10×10 BWR)
- Full NCT suite (1ft drop) of loading evaluations as well as possible hypothetical accident conditions
- Coupled influence of cladding material and burnup (M5$^®$ & ZIRLO™ targeted for extension)
- Influence the absence of a canister can have (cask without canister)
- Rod bowing and bambooing
- Influence of packaging configuration
- Influence of vacuum drying mechanisms
- Influence of intermediate flow mixers
- Degradation influenced parameterization (fretting and oxidation thickness)
- Truck transport

9.2 DUCTILITY DEMANDS ON UNF UNDER NCT

Another of the long term goals of this initiative is to identify the type of ductility demands that would be required to ensure adequate high burnup UNF performance and survivability under a normal transport campaign. The results of analytical assessments using the developed modeling tools performed on a wide variety of UNF geometries and conditions and a wide range of NCT loadings could be used to establish required fuel or cladding properties to ensure generic survivability and avoid detailed simulations for each individual transportation campaign.

9.3 UNF INTEGRITY AND RETRIEVABILITY

Another of the long term goals of this initiative is to answer questions relative to the ability of high burnup UNF to maintain its integrity and retrievability as it moves through each step of the waste management process (storage, transportation, repackaging, and disposal). Such a generic survivability limit previously discussed would undoubtedly be a function of burnup, possibly adding additional limits to storage, transportation, repackaging, and disposal of high burnup UNF relative to low or moderate burnup UNF. These limits could build on any anticipated damage calculated using the current set of tools and build on anticipated cumulative effects.

9.4 DEVELOPMENT OF VALIDATED MODELS AND INFORMATION

Another of the long term goals of this initiative is to develop validated models and information to aid in making decisions regarding determination of storage and disposal paths. A significant level of validation has been performed under this initiative. Other validation initiatives are still needed to capture influences not addressed under this initiative such as:

- Spacer grid influence (ORNL bend fixture modification and testing)

USED FUEL DISPOSITION CAMPAIGN
Used Nuclear Fuel Loading and Structural Performance Under Normal Conditions of Transport -
Demonstration of Approach and Results of Used Fuel Performance Characterization
282   SEPTEMBER 30, 2013

- Influence of vacuum drying mechanisms
- Coupled influence of cladding material and burnup (M5® & ZIRLO™ targeted for extension)
- Influence of packaging configuration
- Shaker tests of an assembly simulating rail related frequencies and displacements
- Collection of prototypic UNF rail conveyance data
- Consideration of other fuel configuration candidates (e.g., GE 10×10)

9.5   TESTS TO ADDRESS TECHNICAL ISSUES TO BE RESOLVED

Another of the long term goals of this initiative is to identify tests that would be sufficient to address technical issues that need to be resolved. In looking at the current failure criteria, several areas for additional testing have been identified including:

- Cyclic bend tests on irradiated fuel segments. Current tests are being performed on PWR 15×15 fuel. Tests should also include PWR 17×17 fuel and BWR 10×10 and BWR 9×9 fuel to determine if the geometry, or reactor conditions impact the fatigue strength of the fuel rods.
- Hydride reorientation. Typical high burnup rods should be subjected to various heat treatments under typical rod internal pressures to determine the magnitude and distribution of hydride reorientation that is expected to occur following vacuum drying operations. Following these heat treatments, the rods should be subjected to fatigue bend testing, and biaxial burst tests or uniaxial tensions tests to determine the impact of this reorientation on fatigue strength, yield strength, elastic modulus, and the possibility of brittle fracture prior to yielding. These data would provide a strong basis for establishing future failure criteria and for future modeling work.
- The impact of grid spacers on fatigue strength. The fatigue bend test fixture should be modified to simulate the impact of radial stress imparted to UNF by the grid spacers during cyclic loading.

9.6   OVERARCHING BLUEPRINT FOR RESOLVING UNF STORAGE AND TRANSPORTATION

The final long term goal of this initiative is to contribute to an overarching blueprint for resolving the numerous technical challenges related to extended storage and subsequent transportation of UNF. Work under this initiative has put comprehensive tools in place to examine the impact of loading of UNF under NCT. A damage fraction has been calculated. This damage fraction may be used as a baseline for other loading conditions such as drop and

USED FUEL DISPOSITION CAMPAIGN
Used Nuclear Fuel Loading and Structural Performance Under Normal Conditions of Transport -
Demonstration of Approach and Results of Used Fuel Performance Characterization
SEPTEMBER 30, 2013   283

accident conditions in examining the combined effects of all the loads placed on UNF prior to final disposition.

10. CONCLUSIONS

A detailed modeling approach and basis for simulating UNF under NCT has been developed and used in an initial demonstration. This approach includes five main modeling inputs;

- Simulated loading histories an AAR specification S-2043 rail conveyance
- Component material properties including irradiated fuel and cladding properties
- Component temperatures
- Fuel and assembly post-irradiation conditions
- Cask, canister, and fuel assembly geometry

The modeling approach includes three main levels;

- Cask-level modeling
- Fuel assembly-level modeling
- Fuel rod-level modeling.

The strains in the fuel rods produced by these models were compared to fatigue failure criteria to assess the possibility for damage during the expected rail journey.

Extensive validation was performed on the model inputs, the FEA models, and the fatigue failure criteria to demonstrate the validity of the results.

Results of a demonstration involving moving high burnup 17×17 OFA fuel in a GBC-32 on a 3000-mile rail journey have been provided. It was determined that peak cladding strains were not large enough to cause structural failure, but cyclic strains roughly projected for the entire route were significant in some cases. The damage ratio for a 3000-mile route was calculated based on a conservative accounting of the vibration and shock loading derived from the representative 10s simulation cases. The total damage for a single rod was then computed by summing the contributions from each of the strain bins. Failure is not expected for damage fractions less than 100%. Cumulative fatigue damage fraction was projected to be 11% of the critical value for the lateral vibration case and 7% for the lateral shock case. Conservatively assuming that the high amplitude shock events occur concurrently with the continuous vibration, the total projected damage is 18% of the critical value. Therefore the fuel rods do not fail during NCT for this demonstration.

Sensitivity studies were performed and the results indicate areas of high, moderate, and low sensitivity. The areas of high sensitivity were found to be;

- Cladding elastic modulus
- Spacer grid stiffness
- Spacer grid location
- Gaps between the assembly and the cask.

USED FUEL DISPOSITION CAMPAIGN
Used Nuclear Fuel Loading and Structural Performance Under Normal Conditions of Transport -
Demonstration of Approach and Results of Used Fuel Performance Characterization
284   **SEPTEMBER 30, 2013**

The areas of moderate sensitivity are;
- Fuel assembly basket location
- In-reactor fretting wear
- Influence of control components
- Pellet-to-clad bonding.

The areas of low or no sensitivity are;
- Cladding yield stress
- Fuel rod location in assembly
- Temperature distribution
- Fuel rod damping
- Pin pressure influence.

A number of long-term goals and objectives of the Used Fuel Disposition Campaign are discussed in this document as they relate to this initiative and the potential for follow-on work is significant.

USED FUEL DISPOSITION CAMPAIGN
Used Nuclear Fuel Loading and Structural Performance Under Normal Conditions of Transport -
Demonstration of Approach and Results of Used Fuel Performance Characterization
SEPTEMBER 30, 2013   285

11. REFERENCES

AAR - Association of American Railroads. 2003. *Standard S-2043 Performance Specification for Trains Used to Carry High-Level Radioactive Material*. Standard S-2043, Association of American Railroads, Washington, D.C. (DIRS 166338).

AAR, 2011. "Manual of Standards and Recommended Practices Section C – Part II: Design, Fabrication, and Construction of Freight Cars," The Association of American Railroads, Washington, DC.

Adkins HA. 2013a. "Used Nuclear Fuel Loading and Structural Performance Under Normal Conditions of Transport – Method and Approach." FCRD-TIO-2011-00050. U.S. Department of Energy, Washington D.C.

Adkins HA. 2013b. "Used Nuclear Fuel Loading and Structural Performance Under Normal Conditions of Transport – Modeling, Simulation and Experimental Integration RD&D Plan." FCRD-TIO-2013-000135. U.S. Department of Energy, Washington D.C.

Adkins HA. 2013c. "Used Nuclear Fuel Loading and Structural Performance Under Normal Conditions of Transport – Loading, M&S Methodology, Sensitivity, Failure, and Associated Development Strategies." FCRD-TIO-2013-000155. U.S. Department of Energy, Washington D.C.

Adkins HA. 2013d. "Used Nuclear Fuel Loading and Structural Performance Under Normal Conditions of Transport – Final UQ development modeling approach and resulting modeling and simulation input." FCRD-TIO-2013-000173. U.S. Department of Energy, Washington D.C.

Adkins HA. 2013e. "Used Nuclear Fuel Loading and Structural Performance Under Normal Conditions of Transport – Final Data, Material Property, and M&S Input Information." FCRD-TIO-2013-000255. U.S. Department of Energy, Washington D.C.

Adkins HA. 2013f. "Used Nuclear Fuel Loading and Structural Performance Under Normal Conditions of Transport – Final M&S Methodology, Basis, Approach, and Initial Sensitivity Results." FCRD-TIO-2013-000254. U.S. Department of Energy, Washington D.C.

Adkins HA, JM Cuta, BJ Koeppel, AD Guzman, and CS Bajwa. 2006. *Spent Fuel Transportation Package Response to the Baltimore Tunnel Fire Scenario*, NUREG/CR-6886 Rev. 1, PNNL-15313, Pacific Northwest National Laboratory, Richland, WA.

ASTM E 1049-85. (Reapproved 2005). *Standard practices for cycle counting in fatigue analysis*. ASTM International.

USED FUEL DISPOSITION CAMPAIGN
Used Nuclear Fuel Loading and Structural Performance Under Normal Conditions of Transport -
Demonstration of Approach and Results of Used Fuel Performance Characterization
286 **SEPTEMBER 30, 2013**

Avallone, EA and T Baumeister III. 1996. *Marks' Standard Handbook for Mechanical Engineers*, Tenth Edition. McGraw-Hill, New York.

BRC - Blue Ribbon Commission. 2012. *Blue Ribbon Commission on America's Nuclear Future, Report to the Secretary of Energy.* Prepared by the Blue Ribbon Commission on America's Nuclear Future for the U.S. Department of Energy, Washington, D.C.

Carter JT, AJ Luptak, J Gastelum, C Stockman, and A Miller. 2012. *Fuel Cycle Potential Waste Inventory for Disposition*. FCR&D-USED-2010-000031 Rev. 5, U.S. Department of Energy, Washington, D.C.

DOE - U.S. Department of Energy. 2013. *Strategy for the Management and Disposal of Used Nuclear Fuel and High-Level Radioactive Waste*. U.S. Department of Energy, Washington, D.C. Available at http://energy.gov/downloads/strategy-management-and-disposal-used-nuclear-fuel-and-high-level-radioactive-waste.

DOE (U.S. Department of Energy). 2009. *National Transportation Plan.* DOE/RW-0603 Revision 0, U.S. Department of Energy, Washington, D.C.

DOE (U.S. Department of Energy). 1987. *Characteristics of Spent Fuel, High-Level Wastes which May Require Long-Term Isolation.* DOE/RW-0184, U.S. Department of Energy, Washington, D.C.

Energy Information Administration. 1995. *Spent Nuclear Fuel Discharges from U.S. Reactors 1993*. SR/CNEAF/95-01, Energy Information Administration, Washington, D.C.

EPRI. 2010. *Impacts Associated with Transfer of Spent Nuclear Fuel from Spent Fuel Storage Pools to Dry Storage After Five Years of Cooling.* TR-1021049, Electric Power Research Institute, Palo Alto, California.

Geelhood KJ, WG Luscher, and CE Beyer. 2010. *FRAPCON-3.4: A Computer Code for the Calculation of Steady-State, Thermal-Mechanical Behavior of Oxide Fuel Rods for High Burnup*, NUREG/CR-7022, Vol. 1, PNNL-19418, Vol. 1, Pacific Northwest National Laboratory, Richland, Washington.

Geelhood KJ. 2013. "Used Nuclear Fuel Loading and Structural Performance Under Normal Conditions of Transport – Supporting Material Properties and Modeling Inputs." FCRD-UFD-2013-000123. U.S. Department of Energy, Washington, D.C. Referred to in the document as the "Material Properties Handbook".

Hanson B, H Alsaed, C Stockman, D Enos, R Meyer, and K Sorenson. 2012. *Gap Analysis to Support Extended Storage of Used Nuclear Fuel,* FCRD-USED-2011-000136, Rev. 0, U.S. Department of Energy, Washington, D.C.

USED FUEL DISPOSITION CAMPAIGN
Used Nuclear Fuel Loading and Structural Performance Under Normal Conditions of Transport -
Demonstration of Approach and Results of Used Fuel Performance Characterization
SEPTEMBER 30, 2013 287

Idaho National Laboratory. 2011. *Software Validation Report for ABAQUS Standard and Explicit Version 6.11-1*, ECAR-1698, Idaho National Laboratory, Idaho Falls, ID.

Klymyshyn NA, SE Sanborn, HE Adkins, Jr, and BD Hanson. 2013. Fuel Assembly Shaker Test Simulation. PNNL-22507, Pacific Northwest National Laboratory, Richland, WA.

Lin. X and G Haichen. 1998. "High cycle fatigue properties and microstructure of zirconium and Zircaloy-4 under reverse bending." *Materials Science and Engineering* A252, pp. 166-173.

LS-DYNA (Version mpp d R6.1.1 Revision 79036 [Software]), 2013. Livermore Software Technology Corporation (LSTC), Livermore, CA.

LSTC 2012. LS-DYNA *Keywords User's Manual Volume I and Volume II*, Version 971 R6.1.0. Livermore Sotfware Technology Corporation (LSTC), Livermore, CA.

Magnuson C.F., 1980. *Shock and Vibration Environments For A Large Shipping Container During Truck Transport (Part II)*. NUREG/CR-0128, SAND78-0337, Sandia National Laboratories, Albuquerque, NM.

Maheras, S.J., E.A. Lahti, S. B. Ross. 2013. "Transportation Shock and Vibration Literature Review," FCRD-TIO-2013-000169. U.S. Department of Energy, Washington D.C.

MATLAB and Statistics Toolbox (Version R2013a [Software]), 2013. The MathWorks, Inc., Natick, MA.

Matsuishi, M. and T. Endo. 1968. "Fatigue of metals subjected to varying stress", *Japan Society of Mechanical Engineering*.

McConnell, P., G. Flores, R. Wauneka, G. Koenig, D. Ammerman, J. Bignell, S. Saltzstein, and K. Sorenson. 2013. *Fuel Assembly Shaker Test for Determining Loads on a PWR Assembly under Simulated Normal Conditions of Truck Transport*, SAND2013-5210P, Rev. 0, FCRD-UFD-2013-000190, Sandia National Laboratory, Albuquerque, NM.

Mehan RL and FW Wiesinger. 1961. *Mechanical Properties of Zircaloy-2*. KAPL-2110, Knolls Atomic Power Laboratory, Schenectady, NY.

NRC - U.S. Nuclear Regulatory Commission. 2007. *Standard Review Plan for the Review of Safety Analysis Report for Nuclear Power Plant: LWR Edition*, Reactor (NUREG-0800, Chapter 4), U.S. Nuclear Regulatory Commission, Washington, D.C.

USED FUEL DISPOSITION CAMPAIGN
Used Nuclear Fuel Loading and Structural Performance Under Normal Conditions of Transport -
Demonstration of Approach and Results of Used Fuel Performance Characterization
288   **SEPTEMBER 30, 2013**

NRC - U.S. Nuclear Regulatory Commission. 2003. *Cladding Considerations for the Transportation and Storage of Spent Fuel,* Interim Staff Guidance Memorandum 11, Revision 3, November 17, 2003, U.S. Nuclear Regulatory Commission, Washington, D.C.

NRC - U.S. Nuclear Regulatory Commission. 1999. *Standard Review Plan for Transportation Packages for Radioactive Material*. NUREG-1609, Spent Fuel Project Office, Office of Nuclear Material Safety and Safeguards, U.S. Nuclear Regulatory Commission, Washington, DC.

O'Donnell WJ and BF Langer. 1964. "Fatigue design basis for zircaloy components." *Nuclear Science and Engineering* (20):1-12.

OECD - Organisation for Economic Co-operation and Development. 2012. *Nuclear Fuel Safety Criteria Technical Review*. OECD NEA No. 7072. Organisation for Economic Co-operation and Development, Nuclear Energy Agency. Available at http://www.oecd-nea.org/nsd/reports/2012/nea7072-fuel-safety-criteria.pdf.

Pandarinathan PR and P Vasudevan. 1980. "Low-Cycle Fatigue Studies on Nuclear Reactor Zircaloy-2 Fuel Tubes at Room Temperature, 300 and 350°C." *Journal of Nuclear Materials* (91):47-58.

Soniak A, S Lansiart, J Royer, J-P Mardon, and N Maeckel. 2004. "Irradiation Effect on Fatigue Behavior of Zircaloy-4 Cladding Tubes." *Zirconium in the Nuclear Industry: Tenth International Symposium*, ASTM STP 1245, pp. 549-558.

TTCI - Transportation Technology Center, Inc. 2013. *NUCARS® Help Manual*, *Version 2013.1*. Transportation Technology Center, Inc., Pueblo, Colorado.

Urban, C., N. Wilson, and A. Keylin. 2013. *NUCARS® Modeling Support for DOE Used Nuclear Fuel Disposition, Task 2: NUCARS® Simulation of Representative Railcar*, ORNL-13-002, Transportation Technology Center, Inc., Pueblo, CO.

Wagner J.C., 2001. Computational Benchmark for Estimation of Reactivity Margin from Fission Products and Minor Actinides in PWR Burnup Credit. NUREG/CR-6747, ORNL/TM-2000/306, Oak Ridge National Laboratory, Oak Ridge, TN.

Wang, J-A and H Wang. 2013. *Progress Report on Reversal Bending Fatigue Testing of Zry-4 Surrogate Rod (Out-of-Cell Fatigue Testing Development, Task 2.4)*, ORNL/TM-2013/297, Oak Ridge National Laboratory, Oak Ridge, TN.

Wang, J-A, H. Jiang, and H Wang. 2013. *The Impact of Interface Bonding Efficiency on High-Burnup Spent Nuclear Fuel Vibration Integrity during Normal Transportation*, ORNL/TM-2013/296, Oak Ridge National Laboratory, Oak Ridge, TN.

USED FUEL DISPOSITION CAMPAIGN
Used Nuclear Fuel Loading and Structural Performance Under Normal Conditions of Transport -
Demonstration of Approach and Results of Used Fuel Performance Characterization
SEPTEMBER 30, 2013 289

Wisner SB, MB Reynolds, and RB Adamson. 2004. "Fatigue Behavior of Irradiated and Unirradiated Zircaloy and Zirconium." *Zirconium in the Nuclear Industry: Tenth International Symposium*, ASTM STP 1245, pp. 499-520.

USED FUEL DISPOSITION CAMPAIGN
**Used Nuclear Fuel Loading and Structural Performance Under Normal Conditions of Transport -
Demonstration of Approach and Results of Used Fuel Performance Characterization**
Appendix A   **SEPTEMBER 30, 2013**

APPENDIX A

USED FUEL DISPOSITION CAMPAIGN
**Used Nuclear Fuel Loading and Structural Performance Under Normal Conditions of Transport -
Demonstration of Approach and Results of Used Fuel Performance Characterization**
A-2
SEPTEMBER 30, 2013

CONTENTS

USED FUEL DISPOSITION CAMPAIGN
Used Nuclear Fuel Loading and Structural Performance Under Normal Conditions of Transport -
Demonstration of Approach and Results of Used Fuel Performance Characterization
A-3   SEPTEMBER 30, 2013

LIST OF FIGURES

USED FUEL DISPOSITION CAMPAIGN
Used Nuclear Fuel Loading and Structural Performance Under Normal Conditions of Transport -
Demonstration of Approach and Results of Used Fuel Performance Characterization
A-4   **SEPTEMBER 30, 2013**

USED FUEL DISPOSITION CAMPAIGN
Used Nuclear Fuel Loading and Structural Performance Under Normal Conditions of Transport -
Demonstration of Approach and Results of Used Fuel Performance Characterization
A-5 **SEPTEMBER 30, 2013**

USED FUEL DISPOSITION CAMPAIGN
**Used Nuclear Fuel Loading and Structural Performance Under Normal Conditions of Transport -
Demonstration of Approach and Results of Used Fuel Performance Characterization**
A-6   **SEPTEMBER 30, 2013**

USED FUEL DISPOSITION CAMPAIGN
**Used Nuclear Fuel Loading and Structural Performance Under Normal Conditions of Transport -
Demonstration of Approach and Results of Used Fuel Performance Characterization**
A-7   **SEPTEMBER 30, 2013**

USED FUEL DISPOSITION CAMPAIGN
Used Nuclear Fuel Loading and Structural Performance Under Normal Conditions of Transport -
Demonstration of Approach and Results of Used Fuel Performance Characterization
A-8   **SEPTEMBER 30, 2013**

USED FUEL DISPOSITION CAMPAIGN
**Used Nuclear Fuel Loading and Structural Performance Under Normal Conditions of Transport -
Demonstration of Approach and Results of Used Fuel Performance Characterization**
A-9   **SEPTEMBER 30, 2013**

INTRODUCTION

This appendix contains a detailed discussion of the cask assembly level analyses results and sensitivity studies that were performed. The specific analysis cases that were performed are listed in Table 8.1. For the discussion that follows the cask assembly model configuration that includes fuel assemblies with control components, "hot" component temperatures, and nominal component-to-component gap sizes will be designated the "nominal" configuration. For the nominal configuration, analyses for all of the P1 and P3 load cases were performed. A detailed discussion of observed response characteristics is provided for each of these analyses. The focus of the discussion is on the average response of the basket at each fuel assembly cell location, as determined from the nodal outputs at those locations. For the other "off-nominal" configurations investigated, analyses for only the P3 shock load cases were performed with the intent of assessing the sensitivity of response characteristics to off-nominal configuration changes. Results from these analyses are discussed in a more limited manner with a focus on pertinent differences in the response characteristics between these off-nominal configurations and their associated nominal configuration counterparts.

Each analysis performed simulated a time eleven seconds in duration. Of these eleven seconds, the first one second was used to apply a gravity load to the cask assembly components to allow them to establish contact with each other and to establish a state of near-static force equilibrium. At one second, the transient dynamic portion of the analysis was commenced. At the beginning of this transient dynamic portion nodal velocities throughout the model were reinitialized to a state consistent with the required initial conditions for the particular load case being performed. This re-initialization ensured that cumulative rigid body displacements and rotations over the course of the ten-second load case were nearly zero. This re-initialization produced some non-physical nodal accelerations in the first several hundred time steps of the analyses preceding the velocity re-initialization (note that each time step was approximately 2.5 microseconds). This non-physical acceleration appeared in only a single output step and was manually corrected before proceeding with any results processing. In addition, to remove some non-physical high frequency numerical noise, output from each basket cell node was processed with a low-pass Butterworth filter which removed frequency content above 150 Hz. Finally, to limit the introduction of additional high frequency noise into the response data by the abrupt start and end of the response data, a Tukey tapered cosine windowing algorithm (MATLAB 2013) with a 0.1 second ramp up and ramp down time was applied.

1.   NOMINAL CONFIGURATION ANALYSES

1.1   P1 SHOCK X (AXIAL)

The P1 Shock X (Axial) case is characterized by a short duration (~1.0 second) shock with peak time-domain acceleration magnitude in the axial direction of 1.269 g. This can be seen in Figure 1.1 which illustrates the acceleration and displacement time-histories for each of the translation and rotation degrees-of-freedom. Figure 1.2 through Figure 1.4 provide FFT, SRS, and PSD plots for both the input excitation and the basket cell response. Transfer functions (input acceleration magnitude versus response acceleration magnitude) for each of the translation and

USED FUEL DISPOSITION CAMPAIGN
Used Nuclear Fuel Loading and Structural Performance Under Normal Conditions of Transport -
Demonstration of Approach and Results of Used Fuel Performance Characterization
A-10   **SEPTEMBER 30, 2013**

rotation degrees-of-freedom are shown in Figure 1.5, along with axial and lateral slip and vertical separation plots (fuel assembly to basket slip or separation) for cell 11 and cell 13. Comparison of the input characteristics versus those of the response in all six degrees-of-freedom at each cell (Figure 1.2, Figure 1.3, and Figure 1.4) indicates that there was a response at each cell location at frequencies above 10 Hz that was not present in the input. This is similarly borne out by the strong peaks in the transfer functions (Figure 1.5) above 10 Hz. This was either the result of amplification of the input at those frequencies through resonance, or the conversion of energy at other frequencies (likely low frequency energy since that is where most of the energy resides – see Figure 1.4) into response in the above 10 Hz range. Investigation of the slip/separation behavior between the fuel assembly and basket for cells 11 and 13 (Figure 1.5) indicates a that a sudden shift axially and laterally at about 2.5 seconds occurred, accompanied by a small vertical separation. In fact, the shock caused all of the fuel assemblies to slide axially in their cells and impact their forward spacer block and then rebound and impact their rear spacer block. Note that the sudden change in axial slip distance at 2.5 seconds was approximately 20 mm in magnitude, which is equal to the total axial clearance between a fuel assembly and its spacer blocks. Lateral slip of the fuel assembly also occurred at 2.5 seconds but the peak-to-peak magnitude of approximately 3 mm was slightly less than the total lateral clearance between the fuel assembly and its cell walls of 5.8 mm. A small amount of vertical separation accompanied the shock but the magnitude of this separation was limited to less than 1 mm in the worst case. This sliding of the fuel assemblies and impact between the fuel assemblies and spacer blocks is likely the mechanism that was resulting in the conversion of low frequency energy (< 10 Hz) in the input excitation into higher frequency energy (> 10 Hz) in the response. It is also interesting to note that in the lateral direction Figure 1.5 indicates that there was amplified response in the 4 to 6 Hz range. From this data it is not clear whether this amplification was due to resonance or some other mechanism. Finally, it is also worth pointing out that the response at each cell location was not identical. For example, comparison of the SRS at each cell in the lateral translation, vertical translation, and axial rotation directions (Figure 1.3) indicates potentially important differences in the response characteristics between each of the cells.

USED FUEL DISPOSITION CAMPAIGN
**Used Nuclear Fuel Loading and Structural Performance Under Normal Conditions of Transport -
Demonstration of Approach and Results of Used Fuel Performance Characterization**
A-11 **SEPTEMBER 30, 2013**
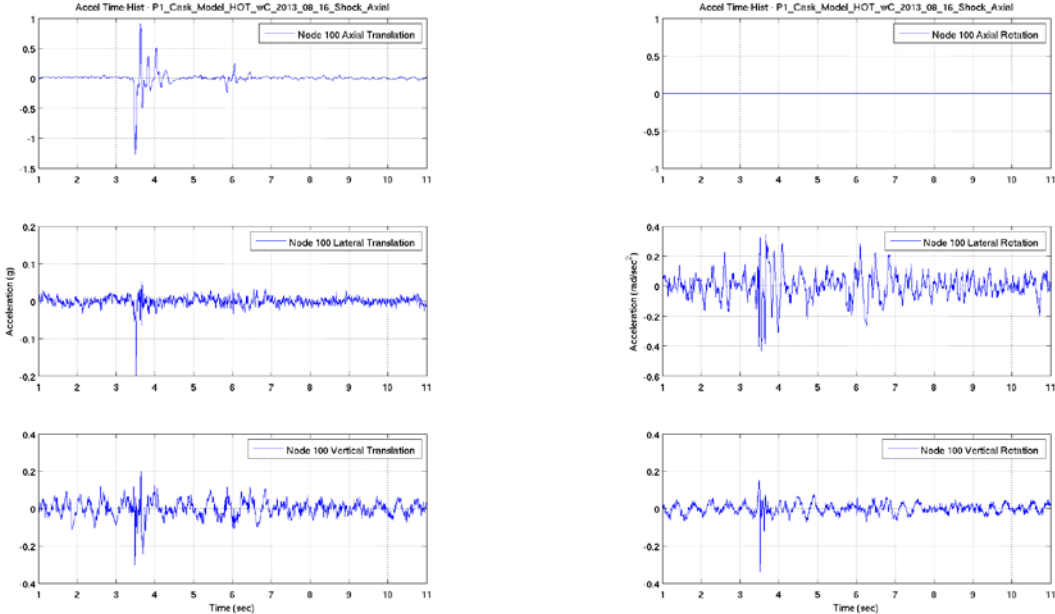
(a) Acceleration Time-Histories

(b) Displacement and Rotation Time-Histories

**Figure 1.1 P1 Shock X (Axial) Load Case, Nominal Model Configuration, Input
Acceleration and Displacement Time-Histories.**

USED FUEL DISPOSITION CAMPAIGN
**Used Nuclear Fuel Loading and Structural Performance Under Normal Conditions of Transport -
Demonstration of Approach and Results of Used Fuel Performance Characterization**
A-12   **SEPTEMBER 30, 2013**

(a) Input   (b) Basket Cell Response

Figure 1.2 P1 Shock X (Axial) Load Case, Nominal Model Configuration, Input and Basket Cell Response FFTs.

USED FUEL DISPOSITION CAMPAIGN
Used Nuclear Fuel Loading and Structural Performance Under Normal Conditions of Transport -
Demonstration of Approach and Results of Used Fuel Performance Characterization
A-13
SEPTEMBER 30, 2013

(a) Input

(b) Basket Cell Response

Figure 1.3 P1 Shock X (Axial) Load Case, Nominal Model Configuration, Input and Basket Cell Response SRSs.

USED FUEL DISPOSITION CAMPAIGN
**Used Nuclear Fuel Loading and Structural Performance Under Normal Conditions of Transport -
Demonstration of Approach and Results of Used Fuel Performance Characterization**
A-14   **SEPTEMBER 30, 2013**

(a) Input   (b) Basket Cell Response
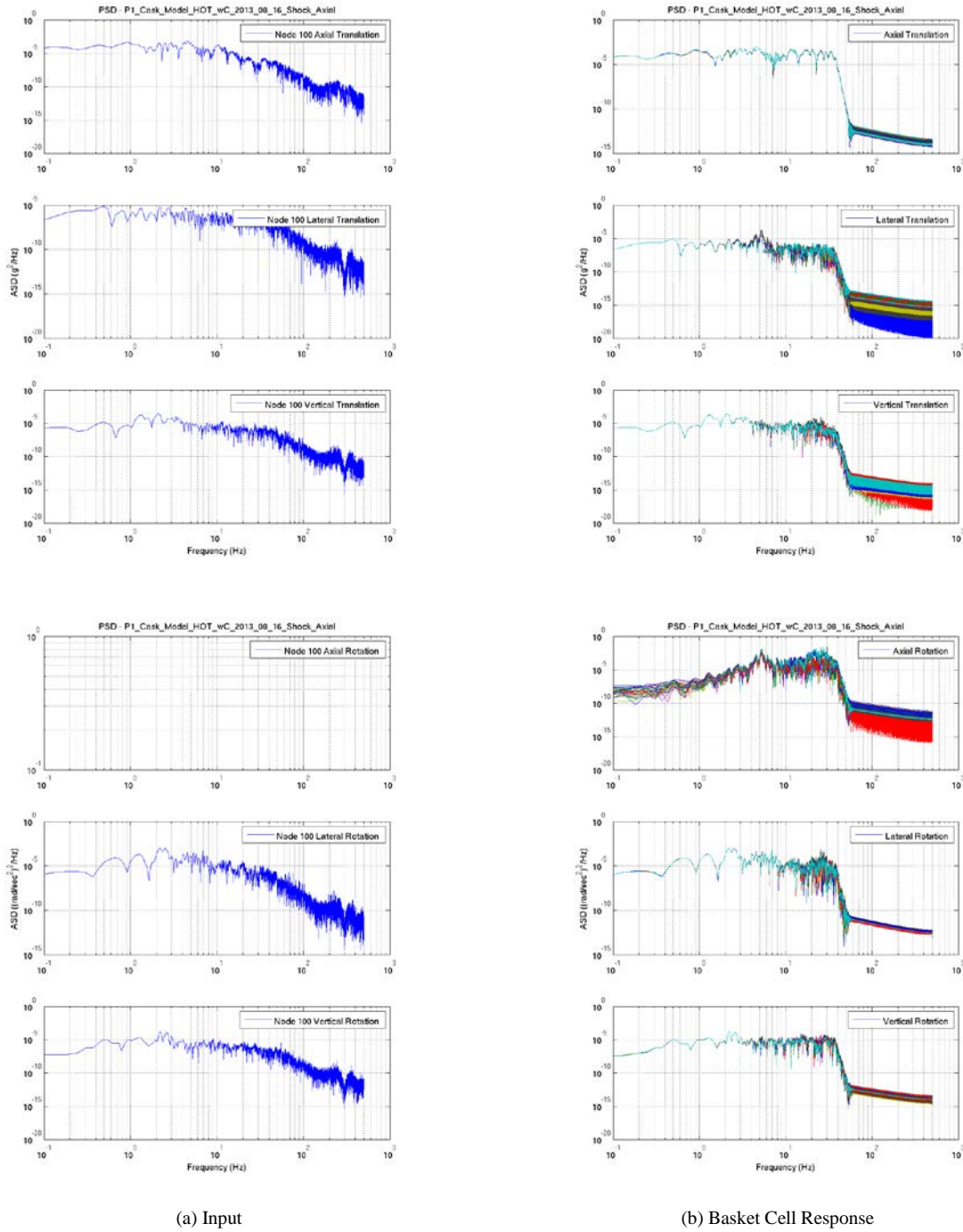
Figure 1.4 P1 Shock X (Axial) Load Case, Nominal Model Configuration, Input and Basket Cell Response PSDs.

USED FUEL DISPOSITION CAMPAIGN
**Used Nuclear Fuel Loading and Structural Performance Under Normal Conditions of Transport -
Demonstration of Approach and Results of Used Fuel Performance Characterization**
A-15   **SEPTEMBER 30, 2013**
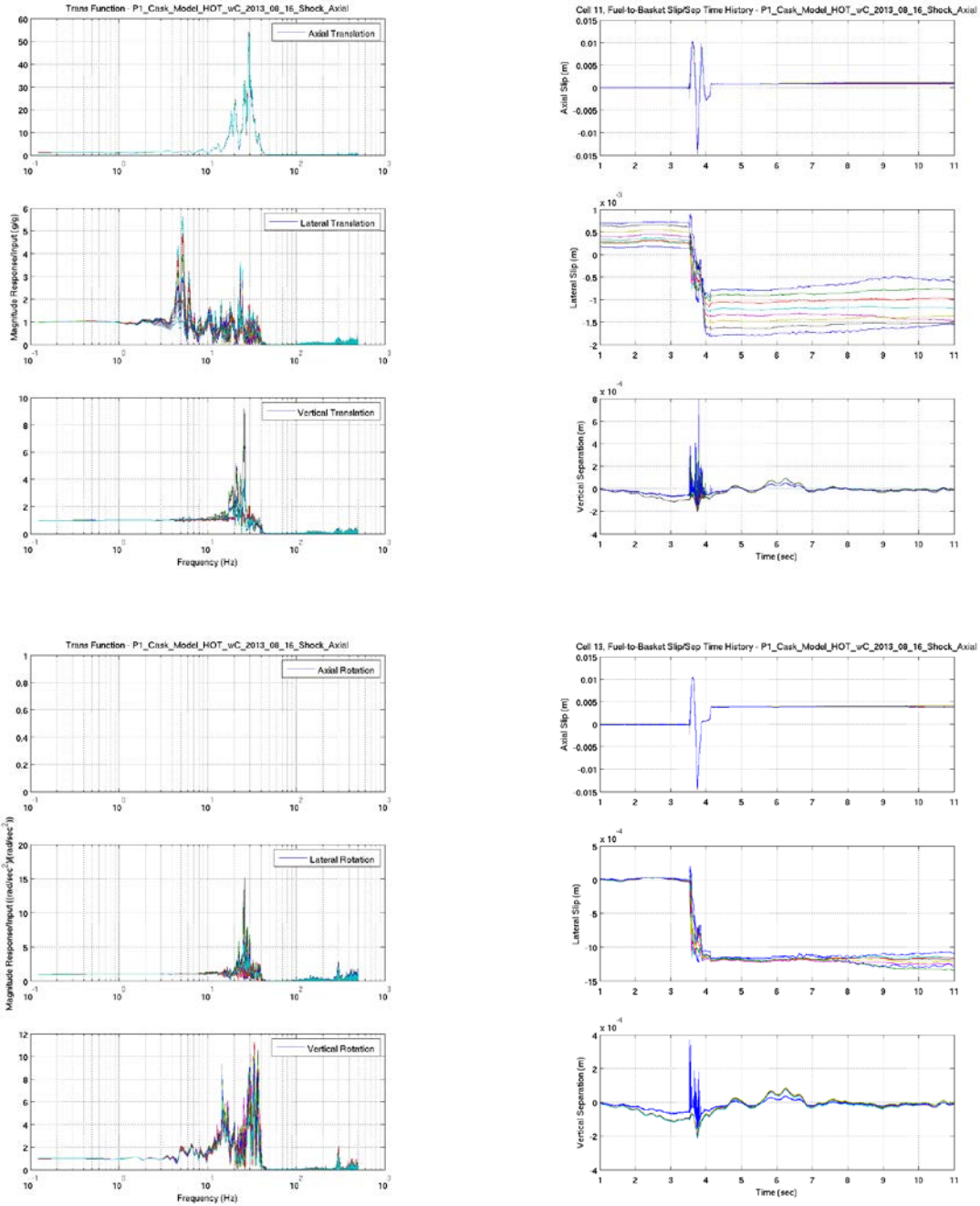
(a) Transfer Functions   (b) Fuel Assembly to Basket Slip/Separation.

**Figure 1.5 P1 Shock X (Axial) Load Case, Nominal Model Configuration, Basket Cell
Response Transfer Functions and Slip/Separation Plots.**

USED FUEL DISPOSITION CAMPAIGN
**Used Nuclear Fuel Loading and Structural Performance Under Normal Conditions of Transport -
Demonstration of Approach and Results of Used Fuel Performance Characterization**
A-16
SEPTEMBER 30, 2013

1.2 P1 SHOCK Y (LATERAL)

The P1 Shock Y (Lateral) case is characterized by two short duration (~1.0 second each) shocks with peak time-domain acceleration magnitude in the lateral direction of 0.492 g. This can be seen in Fig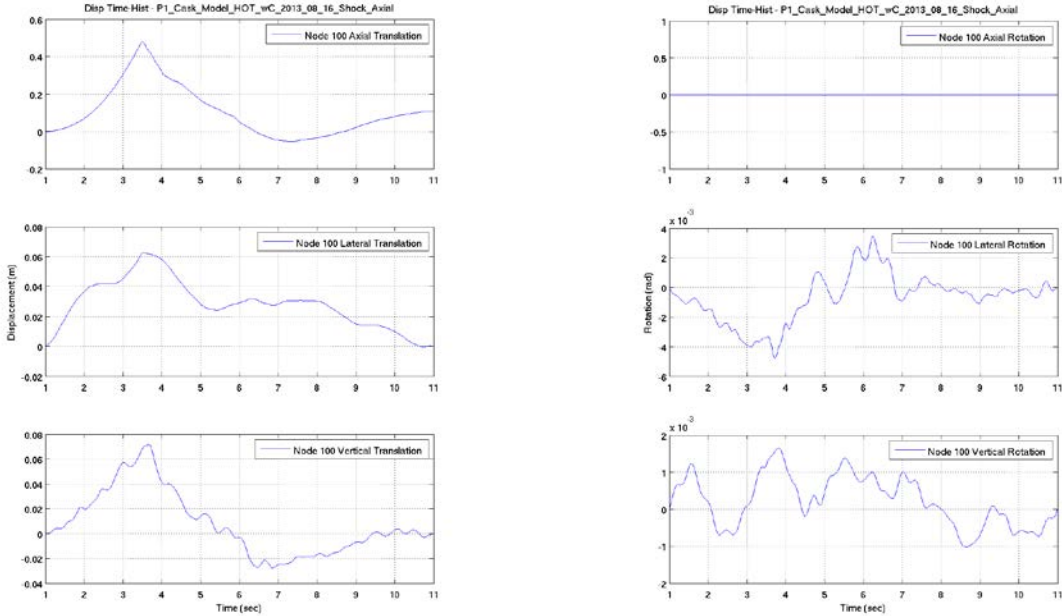ure 1.6 which illustrates the acceleration and displacement time-histories for each of the translation and rotation degrees-of-freedom. Figure 1.7 through Figure 1.9 provide FFT, SRS, and PSD plots for both the input excitation and the basket cell response. Transfer functions for each of the three translation and rotation degrees-of-freedom are shown in Figure 1.10, along with axial and lateral slip and vertical separation plots for cell 11 and cell 13. Investigation of the PSD curves for the input (Figure 1.9) indicates that the input excitations in all degrees-of-freedom contained significant energy in the 10 Hz to 50 Hz frequency range, as well as energy in the 0.5 Hz to 10 Hz range for the lateral and vertical translation and rotation directions. This is in contrast to the P1 Shock X (Axial) case in which the bulk of the energy content was confined to below 10 Hz. Response of the basket cells was predominately at frequencies above 10 Hz, specifically at 18 Hz (Figure 1.7, Figure 1.8, and Figure 1.9). Below 10 Hz there was a significant response in the lateral direction at about 6 Hz which is interesting because the input excitation was minimal at that frequency in that direction. This response is seen as a large peak on the transfer function plot for the lateral direction (Figure 1.10). This behavior may be indicative of a cask-canister-basket mode at approximately 6 Hz in the lateral direction. Investigation of the slip/separation behavior between the fuel assembly and basket for cells 11 and 13 (Figure 1.10) indicates that the fuel assemblies slid around within the basket cells, with slip displacements in the lateral direction of about 3 mm being more pronounced than slip displacements in the axial direction of about 0.5 mm. Some amount of vertical separation between the fuel assembly and basket (~1 mm) was observed in cell 11 (a cell on the exterior of the basket) with a somewhat smaller (~0.8 mm) vertical separation in cell 13 (an interior basket cell). Again the response at each cell location was not identical. For example, comparison of the SRS at each cell in the lateral and vertical translation directions (Figure 1.8) indicates some potentially important differences in the response characteristics between each of the cells.

USED FUEL DISPOSITION CAMPAIGN
**Used Nuclear Fuel Loading and Structural Performance Under Normal Conditions of Transport -
Demonstration of Approach and Results of Used Fuel Performance Characterization**
A-17   **SEPTEMBER 30, 2013**

(a) Acceleration Time-Histories
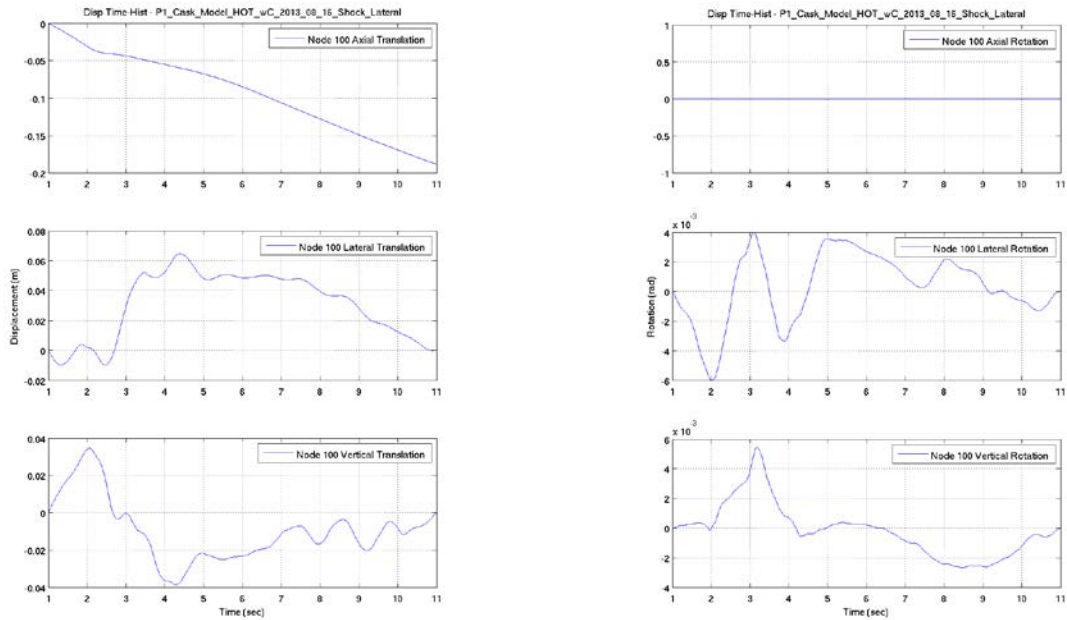
(b) Displacement and Rotation Time-Histories

**Figure 1.6 P1 Shock Y (Lateral) Load Case, Nominal Model Configuration, Input
Acceleration and Displacement Time-Histories.**

USED FUEL DISPOSITION CAMPAIGN
**Used Nuclear Fuel Loading and Structural Performance Under Normal Conditions of Transport -
Demonstration of Approach and Results of Used Fuel Performance Characterization**
A-18   **SEPTEMBER 30, 2013**

(a) Input

(b) Basket Cell Response

Figure 1.7 P1 Shock Y (Lateral) Load Case, Nominal Model Configuration, Input and Basket Cell Response FFTs.
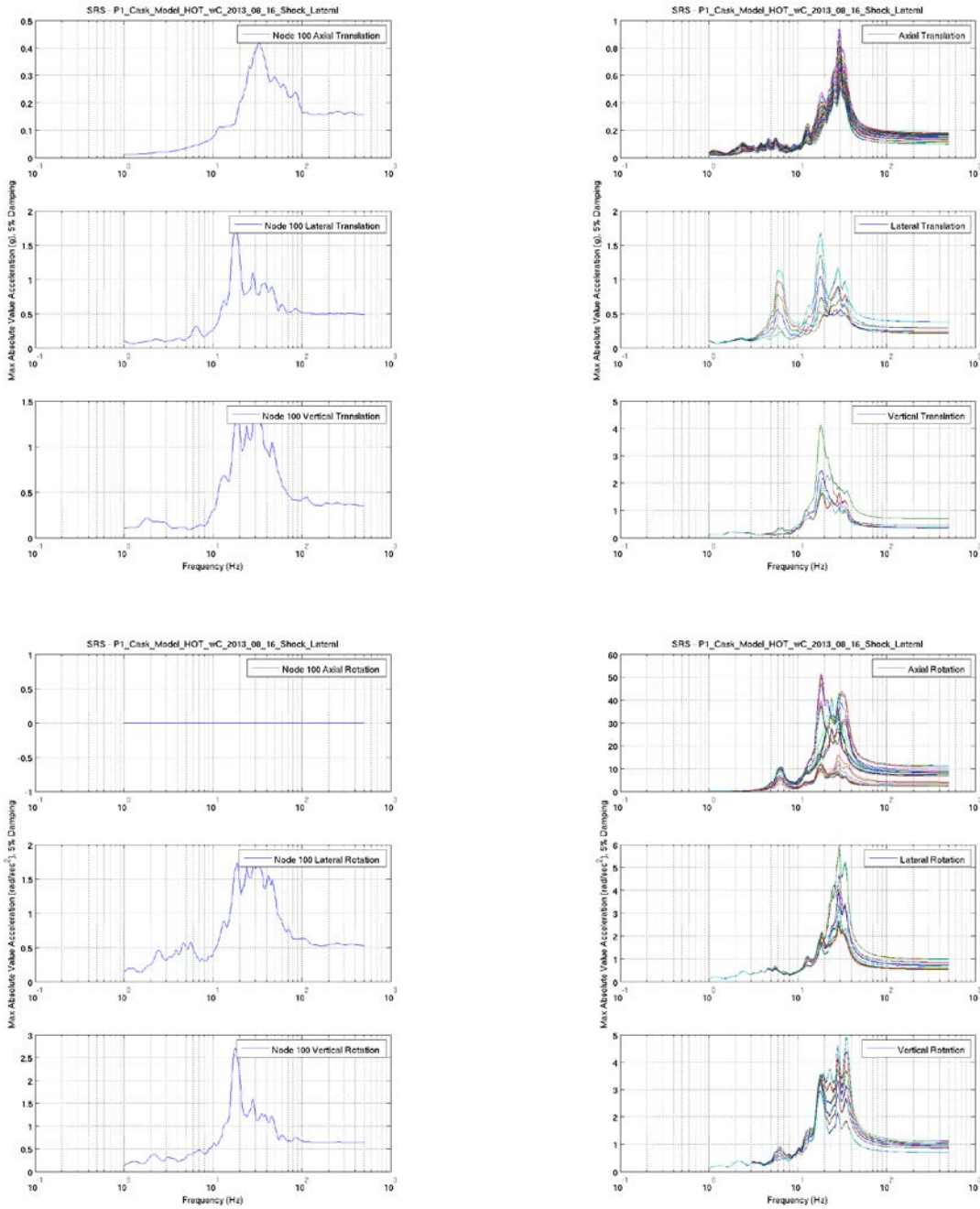
(a) Input   (b) Basket Cell Response

Figure 1.8 P1 Shock Y (Lateral) Load Case, Nominal Model Configuration, Input and Basket Cell Response SRSs.

USED FUEL DISPOSITION CAMPAIGN
**Used Nuclear Fuel Loading and Structural Performance Under Normal Conditions of Transport -
Demonstration of Approach and Results of Used Fuel Performance Characterization**
A-20 **SEPTEMBER 30, 2013**

(a) Input   (b) Basket Cell Response
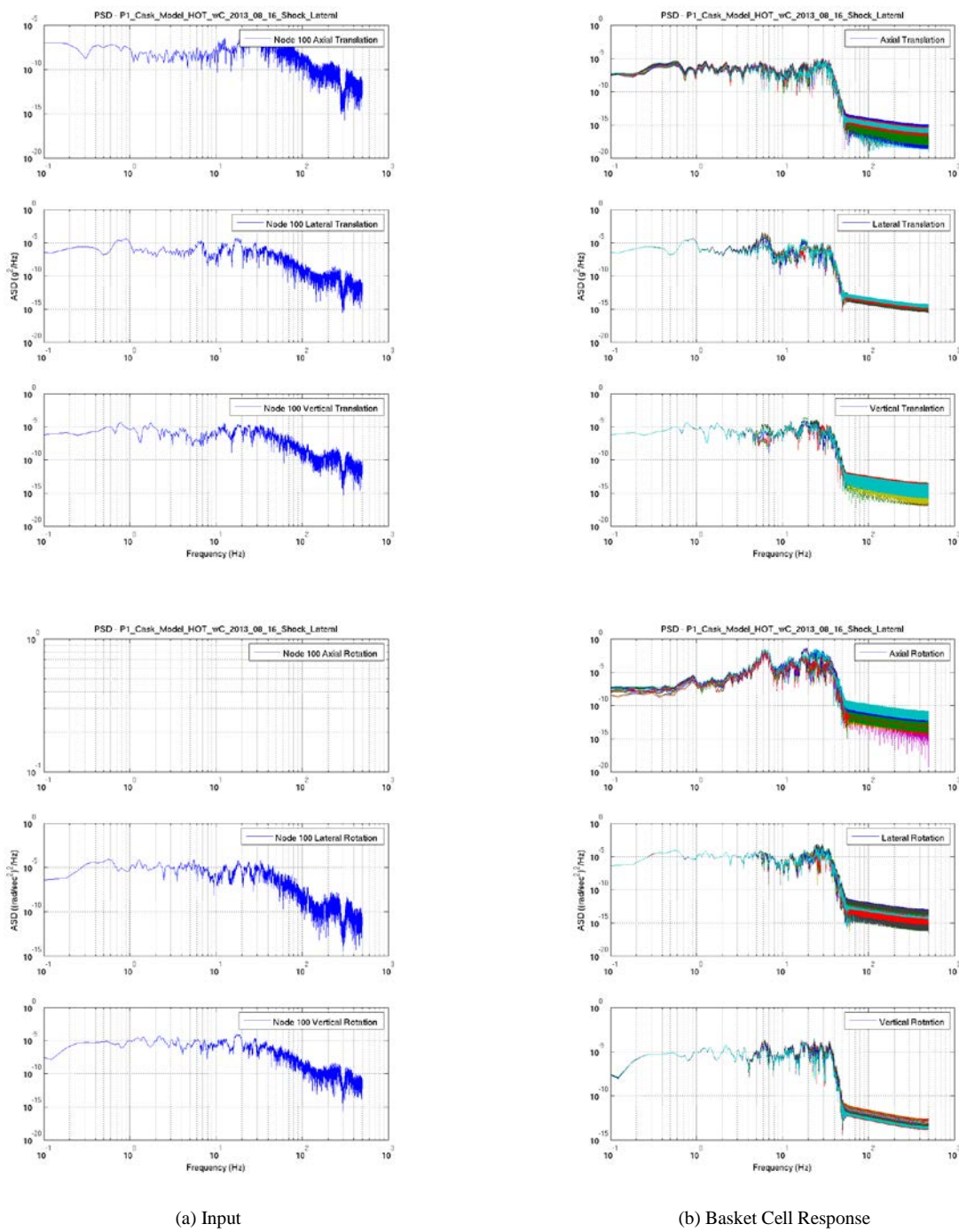
**Figure 1.9 P1 Shock Y (Lateral) Load Case, Nominal Model Configuration, Input and
Basket Cell Response PSDs.**

USED FUEL DISPOSITION CAMPAIGN
**Used Nuclear Fuel Loading and Structural Performance Under Normal Conditions of Transport -
Demonstration of Approach and Results of Used Fuel Performance Characterization**
A-21   **SEPTEMBER 30, 2013**
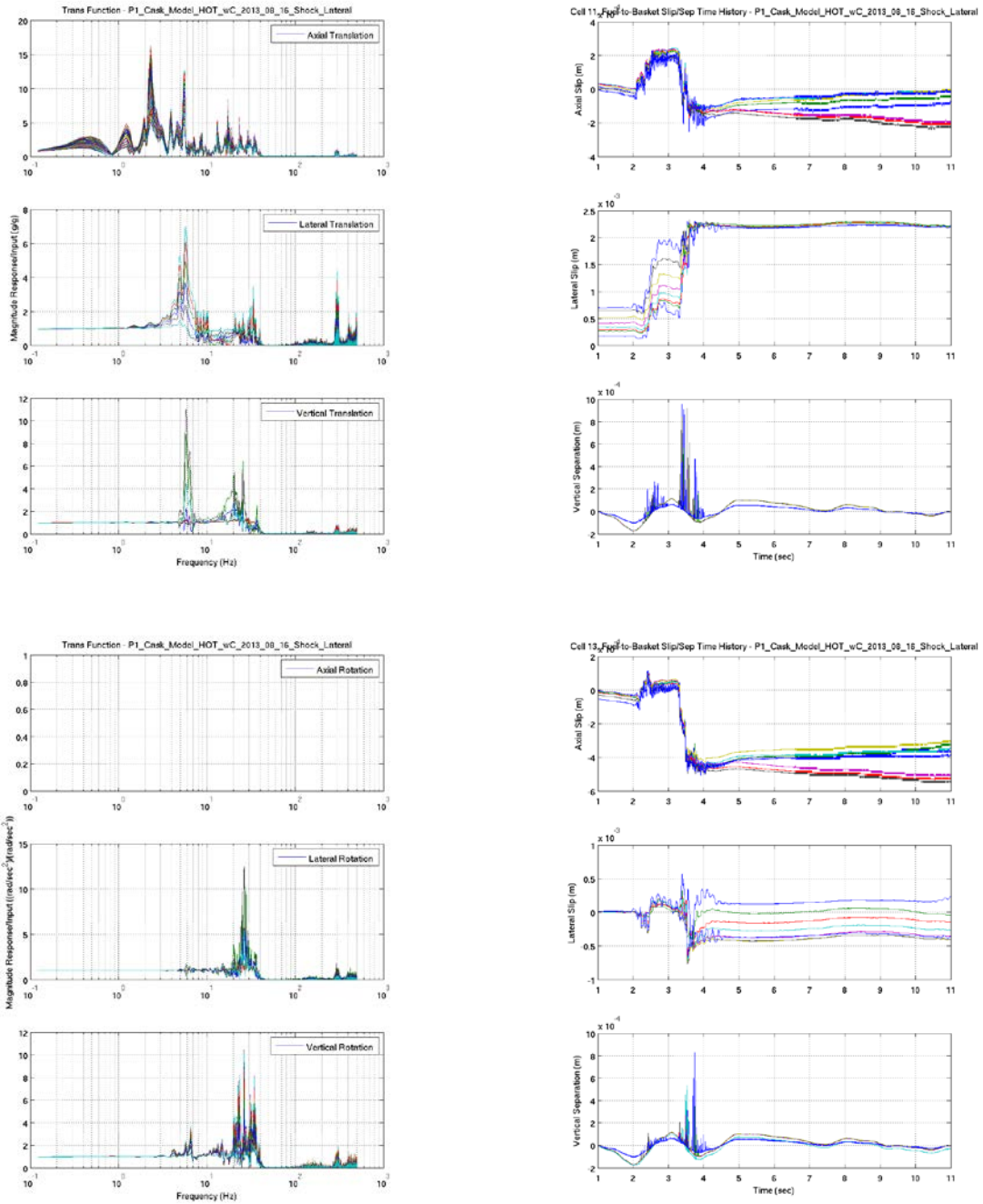
(a) Transfer Functions   (b) Fuel Assembly to Basket Slip/Separation.

**Figure 1.10 P1 Shock Y (Lateral) Load Case, Nominal Model Configuration, Basket Cell
Response Transfer Functions and Slip/Separation Plots.**

USED FUEL DISPOSITION CAMPAIGN
Used Nuclear Fuel Loading and Structural Performance Under Normal Conditions of Transport -
Demonstration of Approach and Results of Used Fuel Performance Characterization
A-22   **SEPTEMBER 30, 2013**

1.3 P1 SHOCK Z (VERTICAL)

The P1 Shock Z (Vertical) case is characterized by a medium duration (~3.0 second) shock with peak time-domain acceleration magnitude in the lateral direction of 1.679 g. This can be seen in Figure 1.11 which illustrates the acceleration and displacement time-histories for each of the translation and rotation degrees-of-freedom. Figure 1.12 through Figure 1.14 provide FFT, SRS, and PSD plots for both the input excitation and the basket cell response. Transfer functions for each of the three translation and rotation degrees-of-freedom are shown in Figure 1.15, along with axial and lateral slip and vertical separation plots for cell 11 and cell 13. Investigation of the input excitation PSD curves (Figure 1.14) indicates that most of the power in the vertical input excitation resided around 1 Hz. The energy in the response in the vertical direction was also largely centered at 1 Hz. There was significant energy at higher frequencies (between 4 and 40 Hz) for rotation about all axes. Figure 1.15 shows that the vertical response in the PSD plot at 1 Hz is merely a reflection of the vertical direction input power at that frequency, and that significant amplification of the input in the vertical direction was almost exclusively confined to frequencies above 10 Hz. It is interesting to note the in the lateral direction, significant amplification of the input at about 5 Hz was occurring, consistent with a cask-canister-basket mode and the observations made for the P1 Shock Y (Lateral) case. Investigation of the slip/separation behavior between the fuel assembly and basket for cells 11 and 13 (Figure 1.15) indicates that significant amounts of lateral and axial slip occurred between the fuel assemblies and basket (on the order of 4 to 6 mm), and that vertical separation was prevalent in both cell 11 and cell 13 particularly between 2 and 3 seconds where it would appear that the assemblies along their entire length lost contact with the basket. The magnitude of the vertical separation between the fuel assemblies and basket cells indicates that they may have impacted the top walls of their cells. Again the response at each cell location was not identical. Differences in the response SRSs can be seen in every direction (with exception of the lateral rotation direction) as shown in Figure 1.13.

USED FUEL DISPOSITION CAMPAIGN
**Used Nuclear Fuel Loading and Structural Performance Under Normal Conditions of Transport -
Demonstration of Approach and Results of Used Fuel Performance Characterization**
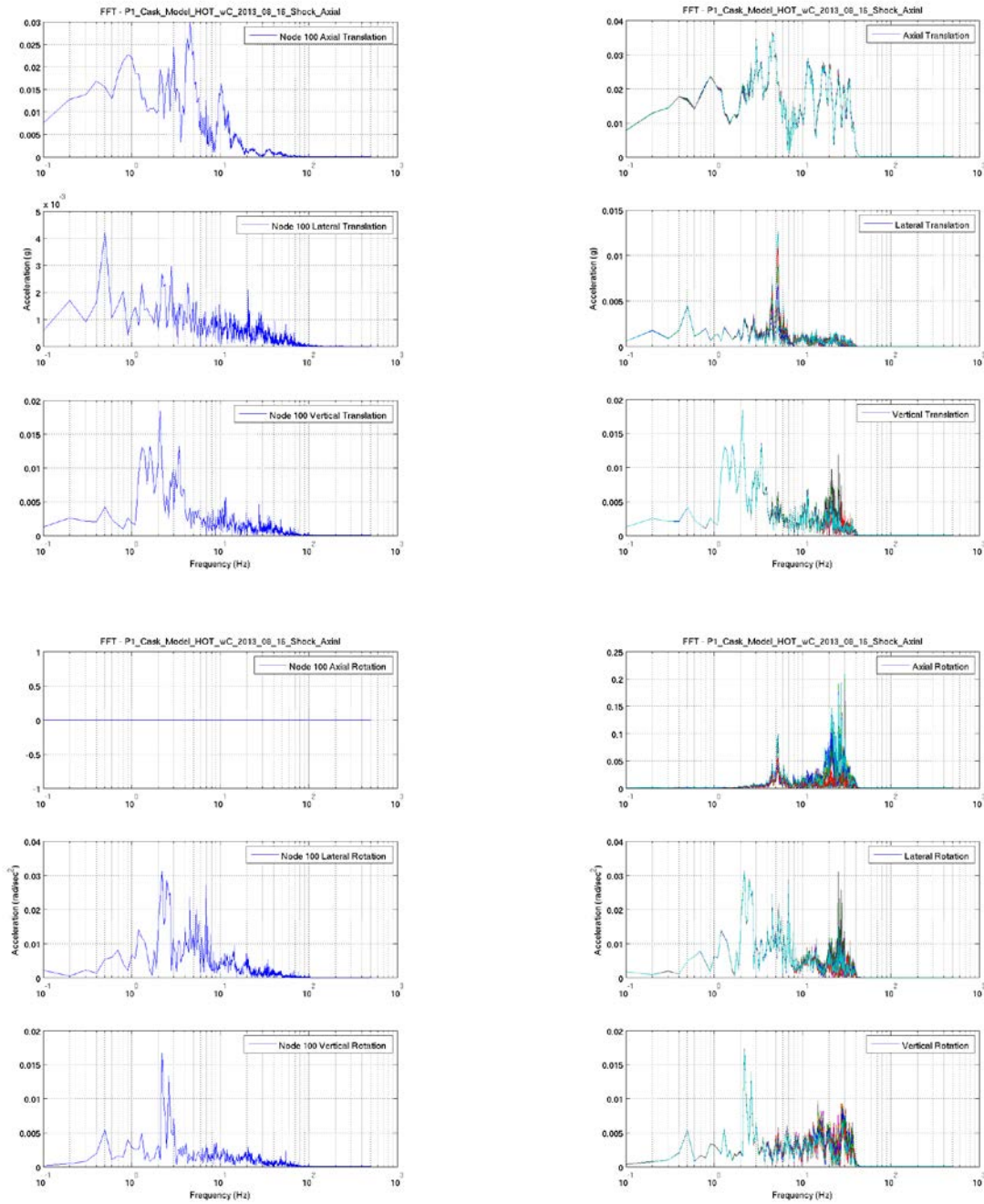**A-23**   **SEPTEMBER 30, 2013**

(a) Acceleration Time-Histories
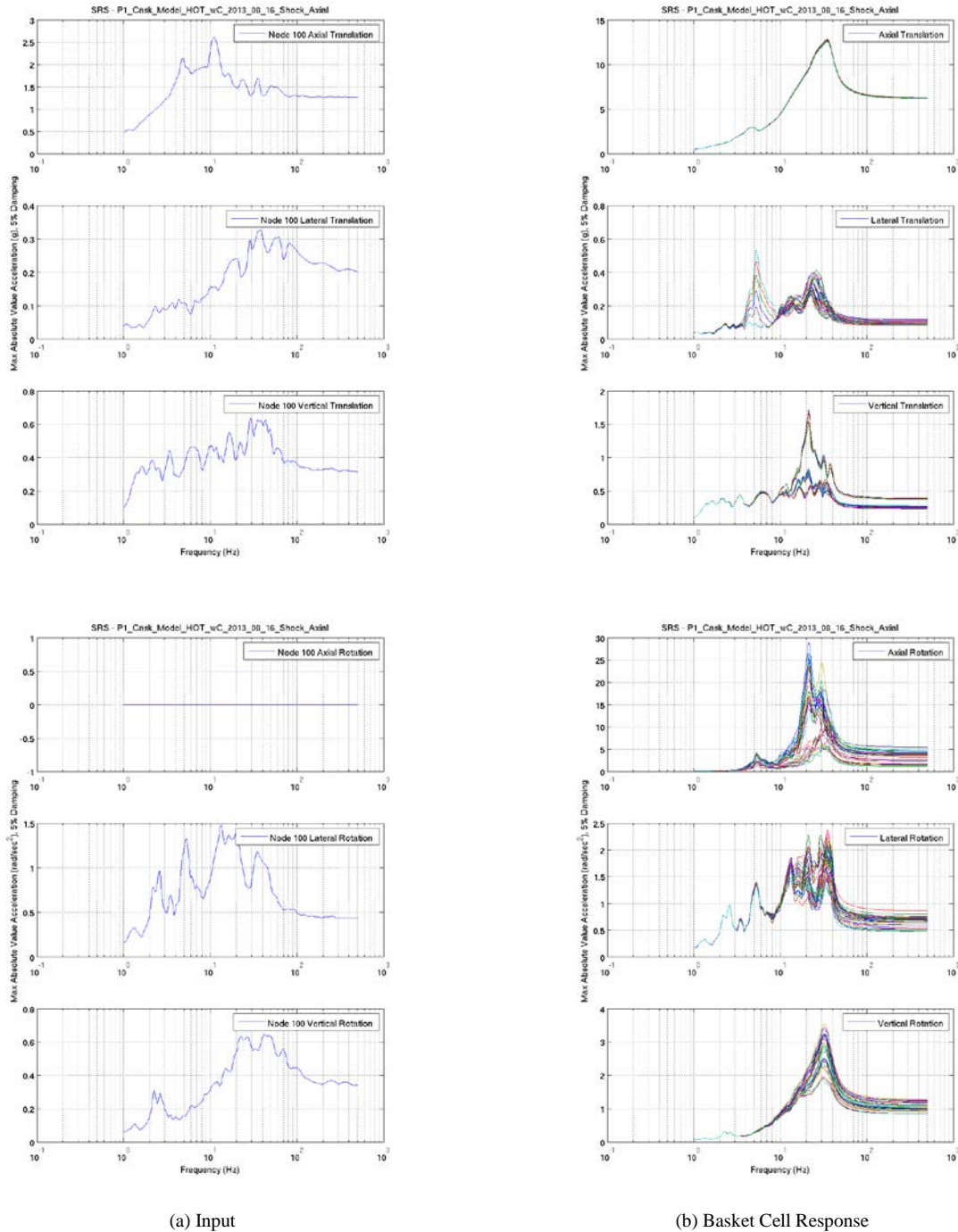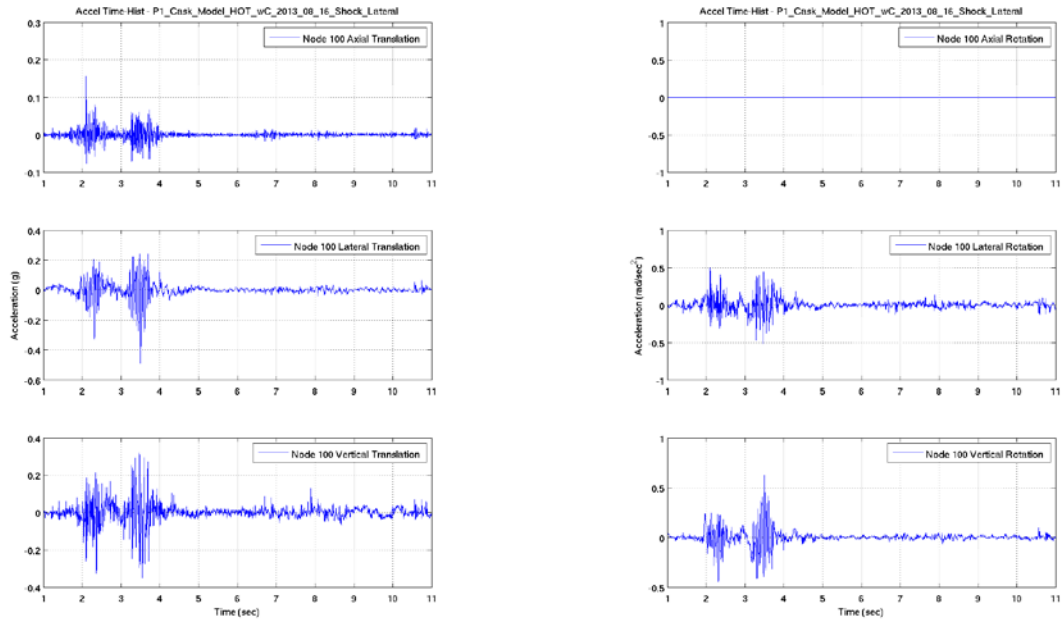

(b) Displacement and Rotation Time-Histories

**Figure 1.11 P1 Shock Z (Vertical) Load Case, Nominal Model Configuration, Input
Acceleration and Displacement Time-Histories.**

USED FUEL DISPOSITION CAMPAIGN
Used Nuclear Fuel Loading and Structural Performance Under Normal Conditions of Transport -
Demonstration of Approach and Results of Used Fuel Performance Characterization
A-24   **SEPTEMBER 30, 2013**

(a) Input

(b) Basket Cell Response
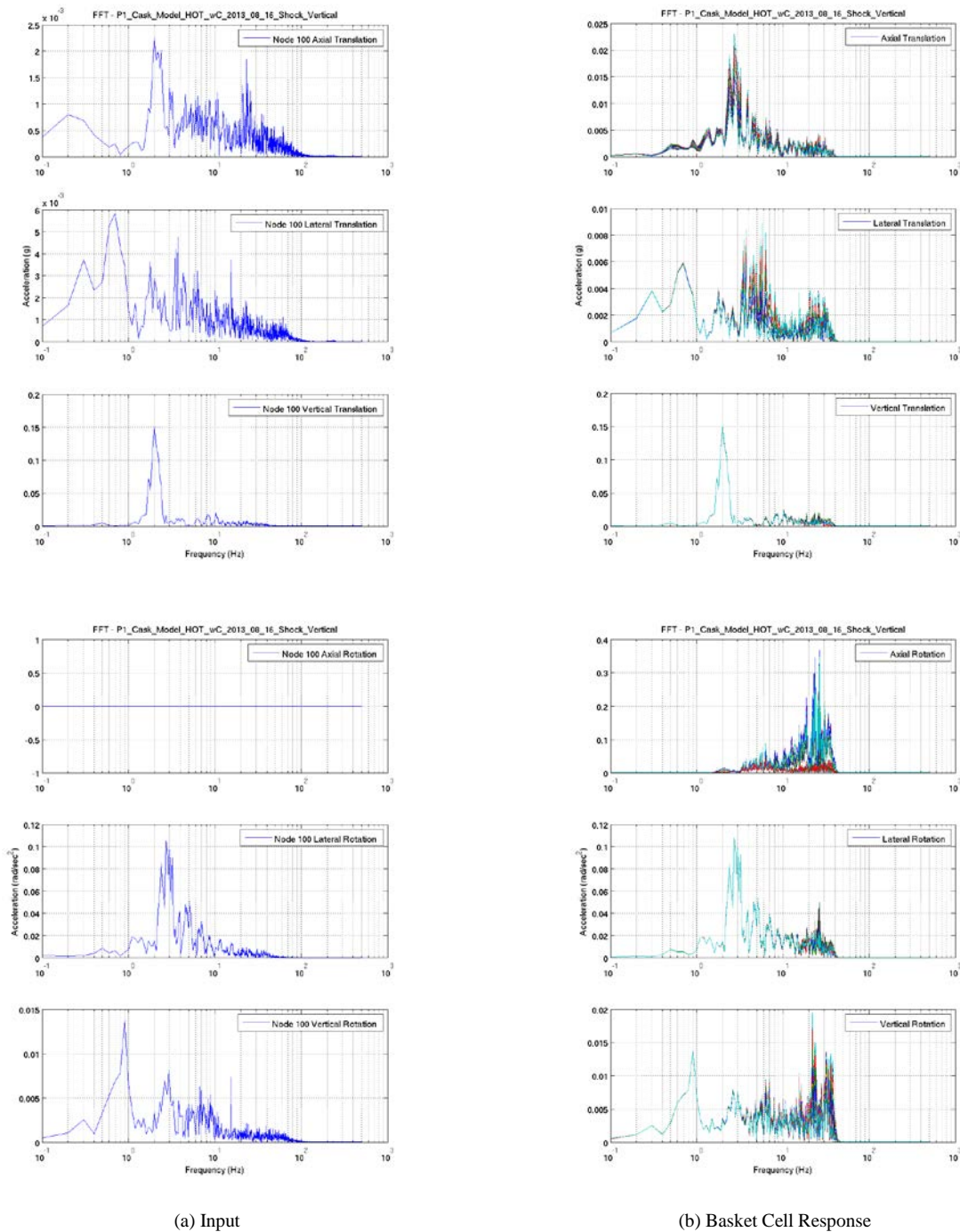
Figure 1.12 P1 Shock Z (Vertical) Load Case, Nominal Model Configuration, Input and Basket Cell Response FFTs.

USED FUEL DISPOSITION CAMPAIGN
**Used Nuclear Fuel Loading and Structural Performance Under Normal Conditions of Transport -
Demonstration of Approach and Results of Used Fuel Performance Characterization**
A-25   **SEPTEMBER 30, 2013**
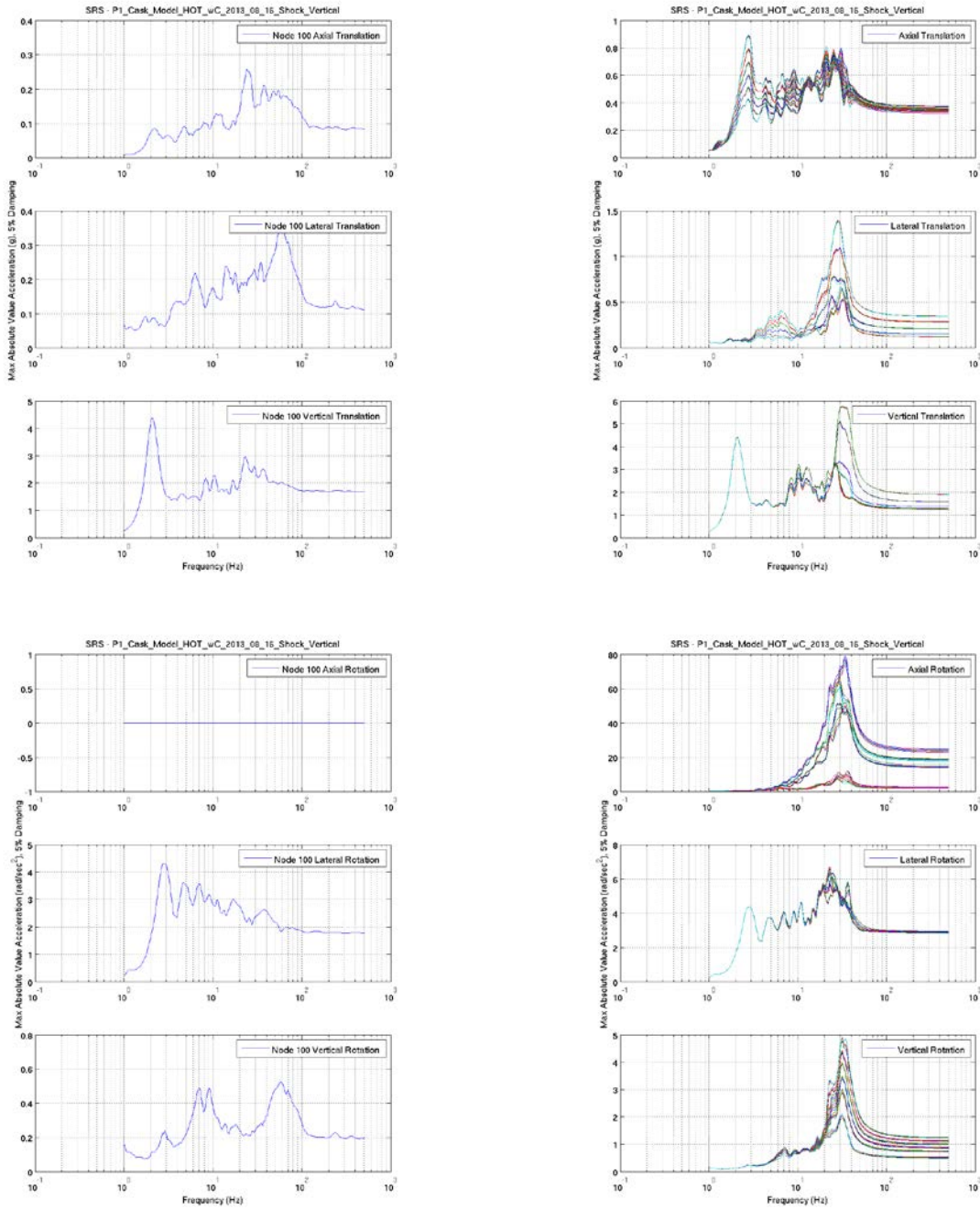
(a) Input   (b) Basket Cell Response

Figure 1.13 P1 Shock Z (Vertical) Load Case, Nominal Model Configuration, Input and Basket Cell Response SRSs.

USED FUEL DISPOSITION CAMPAIGN
Used Nuclear Fuel Loading and Structural Performance Under Normal Conditions of Transport -
Demonstration of Approach and Results of Used Fuel Performance Characterization
A-26   **SEPTEMBER 30, 2013**

(a) Input   (b) Basket Cell Response

Figure 1.14 P1 Shock Z (Vertical) Load Case, Nominal Model Configuration, Input and Basket Cell Response PSDs.

USED FUEL DISPOSITION CAMPAIGN
**Used Nuclear Fuel Loading and Structural Performance Under Normal Conditions of Transport -
Demonstration of Approach and Results of Used Fuel Performance Characterization**
A-27   **SEPTEMBER 30, 2013**
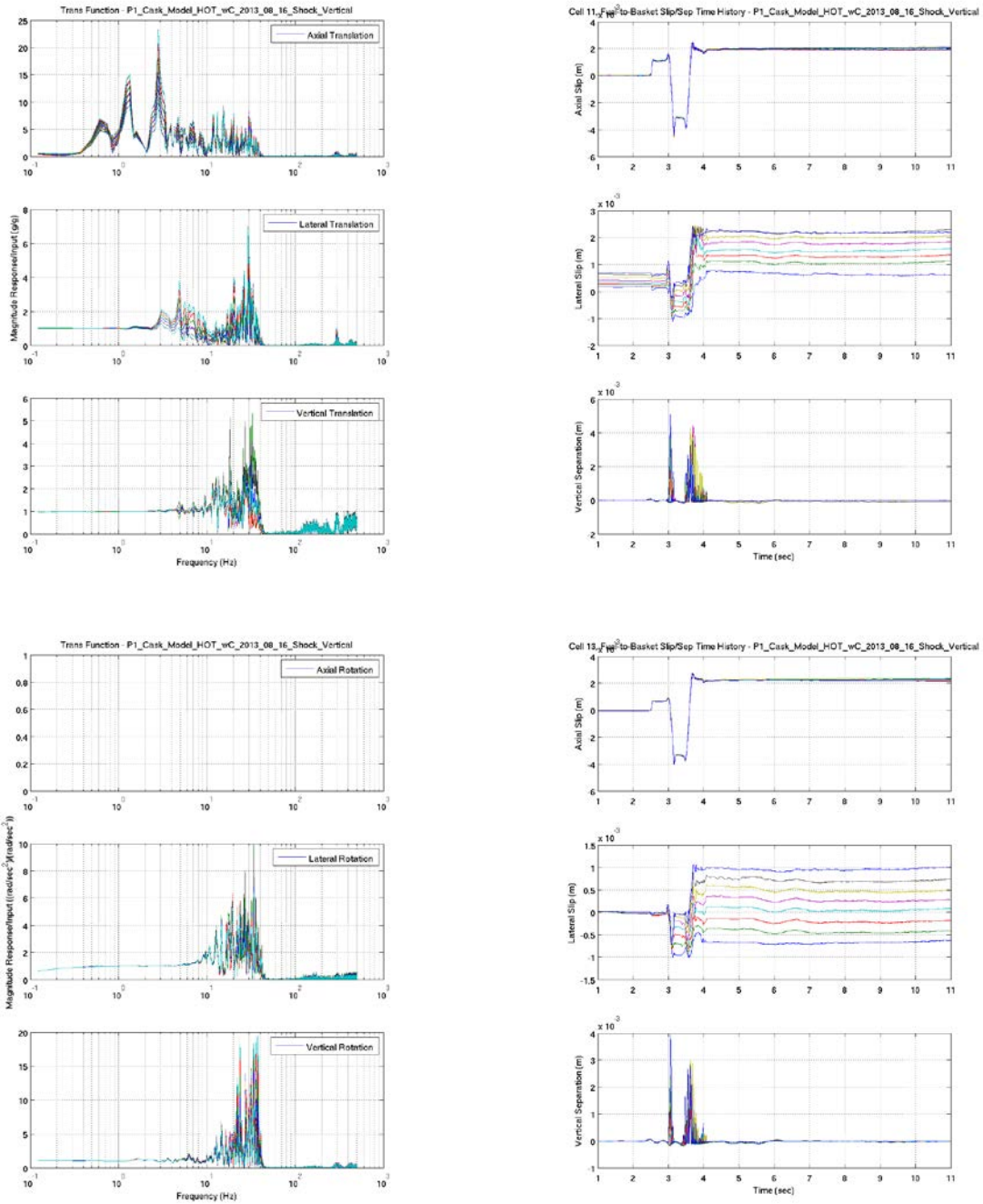
(a) Transfer Functions   (b) Fuel Assembly to Basket Slip/Separation.

**Figure 1.15 P1 Shock Z (Vertical) Load Case, Nominal Model Configuration, Basket Cell
Response Transfer Functions and Slip/Separation Plots.**

USED FUEL DISPOSITION CAMPAIGN
**Used Nuclear Fuel Loading and Structural Performance Under Normal Conditions of Transport -
Demonstration of Approach and Results of Used Fuel Performance Characterization**
A-28   **SEPTEMBER 30, 2013**

1.4   P1 VIBRATION X (AXIAL)

The P1 Vibration X (Axial) case is characterized by a relatively uniform in the time domain vibration in the axial direction with a g_{rms} value of 0.0079 g. The input PSD plots (Figure 1.19) indicate that the majority of the power in the input was located between 2 and 8 Hz in the axial direction, between 1 and 4 Hz in the vertical direction, and between 0.1 and 1 Hz in the lateral direction. The lateral direction input power was somewhat less than the axial and vertical direction components. Figure 1.16 illustrates the acceleration and displacement time-histories for each of the translation and rotation degrees-of-freedom for this load case. Figure 1.17 through Figure 1.19 provide FFT, SRS, and PSD plots for both the input excitation and the basket cell response. Transfer functions for each of the translation and rotation degrees-of-freedom are shown in Figure 1.20, along with axial and lateral slip and vertical separation plots for cell 11 and cell 13. Figure 1.19 indicates that much of the power in the response in the axial direction was centered at about 2.5 and 7 Hz, in the lateral direction at about 5.5 Hz, and in the vertical direction between 1 and 3 Hz. A significant amount of power existed at multiple frequencies for axial rotation, in particular at about 5.5 Hz and at several frequencies above 10 Hz. This is particularly interesting because there was no rotational excitation in the axial direction. Rather, this rotational response must be the result of the lateral translation input excitation. It is probable that the lateral excitation was exciting a rocking mode of the canister in the cask and a racking mode of the basket. Investigation of the transfer functions in Figure 1.20 indicates that the response in the axial direction at 2.5 Hz and 7 Hz was only a slight amplification of the input accelerations in that direction. Most of the amplification in the axial direction occurred above 10 Hz, but the input acceleration did not contain much power at those frequencies (Figure 1.19). In the lateral direction, the transfer function indicates that the response observed at 5.5 Hz was a significant amplification over the input accelerations, indicating a response mode at that frequency. In the vertical direction, the transfer function indicates that little or no amplification of the input accelerations occurred between 1 and 3 Hz, but that the response observed between 20 and 30 Hz was likely indicative of response modes at those frequencies. Investigation of the slip/separation behavior between the fuel assembly and basket for cells 11 and 13 (Figure 1.20) indicates that little or no slip in the axial or lateral directions occurred between the fuel assemblies and basket, and that no vertical separation occurred either. Again, in this case the response at each cell location was not identical. The differences were particularly pronounced in the 3.5 Hz response in the lateral translation direction, and between 10 and 30 Hz in the vertical translation, and axial, lateral, and vertical rotation directions of the SRS plots show in Figure 1.18.

USED FUEL DISPOSITION CAMPAIGN
Used Nuclear Fuel Loading and Structural Performance Under Normal Conditions of Transport -
Demonstration of Approach and Results of Used Fuel Performance Characterization
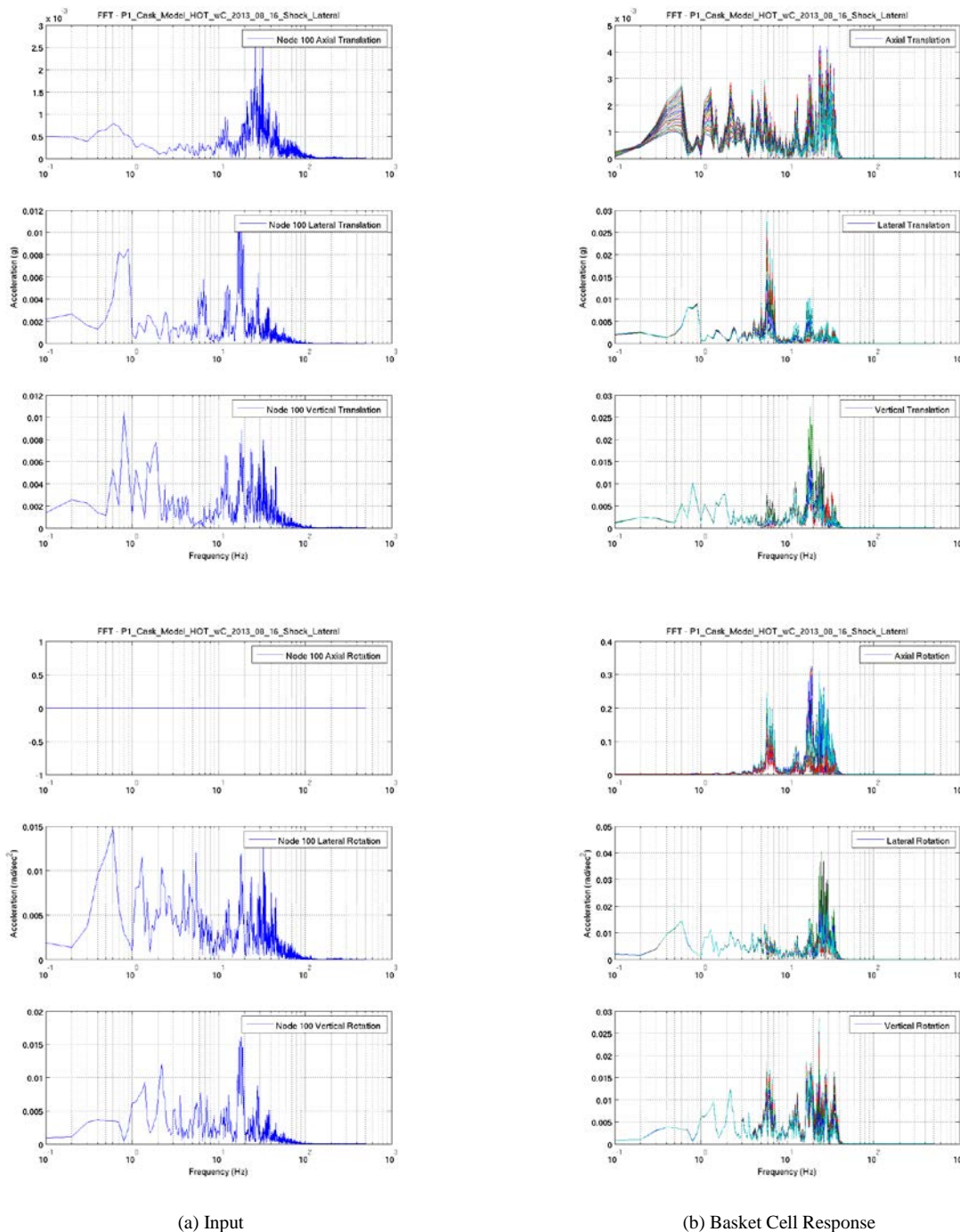A-29   SEPTEMBER 30, 2013
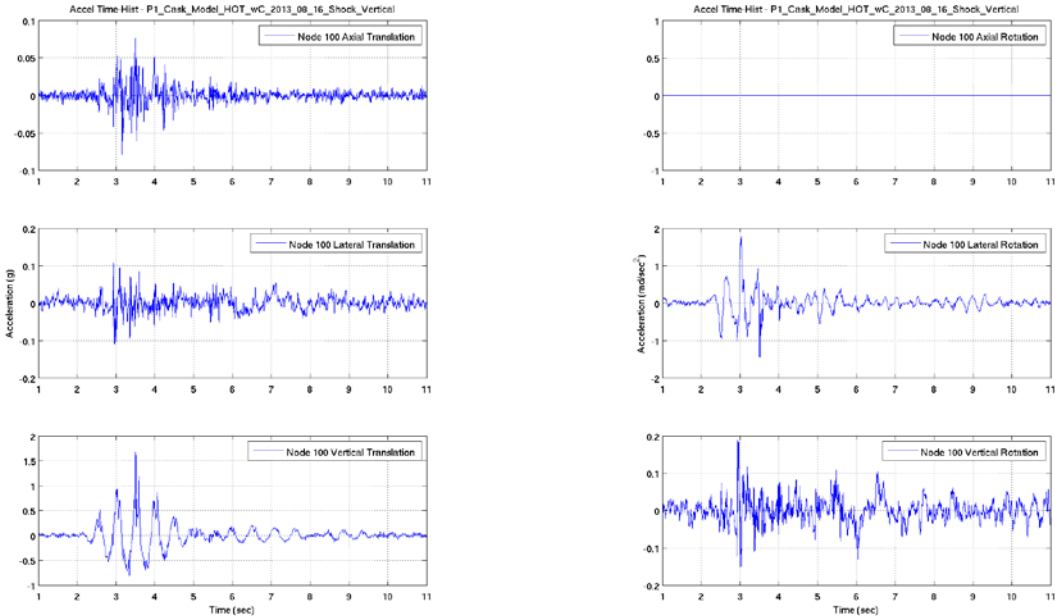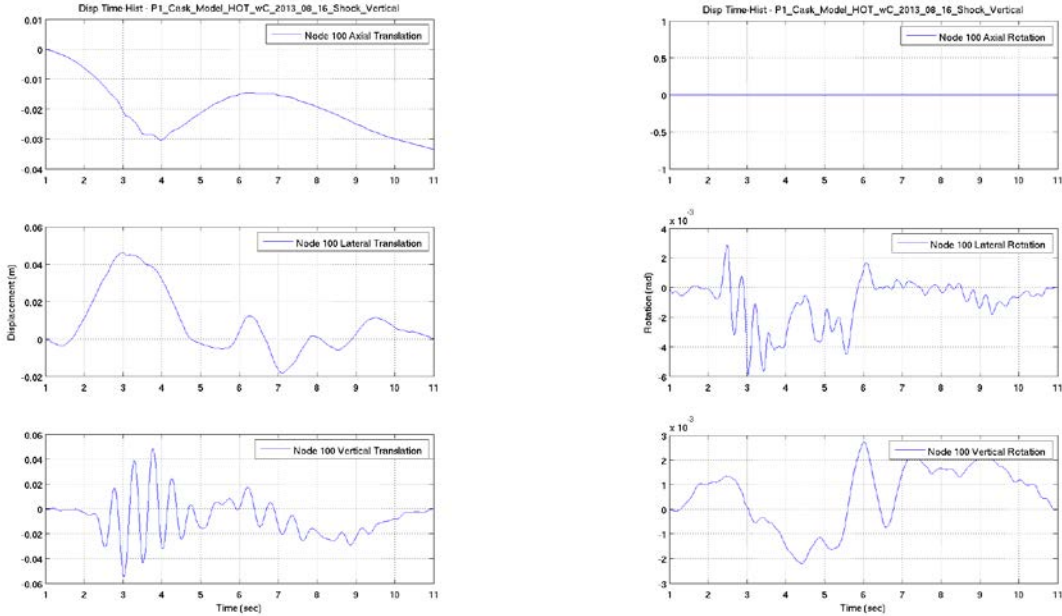

(a) Acceleration Time-Histories

(b) Displacement and Rotation Time-Histories

**Figure 1.16 P1 Vibration X (Axial) Load Case, Nominal Model Configuration, Input
Acceleration and Displacement Time-Histories.**
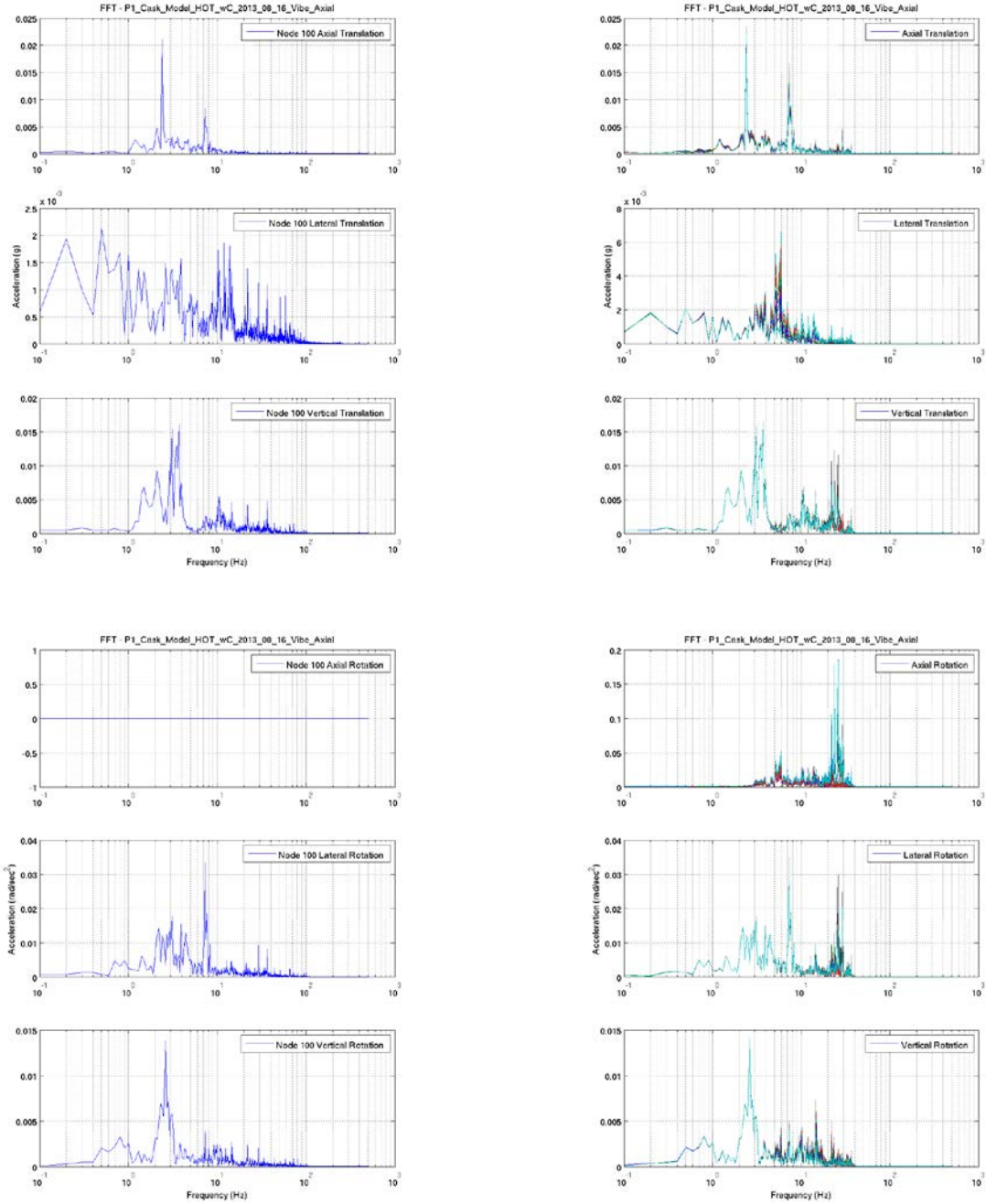
(a) Input

(b) Basket Cell Response

Figure 1.17 P1 Vibration X (Axial) Load Case, Nominal Model Configuration, Input and Basket Cell Response FFTs.

USED FUEL DISPOSITION CAMPAIGN
Used Nuclear Fuel Loading and Structural Performance Under Normal Conditions of Transport -
Demonstration of Approach and Results of Used Fuel Performance Characterization
A-31   **SEPTEMBER 30, 2013**
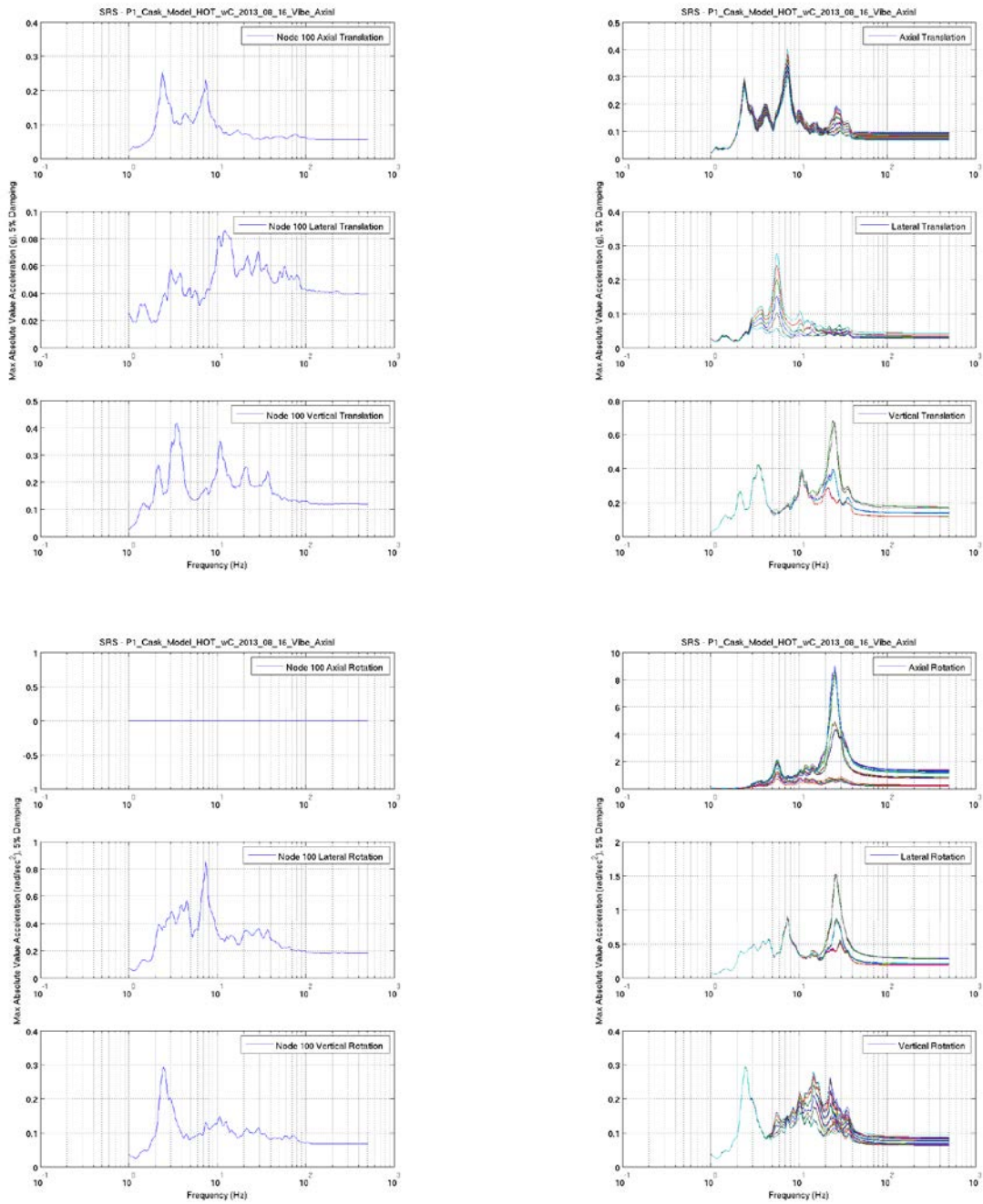
(a) Input   (b) Basket Cell Response

Figure 1.18 P1 Vibration X (Axial) Load Case, Nominal Model Configuration, Input and Basket Cell Response SRSs.

USED FUEL DISPOSITION CAMPAIGN
**Used Nuclear Fuel Loading and Structural Performance Under Normal Conditions of Transport -
Demonstration of Approach and Results of Used Fuel Performance Characterization**
A-32 **SEPTEMBER 30, 2013**

(a) Input

(b) Basket Cell Response

Figure 1.19 P1 Vibration X (Axial) Load Case, Nominal Model Configuration, Input and Basket Cell Response PSDs.

USED FUEL DISPOSITION CAMPAIGN
**Used Nuclear Fuel Loading and Structural Performance Under Normal Conditions of Transport -
Demonstration of Approach and Results of Used Fuel Performance Characterization**
A-33   **SEPTEMBER 30, 2013**
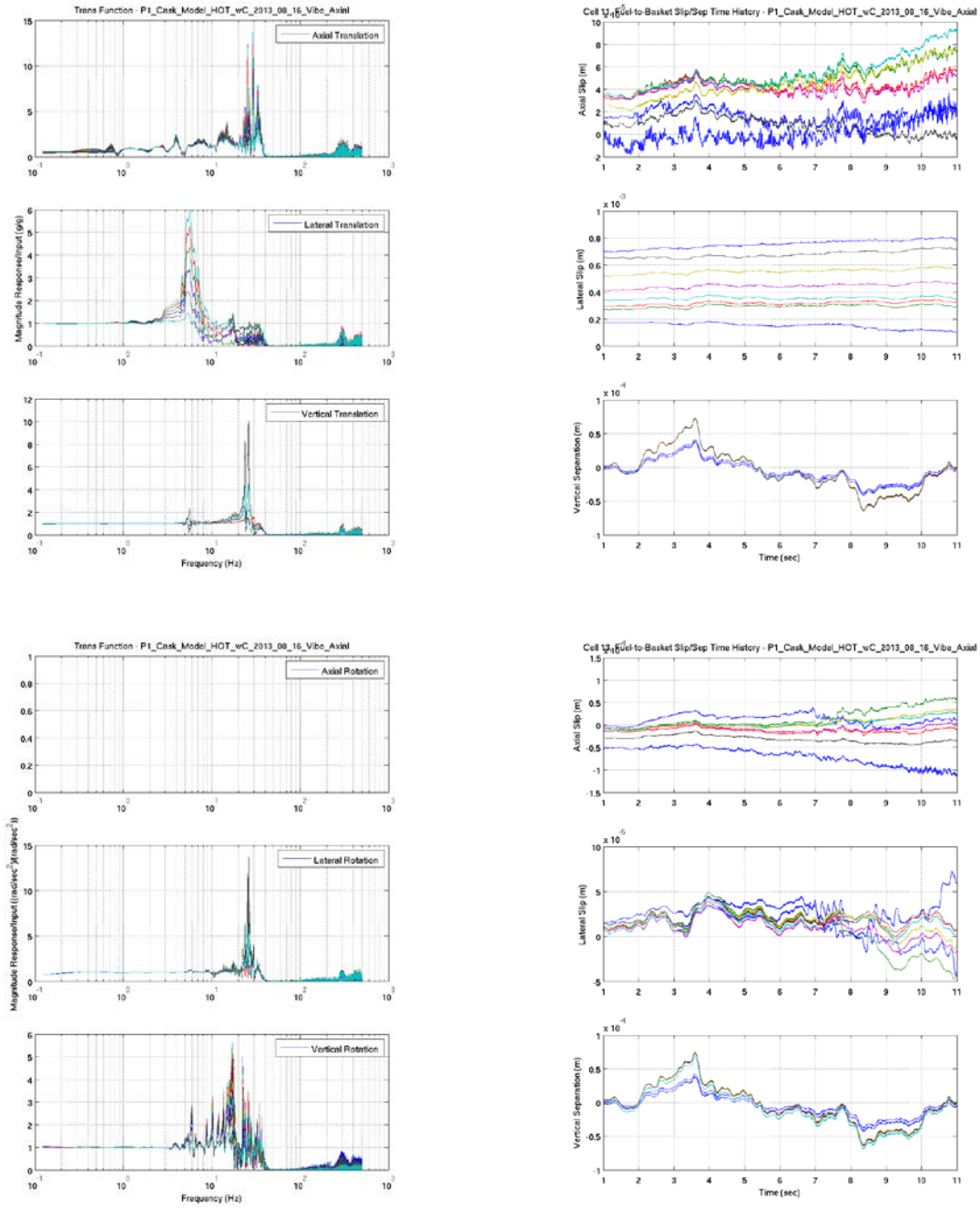
(a) Transfer Functions   (b) Fuel Assembly to Basket Slip/Separation.

**Figure 1.20 P1 Vibration X (Axial) Load Case, Nominal Model Configuration, Basket Cell
Response Transfer Functions and Slip/Separation Plots.**

USED FUEL DISPOSITION CAMPAIGN
Used Nuclear Fuel Loading and Structural Performance Under Normal Conditions of Transport -
Demonstration of Approach and Results of Used Fuel Performance Characterization
A-34   **SEPTEMBER 30, 2013**

1.5   P1 VIBRATION Y (LATERAL)

The P1 Vibration Y (Lateral) case is characterized by a relatively uniform vibration in the time domain in the lateral direction with a g_{rms} value of 0.0105 g. The input PSD plots (Figure 1.24) indicate that the majority of the power in the input was spread across a frequency range from 0.3 to 50 Hz. The power in the input acceleration in the axial direction was significantly lower across that same frequency range. The power in the vertical direction was greater than in both the lateral and axial directions and was centered at about 2 and 10 Hz. Figure 1.21 illustrates the acceleration and displacement time-histories for each of the translation and rotation degrees-of-freedom for this load case. Figure 1.22 through Figure 1.24 provide FFT, SRS, and PSD plots for both the input excitation and the basket cell response. Transfer functions for each of the translation and rotation degrees-of-freedom are shown in Figure 1.25, along with axial and lateral slip and vertical separation plots for cell 11 and cell 13. Figure 1.24 indicates that much of the power in the response in the lateral direction was centered at about 3.5 and 5.5 Hz. In the axial direction there was a significant response at 1, 3, and 5.5 Hz, as well as between 25 and 30 Hz. A significant response was seen in the vertical direction at about 2 Hz and also in the range between 10 and 30 Hz. The axial rotation response contained by far the most power observed in the rotational response degrees-of-freedom, with the response most pronounced at 3.5 and 5.5 Hz, and between 10 and 30 Hz. Investigation of the transfer functions in Figure 1.25 indicates that the response in the lateral direction at 5.5 Hz was the result of significant amplification of the input acceleration at that frequency. The transfer function for the axial direction indicates that the response observed in that direction at 1, 3, and 5.5 Hz was the result of significant amplification of the input excitation accelerations at those frequencies in that direction, whereas the response at 20 to 30 Hz was only modestly amplified. Finally, the transfer function for the response in the vertical direction indicates strong amplification of the excitation accelerations in that direction at about 5.5 and between 20 and 30 Hz. Investigation of the slip/separation behavior between the fuel assembly and basket for cells 11 and 13 (Figure 1.25) indicates that little or no slip in the axial and lateral directions occurred between the fuel assemblies and basket, and that little or no vertical separation occurred either. Differences in response characteristics at each cell location were again pronounced in the SRS data (Figure 1.23), particularly at 3.5 Hz in the lateral direction and between 10 and 30 Hz in the vertical translation, and axial, lateral and vertical rotation directions.

USED FUEL DISPOSITION CAMPAIGN
**Used Nuclear Fuel Loading and Structural Performance Under Normal Conditions of Transport -
Demonstration of Approach and Results of Used Fuel Performance Characterization**
A-35
SEPTEMBER 30, 2013

(a) Acceleration Time-Histories

(b) Displacement and Rotation Time-Histories

**Figure 1.21 P1 Vibration Y (Lateral) Load Case, Nominal Model Configuration, Input
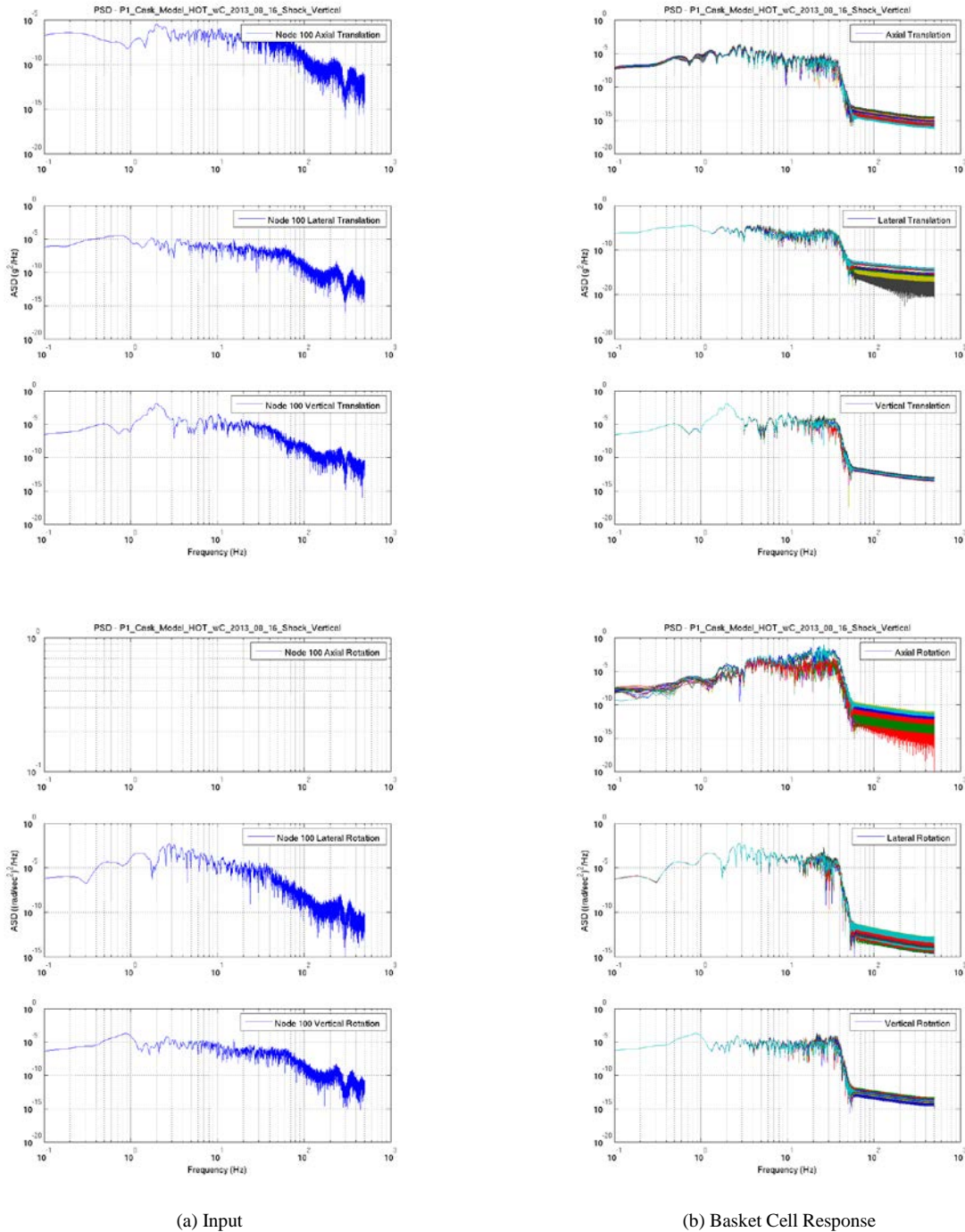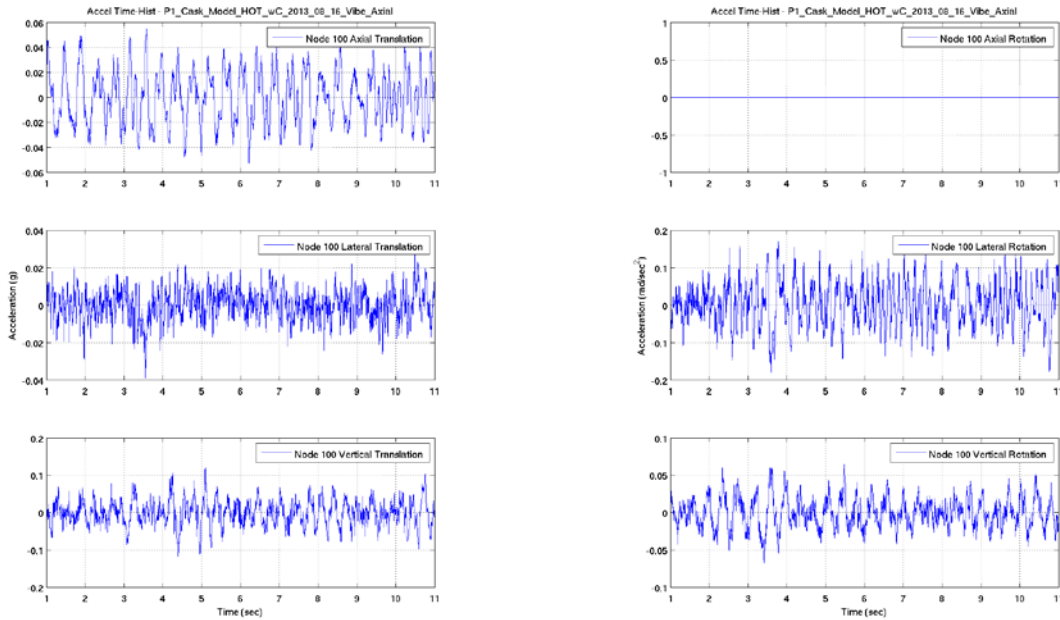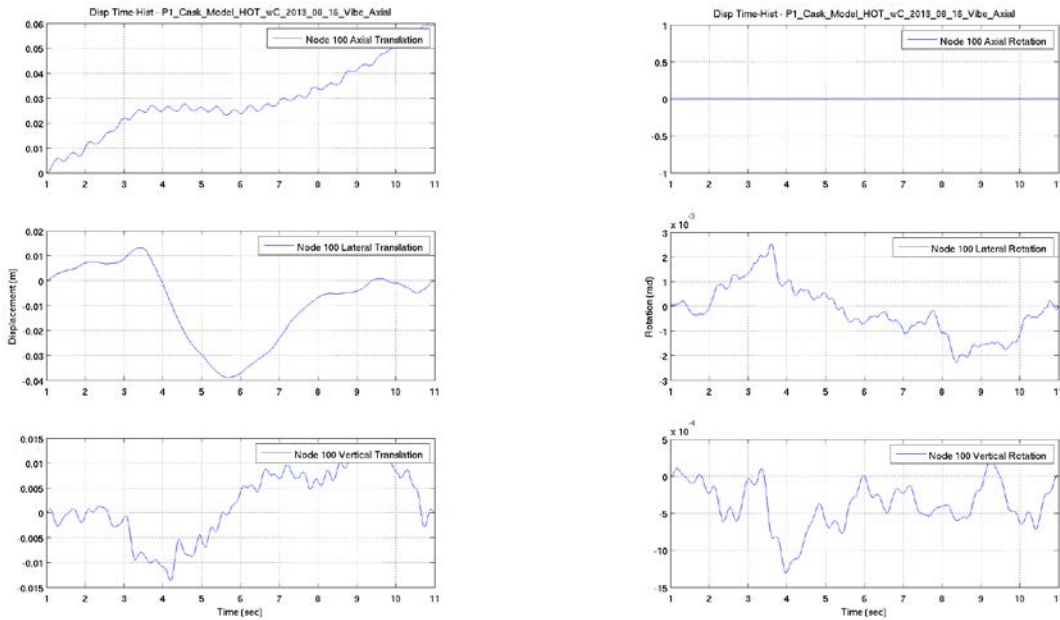Acceleration and Displacement Time-Histories.**

USED FUEL DISPOSITION CAMPAIGN
Used Nuclear Fuel Loading and Structural Performance Under Normal Conditions of Transport -
Demonstration of Approach and Results of Used Fuel Performance Characterization
A-36   **SEPTEMBER 30, 2013**

(a) Input

(b) Basket Cell Response
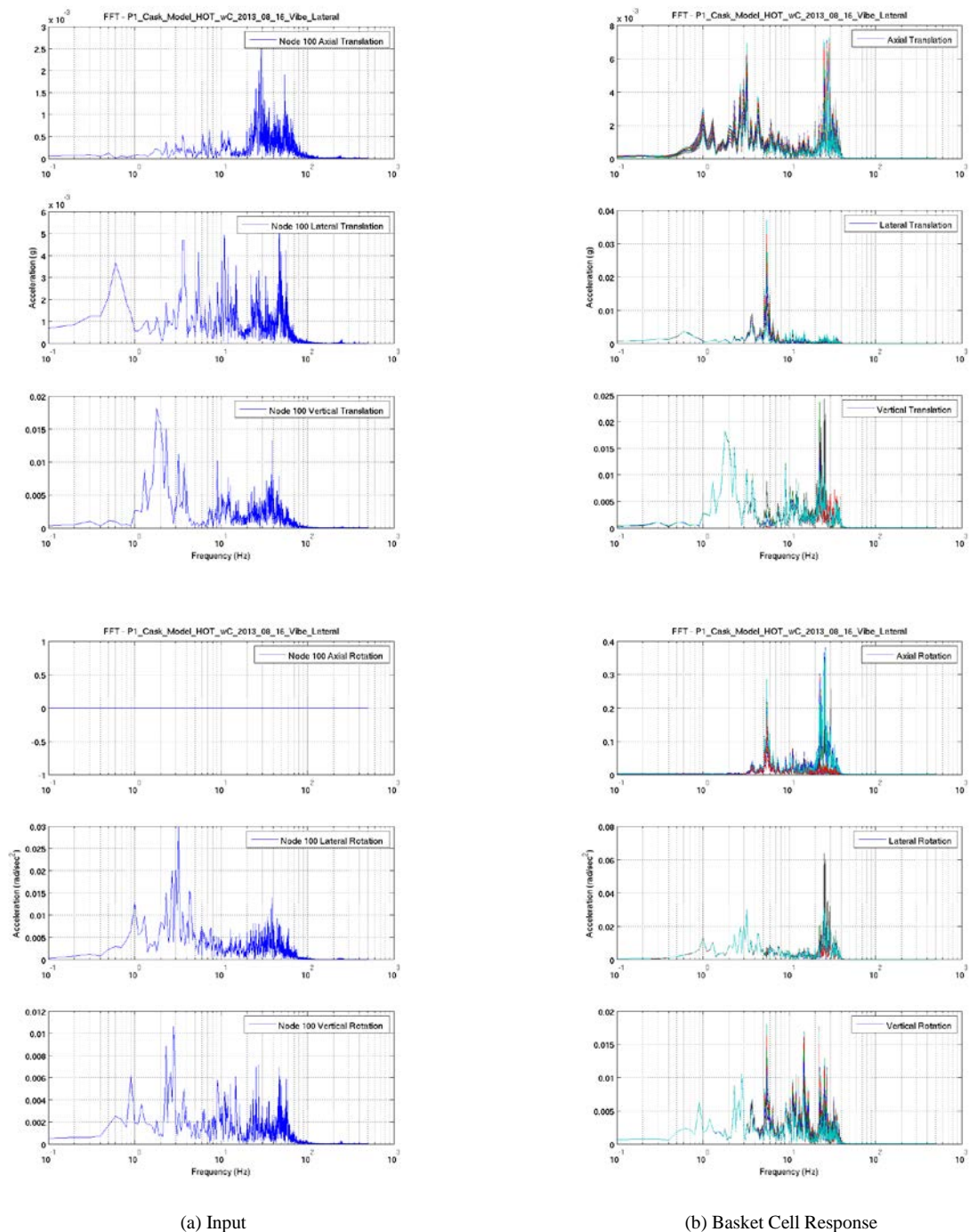
Figure 1.22 P1 Vibration Y (Lateral) Load Case, Nominal Model Configuration, Input and Basket Cell Response FFTs.

USED FUEL DISPOSITION CAMPAIGN
**Used Nuclear Fuel Loading and Structural Performance Under Normal Conditions of Transport -
Demonstration of Approach and Results of Used Fuel Performance Characterization**
A-37   **SEPTEMBER 30, 2013**

(a) Input

(b) Basket Cell Response
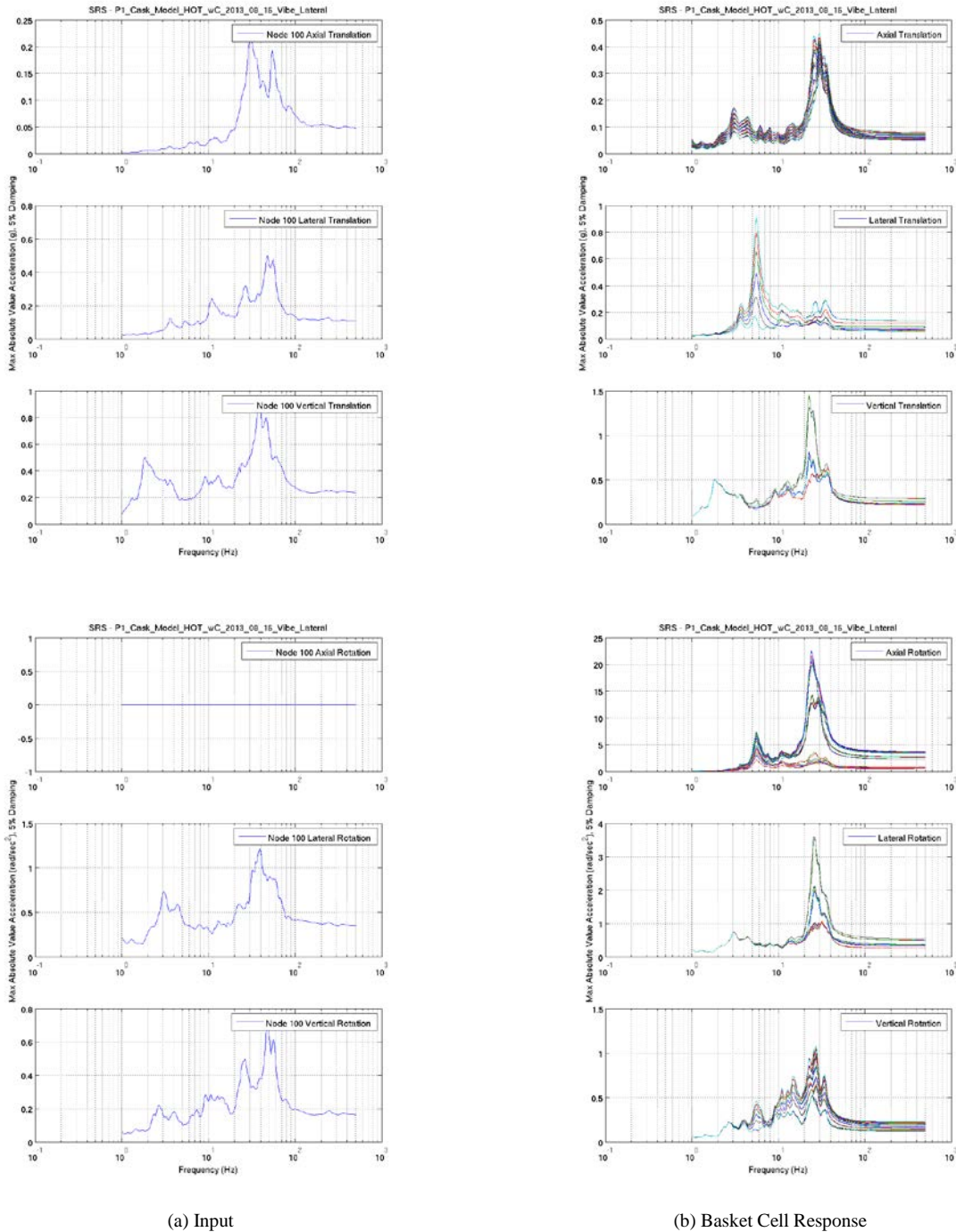
**Figure 1.23 P1 Vibration Y (Lateral) Load Case, Nominal Model Configuration, Input and
Basket Cell Response SRSs.**

USED FUEL DISPOSITION CAMPAIGN
Used Nuclear Fuel Loading and Structural Performance Under Normal Conditions of Transport -
Demonstration of Approach and Results of Used Fuel Performance Characterization
A-38   **SEPTEMBER 30, 2013**
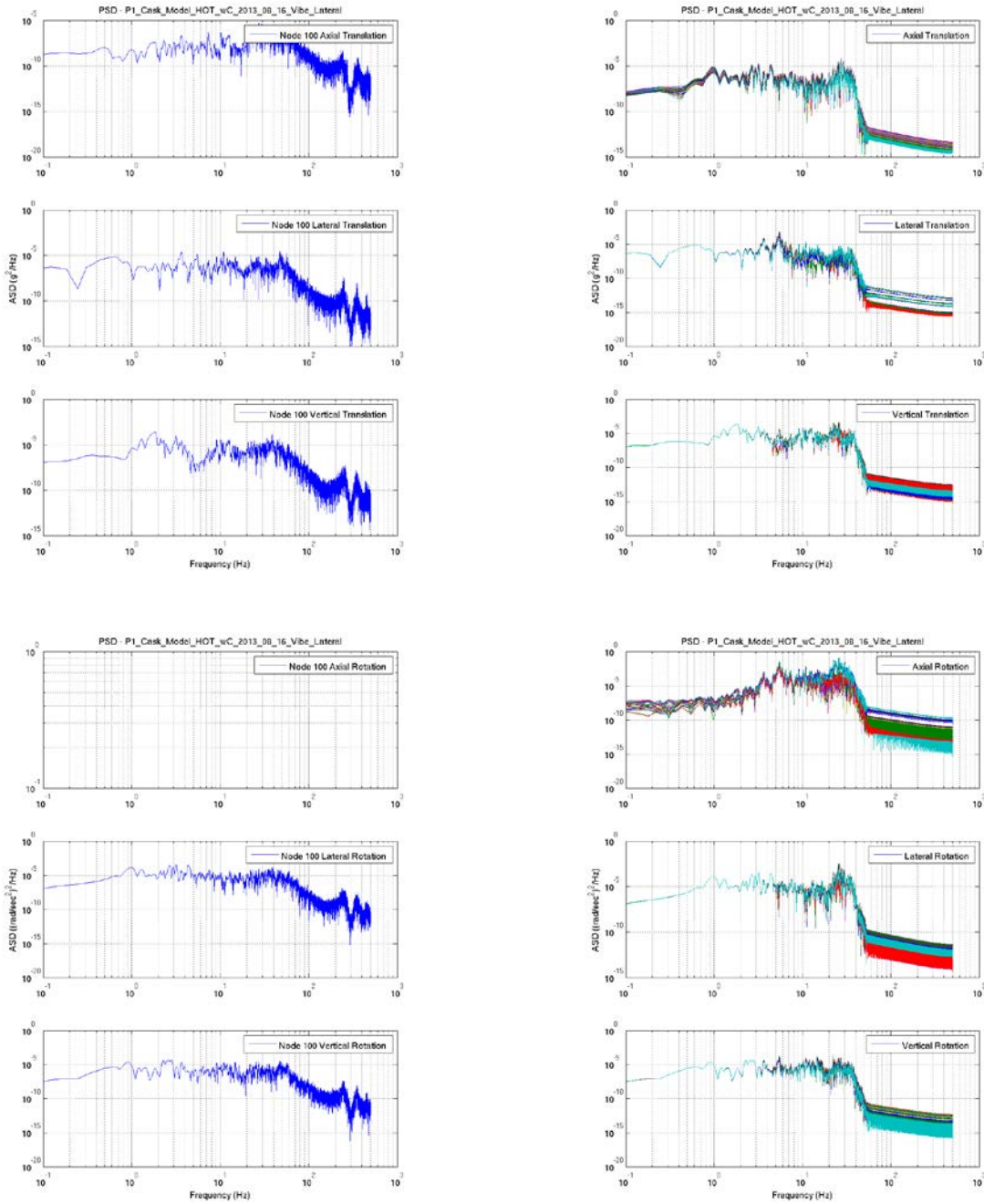
(a) Input

(b) Basket Cell Response

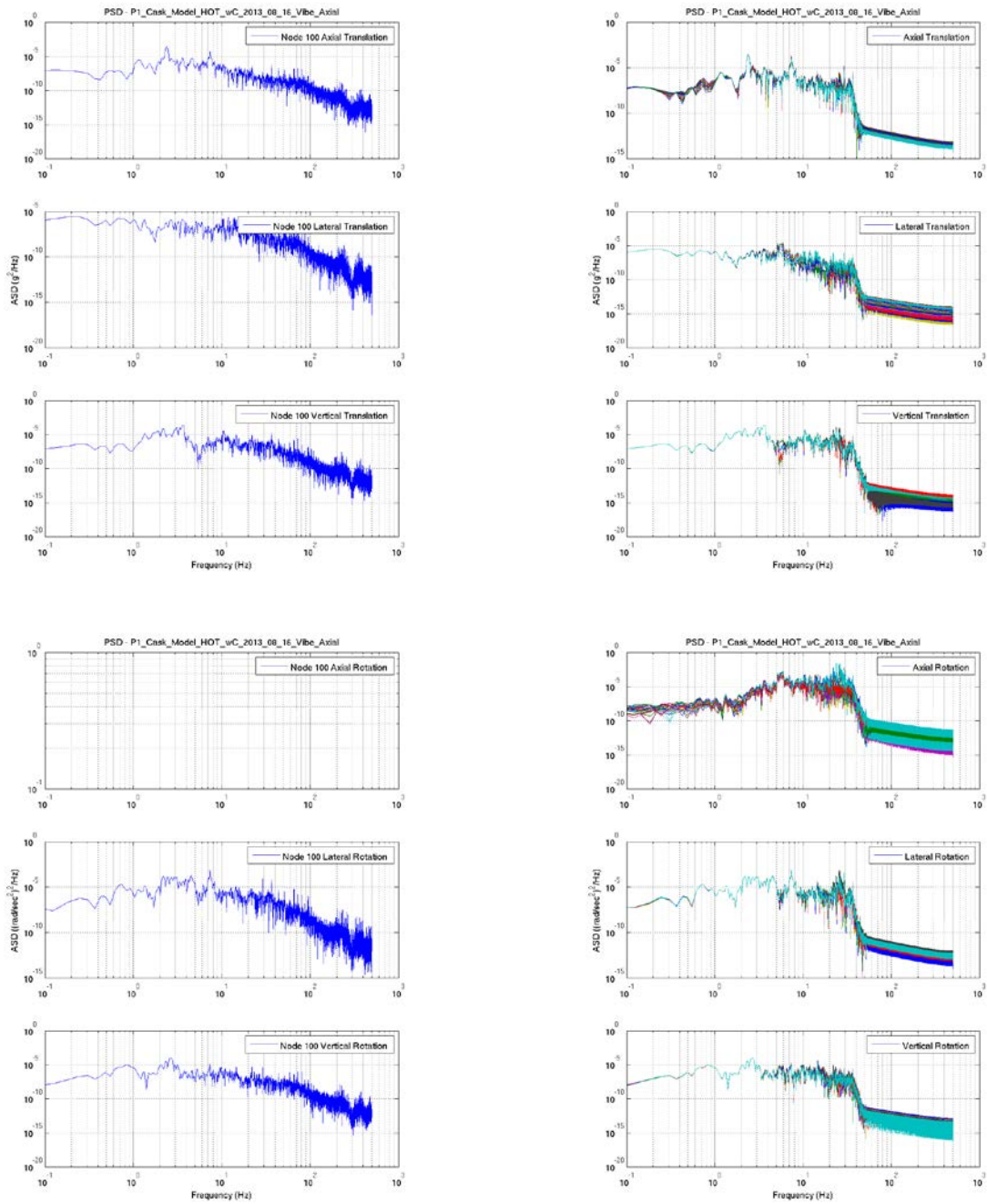**Figure 1.24 P1 Vibration Y (Lateral) Load Case, Nominal Model Configuration, Input and Basket Cell Response PSDs.**

USED FUEL DISPOSITION CAMPAIGN
Used Nuclear Fuel Loading and Structural Performance Under Normal Conditions of Transport -
Demonstration of Approach and Results of Used Fuel Performance Characterization
A-39 **SEPTEMBER 30, 2013**

(a) Transfer Functions   (b) Fuel Assembly to Basket Slip/Separation.

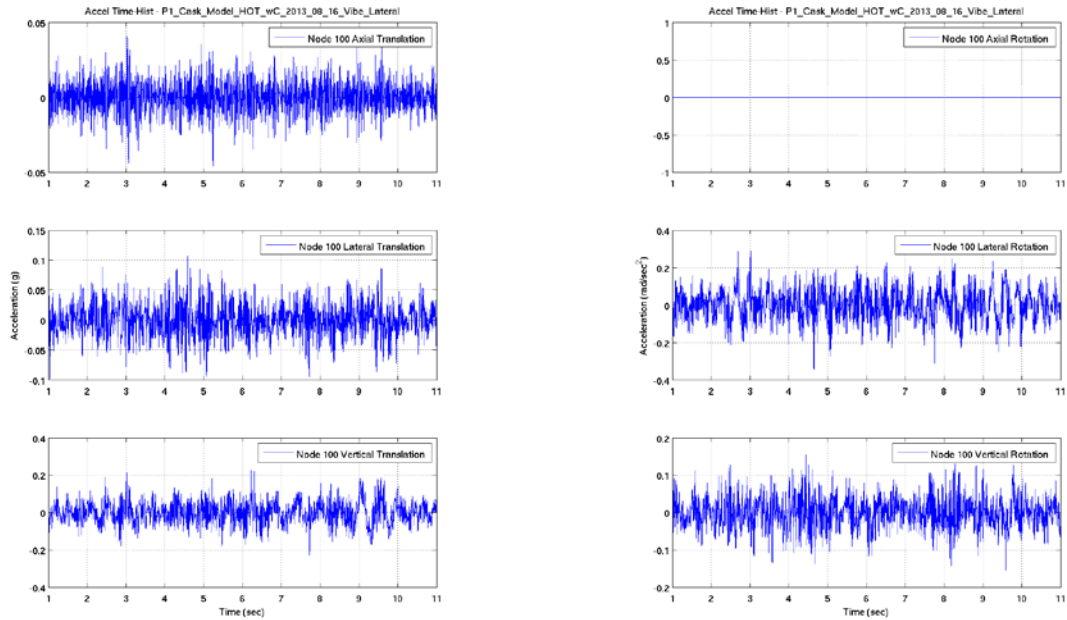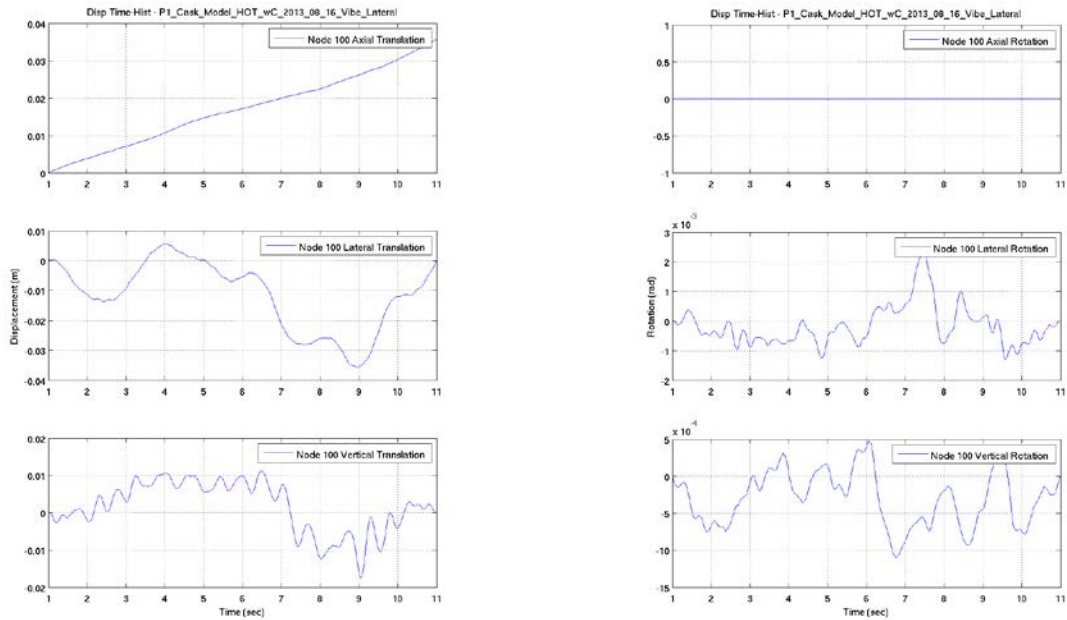**Figure 1.25 P1 Vibration Y (Lateral) Load Case, Nominal Model Configuration, Basket Cell Response Transfer Functions and Slip/Separation Plots.**

USED FUEL DISPOSITION CAMPAIGN
**Used Nuclear Fuel Loading and Structural Performance Under Normal Conditions of Transport -
Demonstration of Approach and Results of Used Fuel Performance Characterization**
A-40   **SEPTEMBER 30, 2013**

1.6   P1 VIBRATION Z (VERTICAL)

The P1 Vibration Z (Vertical) case is characterized by a relatively uniform vibration in the time domain in the vertical direction with a g_{rms} value of 0.0241 g. The input PSD plots (Figure 1.29) indicate that the majority of the power in the input in the vertical direction was concentrated between 1 and 4 Hz, with some power at 10 Hz, and between 20 and 40 Hz. The power in the input accelerations in the lateral direction was of the same magnitude, with peaks at 0.7, 3.5, 5 and 10 Hz. The power in the axial direction was several orders of magnitude lower than both the vertical and lateral directions, and was concentrated in the 20 to 50 Hz frequency range. Figure 1.26 illustrates the acceleration and displacement time-histories for each of the translation and rotation degrees-of-freedom for this load case. Figure 1.27 through Figure 1.29 provide FFT, SRS, and PSD plots for both the input excitation and the basket cell response. Transfer functions for each of the translation and rotation degrees-of-freedom are shown in Figure 1.30, along with axial and lateral slip and vertical separation plots for cell 11 and cell 13. Figure 1.29 indicates that much of the power in the response in the vertical direction was centered between 1 and 4 Hz, and between 9 and 30 Hz. In the axial direction there was a significant response at about 2.5 Hz, and between 20 and 30 Hz. Response in the lateral direction was centered at 0.7, 3.5, 5.5, and 6.5 Hz. Coupled to this was a significant response in the axial rotation direction at 5 and 6 Hz, but with additional response between 20 and 30 Hz. Investigation of the transfer functions in Figure 1.30 indicates that the response in the vertical direction between 1 and 4 Hz was not a result of amplification of the input, but between 5 and 7 Hz there was significant amplification. In addition, amplification between 10 and 20 Hz was significant and particularly strong at about 22 and 25 Hz. The transfer function for the response in the axial direction indicates that all of the significant response characteristics observed in that direction were the result of some amplification of the input excitations in that direction. Finally, the transfer function for the response in the lateral direction indicates that there was strong amplification of the excitation accelerations in that direction at 5.5 Hz. Investigation of the slip/separation behavior between the fuel assembly and basket for cells 11 and 13 (Figure 1.30) indicates that little or no slip in the axial and lateral directions occurred between the fuel assemblies and basket, and that little or no vertical separation occurred. Differences in response characteristics at each cell location were again pronounced in the SRS data (Figure 1.28), particularly in the lateral direction across the frequency range shown, in the vertical direction between 10 and 30 Hz, in the axial direction between 20 and 30 Hz, and in all the rotational directions between 10 and 40 Hz.

USED FUEL DISPOSITION CAMPAIGN
Used Nuclear Fuel Loading and Structural Performance Under Normal Conditions of Transport -
Demonstration of Approach and Results of Used Fuel Performance Characterization
A-41 **SEPTEMBER 30, 2013**

(a) Acceleration Time-Histories

(b) Displacement and Rotation Time-Histories

Figure 1.26 P1 Vibration Z (Vertical) Load Case, Nominal Model Configuration, Input
Acceleration and Displacement Time-Histories.

USED FUEL DISPOSITION CAMPAIGN
Used Nuclear Fuel Loading and Structural Performance Under Normal Conditions of Transport -
Demonstration of Approach and Results of Used Fuel Performance Characterization
A-42 **SEPTEMBER 30, 2013**
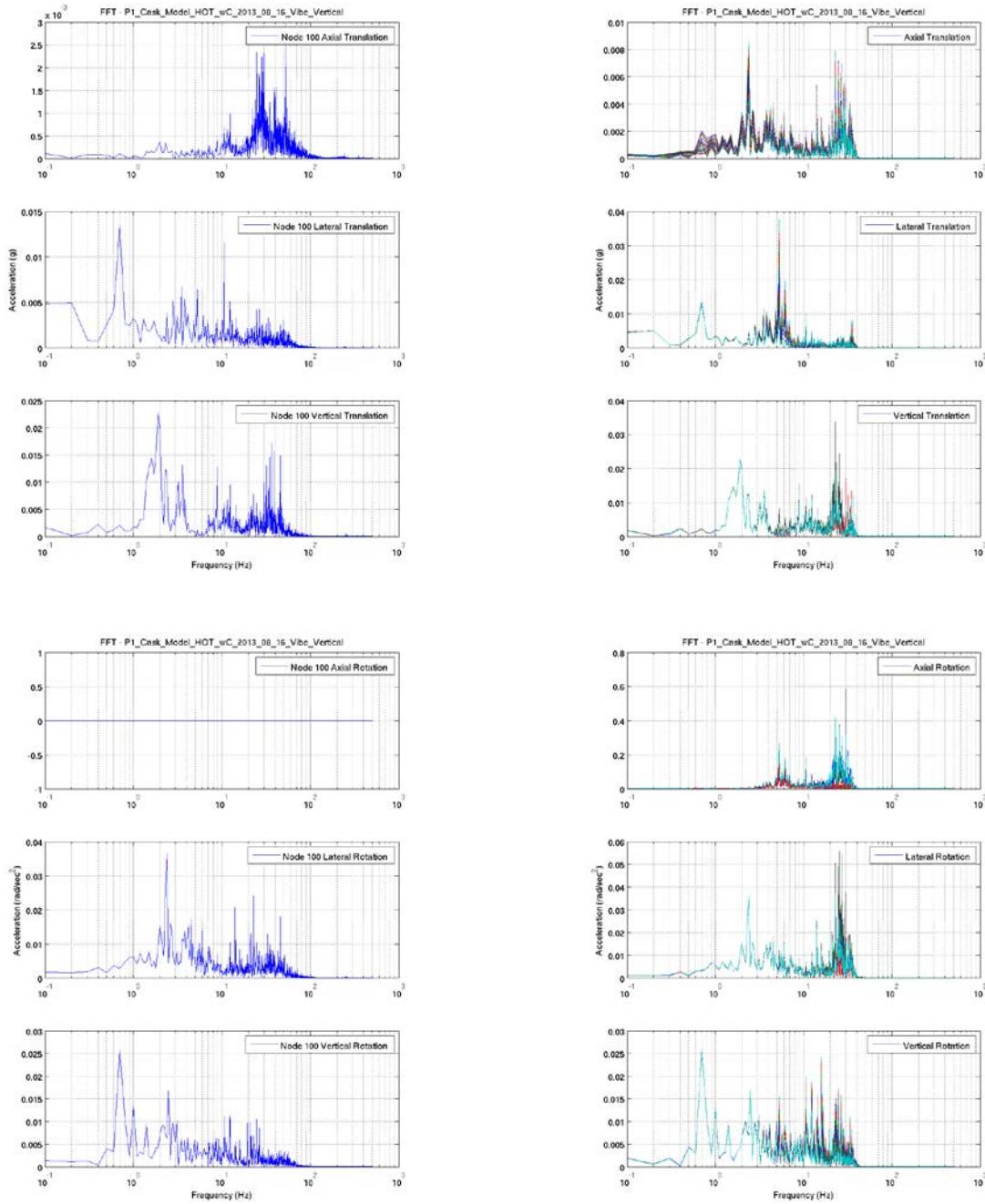
(a) Input   (b) Basket Cell Response

Figure 1.27 P1 Vibration Z (Vertical) Load Case, Nominal Model Configuration, Input and Basket Cell Response FFTs.

USED FUEL DISPOSITION CAMPAIGN
**Used Nuclear Fuel Loading and Structural Performance Under Normal Conditions of Transport -
Demonstration of Approach and Results of Used Fuel Performance Characterization**
A-43
SEPTEMBER 30, 2013
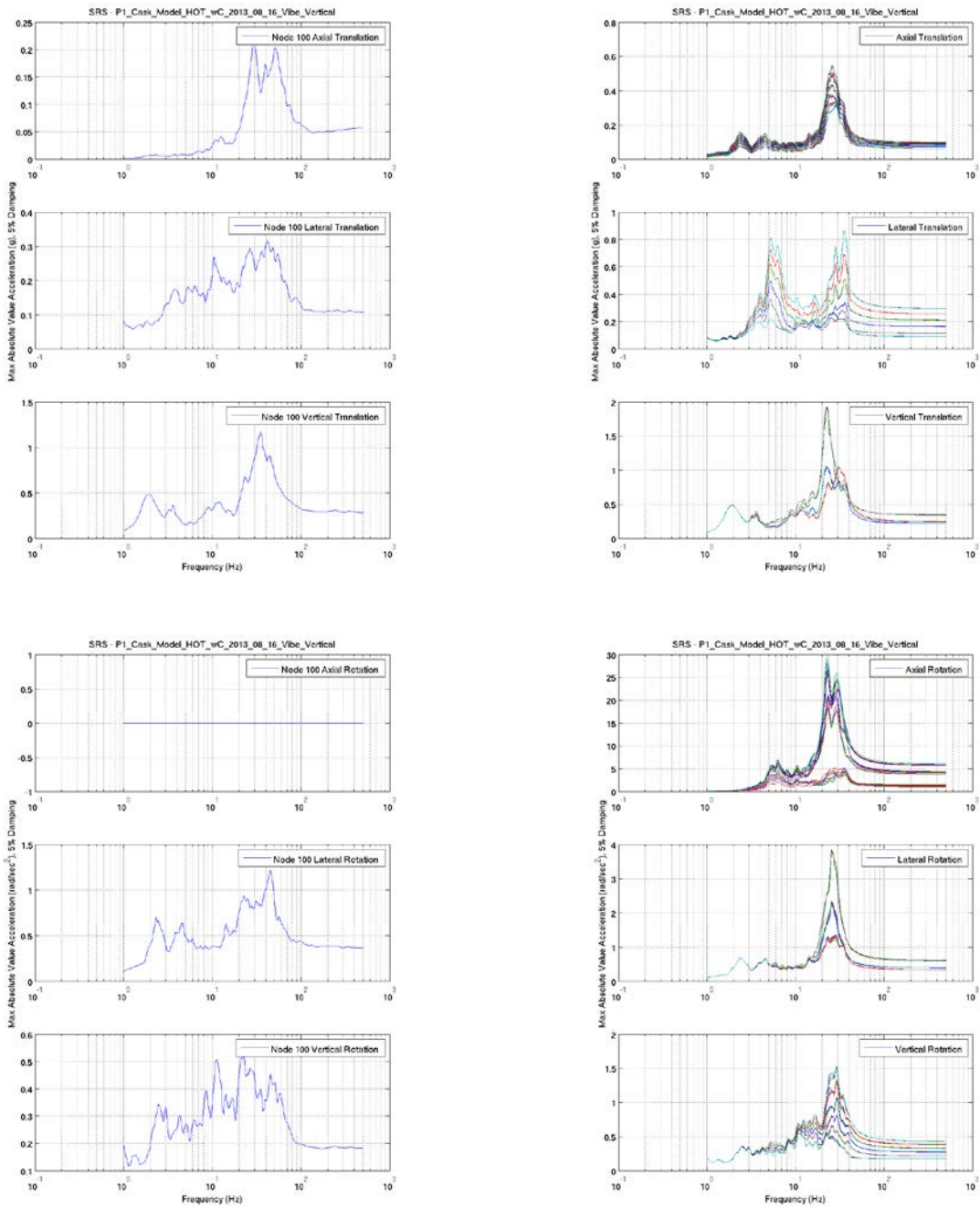
(a) Input

(b) Basket Cell Response

Figure 1.28 P1 Vibration Z (Vertical) Load Case, Nominal Model Configuration, Input and Basket Cell Response SRSs.

USED FUEL DISPOSITION CAMPAIGN
**Used Nuclear Fuel Loading and Structural Performance Under Normal Conditions of Transport -
Demonstration of Approach and Results of Used Fuel Performance Characterization**
A-44   **SEPTEMBER 30, 2013**
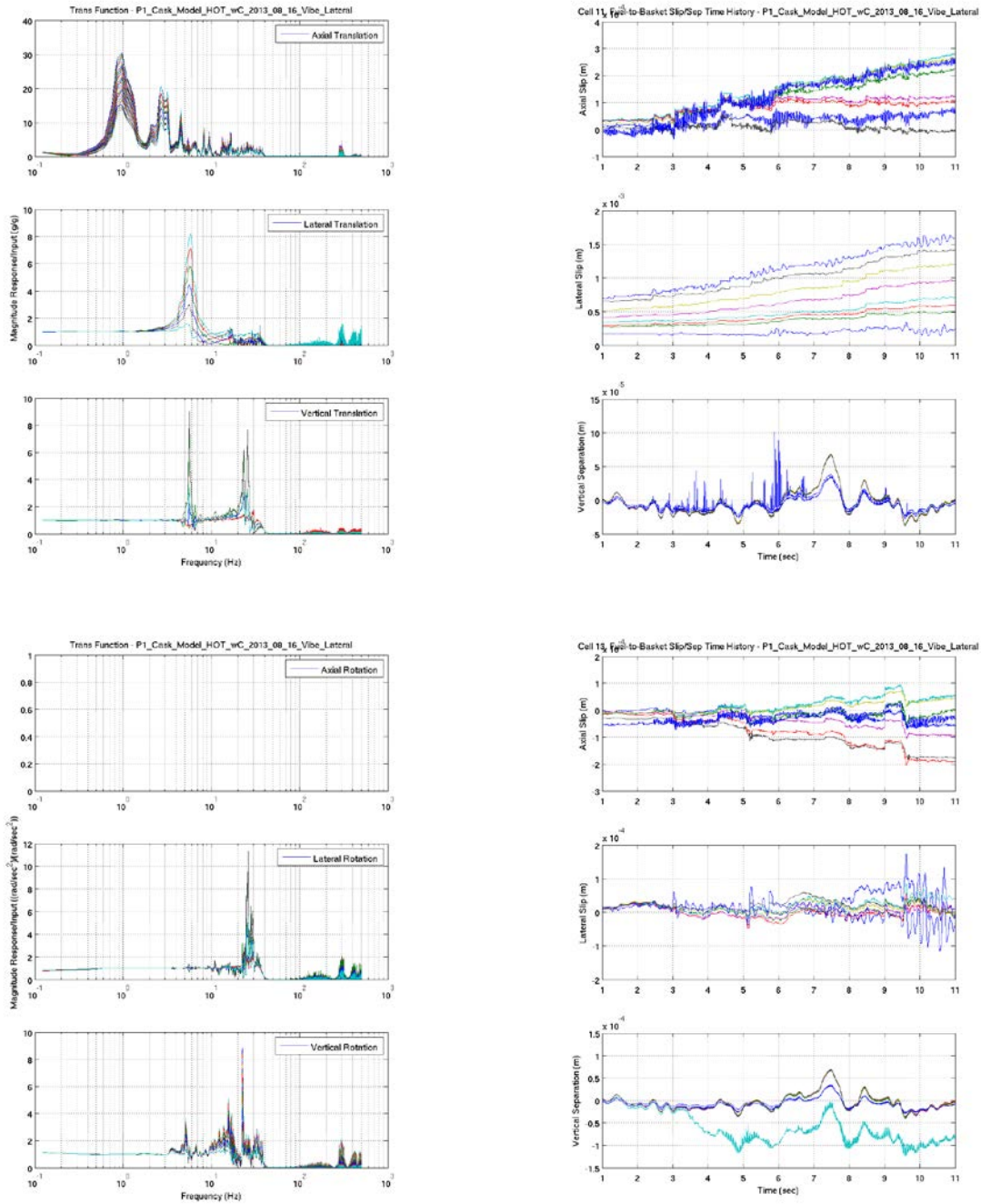

(a) Input

(b) Basket Cell Response
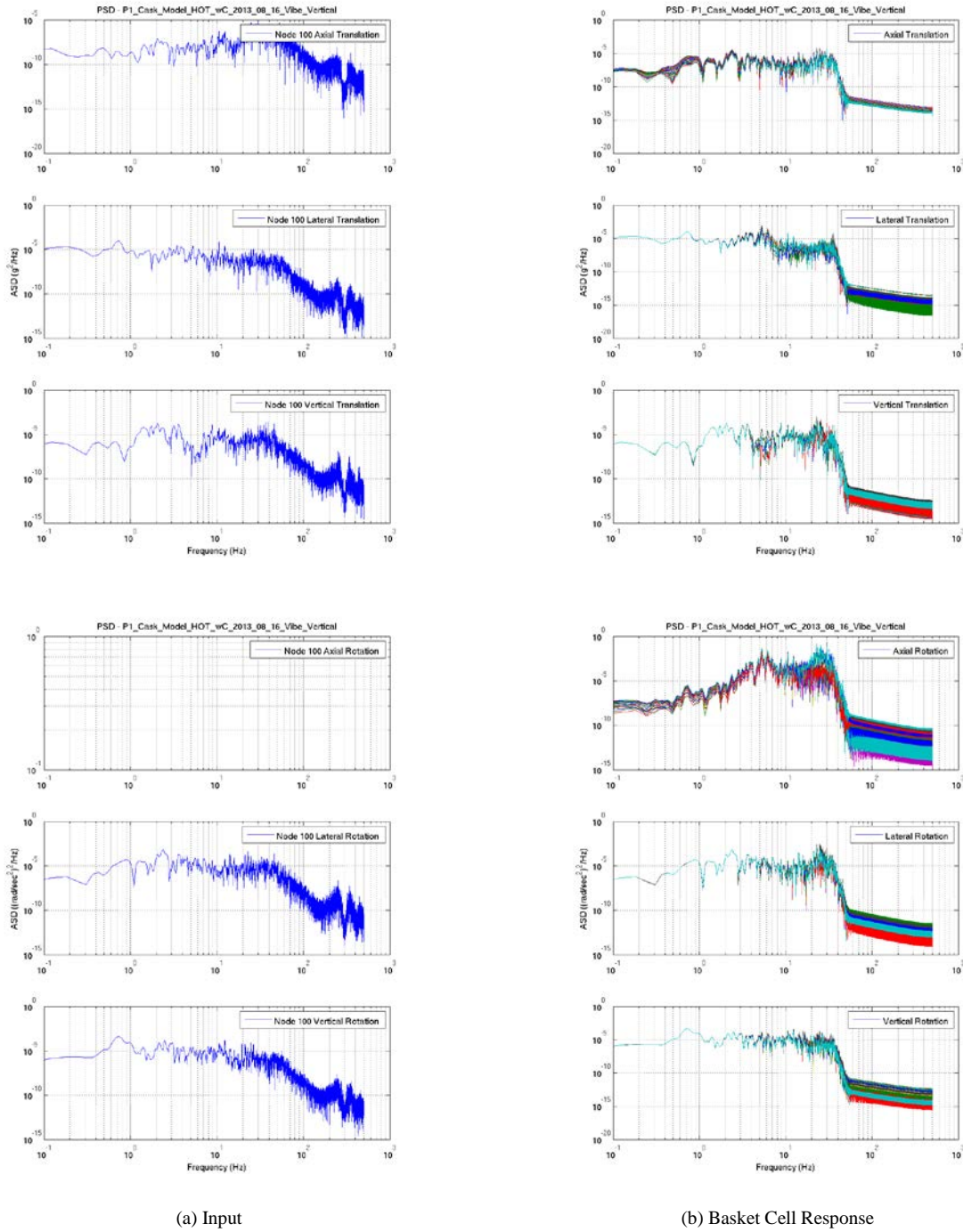
**Figure 1.29 P1 Vibration Z (Vertical) Load Case, Nominal Model Configuration, Input and
Basket Cell Response PSDs.**

USED FUEL DISPOSITION CAMPAIGN
**Used Nuclear Fuel Loading and Structural Performance Under Normal Conditions of Transport -
Demonstration of Approach and Results of Used Fuel Performance Characterization**
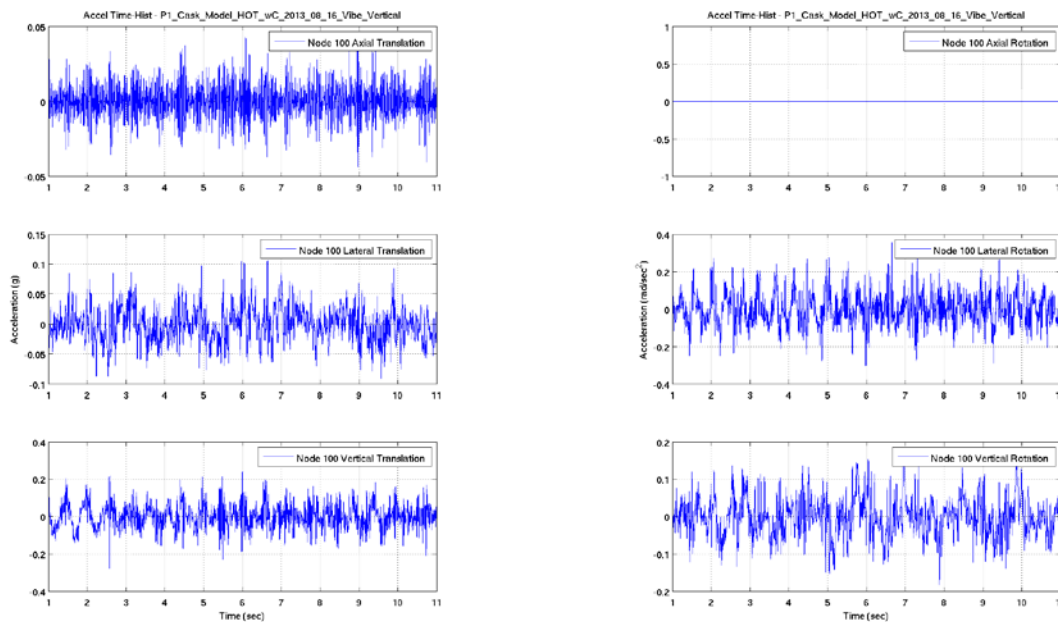**A-45** **SEPTEMBER 30, 2013**

(a) Transfer Functions　　　　　　　　　　(b) Fuel Assembly to Basket Slip/Separation.

**Figure 1.30 P1 Vibration Z (Vertical) Load Case, Nominal Model Configuration, Basket
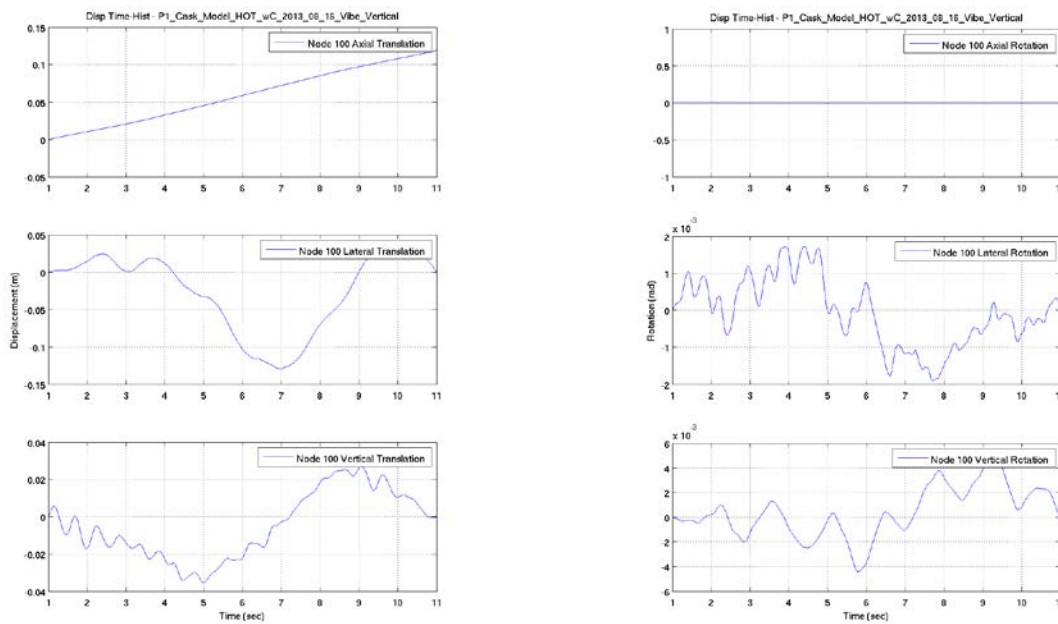Cell Response Transfer Functions and Slip/Separation Plots.**

USED FUEL DISPOSITION CAMPAIGN
Used Nuclear Fuel Loading and Structural Performance Under Normal Conditions of Transport -
Demonstration of Approach and Results of Used Fuel Performance Characterization
A-46 **SEPTEMBER 30, 2013**

1.7   P3 SHOCK Y (LATERAL)

The P3 Shock Y (Lateral) case is characterized by a medium duration (~3.0 second) shock with peak time-domain acceleration magnitude in the lateral direction of 0.101 g. This can be seen in Figure 1.31 which illustrates the acceleration and displacement time-histories for each of the translation and rotation degrees-of-freedom. Figure 1.32 through Figure 1.34 provide FFT, SRS, and PSD plots for both the input excitation and the basket cell response. Transfer functions for each of the three translation and rotation degrees-of-freedom are shown in Figure 1.35, along with axial and lateral slip and vertical separation plots for cell 11 and cell 13. Investigation of the FFT and PSD curves for the input (Figure 1.32 and Figure 1.34) indicate that the input excitations in the lateral and vertical directions contained significant energy in the 1 to 4 Hz range, as well energy in the lateral direction in the 5 to 11 Hz range. In the axial direction, the input energy was somewhat lower than in the lateral and vertical directions. In the axial rotation direction, there was significant energy between 1 and 2 Hz, as was true for input excitations in the vertical rotation direction, but in that direction there was also significant energy in the 6 to 11 Hz range. In the lateral rotation direction, there was significant energy equally distributed between 1 and 11 Hz. Above approximately 30 Hz, all input excitations showed a marked drop in energy (in contrast to the P1 Shock Y (Lateral) load case).

Response of the basket cells in the lateral direction was predominately at 30 Hz, but with significant responses at 1 and 8 Hz as well (Figure 1.32, Figure 1.33, and Figure 1.34). The peak response in the vertical direction was approximately two-thirds of the response in the lateral direction and at a slightly lower frequency of 20 Hz. Response in the lateral direction was also observed between 1 and 4 Hz. The peak response in the axial direction was approximately half of the peak response in the lateral direction and predominately at about 10.5 Hz. Response in the rotational directions were pronounced in the 10 to 40 Hz range, with the response in the axial rotation direction being the most significant and at least one order of magnitude above the peak rotational response in the lateral and vertical rotation directions. Investigation of the transfer functions in Figure 1.35 indicates that the peak response in the lateral direction at 30 Hz was the result of significant amplification of the input in that direction at that frequency, and that the response at 1 and 8 Hz was only slightly amplified. Significant amplification occurred in the lateral direction between 4 and 6 Hz but the input excitation at those frequencies was relatively low. The peak response in the vertical direction at 20 Hz was the result of significant amplification of the input excitation at that frequency in that direction. The peak response in the axial direction at about 10.5 Hz was also somewhat the result of amplification; however, the amplification at other frequencies was more significant, particularly at frequencies between 30 and 40 Hz. The peak responses in the rotational directions between 10 and 40 Hz were all amplified, particularly the response in the axial rotation direction in which amplifications were on the order of 20 to 40 times.

Investigation of the slip/separation behavior between the fuel assembly and basket for cells 11 and 13 (Figure 1.35) indicates that the fuel assemblies are slid around within the basket cells, with slip displacements in the lateral direction of about 4 mm and in the axial direction of about 0.5 mm. No significant vertical separation between the fuel assembly and basket occurred in either cell 11 or 13. As was true for the P1 load case analyses, the response at each cell location

USED FUEL DISPOSITION CAMPAIGN
**Used Nuclear Fuel Loading and Structural Performance Under Normal Conditions of Transport -
Demonstration of Approach and Results of Used Fuel Performance Characterization**
A-47
SEPTEMBER 30, 2013

was not identical. For example, comparison of the SRS at each cell in the lateral and vertical translation directions, and in the axial, lateral, and vertical rotation directions (Figure 1.33) indicates some potentially important differences in the response characteristics between each of the cells.

USED FUEL DISPOSITION CAMPAIGN
**Used Nuclear Fuel Loading and Structural Performance Under Normal Conditions of Transport -
Demonstration of Approach and Results of Used Fuel Performance Characterization**
A-48   **SEPTEMBER 30, 2013**
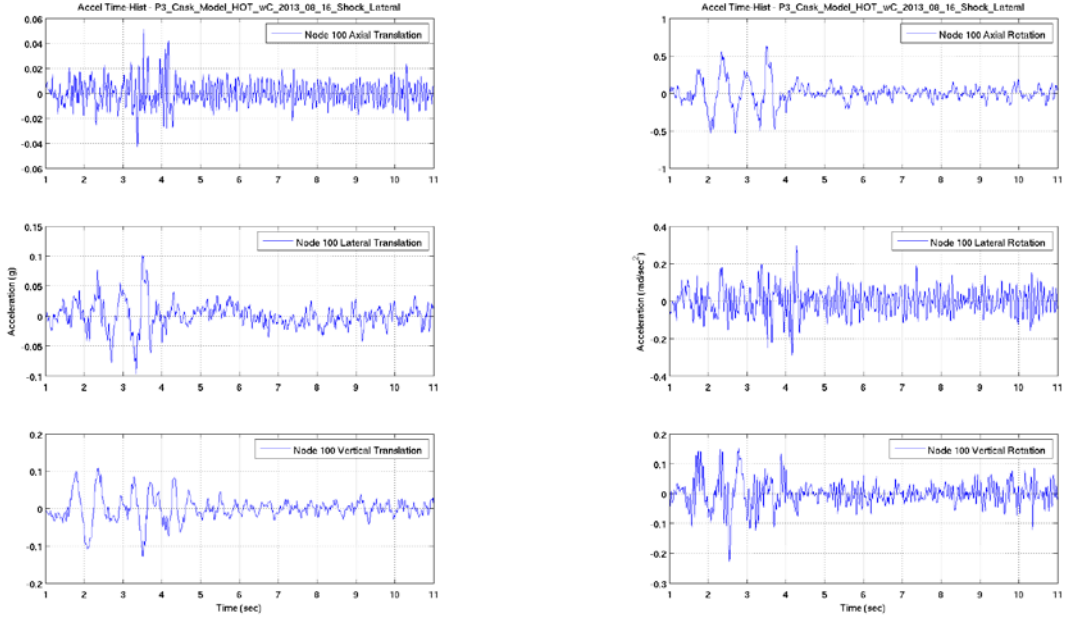
(a) Acceleration Time-Histories

(b) Displacement and Rotation Time-Histories

**Figure 1.31 P3 Shock Y (Lateral) Load Case, Nominal Model Configuration, Input
Acceleration and Displacement Time-Histories.**

USED FUEL DISPOSITION CAMPAIGN
**Used Nuclear Fuel Loading and Structural Performance Under Normal Conditions of Transport -
Demonstration of Approach and Results of Used Fuel Performance Characterization**
A-49
SEPTEMBER 30, 2013
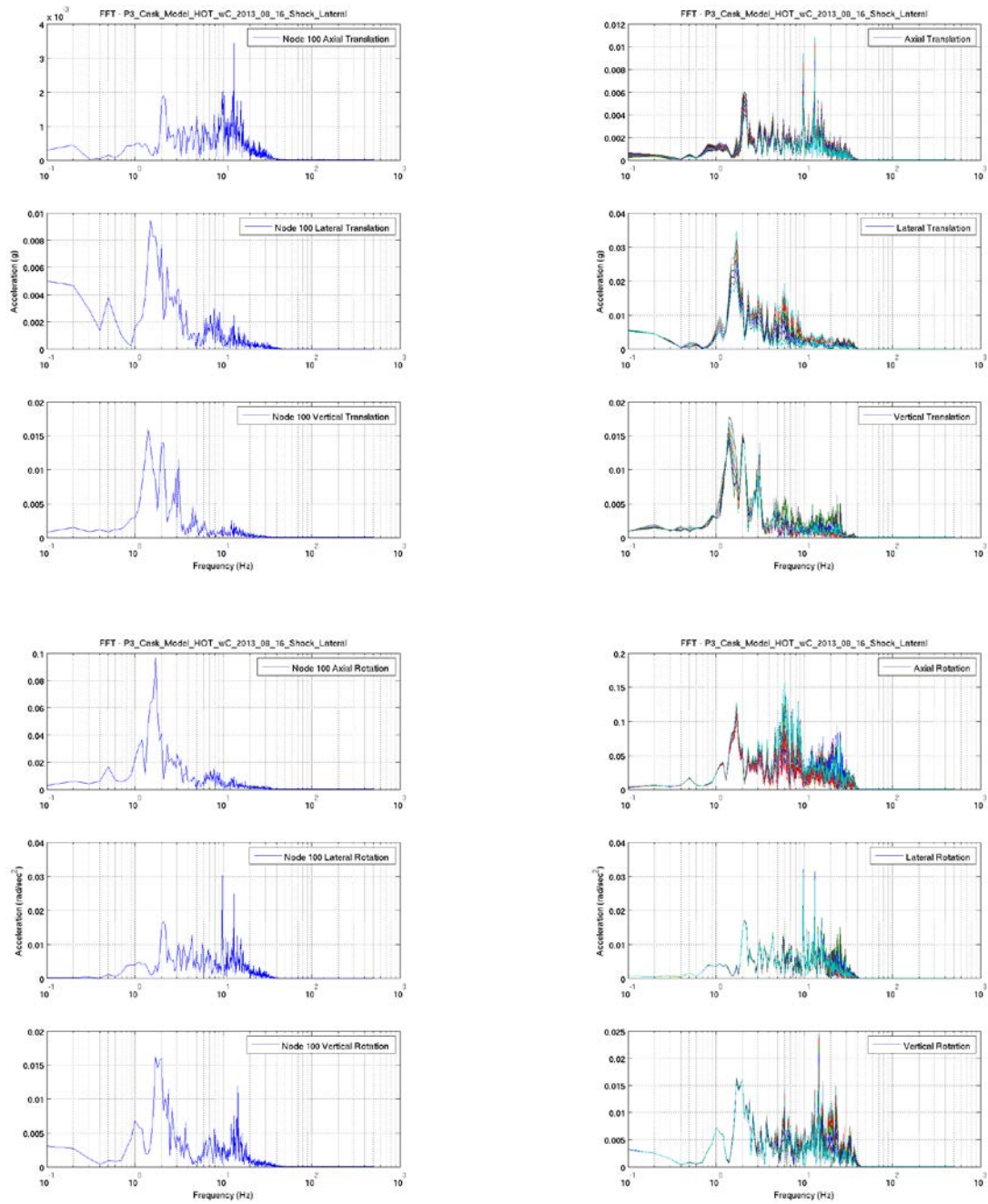
(a) Input

(b) Basket Cell Response

**Figure 1.32 P3 Shock Y (Lateral) Load Case, Nominal Model Configuration, Input and
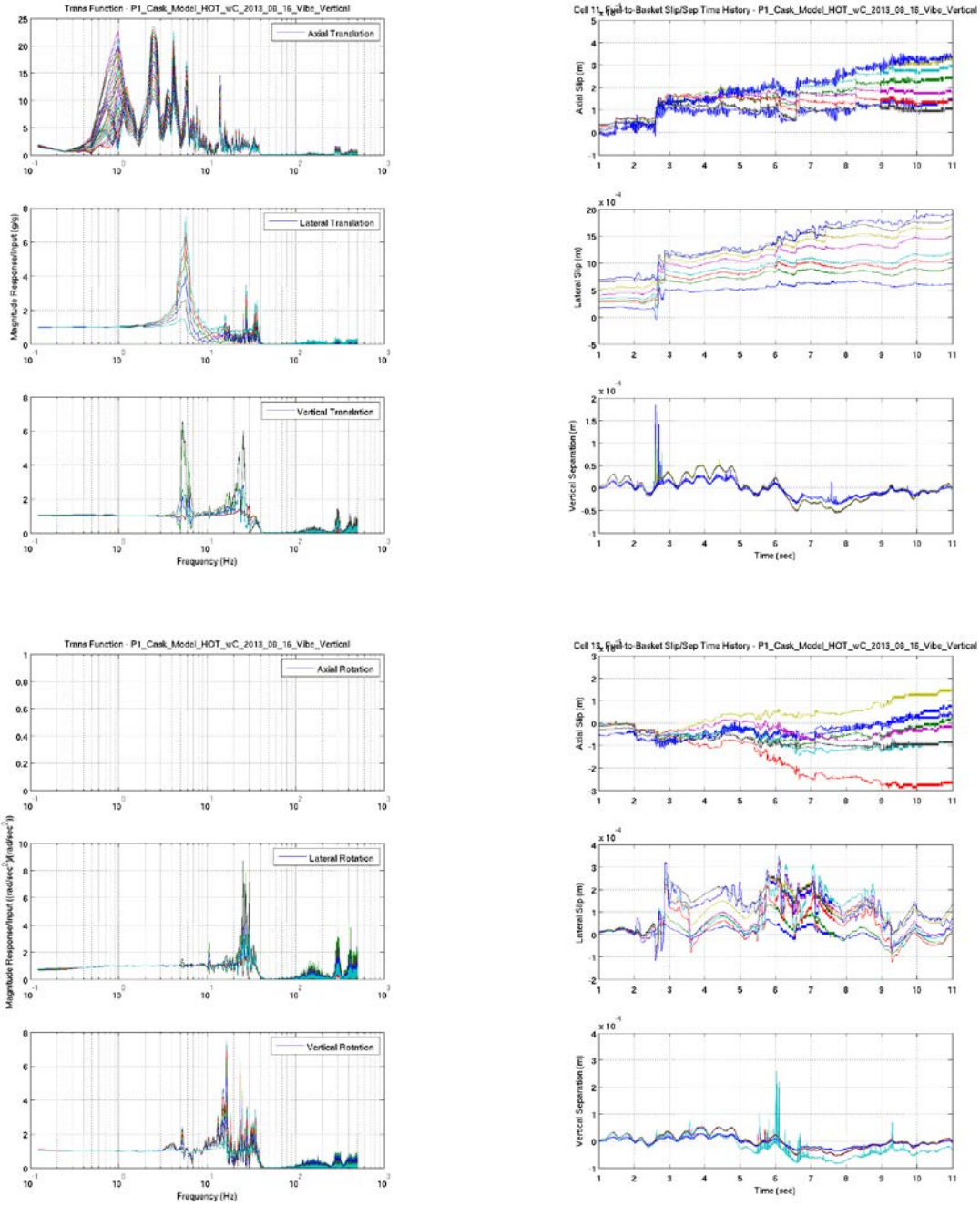Basket Cell Response FFTs.**

USED FUEL DISPOSITION CAMPAIGN
**Used Nuclear Fuel Loading and Structural Performance Under Normal Conditions of Transport -
Demonstration of Approach and Results of Used Fuel Performance Characterization**
A-50
SEPTEMBER 30, 2013
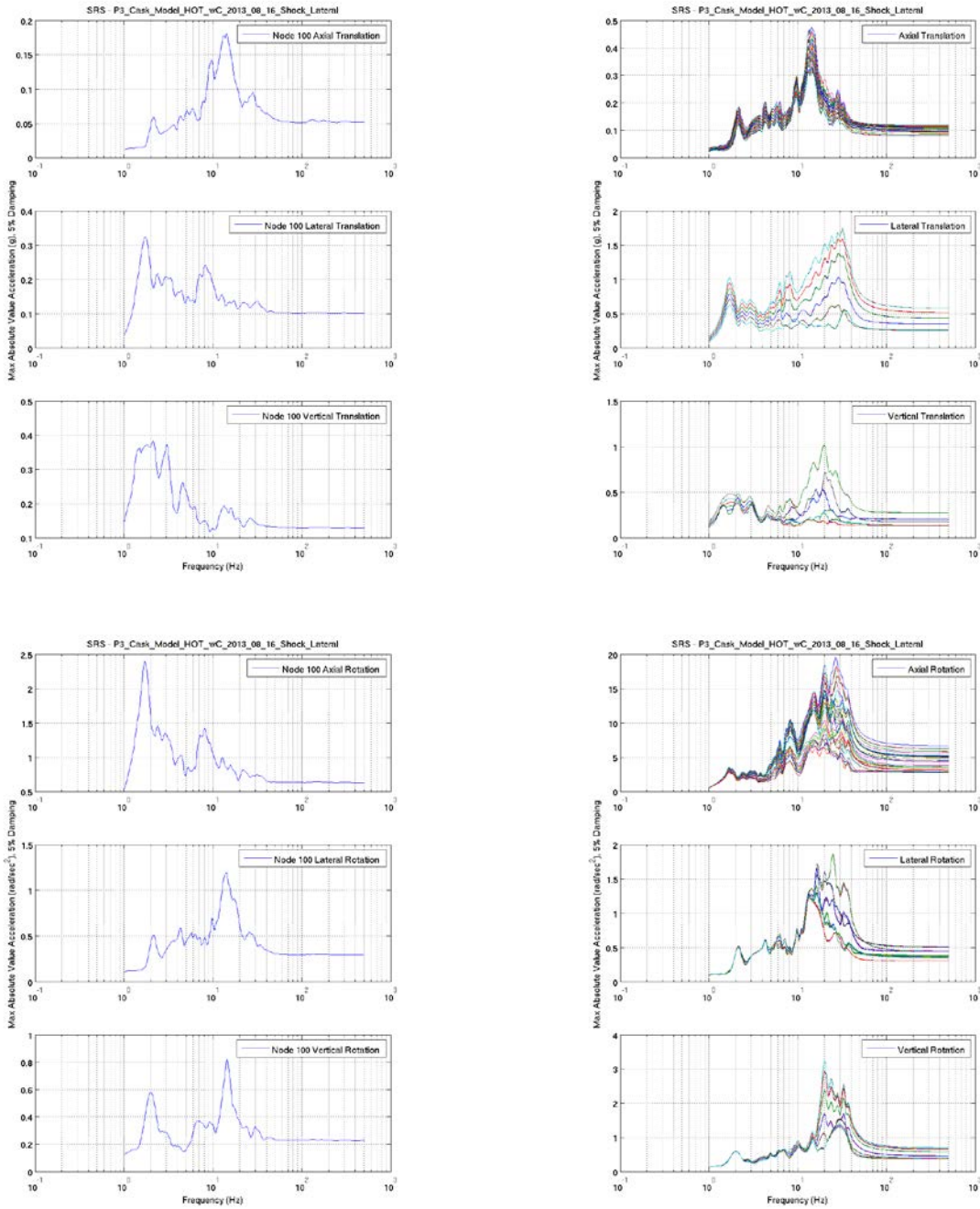
(a) Input

(b) Basket Cell Response

**Figure 1.33 P3 Shock Y (Lateral) Load Case, Nominal Model Configuration, Input and
Basket Cell Response SRSs.**

USED FUEL DISPOSITION CAMPAIGN
**Used Nuclear Fuel Loading and Structural Performance Under Normal Conditions of Transport -
Demonstration of Approach and Results of Used Fuel Performance Characterization**
A-51   **SEPTEMBER 30, 2013**

(a) Input   (b) Basket Cell Response
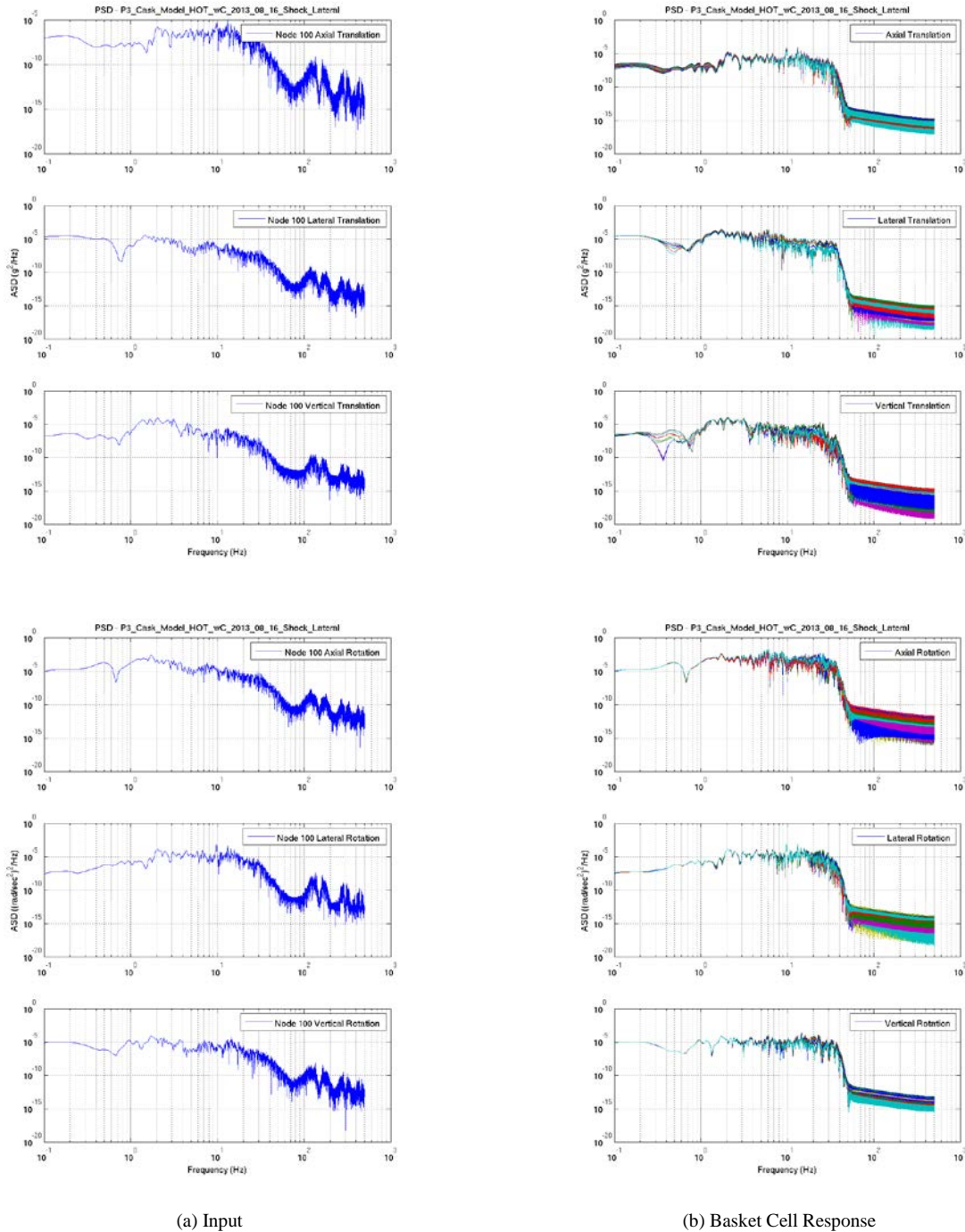
**Figure 1.34 P3 Shock Y (Lateral) Load Case, Nominal Model Configuration, Input and
Basket Cell Response PSDs.**

USED FUEL DISPOSITION CAMPAIGN
**Used Nuclear Fuel Loading and Structural Performance Under Normal Conditions of Transport -
Demonstration of Approach and Results of Used Fuel Performance Characterization**
A-52   **SEPTEMBER 30, 2013**
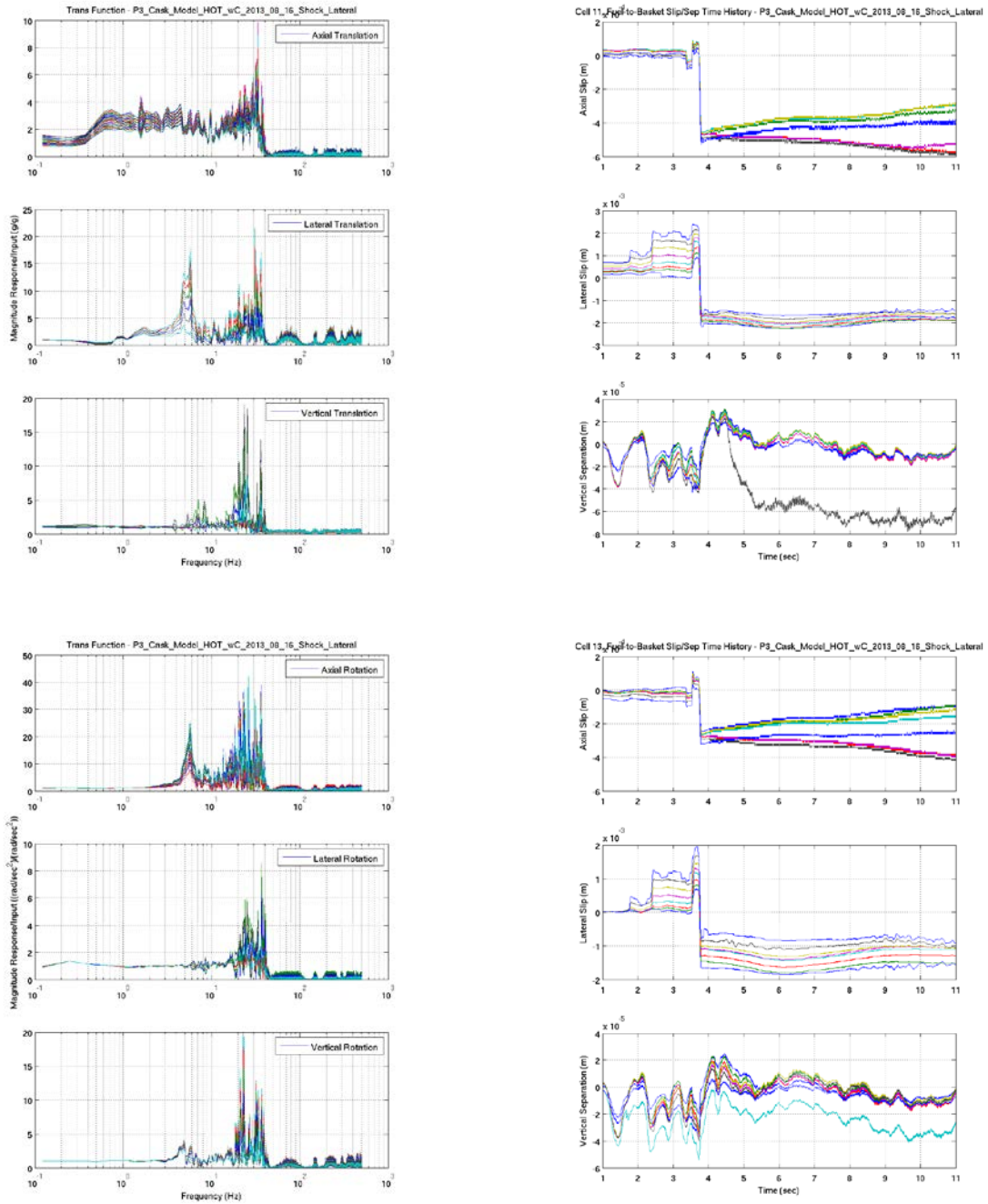
(a) Transfer Functions   (b) Fuel Assembly to Basket Slip/Separation.

**Figure 1.35 P3 Shock Y (Lateral) Load Case, Nominal Model Configuration, Basket Cell
Response Transfer Functions and Slip/Separation Plots.**

USED FUEL DISPOSITION CAMPAIGN
**Used Nuclear Fuel Loading and Structural Performance Under Normal Conditions of Transport -
Demonstration of Approach and Results of Used Fuel Performance Characterization**
A-53   **SEPTEMBER 30, 2013**

1.8   P3 SHOCK Z (VERTICAL)

The P3 Shock Z (Vertical) case is characterized by a medium duration (~3.0 second) shock with peak time-domain acceleration magnitude in the vertical direction of 0.335 g. The P3 Shock Z (Vertical) case also encompassed the peak axial shock event. The axial shock event is characterized by a short duration (~1.0 second) shock with peak time-domain acceleration magnitude in the axial direction of 0.087 g. This can be seen in Figure 1.36 which illustrates the acceleration and displacement time-histories for each of the translation and rotation degrees-of-freedom. Figure 1.37 through Figure 1.39 provide FFT, SRS, and PSD plots for both the input excitation and the basket cell response. Transfer functions for each of the three translation and rotation degrees-of-freedom are shown in Figure 1.40, along with axial and lateral slip and vertical separation plots for cell 11 and cell 13. Investigation of the FFT and PSD curves for the input (Figure 1.37 and Figure 1.39) indicate that the input excitation in the vertical direction contained significant energy in the 1 to 2 Hz frequency range. The energy in the lateral direction was somewhat less than in the vertical direction, and was also largely contained in the frequency range between 1 and 2 Hz. In the axial direction, the input energy was somewhat lower than in the lateral and vertical directions; however, there was significant energy in the axial direction between 5 and 10 Hz. In all the rotation directions there was significant energy between 1 and 10 Hz, with energy in the axial rotation direction somewhat higher than in the other two directions for frequencies below 2 Hz. Above approximately 30 Hz, all input excitations showed a marked drop in energy (in contrast to the P1 Shock Z (Vertical) load case).

Response of the basket cells is the vertical direction was predominately at about 1.5 Hz, but with significant responses at 6 and 20 Hz (Figure 1.37, Figure 1.38, and Figure 1.39). The peak response in the lateral and axial directions was approximately two-thirds of the response in the vertical direction, with the response predominately at 2 and 6 Hz in the lateral direction, and at 20 Hz in the axial direction. Responses in the rotational directions were all significant between 10 and 30 Hz, and between 5 and 8 Hz, with the response in the axial rotation direction being most significant, nearly three times larger than the peak rotational response in the lateral and vertical rotation directions. Investigation of the transfer functions in Figure 1.40 indicates that the peak response in the vertical direction at about 1.5 Hz was not the result of amplification of the input excitation in that direction at that frequency, but rather an indication of the significant energy in the input at that frequency. In the vertical direction the largest amplification occurred at frequencies between 20 and 30 Hz, which likely contributed to the peak in the response centered around 20 Hz. The peak response in the lateral direction at 6 Hz was the result of significant amplification of the input excitation in that direction at that frequency, and the response at 2 Hz was to a lesser extent. The response in the axial direction from 5 to 20 Hz represented an amplification of the input excitations in that direction at those frequencies. Responses in all three rotational directions between 10 and 30 Hz, and in the axial and vertical rotation directions between 5 and 8 Hz were all amplified over the input excitation in those directions at those frequencies, with amplification in the axial rotation direction being the most significant at between 20 and 60 times.
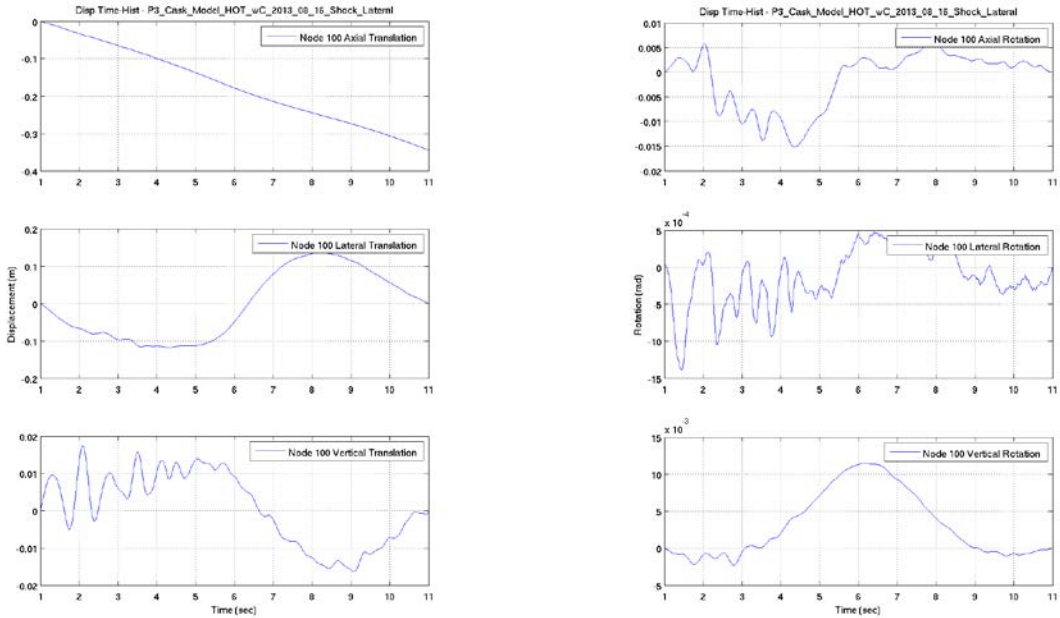
Investigation of the slip/separation behavior between the fuel assembly and basket for cells 11 and 13 (Figure 1.40) indicates that little or no slip of the fuel assemblies in the axial and lateral

USED FUEL DISPOSITION CAMPAIGN
**Used Nuclear Fuel Loading and Structural Performance Under Normal Conditions of Transport -
Demonstration of Approach and Results of Used Fuel Performance Characterization**
A-54
SEPTEMBER 30, 2013

directions is occurred, with the exception being a small (~0.2 mm) slip in the axial direction at between 3 and 4 seconds. No significant vertical separation between the fuel assembly and basket occurred in either cell 11 or 13. As was true for the P1 load case analyses, the response at each cell location was not identical. The differences were particularly pronounced in the cell SRS in the lateral translation and axial rotation directions (Figure 1.38).

USED FUEL DISPOSITION CAMPAIGN
**Used Nuclear Fuel Loading and Structural Performance Under Normal Conditions of Transport -
Demonstration of Approach and Results of Used Fuel Performance Characterization**
A-55   **SEPTEMBER 30, 2013**
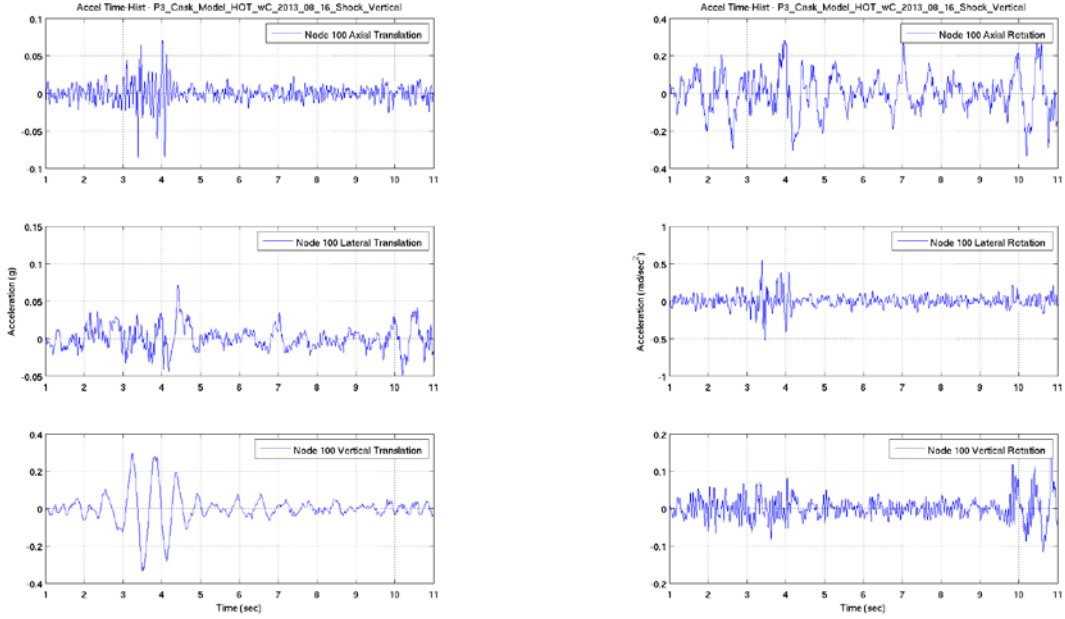
(a) Acceleration Time-Histories
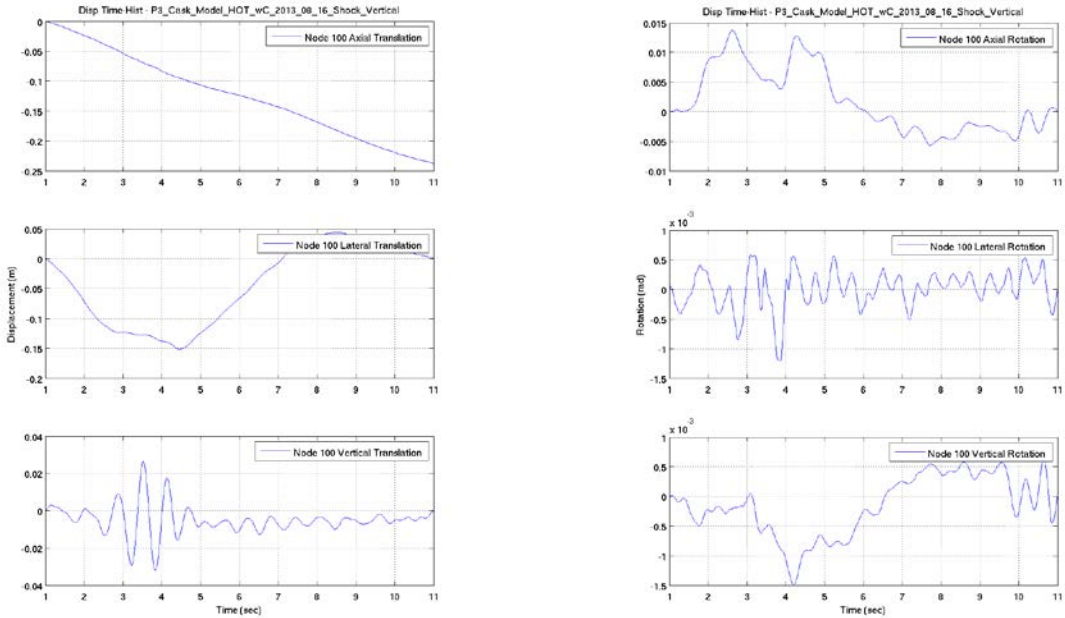
(b) Displacement and Rotation Time-Histories

**Figure 1.36 P3 Shock Z (Vertical) Load Case, Nominal Model Configuration, Input
Acceleration and Displacement Time-Histories.**

USED FUEL DISPOSITION CAMPAIGN
Used Nuclear Fuel Loading and Structural Performance Under Normal Conditions of Transport -
Demonstration of Approach and Results of Used Fuel Performance Characterization
A-56   **SEPTEMBER 30, 2013**
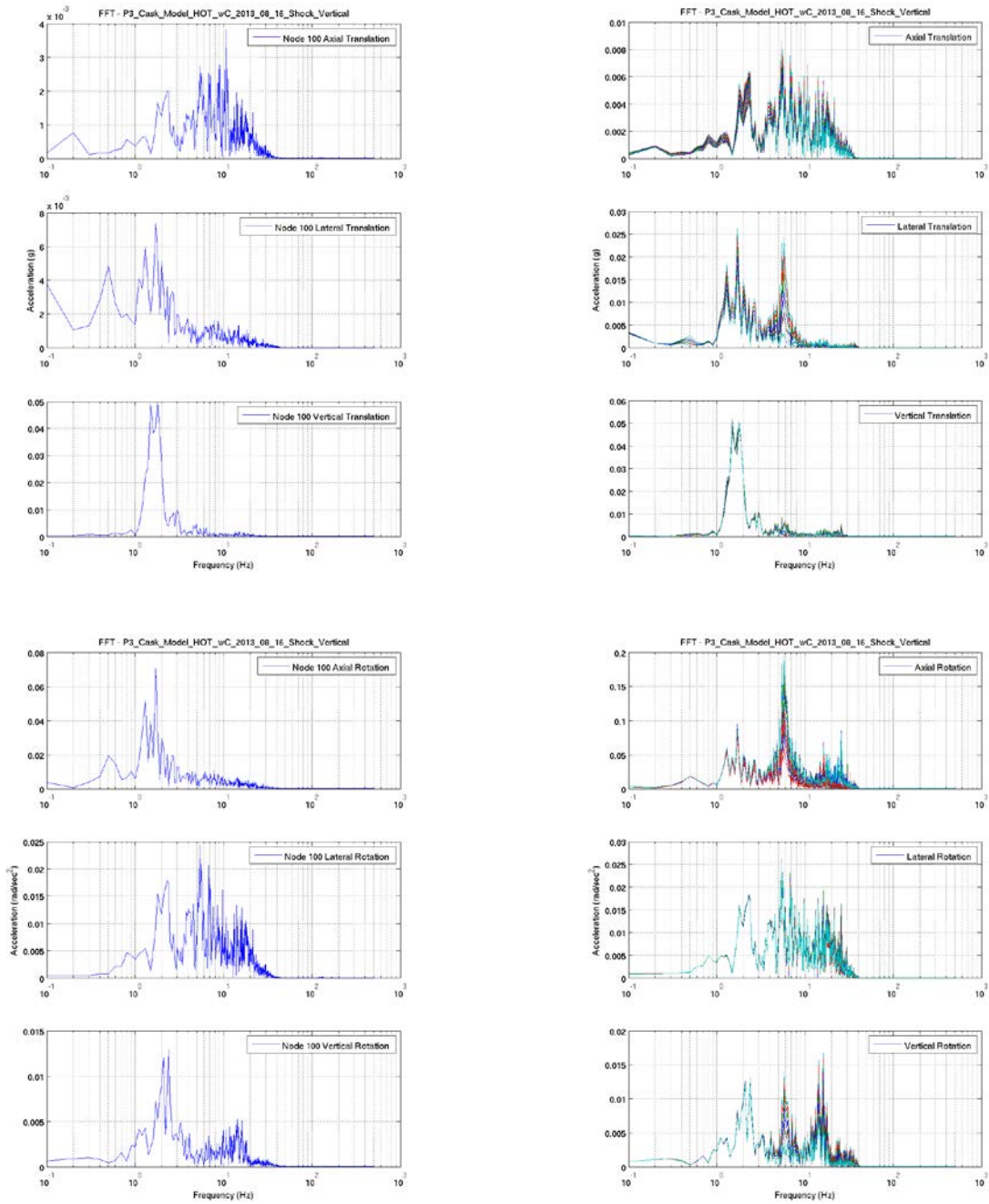
(a) Input   (b) Basket Cell Response

Figure 1.37 P3 Shock Z (Vertical) Load Case, Nominal Model Configuration, Input and Basket Cell Response FFTs.

USED FUEL DISPOSITION CAMPAIGN
**Used Nuclear Fuel Loading and Structural Performance Under Normal Conditions of Transport -
Demonstration of Approach and Results of Used Fuel Performance Characterization**
A-57   **SEPTEMBER 30, 2013**

(a) Input

(b) Basket Cell Response
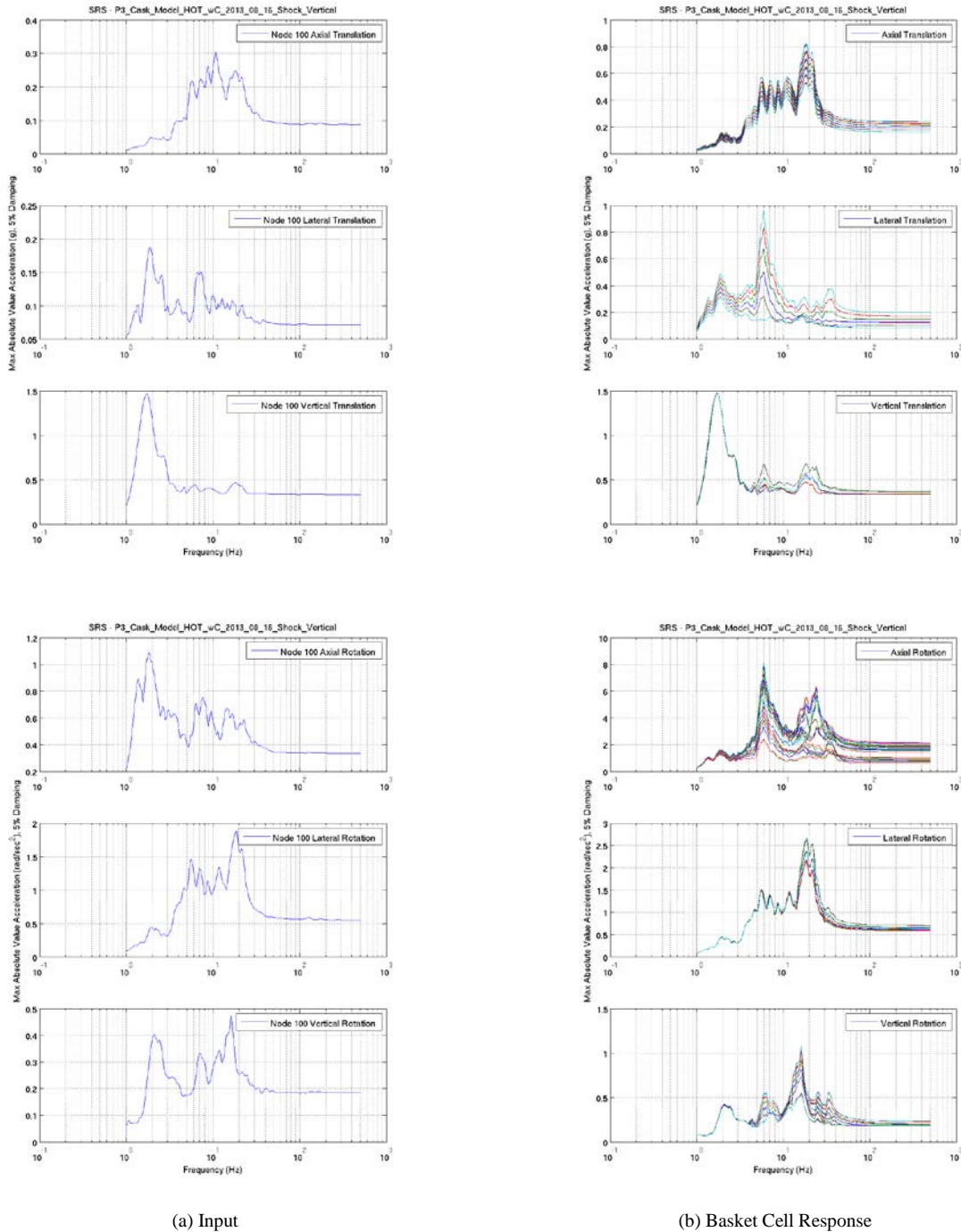
Figure 1.38 P3 Shock Z (Vertical) Load Case, Nominal Model Configuration, Input and Basket Cell Response SRSs.

USED FUEL DISPOSITION CAMPAIGN
Used Nuclear Fuel Loading and Structural Performance Under Normal Conditions of Transport -
Demonstration of Approach and Results of Used Fuel Performance Characterization
A-58
SEPTEMBER 30, 2013

(a) Input

(b) Basket Cell Response
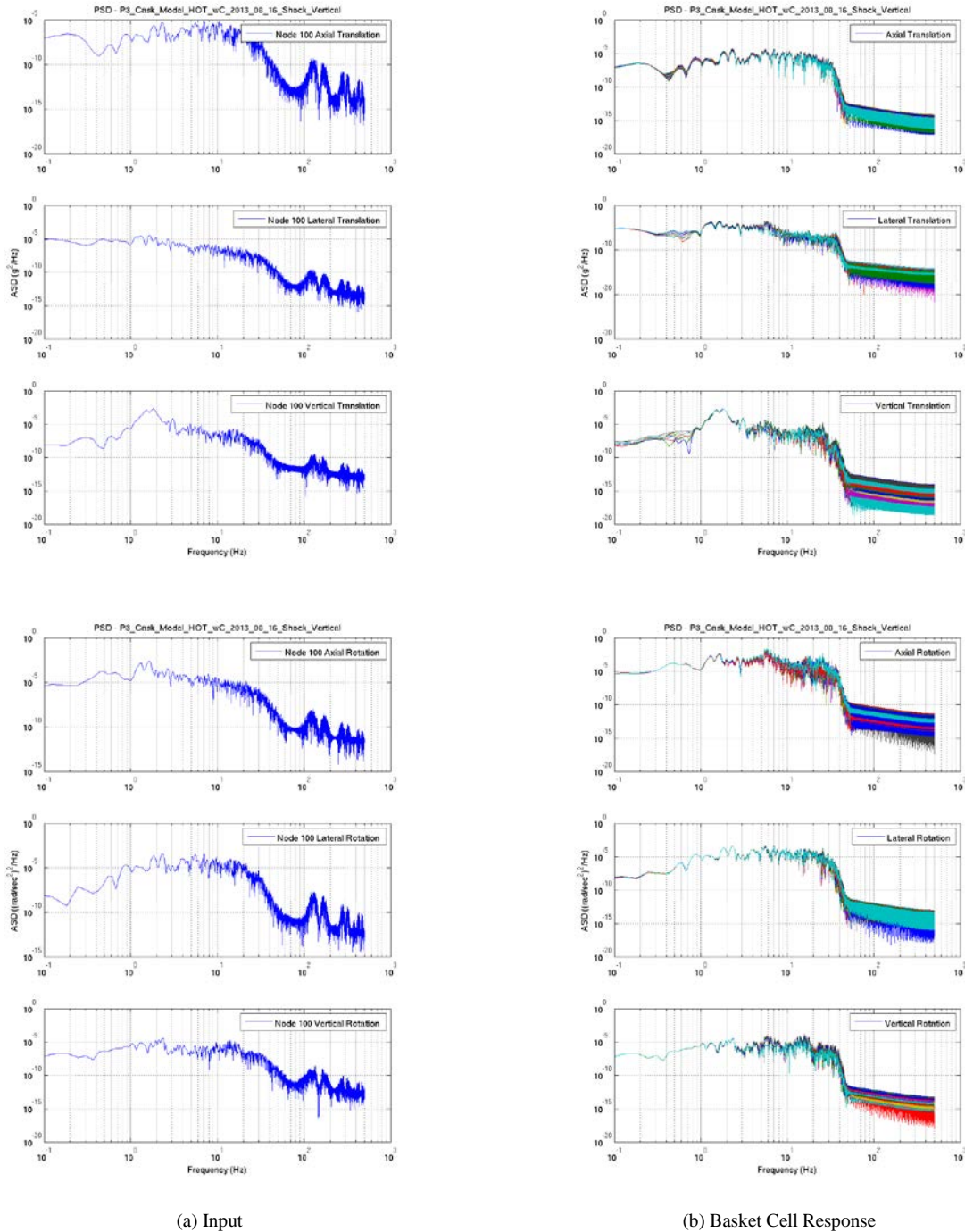
Figure 1.39 P3 Shock Z (Vertical) Load Case, Nominal Model Configuration, Input and Basket Cell Response PSDs.

USED FUEL DISPOSITION CAMPAIGN
Used Nuclear Fuel Loading and Structural Performance Under Normal Conditions of Transport -
Demonstration of Approach and Results of Used Fuel Performance Characterization
A-59   **SEPTEMBER 30, 2013**
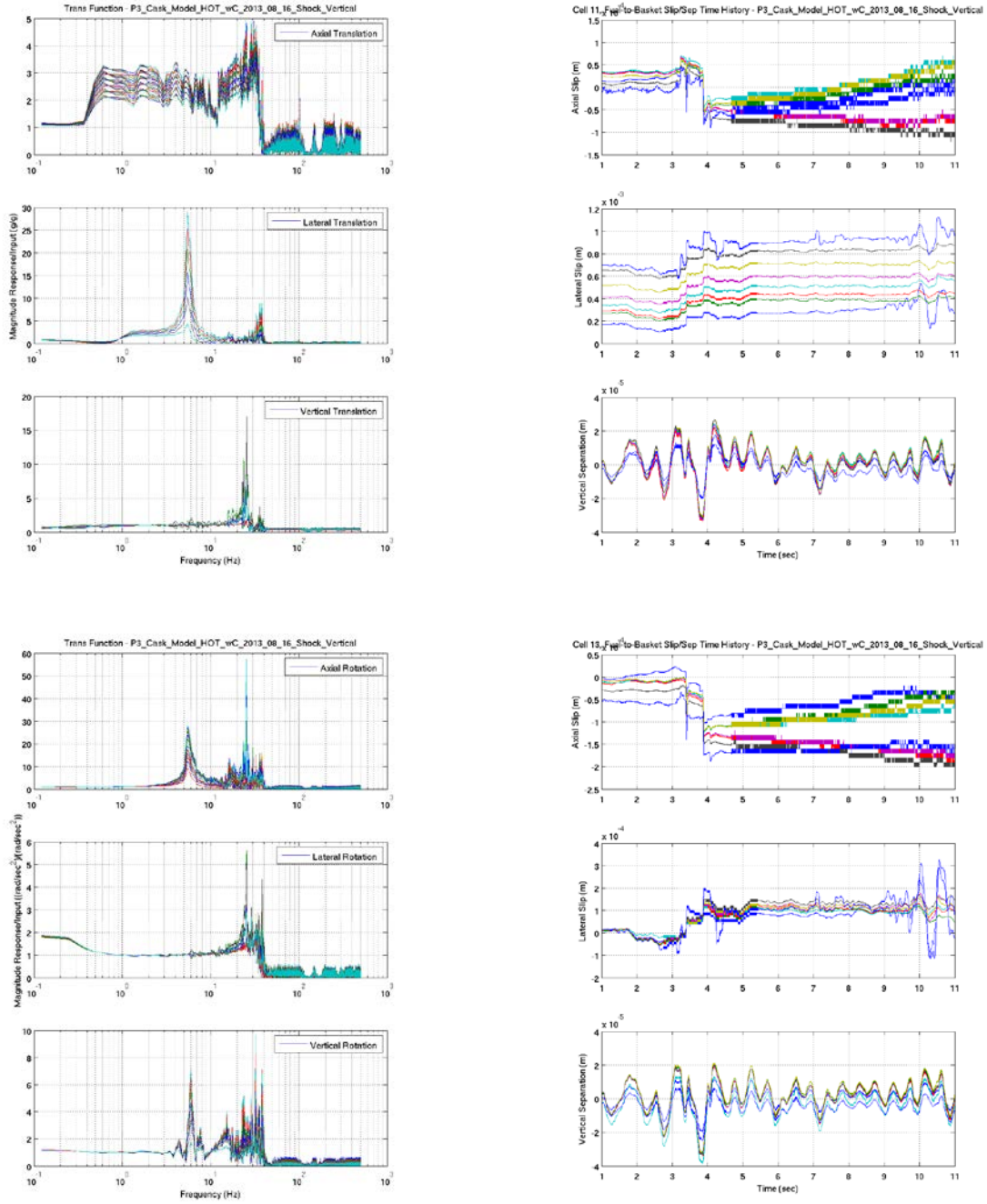
(a) Transfer Functions   (b) Fuel Assembly to Basket Slip/Separation.

Figure 1.40 P3 Shock Z (Vertical) Load Case, Nominal Model Configuration, Basket Cell Response Transfer Functions and Slip/Separation Plots.

USED FUEL DISPOSITION CAMPAIGN
**Used Nuclear Fuel Loading and Structural Performance Under Normal Conditions of Transport -
Demonstration of Approach and Results of Used Fuel Performance Characterization**
A-60   **SEPTEMBER 30, 2013**

1.9   P3 VIBRATION X (AXIAL)

The P3 Vibration X (Axial) case is characterized by a relatively uniform in the time domain vibration in the axial direction with a g_{rms} value of 0.00221 g. The input FFT and PSD plots (Figure 1.42 and Figure 1.44) indicate that the majority of the power in the input was distributed relatively evenly between 2 and 12 Hz in the axial direction and between 1 and 3 Hz in the lateral and vertical directions. Significant energy exited in the vertical direction at 1 and 10 Hz, and between 15 and 20 Hz. The axial direction power (g_{rms} of 0.00221 g) was somewhat below that of both the lateral and vertical direction powers (g_{rms} of 0.00268 g and 0.00918 g, respectively). The power of the excitation in the vertical direction was by far the largest. In the axial rotation direction, the power was highest in the frequency range between 1 and 2 Hz. In the lateral rotation direction there was a significant power spike at about 10 Hz and a somewhat less pronounced spike between 2 and 3 Hz. The power in the vertical rotation direction (g_{rms} of 0.0052 rad/sec^2) was significantly less than in either the axial or lateral rotation directions (g_{rms} of 0.0164 rad/sec^2 and 0.0183 rad/sec^2, respectively). Above approximately 30 Hz, all input excitations showed a marked drop in energy (in contrast to the P1 Vibration X (Axial) load case). Figure 1.41 illustrates the acceleration and displacement time-histories for each of the translation and rotation degrees-of-freedom for this load case. Figure 1.42 through Figure 1.44 provide FFT, SRS, and PSD plots for both the input excitation and the basket cell response. Transfer functions for each of the translation and rotation degrees-of-freedom are shown in Figure 1.45, along with axial and lateral slip and vertical separation plots for cell 11 and cell 13.

Figure 1.43 indicates that the peak response in the axial direction was centered at about 10 Hz, and was generally significant across the frequency range of 6 to 30 Hz. In the lateral direction the peak response was centered at about 5 Hz, and in the vertical direction at about 1 and 2 Hz. In the axial rotation direction the peak response was centered between 20 and 30 Hz, but there was also a significant response at about 5.5 Hz and about 17 Hz. Investigation of the transfer functions in Figure 1.45 indicates that the peak response in the axial direction centered at about 10 Hz, as well as the response across the frequency range of 6 to 30 Hz, represented an amplification over the input excitations at those frequencies in that direction. The peak response in the lateral direction centered at about 5 Hz was highly amplified over the input in that direction at that frequency and is likely indicative of a significant response mode at that frequency. The peak response in the vertical direction at about 1 and 2 Hz did not represent an amplification of the input excitation. Instead, the amplification in the vertical direction was confined to frequencies above 10 Hz and most pronounced at about 23 Hz. The peak response in the axial rotation direction centered between 20 and 30 Hz was the result of a huge amplification of the input excitations in that direction at a frequency of approximately 25 Hz. In fact, the amplitude of the transfer function at that frequency was nearly 100. In the axial rotation direction there was also significant amplification indicated at the other peak response frequencies of 5.5 Hz and about 17 Hz.

Investigation of the slip/separation behavior between the fuel assembly and basket for cells 11 and 13 (Figure 1.45) indicates that essentially no slip in either the axial or lateral directions occurred between the fuel assemblies and basket, and that no vertical separation occurred. Again,

USED FUEL DISPOSITION CAMPAIGN
**Used Nuclear Fuel Loading and Structural Performance Under Normal Conditions of Transport -
Demonstration of Approach and Results of Used Fuel Performance Characterization**
A-61 **SEPTEMBER 30, 2013**

the response at each cell location was not identical. The differences are easily identified in the cell SRSs shown in Figure 1.43.

USED FUEL DISPOSITION CAMPAIGN
**Used Nuclear Fuel Loading and Structural Performance Under Normal Conditions of Transport -
Demonstration of Approach and Results of Used Fuel Performance Characterization**
A-62   **SEPTEMBER 30, 2013**
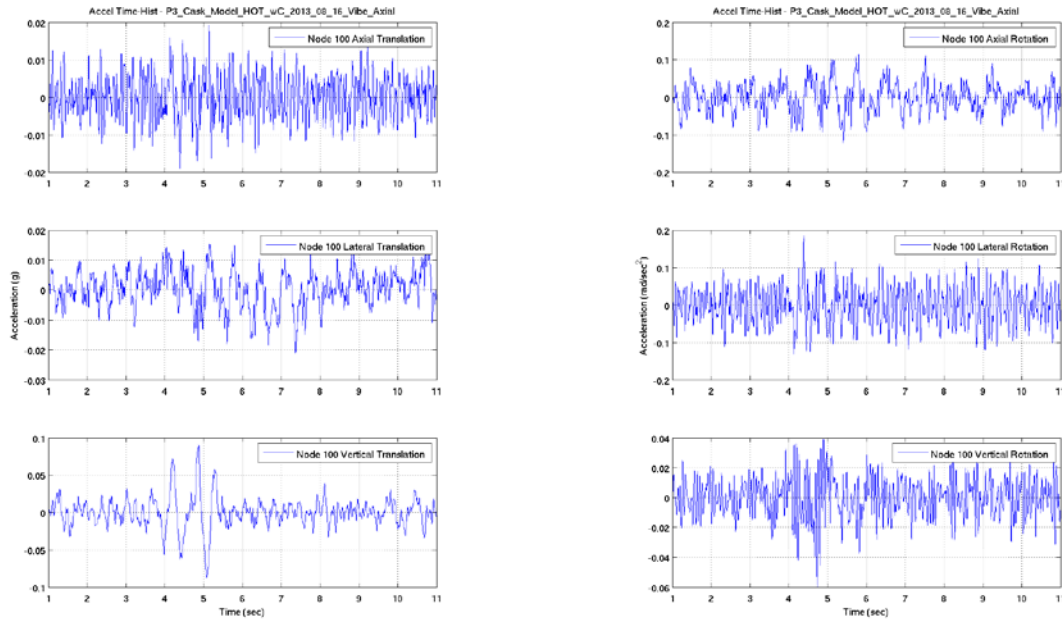
(a) Acceleration Time-Histories
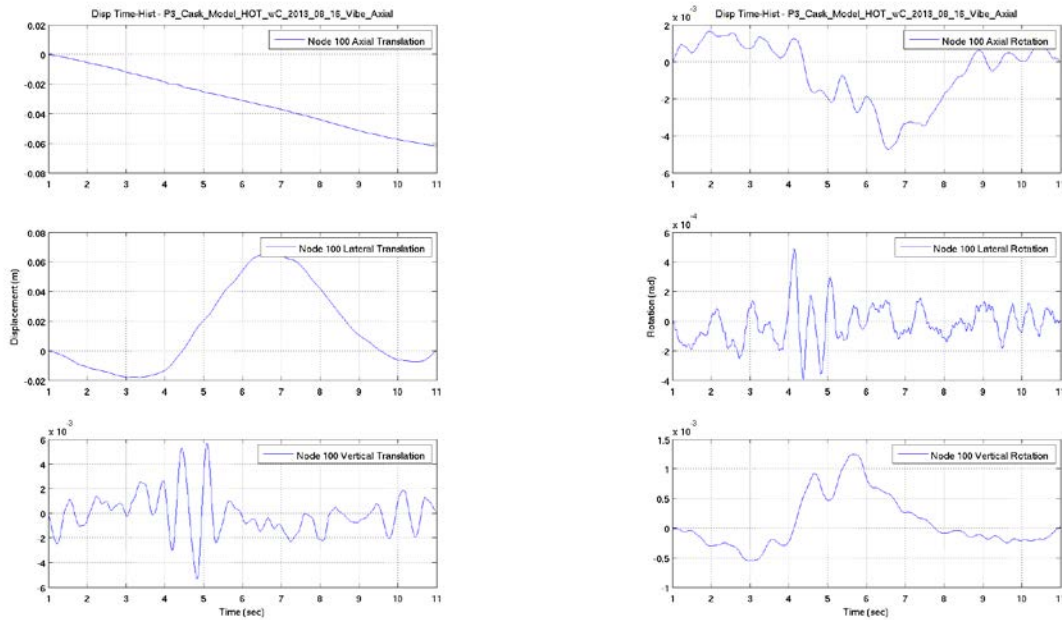
(b) Displacement and Rotation Time-Histories

**Figure 1.41 P3 Vibration X (Axial) Load Case, Nominal Model Configuration, Input
Acceleration and Displacement Time-Histories.**

USED FUEL DISPOSITION CAMPAIGN
Used Nuclear Fuel Loading and Structural Performance Under Normal Conditions of Transport -
Demonstration of Approach and Results of Used Fuel Performance Characterization
A-63   **SEPTEMBER 30, 2013**
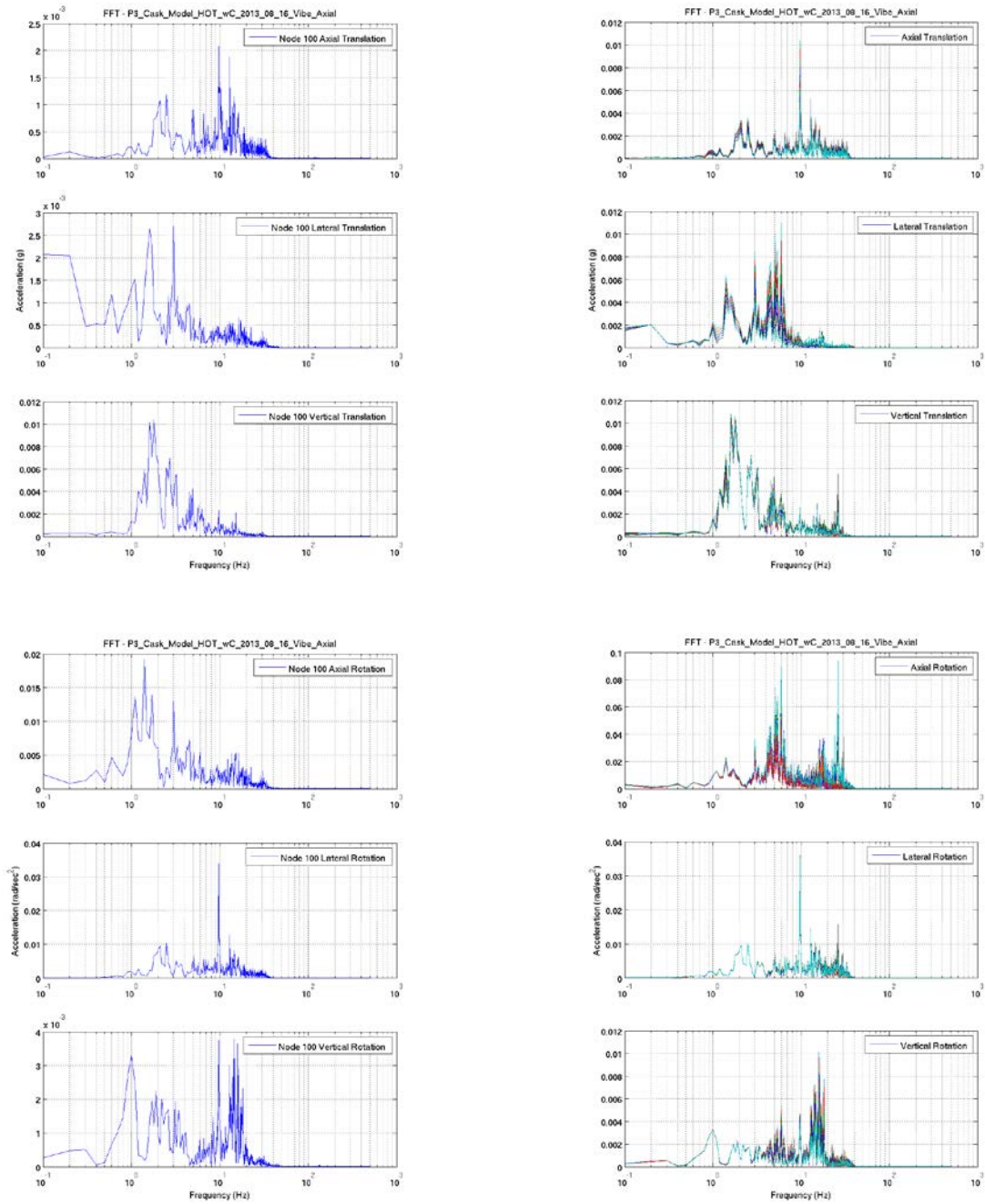
(a) Input

(b) Basket Cell Response

Figure 1.42 P3 Vibration X (Axial) Load Case, Nominal Model Configuration, Input and Basket Cell Response FFTs.

USED FUEL DISPOSITION CAMPAIGN
**Used Nuclear Fuel Loading and Structural Performance Under Normal Conditions of Transport -
Demonstration of Approach and Results of Used Fuel Performance Characterization**
A-64
SEPTEMBER 30, 2013
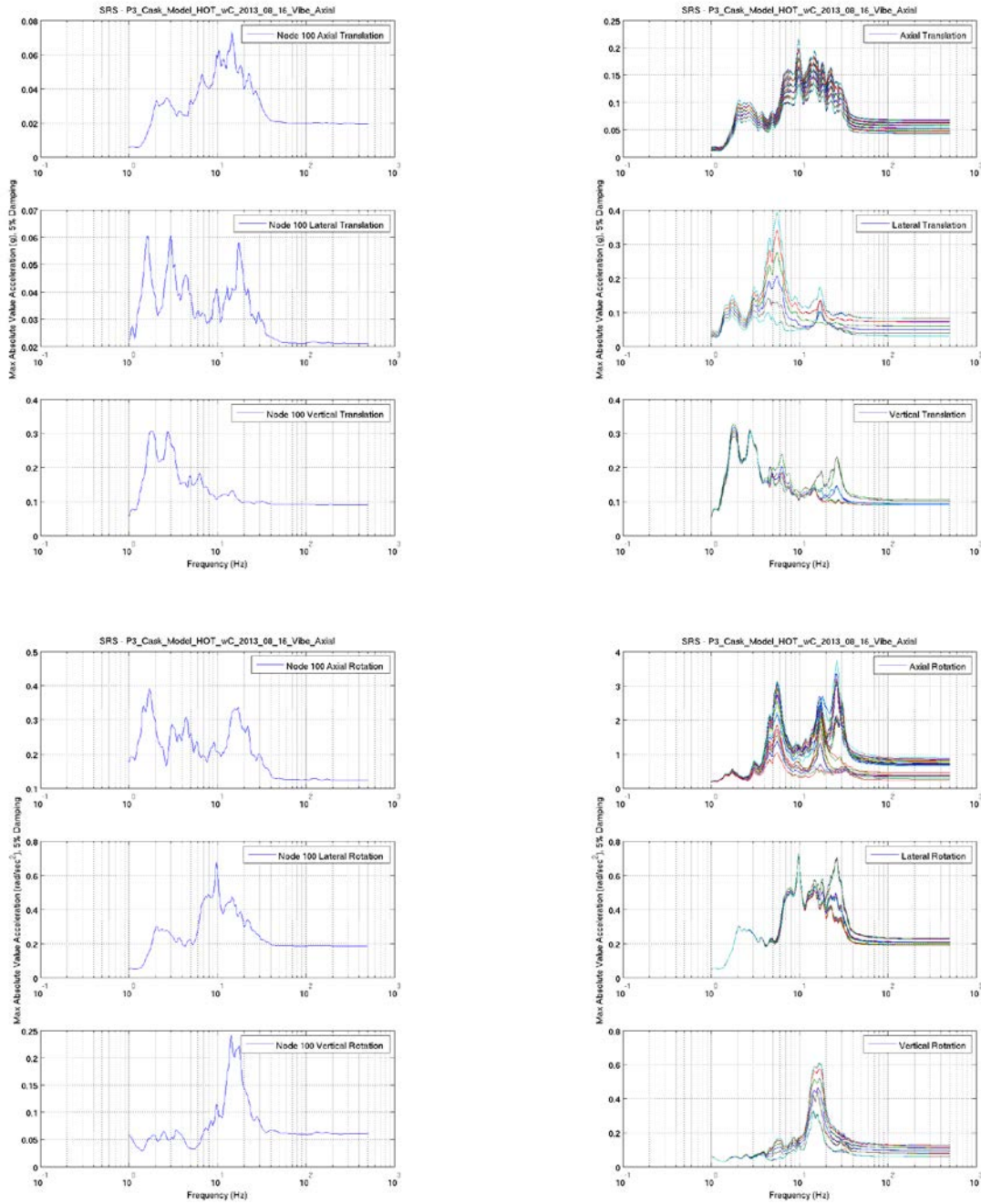
(a) Input

(b) Basket Cell Response

**Figure 1.43 P3 Vibration X (Axial) Load Case, Nominal Model Configuration, Input and
Basket Cell Response SRSs.**

USED FUEL DISPOSITION CAMPAIGN
**Used Nuclear Fuel Loading and Structural Performance Under Normal Conditions of Transport -
Demonstration of Approach and Results of Used Fuel Performance Characterization**
A-65   **SEPTEMBER 30, 2013**
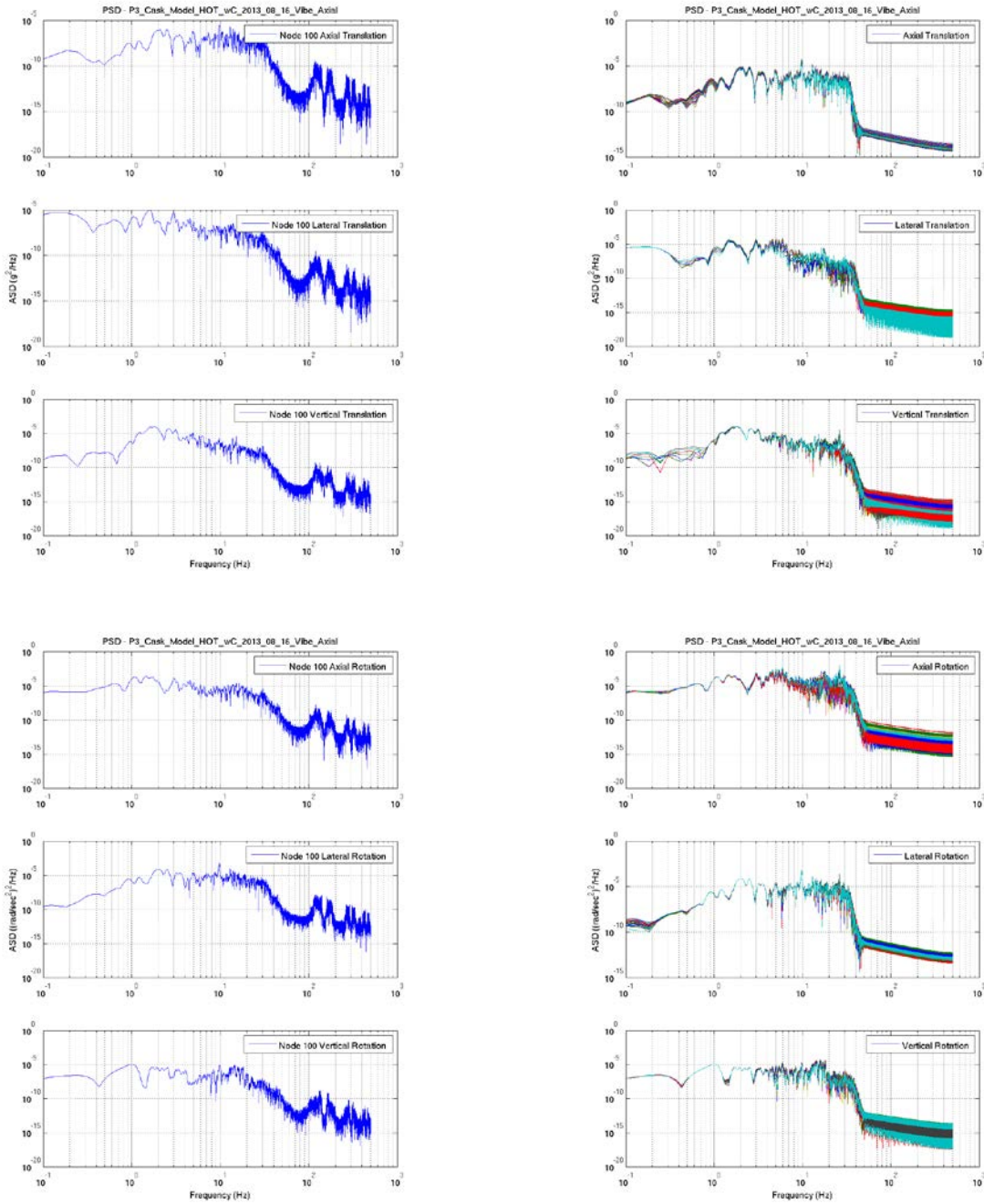
(a) Input   (b) Basket Cell Response

**Figure 1.44 P3 Vibration X (Axial) Load Case, Nominal Model Configuration, Input and
Basket Cell Response PSDs.**

USED FUEL DISPOSITION CAMPAIGN
**Used Nuclear Fuel Loading and Structural Performance Under Normal Conditions of Transport -
Demonstration of Approach and Results of Used Fuel Performance Characterization**
A-66   **SEPTEMBER 30, 2013**
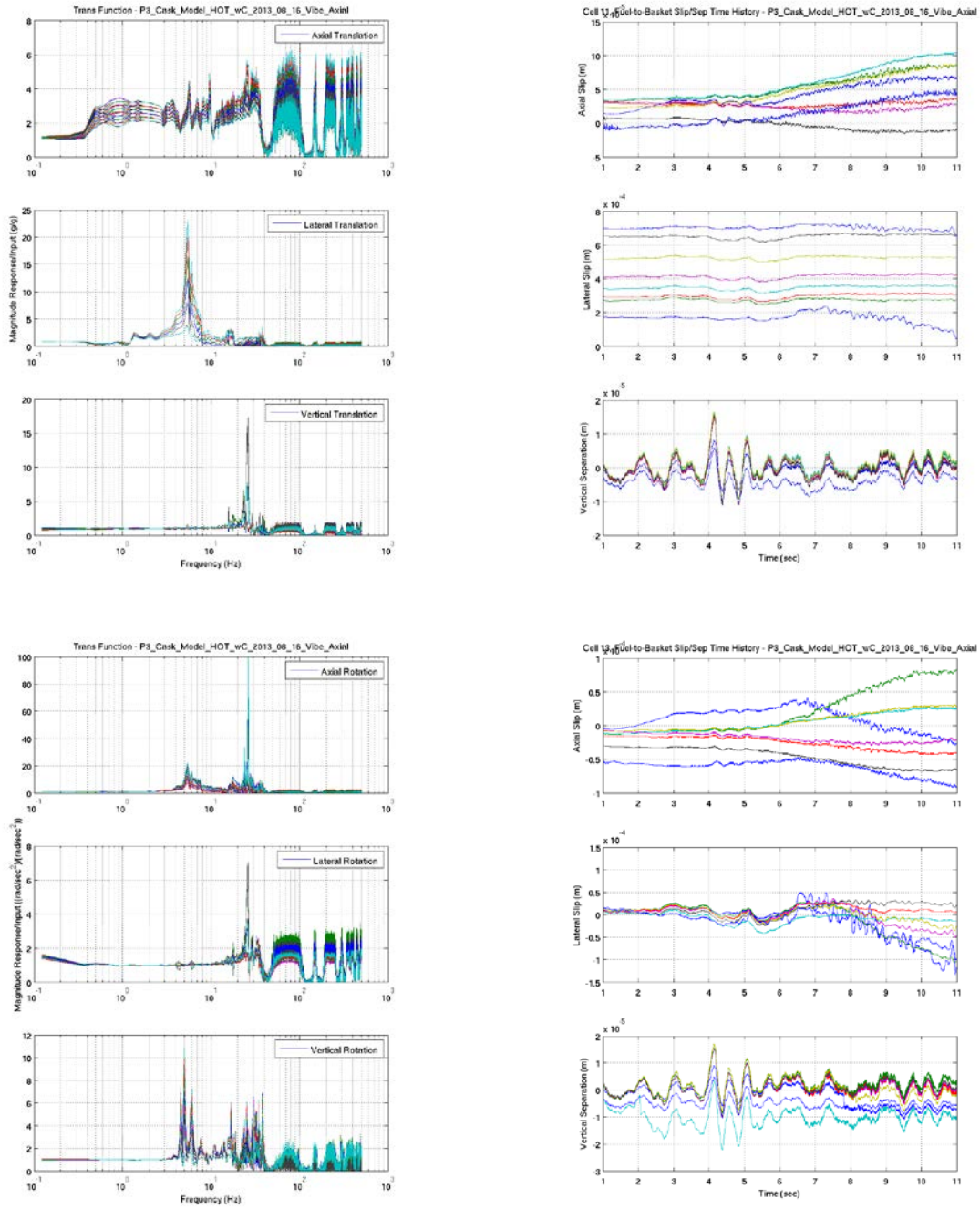
(a) Transfer Functions   (b) Fuel Assembly to Basket Slip/Separation.

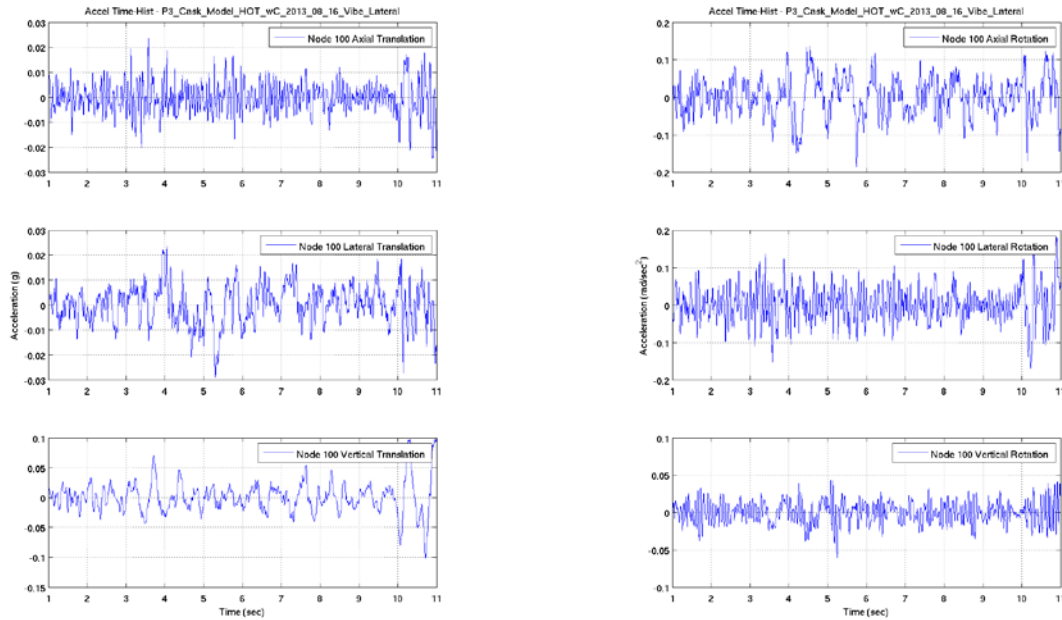**Figure 1.45 P3 Vibration X (Axial) Load Case, Nominal Model Configuration, Basket Cell
Response Transfer Functions and Slip/Separation Plots.**

USED FUEL DISPOSITION CAMPAIGN
**Used Nuclear Fuel Loading and Structural Performance Under Normal Conditions of Transport -
Demonstration of Approach and Results of Used Fuel Performance Characterization**
A-67   **SEPTEMBER 30, 2013**
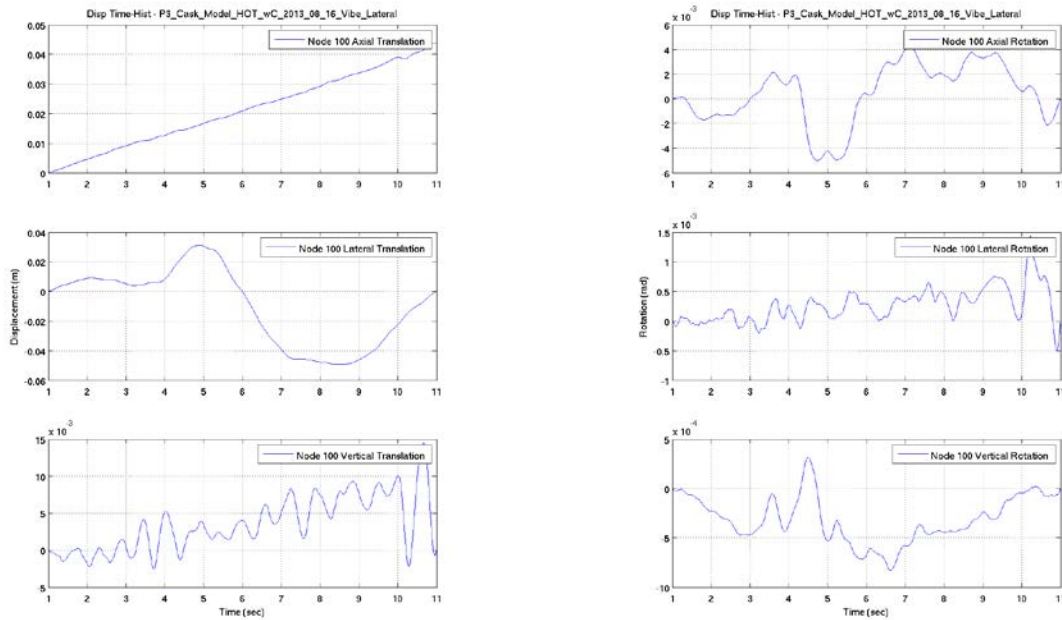
1.10 P3 VIBRATION Y (LATERAL)

The P3 Vibration Y (Lateral) case is characterized by a relatively uniform in the time domain vibration in the lateral direction with a g_{rms} value of 0.00318 g. The input FFT and PSD plots (Figure 1.47 and Figure 1.49) indicate that the majority of the power in the axial translation direction input was at frequencies between 0.2 and 0.4 Hz, and between 1 and 2 Hz. In the vertical translation direction the majority of the power was at frequencies between 1 and 2 Hz. In the axial translation direction the power was distributed across a wider range of frequencies from 1 to 20 Hz. The excitation power was greatest in the vertical direction (g_{rms} of 0.00692 g), with the lateral direction power (g_{rms} of 0.00318 g) being significantly lower. The axial direction excitation power (g_{rms} of 0.00209g) was lower still than both the power in the lateral and vertical directions. In the axial rotation direction there was a significant power spike between 1 and 2 Hz. The power in the axial rotation direction (g_{rms} of 0.0202 rad/sec^2) was somewhat greater than in either the lateral or vertical rotation directions (g_{rms} of 0.0151 rad/sec^2 and 0.0053 rad/sec^2, respectively). Significant energy in the lateral rotation direction existed between 2 and 20 Hz. In the vertical rotation direction, the power was concentrated in the 1 to 4 Hz, and 10 to 20 Hz ranges. Above approximately 30 Hz, all input excitations showed a marked drop in energy (in contrast to the P1 Vibration Y (Lateral) load case). Figure 1.46 illustrates the acceleration and displacement time-histories for each of the translation and rotation degrees-of-freedom for this load case. Figure 1.47 through Figure 1.49 provide FFT, SRS, and PSD plots for both the input excitation and the basket cell response. Transfer functions for each of the translation and rotation degrees-of-freedom are shown in Figure 1.50, along with axial and lateral slip and vertical separation plots for cell 11 and cell 13.

Figure 1.48 indicates that the peak response in the lateral direction was centered at about 5 Hz. In the axial direction the peak response was approximately half that of the peak response in the lateral direction and was centered at about 12 Hz, and was generally most pronounced across the frequency range of 6 to 30 Hz. In the vertical direction the peak response was approximately equal in magnitude to that in the axial direction and was centered at approximately 2, 3, and 25 Hz. The response in the rotational directions was largest for rotations about the axial axis. The axial rotation peak response was at about 5 Hz and some of the cells also show a significant response at about 25 Hz. Investigation of the transfer functions in Figure 1.50 indicate that the peak response in the lateral direction centered at about 5 Hz was significantly amplified above the input acceleration in that direction at that frequency. The magnitude of the transfer function at that frequency was greater than 25 for some of the cells. The axial direction peak response across the frequency range of 6 to 30 Hz was generally in excess of the input frequencies in that direction across that frequency range by a factor of 1.5 to 5. In the vertical direction, only the peak response centered at approximately 25 Hz was significantly amplified above the input excitation at that frequency in that direction. The peak responses at 2 and 3 Hz were simply a reflection of the input energy at those frequencies. No significant amplification at those frequencies was indicated. The axial rotation peak response at about 5 Hz and in some of the cells at about 25 Hz were significantly amplified (approximately 25 and 65 times, respectively) above the input accelerations at those frequencies in that direction.

USED FUEL DISPOSITION CAMPAIGN
**Used Nuclear Fuel Loading and Structural Performance Under Normal Conditions of Transport -
Demonstration of Approach and Results of Used Fuel Performance Characterization**
A-68
SEPTEMBER 30, 2013

Investigation of the slip/separation behavior between the fuel assembly and basket for cells 11 and 13 (Figure 1.50) indicates that essentially little or no slip in either the axial or lateral directions occurred between the fuel assemblies and basket, and that no vertical separation occurred. Again, the response at each cell location was not identical. The differences are easily identified in the cell SRSs shown in Figure 1.48.

USED FUEL DISPOSITION CAMPAIGN
**Used Nuclear Fuel Loading and Structural Performance Under Normal Conditions of Transport -
Demonstration of Approach and Results of Used Fuel Performance Characterization**
A-69 **SEPTEMBER 30, 2013**

(a) Acceleration Time-Histories

(b) Displacement and Rotation Time-Histories

**Figure 1.46 P3 Vibration Y (Lateral) Load Case, Nominal Model Configuration, Input
Acceleration and Displacement Time-Histories.**

USED FUEL DISPOSITION CAMPAIGN
Used Nuclear Fuel Loading and Structural Performance Under Normal Conditions of Transport -
Demonstration of Approach and Results of Used Fuel Performance Characterization
A-70
SEPTEMBER 30, 2013
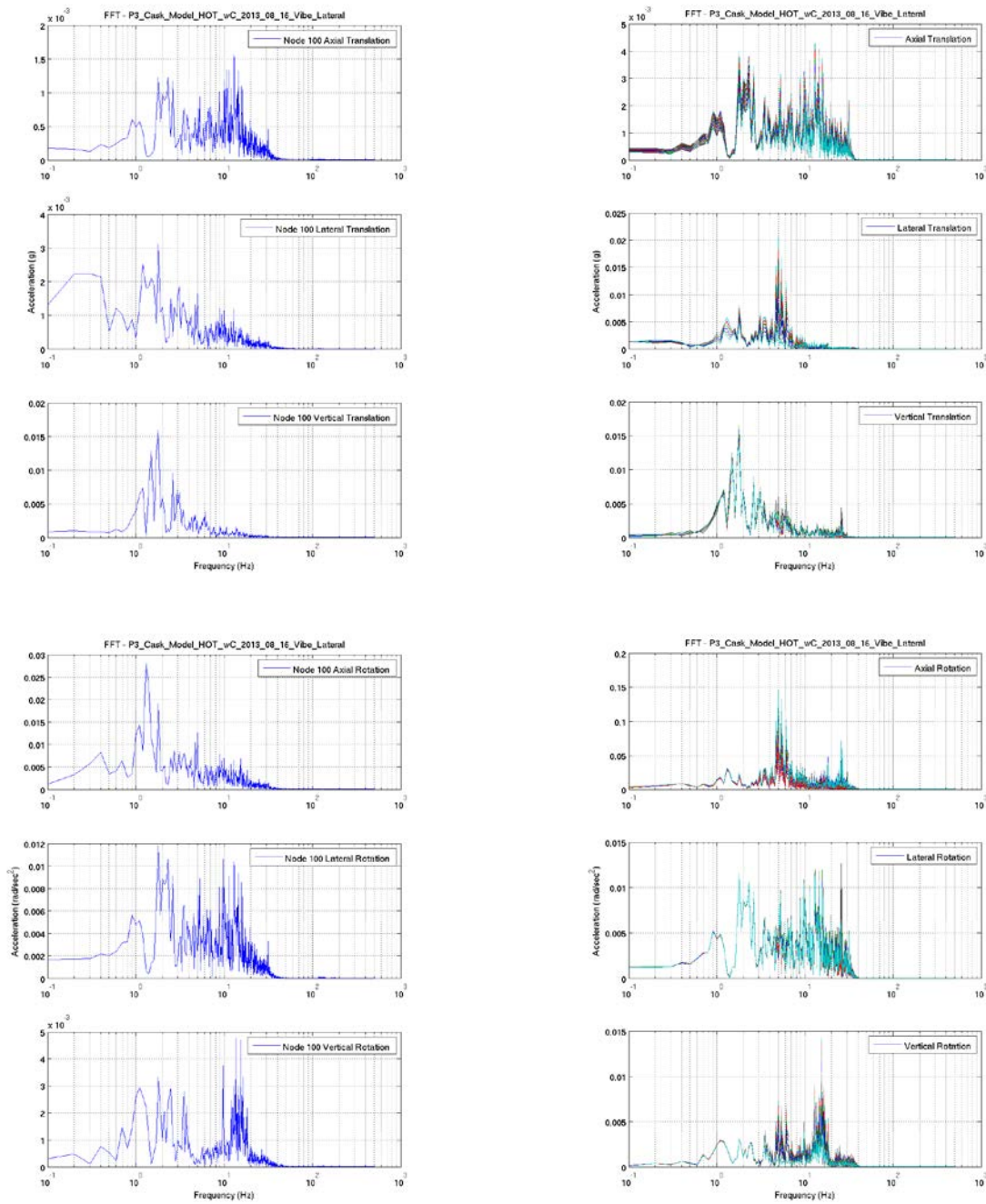
(a) Input

(b) Basket Cell Response

Figure 1.47 P3 Vibration Y (Lateral) Load Case, Nominal Model Configuration, Input and Basket Cell Response FFTs.

USED FUEL DISPOSITION CAMPAIGN
**Used Nuclear Fuel Loading and Structural Performance Under Normal Conditions of Transport -
Demonstration of Approach and Results of Used Fuel Performance Characterization**
A-71   **SEPTEMBER 30, 2013**
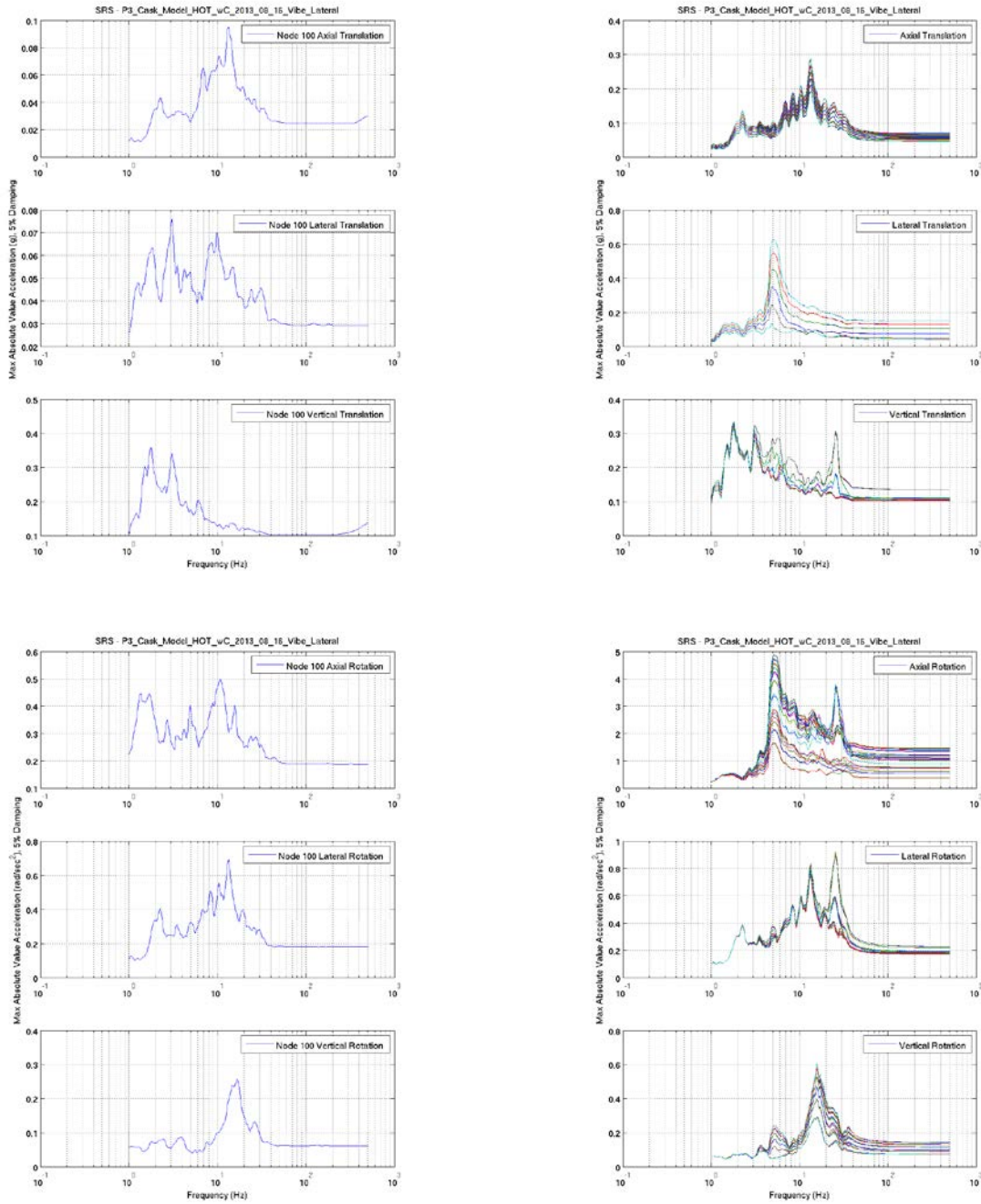
(a) Input   (b) Basket Cell Response

**Figure 1.48 P3 Vibration Y (Lateral) Load Case, Nominal Model Configuration, Input and
Basket Cell Response SRSs.**

USED FUEL DISPOSITION CAMPAIGN
**Used Nuclear Fuel Loading and Structural Performance Under Normal Conditions of Transport -
Demonstration of Approach and Results of Used Fuel Performance Characterization**
A-72   **SEPTEMBER 30, 2013**

(a) Input

(b) Basket Cell Response
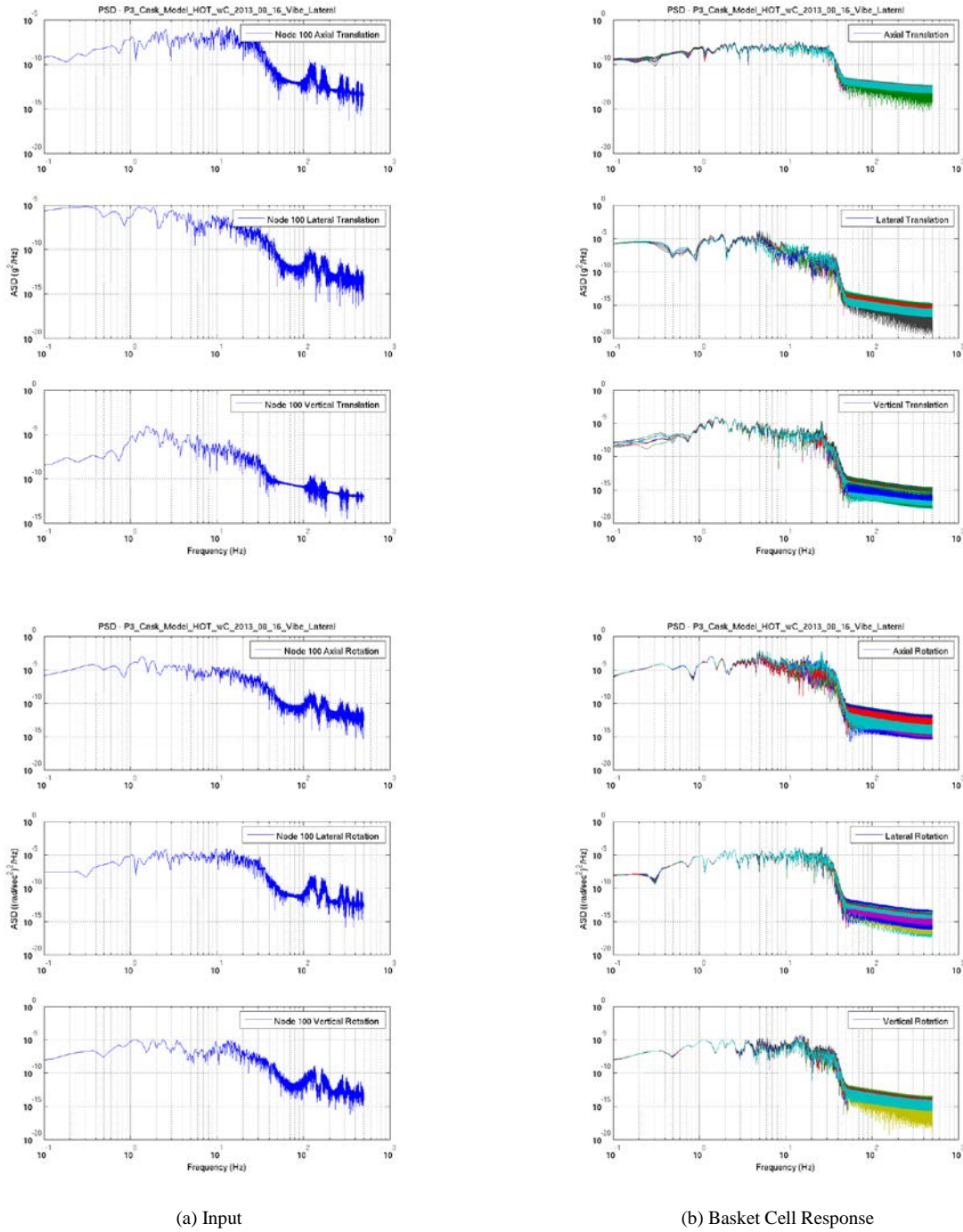
**Figure 1.49 P3 Vibration Y (Lateral) Load Case, Nominal Model Configuration, Input and
Basket Cell Response PSDs.**

USED FUEL DISPOSITION CAMPAIGN
Used Nuclear Fuel Loading and Structural Performance Under Normal Conditions of Transport -
Demonstration of Approach and Results of Used Fuel Performance Characterization
A-73   **SEPTEMBER 30, 2013**
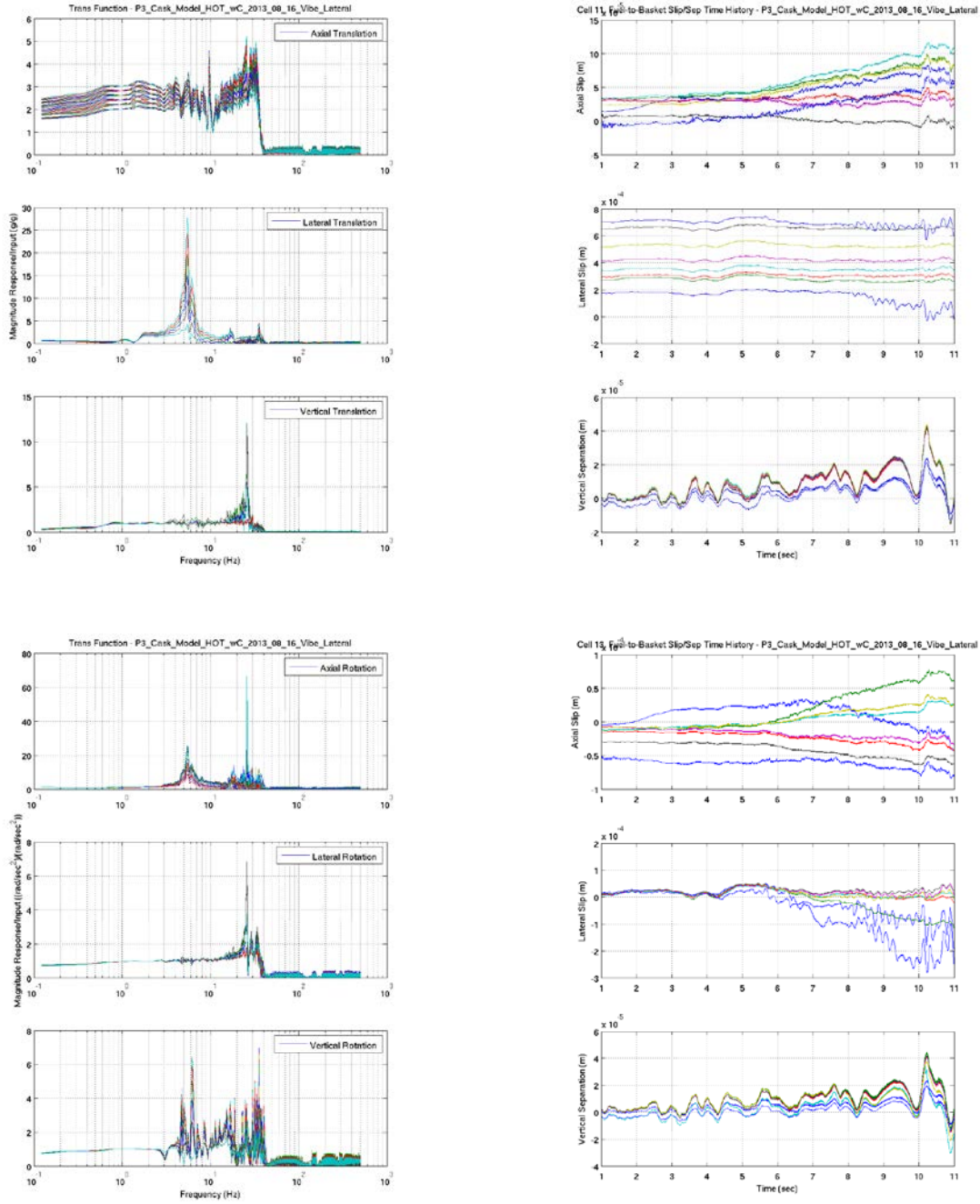
(a) Transfer Functions   (b) Fuel Assembly to Basket Slip/Separation.

**Figure 1.50 P3 Vibration Y (Lateral) Load Case, Nominal Model Configuration, Basket
Cell Response Transfer Functions and Slip/Separation Plots.**

USED FUEL DISPOSITION CAMPAIGN
**Used Nuclear Fuel Loading and Structural Performance Under Normal Conditions of Transport -
Demonstration of Approach and Results of Used Fuel Performance Characterization**
**A-74** **SEPTEMBER 30, 2013**

1.11 P3 VIBRATION Z (VERTICAL)

The P3 Vibration Z (Vertical) case is characterized by a relatively uniform in the time domain vibration in the vertical direction with a g_{rms} value of 0.00805 g. The input FFT and PSD plots (Figure 1.52 and Figure 1.54) indicate that the majority of the power in the vertical translation direction input was at frequencies between 1 and 3 Hz. In the lateral translation direction the majority of the power was at frequencies between 1 and 2 Hz, but there was also significant power at 0.2 Hz and 3 Hz. In the axial translation direction the power was more heavily concentrated between 10 and 20 Hz. The excitation was most powerful in the vertical direction (g_{rms} of 0.00805 g) with the power in the axial and lateral directions somewhat lower (g_{rms} of 0.00231 g and 0.00260 g, respectively). In the axial rotation direction the power existed across the frequency range from 1 to 20 Hz, with a significant peak between 1 and 2 Hz. The power in the axial rotation direction (g_{rms} of 0.0173 rad/sec^2) was approximately equal to the power in the lateral rotation direction (g_{rms} of 0.0173 rad/sec^2) and significantly greater than the power in the vertical rotation direction (g_{rms} of 0.0051 rad/sec^2). The energy in the lateral rotation direction existed in the frequency range from 2 to 20 Hz, with a somewhat heavier concentration of energy in the frequencies between 10 Hz and 15 Hz. The energy in the vertical rotation direction existed in frequencies between 1 and 4 Hz, and 10 and 20 Hz, with the energy in the latter range being somewhat more significant. Above approximately 30 Hz, all input excitations showed a marked drop in energy (in contrast to the P1 Vibration Z (Vertical) load case). Figure 1.51 illustrates the acceleration and displacement time-histories for each of the translation and rotation degrees-of-freedom for this load case. Figure 1.52 through Figure 1.54 provide FFT, SRS, and PSD plots for both the input excitation and the basket cell response. Transfer functions for each of the translation and rotation degrees-of-freedom are shown in Figure 1.55, along with axial and lateral slip and vertical separation plots for cell 11 and cell 13.

Figure 1.53 indicates that the peak response in the vertical direction occurred at about 3 Hz, with a somewhat reduced response in some of the cells at frequencies of 5.5 and 23 Hz. The response in the lateral direction was nearly twice that of the response in the vertical direction, and was centered exclusively at about 6 Hz. The magnitude of the response was heavily dependent on cell location. The peak response in the axial direction was of similar magnitude to the response in the vertical direction, with the peak response occurring at about 12 Hz. The peak response in the rotational directions was greatest for rotations about the axial axis. The axial rotation peak response was centered at about 6 Hz, with some of the cells also showing a significant response at about 25 Hz. The peak response in the lateral and vertical rotation directions was nearly an order of magnitude lower than in the axial rotation direction, with the peak response in those directions occurring between 10 and 20 Hz. Investigation of the transfer functions in Figure 1.55 indicate that the peak response in the vertical direction at about 3 Hz was not amplified above the input excitation at that frequency in that direction, indicating the peak in the response in the vertical direction was merely a reflection of the input excitation characteristics. Significant amplification in the vertical direction was only indicated at frequencies between 20 and 30 Hz. The peak response in the lateral rotation direction at about 6 Hz was significantly greater than the magnitude of the input excitation at that frequency in that direction, indicating the presence of a response mode at 6 Hz. The magnitude of the amplification was dependent on cell location and ranged from less than 5 to over 20 times. This peak response was strongly coupled to the

USED FUEL DISPOSITION CAMPAIGN
**Used Nuclear Fuel Loading and Structural Performance Under Normal Conditions of Transport -
Demonstration of Approach and Results of Used Fuel Performance Characterization**
A-75
SEPTEMBER 30, 2013

response in the axial rotation direction at 6 Hz indicating that rocking of the cask about its longitudinal axis was generating this amplification. The peak response in the axial translation direction at about 12 Hz was somewhat amplified above the input excitation at that frequency in that direction. Amplification in the axial direction was more significant for other frequencies, particularly in the range from 0.8 to 10 Hz, and from 11 to 30 Hz. The peak response in the axial rotation direction centered at about 6 Hz was significantly amplified, with the amplification ranging from about 5 to 20, depending on cell location. Significant amplification also occurred at frequencies just below 20 Hz, and at frequencies between 20 and 40 Hz. The peak response in the lateral and vertical rotation directions between 10 and 20 Hz were not significantly amplified, but responses at frequencies between 20 and 30 in the lateral rotation direction, and between 5 and 6 Hz in the vertical rotation direction, were significantly amplified.

Investigation of the slip/separation behavior between the fuel assembly and basket for cells 11 and 13 (Figure 1.55) indicates that essentially little or no slip in either the axial or lateral directions occurred between the fuel assemblies and basket, and that no vertical separation occurred. Again, the response at each cell location was not identical. The differences are easily identified in the cell SRSs shown in Figure 1.53.
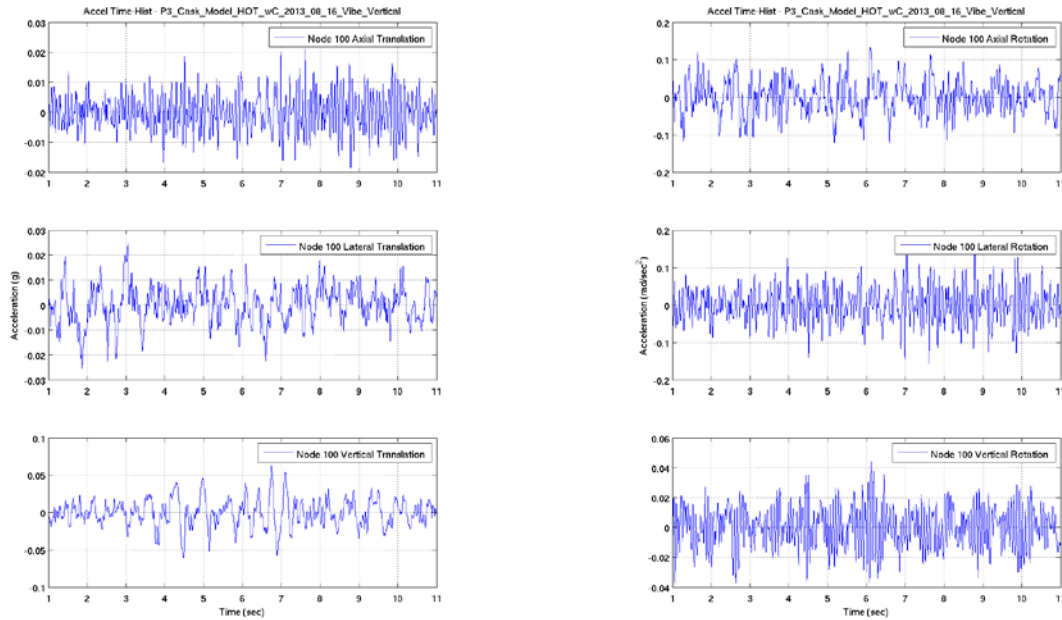
(a) Acceleration Time-Histories
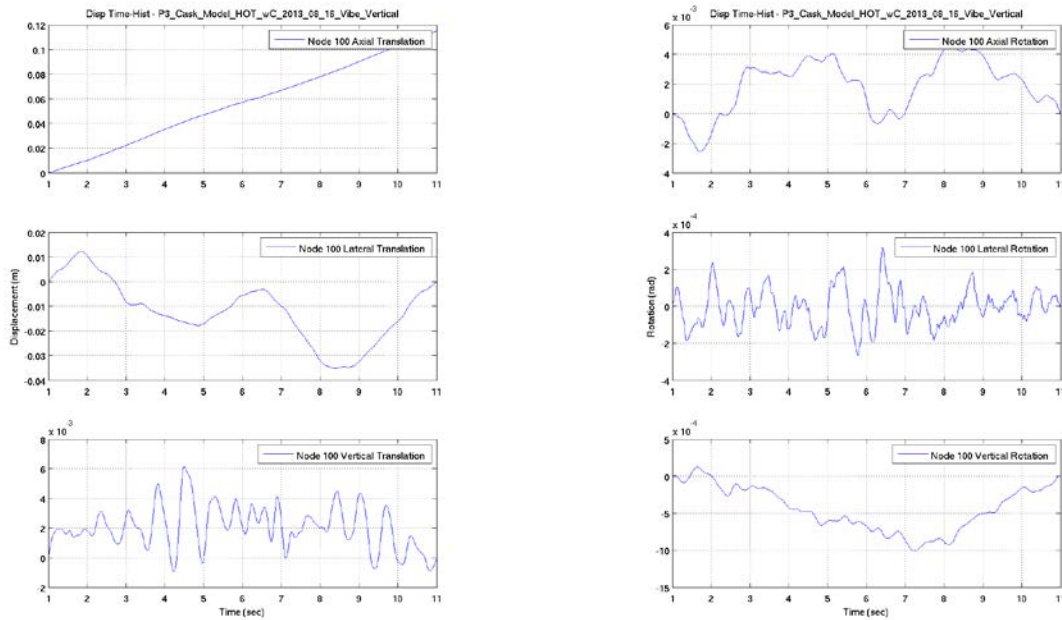
(b) Displacement and Rotation Time-Histories

Figure 1.51 P3 Vibration Z (Vertical) Load Case, Nominal Model Configuration, Input Acceleration and Displacement Time-Histories.

USED FUEL DISPOSITION CAMPAIGN
Used Nuclear Fuel Loading and Structural Performance Under Normal Conditions of Transport -
Demonstration of Approach and Results of Used Fuel Performance Characterization
A-77   **SEPTEMBER 30, 2013**
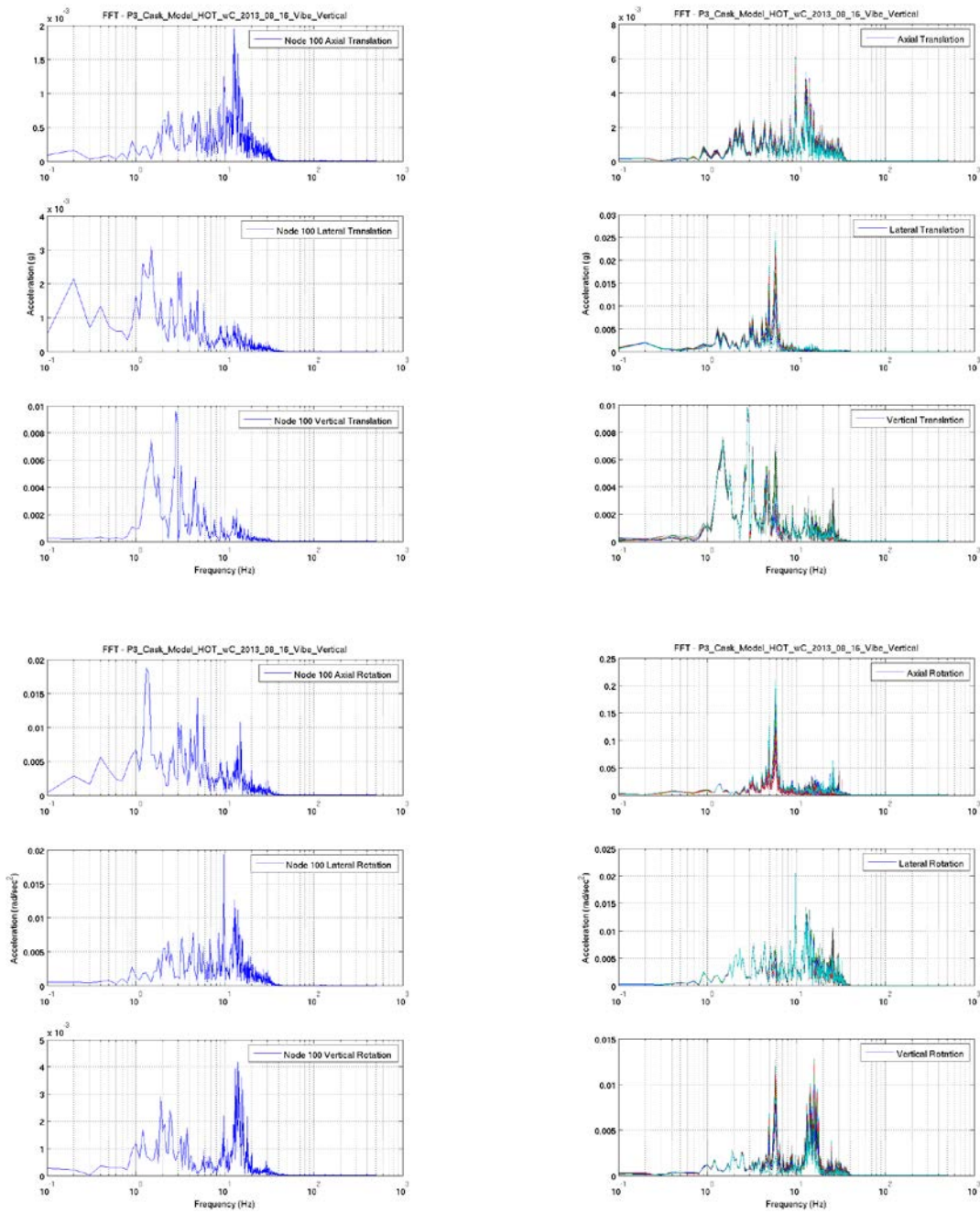
(a) Input

(b) Basket Cell Response

Figure 1.52 P3 Vibration Z (Vertical) Load Case, Nominal Model Configuration, Input and Basket Cell Response FFTs.

USED FUEL DISPOSITION CAMPAIGN
Used Nuclear Fuel Loading and Structural Performance Under Normal Conditions of Transport -
Demonstration of Approach and Results of Used Fuel Performance Characterization
A-78
SEPTEMBER 30, 2013
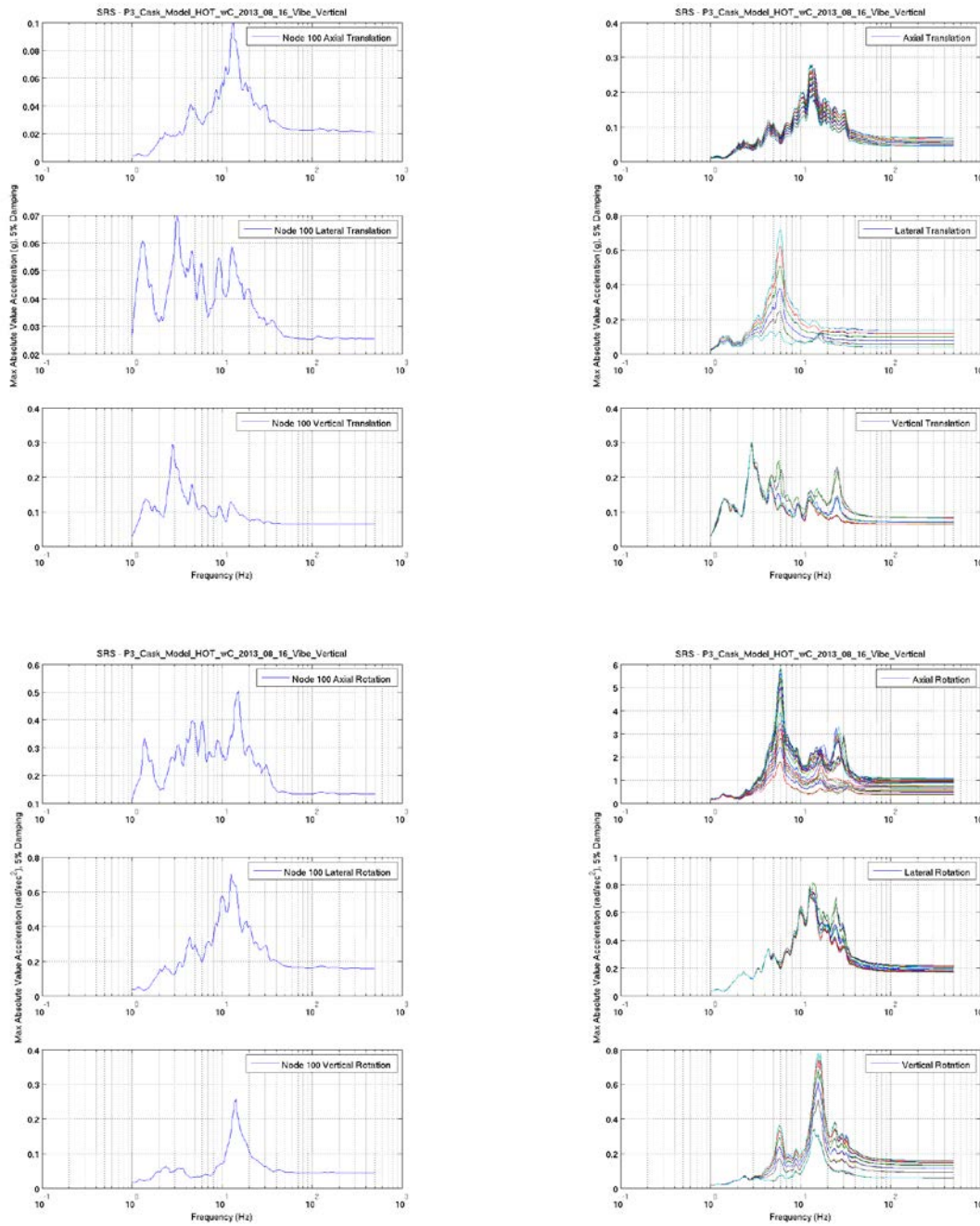
(a) Input

(b) Basket Cell Response

Figure 1.53 P3 Vibration Z (Vertical) Load Case, Nominal Model Configuration, Input and Basket Cell Response SRSs.

USED FUEL DISPOSITION CAMPAIGN
**Used Nuclear Fuel Loading and Structural Performance Under Normal Conditions of Transport -
Demonstration of Approach and Results of Used Fuel Performance Characterization**
A-79   **SEPTEMBER 30, 2013**

(a) Input

(b) Basket Cell Response
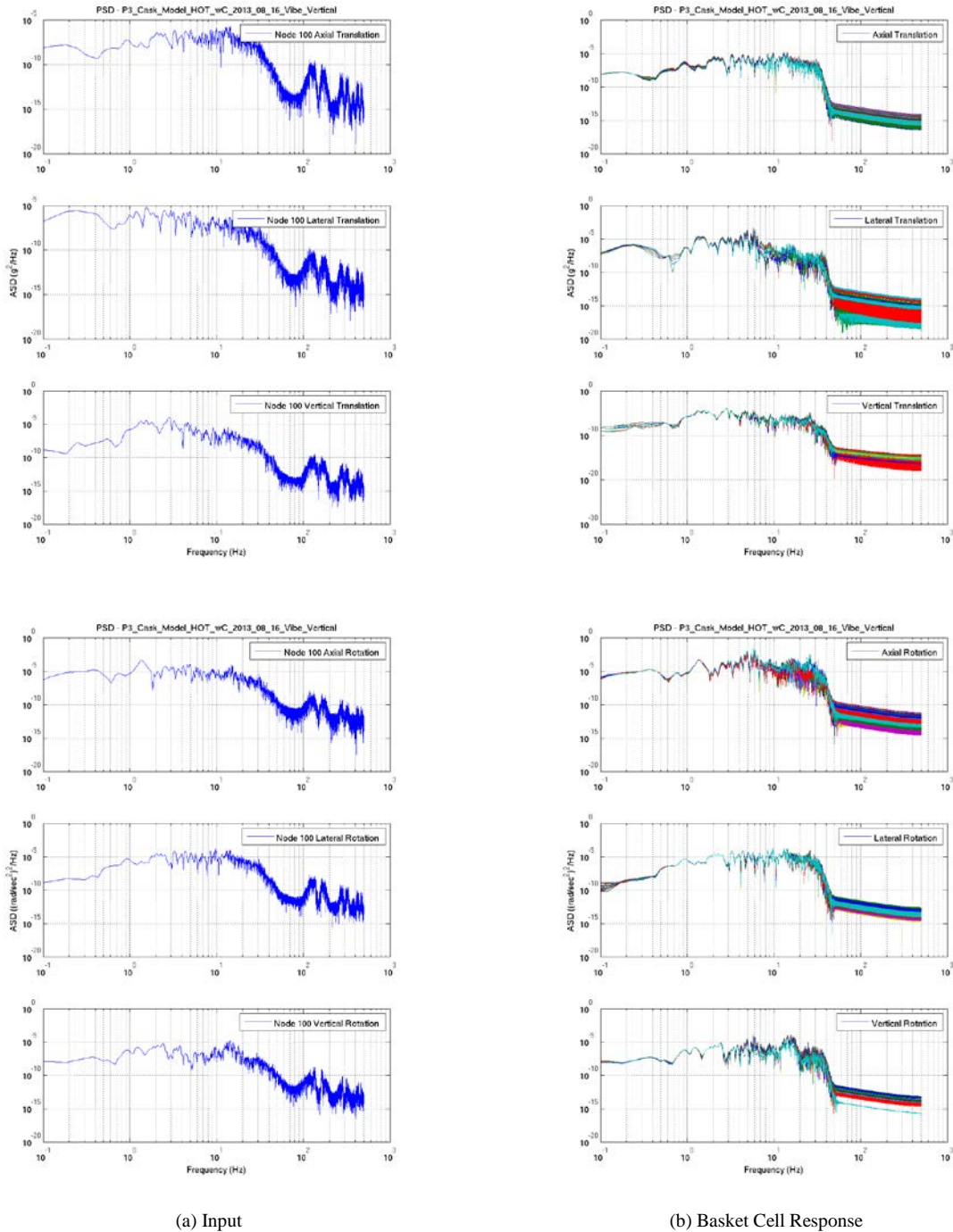
Figure 1.54 P3 Vibration Z (Vertical) Load Case, Nominal Model Configuration, Input and Basket Cell Response PSDs.

USED FUEL DISPOSITION CAMPAIGN
**Used Nuclear Fuel Loading and Structural Performance Under Normal Conditions of Transport -
Demonstration of Approach and Results of Used Fuel Performance Characterization**
A-80   **SEPTEMBER 30, 2013**
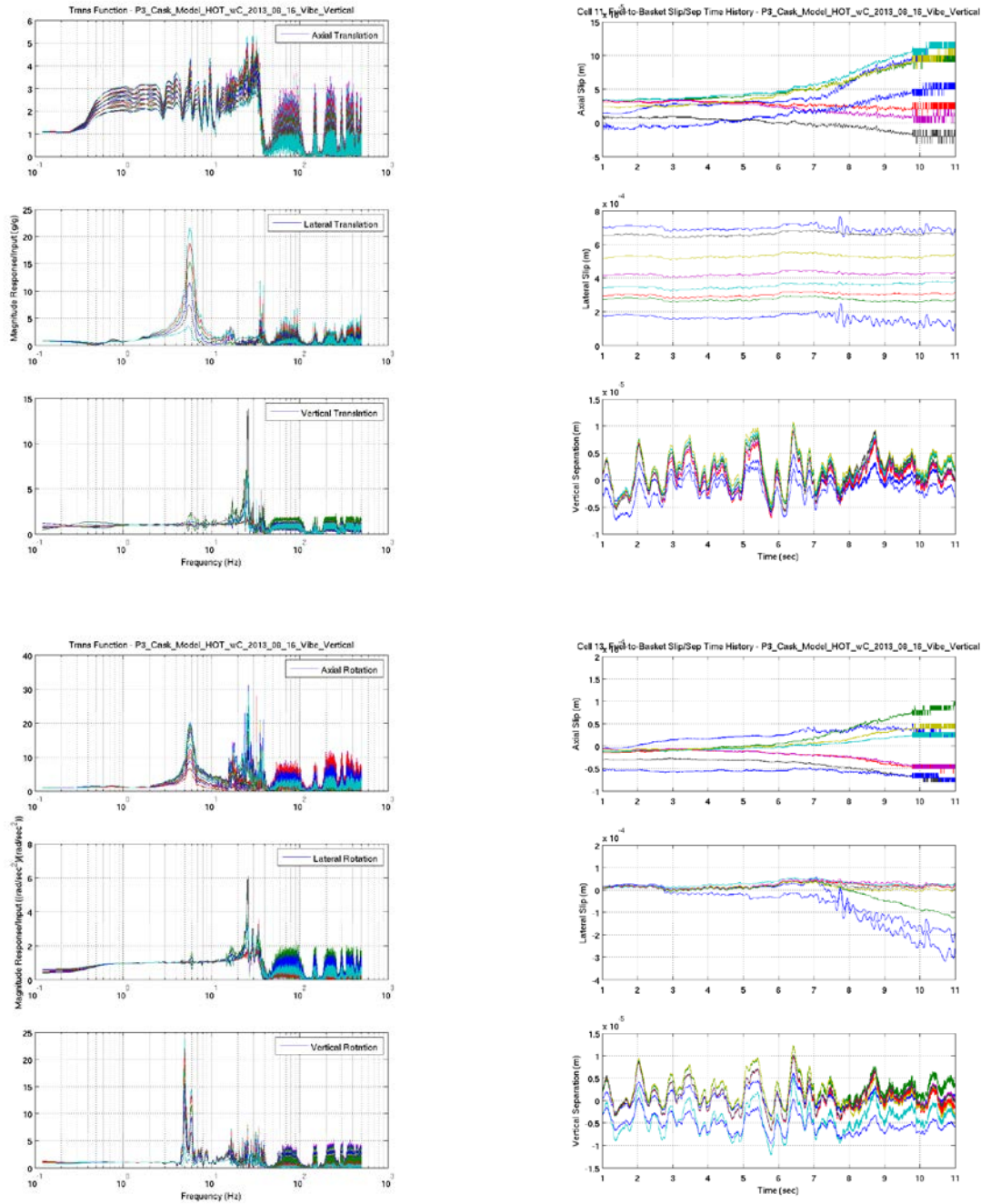
(a) Transfer Functions   (b) Fuel Assembly to Basket Slip/Separation.

**Figure 1.55 P3 Vibration Z (Vertical) Load Case, Nominal Model Configuration, Basket
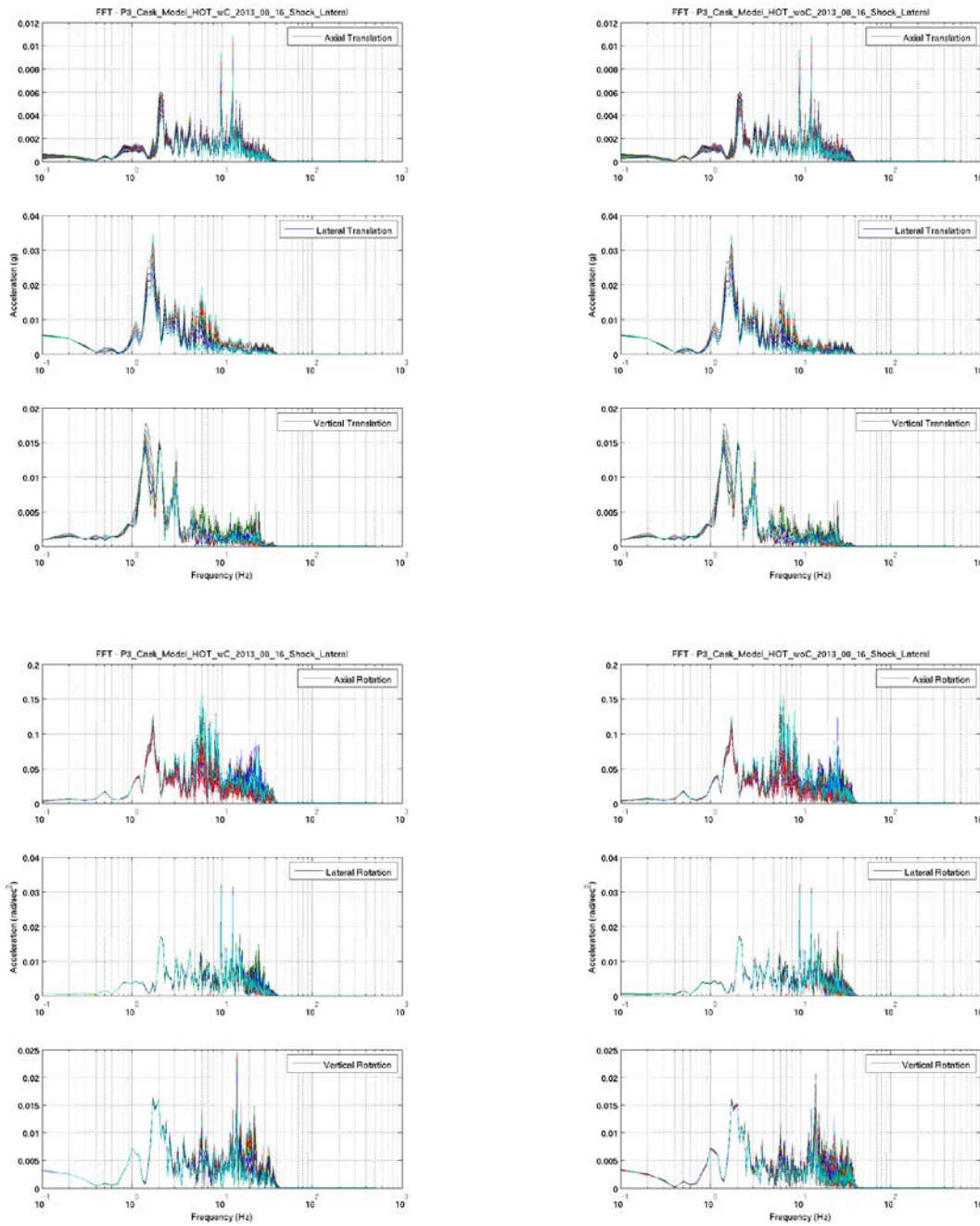Cell Response Transfer Functions and Slip/Separation Plots.**

USED FUEL DISPOSITION CAMPAIGN
**Used Nuclear Fuel Loading and Structural Performance Under Normal Conditions of Transport -
Demonstration of Approach and Results of Used Fuel Performance Characterization**
A-81 **SEPTEMBER 30, 2013**

2. SENSITIVITY ANALYSES

2.1 WITHOUT CONTROL COMPONENTS

2.1.1 P3 SHOCK Y (LATERAL)

Figure 2.1 through Figure 2.5 provide a comparison of FFT, SRS, PSD, transfer function, and cell 11 and 13 slip/separation response plots for the nominal configuration model and the without control components configuration model for the P3 Shock Y (Lateral) load case. In general, the response between the two models differed only slightly. Figure 2.2 illustrates that the peak response for the without control assembly configuration was slightly lower than that of the nominal configuration. In the vertical translation direction, the peak SRS magnitude at about 22 Hz was lower by about 30%, and the peak in the lateral direction at about 30 Hz was lower by about 5%. The peak response in the axial rotation direction at just under 30 Hz was also lower by 15%, the peak response in the lateral rotation direction at about 15 and 25 Hz was lower by about 20%, and the peak response in the vertical rotation direction at about 20 Hz was lower by approximately 50%. In contracts to these reductions, the response in the axial translation direction between 20 and 40 Hz (which was not the peak response in that direction) was higher by about 40%. The trends in the PSD plots (Figure 2.3) support these observations. The average g_{rms} value in the axial translation direction was approximately equal between the nominal model configuration case and the without control components model configuration case, whereas the g_{rms} values for the without control components configuration model in the lateral translation, vertical translation, axial rotation, lateral rotation, and vertical rotation directions were all lower (by approximately 3%, 3%, 10%, 3%, and 14%, respectively). Minor differences are also seen in the FFT and transfer functions (Figure 2.1 and Figure 2.4), particularly at frequencies between 20 and 40 Hz. Finally, differences in response ware also observed in the cell 11 and 13 slip/separation plots (Figure 2.5), specifically the total axial slip was somewhat larger in the without control component configuration case (by approximately 16% and 50% for cell 11 and 13, respectively) and the total lateral slip was somewhat lower (by approximately 25% and 15% for cell 11 and 13, respectively).

Which model configuration represents the worst configuration for this load case is difficult to determine. The response of the fuel assembly will depend not only on the magnitude of any input excitation, but also upon the specific frequencies at which that excitation occurs. There were some potentially important differences in the response at each cell between these two configurations, particularly in the range of frequencies from 20 to 40 Hz in which the fuel assembly rods are expected to respond.

USED FUEL DISPOSITION CAMPAIGN
Used Nuclear Fuel Loading and Structural Performance Under Normal Conditions of Transport -
Demonstration of Approach and Results of Used Fuel Performance Characterization
A-82   **SEPTEMBER 30, 2013**

(a) Nominal Configuration   (b) Without Control Components Configuration

Figure 2.1 P3 Shock Y (Lateral) Load Case, Without Control Components Model
Configuration, Basket Cell Response FFTs.

USED FUEL DISPOSITION CAMPAIGN
Used Nuclear Fuel Loading and Structural Performance Under Normal Conditions of Transport -
Demonstration of Approach and Results of Used Fuel Performance Characterization
A-83 **SEPTEMBER 30, 2013**

(a) Nominal Configuration   (b) Without Control Components Configuration

**Figure 2.2 P3 Shock Y (Lateral) Load Case, Without Control Components Model
Configuration, Basket Cell Response SRSs.**

USED FUEL DISPOSITION CAMPAIGN
Used Nuclear Fuel Loading and Structural Performance Under Normal Conditions of Transport -
Demonstration of Approach and Results of Used Fuel Performance Characterization
A-84　　　　　　　　　　　　　　　　　　　　　　　　　　　　**SEPTEMBER 30, 2013**

(a) Nominal Configuration　　　　　　　　　　　(b) Without Control Components Configuration

Figure 2.3 P3 Shock Y (Lateral) Load Case, Without Control Components Model Configuration, Basket Cell Response PSDs.

USED FUEL DISPOSITION CAMPAIGN
**Used Nuclear Fuel Loading and Structural Performance Under Normal Conditions of Transport -
Demonstration of Approach and Results of Used Fuel Performance Characterization**
A-85   **SEPTEMBER 30, 2013**

(a) Nominal Configuration   (b) Without Control Components Configuration

**Figure 2.4 P3 Shock Y (Lateral) Load Case, Without Control Components Model
Configuration, Basket Cell Response Transfer Functions.**

USED FUEL DISPOSITION CAMPAIGN
**Used Nuclear Fuel Loading and Structural Performance Under Normal Conditions of Transport -
Demonstration of Approach and Results of Used Fuel Performance Characterization**
A-86   **SEPTEMBER 30, 2013**

(a) Nominal Configuration   (b) Without Control Components Configuration

**Figure 2.5 P3 Shock Y (Lateral) Load Case, Without Control Components Model
Configuration, Basket Cell Response Slip/Separation Plots.**

USED FUEL DISPOSITION CAMPAIGN
**Used Nuclear Fuel Loading and Structural Performance Under Normal Conditions of Transport -
Demonstration of Approach and Results of Used Fuel Performance Characterization**
A-87 **SEPTEMBER 30, 2013**

2.1.2 P3 SHOCK Z (VERTICAL)

Figure 2.6 through Figure 2.10 provide a comparison of FFT, SRS, PSD, transfer function, and cell 11 and 13 slip/separation response plots for the nominal configuration model and the without control components configuration model for the P3 Shock Z (Vertical) load case. In general, the response between the two models differed only slightly. Figure 2.7 illustrates that the peak response for the without control assembly configuration in some instances was somewhat lower than that of the nominal configuration case and in some instances somewhat higher. In the vertical translation direction, the peak SRS magnitude at about 2 Hz was essentially equivalent between the two cases, whereas the response in that direction at about 20 Hz was higher in the without control components case by approximately 30%. Similarly, the peak response in the lateral direction at about 6 Hz was essentially equivalent, whereas the response between 20 and 30 Hz was higher in the without control components case by about 30%. The response in the axial translation direction was essentially equivalent between the two cases. The peak response in the axial rotation direction at about 6 Hz was lower by about 10% in the without control components case and replaced by a 40% higher peak response at a frequency of about 20 Hz. A similar difference was observed in the response in the vertical rotation direction, with the peak response at about 15 Hz in the nominal model configuration being replaced by a 65% higher peak response in the without control assembly model configuration at a frequency of about 32 Hz. The peak response in the lateral rotation direction was essentially equivalent between the two cases. The trends in the PSD plots (Figure 2.3) support these observations. The average g_{rms} value in the axial translation, vertical translation, and lateral rotation directions were equal between the nominal model configuration case and the without control components model configuration case, whereas the g_{rms} values for the without control components configuration model in the lateral translation and axial rotation directions were lower (by approximately 4% and 5%, respectively) and in the vertical rotation direction higher (by approximately 7%). Minor differences were also seen in the FFT and transfer functions (Figure 2.6 and Figure 2.9), particularly at a frequency of 6 Hz and frequencies between 20 and 40 Hz. Finally, differences in response were also observed in the cell 11 and 13 slip/separation plots (Figure 2.5), specifically the total axial and lateral slip was somewhat higher in the case of the without control component configuration model (by approximately 230% and 150%, and 230% and 100% for cell 11 and 13, respectively). Vertical separation, while very small in amplitude, did occur in the without control assembly model configuration case, and did not occur in the nominal configuration case.
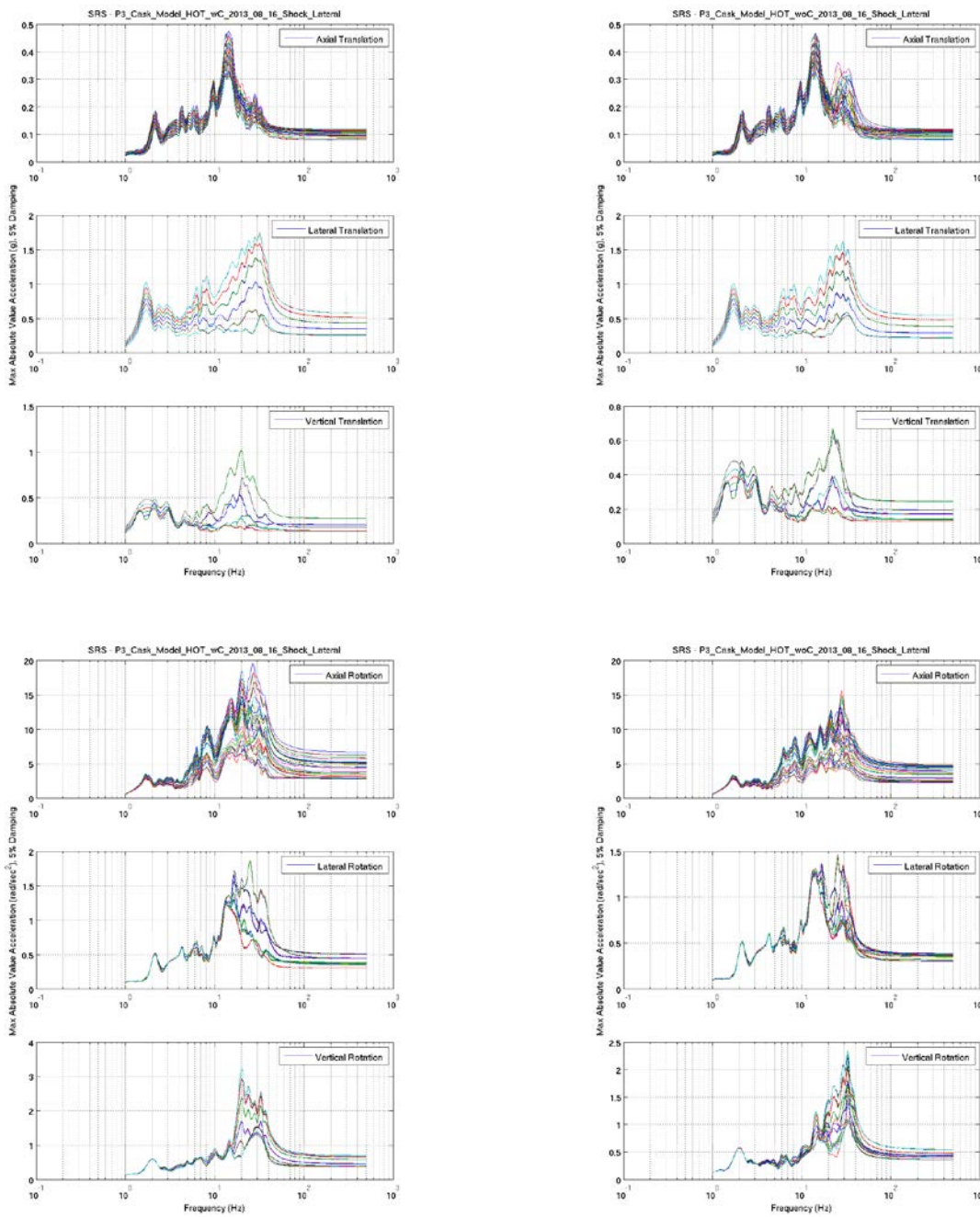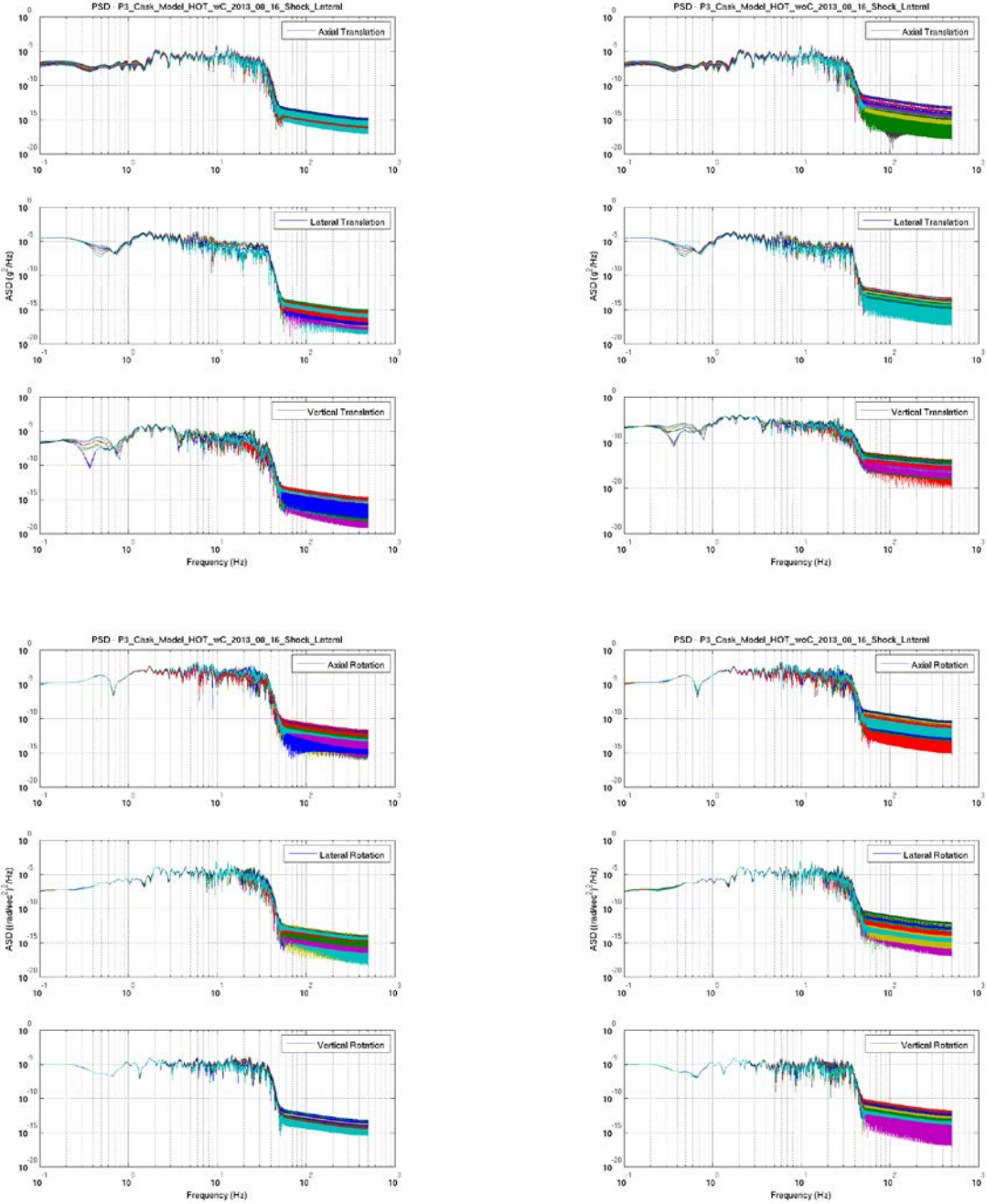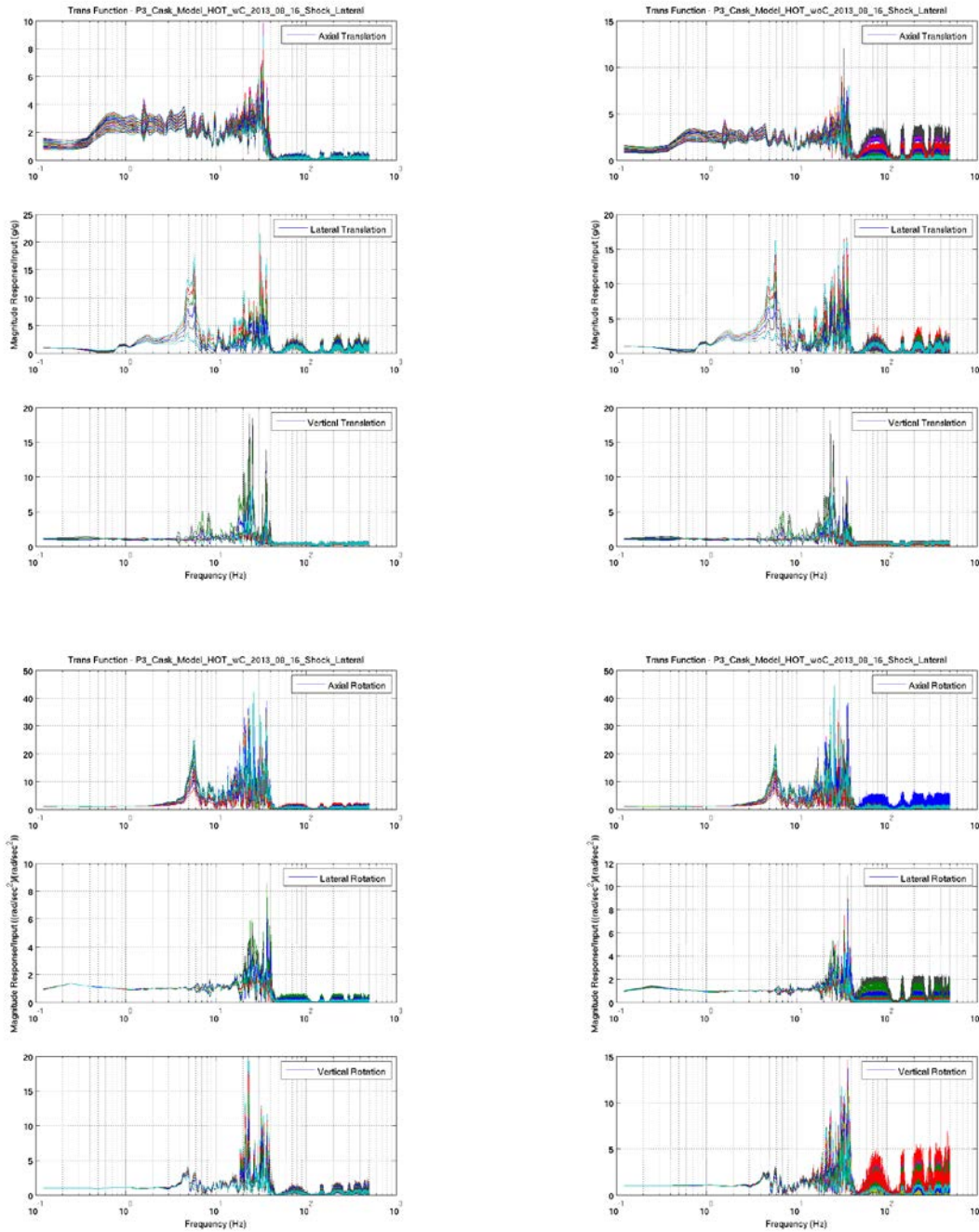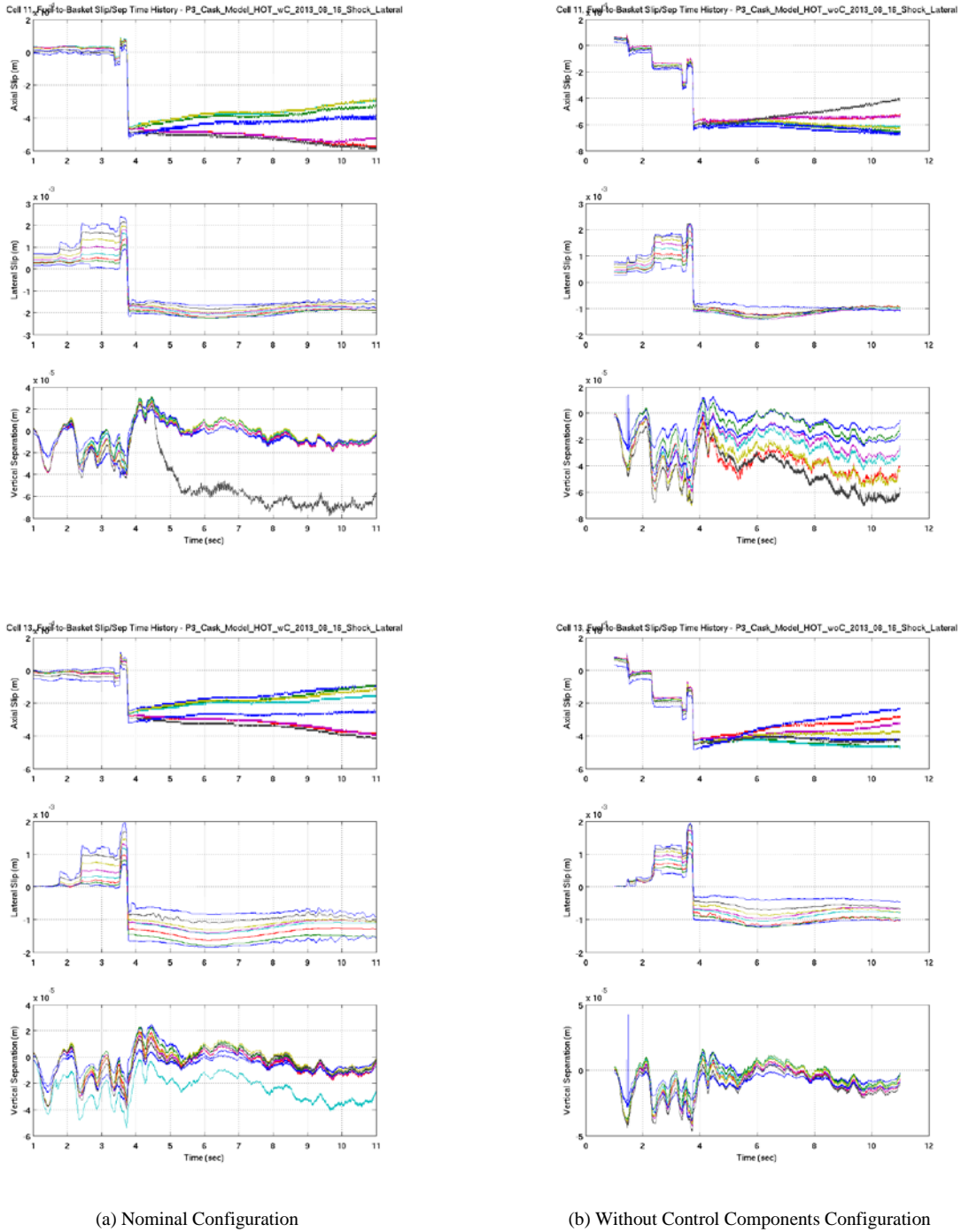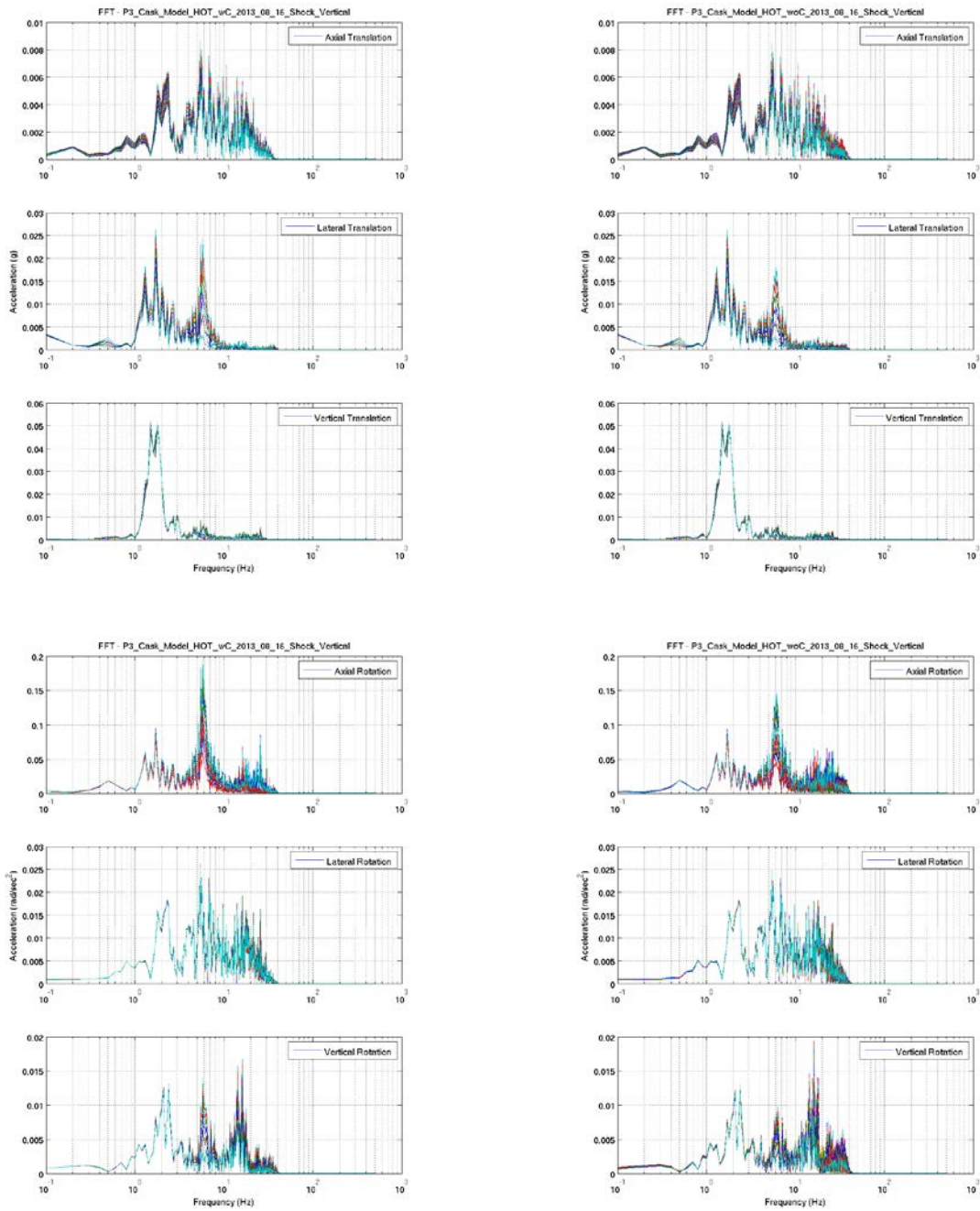
Which model configuration represents the worst configuration for this load case is difficult to determine. The response of the fuel assembly will depend not only on the magnitude of any input excitation, but also upon the specific frequencies at which that excitation occurs. There were some potentially important differences in the response at each cell between these two configurations, particularly in the range of frequencies from 20 to 40 Hz in which the fuel assembly rods are expected to respond.

USED FUEL DISPOSITION CAMPAIGN
**Used Nuclear Fuel Loading and Structural Performance Under Normal Conditions of Transport -
Demonstration of Approach and Results of Used Fuel Performance Characterization**
A-88   **SEPTEMBER 30, 2013**

(a) Nominal Configuration   (b) Without Control Components Configuration

**Figure 2.6 P3 Shock Z (Vertical) Load Case, Without Control Components Model
Configuration, Basket Cell Response FFTs.**

USED FUEL DISPOSITION CAMPAIGN
**Used Nuclear Fuel Loading and Structural Performance Under Normal Conditions of Transport -
Demonstration of Approach and Results of Used Fuel Performance Characterization**
A-89   **SEPTEMBER 30, 2013**

(a) Nominal Configuration   (b) Without Control Components Configuration

**Figure 2.7 P3 Shock Z (Vertical) Load Case, Without Control Components Model
Configuration, Basket Cell Response SRSs.**

USED FUEL DISPOSITION CAMPAIGN
**Used Nuclear Fuel Loading and Structural Performance Under Normal Conditions of Transport -
Demonstration of Approach and Results of Used Fuel Performance Characterization**
A-90
SEPTEMBER 30, 2013

(a) Nominal Configuration   (b) Without Control Components Configuration

**Figure 2.8 P3 Shock Z (Vertical) Load Case, Without Control Components Model
Configuration, Basket Cell Response PSDs.**

USED FUEL DISPOSITION CAMPAIGN
**Used Nuclear Fuel Loading and Structural Performance Under Normal Conditions of Transport -
Demonstration of Approach and Results of Used Fuel Performance Characterization**
A-91   **SEPTEMBER 30, 2013**

(a) Nominal Configuration   (b) Without Control Components Configuration

**Figure 2.9 P3 Shock Z (Vertical) Load Case, Without Control Components Model
Configuration, Basket Cell Response Transfer Functions.**

USED FUEL DISPOSITION CAMPAIGN
**Used Nuclear Fuel Loading and Structural Performance Under Normal Conditions of Transport -
Demonstration of Approach and Results of Used Fuel Performance Characterization**
A-92   **SEPTEMBER 30, 2013**
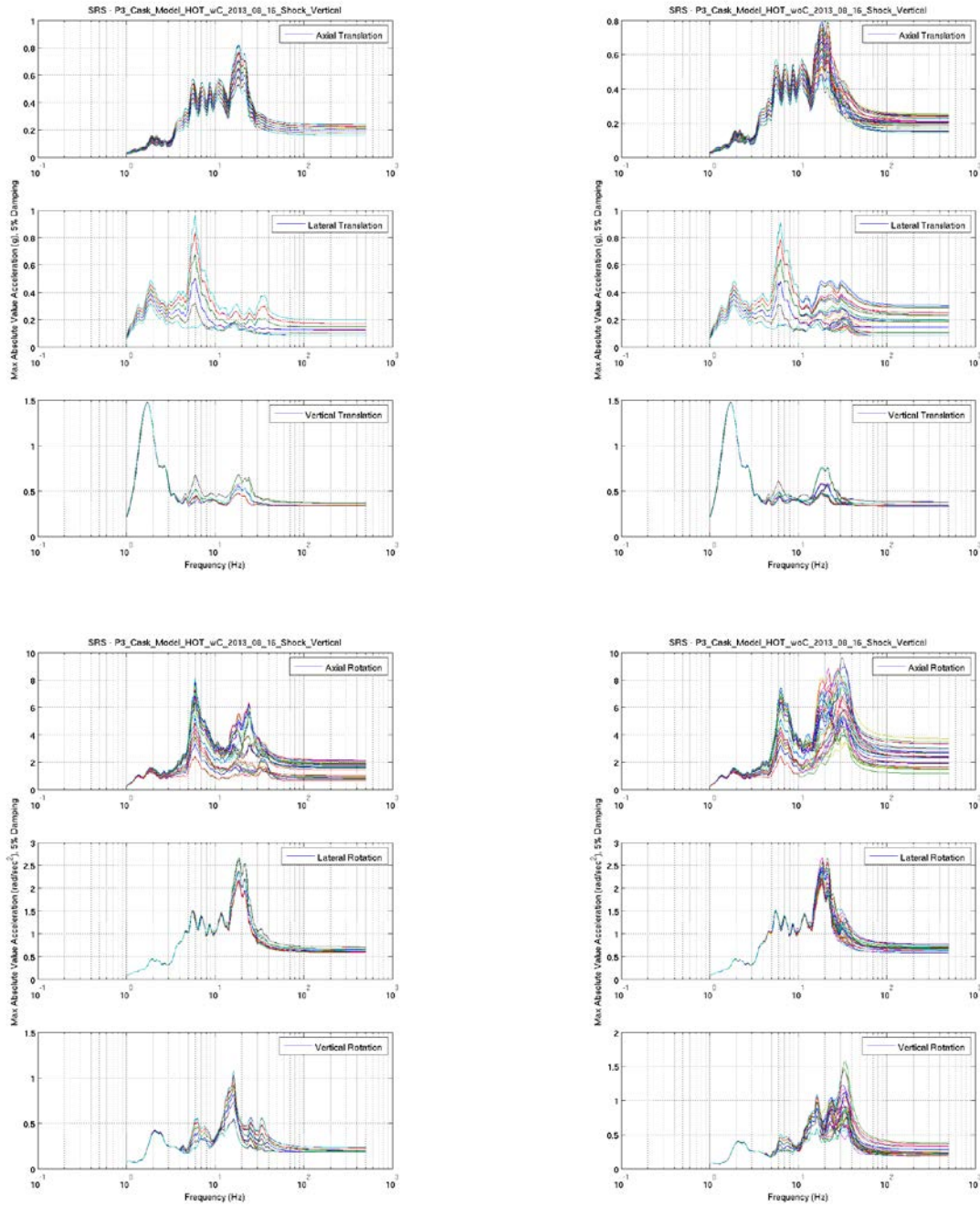

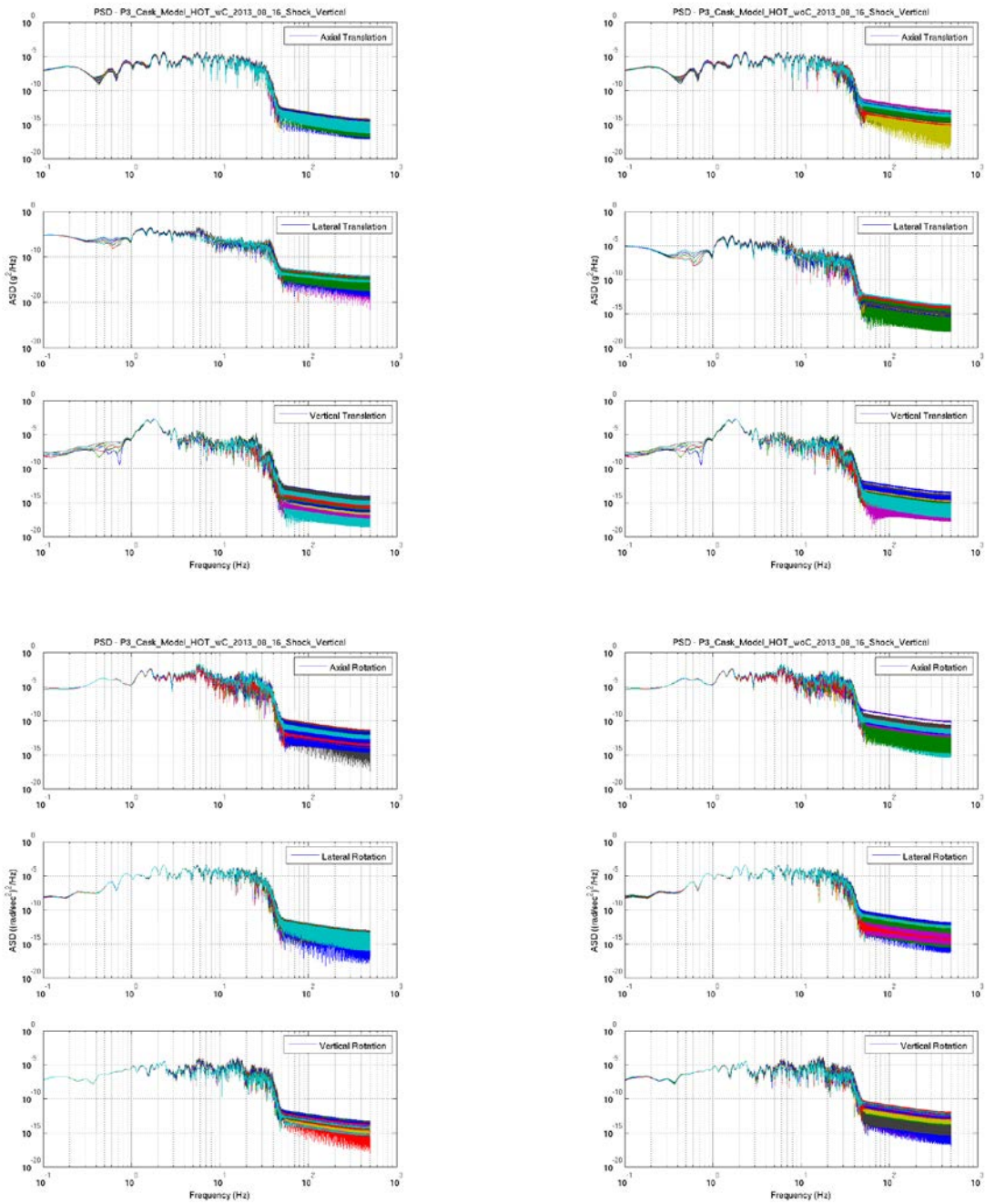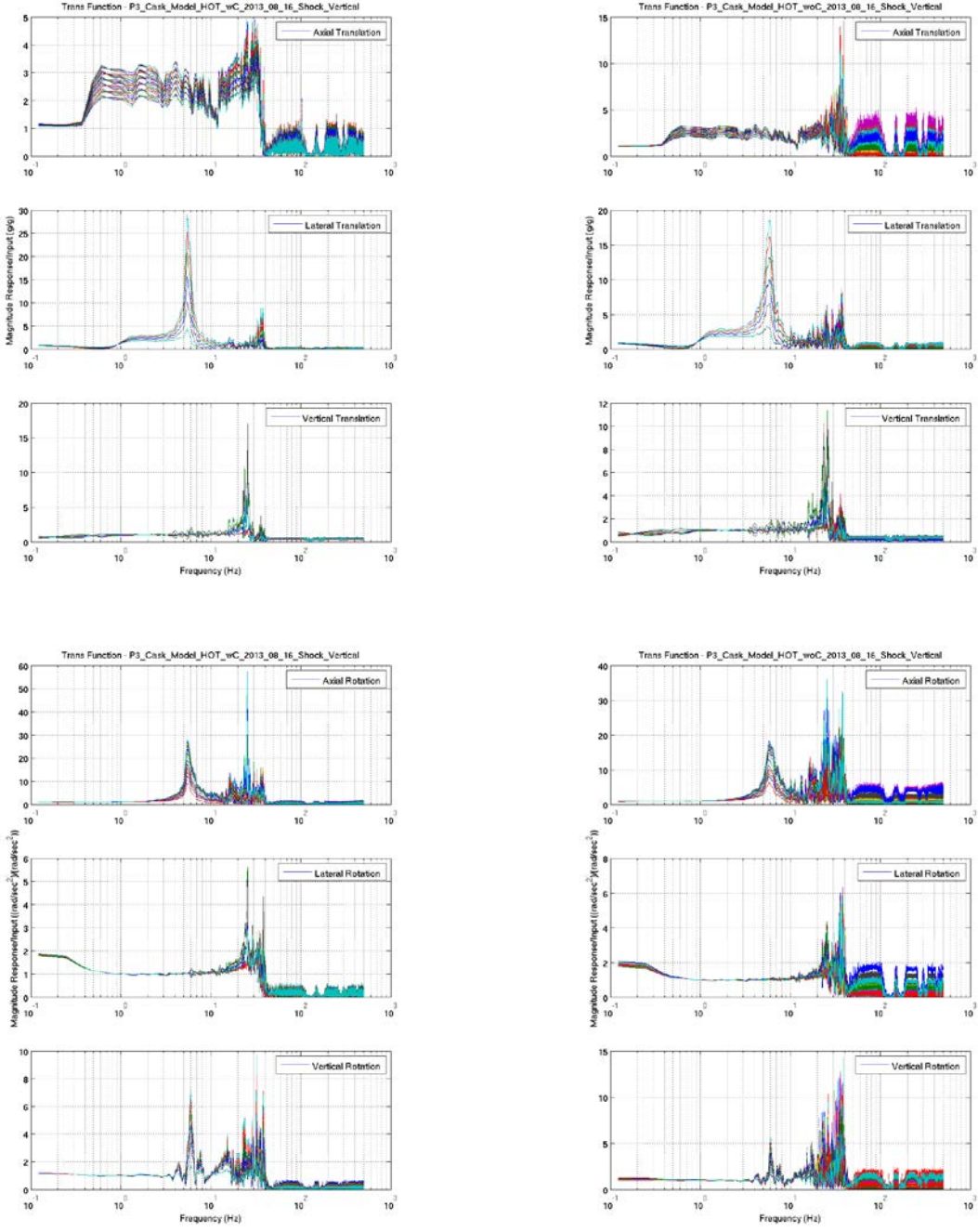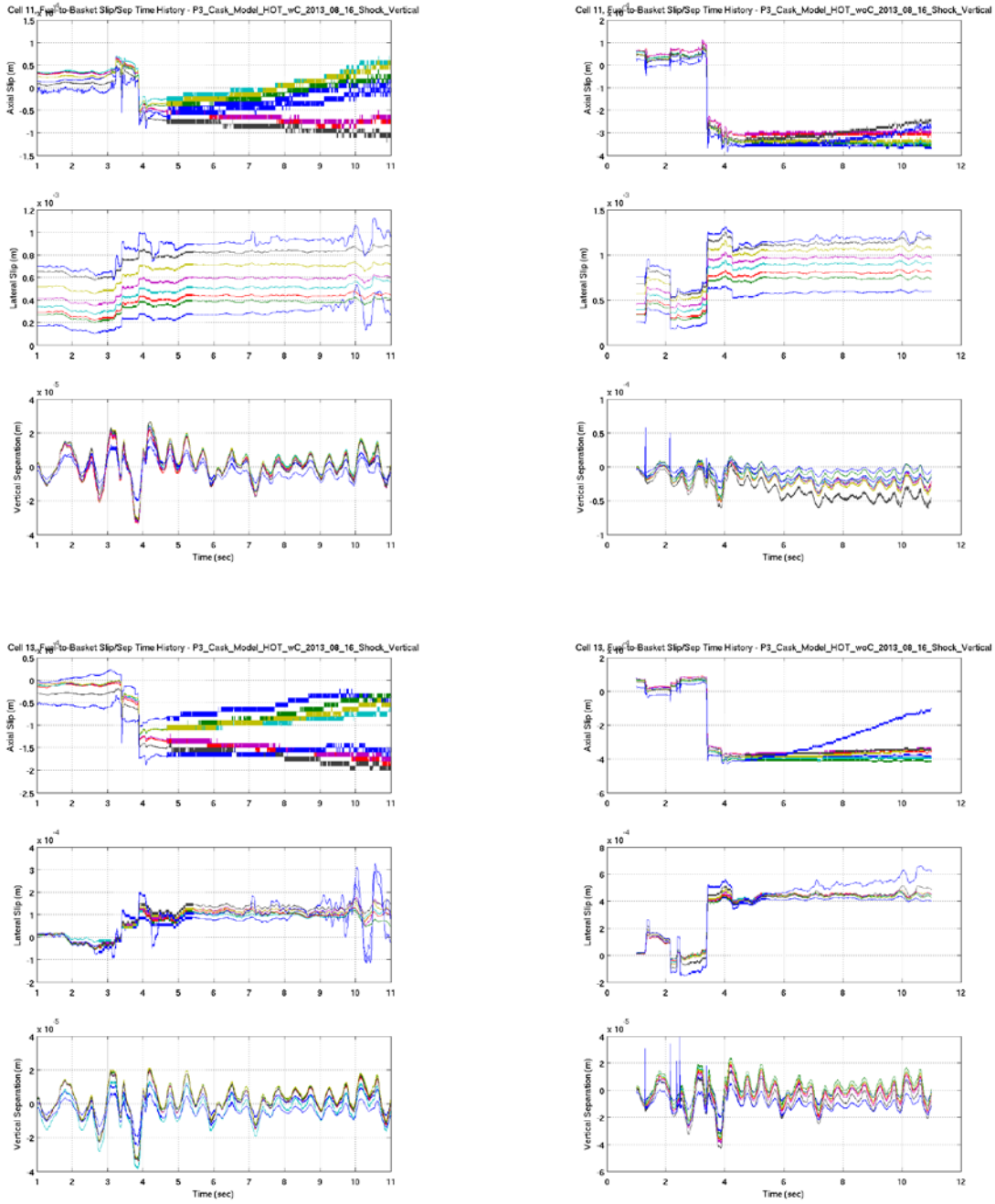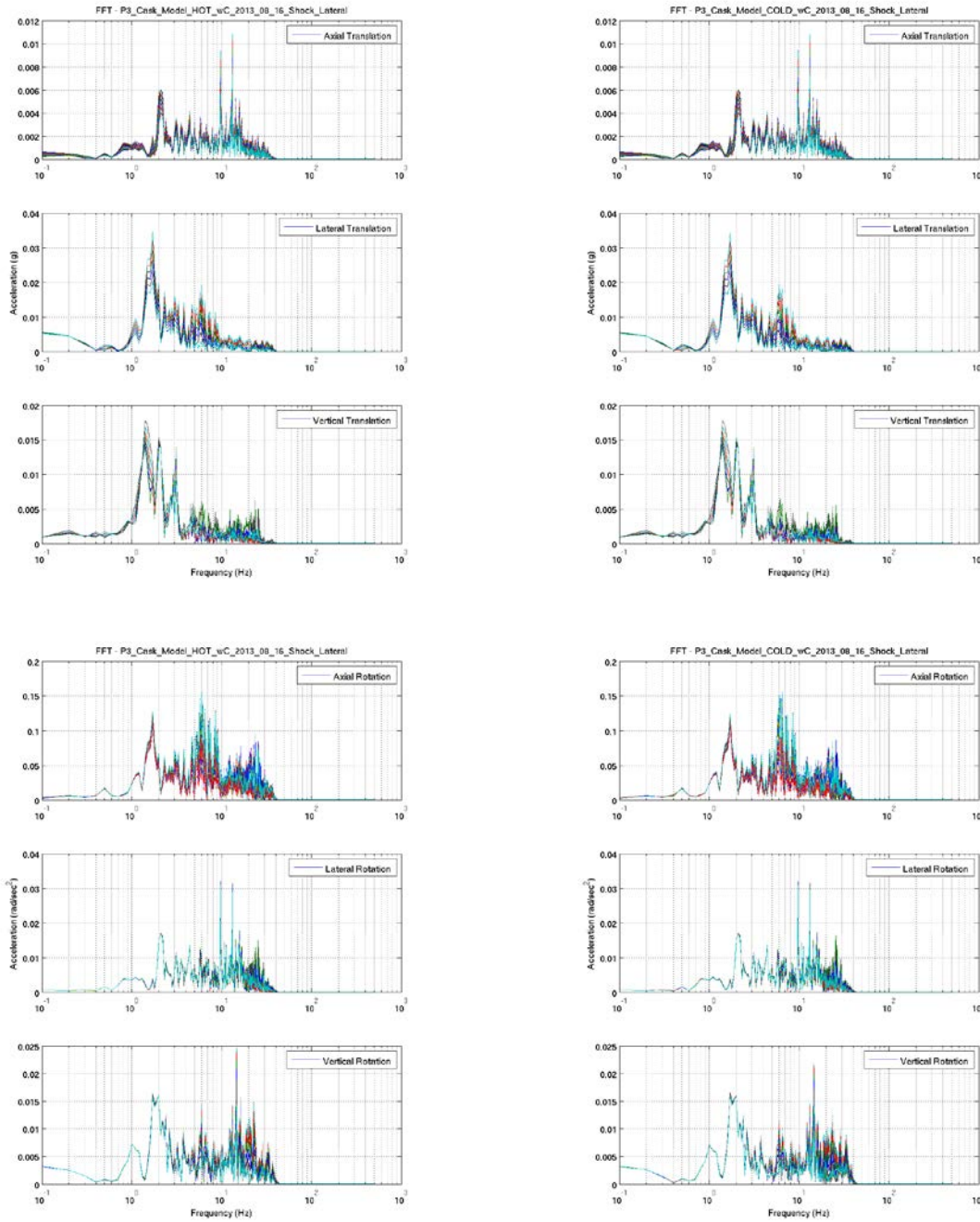(a) Nominal Configuration   (b) Without Control Components Configuration

**Figure 2.10 P3 Shock Z (Vertical) Load Case, Without Control Components Model
Configuration, Basket Cell Response Slip/Separation Plots.**

USED FUEL DISPOSITION CAMPAIGN
**Used Nuclear Fuel Loading and Structural Performance Under Normal Conditions of Transport -
Demonstration of Approach and Results of Used Fuel Performance Characterization**
A-93   **SEPTEMBER 30, 2013**

2.2   COLD TEMPERATURE

2.2.1   P3 SHOCK Y (LATERAL)

Figure 2.11 through Figure 2.15 provide a comparison of FFT, SRS, PSD, transfer function, and cell 11 and 13 slip/separation response plots for the nominal configuration model and the cold temperature configuration model for the P3 Shock Y (Lateral) load case. In general, the response between the two models was essentially the same. Figure 2.12 illustrates that the peak response for the cold temperature configuration in some instances was somewhat lower than that of the nominal configuration and in some instances somewhat higher. Additionally, in some instances the peak response remained unchanged, but a small shift in the frequency at which the peak response occurred was observed. In the lateral translation direction, the peak SRS magnitude at about 30 Hz was essentially identical between the two cases, but the precise frequency at which the peak occurred was several hertz lower in the cold temperature model configuration case. A similar frequency shift was observed in the vertical rotation response between 20 and 40 Hz, with the peak response shifted from 20 Hz in the nominal case to 40 Hz in the cold temperature case. The peak response in the vertical translation direction at 20 Hz was lower by about 15%, whereas the peak response in the lateral rotation direction was higher by 25% for the cold temperature case. The response in the axial translation, lateral translation, and axial rotation directions were essentially identical between the two cases. The trends in the PSD plots (Figure 2.13) support these observations. The average g_{rms} value in the axial translation, vertical translation, and lateral rotation directions were essentially the same between the two cases, whereas the average g_{rms} values for the cold temperature case in the lateral translation, axial rotation, and vertical rotation directions were each slightly lower (by approximately 2%, 6%, and 8%, respectively). Minor differences were also seen in the FFT and transfer functions (Figure 2.11 and Figure 2.14), particularly at frequencies between 20 and 40 Hz. Finally, essentially no significant differences were observed in the cell 11 and 13 slip/separation plots (Figure 2.15), with the total axial and lateral slip and vertical separation between the two cases at both cell 11 and cell 13 being identical.

Which model configuration represents the worst configuration for this load case is difficult to determine definitively as the response of the fuel assembly will depend not only on the magnitude of any input excitation, but also upon the specific frequencies at which that excitation occurs. However, the change in component temperatures investigated here appears to have a relatively small impact on the loading environments generated at each cell as determined by the metrics discussed above, and based on this the hot and cold temperature configurations can be considered essentially identical for this load case.

USED FUEL DISPOSITION CAMPAIGN
**Used Nuclear Fuel Loading and Structural Performance Under Normal Conditions of Transport -
Demonstration of Approach and Results of Used Fuel Performance Characterization**
A-94   **SEPTEMBER 30, 2013**

(a) Nominal Configuration   (b) Without Control Components Configuration

**Figure 2.11 P3 Shock Y (Lateral) Load Case, Cold Temperatures Model Configuration,
Basket Cell Response FFTs.**

USED FUEL DISPOSITION CAMPAIGN
**Used Nuclear Fuel Loading and Structural Performance Under Normal Conditions of Transport -
Demonstration of Approach and Results of Used Fuel Performance Characterization**
A-95
SEPTEMBER 30, 2013
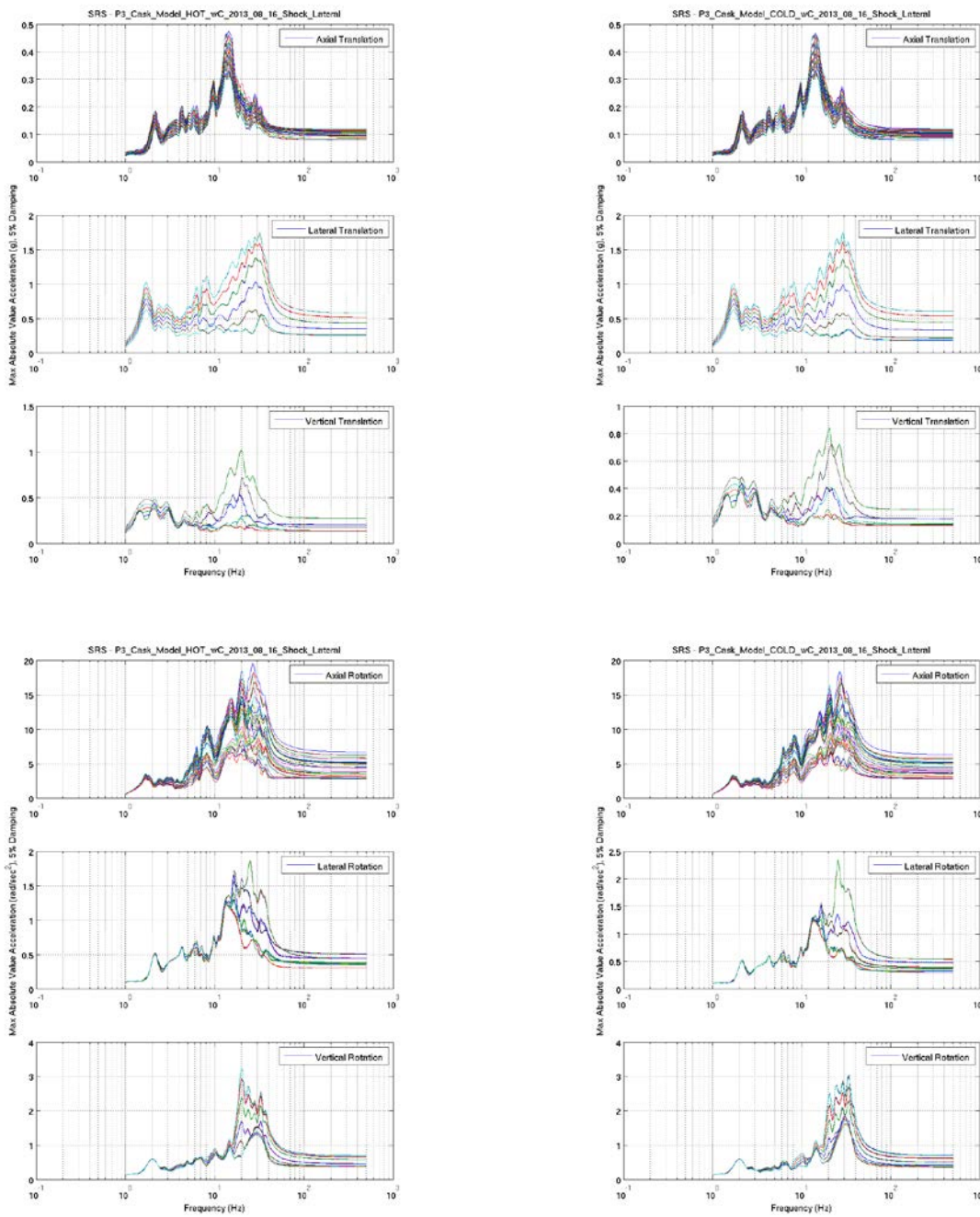
(a) Nominal Configuration

(b) Without Control Components Configuration

**Figure 2.12 P3 Shock Y (Lateral) Load Case, Cold Temperatures Model Configuration,
Basket Cell Response SRSs.**

USED FUEL DISPOSITION CAMPAIGN
Used Nuclear Fuel Loading and Structural Performance Under Normal Conditions of Transport -
Demonstration of Approach and Results of Used Fuel Performance Characterization
A-96
SEPTEMBER 30, 2013

(a) Nominal Configuration

(b) Without Control Components Configuration

Figure 2.13 P3 Shock Y (Lateral) Load Case, Cold Temperatures Model Configuration, Basket Cell Response PSDs.

USED FUEL DISPOSITION CAMPAIGN
**Used Nuclear Fuel Loading and Structural Performance Under Normal Conditions of Transport -
Demonstration of Approach and Results of Used Fuel Performance Characterization**
A-97   **SEPTEMBER 30, 2013**

(a) Nominal Configuration   (b) Without Control Components Configuration

**Figure 2.14 P3 Shock Y (Lateral) Load Case, Cold Temperatures Model Configuration,
Basket Cell Response Transfer Functions.**

USED FUEL DISPOSITION CAMPAIGN
**Used Nuclear Fuel Loading and Structural Performance Under Normal Conditions of Transport -
Demonstration of Approach and Results of Used Fuel Performance Characterization**
A-98   **SEPTEMBER 30, 2013**
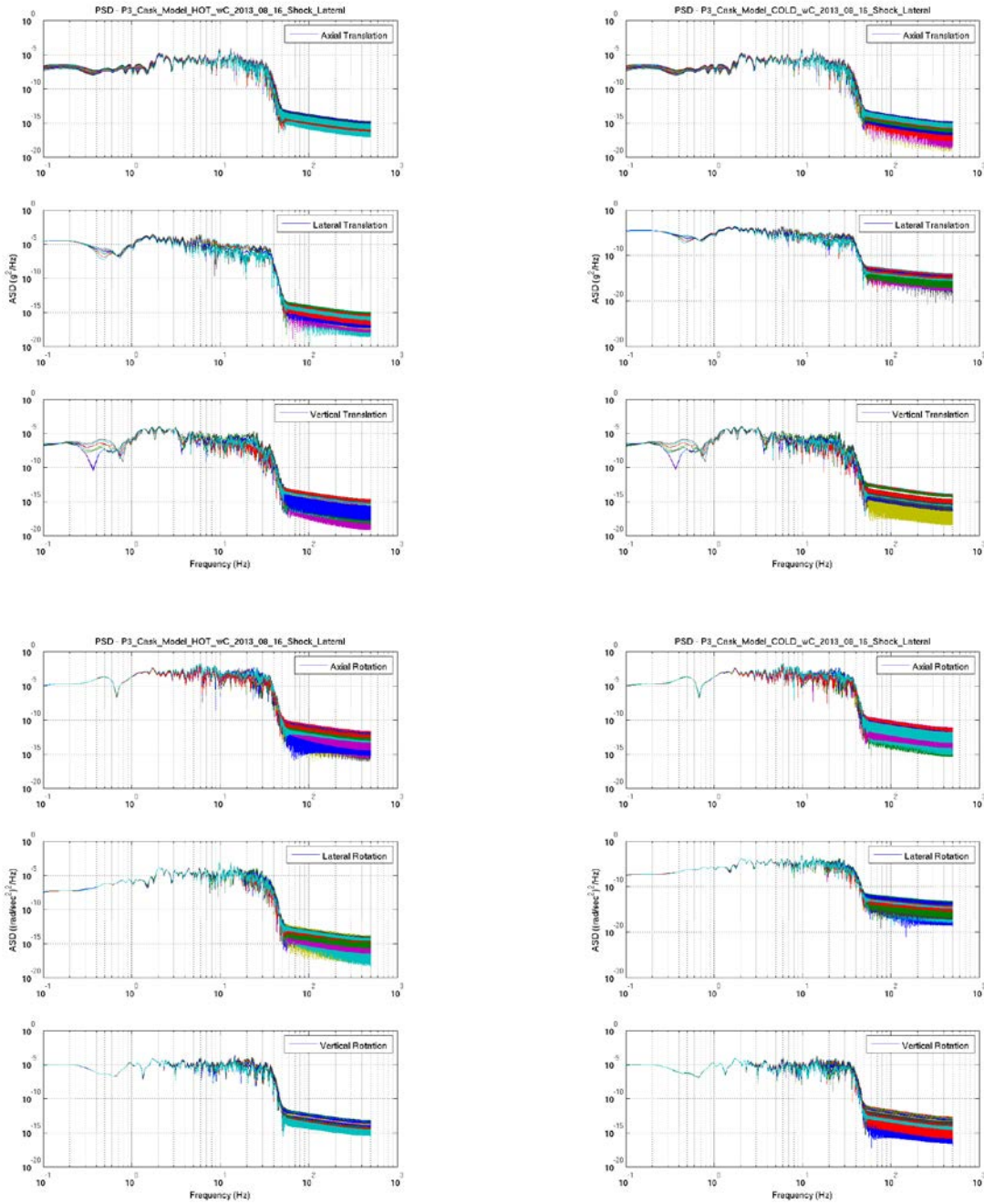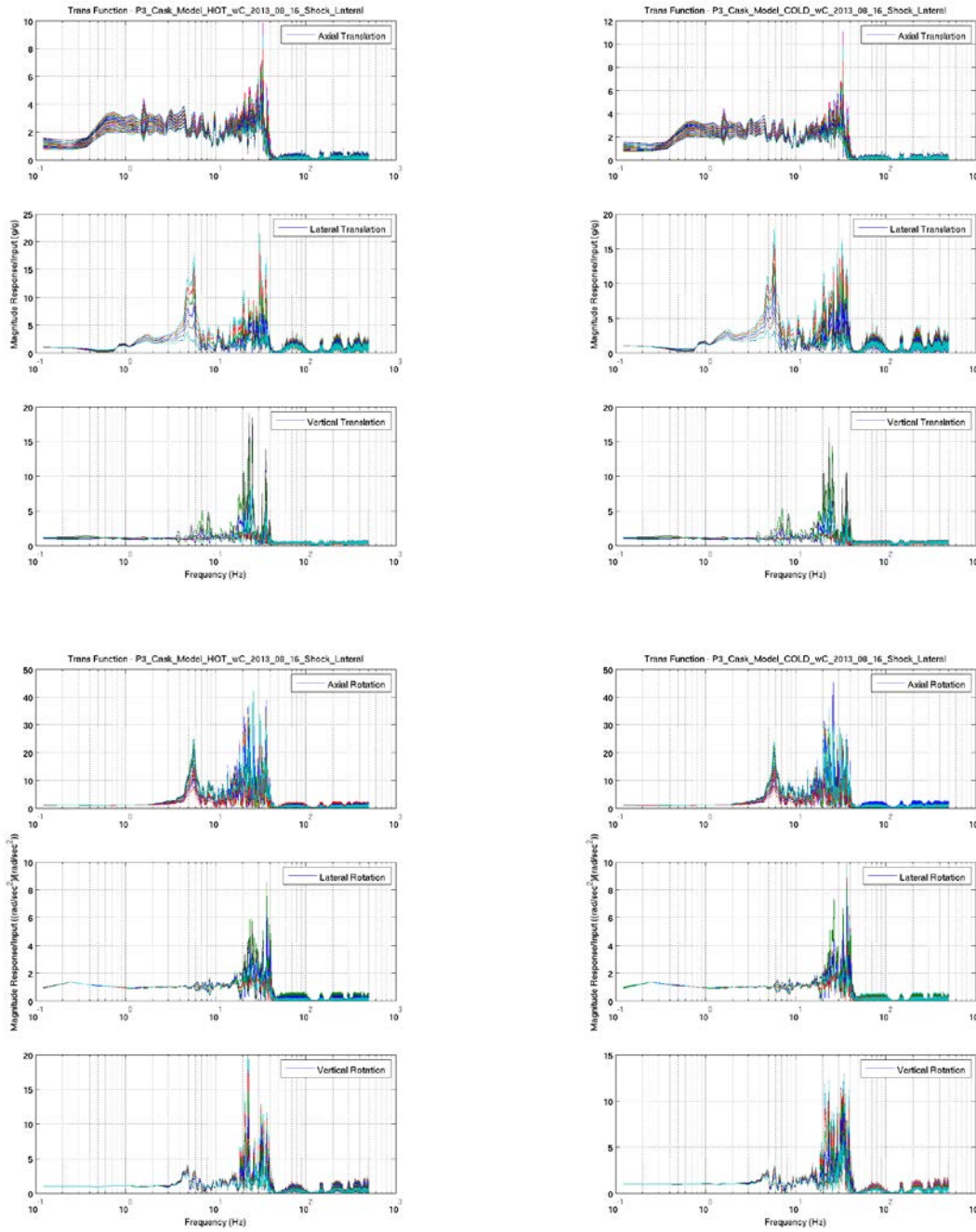

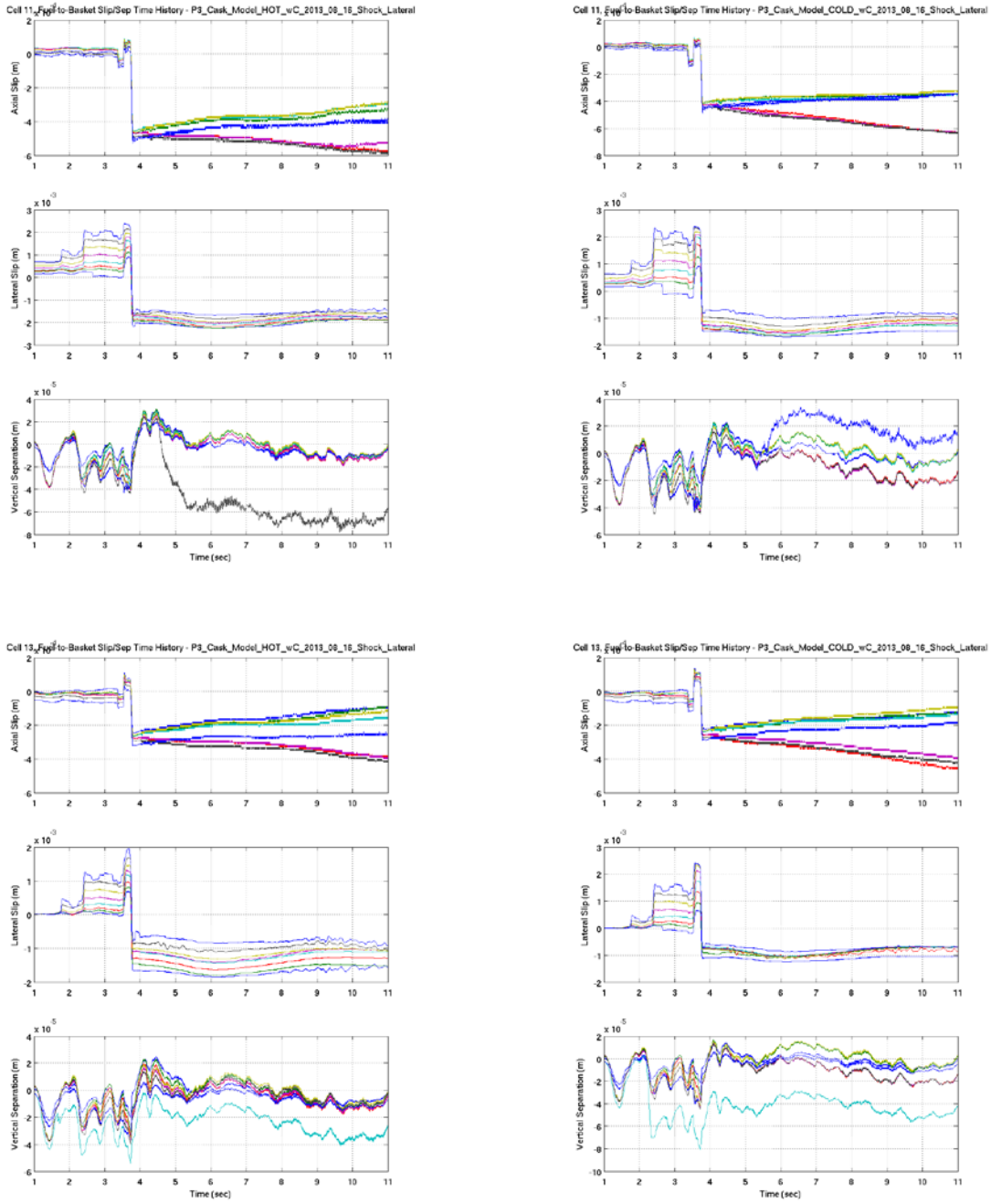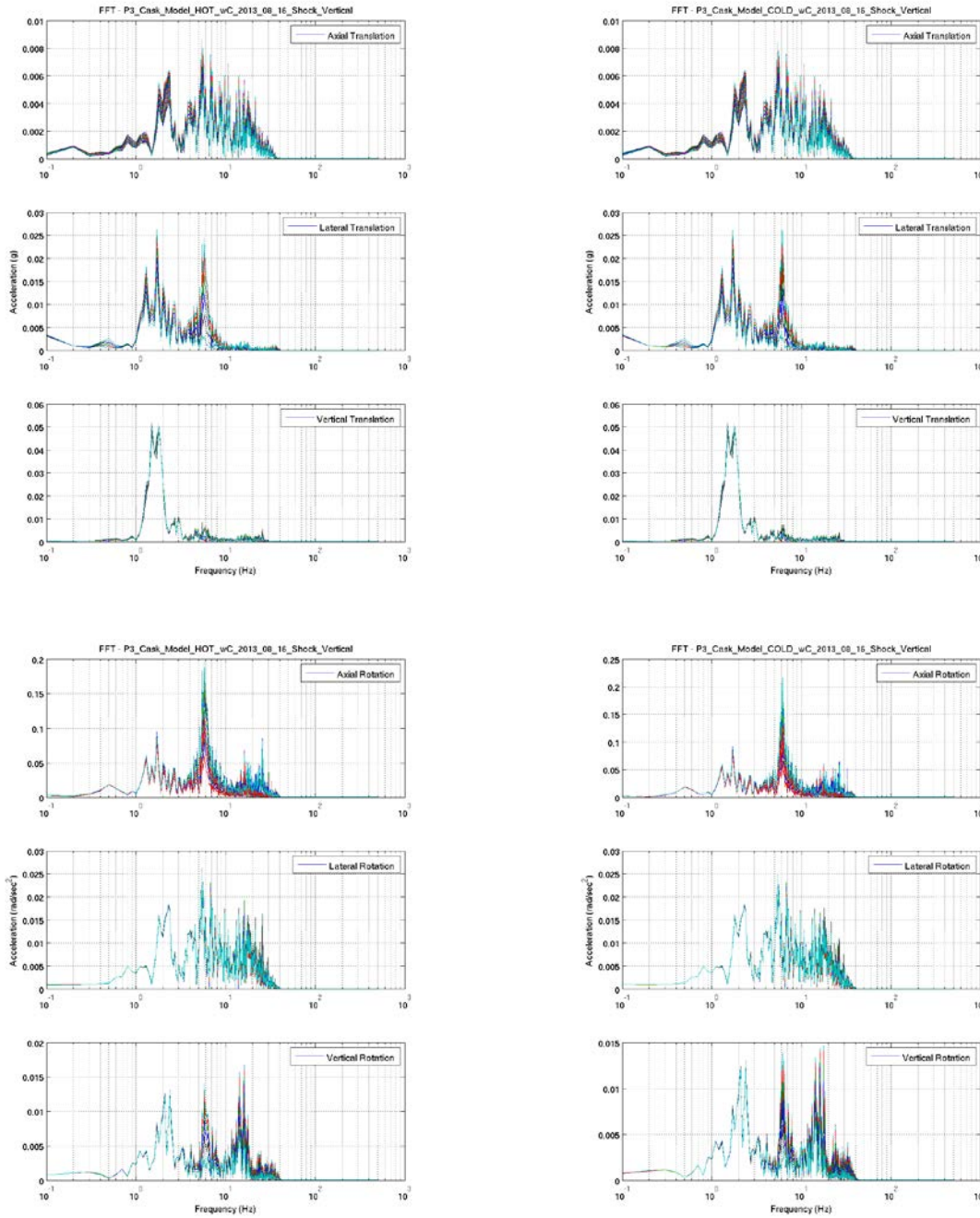(a) Nominal Configuration   (b) Without Control Components Configuration

**Figure 2.15 P3 Shock Y (Lateral) Load Case, Cold Temperatures Model Configuration,
Basket Cell Response Slip/Separation Plots.**

USED FUEL DISPOSITION CAMPAIGN
**Used Nuclear Fuel Loading and Structural Performance Under Normal Conditions of Transport -
Demonstration of Approach and Results of Used Fuel Performance Characterization**
A-99
SEPTEMBER 30, 2013

2.2.2   P3 SHOCK Z (VERTICAL)

Figure 2.16 through Figure 2.20 provide a comparison of FFT, SRS, PSD, transfer function, and cell 11 and 13 slip/separation response plots for the nominal configuration model and the cold temperature configuration model for the P3 Shock Z (Vertical) load case. In general, the response between the two models was essentially the same, with only minor differences observed. Figure 2.17 illustrates that the peak response for the cold temperature configuration was generally equal to that of the nominal configuration or only modestly higher. In the vertical translation direction, the peak SRS magnitude at about 6 Hz was higher by approximately 5% in the cold configuration case, and the peak response in the vertical rotation direction at about 15 Hz was higher by approximately 15%. In all other directions the peak response was essentially identical for the two cases. The trends in the PSD plots (Figure 2.18) support these observations. The average g_{rms} value in the axial translation, lateral translation, vertical translation, and lateral rotation directions were essentially equal for the two cases, whereas the average g_{rms} values for the cold temperature case in the axial rotation and vertical rotation directions were slightly lower (by approximately 3% in each direction). Minor differences were also seen in the FFT and transfer functions (Figure 2.16 and Figure 2.19), particularly at a frequency of 6 Hz and at frequencies between 20 and 40 Hz. Finally, only small differences were observed in the cell 11 and 13 slip/separation plots (Figure 2.20), with the total axial and lateral slip being somewhat higher for the cold temperature configuration (by between 25 and 30%). The vertical separation behavior at both cell 11 and cell 13 were essentially identical for the two cases.

Which model configuration represents the worst configuration for this load case is difficult to determine definitively as the response of the fuel assembly will depend not only on the magnitude of any input excitation, but also upon the specific frequencies at which that excitation occurs. However, the change in component temperatures investigated here appeared to have a relatively small impact on the loading environments generated at each cell as determined by the metrics discussed above, and based on this the hot and cold temperature configurations can be considered essentially identical for this load case.

USED FUEL DISPOSITION CAMPAIGN
Used Nuclear Fuel Loading and Structural Performance Under Normal Conditions of Transport -
Demonstration of Approach and Results of Used Fuel Performance Characterization
A-100   **SEPTEMBER 30, 2013**

(a) Nominal Configuration   (b) Without Control Components Configuration

Figure 2.16 P3 Shock Z (Vertical) Load Case, Cold Temperatures Model Configuration, Basket Cell Response FFTs.

USED FUEL DISPOSITION CAMPAIGN
**Used Nuclear Fuel Loading and Structural Performance Under Normal Conditions of Transport -
Demonstration of Approach and Results of Used Fuel Performance Characterization**
A-101   **SEPTEMBER 30, 2013**
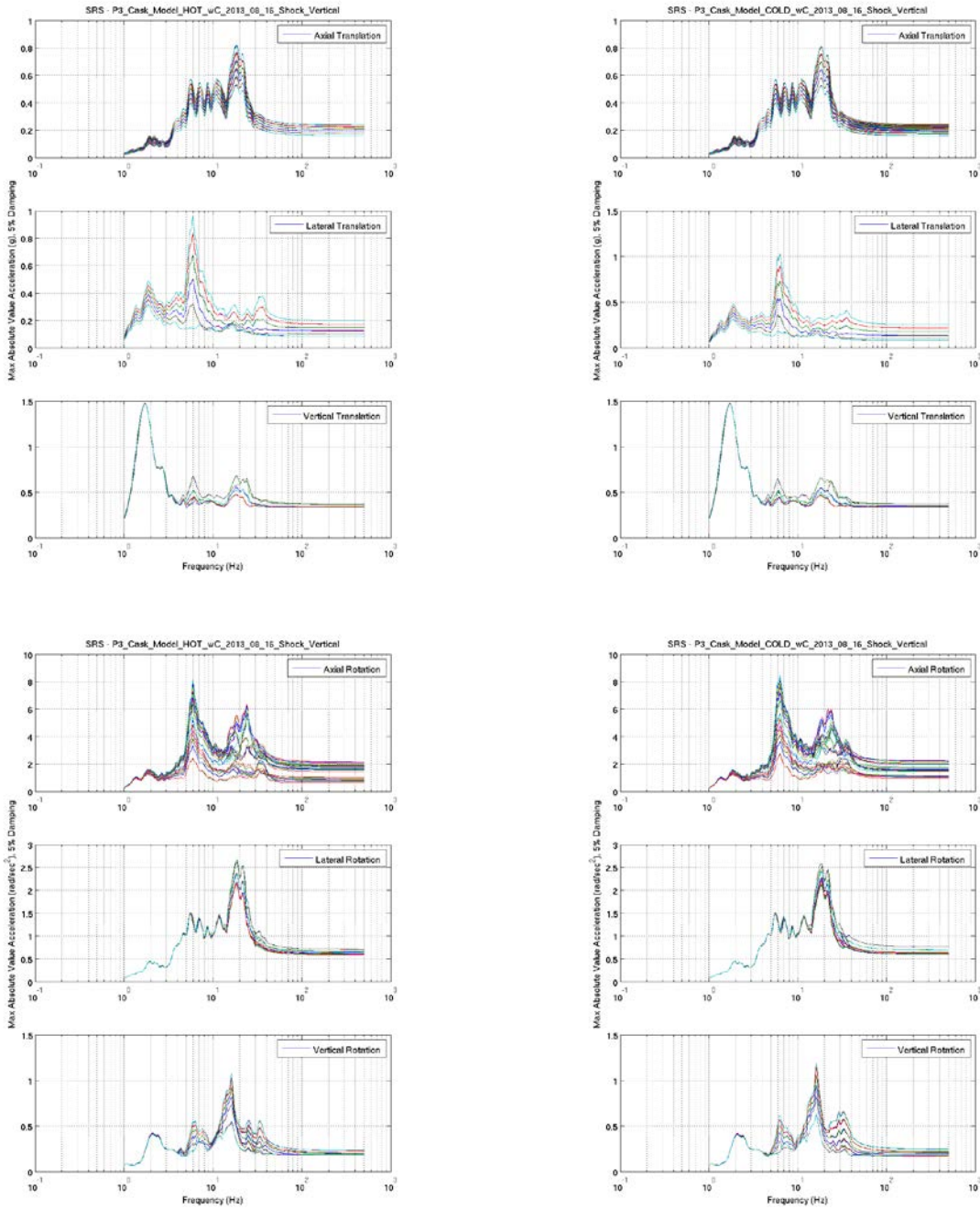
(a) Nominal Configuration   (b) Without Control Components Configuration

**Figure 2.17 P3 Shock Z (Vertical) Load Case, Cold Temperatures Model Configuration,
Basket Cell Response SRSs.**

USED FUEL DISPOSITION CAMPAIGN
**Used Nuclear Fuel Loading and Structural Performance Under Normal Conditions of Transport -
Demonstration of Approach and Results of Used Fuel Performance Characterization**
A-102
SEPTEMBER 30, 2013
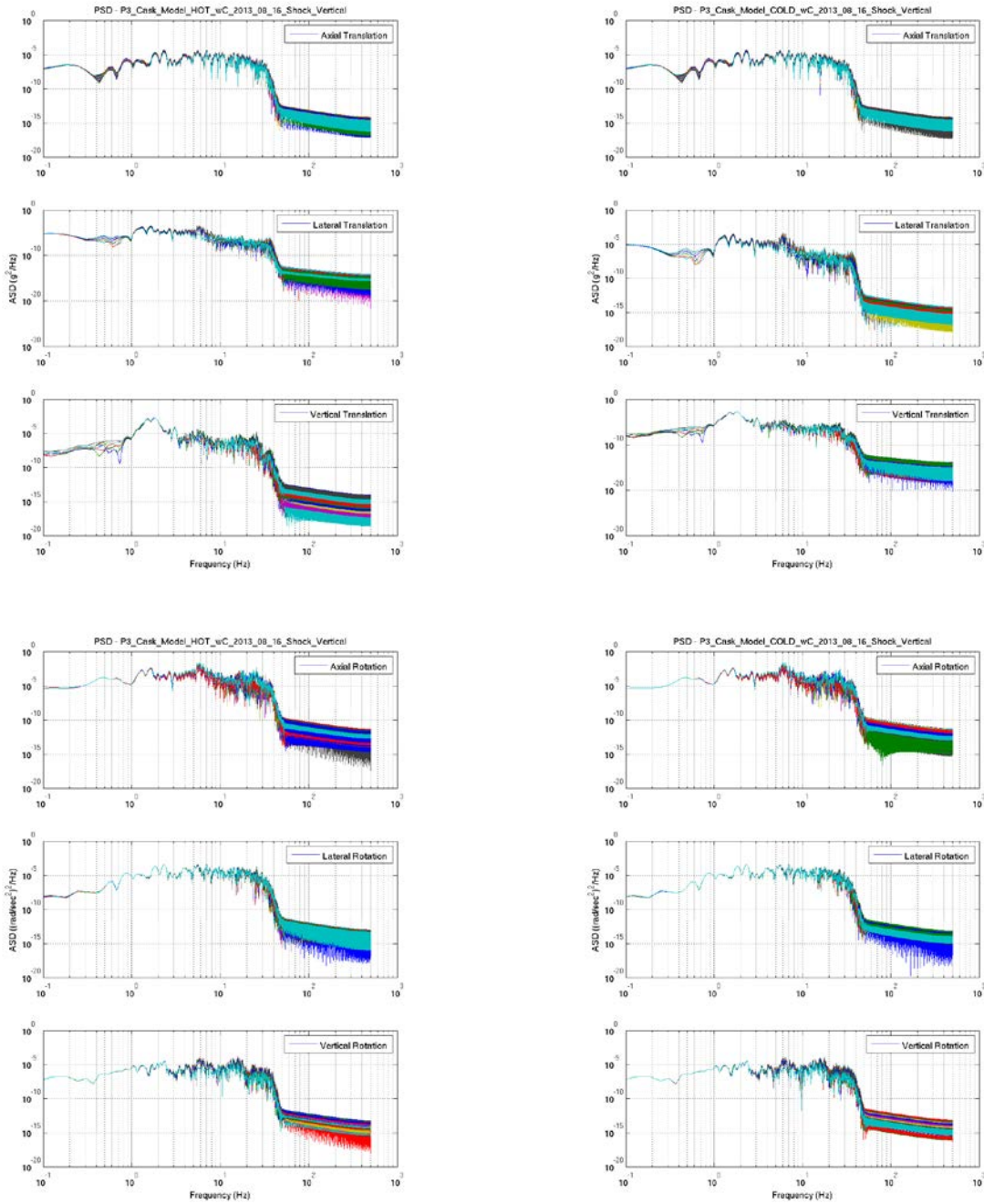
(a) Nominal Configuration

(b) Without Control Components Configuration

Figure 2.18 P3 Shock Z (Vertical) Load Case, Cold Temperatures Model Configuration, Basket Cell Response PSDs.

USED FUEL DISPOSITION CAMPAIGN
**Used Nuclear Fuel Loading and Structural Performance Under Normal Conditions of Transport -
Demonstration of Approach and Results of Used Fuel Performance Characterization**
A-103   **SEPTEMBER 30, 2013**

(a) Nominal Configuration   (b) Without Control Components Configuration

**Figure 2.19 P3 Shock Z (Vertical) Load Case, Cold Temperatures Model Configuration,
Basket Cell Response Transfer Functions.**

USED FUEL DISPOSITION CAMPAIGN
**Used Nuclear Fuel Loading and Structural Performance Under Normal Conditions of Transport -
Demonstration of Approach and Results of Used Fuel Performance Characterization**
A-104   **SEPTEMBER 30, 2013**

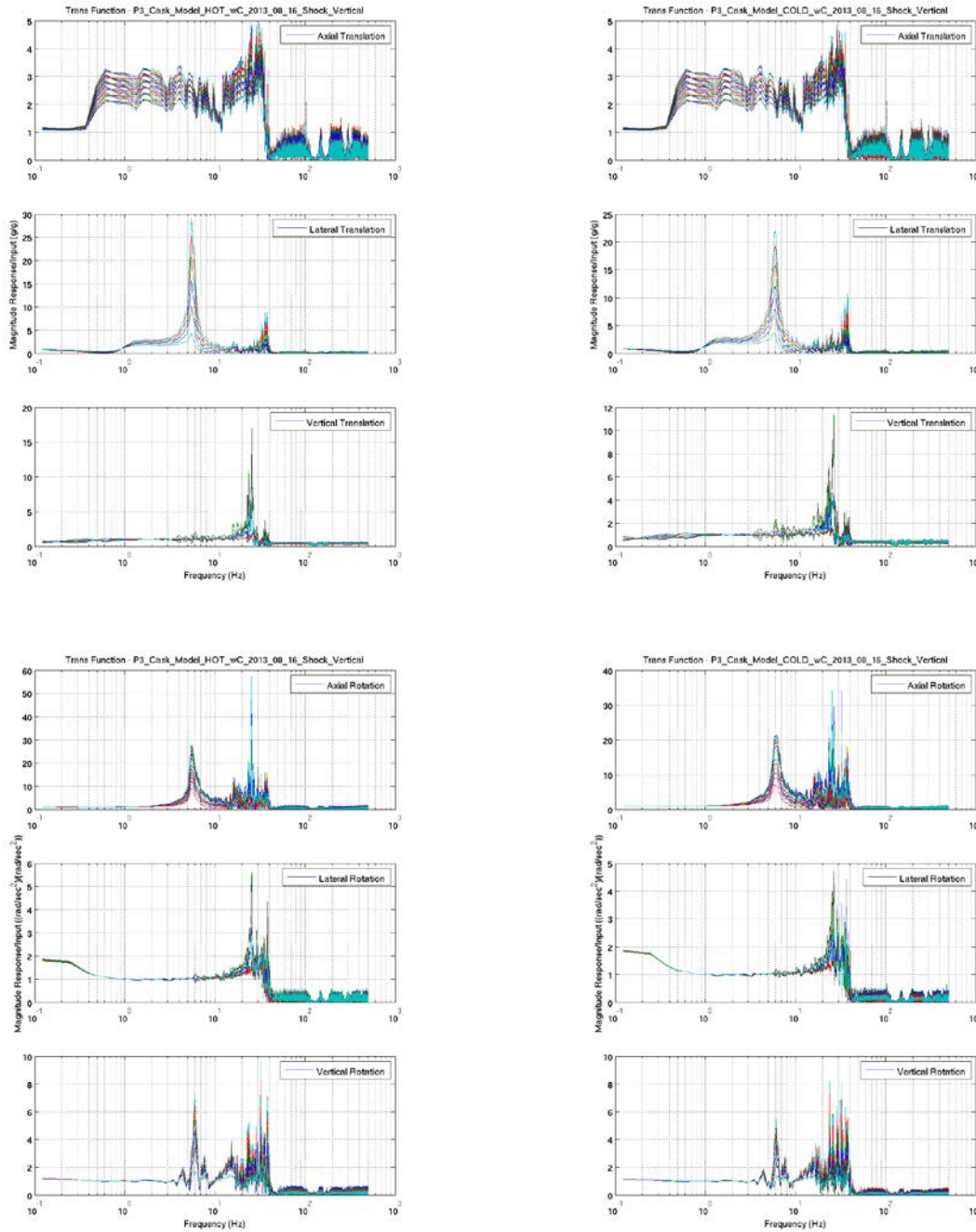(a) Nominal Configuration   (b) Without Control Components Configuration

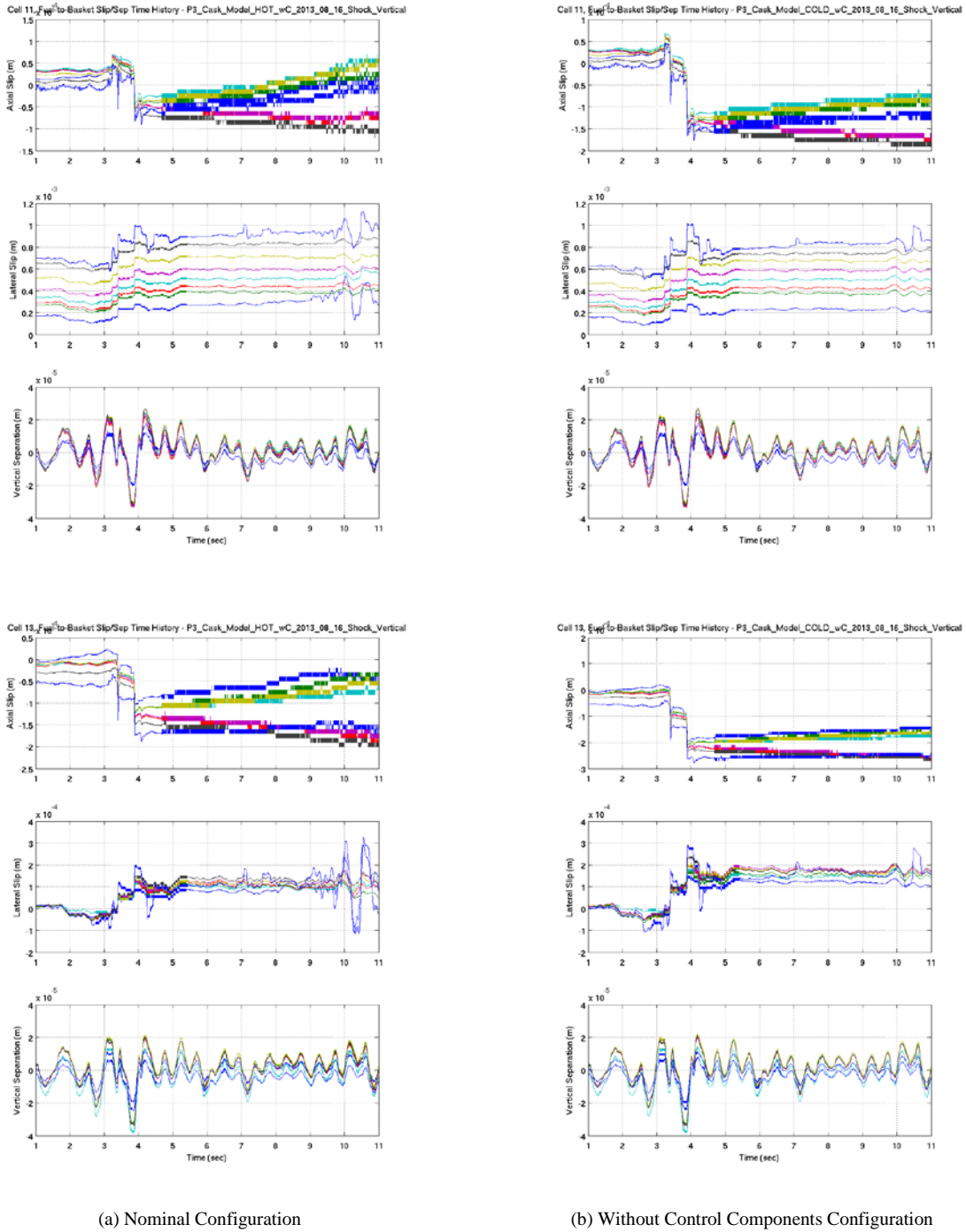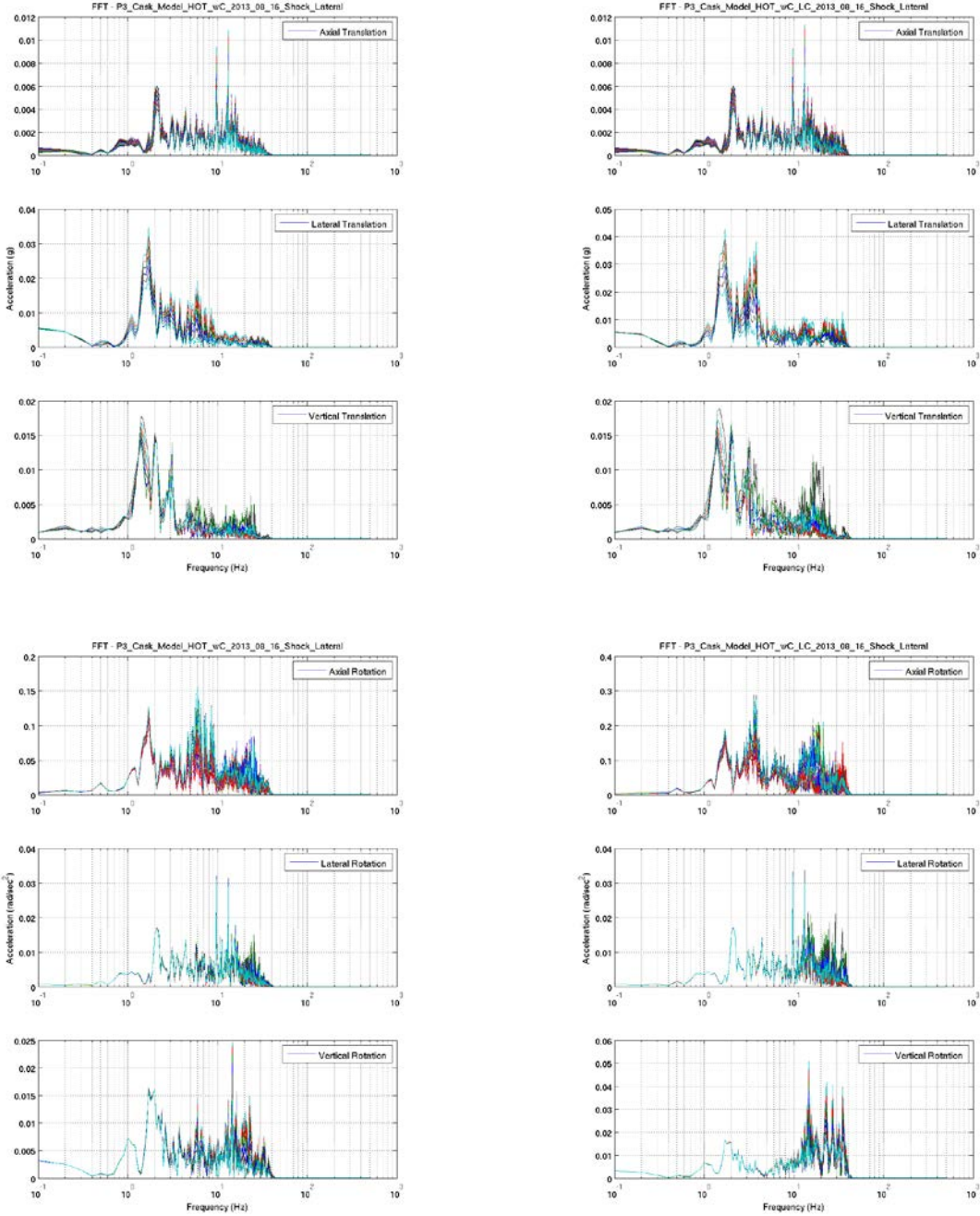**Figure 2.20 P3 Shock Z (Vertical) Load Case, Cold Temperatures Model Configuration,
Basket Cell Response Slip/Separation Plots.**

USED FUEL DISPOSITION CAMPAIGN
**Used Nuclear Fuel Loading and Structural Performance Under Normal Conditions of Transport -
Demonstration of Approach and Results of Used Fuel Performance Characterization**
A-105 **SEPTEMBER 30, 2013**

2.3 LARGE CLEARANCE

2.3.1 P3 SHOCK Y (LATERAL)

Figure 2.21 through Figure 2.25 provide a comparison of FFT, SRS, PSD, transfer function, and cell 11 and 13 slip/separation response plots for the nominal configuration model and the large clearance configuration model for the P3 Shock Y (Lateral) load case. In general, the response of the large clearance model was larger than the nominal configuration model. Figure 2.22 illustrates that the peak response for the large clearance configuration was higher than that of the nominal configuration and in some instances significantly higher. In the lateral translation direction, the peak SRS magnitude at about 30 Hz was significantly higher (by approximately 90%) than in the large clearance case, where the peak response was shifted down in frequency by approximately 5 Hz. The peak responses in the other translation directions were higher for the large clearance case as well, with the increase in response being greater than in the lateral translation direction. In the vertical translation direction the peak response at 20 Hz was higher by 150% and in the axial translation direction the peak at approximately 12 Hz was overtaken by a peak response at approximately 30 Hz that was 50% higher. Peak responses in the rotational directions were also significantly higher in the large clearance case, with the peak responses being nearly 165% higher in all rotation directions than in the nominal case. The trends in the PSD plots (Figure 2.23) support these observations. The average g_{rms} value in the axial, lateral, and vertical translation directions were all higher for the large clearance case (by approximately 4%, 63%, and 28%, respectively), and the average g_{rms} values in the axial, lateral, and vertical rotation directions were all also higher (by approximately 102%, 17%, and 178% respectively). Major differences were also seen in the FFT and transfer functions (Figure 2.21 and Figure 2.24), particularly at frequencies centered around 3 Hz and at frequencies between 20 and 40 Hz. Finally, significant differences were also observed in the cell 11 and 13 slip/separation plots (Figure 2.25), particularly in the peak lateral slip amounts between the two cases at both cell 11 and cell 13 in which the lateral slip in the large clearance case was more than double (125% and 133% larger for the two cell locations, respectively) that of the lateral slip in the nominal case. Lateral sliding of the fuel assemblies within the basket cells and subsequent impact with the cell walls appeared to play an important role in the severity of the response in the large clearance case. Larger clearances appeared to facilitate the conversion of input energy at low frequencies (<10 Hz) into energy at higher frequencies, which are more in range with the response frequencies of interest for the fuel assemblies, namely 10 to 40 Hz.

Which model configuration represents the worst configuration for this load case is difficult to determine definitively as the response of the fuel assembly will depend not only on the magnitude of any input excitation, but also upon the specific frequencies at which that excitation occurs. However, in this instance it is pretty clear that the large clearance case will likely result in more severe excitations being imparted to the fuel assemblies.

USED FUEL DISPOSITION CAMPAIGN
**Used Nuclear Fuel Loading and Structural Performance Under Normal Conditions of Transport -
Demonstration of Approach and Results of Used Fuel Performance Characterization**
A-106   **SEPTEMBER 30, 2013**

(a) Nominal Configuration   (b) Without Control Components Configuration

**Figure 2.21 P3 Shock Y (Lateral) Load Case, Large Clearances Model Configuration,
Basket Cell Response FFTs.**

USED FUEL DISPOSITION CAMPAIGN
**Used Nuclear Fuel Loading and Structural Performance Under Normal Conditions of Transport -
Demonstration of Approach and Results of Used Fuel Performance Characterization**
A-107   **SEPTEMBER 30, 2013**

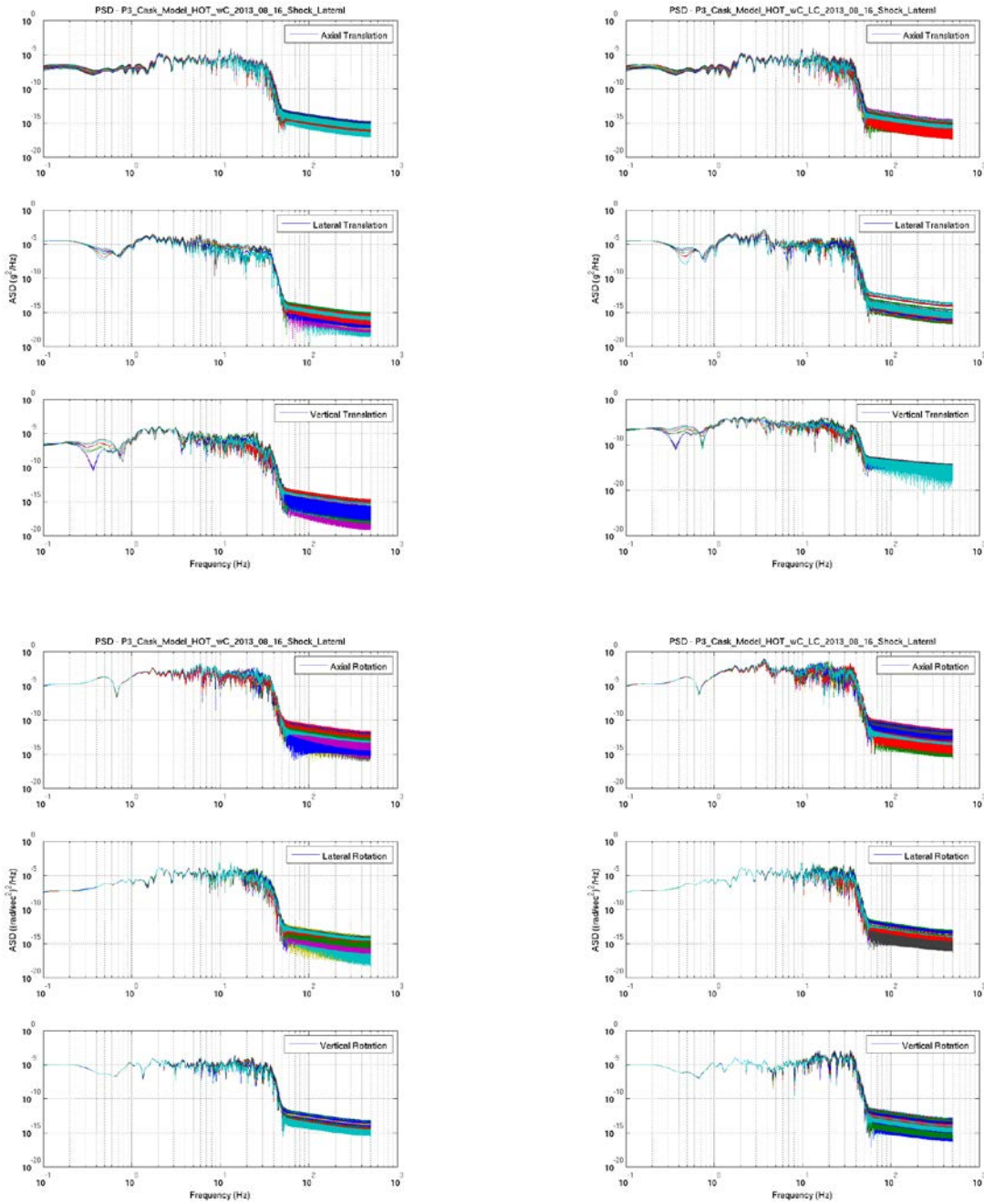(a) Nominal Configuration   (b) Without Control Components Configuration

**Figure 2.22 P3 Shock Y (Lateral) Load Case, Large Clearances Model Configuration,
Basket Cell Response SRSs.**

USED FUEL DISPOSITION CAMPAIGN
Used Nuclear Fuel Loading and Structural Performance Under Normal Conditions of Transport -
Demonstration of Approach and Results of Used Fuel Performance Characterization
A-108   **SEPTEMBER 30, 2013**

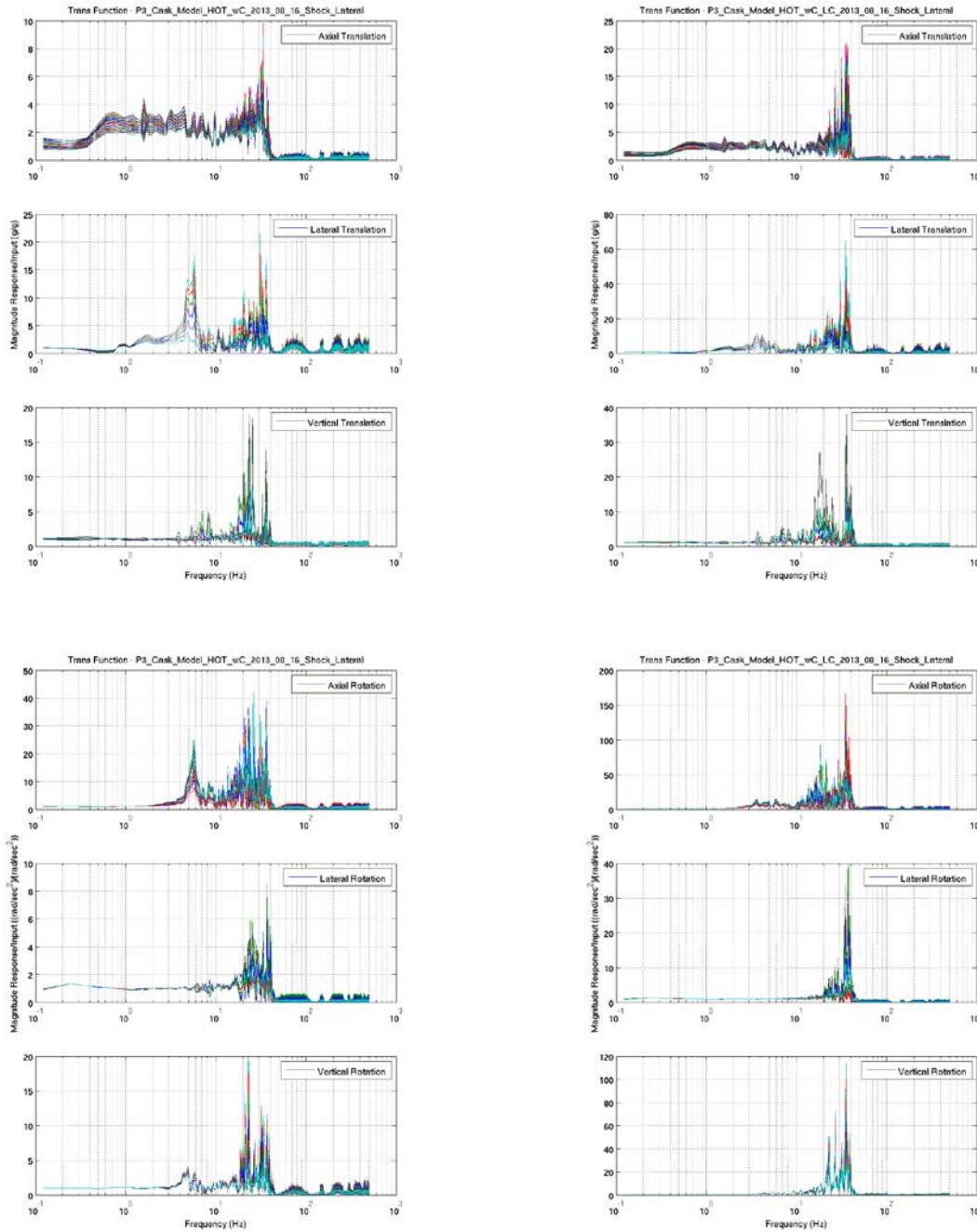(a) Nominal Configuration   (b) Without Control Components Configuration

Figure 2.23 P3 Shock Y (Lateral) Load Case, Large Clearances Model Configuration, Basket Cell Response PSDs.

USED FUEL DISPOSITION CAMPAIGN
**Used Nuclear Fuel Loading and Structural Performance Under Normal Conditions of Transport -
Demonstration of Approach and Results of Used Fuel Performance Characterization**
A-109   **SEPTEMBER 30, 2013**

(a) Nominal Configuration   (b) Without Control Components Configuration

**Figure 2.24 P3 Shock Y (Lateral) Load Case, Large Clearances Model Configuration,
Basket Cell Response Transfer Functions.**

USED FUEL DISPOSITION CAMPAIGN
**Used Nuclear Fuel Loading and Structural Performance Under Normal Conditions of Transport -
Demonstration of Approach and Results of Used Fuel Performance Characterization**
A-110 **SEPTEMBER 30, 2013**

(a) Nominal Configuration   (b) Without Control Components Configuration
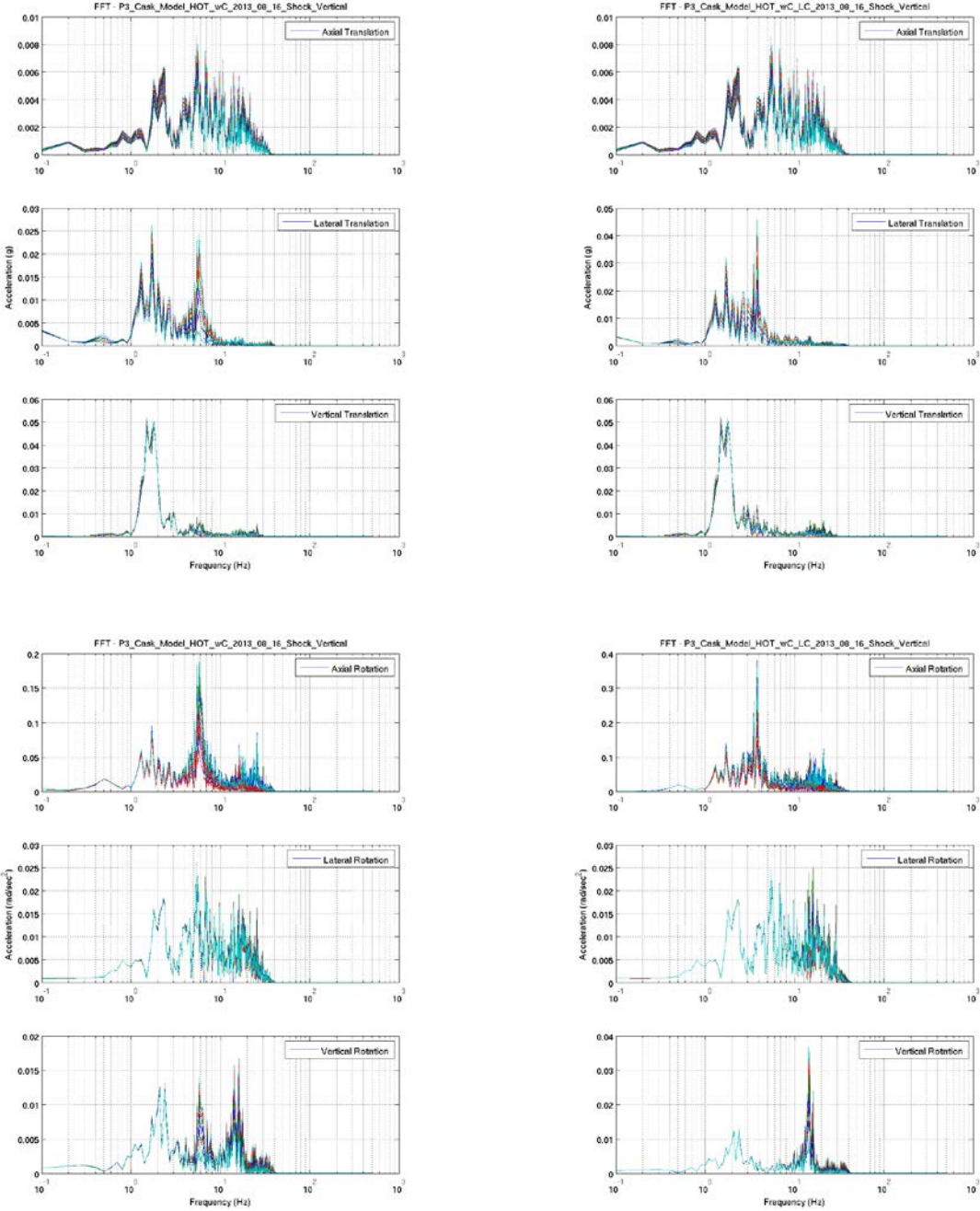
**Figure 2.25 P3 Shock Y (Lateral) Load Case, Large Clearances Model Configuration,
Basket Cell Response Slip/Separation Plots.**

USED FUEL DISPOSITION CAMPAIGN
**Used Nuclear Fuel Loading and Structural Performance Under Normal Conditions of Transport -
Demonstration of Approach and Results of Used Fuel Performance Characterization**
A-111   **SEPTEMBER 30, 2013**

2.3.2   P3 SHOCK Z (VERTICAL)

Figure 2.26 through Figure 2.30 provide a comparison of FFT, SRS, PSD, transfer function, and cell 11 and 13 slip/separation response plots for the nominal configuration model and the large clearances configuration model for the P3 Shock Z (Vertical) load case. In general, the response of the large clearances model is higher than the nominal configuration model. Figure 2.27 illustrates that the peak response for the large clearances configuration was higher than that of the nominal configuration and in some instances significantly higher. In the lateral translation direction, the peak SRS magnitude in the large clearances case at about 3.5 Hz was significantly higher (by approximately 50%) than the peak at 6 Hz in the nominal case. The peak responses in the other translation directions were essentially equal between the two cases. The peak responses in the axial and vertical rotation directions were significantly higher in the large clearance case (25% and 125%, respectively). The trends in the PSD plots (Figure 2.28) support these observations. The average basket cell PSD g_{rms} value in the lateral translation direction was approximately 32% higher in the large clearances case, whereas the average basket cell PSD g_{rms} value in the axial and vertical translation directions were essentially equal between the two cases. The average basket cell PSD g_{rms} values in the axial and vertical rotation directions were all also higher in the large clearance case, being 56% and 21% higher, respectively. Major differences were also seen in the FFT and transfer functions (Figure 2.26 and Figure 2.29), particularly at frequencies between 3 and 6 Hz in the lateral translation direction and at frequencies between 10 and 40 Hz in the vertical translation and axial, lateral, and vertical rotation directions. Finally, significant differences were also observed in the cell 11 and 13 slip/separation plots (Figure 2.30), particularly in the total lateral slip amounts between the two cases at both cell 11 and cell 13 in which the lateral slip in the large clearance case was an order of magnitude larger than in the nominal case. Lateral sliding of the fuel assemblies within the basket cells and subsequent impact of the fuel assemblies against the cell walls appeared to play an important role in the severity of the response in the large clearance case. Larger clearances appear to facilitate the conversion of input energy at low frequencies (< 10 Hz) into energy at higher frequencies which are more in range with the response frequencies of interest for the fuel assemblies, namely 10 to 40 Hz. In this case, the increased vertical clearance between the fuel assembly and cell upper wall appears to be unimportant because the fuel assemblies did not separate vertically from the basket at this level of excitation. For larger excitation levels, the amount of vertical clearance will undoubtedly become more of an important factor in determining the severity of the excitations imparted to the fuel assemblies.

Which model configuration represents the worst configuration for this load case is difficult to determine definitively as the response of the fuel assembly will depend not only on the magnitude of any input excitation, but also upon the specific frequencies at which that excitation occurs. However, in this instance it is likely that the large clearance case will result in more severe excitations being imparted to the fuel assemblies.
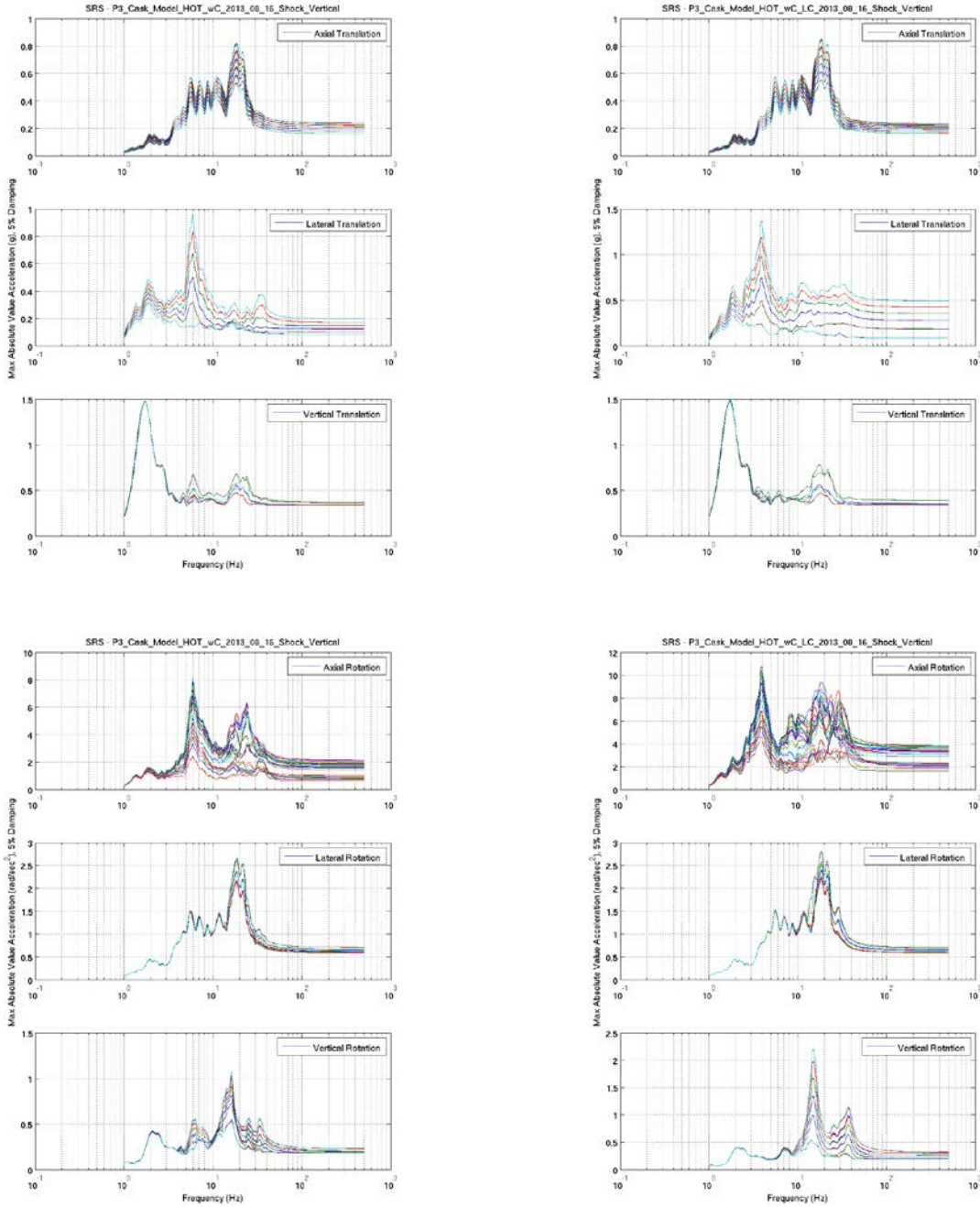
USED FUEL DISPOSITION CAMPAIGN
**Used Nuclear Fuel Loading and Structural Performance Under Normal Conditions of Transport -
Demonstration of Approach and Results of Used Fuel Performance Characterization**
A-112   **SEPTEMBER 30, 2013**

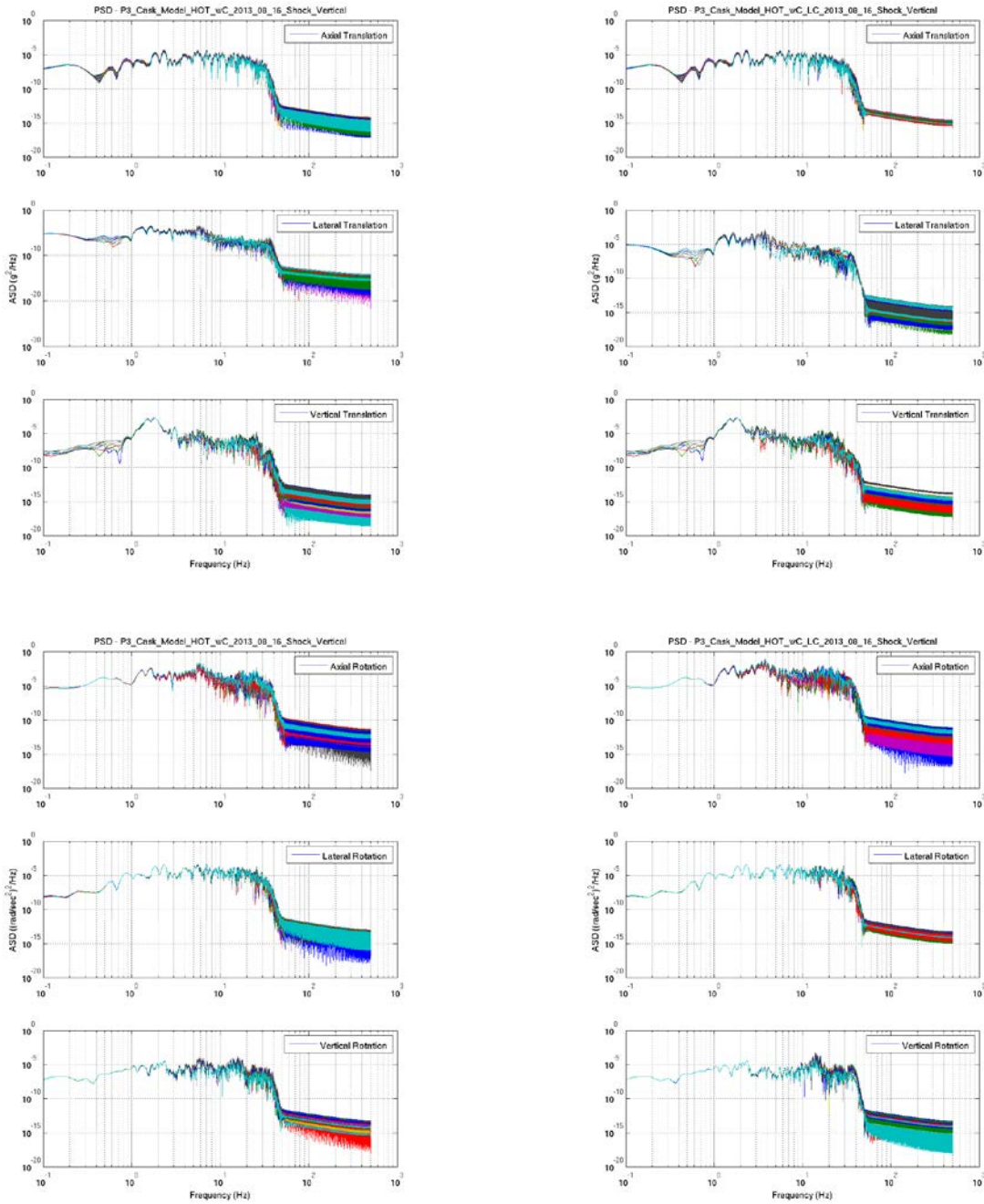

(a) Nominal Configuration   (b) Without Control Components Configuration

**Figure 2.26 P3 Shock Z (Vertical) Load Case, Large Clearances Model Configuration,
Basket Cell Response FFTs.**

USED FUEL DISPOSITION CAMPAIGN
**Used Nuclear Fuel Loading and Structural Performance Under Normal Conditions of Transport -
Demonstration of Approach and Results of Used Fuel Performance Characterization**
A-113   **SEPTEMBER 30, 2013**

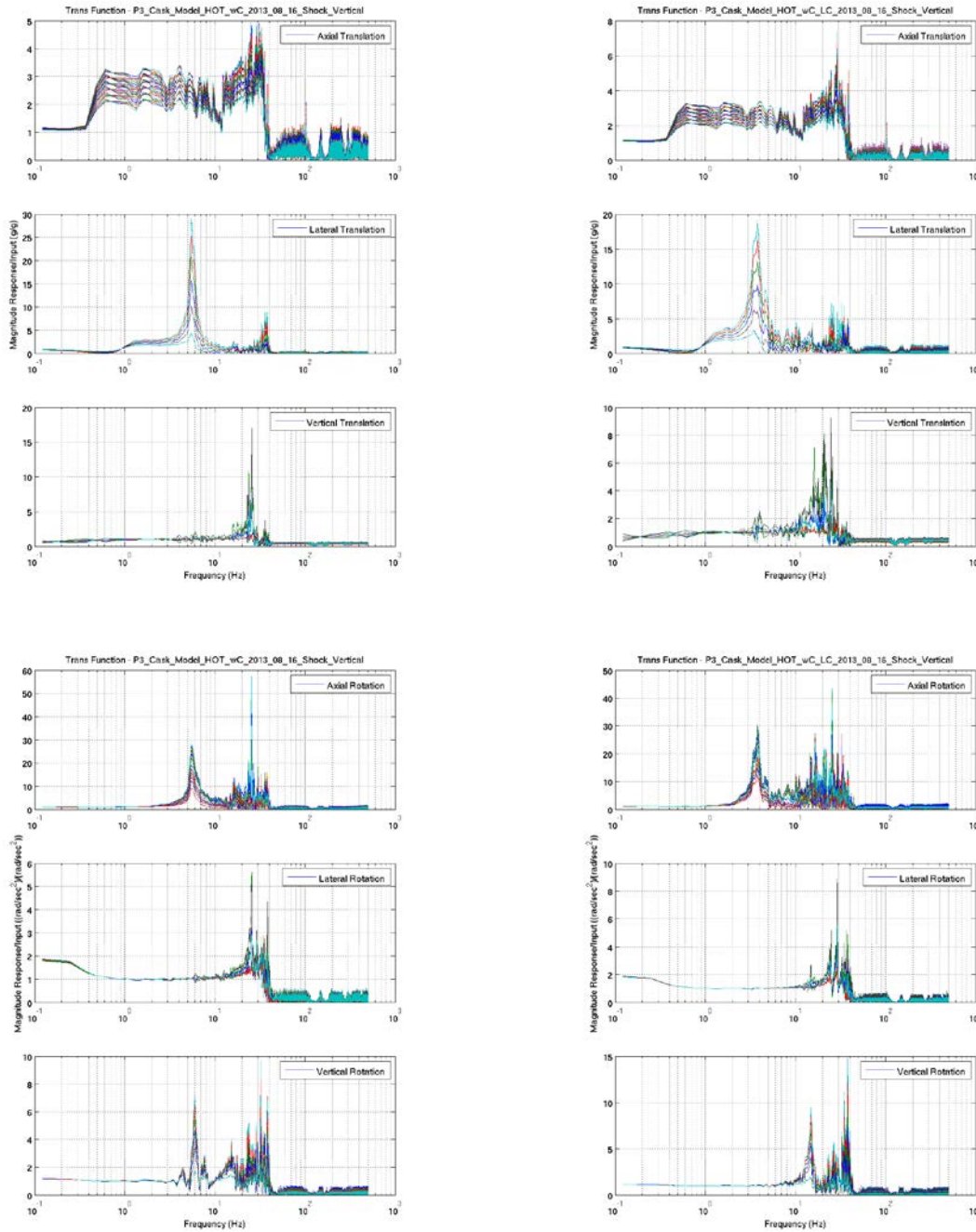(a) Nominal Configuration   (b) Without Control Components Configuration

**Figure 2.27 P3 Shock Z (Vertical) Load Case, Large Clearances Model Configuration,
Basket Cell Response SRSs.**

USED FUEL DISPOSITION CAMPAIGN
**Used Nuclear Fuel Loading and Structural Performance Under Normal Conditions of Transport -
Demonstration of Approach and Results of Used Fuel Performance Characterization**
A-114   **SEPTEMBER 30, 2013**

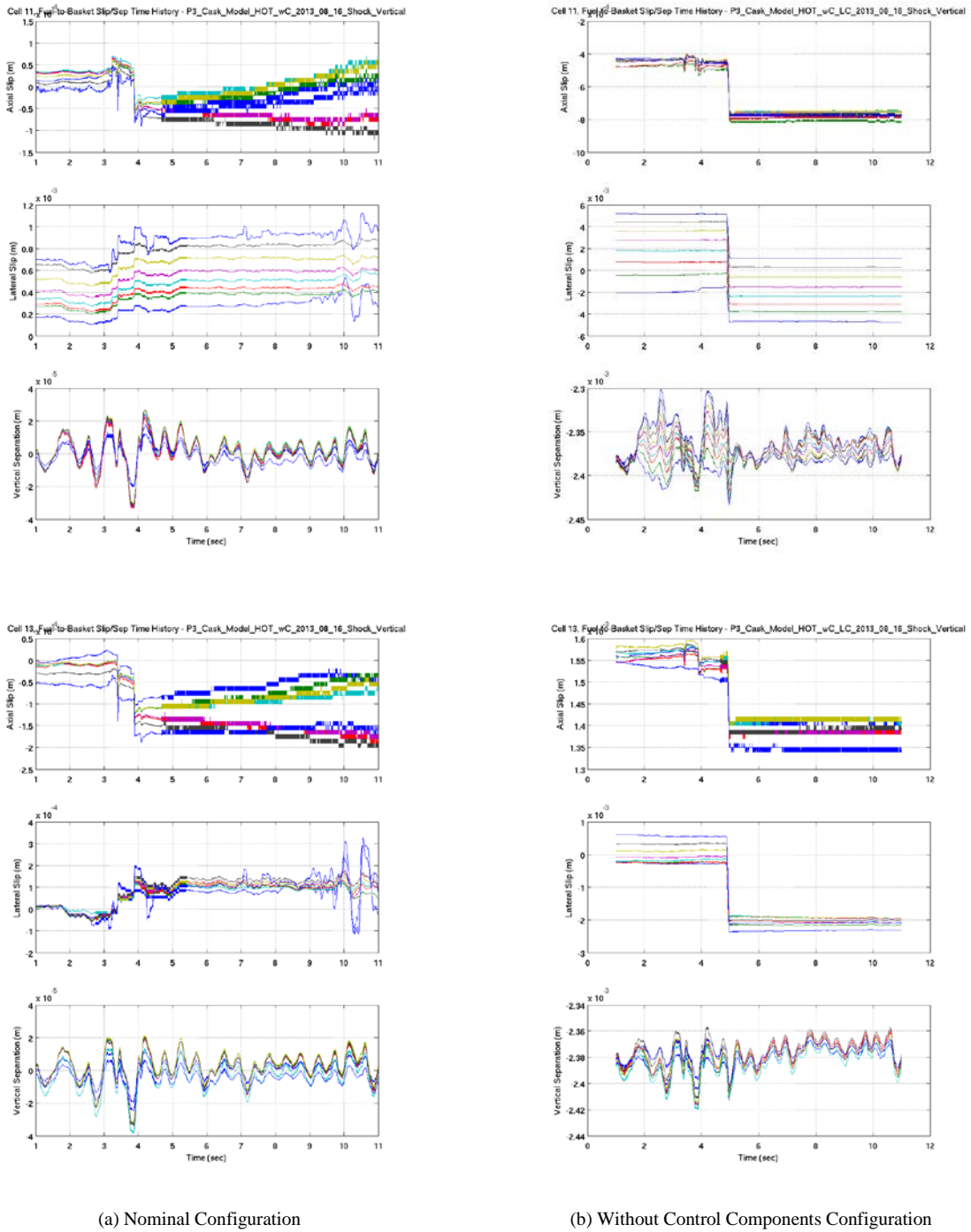(a) Nominal Configuration   (b) Without Control Components Configuration

**Figure 2.28 P3 Shock Z (Vertical) Load Case, Large Clearances Model Configuration,
Basket Cell Response PSDs.**

(a) Nominal Configuration

(b) Without Control Components Configuration

Figure 2.29 P3 Shock Z (Vertical) Load Case, Large Clearances Model Configuration, Basket Cell Response Transfer Functions.
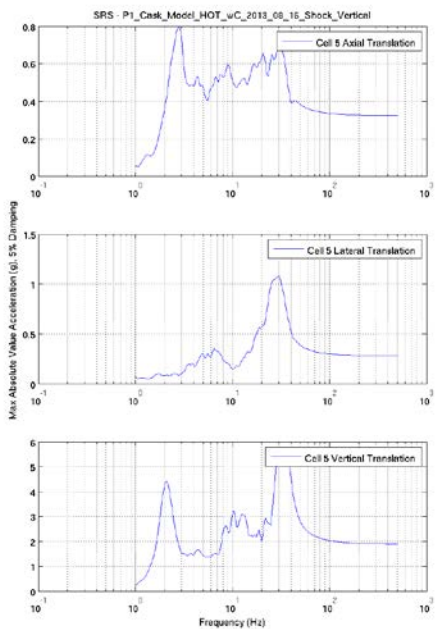
USED FUEL DISPOSITION CAMPAIGN
**Used Nuclear Fuel Loading and Structural Performance Under Normal Conditions of Transport -
Demonstration of Approach and Results of Used Fuel Performance Characterization**
A-116
SEPTEMBER 30, 2013

(a) Nominal Configuration   (b) Without Control Components Configuration

**Figure 2.30 P3 Shock Z (Vertical) Load Case, Large Clearances Model Configuration,
Basket Cell Response Slip/Separation Plots.**

USED FUEL DISPOSITION CAMPAIGN
**Used Nuclear Fuel Loading and Structural Performance Under Normal Conditions of Transport -
Demonstration of Approach and Results of Used Fuel Performance Characterization**
A-117   **SEPTEMBER 30, 2013**

2.4   SENSITIVITY OF RESULTS TO INPUT PARAMETERS

Analyses to investigate the sensitivity of the basket cell response to the input parameters of cask component temperature, component-to-component gap size, and inclusion or exclusion of control components with the fuel assembly have been completed for the P3 shock load cases. Results from these analyses indicate that cask component temperature, for loads consistent with the P3 shock loads and for the range of temperatures expected, are relatively unimportant in determining the severity of the excitations at each fuel assembly. Loads generated at each cell location were essentially identical for the hot and cold temperature configurations. The inclusion or exclusion of the control assembly components with each fuel assembly, again for loads consistent with the P3 shock loads and for the fuel assembly investigated, was only of moderate importance in determining the severity of the excitations at each fuel assembly. Significant differences did exist between the excitation produced at each cell location when control components were included or excluded from the model. The component-to-component gap size, again for loads consistent with the P3 shock loads and for the range of clearances investigated, was of significant importance in determining the severity of the excitations at each fuel assembly, particularly for excitations in the lateral and axial rotation directions. In general larger clearances between components resulted in increased excitation levels at each fuel assembly and therefore larger clearance configurations can generally be considered more severe.

Results from all of the analyses performed indicate that cell location within the basket is also of critical importance, with the characteristics of the response at each cell location significantly affected by cell location. For example, cells located on the exterior edges of the basket displayed different response characteristics when excited in the vertical direction. Consider the response of exterior cell 5 and interior cell 7 given in Figure 2.31 to the loading of the P1 Shock Z (Vertical) load case. It is clear from the figure that the magnitude of the response in the vertical direction at 30 Hz was significantly different between the exterior cell (cell 5) which had a greater magnitude of response at 30 Hz, than at the interior cell (cell 7) at the same frequency. This difference resulted in differing amplitudes of vertical separation between the fuel assembly and basket at the two locations. Or, alternatively consider the response of cell 2 located on the upper side of the basket and cell 30 located on the lower side of the basket given in Figure 2.32 to the loading of the P1 Vibration Y (Lateral) load case. It is clear from the figure that the magnitude of the responses in the lateral direction at 6 and 30 Hz were significantly different between these two cells, with greater SRS acceleration magnitudes experienced at cell 2 on the upper side of the basket than at cell 30 located on the lower side of the basket. This was likely the result of rocking of the canister in the cask and racking of the basket.
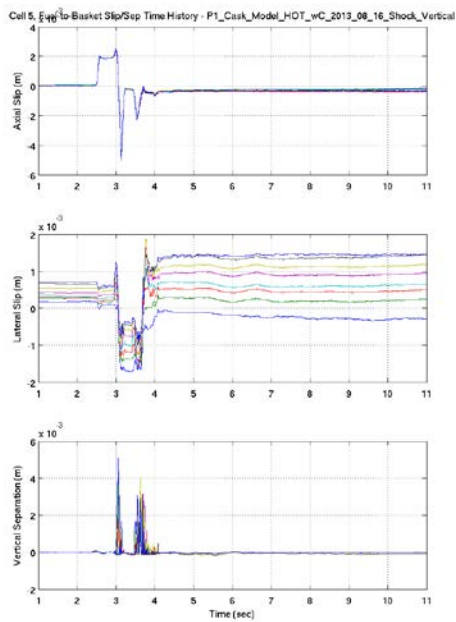
Other potentially important parameters that should have been considered but were not are the static and dynamics coefficients of friction between interacting bodies (most notably between the cell and basket), structural damping, specifics related to contact and how contact is handled within the analysis code, input load characteristics, and variations in design characteristics of the cradle-cask-canister-basket assembly. Each of these parameters are likely important and could potentially affect important characteristics of the response including response magnitude, frequency content, the occurrence of slip/separation/impact, etc..
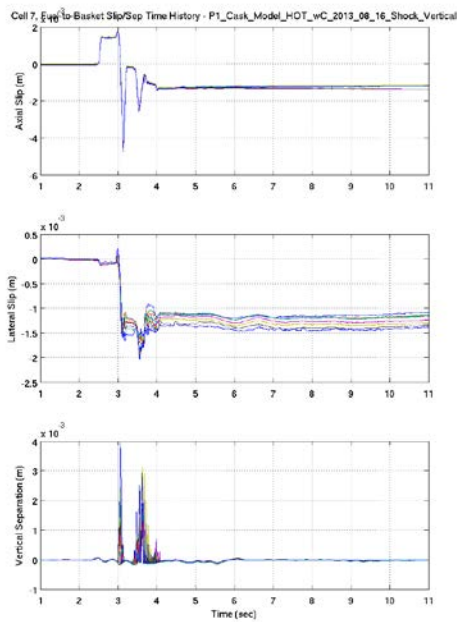
USED FUEL DISPOSITION CAMPAIGN
**Used Nuclear Fuel Loading and Structural Performance Under Normal Conditions of Transport -
Demonstration of Approach and Results of Used Fuel Performance Characterization**
A-118   **SEPTEMBER 30, 2013**

(c) Exterior Cell 5 – SRS   (d) Interior Cell 7 – SRS
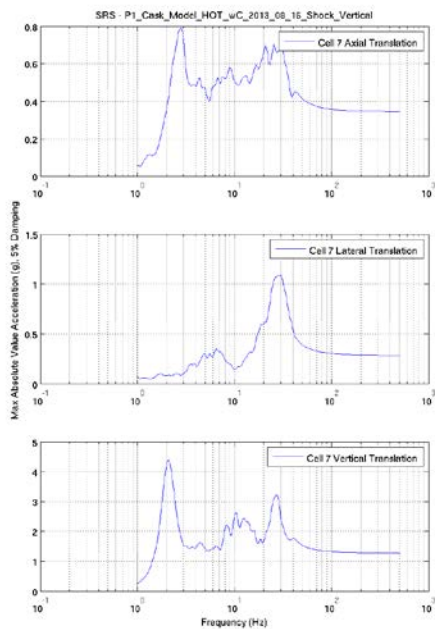
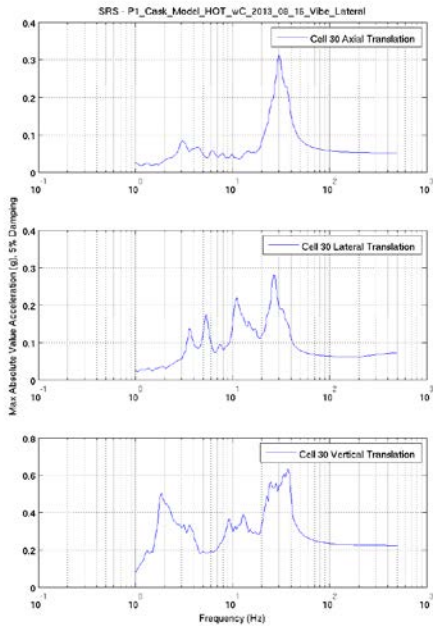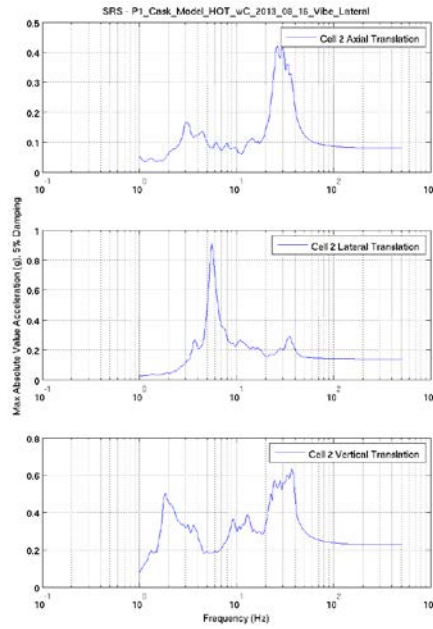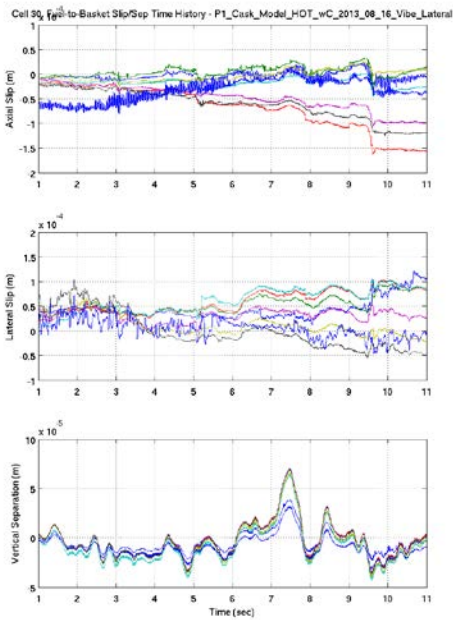(c) Exterior Cell 5 – Slip/Sep   (d) Interior Cell 7 – Slip/Sep

**Figure 2.31 Comparison of Response in the Vertical Direction Between an Interior and
Exterior Cell.**

USED FUEL DISPOSITION CAMPAIGN
Used Nuclear Fuel Loading and Structural Performance Under Normal Conditions of Transport -
Demonstration of Approach and Results of Used Fuel Performance Characterization
A-119   **SEPTEMBER 30, 2013**
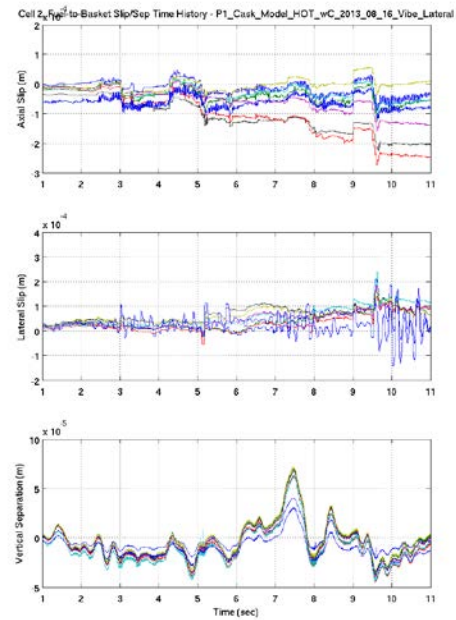
(c) Upper Cell 30 – SRS   (d) Lower Cell 2 – SRS

(c) Upper Cell 30 – Slip/Sep   (d) Lower Cell 2 – Slip/Sep

Figure 2.32 Comparison of Response in the Lateral Direction Between an Upper and Lower Cell.

USED FUEL DISPOSITION CAMPAIGN
**Used Nuclear Fuel Loading and Structural Performance Under Normal Conditions of Transport -
Demonstration of Approach and Results of Used Fuel Performance Characterization**
A-120   **SEPTEMBER 30, 2013**

3.   SUMMARY

For the cask assembly as realized in the cask assembly FEM, the shock and vibration loads derived from the P1 data provided by TTCI produced significant excitations at the fuel assembly level. In the axial and vertical shock cases, the rail car loads were sufficient enough to result in slip and/or vertical separation of the fuel assemblies in the basket and impact of the fuel assemblies against either the basket cell walls or the top or bottom spacer blocks. P1 vibration loads were more benign than the P1 shock loads with respect to their ability to produce fuel assembly slip and vertical separation, but they still tended to produce excitations at the fuel assemblies of significant magnitude in the frequency range of concern, namely between 10 and 60 Hz.

The P3 shock and vibration loads derived from the NUCARS simulations performed by TTCI produced basket cell excitations significantly reduced from those of the P1 shock load cases. However, the P3 shock loads were still sufficient enough to induce sliding of the fuel assemblies in the basket and impact of the fuel assemblies against either the basket cell walls or the top or bottom spacer blocks. Vertical separation between the fuel assembly and basket cell wall was significantly reduced or entirely eliminated in the P3 simulations. The P3 vibration loads were generally more benign than even the P1 vibration loads, but still produced excitations at the fuel assemblies of significant magnitude in the frequency range between 10 and 60 Hz.